RECENT ADVANCES on MECHANICS, MATERIALS, MECHANICAL ENGINEERING and CHEMICAL ENGINEERING

International Conference on Mechanics, Materials, Mechanical Engineering and Chemical Engineering (MMMCE 2015)

Barcelona, Spain
April 7-9, 2015

RECENT ADVANCES on MECHANICS, MATERIALS, MECHANICAL ENGINEERING and CHEMICAL ENGINEERING

Proceedings of the International Conference on Mechanics, Materials, Mechanical Engineering and Chemical Engineering (MMMCE 2015)

Barcelona, Spain
April 7-9, 2015

All papers of the present volume were peer reviewed by no less than two independent reviewers. Acceptance was granted when both reviewers' recommendations were positive.

Series: Recent Advances in Mechanical Engineering Series | 14

ISSN: 2227-4596
ISBN: 978-1-61804-295-8

RECENT ADVANCES on MECHANICS, MATERIALS, MECHANICAL ENGINEERING and CHEMICAL ENGINEERING

Proceedings of the International Conference on Mechanics, Materials, Mechanical Engineering and Chemical Engineering (MMMCE 2015)

Barcelona, Spain
April 7-9, 2015

Organizing Committee

Editors:
Professor Nikos E. Mastorakis, Technical University of Sofia, Bulgaria
Professor Imre Rudas, Obuda University, Budapest, Hungary
Professor Marina V. Shitikova, Voronezh State University of Architecture and Civil Engineering, Russia
Professor Yuriy S. Shmaliy, Universidad de Guanajuato, Salamanca, Mexico

Program Committee:
Prof. Cho W. Solomon To, ASME Fellow, University of Nebraska, Lincoln, Nebraska, USA
Prof. Kumar Tamma, University of Minnesota, Minneapolis, MN, USA
Prof. Mihaela Banu, Department of Mechanical Engineering, University of Michigan, Ann Arbor, MI USA
Prof. Pierre-Yves Manach, Universite de Bretagne-Sud, Bretagne, France
Prof. Jiin-Yuh Jang, University Distinguished Professor, ASME Fellow, National Cheng-Kung University, Taiwan
Prof. Hyung Hee Cho, ASME Fellow, Yonsei University (and National Acamedy of Engineering of Korea), Korea
Prof. Robert Reuben, Heriot-Watt University, Edinburgh, Scotland, UK
Prof. Ali K. El Wahed, University of Dundee, Dundee, UK
Prof. Yury A. Rossikhin, Voronezh State University of Architecture and Civil Engineering, Voronezh, Russia
Prof. Igor Sevostianov, New Mexico State university, Las Cruces, NM, USA
Prof. Ramanarayanan Balachandran, University College London, Torrington Place, London, UK
Prof. Sorinel Adrian Oprisan, Department of Physics and Astronomy, College of Charleston, USA
Prof. Yong Ding, Georgia Institute of Technology, Atlanta, GA, USA
Prof. Yulin Deng, Georgia Institute of Technology, Atlanta, GA, USA
Prof. Paul H. Holloway, Distinguished Professor, University of Florida, Gainesville FL, USA
Prof. Saad Khan, North Carolina State University, Raleigh, North Carolina, USA
Prof. Manijeh Razeghi, Northwestern University, Evanston, IL, USA
Prof. Igor Sevostianov, New Mexico State University, Las Cruces, New Mexico, USA
Prof. Yoshihiro Tomita, Kobe University, Kobe, Hyogo, Japan
Prof. Mohindar S. Seehra, West Virginia University, Morgantown, West Virginia, USA
Prof. Tao Liu, Florida State University, Tallahassee, Florida, USA
Prof. Samuel Lofland, Rowan University, Glassboro, New Jersey, USA
Prof. Daniel Guay, Institut National de la Recherche Scientifique (INRS), Universite du Quebec,Quebec, Canada
Prof. Tian Tang, University of Alberta, Edmonton, Alberta, Canada
Prof. Roland Frankenberger, University of Marburg, Marburg, Germany
Prof. Mohamedally Kurmoo, Universite de Strasbourg, Strasbourg, France
Prof. C. C. Sorrell, University of New South Wales, Sydney, NSW, Australia
Prof. Concepcion Lopez, Universitat de Barcelona, Barcelona, Spain
Prof. Alan Dalton, University of Surrey, Guildford, Surrey, UK
Prof. Kourosh Kalantar-Zadeh, RMIT University, Melbourne, Australia
Prof. Tetsu Yonezawa, Hokkaido University, Kita Ward, Sapporo, Hokkaido Prefecture, Japan
Prof. Daolun Chen, Ryerson University, Toronto, Ontario, Canada
Prof. Mohamed M. Chehimi, Universite Paris Diderot, Paris, France
Prof. Vincenzo Fiorentini, Universita degli studi di Cagliari, Cagliari, Italy
Prof. Tamas Ungar, Eotvos Lorand University (ELTE), Budapest, Hungary
Prof. Anthony W. Coleman, Universite Claude Bernard Lyon 1, Lyon, France
Prof. Albert Chin, IEEE Fellow, OSA Fellow, National Chiao Tung University, Hsinchu, Taiwan
Prof. Artur Cavaco-Paulo, Universidade do Minho, Braga, Portugal
Prof. Yoshihiro Tomita, Kobe University, Kobe, Japan
Prof. Jian Wang, Los Alamos National Laboratory, Los Alamos, NM, USA
Prof. Byung K. Kim, Pusan National University, Busan, South Korea

Additional Reviewers

Francesco Zirilli	Sapienza Universita di Roma, Italy
Sorinel Oprisan	College of Charleston, CA, USA
Xiang Bai	Huazhong University of Science and Technology, China
Philippe Dondon	Institut polytechnique de Bordeaux, France
Yamagishi Hiromitsu	Ehime University, Japan
Frederic Kuznik	National Institute of Applied Sciences, Lyon, France
George Barreto	Pontificia Universidad Javeriana, Colombia
Takuya Yamano	Kanagawa University, Japan
Imre Rudas	Obuda University, Budapest, Hungary
Tetsuya Shimamura	Saitama University, Japan
M. Javed Khan	Tuskegee University, AL, USA
Eleazar Jimenez Serrano	Kyushu University, Japan
Valeri Mladenov	Technical University of Sofia, Bulgaria
Jon Burley	Michigan State University, MI, USA
Andrey Dmitriev	Russian Academy of Sciences, Russia
Moran Wang	Tsinghua University, China
Jose Flores	The University of South Dakota, SD, USA
Hessam Ghasemnejad	Kingston University London, UK
Santoso Wibowo	CQ University, Australia
Kazuhiko Natori	Toho University, Japan
Konstantin Volkov	Kingston University London, UK
Kei Eguchi	Fukuoka Institute of Technology, Japan
Abelha Antonio	Universidade do Minho, Portugal
Tetsuya Yoshida	Hokkaido University, Japan
Matthias Buyle	Artesis Hogeschool Antwerpen, Belgium
Deolinda Rasteiro	Coimbra Institute of Engineering, Portugal
Masaji Tanaka	Okayama University of Science, Japan
Bazil Taha Ahmed	Universidad Autonoma de Madrid, Spain
Zhong-Jie Han	Tianjin University, China
James Vance	The University of Virginia's College at Wise, VA, USA
Angel F. Tenorio	Universidad Pablo de Olavide, Spain
Genqi Xu	Tianjin University, China
João Bastos	Instituto Superior de Engenharia do Porto, Portugal
Miguel Carriegos	Universidad de Leon, Spain
Shinji Osada	Gifu University School of Medicine, Japan
Ole Christian Boe	Norwegian Military Academy, Norway
Lesley Farmer	California State University Long Beach, CA, USA
Dmitrijs Serdjuks	Riga Technical University, Latvia
Alejandro Fuentes-Penna	Universidad Autónoma del Estado de Hidalgo, Mexico
Francesco Rotondo	Polytechnic of Bari University, Italy
Stavros Ponis	National Technical University of Athens, Greece
José Carlos Metrôlho	Instituto Politecnico de Castelo Branco, Portugal
Minhui Yan	Shanghai Maritime University, China

Table of Contents

Plenary Lecture 1

Professor Marina Shitikova
Research Center on Dynamics of Solids and Structures
Voronezh State University of Architecture and Civil Engineering
Russia
E-mail: shitikova@vmail.ru

Abstract: The analytical review of the existing dynamic technical theories of thin-walled beams of open profile is carried out, from which it follows that all papers in the field can be divided into three groups. The papers, wherein the governing set of equations is both hyperbolic and correct from the viewpoint of the physically admissible magnitudes of the velocities of the transient waves resulting from these equations, fall into the first category. The second category involves the articles presenting hyperbolic but incorrect equations from the above mentioned viewpoint, i.e. resulting in incorrect magnitudes of the transient wave velocities. The papers providing the governing system of equations which are not hyperbolic fall into the third group. The simple but effective procedure for checking for the category, within which this or that paper falls in, has been proposed and illustrated by several examples. It has been shown that only the theories of the first group could be used for solving the problems dealing with transient wave propagation, while the theories belonging to the second and third group could be adopted for static problems only. However, in the theories of the first group, only the velocity of the longitudinal-flexural-warping wave has been found correctly, and it is equal to $v_1 = \sqrt{E / \rho}$, where E is the Young modulus and ρ is the density, while these theories produce three shear waves, the velocities of which depend on the geometry of the beam. But the correct theory should provide a researcher with only one shear-torsional wave propagating with the velocity $v_2 = \sqrt{\mu / \rho}$, where μ is the shear modulus. Such a theory has been recently proposed by the authors, and it would be discussed in the last part of the presentation. This theory is based on three-dimentional equations of the theory of elasticity, theory of discontinuities and ray expansions.

Brief Biography of the Speaker: Marina V. Shitikova is a Soros Professor of the Department of Structural Mechanics and a leading Researcher of the Research Center of Dynamics of Solids and Structures at Voronezh State University of Architecture and Civil Engineering in Russia. She received her MEng in Civil Engineering in 1982, a PhD degree in Structural Mechanics in 1987 from Voronezh Civil Engineering Institute, a DSc degree in Solid Mechanics in 1995 from the Institute for Problems in Mechanics, Russian Academy of Sciences and a Professorship in 1995 from Voronezh State University of Architecture and Civil Engineering. Since 1994, she has been an Associate Member of the Acoustical Society of America, since 1995 she has been a Member of the EUROMECH, GAMM, the ASME International, and Russian Association “Women in Science and Education”. She has published more than 200 papers dealing with structural mechanics, vibrations, wave dynamics, and acoustics. Her biography has been included in Who's Who in the World, Who's Who in Science and Technology, 2000 Outstanding Scientists of the 20th Century. She received a Commemorative Medal "1997 Woman of the Year" from the American Biographical Institute. In 1998 she was awarded the Russian President Fellowship for Outstanding Young Doctors of Sciences. Since 2009 she is the Head of the Department of International Education and Cooperation at Voronezh State University of Architecture and Civil Engineering. She was a Fulbright Fellow at Rice University, Houston, Texas in 2007-2008 and a Visiting Professor in different universities.

ISBN: 978-1-61804-295-8

Plenary Lecture 2

Cloud Robotics

Prof. Imre J. Rudas
Obuda University
Budapest, Hungary
E-mail: rudas@uni-obuda.hu

Abstract: Cloud Robotics is an emerging field within robotics, currently covering various application domains and robot network paradigms. Cloud Robotics was born from the merger of cloud technologies and robotics. Cloud technology-based computing—or simply Cloud Computing—is one of the most dynamically growing areas of Info-Communication Technologies (ICT). The presentation summarizes the basics of cloud computing, namely the main idea, the definition, the cloud model composed of essential characteristics, service models and deployment models. The next part provides a structured, systematic overview of the numerous definitions, concepts and technologies linked to Cloud Robotics and cloud technologies in a broader sense. It also presents a roadmap for the near future, describing development trends and emerging application areas. Cloud Robotics may have a significant role in the future as an explicitly human-centered technology, capable of addressing the dire needs of our society. Finally some cloud robotics projects are discussed. The last part of the presentation summarizes the results and ideas of a new generation internet and Cloud Technology based Virtual Collaboration Arena (VirCA) developed in Hungary and some of its application possibilities in Cloud Robotics. VirCA provides a platform where users can build, share and manipulate 3D content, and collaboratively interact with real-time processes in a 3D context, while the participating hardware and software devices can be spatially and/or logically distributed and connected together via IP network. The 3D content and processes in VirCA can be synchronized with the real world, which allows the combination of reality and virtual world in the collaboration arena.

Brief Biography of the Speaker: Imre J. Rudas graduated from Banki Donat Polytechnic, Budapest in 1971, received the Master Degree in Mathematics from the Eotvos Lorand University, Budapest, the Ph.D. in Robotics from the Hungarian Academy of Sciences in 1987, while the Doctor of Science degree from the Hungarian Academy of Sciences in 2004. He received his first Doctor Honoris Causa degree from the Technical University of Kosice, Slovakia and the second one from "Polytechnica" University of Timisoara, Romania. He is active as a full university professor He served as the President of Budapest Tech from 2003 till 2010. He was elected in 2010 as the President of Obuda University, the successor of Budapest Tech till April 2014. Now he is the Head of the Steering Committee of the University Research and Innovation Center. He is a Fellow of IEEE, Senior AdCom member of Industrial Electronics Society (IES), he served IES as a Vice-President in 2000-2001, he is Board of Governors member of IEE System, Man and Cybernetics Society. He is the Junior Past Chair of IEEE Hungary Section.

He served IFSA (International Fuzzy System Association) as Vice-President and Treasure for a period of 7 years; he had been the President of Hungarian Fuzzy Association for ten years. He serves as an associate editor of some scientific journals, including IEEE Transactions on Industrial Electronics, member of editorial board of Journal of Advanced Computational Intelligence, member of various national and international scientific committees. He is the founder of the IES Sponsored IEEE International Conference Series on Intelligent Engineering Systems (INES), IEEE International Conference on Computational Cybernetics (ICCC), IEEE International Symposium on Computational Intelligence and

ISBN: 978-1-61804-295-8

Informatics (CINTI, since 2000), IEEE International Symposium on Machine Intelligence and Informatics (SAMI, since 2003), IEEE International Symposium on Intelligent Systems and Informatics (SISY, since 2003), IEEE International Symposium on Applied Computational Intelligence and Informatics (SACI, since 2004), IEEE International Symposium on Logistics and Industrial Informatics (LINDI, since 2007). He has served as General Chairman and Program Chairman of numerous scientific international conferences. His present areas of research activities are Computational Cybernetics, Robotics with special emphasis on Robot Control, Soft Computing, Fuzzy Control and Fuzzy Sets. He has published six books, more than 690 papers in international scientific journal, conference proceedings and book chapters, he has more than 1000 independent citations.

Analysis and Comparison of Project Management Standards and Guides

Rui XUE[1, a *], Claude Baron[1, b], Philippe ESTEBAN[1,c] and Li ZHENG[1,d]

[1]CNRS, LAAS, 7 av. du colonel. Roche, F-31400 Toulouse, France

{[a]rui.xue, [b]claude.baron, [c]philippe.esteban, [d]li.zheng}@laas.fr

Keywords: project management; standards; guides; references; PMBoK; ISO 21500; ISO/IEC 29110.

Abstract. With the increasing scale of systems and products, many large companies ask different suppliers to manufacture the components of the final systems or products. Thus, managing projects dedicated to complex systems engineering is very tricky and ensuring the success of projects is a real issue. Many project management tools, techniques and even standards or guides have been developed by different organizations in order to support the management of such projects. For project managers, selecting and relying on immediately operational methods, tools and references (standards and guides) for a project manager to lead his project represents a true difficulty. The purpose of this paper is to introduce, analyze and compare the most famous project management references (PMBoK, ISO 21500 and ISO/IEC 29110) to provide a global and a detailed views on project management methodological guidelines, in order to facilitate the choice of a project management reference to help the project manager to manage the project effectively, thus to improve the success rate of projects.

Introduction

Project Management (PM) plays a critical role in the implementation of projects in all the organizations or companies, wherever they are small or large. Using PM methods and tools cannot ensure the success of a project, but it can improve its chances of success. PM has been practiced for thousands of years that can be dated back to the Great Pyramid of Giza [1,2]. Many methods and tools have been developed since and are now available and routinely used by projects managers. Among them, the Gantt chart, the Critical Path Method (CPM), the Work Breakdown Structure (WBS) and the Earned Value Management (EVM) [3]. If some methods for developing systems are easier to manage than others and some more likely to succeed, particularly in large-scale projects, using project management references, standards or compendiums of good practices, is also a way to support and guide project management [4,5]. The first PM reference was the PMBoK Guide, a Guide to the Project Management Body of Knowledge; it was published by Project Management Institute (PMI) in 1987; the fifth version was edited in 2013 [6]. The ISO 21500 Standard for Project Management is a standard developed by ISO (International Organization for Standardization) from 2007, later released in the September 2012 [7]. The last international standard is the ISO/IEC 29110 elaborated by the sub-committee 7 of Joint Technical Committee 1 of the ISO and IEC (International Electrotechnical Commission) and dedicated to the very small entities [8]. It was first published in 2012. For project managers, determining which standard or guide is more suitable for their projects means spending a lot of time to read, analyze and compare these three references. So the purpose of this paper is to make this analysis and to compare the three project management standards or guides to help the project managers to facilitate their selection.

The current situation in the domain of PM is stated in section 2. Section 3 briefly introduces and compares the three PM references. A conclusion on the comparison of them is given in section 4.All manuscripts must be in English, also the table and figure texts, otherwise we cannot publish your paper.

Current situation

History and definition of Project management. The Great Pyramid of Giza, the Colosseum in Rome and the Great Wall of China are testimonies of successful construction projects. In the 2570's BC, the ancient records show that there were managers for each of the four faces for the Great Pyramid when they were built. According to historical data, the labor force was organized into three groups: soldiers, common people and criminals when the Great Wall of China was built [9]. The origins of the theory of project management correspond with the development of Gantt chart, named by the creator Henry Gantt, in 1917. It is the forefather of project management. In the 1950s, the Navy employed the modern project management methodologies in their Polaris project. During the 1960s and 1970s, many methods or tools were developed, for instance, the CPM, Program Evaluation Review Technique (PERT) and WBS. At the same time, a lot of organizations were built to promote the methodology of project management, such as the American Association of Cost Engineers (AACE), the International Project Management Association (IPMA) and the PMI. Indeed, PM covers a wide field of applications where associations historically played and still play an important role [1,9].

Many organizations define what project management is. The PMI states that "Project management is the application of knowledge, skills, tools, and techniques to project activities to meet the project requirements" [6]. The ISO 21500 defines the PM this way: "Project Management is the application of methods, tools, techniques and competencies to a project" [7]. The definition of PMI emphasizes the purpose of PM is to meet the project requirements. The application of project management can meet the requirements better; short the cost and time to finish the project [6,7].

Evolution of project management references. Many standards or guides were developed by the different organizations from the 1987's. PMBoK Guide was first published as a white paper by PMI in 1987; it was an attempt to document and standardize project management practices [6]. The first edition appeared in 1996, the second edition in 2000, a third in 2004, a fourth in 2009 and the last version in 2013. In 2012, the International Organization for Standardization (ISO) recognized the importance of formalizing the practices of project management; they published the standard ISO 21500 in 2012 [7]. Last but not least, another standard for project management, focusing on very little companies, ISO/IEC 29110, appeared in also appeared at the same date [8].

Next section introduces the three project management standards or guide.

Analysis and comparison of project management standards and guides

This section introduces the three project management references then analyzes, compares and aligns them.

Introduction of the three references

PMBoK. With the development of project management, the PMBoK has been released many times from 1996 to now. This guide aims at providing knowledge, processes, skills, tools and techniques that have a significant impact on the project success [6]. The first part of this guide provides the subset of the project management body of knowledge that is generally recognized as good practices.

It defines 47 processes in the first part of this guide into 10 Knowledge Areas (KA) about the professional field, project management field or area of specialization, such as the project scope management and project cost management. In the second part, this guide re-groups the processes to form a project management standard. It defines the five process groups based on the five stages of the project implementation: initiating process group, planning process group, executing process group, monitoring and controlling process groups and closing process groups [6]. It details the input, tools and techniques, output and the data flow diagram of each process in the ten KA. At each stage of the systems engineering (SE), one can use all or part of the five process groups; any set of processes can also be reused for any stage of SE.

It defines a table that provides the project management process group and knowledge area mapping for the readers in order to help them better under the processes . The Fig. 1 shows the structure of PMBoK.

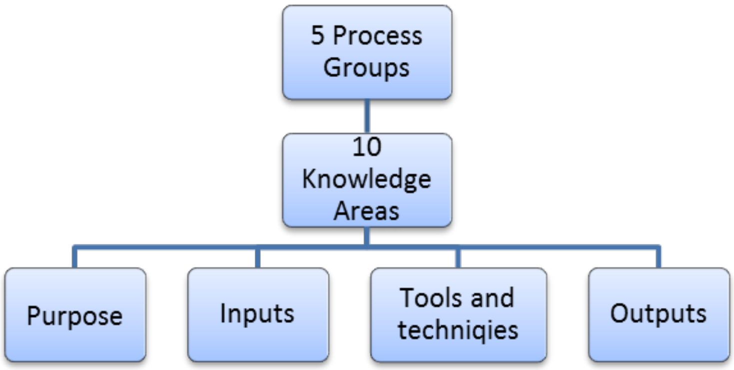

Fig. 1 structure of PMBoK

ISO 21500. Like the PMI, the ISO organization also recognized the importance of improving the performance of project management in order to enhance the competition of companies, and published the ISO 21500 Guidance in project management in 2012 [7]. It is an international standard on project management. The ISO started to edit this standard from 2007 and finished in 2012. This guide aims to provide guidance for project management and can be used by any type of organizations.

It defines 39 processes that group into 5 process groups (like the 5 process groups of PMBoK) and 10 groups of subject (like the 10 KAs of PMBoK). The five process groups can be used at any stage or sub-project or throughout the project. Each process contains the purpose, input and output (deliverable, a result, a document ...). The structure of ISO 21500 is shown in the Fig. 2.

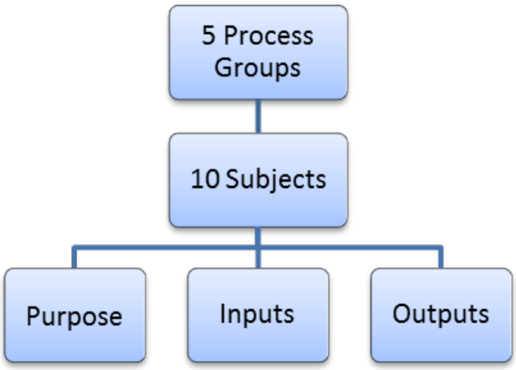

Fig. 2 the structure of ISO 21500

ISO/IEC 29110. With today's large scale projects, it is compulsory for companies to buy the product as the components of large systems or products from suppliers, often small companies, so many small companies were created quickly to meet this requirement. For ensuring the quality of projects or systems, it is necessary to help the very small entities (VSEs) develop high quality products. Considering this, the ISO organization developed a guide named "Software engineering – Lifecycle profiles for very small entities" [8]. This guide considers VSEs as entities with less than 25 employees [8]. There are five parts of this guide: 1) Overview (ISO/IEC TR 29110-1), 2) Framework and taxonomy (ISO/IEC TR 29110-2), 3) Assessment guide (ISO/IEC TR 29110-3), 4) Profile specification (ISO/IEC TR 29110-4) and 5) Management and engineering guide (ISO/IEC TR 29110-5). The fifth part deals about implementation management and engineering guide for the small entities. This guide is suggested to be used with some project management and software implementation processes and outcomes from the standard ISO/IEC 12207 and products from ISO/IEC 15289 [8].

The first part of this guide aims at introducing the guide briefly, such as the processes, lifecycle and some other concepts. The purpose of the second part of this guide is to introduce the concepts for software engineering standardized profiles for VSEs and defines the terms common to the documents of the VSE profile set. The third part provides the definitions of the process assessment guidelines and the compliance requirements that are used to meet the purpose of the defined VSEs profiles. It defines the specification for all the profiles of the Generic Profile Group (GPG) in the fourth part. In the last part, it gives an implementation management and engineering guide for the entry profile of the GPG. According to the purpose of this paper, we focus on the fifth part of this guide.

In fact, according the reports and studies, it is obvious that the VSEs have difficulties to use the international standard during their project because the scale, the time and the resource of the VSEs [8]. For those reasons, this guide just defines two processes: the project management (PM) process and the software implementation (SI) process. But this guide allows the VSEs to adapt themselves to this guide by adding their processes and tailoring the activities or processes. The structure of ISO/IEC 29110 is shown in the Fig. 3.

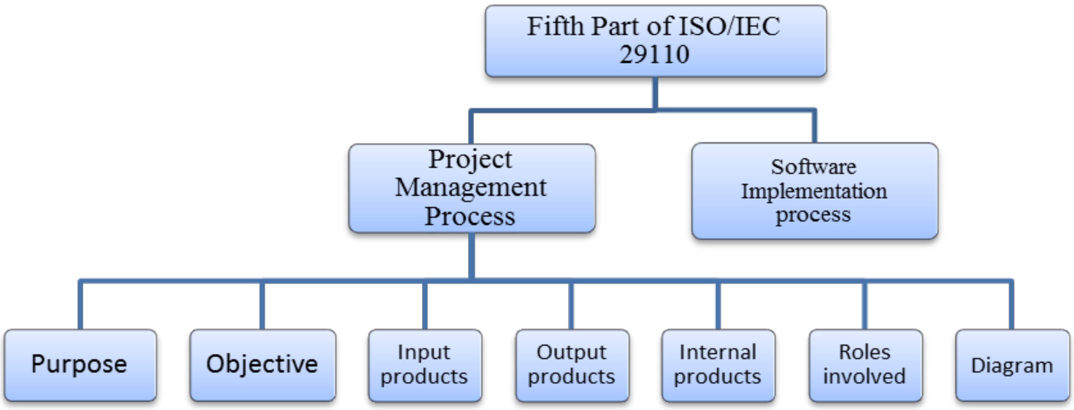

Fig. 3 Structure of the fifth part of ISO/IEC 29110

Analysis and comparison of the three references. The three references introduced above are the most famous standards or guides for project management. After a brief introduction to them, the purpose of this section is to compare them generally and in details to provide the project managers a global view in order to choose the suitable standard or guides to implement their project.

General Comparison of the three references. This section compares the three references according a set of general criteria: the number of processes of references, the target audience, level of details, proposition on tools and techniques, year of publication and the revision frequency.

The PMBoK has the largest number of project management processes, the ISO 21500 has 39 processes and the ISO/IEC 29110 just has one process management process; note that the detailed comparison of processes in the three references will be addressed where processes from each reference will be identified, detailed and aligned. The target audiences for them are different. The PMBoK and ISO 21500 are intended to be used by any scale company, although there are some studies pointed out that the VSEs have the difficulties to relate themselves with the international standards. The ISO/IEC 29110 focuses on the VSEs, and it allows the VSEs to adapt themselves to the guide by adding some elements from their own practices.

The PMBoK almost has 600 pages, it is the most detailed PM reference; it not only provides the purpose, input and output of each process, and it also presents some PM tools and techniques. The ISO 21500 is a standard without suggestion on tools and techniques. The ISO/IEC 29110 is the least detailed guide among the three references because it focuses on the VSEs. Indeed, considering the scale, budget, number of employees of the VSEs, it just defines some example process or activates of project management to give the referencse to the VSEs. The three references are all very new, there are all published recently and the PMBoK is the fifth edition because the wide use of this guide.

In the next section, we will compare the three references in the term of the structure in order to align them at the structure level. The Table 1summarizes the result of comparison briefly.

Table 1 comparison between the three project management references

	PMBoK	ISO 21500	ISO /IEC 29110

Processes of references	39 processes	47 processes	2 processes
The target audience	Any company	Any company	VSEs
Level of details	◆◆◆◆◆	◆◆◆◇◇	◆◇◇◇◇
Proposition on tools and techniques	Yes	No	No
Year of publication	2013	2012	2012
Revision frequency	◆◆◆◆◆	◇◇◇◇◇	◇◇◇◇◇

Detailed Comparison on the structure level of three references. This section compares the process groups of PMBoK and ISO 21500, and analyzes the PM objective and activities to align the three references at the structure level.

The ISO/IEC 29110 defines 2 processes: project management (PM) process and software implementation (SI) process. The project management process aims to establish and carry out in a systematic way the tasks of the software implementation project [8], and the purpose of the SI process is the systematic performance of the analysis, software component identification, construction, integration and tests [8]. Related to this aim of this paper, we should select the PM process to compare with the other reference because the SI process is related to the systems engineering domain.

As we introduce above, the PMBoK has 47 processes and they are grouped into five process groups and the processes are regrouped into 10 KAs. The ISO 21500 nearly has the same structure. It defines 39 processes organized into 5 groups, instead of the KAs; it defines the 10 subjects related to knowledge of project management field. All the two references (PMBoK and ISO 21500) define the purpose, inputs and outputs in each process, and the PMBoK provides the tools and techniques extraordinarily.

The PM process of ISO/IEC 29110 has a completely different way to present the process. It defines the purpose, objectives, input products, outputs products, internal products, roles involved and the PM diagram. In the section of PM diagram, it defines four activities of the PM process: project planning, project plan executin, project assessment and control and the project closure. Outwardly, the ISO/IEC 29110 has a different way to organize the processes by regarding to the PMBoK and ISO 21500. In fact, aligning to the structures of the other two references, this guide defines two process groups: the project management process group and the software implementation process group. The PM process group presents four process groups (named PM activities in the guide). But at the same time, it also defines 7 PM objectives. In each PM objectives, it suggests to use some processes from the ISO/IEC 12207. So after aligning to the other structure, the 4 PM activities are corresponding to the process groups in the PMBoK and ISO 21500. The 7 PM objectives are corresponding to the KAs of PMBoK or subjects of ISO 21500. In each objective, the ISO/IEC 29110 selects some processes from the standard ISO/IEC 12207. There are 11 processes presented in the PM objectives that are selected from the ISO/IEC 12207.

The corresponding between the structures of the three references is show in the Table 2.

Table 2 corresponding between the structures of the three references

	PMBoK	ISO 21500	ISO/IEC 29110
Process groups	• Initiating • Planning • Executing • Monitoring and Controlling • Closing	• Initiating • Planning • Implementing • Controlling • Closing	• Planning • Executing • Assessment and Controlling • Closure

KAs, subjects or activities	10 KAs	10 subjects	7 objectives

In the next section, we analyze and compare all the processes from the three references in order to align them at the process level.

Detailed Comparison on the processes level of three references. In this section, we first analyze the processes from the three references, then we compare them in order to find if processes are identical or can be aligned; at last we give the detail on the same processes, the process merged of same activities and the special processes in each reference.

To compare processes, we proceed this way: we consider the ISO 21500 and the ISO/IEC 29110 referred to PMBoK. First we compare the ISO 21500 with the PMBoK, then we compare the ISO/IEC 29110 with the PMBoK. The comparison of the ISO 21500 with the PMBoK revealed 27 identical processes, the ISO 21500 having 2 processes less than PMBoK (validate scope process and plan stakeholder management process) and it introduces two new process (collect lesson learned process and control resource process). It replace the “define activities process” of project time management knowledge area into the project scope management subject. The ISO 21500 defines the “manage stakeholder process” instead of the “manage stakeholder process’’ and the “control stakeholder process” of PMBoK; the “define scope process” instead of the “collect requirements process” and “define scope process” of PMBoK; the “assess risk process” instead of the “perform quantitative risk analysis process” and “perform quantitative risk analysis process” of PMBoK; the “administer contracts process” instead of the “control procurement process” and “close procurement process” of PMBoK; the “define project plan process” instead of “develop project management plan process ”. The ISO 21500 rewrite the “estimate activity resource process”, “acquire project team” and “develop project team” of PMBoK with the “establish project team process”, “estimate resource process”, “define organization process” and “develop project team process”, “plan scope management process”, “plan schedule management process”, “plan cost management process”, “plan human resource management process” and “plan risk management process”.

According to the PMBoK, there is no identical process in the ISO/IEC 29110. But after analyzing the elements of the processes in the 7 PM activities, there are 9 processes selected from the ISO/IEC 12207: Project Planning Process, Measurement Process, Project Assessment and Control Process, Software Acceptance Support Process, Software Requirements Analysis Process, Software Review Process, Risk Management Process, Software Configuration Management Process and Software Quality Assurance Process. All the 9 processes can be all covered by the processes of PMBoK. The result of the comparison on the three references at the process level is shown in the Table 3.

Table 3 differences and similarities between PMBoK and ISO 21500 (PMI)

	PMBoK	ISO 21500	ISO/IEC 29110
The same processes emerge in both references	27	27	_
The process replaced	1	1	
The process combined	14	5	
the process rewrited	3	4	9
The processes only emerges in PMBoK	2	_	_
The processes only emerges in ISO 21500	_	2	_
Total	47	39	

Conclusion on the comparison of the three references. After this comparison of the three project management references, we come to the conclusion that the PMBoK is suitable for the large scale projects, even if it can be used at any time and at any level of projects. Regarding the profile of the VSEs, the implementation of the PMBoK would cost too much time and money; this does not suit the required flexibility of VSEs. The ISO 21500 almost has the same PM processes as the PMBoK, but it does not provide the tools and techniques for the project manager to manage projects. If the project managers do not consider the suggestion on PM tools and techniques, they can choose any one of the PMBoK and ISO 21500 as the reference. Based on the purpose and the character of ISO/IEC 29110, this standard is better for VSEs because of their features and flexibility. The VSEs also can select the processes from another standard based on the projects, for example the ISO/IEC 12207 and ISO/IEC 15289.

Conclusion

According to the scale of projects, the project managers play an important role in order to assurance the success of project. There is a trend that the large companies buy the components of product from other smaller companies and assemble them at their own companies, and then they deliver the products to the customer [10]. The most famous example is Airbus; many companies want to be selected by the Airbus as its suppliers. So for large projects, project managers constitute a key point because they implement, lead, monitor and control the global project. Although systems engineers still remain essential in engineering projects, their importance declines while the one of project managers rise [11,12]. So in order to help the project managers be familiar with the project management standards or guides, the comparison made in this paper is necessary. This paper introduced, analyzed and compared the most used PM references: PMBoK, ISO 21500 and ISO/IEC 29110 to help the project managers choose the PM reference easier. Based on the comparison, the PMBoK is the most detailed PM guide with the suggestion of PM tools and techniques; the ISO 21500 nearly has the same structure and processes as the PMBoK with the introduction of PM tools and techniques. These two PM references are more suitable for the large companies and large projects with the regular project management implementation. We suggest thta the VSEs use the ISO/IEC 29110 because of the special purpose of this guide. The aim of this guide is to help the VSEs manager their projects effectively and successfully. However, other means must be associated to improve the success of projects, such as the alignment of project management and systems engineering. Some studies [13,14] also analyzed and compared the systems engineering standards and guides, so the development of the tools to aligning the PM and SE can be considered as an interest method assure the success of projects.

References

[1] Y.H. Kwak, Brief history of project management (2003)

[2] H. S. Beiryaei, and S. E. Vaghefim, Implementing knowledge life cycle in the body of project life cycle by using knowledge management system (KLC in PLC), 2010 3rd International Conference on Computer Science and Information Technology, 2010, pp. 643-647.

[3]S. Maserang, Project Management: Tools & Techniques, Systems Analysis & Design,[online]:http://www.umsl.edu/~sauterv/analysis/488_f02_papers/ProjMgmt.html

[4] R. Xue, C. Baron, P. Esteban, Managing systems engineering processes: a multi-standard approach, processing of the 8th annual IEEE International Systems Conference (SYSCON), Ottawa, Canada, March 31-April 3, 2014.

[5] AK Munns, B.F. Bjeirmi, The role of project management in achieving project success, International Journal of Project Management,Vol 14, 1996, pp:81–87

[6] PMI. A Guide to the Project Management Body of Knowledge: PMBOK® Guide. Project Management Institute, 2013.

[7] ISO, «ISO 21500 Guidance on Project Management. A Pocket Guide». Van Haren Pub, 2013.

[8] ISO/IEC, ISO/IEC 29110 Software engineering — Lifecycle profiles for Very Small Entities (VSEs)

[9]D. Haughey, A Brief History of Project Management, [online] http://www.projectsmart.co.uk/brief-history-of-project-management.php

[10] X.Q. Liang, Research on project management of company's marketing system, 2010 2nd IEEE International Conference on Information and Financial Engineering (ICIFE), 17-19 Sept. 2010,Pp:319-322.

[11] R. Vermaa, M.E. Pullmanb, An analysis of the supplier selection process, Omega, Vol 26, 1998, Pp: 739–750

[12] G.Y. Xu, How to Choose the Supplier in Logistics Outsourcing Based on Membership Degree, International Conference on Management Science and Engineering, 2007, 20-22 Aug. 2007,Pp:286-292.

[13] PMI-france, ISO 21500 ou PMI, faut-il choisir ? [online] http://pmi-france.org/branches/nord-de-france/ressources-des-conferences-passees/239-iso-21500-ou-pmi-faut-il-choisir

[14]S. Gasik, Comparison of ISO 21500 and PMBOK® Guide

Application of advanced signal processing techniques to the diagnostic of induction motors

Jose Antonino-Daviu

Universitat Politecnica de Valencia, Instituto de Ingeniería Energética,

Camino de Vera s/n, 46022 Valencia

joanda@die.upv.es

Keywords: Induction motors; signal processing; fault diagnosis; wavelet transforms, Hilbert-Huang transform, transient analysis.

Abstract. The application of signal processing tools in electrical machines-related areas has lived an extraordinary advance over recent years. This has been partially due to the extrapolation of recent techniques that have shown very satisfactory results in other scientific areas. More specifically, the application of these tools to determine the health of the machine is a research field that has attracted the interest of industry and academia. The idea is to apply these techniques to the machine quantities, regardless of its operation regime, in order to obtain additional information about its condition that is not available with the conventional tools. This paper reviews the application of diverse recent signal processing tool in the electric machines condition monitoring area. The paper discussions presented in the paper cover from the conventional tools, as the Fourier transforms, to more modern alternatives based on time-frequency analysis. The paper includes a section where a didactic explanation of the operation of some of these advanced tools is presented.

Introduction

The use of signal processing tools in the electrical machines area has lived an extraordinary advance over recent decades [1-2]. This is a classical area that has been always characterized by importing the advances and new findings in other scientific areas but with a certain delay. More specifically, the electrical machines condition monitoring research area has been applying tools and methodologies that have been employed with great success in other research fields. As an example, nuclear engineering is an area that has been pioneer in the development and application of advanced signal processing tools in order to develop techniques aimed to guarantee the reliability of nuclear processes that are often critical. Some of these techniques have been later extrapolated to the electrical machines fault diagnosis and prognosis areas [3].

This progressive use of validated and optimized signal processing tools has been very beneficial for the electrical machines diagnosis community, whose primary goal is to develop advanced methods to reliably detect the eventual presence of failure in these machines, while these failures are still in their early stages of development. In this way, the industrial users can adopt proper maintenance actions in advance, minimizing the possible economic losses derived from unplanned interruptions. The use of advanced and modern signal processing tools enables to reach a higher reliability and accuracy in the conclusions relative to the machine condition, since much more information can be obtained when applying these tools (in comparison with that obtained with the conventional methods).

A recent trend that has drawn a significant attention is the analysis of machine quantities (currents, fluxes, vibrations, voltages…) that are captured during transient operation [2-4]. Current analysis has drawn a significant attention, since this is a quantity that can be measured in a non-invasive way and the necessary equipment for its measurement and processing is rather simple [5]. However, currents and other quantities are often characterized by their non-stationary nature, a fact that makes difficult (or even impossible) the application of classical signal processing tools (as the

ISBN: 978-1-61804-295-8

Fourier transform). To analyze such quantities and obtain the most information possible, advanced signal processing tools, suited for the analysis of non-stationary signals must be used. In this context, modern time-frequency tools, as wavelet transforms, Wigner-Ville distributions or Hilbert-Huang transforms have proven to provide very useful information for fault diagnosis purposes [1-2]. In fact, these tools are able to track the evolutions of multiple harmonics that are introduced by the corresponding fault in the analyzed signal (current or vibration). The detection of these harmonics evolutions is a reliable indicator or the presence of the fault, since it is very unlikely that other phenomenon leads to harmonics with such evolutions.

One interesting application within the electrical machines condition monitoring area where the use of these tools has provided very satisfactory results is the rotor assessment of induction motors [4]. Several works have shown that the application of tools as the Discrete Wavelet Transform (DWT) [4] or the Hilbert-Huang Transform (HHT) [3,6] enables to obtain very complete 'pictures' of the time-frequency content of the analyzed signal. More specifically, the application of these tools to the phase stator startup current yields time-frequency maps represented in different manners, where the rotor fault related harmonics can be tracked. Moreover, it is even possible to quantify the level of cage failure by computing the energies of different regions of these maps [4].

The present paper is aimed to present an overview of the basic operation of these two transforms (DWT and HHT), illustrating their operation through several didactic examples. In addition, the paper will review the application of these tools to the rotor assessment in induction motors. The results included here show the powerfulness of these signal processing techniques as well as their potential for the further extrapolation to the detection to other faults.

Advanced Time-Frequency tools

Discrete Wavelet Transform (DWT). When the Discrete Wavelet Transform (DWT) is applied to a certain sampled signal *s(t)*, this signal is decomposed as the addition of a set of signals (*wavelet signals)*: an *approximation signal* at a certain decomposition level *n* (a_n) plus *n detail signals* (d_j with *j* varying from 1 to *n*) [7].

Each wavelet signal (approximation and detail) has an associated frequency band, the limits of which are well-established, once the sampling rate (f_s) of the original analyzed signal is known, in accordance with an algorithm enunciated by S. Mallat (*Subband Coding Algorithm*) [8]. The formulae that are employed to calculate the limits of the frequency bands associated with each wavelet signal, according to the Mallat algorithm, are specified in Fig. 1. Note how the limits of the frequency band for each wavelet signal depend on the sampling rate (f_s) as well as on the level of the corresponding wavelet signal (*j*). As an example, if the sampling rate used for capturing *s(t)* is f_s=5000 samples/second, and we perform the DWT decomposition in *n*=8 levels, the frequency bands associated with each wavelet signal are those shown in Table 1 [9].

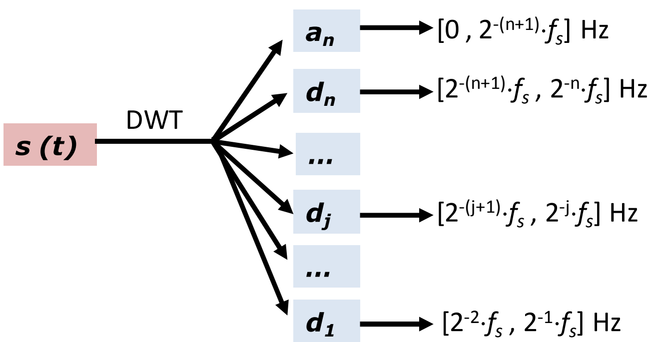

Fig. 1 DWT decomposition in wavelet signals and associated frequency bands [9]

Table 1. Frequency bands associated with wavelet signals for f_s=5 kHz and n=8

Wavelet signal	Frequency band
a_8	[0-9'2] Hz
d_8	[9'2-19'5] Hz
d_7	[19'5-39] Hz
d_6	[39-78'1] Hz
d_5	[78'1-156'2] Hz
d_4	[156'2-312'5] Hz
d_3	[312'5-625] Hz
d_2	[625-1250] Hz
d_1	[1250-2500] Hz

The intuitive idea underlying the application of the DWT is the next: each one of the wavelet signal acts as a filter, extracting the temporal evolution of the components of the original signal contained within the frequency band associated with that wavelet signal [4, 9]. For instance, in the previous example, the wavelet signal d_6 (*detail signal 6*) will reflect the time evolution of every harmonic component of the original signal when its frequency falls in the band [39-78'1] Hz. For instance, if the signal is a pure 50Hz sinusoidal waveform, the whole signal evolution would be reflected in that signal d_6. Some examples that illustrate the operation of the DWT are presented next [9]:

Example 1: DWT analysis of a pure sinusoidal signal

Fig. 2 shows the DWT of a 50 Hz pure sinusoidal signal (depicted at the top). Note how, in agreement with the filtering process carried out by the DWT, the whole signal is filtered into the detail signal d7. The reason for this is that this signal reflects the evolution of every component evolving within the range [39-78,1]Hz. Hence, since there is a single 50 Hz component in the original signal, d7 exactly reflects the evolution of the whole component. The other wavelet signals are approximately zero, since no other frequency components exist in the original signal.

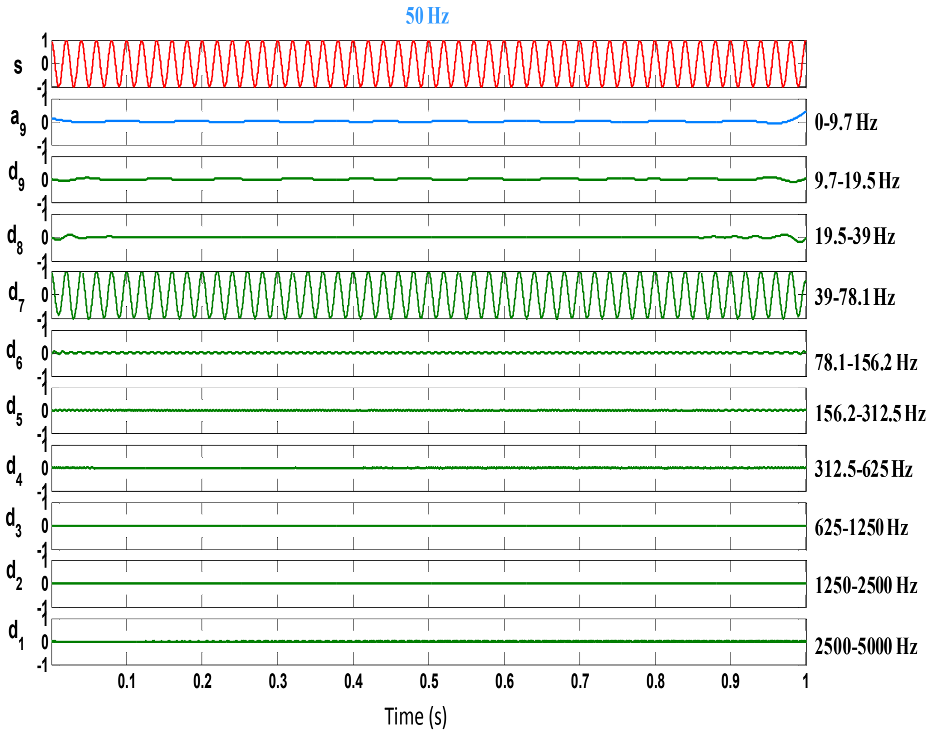

Fig. 2 Example 1: DWT decomposition of a pure sinusoidal signal [9]

ISBN: 978-1-61804-295-8

Example 2: Superposition of sinusoidal signals

Fig. 3 shows the DWT analysis of a signal s (that is depicted plotted on the top) that has been built by adding four sinusoidal signals with frequencies: 5 Hz, 15 Hz, 30 Hz and 50 Hz. The result is a stationary signal in which all four frequencies are present at every time. The filtering nature of the DWT allows extracting each frequency component in a separate wavelet signal, in concordance with the values of their respective band limits. Note that the 5Hz component is filtered in a9, the 15 Hz component in d9, the 30 Hz component in d8 and the 50 Hz component in d7, remaining almost zero the rest of signals, since no other components exist within their bands. This is an illustrative example of the filtering process carried out by the transform. It also proves its ability to separate the different components of the signals, provided that they fall in different frequency bands covered by the wavelet signals [9].

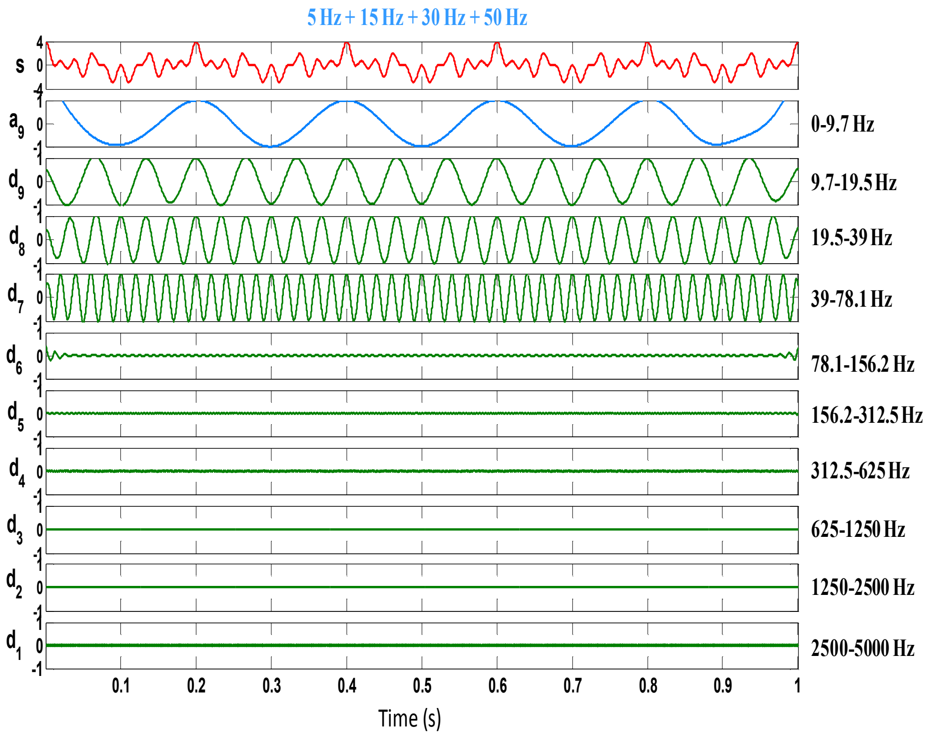

Fig. 3 Example 2: DWT analysis of a signal based on the superposition of four sinusoidal signals with frequencies 5 Hz, 15 Hz, 30 Hz and 50 Hz [9].

Example 3: Concatenation of sinusoidal signals

Fig. 4 shows the DWT of a signal s that is plotted at the top of the figure) which has been built by concatenating four sinusoidal signals with respective frequencies 5 Hz, 15 Hz, 30 Hz and 50 Hz. The result is a non-stationary signal, where each frequency component is present only during its corresponding time interval. The DWT of that signal implies to filter each component in the wavelet signal covering the frequency band where it is included. Therefore, the 5Hz component is filtered in a9, the 15 Hz component in d9, the 30 Hz component in d8 and the 50 Hz component in d7. The rest of signals are almost zero since no components exist within their bands. Furthermore, the wavelet signals indicate when each component starts and ends in the analyzed signal. As an example, a9 shows how the 5 Hz component is present during the initial 0,25 seconds, d9 shows that the 15 Hz component is present between 0,25 and 0,5 s, d8 reveals that the 30 Hz component occurs between 0,5 and 0,75 seconds and, finally, d7 shows that the 50 Hz component is present between 0,75 and 1 second. This is an illustrative example of one of the most important advantages of the DWT in comparison with the FFT [9]: whereas with the FFT, the time information is lost and two rather different signals (such as those analyzed in Examples 2 and 3) could be represented by

ISBN: 978-1-61804-295-8

similar FFT spectra, the DWT preserves the time information, enabling to identify which frequencies and when they occur. Hence, the DWT leads to a three-dimensional representation of the analyzed signal: frequency (because each wavelet signal covers a frequency band), time (since each wavelet signal is represented versus time) and amplitude (the amplitude of the wavelet signal informs on the corresponding amplitude of its filtered components in the analyzed signal) [9].

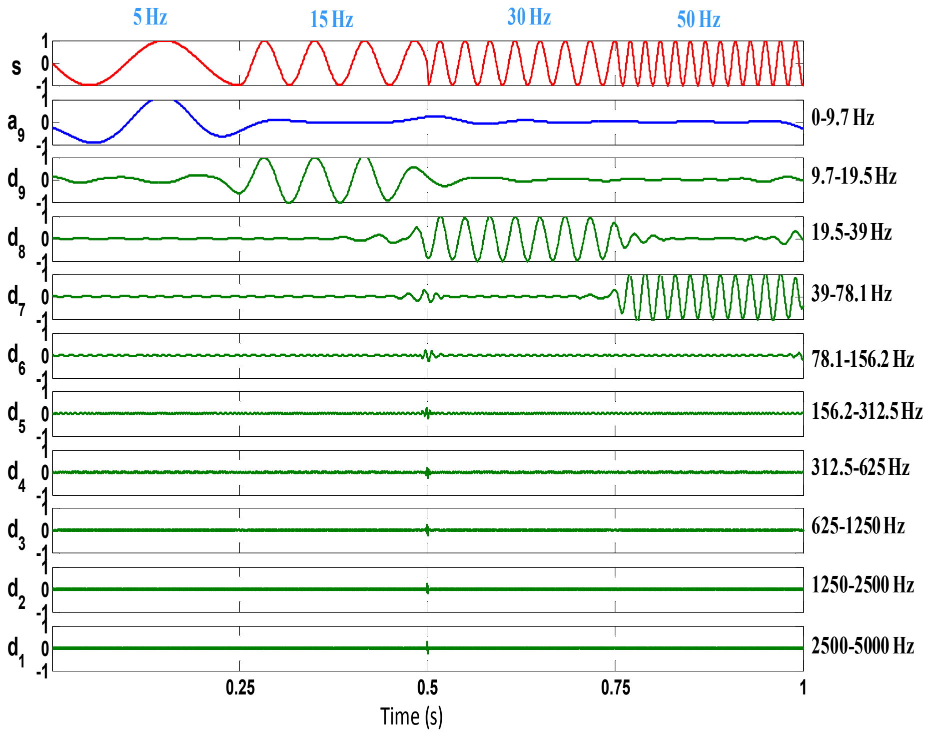

Fig. 4 Example 3: DWT analysis of a signal based on the concatenation of four sinusoidal signals with frequencies 5 Hz, 15 Hz, 30 Hz and 50 Hz [9].

Hilbert-Huang Transform. The Hilbert-Huang transform (HHT) is a modern tool that has provided very good results in other engineering areas, as nuclear technology, to analyze multi-component signals [3, 6, 10]. In synthesis, the HHT decomposes the analyzed signal into a set of intrinsic mode functions (imfs). Each imf filters the components of the original signal into a certain frequency band. However, unlike what happens in the DWT, the frequency band associated to each imf is not known 'a priori'. The HHT performs an 'adaptive filtering' process so that the predominant frequencies are filtered in the first imfs, while the latter imfs contain the components with reduced amplitudes [10].

In order to know the exact frequencies covered and obtain a proper time-frequency representation of each imf, it is necessary to perform the Hilbert spectrum of the imf, that shows how all components contained in that imf evolve in the t-f map. Some examples that illustrate the operation of the HHT are presented next [10]:

Example 4: HHT of the addition of sinusoidal signals

Fig. 5 depicts a signal based on the addition of two sinusoidal signals with frequencies 50 Hz and 15 Hz and respective amplitudes 5 and 1. Fig. 6 shows the application of the HHT to the previous signal (two imfs are considered) [10]. Fig. 6(a) depicts: the imf1 waveform (Fig. 6(a), top), the imf1 Hilbert Huang spectrum (Fig. 6(a), middle) and the imf1 marginal spectrum ((Fig. 6(a), bottom). Fig. 6(b) is equivalent but for the imf2. This figure is very illustrative on how the HHT operates: the imf1 extracts the largest component present in the signal (i.e., the 50 Hz sinusoidal component with amplitude 5). This is observed in the imf1 waveform. On the other hand, the Hilbert Huang spectrum of this imf1, logically, shows a single line at 50 Hz at every time instant. Finally, the imf1 marginal spectrum shows a peak at 50 Hz. On the other hand, imf2 extracts the evolution of the rest of components in the analyzed signal (in this case, the 15 Hz sinusoidal component with amplitude 1); this is observed in Fig. 4(b) (top), that depicts the imf2 waveform and reveals a sinusoidal component with lower frequency (and amplitude) than that in Fig. 6(a), top. Hilbert spectrum of imf2 shows a single line at 15 Hz at every time instant. Accordingly, the marginal spectrum of imf2 reveals a single frequency peak at 15 Hz.

This example illustrates the adaptive filtering nature of the HHT, extracting the components present in the signal in the different imfs.

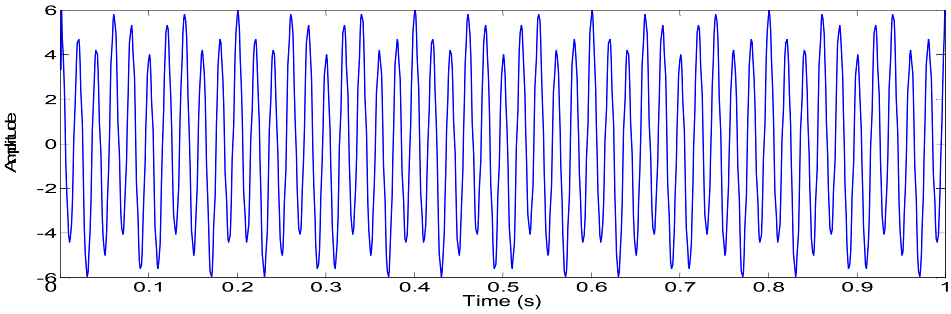

Fig. 5 Signal based on the addition of two sinusoidal signals [10]

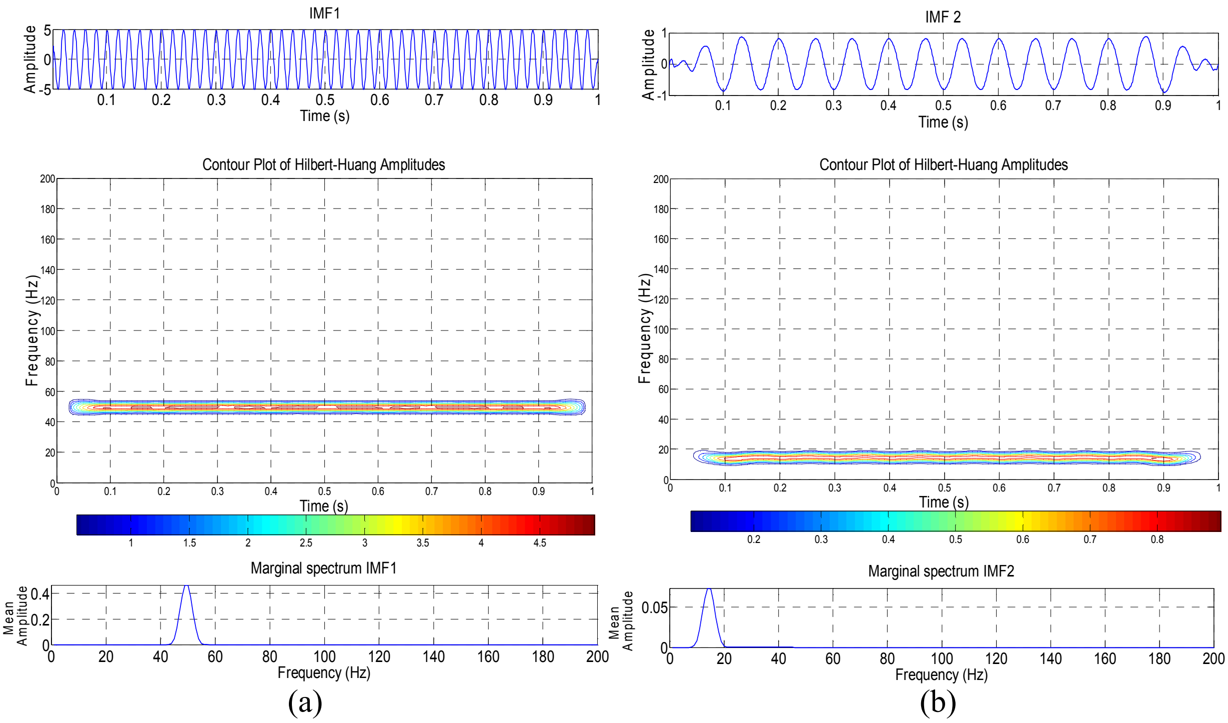

Fig. 6 Example 4: HHT of the previous signal: (a) IMF1: waveform (top), Hilbert spectrum (middle) and marginal spectrum (bottom); (b) IMF2: waveform (top), Hilbert spectrum (middle) and marginal spectrum (bottom) [10].

ISBN: 978-1-61804-295-8

Example 5: HHT of the concatenation of two sinusoidal signals

This example is based on the HHT analysis of the signal plotted in Fig. 7, that is the concatenation of two sinusoidal signals with respective frequencies 50 Hz and 15 Hz and respective amplitudes 5 and 1. In this case, the HHT analysis leads to a single imf (imf1) that reflects the evolution of both components. Fig. 8 shows the HHT results: the imf1 waveform (top), Hilbert spectrum of the IMF1 (middle) and marginal spectrum of imf1 (bottom). The waveform of the imf1 corresponds to that of the original signal (concatenation of the two aforementioned components). The Hilbert spectrum of imf1 is especially interesting; a single line at 50 Hz reveals the presence of the first frequency component during the initial 0,5s. A second trace at 15 Hz shows the occurrence of the second component during the last 0,5 s. The lower color intensity of this second trace is due to the lower amplitude of the 15Hz frequency component. This Hilbert spectrum illustrates rather well the time-frequency nature of the tool, since it informs not only on which frequency components are present in the analyzed signal, but also when they occur. Finally, the marginal spectrum of imf1 shows two peaks at the corresponding frequencies present in the signal (15 Hz and 50 Hz), the amplitudes of which reflect the amplitude of the associated sinusoidal signals [10].

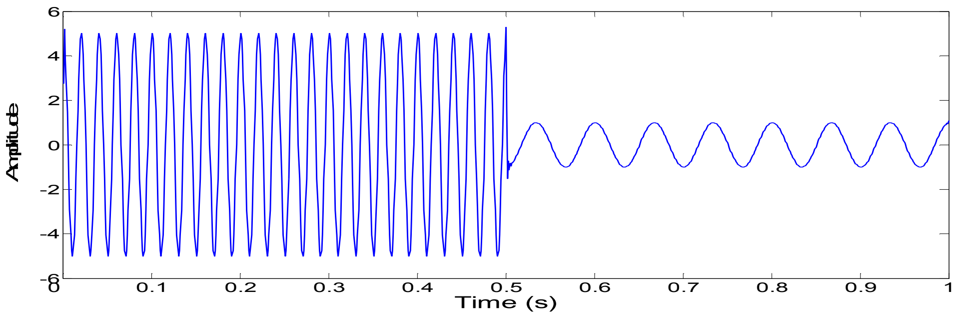

Fig. 7 Signal based on the concatenation of two sinusoidal signals [10]

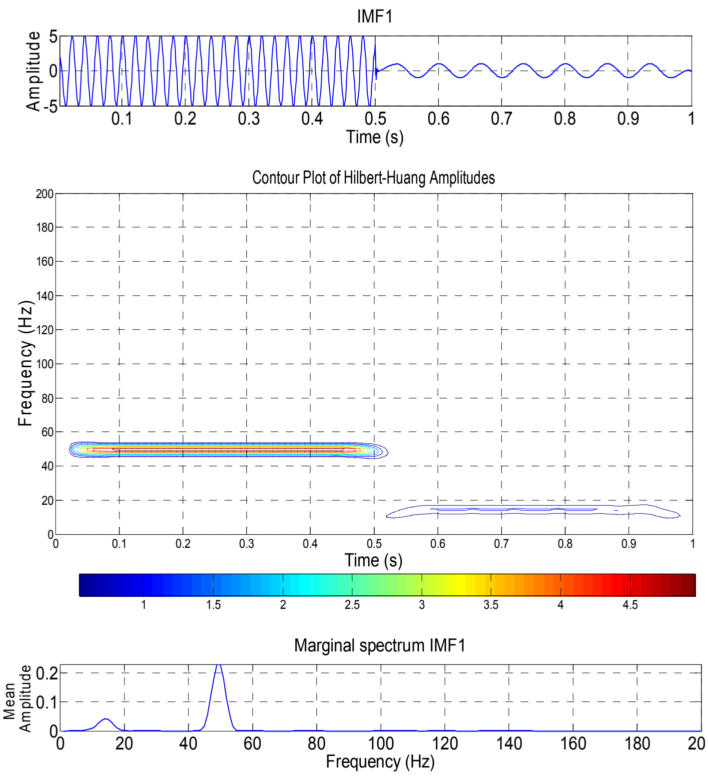

Fig. 8 Example 5: HHT of the previous signal: waveform of the IMF1 (top), Hilbert spectrum of IMF1 (middle) and marginal spectrum of IMF1 (bottom) [10].

Application of Signal Processing Techniques to Fault Diagnosis

As explained before, the application of some of the aforementioned signal processing tools in the electric motor condition monitoring area has provided very beneficial results; these tools enable a more accurate tracking of the evolutions of the fault related components in the analyzed signals (e.g. the startup current). These evolutions are reliable indicators of the presence of the failure since it is very unlikely that other phenomena can lead to the same evolutions.

A clear example that illustrates all these statements relies on the determination of the rotor condition in induction motors. In previous works [5], it has been shown that when the rotor of an induction motor is faulty, several harmonics appear in the stator current signal (i.e. the current demanded by the motor). The most relevant harmonics are known as *sideband components*; their frequencies are given by the well-known expression (1) (with f=supply frequency and s=slip). The *lower sideband component* (LSC) is the one with negative sign in (1), whereas the *upper sideband component* (USH) is that with positive sign [5].

$$f_{sc} = f\cdot(1-2\cdot s) \qquad (1)$$

In recent works [4, 6], it has been shown that the application of advanced tools, as the DWT or the HHT, enables to track the evolution of both harmonics (especially, the evolution of the LSC that is the most relevant component) during the startup transient. During this transient, as the slip changes from 1 to near 0 in a direct-on-line start), the frequency of the LSC (f_{LSC}) drops from f (=50 Hz in Europe) to 0 and then increases again to near f. This evolution can be clearly identified with the aforementioned tools, as proven in recent works [4].

Fig. 9 shows the DWT of the startup current for a healthy motor (Fig. 9(a)) and for a motor with broken rotor bars (faulty rotor, Fig. 9 (b)). Note the appearance of a Λ-shaped pattern in the high-level wavelet signals for these latter case [4]. This pattern is caused by the time-frequency evolution of the LSC during the startup; as its frequency changes in the way commented before (50→0→50Hz), some oscillations appear in the wavelet signals covering that frequency band. These oscillations are reflecting the evolution of the LSC and their detection enables to diagnose the presence of the fault [4].

Moreover, it is even possible to determine the severity of the rotor failure; to this end, several fault indicators have been developed based on the amplitudes or energies of the wavelet signals affected by the evolution of the LSC [4, 11]. The practical experience has shown that indicators based on the energies of signals as d7 in Fig. 9 have provided very good results for the diagnostic. The indicators have been defined in such a way that a low value indicates faulty condition, while high values show a healthy condition of the rotor [12].

The application of the HHT to the startup current has provided also good results for rotor fault diagnosis purposes. In this case, the HHT can provide complete maps (either in 2-D or 3-D) of the time-frequency content of the startup current signal. These maps enable to visualize the fault components evolutions and, among them, the evolution of the LSC [3, 6]. Fig. 10 shows the 3-D Hilbert Huang spectrum of the imf2 of the startup current for the healthy motor (Fig. 10 (a)) and for the motor with faulty rotor (Fig. 10(b)). The time-frequency evolution of the LSC, that was previously described, is clearly noticed in that figure.

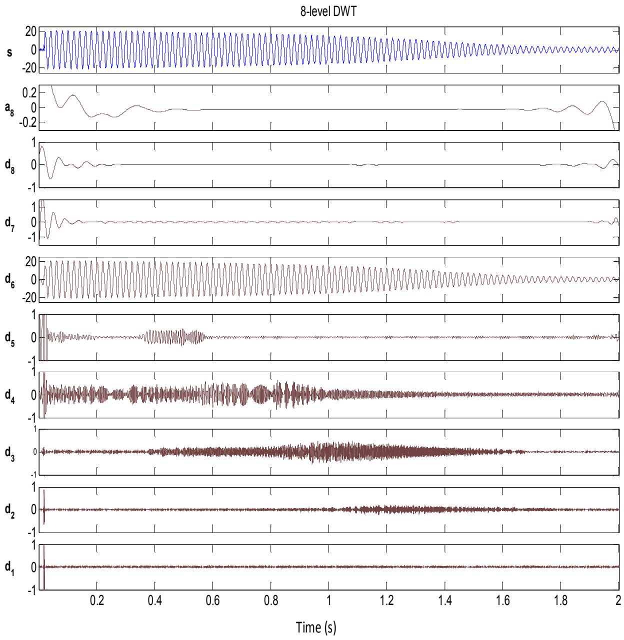

(a) (b)

Fig. 9 Application of the 8-level DWT to the startup current of: (a) a healthy motor, (b) a motor with faulty rotor [4].

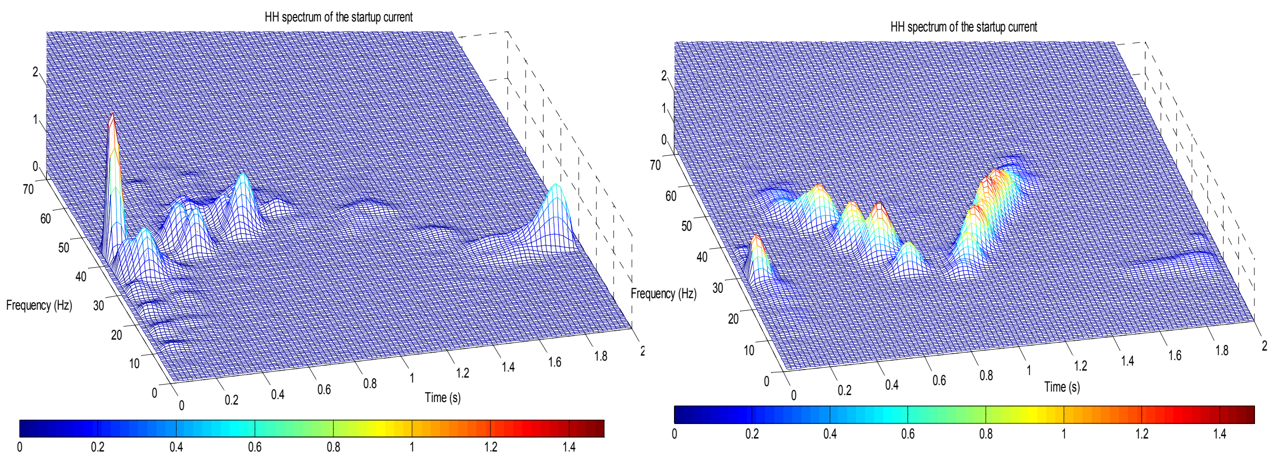

(a) (b)

Fig. 10 Application of the HHT to the startup current. HH spectrum of: (a) a healthy motor, (b) a motor with faulty rotor [6].

Conclusions

This paper reviews the application of advanced signal processing techniques to the electric motors condition monitoring area. More specifically, the work describes the utilization of two time-frequency decomposition tools (the Discrete Wavelet Transform and the Hilbert-Huang Transform) for the rotor assessment of induction motors. The paper includes a didactic explanation of both tools, including several examples that illustrate the operation of these transforms. As justified in the work, these tools enable a reliable diagnostic of the possible rotor failures based on tracking the evolutions of fault-related harmonics in the time-frequency map. The results included in the paper, obtained with real machines, prove the usefulness of the extrapolation of advance tools that have shown very satisfactory results in other scientific fields.

References

[1] J. Pons-Llinares, V. Climente-Alarcón, F. Vedreño-Santos, J. Antonino-Daviu, and M. Riera-Guasp, Electric Machines Diagnosis Techniques via Transient Current Analysis, Proceedings of the 38th Annual Conference of the IEEE Industrial Electronics Society, IECON 2012, 25-28 October, Montreal, Canada (2012).

[2] S. H. Kia, H. Henao, and G.-A. Capolino, Efficient digital signal processing techniques for induction machine fault diagnosis," Proc. IEEE Workshop Electrical Machines Design, Control and Diagnosis (WEMDCD'2013), Paris, France, Mar. 11–12, pp. 230–244 (2013).

[3] J.A. Antonino-Daviu, M. Riera-Guasp, M. Pineda-Sanchez, R. Puche-Panadero, R.B. Pérez, P. Jover-Rodriguez, A. Arkkio, Fault Diagnosis in Induction Motors using the Hilbert-Huang Transform, Nuclear technology (American Nuclear Society), Vol. 173, pp. 26-34 (2011).

[4] J. A. Antonino-Daviu, M. Riera-Guasp, J. R. Folch, and M. Pilar Molina Palomares, Validation of a new method for the diagnosis of rotor bar failures via wavelet transform in industrial induction machines, IEEE Trans. Ind. Appl., vol. 42, pp. 990-996 (2006).

[5] W.T. Thomson, M. Fenger, Current signature analysis to detect induction motor faults, IEEE Industry Applications Magazine, pp. 26-34 (2001)

[6] J.A. Antonino-Daviu, M. Riera-Guasp, M. Pineda-Sánchez, R.B. Pérez, A Critical Comparison Between DWT and Hilbert–Huang-Based Methods for the Diagnosis of Rotor Bar Failures in Induction Machines, IEEE Transactions on Industry Applications, vol. 45, no 5, pp. 1794 – 1803, (2009).

[7] C.S. Burrus, R.A. Gopinath and H. Guo, Introduction to Wavelets and Wavelet Transforms a primer, Prentice Hall (1998)

[8] S. Mallat, A Wavelet Tour of Signal Processing. New York: Academic Press, (1999).

[9] J.A. Antonino Daviu, Operation of the Discrete Wavelet Transform: basic overview with examples. Docent article UPV. http://hdl.handle.net/10251/30739 (2013)

[10] J.A. Antonino Daviu, Operation of the Hilbert-Huang Transform: basic overview with examples. Docent article UPV. http://hdl.handle.net/10251/30740 (2013)

[11] M. Riera-Guasp, J. A. Antonino-Daviu, M. Pineda-Sanchez, R. Puche-Panadero, and J. Perez-Cruz, A General Approach for the Transient Detection of Slip-Dependent Fault Components Based on the Discrete Wavelet Transform," IEEE Trans. Ind. Electron., vol. 55, pp. 4167-4180 (2008).

[12] C. Yang, T. Kang, D. Hyun, S.B. Lee, J. Antonino-Daviu, J. Pons-Llinares, Reliable Detection of Induction Motor Rotor Faults Under the Rotor Axial Air Duct Influence, IEEE Transactions on Industry Applications, vol.50, no.4, pp.2493-2502 (2014).

ISBN: 978-1-61804-295-8

Porous composite biomaterials based on silicon nitride and bioglass

Františka Frajkorová[1,a*], KatarínaBodišová[2,b], Martin Boháč[1,c], EvaBartoníčková[1,d], Jaroslav Sedláček[3,e]

[1] Faculty of Chemistry, Brno University of Technology, Purkyňova 464/118, 612 00 Brno, CzechRepublic
[2] Department of Ceramics, Glass and Cements, Faculty of Chemical and Food Technology, Slovak University of Technology in Bratislava, Radlinského 9, 812 37 Bratislava, Slovak Republic
[3] Institute of Inorganic Chemistry, Slovak Academy of Sciences, 84536 Bratislava, Slovak Republic
[a]frajkorova@fch.vutbr.cz, [b] gghillanyova@stuba.sk, [c] bohac@fch.vutbr.cz, [d] bartonickova@fch.vutbr.cz,[e] jaroslav.sedlacek@savba.sk

Keywords: Sintering, Composites, Glass, Nitrides, Biomedicalapplications

Abstract

The combination of bioinert and bioactive material offers new potentialities in bone tissue engineering. The present paper deals with preparation of novel biomaterial composite based on silicon nitride (Si_3N_4) and bioglass (in amount of 10 and 30 wt%) by free sintering at 980 °C for 1h in nitrogen atmosphere. The obtained material was characterized by differential thermal analysis (DTA) and X-ray powder diffraction (XRD). The bioactivity was examined *in vitro* with respect to the ability of hydroxyapatite layer formation on the surface of materials as a result of contact with simulated body fluid (SBF). All composites were studied by Fourier transform infrared spectroscopy (FTIR) and scanning electron microscopy (SEM) before and after immersion in SBF. Thebioglass-free sample was prepared as a reference material to compare the microstructure and bioactivity to the composites.

1. Introduction

Silicon nitride (Si_3N_4) based ceramics represent a combination of mechanical, tribological, thermal and chemical properties that makes them suitable for high performance components in severe environments in several industrial applications. These properties, namely hardness, fracture toughness, friction and wear coefficient, are also very important for many high-load medical application of bioceramics in the human body. Another desirable property of ceramic-based implants is bioactivity.

On the basis of potentialities, silicon nitride attracts interest for orthopedic and dental applications [1-7] in the human body, but is not yet established as a biomaterial in medicine. This is related to some controversy in the literature about the biocompatibility [1,4-6]. Several works on biocompatibility and bioactivity of silicon nitride outline that silicon nitride based ceramics can be used as materials for clinical applications in the field of hard tissue surgery. The absence of toxic behaviour was ascertained during toxicity tests [8].

In the application of silicon nitride as a biomaterial a key aspect is the presence of grain boundary phases deriving from the necessary use of sintering aids. The grain boundary phasecomposition and amount depend on the selected additives which, during sintering, react with the silica presents on the silicon nitride particles and other impurities, leading to the formation of a liquid phase. This allows the sintering of silicon nitride, but the final dense ceramics contains amorphous or partially crystalline grain boundary phases. It has to be taken into account that the glassy phases may exhibit bioactivity different from silicon nitride crystalline phases. Generally used additives for sintering of silicon nitride there are Mg, Al, rare earthand bioactive glass as novel sintering aid [9].

The first bioactive material reported was a four component glass composed of SiO_2, CaO, Na_2O, and P_2O_5 by Hench et al in 1971 [10]. Bioglass®45S5 has the following chemical composition: 45.0 SiO_2–24.5 Na_2O –24.5 CaO–6.0 P_2O_5 in wt%. It is a silicate glass based on the 3-D glass forming SiO_2 network in which Si is fourfold coordinated to O. The key compositional features that are responsible for bioactivity of 45S5 glass are its low SiO_2 content (compared to more chemically durable silicate glasses), high Na_2O and CaO (glass network modifiers) content and high CaO/ P_2O_5 ratio [11]. When implanted, the low silica content and the presence of sodium ions in the glass results in very rapid ion exchange with the protons and hydronium ions of physiological solutions [12]. The ion exchange creates an alkali pH at the implant interface with the body fluids, leading to nucleation and crystallisation of hydroxyl carbonate apatite (HCA) bone mineral at the surface of the glass. The growing bone mineral layer bonds to collagen, produced by the bone cells, and forms a strong interfacial bond between the implant and the living tissue [13,14].

However, medical applications of bioglass have been centred on low stress fields, mainly due to its non-adequate fracture toughness compared to that of cortical bone. This limitation is unfortunately a common characteristic of glasses, ceramics and glass ceramics used in medical applications. Theoretically, Si_3N_4-bioglass composites would lead to medical implants that combine the advantageous properties of each material individually. Amaral, Santos et al. [3,15] have prepared almost fully dense Si_3N_4-bioglass composite by hot pressing technique with exceptional mechanical properties that make it suitable for high-load application.

The present work describes the preparation of porous bioactive composite, based on silicon nitride and 45S5 Bioglass®,using free sintering. The pressureless sintering allows preparation of porous material by economic and simple way. A complete description of preparation, sinteringand microstructural characterization and also bioactivity is reported.

2. Experimental Procedure

Si_3N_4 –bioglass composites were prepared from a mixture of a Si_3N_4 commercial powder (Yantai, Tomley Hi-Tech Ind. &Tra. Co., Ltd., D_{90}=1.0 μm, O < 1.4%) and a bioglass. The bioglass (with the similar composition to Bioglass® 45S5) was prepared by sol-gel method according to the procedure [16] and has the following chemical composition: 45.0 SiO_2–24.5 Na_2O –24.5 CaO–6.0 P_2O_5 in wt%. The bioglass powder was then mixed with Si_3N_4 powder in a 0-30 % weight proportion in isopropanol by planetary milling for 2 h in a silicon nitride jar using silicon nitride balls. The homogenised suspension was dried and subsequently screened through 71 μm sieve in order to avoid large hard agglomerates. The pellets were uniaxially pressed at 100 MPa. The samples were free sintered at 980°C for 1h in nitrogen atmosphere. After the dwell time the samples were taken out from the furnace to inhibit the crystallisation of the bioglassas, according to Clupper and Hench [17-20], the crystal phase $Na_2Ca_2Si_3O_9$ slightly decreased the formation kinetics of an apatite layer on the Bioglass® sample surface but it did not totally suppress the formation of such a layer [20]. The sintering temperature of the composites was chosen on the basis of results obtained from the differential thermal analysis (DTA). The analysis was performed on TA Instruments Q600 equipment using a heating rate of 10°C/min and Al_2O_3 as reference.

The bioglass-free sample (referred as Si_3N_4-0) was prepared as a reference material to compare the microstructure and bioactivity to the composites. The sample was sintered in air at 1150 °C for 1h. The composition of studied systems are listed in Table 1.

Table 1. Chemical composition of studied systems.

Sample	Composition [wt%]	
	Si_3N_4	45S5 Bioglass®
Si_3N_4-0	100	0
Si_3N_4-10	90	10
Si_3N_4-30	70	30

The densities of the samples were measured by Archimedes method in water. The theoretical densities were calculated according to the rule of mixtures. The microstructure was observed by scanning electron microscopy (Zeiss, EVO 40 HV,Germany). The crystalline phases present in the ground samples were identified using X-ray diffraction (XRD) (Bruker AXS D8 Discover X-ray diffractometer).

The assessment of *in vitro* bioactivity was carried out by soaking samples in simulated body fluid (SBF) maintained at 36.5°C in incubation apparatus (Binder BD 115) for 7 and 21 days under a static regime. The SBF solution was preparedaccording to the standard procedure described by Kokubo and Takadama [21].After the soaking, the sample surface was characterized with scanning electron microscopy (Zeiss, EVO 40 HV, Germany) and Fourier transform infrared spectroscopy. The FTIR spectra were obtained using a Nicolet 6700 FTIR spectrometer from Thermo Scientific.The solutions were analysed using inductively coupled plasma optical emission spectrometer (ICP-OES) spectroscopy (HORIBA JY Ultima2) to determine the elemental concentration of Ca^{2+}, P^{5+} and Si^{4+} as a function of immersion time.

3. Results and Discussion

3.1 Thermal property analysis and phase characterisation

Fig. 1 shows the DTA curve of the Bioglass® powder prepared by sol-gel method. DTA curve presents two exothermic peaks, the first one at 305°C, the second one at 698°C and one endothermic effect in the region of 980-1030°C. Smaller exothermic peak at 305°C is probably a result of loss of residual organics from sol-gel process while large exothermic peak at 698°C corresponds to Bioglass® crystallisation. During the crystallisation process the development of new crystalline phase is detected. Theseresults are in agreement with those presented by Clupper and Hench [22]. Endothermic effect between 980 and 1030°C is attributed to glass transition region of bioglass, therefore the temperature of 980°C has been chosen as the sintering temperature. Bioglass at such a temperature acts as a sintering additive due to the transition of solid state to soften viscous liquid.

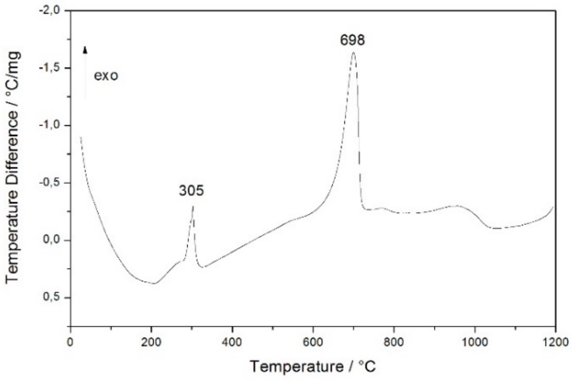

Fig. 1. DTA analysis of bioglass using a heating rate of 10°C/min.

The crystalline phase mentioned above is a sodium calcium silicate $Na_2Ca_2Si_3O_9$.X-ray powder patterns of Si_3N_4-composites are presented in Fig. 2. XRD phase analysis of the composite contains 30% of bioglass (Si_3N_4-30) confirmed the presence of $Na_2Ca_2Si_3O_9$ together with β- Si_3N_4 and SiO_2 (tridymit) as minority phases and α-Si_3N_4 as a majority phase.The XRD analysis of the composite contains 10% of bioglass (Si_3N_4-10)showed the presence of α-Si_3N_4 as a majority phase and β-Si_3N_4 and SiO_2 (cristobalite) as minority phases. The fact, that no further crystalline phases were not detected could indicate that no significant reactions occurred between silicon nitride and bioglass. However, the EDX analysis of the composite Si_3N_4-10 showed the presence of $Na_2Ca_2Si_3O_9$. It means that 45S5 bioglasshascrystallised to $Na_2Ca_2Si_3O_9$ but its concentration may be below the detection limit of XRD analysis.The XRD pattern of bioglass-free sample, Si_3N_4-0, sintered at 1150°C in air, is presented in Fig. 3. The results of phase analysis have revealed that α→β-Si_3N_4 phase transformation has occurred at sintering temperature, besides α-Si_3N_4 alsoβ- Si_3N_4, both hexagonal, was detected. The α→βphase transformation is proceeding through solution–diffusion–reprecipitation process [23].

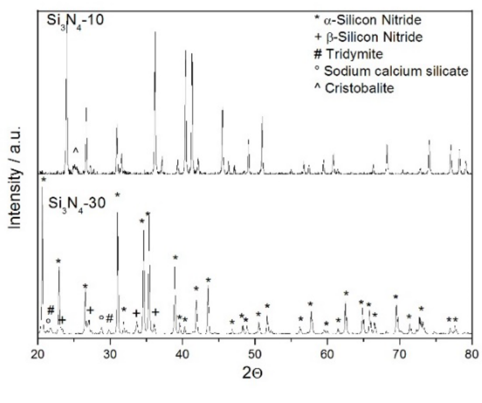

Fig. 2. XRD pattern of the silicon nitride-bioglass composites, Si_3N_4-10 and Si_3N_4-30

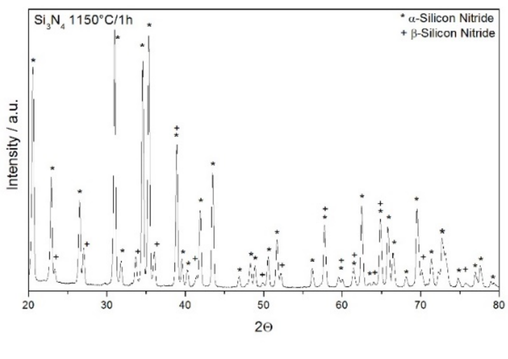

Fig. 3. XRD pattern of the bioglass-free sample, Si_3N_4-0.

3.2 Microstructural characterisation

The values of densities, relative densities and porosity of the Si_3N_4-bioglass composites and bioglass-free sample are summarized in Table 2.

ISBN: 978-1-61804-295-8

Table 2. Densities, relative densities and porosity of samples.

Sample	Density [g cm^{-3}]	Relative density [%]	Porosity [%]		
			Overall	Open	Close
Si_3N_4-0	1.7	52.5	47.5	40.1	7.4
Si_3N_4-10	1.9	60.3	39.7	33.9	5.9
Si_3N_4-30	2.0	65.7	34.3	24.0	10.3

From the results listed in the Table 2 is obvious that relative density of Si_3N_4-bioglass composites increases with the addition of bioglass. Relative densities of composites is higher in comparison with bioglass-free sample Si_3N_4-0 so it can be assumed that bioglass plays the role of sintering additive and promotes the sintering process of composites. However the changes in relative density as well as in porosity could have been more significantif the sintering temperature had been closer to the melting point of bioglass. Due to the lack of liquid phase which wets the solid grains of Si_3N_4 is not possible to speak about liquid phase sintering.

The microstructure of materials designed for bioapplications is of great importance.Overall porosity of the Si_3N_4-bioglass composites decrease with increased content of bioglass. This is in accordance with observed increasing density with the rising bioglass content. The porosity of the Si_3N_4-bioglass composites and bioglass-free sample was calculated using Archimedes method of weighing in water.

Complex microstructural characterisation offers SEM analysis. The micrographs of reference Si_3N_4-0 sample and as well as Si_3N_4-bioglass composites with 10 and 30% of bioglass are shown in Fig. 4. The final microstructures of Si_3N_4-bioglass composites shown in Fig. 4a), b) reveal irregularly distributed prolonged crystals of bioglass in α-Si_3N_4 matrix. With increasing content of bioglass in the composite also grows the amount of crystals with lath-like morphology overlapping the equiaxial α-Si_3N_4 grains. The microstructure of bioglass-free sample in Fig. 4c) shows a few elongated β- Si_3N_4 grains in matrix formed of equiaxial α-Si_3N_4 grains.

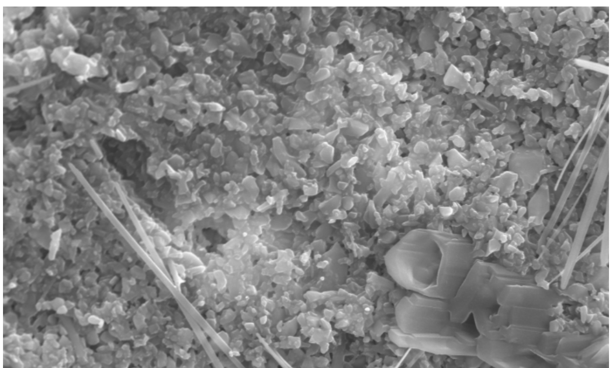

a) Si_3N_4-10

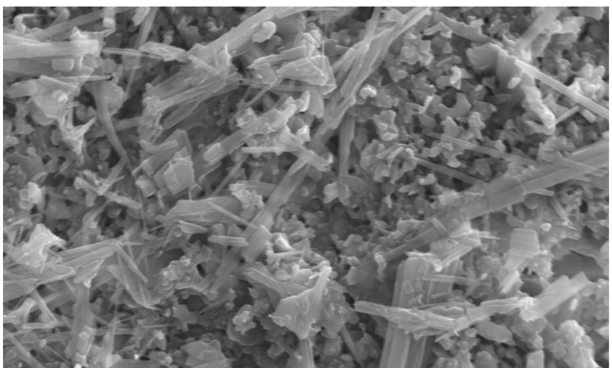

b) Si_3N_4-30

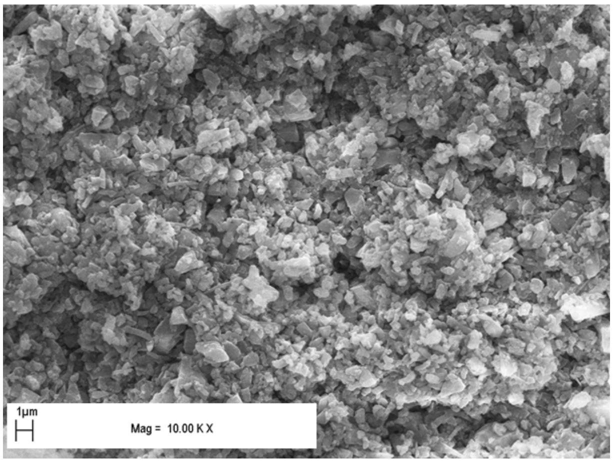

c) Si_3N_4-0

Fig. 4. The microstructures of Si_3N_4-bioglass composites with 10 a 30% of bioglass and reference bioglass-free sample (magnification x1000).

3.3 Bioactivity

In vivo bone bioactivity of a material can be predicted from the apatite formation on its surface in SBF. SEM micrographs of the surfaces of the Si_3N_4-bioglass composites after soaking in SBF for 7 (Fig. 5a), b))and 21 days (Fig. 6a), b)) show that the samples remained porous after a soaking period and the surface changes, typical for a bioactive material, can be observed. The morphological evolution in SBF follows a profile analogous to that reported for hydroxyapatite (HA) coatings [24]. After immersion for 7 day in SBF a newly formed hydroxyapatite plates of irregular shape are visible on the surface of sample Si_3N_4-10 (Fig. 5a)). As presented in Fig. 5b), after immersion for 7 days in SBF on the surface of sample Si_3N_4-30 locally grown small spherical hydroxyapatite granules. After soaking in SBF for 21 days, is the surface of sample Si_3N_4-10 almost totally covered with hydroxyapatite plates of irregular shape (Fig. 6a)), while the surface of sample Si_3N_4-30 is completely coated with HA film (Fig. 6b)) and the detailed picture revealed that the hydroxyapatite particles have spherical shape.

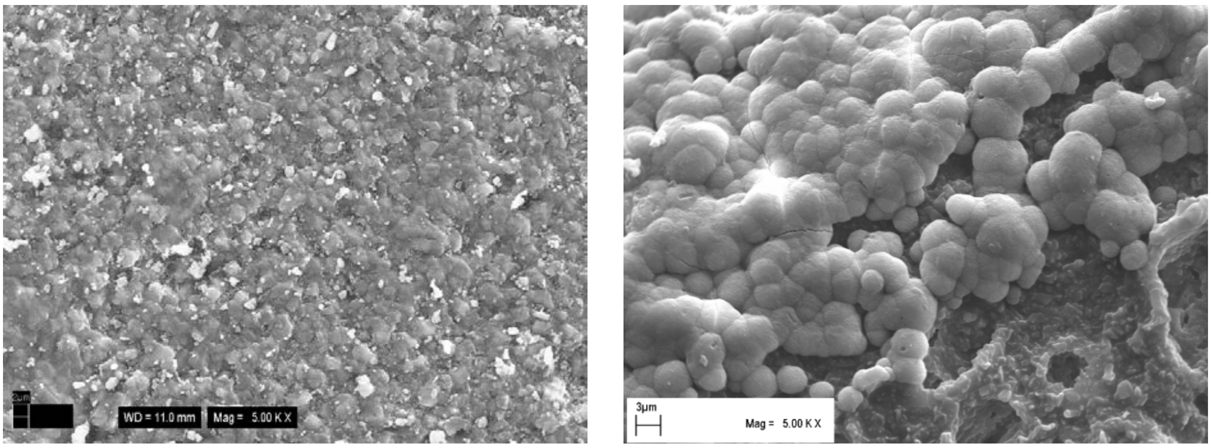

a) Si_3N_4-10_7 b) Si_3N_4-30_7

Fig. 5. SEM micrographs showing the surface microstructure of the Si_3N_4-bioglass composites after soaking in SBF for 7 days (magnification 5000x):

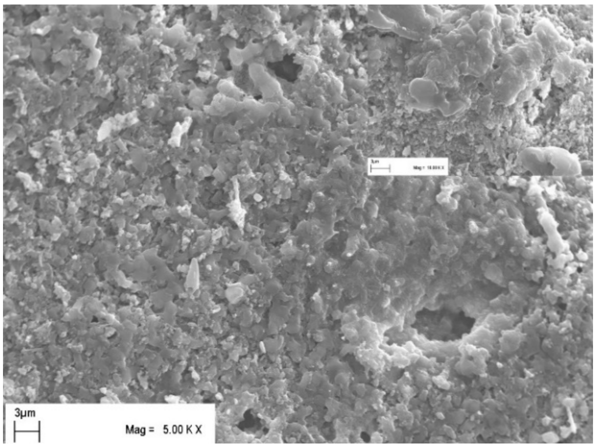

a) Si_3N_4-10_21

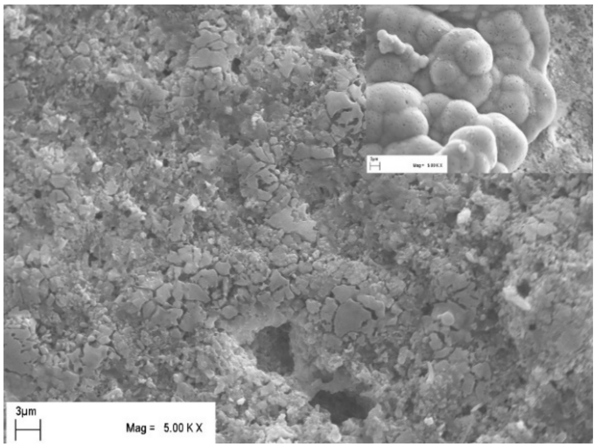

b) Si_3N_4-30_21

Fig. 6. SEM micrographs showing the surface microstructure of the Si_3N_4-bioglass composites after soaking in SBF for 21 days (magnification 5000x). The surface details are shown in the pictures placed at the top-right corner of micrograph:

Control experiments in SBF were also performed with the bioglass-free sample Si_3N_4-0. In accordance with the expectations no surface changes, associated with the formation of hydroxyapatite, have occurred, as the silicon nitride is abioinert material.

3.4 Analysis of leachates

Examining the compositional change of SBF solution with time may provide insight into the mechanism of enhanced bioactivity of the Si_3N_4-bioglass composites. Fig. 7 - Fig. 9 show the changes in Ca^{2+}, P^{5+} and Si^{4+} concentration of the SBF as a function of soaking time, examined by ICP analysis. These results are very useful for understanding the phenomenon of ion transfer which takes place between the glass-ceramic surface and the synthetic physiological liquid. The variations of calcium concentration of the SBF after 7 and 21 days of immersion are shown in the Fig. 7. The marked release of Ca^{2+} ions into the SBF medium during 7 day test are due to partial dissolution of the surface. The concentration of Ca^{2+} ions increased from 2.5 mmol.dm^{-3} to 3.2 mmol.dm^{-3} in case of Si_3N_4-10 sample and from 2.5 mmol.dm^{-3} to 3.4 mmol.dm^{-3} for Si_3N_4-30 sample. After 21 days the concentration of Ca^{2+} decreased because SBF is already supersaturated with calcium ions regarding the HA formation. The decrease in the phosphorus concentrations, shown in Fig. 8, is likely due to the precipitation of the calcium phosphate layer, which consumes Ca^{2+} and P^{5+} ions from the SBF medium [25,26]. Changes in Ca^{2+} concentration correlated with changes in P^{5+} concentration and correspond to chemical composition of the composites. After 7 days test the concentration of P^{5+} fell from 1.0 mmol.dm^{-3} to 0.9 mmol.dm^{-3} for Si_3N_4-10 sample and from 1.0 mmol.dm^{-3} to0.8 mmol.dm^{-3} for Si_3N_4-30 sample. Regarding bioglass-free sample (Si_3N_4-0), the concentrations of Ca^{2+} and P^{5+} did not change, as silicon nitride is a bioinert material. As shown in Fig. 9, silicon concentration released into the SBF medium increases steadily with time of immersion in case of the composites and even in case of the bioglass-free Si_3N_4 sample, as silicon nitride grains are on their surface covered by a silica layer. The increase in Si^{4+} indicates the first stage of dissolution by the breaking of the outer silica layers of the network. The solid silica dissolves in the form of monosilicic acid $Si(OH)_4$ to the solution resulting from breaking of Si-O-Si bonds and formation of Si-OH (silanols) groups, which act as nucleation sites of the apatite layer [25].

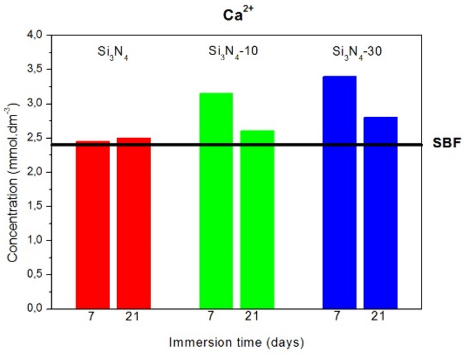

Fig. 7. Variation of Ca^{2+} concentration in SBF afte soaking the samples for 7 and 21 days.

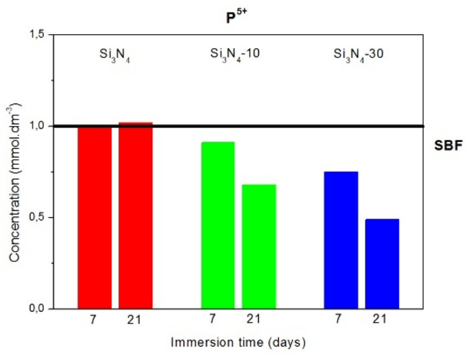

Fig. 8. Variation of P^{5+} concentration in SBF aft soaking the samples for 7 and 21 days.

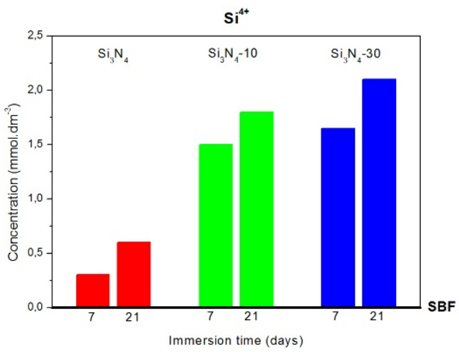

Fig. 9. Variation of Si^{4+} concentration in SBF after soaking the samples for 7 and 21 days

3.5 FTIR spectroscopy

In Fig. 10 and Fig. 11 can be seen FTIR spectra of composites with 10 and 30% of bioglass after7 and 21 days of immersion in SBF. The presented spectra report the characteristic vibrations of silicon nitride, bioglass and newly formed hydroxyapatite. The most characteristic stretching vibration bands of silicon nitride were observed at 670 cm^{-1} (Si-N-Si) and at 880 cm^{-1} (Si-N). The group vibrations of Si-O-Si bending mode and Si-O stretching mode, in the regions of 550 cm^{-1} - 400 cm^{-1} and 1200 cm^{-1} - 850 cm^{-1} respectively are assigned to the nucleant agent, bioglass[27,28]. Bands at ~920 cm^{-1}and ~ 1030 cm^{-1} are attributed to P-O stretching vibration due to formation of hydroxyapatite (HA) layer on the surface of composites exposed to the SBF solution. Development of HA is also confirmed by the rise of peaks at ~560 cm^{-1} and ~ 590 cm^{-1} assigned to P-O bending vibration mode [29].

FTIR spectra of Si_3N_4-10 sample after 7 and 21 days of immersion in SBF, presented in Fig. 10 are almost identical while the spectra obtained from Si_3N_4-30 sample after 7 and 21 days in SBF (Fig 11) are slightly different. The characteristic peak of HA near 560 cm^{-1} belongs to the P-O bending vibration becomes stronger after 21 days test (solid curve) and is shifted to the characteristic peak position of pure HA (560 cm^{-1}).

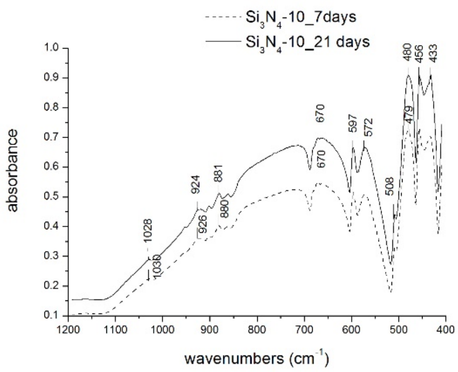

Fig. 10. FTIR spectra of Si_3N_4-10 sample after 7 (dashed curve) and 21 days (solid curve) of immersi in SBF.

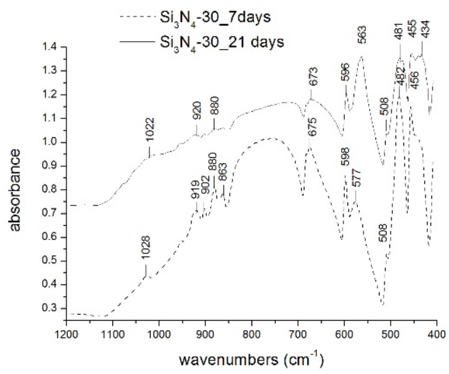

Fig. 11. FTIR spectra of Si_3N_4-30 sample after 7(dasl curve) and 21 days (solid curve) of immersion in SBl

4. Conclusion

Novel Si_3N_4 – bioglass composites (with 10 and 30 wt% of bioglass) were prepared using free sintering at 980 °C. Bioglass, with the similar composition to Bioglass® 45S5, was prepared using sol-gel method. Bioactive glass plays the role of sintering additive which partially supports the sintering of composite but mainly promotes the bioactivity of prepared materials. The bioactive behavior was confirmed by immersion of composites in simulated body fluid for different time period whereby the hydroxyapatite layer was developed on their surface. The presence of the hydroxyapatite was assessed by means of SEM and FTIR and also ICP analysis of the leachates shown the changes in Ca^{2+}, P^{5+} and Si^{4+} concentration of the SBF due to the hydroxyapatite formation. The bioglass-free sample prepared as a reference material exhibited no bioactivity which clearly confirmed the positive effect of bioglass addition.

Acknowledgments

This work was supported by project ‘‘Excellent young researcher at BUT’’No. CZ.1.07./2.3.00/30.0039 and No. CZ.1.07/2.3.00/30.0005.

References

[1] C.C. Sorell, P.H. Hardcastle, R.K. Druitt, E.R. Mc Cartney, in: A. Ravaglioli, A. Krajewski (Eds.), Proceedings 5th Meeting and seminar on: Implants for spine, ceramics, cell and tissue annual conferences, ISTEC-CNR, Faenza, Italy, 1999, pp. 47.

[2] Y.S. Zhou, K. Ikeuchi, M. Ohashi, Comparison of the friction properties of four ceramic materials for joint replacements, Wear 210 (1997) 171-177.

[3] M. Amaral, M. A. Lopez, R.F. Silva, J.D Santos, Densification route and mechanical properties of Si_3N_4-bioglass biocomposites, Biomaterial 23 (2002) 857-862.

[4] H.R Maier, C. Ragoss, M. Held, T. Reske, A. Neumann, K. Jahnke, Design and biocompatibility aspects of a minifixation system from Si_3N_4 for osteosynthesis, cfi/Ber. DKG81(2004) 33-38.

[5] Y.S. Zhou, N. Tomita, K. Ikeuchi, M. Ohashi, K. Takashima, Study on the possibility of silicon nitride – silicon nitride as a material for hip prostheses, Mater. Sci. Eng.: C 5 (1977) 125-129.

[6] A. Neumann, M. Kramps, C. Ragoss, H. R. Maier, K. Jahnke, Histological and microradiographic appearances of silicon nitride and aluminium oxide in a rabit femur implantation model, Materialwiss. Werkst. 35 (2004) 569-573.

[7] K. Olsson, J. Li, L. Urban, EP Patent No. 1064238, 2003.

[8] C.C. Guedes e Silva, O.Z. Higa, J.C. Bressiani, Cytotoxic evaluation of silicon nitride based ceramics, Mater. Sci. Eng.: C 24 (2004) 643-646.

[9] M. Mazzochi, A. Bellosi, On the possibility of silicon nitride as a ceramic for structural orthopaedic implants, Part I: processing, microstructure, mechanical properties, cytotoxicity, J. Mater. Sci. 19 (2008), 2881-2887.

[10] P. Saravanapavan, J.R. Jones, R. S. Pryce, L.L. Hench, Bioactivity of gel-glass powder in the CaO-SiO_2 system: A comparison with ternary (CaO-P_2O_5-SiO_2) and quaternary glasses (SiO_2-CaO-P_2O_5-Na_2O), J. Biomed. Mater. Res. Part A 66 (1) (2003) 110-119.

[11] M.N. Rahaman, D.E. Day, B. Sonny Bal, Q. Fu, S.B. Jung, L.F. Bonewald, A.P. Tomsia, Bioaactive glass in tissue engineering, ActaBiomat. 7 (2011) 2355-2373.

[12] L.L. Hench, J. Wilson, Introduction, In. L.L. Hench, J. Wilson (Eds.), Introduction to bioceramics, Singapore: World Scientific, 1993, pp.1-17.

[13] L.L. Hench,J.K. West, Biological applications of bioactive glasses, Life Chem. Rep. 13 (1996) 187-241.

[14] L.L Hench, R.J. Splinter, W.C. Allen, Bonding mechanism at the interface of ceramic prosthetic materials, J. Biomed. Mater. Res. 2 (1971) 117-141.

[15] J.D. Santos, M. Amaral, S.M. Oliveira, M.A. Lopes, R.F. Silva, Silicon Nitride – bioglass® 45S5 composite for biomedical applications, Key Eng. Mat. 192-195 (2001) 589-592.

[16] Q.-Z. Chen, Y. Li, L.-Y. Jin, J.M.W. Quinn, P.A. Komesaroff, A new sol-gel process for producing Na_2O-containing bioactive glass ceramics, ActaBiomat. 6 (2010) 4143-4153.

[17] O. PeitlFilho, G.P. LaTorre, L.L. Hench, Effect of crystallization on apatite-layer formation of bioactive glass 45S5, J. Biomed. Mater. Res. 30 (1996) 509-514.

[18] O. PeitlFilho, E.D. Zanotto, L.L. Hench, Highly bioactive $P_2O_5 – Na_2O – CaO – SiO_2$ glass ceramics, J. Non.-Cryst. Solid 292 (2001) 115-126.

[19] D.C Clupper, J.J. Mecholsky Jr., G.P. LaTorre, D.C. Greenspan, Sintering temperature effects on the in vivo bioactive response of tape cast and sintered bioactive glass-ceramic in Tris buffer, J. Biomed. Mater. Res. 57 (2001) 532-540.

[20] D.C Clupper, J.J. Mecholsky Jr., G.P. LaTorre, D.C. Greenspan, Bioactivity oftape cast and sintered bioactive glass-ceramic in simulated body fluid, Biomaterials 23(2002) 2599-2606.

[21] T. Kokubo,H. Takadama, How useful is SBF in predicting in vivo bone bioactivity? Biomaterias27 (2006) 2907-2915.

[22] D.C. Clupper, L.L. Hench, Crystallization kinetics of tape cast bioactive glass 45S5, J. Non-Cryst. Solids 318 (2003) 43-48.

[23] S. Hampshire, Silicon nitride ceramics - review of structure, processing and properties, J. Achiev. Mater. Manuf. 24/1 (2007) 43-50.

[24] Y.W. Gu, K.A. Khor, P. Cheang, In vitro studies of plasma-sprayed hydroxyapatite/Ti-6Al-4V composite coatings in simulated body fluid (SBF), Biomaterials 24 (2003) 1603-1611.

[25] L.L Hench, Bioceramics: From concept to clinic, J. Am. Ceram. Soc. 74 (11) (1991) 1487-1510.

[26] P.B. Malafaya, G.A. Silva, R.L. Reis, Natural-origin polymers as carriers and scaffolds for biomolecules and cell delivery in tissue engineering applications, Adv. Drug. Deliver. Rev. 59 (2007) 207-203.

[27] T. Kokubo, H. Kushitani, S. Sakka, T. Kitsugi, T. Yamamuro, Solutions able to reproduce in vivo surface-structure changes in bioactive glass-ceramic A-W, J. Biomed. Mater. Res. 24 (1990) 721-734.

[28] M. Ogino, F. Ohuchi, L.L. Hench, Compositional dependence of the formation of calcium phosphate films on bioglass, J. Biom. Mater. Res. 14 (1980) 55-64.

[29] X. Chatzistavrou, N. Kantiranis, E. Kontonasaki, K. Chrissafis, L. Papadopoulou, P. Koidis, A.R. Boccaccini, K.M. Paraskevopoulos, Thermal analysis and in vivo bioactivity of bioactive glass-alumina composites, Mater. Charact. 62 (2011) 118-129.

The Impact Induced 2:1 Internal Resonance in a Nonlinear Doubly Curved Shallow Shell with Rectangular Base

Yury Rossikhin[1,a], Marina Shitikova[1,b*] and Muhammed Salih Khalid J.M.[1,2,c]

[1]Research Center of Wave Dynamics, Voronezh State University of Architecture and Civil Engineering, Voronezh 394006, Russia

[2] on leave from the Ministry of Higher Education of Iraq, Iraq

[a]yar@vgasu.vrn.ru , [b]mvs@vgasu.vrn.ru , [c]Khalid_bus@yahoo.com

* the corresponding author

Keywords: Doubly curved shallow shell rectangular in base, method of multiple time scales, two-to-one-to-one internal resonance, impact induced resonance

Abstract. Large amplitude (geometrically nonlinear) vibrations of doubly curved shallow shells with rectangular base under the low-velocity impact by an elastic sphere are investigated when only two natural modes of vibrations dominate during the process of impact and the two-to-one internal resonance is induced by the falling impactor. It is assumed that the shell is simply supported and partial differential equations are obtained in terms of shell's transverse displacement and Airy's stress function. The local bearing of the shell and impactor's materials is neglected with respect to the shell deflection in the contact region. The equations of motion are reduced to a set of infinite nonlinear ordinary differential equations of the second order in time and with cubic and quadratic nonlinearities in terms of the generalized displacements. The time dependence of the contact force is found, resulting in the determination of the contact duration and the maximal contact force.

Introduction

Doubly curved panels are widely used in aeronautics, aerospace and civil engineering and are subjected to dynamic loads that can cause vibration amplitude of the order of the shell thickness, giving rise to significant nonlinear phenomena [1-4].

A review of the literature devoted to dynamic behavior of curved panels and shells could be found in [5], wherein it has been emphasized that free vibrations of doubly curved shallow shells were studied in the majority of papers either utilizing a slightly modified version of the Donnell theory taking into account the double curvature [1] or the nonlinear first-order theory of shells [5, 6].

Large-amplitude vibrations of doubly curved shallow shells with rectangular base, simply supported at the four edges and subjected to harmonic excitation were investigated in [3], while chaotic vibrations were analyzed in [4]. It has been revealed that such an important nonlinear phenomenon as the occurrence of internal resonances in the problems considered in [3] and [4] is of fundamental importance in the study of curved shells.

In spite of the fact that the impact theory is substantially developed, there is a limited number of papers devoted to the problem of impact over geometrically nonlinear shells [7-10].

In the present paper, a new approach is proposed for the analysis of the impact interactions of nonlinear doubly curved shallow shells with rectangular base under the low-velocity impact by an elastic sphere. It is assumed that the shell is simply supported and partial differential equations are obtained in terms of shell transverse displacement and Airy stress function. The local bearing of the shell and impactor materials is neglected with respect to the shell deflection in the contact region. The equations of motion are reduced to a set of infinite nonlinear ordinary differential equations of the second order in time with cubic and quadratic nonlinearities in terms of the generalized displacements. Assuming that only two natural modes of vibrations dominate during impact and applying the method of multiple time scales, the set of dynamic equations is obtained, which allows one to investigate a new nonlinear phenomenon resulting in the 2:1 internal resonance induced by the impactor and to find the time dependence of the contact force.

Problem Formulation and Governing Equations

Assume that an elastic or rigid sphere of mass M moves along the z-axis towards a thin walled doubly curved shell with thickness h, curvilinear lengths a and b, principle curvatures k_x and k_y and rectangular base. Impact occurs at the moment $t=0$ with the velocity εV_0 (ε is a small value) at the point N with Cartesian coordinates x_0, y_0.

According to Donnell's nonlinear shallow shell theory, the equations of motion could be obtained in terms of lateral deflection w and Airy's stress function φ [2]

$$\frac{D}{h}\left(\frac{\partial^4 w}{\partial x^4}+2\frac{\partial^4 w}{\partial x^2\partial y^2}+\frac{\partial^4 w}{\partial y^4}\right)=\frac{\partial^2 w}{\partial x^2}\frac{\partial^2 \varphi}{\partial y^2}+\frac{\partial^2 w}{\partial y^2}\frac{\partial^2 \varphi}{\partial x^2}-2\frac{\partial^2 w}{\partial x\partial y}\frac{\partial^2 \varphi}{\partial x\partial y}+k_y\frac{\partial^2 \varphi}{\partial x^2}+k_x\frac{\partial^2 \varphi}{\partial y^2}+\frac{F}{h}-\rho\ddot{w}, \quad (1)$$

$$\frac{1}{E}\left(\frac{\partial^4 \varphi}{\partial x^4}+2\frac{\partial^4 \varphi}{\partial x^2\partial y^2}+\frac{\partial^4 \varphi}{\partial y^4}\right)=-\frac{\partial^2 w}{\partial x^2}\frac{\partial^2 w}{\partial y^2}+\left(\frac{\partial^2 w}{\partial x\partial y}\right)^2-k_y\frac{\partial^2 w}{\partial x^2}-k_x\frac{\partial^2 w}{\partial y^2}, \quad (2)$$

where $D=\dfrac{Eh^3}{12(1-\nu^2)}$ is the cylindrical rigidity, ρ is the density, E and ν are the elastic modulus and Poisson's ratio, respectively, t is time, $F=P(t)\delta(x-x_0)\delta(y-y_0)$ is the contact force, $P(t)$ is yet unknown function, δ is the Dirac delta function, x and y are Cartesian coordinates, overdots denote time-derivatives, $\varphi(x,y)$ is the stress function which is the potential of the in-plane force resultants.

The equation of motion of the sphere is written as

$$M\ddot{z}=-P(t) \quad (3)$$

subjected to the initial conditions

$$z(0)=0, \qquad \dot{z}(0)=\varepsilon V_0, \quad (4)$$

where $z(t)$ is the displacement of the sphere, in so doing

$$z(t)=w(x_0,y_0,t). \quad (5)$$

Considering a simply supported a simply supported shell with movable edges, the following conditions should be imposed at each edge: at $x=0,a$

$$w=0,\ \int_0^b N_{xy}dy=0,\ N_x=0,\ M_x=0, \quad (6)$$

and at $y=0,b$

$$w=0,\ \int_0^a N_{xy}dx=0,\ N_y=0,\ M_y=0, \quad (7)$$

where M_x and M_y are the moment resultants, and N_x, N_y and N_{xy} are the in-plane force resultants.

The suitable trial function that satisfies the geometric boundary conditions is

$$w(x,y,t)=\sum_{p=1}\sum_{q=1}\xi_{pq}(t)\sin\left(\frac{p\pi x}{a}\right)\sin\left(\frac{q\pi y}{b}\right), \quad (8)$$

where p and q are the number of half-waves in x and y directions, respectively, and $\xi_{pq}(t)$ are the generalized coordinates. Substituting (8) in (5) and using (3), we obtain

$$P(t)=-M\sum_{p=1}^{\tilde{p}}\sum_{q=1}^{\tilde{q}}\ddot{\xi}_{pq}(t)\sin\left(\frac{p\pi x_0}{a}\right)\sin\left(\frac{q\pi y_0}{b}\right). \quad (9)$$

ISBN: 978-1-61804-295-8

In order to find the solution of the set of Eqs. 1 and 2, it is necessary first to obtain the solution of Eq. 2. For this purpose, let us substitute (8) in the right-hand side of Eq. 2 and seek the solution of the equation obtained in the form

$$\varphi(x,y,t)=\sum_{m=1}^{\tilde{m}}\sum_{n=1}^{\tilde{n}}A_{mn}(t)\sin\left(\frac{m\pi x}{a}\right)\sin\left(\frac{n\pi y}{b}\right), \tag{10}$$

where $A_{mn}(t)$ are yet unknown functions.

Substituting (8) and (10) in Eq. 2 and using the orthogonality conditions of sines within the segments $0\le x\le a$ and $0\le y\le b$, we have [11]

$$A_{mn}(t)=\frac{E}{\pi^2}K_{mn}\xi_{mn}(t)+\frac{4E}{a^3b^3}\left(\frac{m^2}{a^2}+\frac{n^2}{b^2}\right)^{-2}\sum_k\sum_l\sum_p\sum_q B_{pqklmn}\xi_{pq}(t)\xi_{kl}(t), \tag{11}$$

where

$$B_{pqklmn}=pqklB^{(2)}_{pqklmn}-p^2l^2B^{(1)}_{pqklmn},\quad K_{mn}=\left(k_y\frac{m^2}{a^2}+k_x\frac{n^2}{b^2}\right)^2\left(\frac{m^2}{a^2}+\frac{n^2}{b^2}\right)^{-2}$$

$$B^{(1)}_{pqklmn}=\int_0^a\int_0^b\sin\left(\frac{p\pi x}{a}\right)\sin\left(\frac{q\pi y}{b}\right)\sin\left(\frac{k\pi x}{a}\right)\sin\left(\frac{l\pi y}{b}\right)\sin\left(\frac{m\pi x}{a}\right)\sin\left(\frac{n\pi y}{b}\right)dxdy, \tag{12}$$

$$B^{(2)}_{pqklmn}=\int_0^a\int_0^b\cos\left(\frac{p\pi x}{a}\right)\cos\left(\frac{q\pi y}{b}\right)\cos\left(\frac{k\pi x}{a}\right)\cos\left(\frac{l\pi y}{b}\right)\sin\left(\frac{m\pi x}{a}\right)\sin\left(\frac{n\pi y}{b}\right)dxdy.$$

Substituting then Eqs. 9-12 in Eq. 1 and using the orthogonality condition of sines within the segments $0\le x\le a$ and $0\le y\le b$, we obtain an infinite set of coupled nonlinear ordinary differential equations of the second order in time for defining the generalized coordinates

$$\begin{aligned}\ddot{\xi}_{mn}(t)\ &+\ \Omega^2_{mn}\xi_{mn}(t)+\frac{8\pi^2E}{a^3b^3\rho}\sum_p\sum_q\sum_k\sum_l B_{pqklmn}\left(K_{kl}-\frac{1}{2}K_{mn}\right)\xi_{pq}(t)\xi_{kl}(t)\\ &+\ \frac{32\pi^4E}{a^6b^6\rho}\sum_r\sum_s\sum_i\sum_j\sum_k\sum_l\sum_p\sum_q B_{rsijmn}B_{pqklij}\xi_{rs}(t)\xi_{pq}(t)\xi_{kl}(t)\\ &+\ \frac{4M}{ab\rho h}\sin\left(\frac{m\pi x_0}{a}\right)\sin\left(\frac{n\pi y_0}{b}\right)\sum_p\sum_q\ddot{\xi}_{pq}(t)\sin\left(\frac{p\pi x_0}{a}\right)\sin\left(\frac{q\pi y_0}{b}\right)=0,\end{aligned} \tag{13}$$

where Ω^2_{mn} are natural frequencies of the target defined as

$$\Omega^2_{mn}=\frac{E}{\rho}\left[\frac{\pi^4h^2}{12(1-\nu^2)}\left(\frac{m^2}{a^2}+\frac{n^2}{b^2}\right)^2+K_{mn}\right]. \tag{14}$$

The last term in each equation from the set of Eqs. 13 describes the influence of the coupled impact interaction of the target with the impactor of the mass M applied at the point with the coordinates x_0, y_0.

In order to study this additional nonlinear phenomenon induced by the coupled impact interaction, we suppose that only two natural modes of vibrations are excited during the process of impact, namely, $\Omega_{\alpha\beta}$ and $\Omega_{\gamma\delta}$. Then the set of Eqs. 13 is reduced to the following two nonlinear differential equations:

$$p_{11}\ddot{\xi}_{\alpha\beta}+p_{12}\ddot{\xi}_{\gamma\delta}+\Omega^2_{\alpha\beta}\xi_{\alpha\beta}+p_{13}\xi^2_{\alpha\beta}+p_{14}\xi^2_{\gamma\delta}+p_{15}\xi_{\alpha\beta}\xi_{\gamma\delta}+p_{16}\xi^3_{\alpha\beta}+p_{17}\xi_{\alpha\beta}\xi^2_{\gamma\delta}=0, \tag{15}$$

$$p_{21}\ddot{\xi}_{\alpha\beta}+p_{22}\ddot{\xi}_{\gamma\delta}+\Omega^2_{\gamma\delta}\xi_{\gamma\delta}+p_{23}\xi^2_{\gamma\delta}+p_{24}\xi^2_{\alpha\beta}+p_{25}\xi_{\alpha\beta}\xi_{\gamma\delta}+p_{26}\xi^3_{\gamma\delta}+p_{27}\xi^2_{\alpha\beta}\xi_{\gamma\delta}=0, \tag{16}$$

where

$$p_{11}=1+\frac{4M}{\rho hab}s_1^2,\quad p_{22}=1+\frac{4M}{\rho hab}s_2^2,\quad p_{12}=p_{21}=\frac{4M}{\rho hab}s_1s_2,\quad s_1=\sin\left(\frac{\alpha\pi x_0}{a}\right)\sin\left(\frac{\beta\pi y_0}{b}\right),$$

ISBN: 978-1-61804-295-8

$$s_2 = \sin\left(\frac{\gamma\pi x_0}{a}\right)\sin\left(\frac{\delta\pi y_0}{b}\right), \quad p_{13} = \frac{8\pi^2 E}{a^3 b^3 \rho} B_{\alpha\beta\alpha\beta\alpha\beta}\frac{1}{2}K_{\alpha\beta}, \quad p_{14} = \frac{8\pi^2 E}{a^3 b^3 \rho} B_{\gamma\delta\gamma\delta\alpha\beta}\left(K_{\gamma\delta} - \frac{1}{2}K_{\alpha\beta}\right),$$

$$p_{15} = \frac{8\pi^2 E}{a^3 b^3 \rho}\left[B_{\gamma\delta\alpha\beta\alpha\beta}\frac{1}{2}K_{\alpha\beta} + B_{\alpha\beta\gamma\delta\alpha\beta}\left(K_{\gamma\delta} - \frac{1}{2}K_{\alpha\beta}\right)\right], \quad p_{23} = \frac{8\pi^2 E}{a^3 b^3 \rho} B_{\alpha\beta\alpha\beta\gamma\delta}\left(K_{\alpha\beta} - \frac{1}{2}K_{\gamma\delta}\right),$$

$$p_{24} = \frac{8\pi^2 E}{a^3 b^3 \rho} B_{\gamma\delta\gamma\delta\gamma\delta}\frac{1}{2}K_{\gamma\delta}, \quad p_{25} = \frac{8\pi^2 E}{a^3 b^3 \rho}\left[B_{\alpha\beta\gamma\delta\gamma\delta}\frac{1}{2}K_{\gamma\delta} + B_{\gamma\delta\alpha\beta\gamma\delta}\left(K_{\alpha\beta} - \frac{1}{2}K_{\gamma\delta}\right)\right],$$

$$p_{16} = \frac{32\pi^2 E}{a^3 b^3 \rho}\sum_i\sum_j B_{\alpha\beta ij\alpha\beta}B_{\alpha\beta\alpha\beta ij}, \quad p_{26} = \frac{32\pi^2 E}{a^3 b^3 \rho}\sum_i\sum_j B_{\gamma\delta ij\gamma\delta}B_{\gamma\delta\gamma\delta ij},$$

$$p_{17} = \frac{32\pi^2 E}{a^3 b^3 \rho}\sum_i\sum_j\left(B_{\alpha\beta ij\alpha\beta}B_{\gamma\delta\gamma\delta ij} + B_{\gamma\delta ij\alpha\beta}B_{\alpha\beta\gamma\delta ij} + B_{\gamma\delta ij\alpha\beta}B_{\gamma\delta\alpha\beta ij}\right),$$

$$p_{27} = \frac{32\pi^2 E}{a^3 b^3 \rho}\sum_i\sum_j\left(B_{\alpha\beta ij\gamma\delta}B_{\gamma\delta\gamma\delta ij} + B_{\gamma\delta ij\gamma\delta}B_{\alpha\beta\gamma\delta ij} + B_{\gamma\delta ij\gamma\delta}B_{\gamma\delta\alpha\beta ij}\right).$$

Method of solution

In order to solve a set of two nonlinear Eqs. 15 and 16, we apply the method of multiple time scales [12] via the following expansions:

$$\xi_{\alpha\beta}(t) = \varepsilon X^1_{\alpha\beta}(T_0, T_1) + \varepsilon^2 X^2_{\alpha\beta}(T_0, T_1), \qquad \xi_{\gamma\delta}(t) = \varepsilon X^1_{\gamma\delta}(T_0, T_1) + \varepsilon^2 X^2_{\gamma\delta}(T_0, T_1), \tag{17}$$

where $T_n = \varepsilon^n t$ are new independent variables, among them: $T_0 = t$ is a fast scale characterizing motions with the natural frequencies, and $T_1 = \varepsilon t$ is a slow scale characterizing the modulation of the amplitudes and phases of the modes with nonlinearity. Considering that

$$\frac{d^2}{dt^2}\xi_{ij} = \varepsilon\left(D_0^2 X^1_{ij}\right) + \varepsilon^2\left(D_0^2 X^2_{ij} + 2D_0 D_1 X^1_{ij}\right),$$

where $ij = \alpha\beta$ or $\gamma\delta$, and $D_i^n = \partial^n / \partial T_i^n$ ($n = 1,2,\ i = 0,1$), and substituting the proposed solution (17) in (15) and (16), after equating the coefficients at like powers of ε to zero, we are led to a set of recurrence equations to various orders:

to order ε

$$p_{11}D_0^2 X_1^1 + p_{12}D_0^2 X_2^1 + \Omega_1^2 X_1^1 = 0, \qquad p_{21}D_0^2 X_1^1 + p_{22}D_0^2 X_2^1 + \Omega_2^2 X_2^1 = 0; \tag{18}$$

to order ε^2

$$p_{11}D_0^2 X_1^2 + p_{12}D_0^2 X_2^2 + \Omega_1^2 X_1^2 = -2p_{11}D_0 D_1 X_1^1 - 2p_{12}D_0 D_1 X_2^1 - p_{13}(X_1^1)^2 - p_{14}(X_2^1)^2 - p_{15}X_1^1 X_2^1, \tag{19}$$

$$p_{21}D_0^2 X_1^2 + p_{22}D_0^2 X_2^2 + \Omega_2^2 X_2^2 = -2p_{21}D_0 D_1 X_1^1 - 2p_{22}D_0 D_1 X_2^1 - p_{23}(X_1^1)^2 - p_{24}(X_2^1)^2 - p_{25}X_1^1 X_2^1, \tag{20}$$

where for simplicity is it denoted $X_1^1 = X_{\alpha\beta}^1$, $X_2^1 = X_{\gamma\delta}^1$, $X_1^2 = X_{\alpha\beta}^2$, $X_2^2 = X_{\gamma\delta}^2$, $\Omega_1 = \Omega_{\alpha\beta}$, and $\Omega_2 = \Omega_{\gamma\delta}$.

Solution of equations at order of ε. Following [11], we seek the solution of Eqs. 18 in the form:

$$X_1^1 = A_1(T_1)e^{i\omega_1 T_0} + A_2(T_1)e^{i\omega_2 T_0} + \mathrm{cc}, \qquad X_2^1 = \alpha_1 A_1(T_1)e^{i\omega_1 T_0} + \alpha_2 A_2(T_1)e^{i\omega_2 T_0} + \mathrm{cc}, \tag{21}$$

where $A_1(T_1)$ and $A_2(T_1)$ are unknown complex functions, cc is the complex conjugate part to the preceding terms, and $\overline{A}_1(T_1)$ and $\overline{A}_2(T_1)$ are their complex conjugates, ω_1 and ω_2 are unknown frequencies of the coupled process of impact interaction of the impactor and the target, and α_1 and α_2 are yet unknown coefficients.

ISBN: 978-1-61804-295-8

Substituting relationships (21) in Eqs. 17 and gathering the terms with $e^{i\omega_1 T_0}$ and $e^{i\omega_2 T_0}$ yields

$$\left(-p_{11}\omega_1^2 - p_{12}\alpha_1\omega_1^2 + \Omega_1^2\right)A_1 e^{i\omega_1 T_0} + \left(-p_{11}\omega_2^2 - p_{12}\alpha_2\omega_2^2 + \Omega_1^2\right)A_2 e^{i\omega_2 T_0} + \text{cc} = 0, \tag{22}$$

$$\left(-p_{21}\omega_1^2 - p_{22}\alpha_1\omega_1^2 + \alpha_1\Omega_2^2\right)A_1 e^{i\omega_1 T_0} + \left(-p_{21}\omega_2^2 - p_{22}\alpha_2\omega_2^2 + \Omega_2^2\alpha_2\right)A_2 e^{i\omega_2 T_0} + \text{cc} = 0. \tag{23}$$

In order to satisfy Eqs. 22 and 23, it is a need to vanish to zero each bracket in these equations. As a result, from four different brackets we have

$$\alpha_1 = -\frac{p_{11}\omega_1^2 - \Omega_1^2}{p_{12}\omega_1^2}, \qquad \alpha_1 = -\frac{p_{21}\omega_1^2}{p_{22}\omega_1^2 - \Omega_2^2}, \tag{24}$$

$$\alpha_2 = -\frac{p_{11}\omega_2^2 - \Omega_1^2}{p_{12}\omega_2^2}, \qquad \alpha_2 = -\frac{p_{21}\omega_2^2}{p_{22}\omega_2^2 - \Omega_2^2}. \tag{25}$$

Since the left-hand side parts of Eqs. 24 as well as 25 are equal, then their right-hand side parts should be equal as well. Now equating the corresponding right-hand side parts of Eqs. 24 and 25, we are led to one and the same characteristic equation for determining the frequencies ω_1 and ω_2:

$$\left(\Omega_1^2 - p_{11}\omega^2\right)\left(\Omega_2^2 - p_{22}\omega^2\right) - p_{12}^2\omega^4 = 0, \tag{26}$$

whence it follows that

$$\omega_{1,2}^2 = \frac{\left(p_{22}\Omega_1^2 + p_{11}\Omega_2^2\right) \pm \sqrt{\Delta}}{2\left(p_{11}p_{22} - p_{12}^2\right)}, \qquad \Delta = \left(p_{22}\Omega_1^2 - p_{11}\Omega_2^2\right)^2 + 4\Omega_1^2\Omega_2^2 p_{12}^2. \tag{27}$$

Solution of equations at order of ε^2 at two-to-one internal resonance. Now substituting (21) in Eqs. 19 and 20, we obtain

$$\begin{aligned} p_{11}D_0^2 X_1^2 + p_{12}D_0^2 X_2^2 + \Omega_1^2 X_1^2 &= -2i\omega_1(p_{11} + \alpha_1 p_{12})e^{i\omega_1 T_0}D_1A_1 - 2i\omega_2(p_{11} + \alpha_2 p_{12})e^{i\omega_2 T_0}D_1A_2 \\ &-(p_{13} + \alpha_1^2 p_{14} + \alpha_1 p_{15})A_1\left[A_1 e^{2i\omega_1 T_0} + \bar{A}_1\right] - (p_{13} + \alpha_2^2 p_{14} + \alpha_2 p_{15})A_2\left[A_2 e^{2i\omega_2 T_0} + \bar{A}_2\right] \\ &-2\left[p_{13} + \alpha_1\alpha_2 p_{14} + (\alpha_1 + \alpha_2)p_{15}\right]A_1\left[A_2 e^{i(\omega_1+\omega_2)T_0} + \bar{A}_2 e^{i(\omega_1-\omega_2)T_0}\right] + \text{cc}, \end{aligned} \tag{28}$$

$$\begin{aligned} p_{21}D_0^2 X_1^2 + p_{22}D_0^2 X_2^2 + \Omega_2^2 X_2^2 &= -2i\omega_1(p_{21} + \alpha_1 p_{22})e^{i\omega_1 T_0}D_1A_1 - 2i\omega_2(p_{21} + \alpha_2 p_{22})e^{i\omega_2 T_0}D_1A_2 \\ &-(p_{23} + \alpha_1^2 p_{24} + \alpha_1 p_{25})A_1\left[A_1 e^{2i\omega_1 T_0} + \bar{A}_1\right] - (p_{23} + \alpha_2^2 p_{24} + \alpha_2 p_{25})A_2\left[A_2 e^{2i\omega_2 T_0} + \bar{A}_2\right] \\ &-2\left[p_{23} + \alpha_1\alpha_2 p_{24} + (\alpha_1 + \alpha_2)p_{25}\right]A_1\left[A_2 e^{i(\omega_1+\omega_2)T_0} + \bar{A}_2 e^{i(\omega_1-\omega_2)T_0}\right] + \text{cc}. \end{aligned} \tag{29}$$

Reference to Eqs. 28 and 29 shows that the following two-to-one internal resonance could occur:

$$\omega_1 = 2\omega_2. \tag{30}$$

With due account for (30) Eqs. 28 and 29 could be rewritten in the following form:

$$p_{11}D_0^2 X_1^2 + p_{12}D_0^2 X_2^2 + \Omega_1^2 X_1^2 = B_1\exp(i\omega_1 T_0) + B_2\exp(i\omega_2 T_0) + \text{Reg} + \text{cc}, \tag{31}$$

$$p_{21}D_0^2 X_1^2 + p_{22}D_0^2 X_2^2 + \Omega_2^2 X_2^2 = B_3\exp(i\omega_1 T_0) + B_4\exp(i\omega_2 T_0) + \text{Reg} + \text{cc}, \tag{32}$$

where all regular terms are designated by Reg, and

$$B_1 = -2i\Omega_1^2\omega_1^{-1}D_1A_1 - \left(p_{13} + \alpha_2^2 p_{14} + \alpha_2 p_{15}\right)A_2^2,$$

ISBN: 978-1-61804-295-8

$$B_2 = -2i\Omega_1^2\omega_2^{-1}D_1A_2 - 2[p_{13} + \alpha_1\alpha_2 p_{14} + (\alpha_1 + \alpha_2)\, p_{15}]A_1\bar{A}_2,$$
$$B_3 = -2i\Omega_2^2\omega_1^{-1}\alpha_1 D_1 A_1 - \left(p_{23} + \alpha_2^2 p_{24} + \alpha_2 p_{25}\right)A_2^2,$$
$$B_4 = -2i\Omega_2^2\omega_2^{-1}\alpha_2 D_1 A_2 - 2[p_{23} + \alpha_1\alpha_2 p_{24} + (\alpha_1 + \alpha_2)\, p_{25}]A_1\bar{A}_2.$$

Let us show that the terms with the exponents $\exp(\pm i\omega_i T_0)$ ($i = 1,2$) produce circular terms. For this purpose we choose a particular solution in the form

$$X_{1p}^2 = C_1 \exp(i\omega_1 T_0) + \text{cc}, \qquad X_{2p}^2 = C_2 \exp(i\omega_1 T_0) + \text{cc}, \tag{33}$$

or

$$X_{1p}^2 = C_1' \exp(i\omega_2 T_0) + \text{cc}, \qquad X_{2p}^2 = C_2' \exp(i\omega_2 T_0) + \text{cc}, \tag{34}$$

where C_1, C_2 and C_1', C_2' are arbitrary constants.

Substituting the proposed solution in Eqs. 31 and 32, we are led to the following sets of equations, respectively:

$$\begin{cases} p_{12}\omega_1^2\left(\alpha_1 C_1 - C_2\right) = B_1, \\ p_{21}\omega_1^2\left(-C_1 + \dfrac{1}{\alpha_1}C_2\right) = B_3, \end{cases} \tag{35}$$

or

$$\begin{cases} p_{12}\omega_2^2\left(\alpha_2 C_1' - C_2'\right) = B_2, \\ p_{21}\omega_2^2\left(-C_1' + \dfrac{1}{\alpha_2}C_2'\right) = B_4. \end{cases} \tag{36}$$

From the sets of Eqs. 35 and 36 it is evident that the determinants comprised from the coefficients standing at C_1, C_2 and C_1', C_2' are equal to zero, therefore, it is impossible to determine the arbitrary constants C_1, C_2 and C_1', C_2' of the particular solutions (33) and (34), what proves the above proposition concerning the circular terms.

In order to eliminate the circular terms, the terms proportional to $e^{i\omega_1 T_0}$ and $e^{i\omega_2 T_0}$ should be vanished to zero putting $B_i = 0$ ($i = 1,2,3,4$). So we obtain four equations for defining two unknown amplitudes $A_1(t)$ and $A_2(t)$. However, it is possible to show that not all of these four equations are linear independent from each other.

For this purpose, let us first apply the operators $(p_{22}D_0^2 + \Omega_2^2)$ and $(-p_{12}D_0^2)$ to Eqs. 31 and 32, respectively, and then add the resulting equations. This procedure will allow us to eliminate X_2^2. If we apply the operators $(-p_{12}D_0^2)$ and $(p_{11}D_0^2 + \Omega_1^2)$ to Eqs. 31 and 32, respectively, and then add the resulting equations. This procedure will allow us to eliminate X_1^2. Thus, we obtain

$$\begin{aligned} &\left[(p_{11}p_{22} - p_{12}^2)D_0^4 + (p_{11}\Omega_2^2 + p_{22}\Omega_1^2)D_0^2 + \Omega_1^2\Omega_2^2\right]X_1^2 = \left[(p_{22}D_0^2 + \Omega_2^2)B_1 - p_{12}D_0^2 B_3\right]\exp(i\omega_1 T_0) \\ &+ \left[(p_{22}D_0^2 + \Omega_2^2)B_2 - p_{12}D_0^2 B_4\right]\exp(i\omega_2 T_0) + \text{Reg+cc}, \end{aligned} \tag{37}$$

$$\begin{aligned} &\left[(p_{11}p_{22} - p_{12}^2)D_0^4 + (p_{11}\Omega_2^2 + p_{22}\Omega_1^2)D_0^2 + \Omega_1^2\Omega_2^2\right]X_2^2 = \left[-p_{12}D_0^2 B_1 + (p_{11}D_0^2 + \Omega_1^2)B_3\right]\exp(i\omega_1 T_0) \\ &+ \left[-p_{12}D_0^2 B_2 + (p_{11}D_0^2 + \Omega_1^2)B_4\right]\exp(i\omega_2 T_0) + \text{Reg+cc}. \end{aligned} \tag{38}$$

To eliminate the circular terms from Eqs. 37 and 38, it is necessary to vanish to zero the terms in each square bracket. As a result we obtain

$$\begin{cases} (\Omega_2^2 - p_{22}\omega_1^2)B_1 + p_{12}\omega_1^2 B_3 = 0 \\ p_{12}\omega_1^2 B_1 + (\Omega_1^2 - p_{11}\omega_1^2)B_3 = 0 \end{cases} \tag{39}$$

and

$$\begin{cases}(\Omega_2^2 - p_{22}\omega_2^2)B_2 + p_{12}\omega_2^2 B_4 = 0 \\ p_{12}\omega_2^2 B_2 + (\Omega_1^2 - p_{11}\omega_2^2)B_4 = 0\end{cases} \tag{40}$$

From Eqs. 39 and 40 it is evident that the determinant of each set of equations is reduced to the characteristic Eq. 26, whence it follows that each pair of equations is linear dependent, therefore for further treatment we should take only one equation from each pair in order that these two chosen equations are to be linear independent. Thus, for example, taking the first equations from each pair, we have

$$2i\omega_1 k_1 D_1 A_1 + b_1 A_2^2 = 0, \tag{41}$$

$$2i\omega_2 k_2 D_1 A_2 + b_2 A_1 \bar{A}_2 = 0, \tag{42}$$

where

$$k_i = \frac{\Omega_1^2 + \alpha_i^2 \Omega_2^2}{\omega_i^2} \quad (i = 1,2), \qquad b_1 = p_{13} + \alpha_2^2 p_{14} + \alpha_2 p_{15} + \alpha_1 (p_{23} + \alpha_2^2 p_{24} + \alpha_2 p_{25}),$$

$$b_2 = 2\{p_{13} + \alpha_1\alpha_2 p_{14} + (\alpha_1 + \alpha_2) p_{15} + \alpha_2 [p_{23} + \alpha_1\alpha_2 p_{24} + (\alpha_1 + \alpha_2) p_{25}]\}.$$

Multiplying Eqs. 41 and 42 by $\bar{A}_1$ and $\bar{A}_2$, respectively, finding their complex conjugates, adding every pair of the mutually adjoint equations with each other and subtracting one from another, and representing $A_1(T_1)$ and $A_2(T_2)$ in the polar form

$$A_i(T_1) = a_i(T_1) e^{i\varphi_i(T_1)} \quad (i = 1,2), \tag{43}$$

we are led to a set of four nonlinear differential equations in $a_1(T_1)$, $a_2(T_1)$, $\varphi_1(T_1)$, and $\varphi_2(T_1)$

$$(a_1^2)^{\cdot} = -\frac{b_1}{k_1\omega_1} a_1 a_2^2 \sin\delta, \tag{44}$$

$$\dot{\varphi}_1 - \frac{b_1}{2k_1\omega_1} a_1^{-1} a_2^2 \cos\delta = 0, \tag{45}$$

$$(a_2^2)^{\cdot} = \frac{b_2}{k_2\omega_2} a_1 a_2^2 \sin\delta, \tag{46}$$

$$\dot{\varphi}_2 - \frac{b_2}{2k_2\omega_2} a_1 \cos\delta = 0, \tag{47}$$

where $\delta = 2\varphi_2 - \varphi_1$, and a dot denotes differentiation with respect to T_1.

It could be shown utilyzing the procedure suggested in [13] that the set of Eqs. 44-47 has two first integrals, namely: (1) the law of conservation of energy

$$MV_0 \left(\frac{b_2}{k_2\omega_2} a_1^2 + \frac{b_1}{k_1\omega_1} a_2^2 \right) = T_0, \tag{48}$$

and (2) the stream function $G(\delta, \xi)$ of the phase fluid on the plane $\delta\xi$

$$G(\delta, \xi) = \sqrt{\xi}(1 - \xi)\cos\delta = G_0(\delta_0, \xi_0), \tag{49}$$

where $T_0 = \frac{1}{2} MV_0^2$ is the initial energy, a new function $\xi(T_1)$ is connected with the amplitude functions by the following relationships:

$$a_1^2 = \frac{k_2\omega_2}{b_2}\frac{V_0}{2}\xi(T_1), \quad a_2^2 = \frac{k_1\omega_1}{b_1}\frac{V_0}{2}[1 - \xi(T_1)], \tag{50}$$

ISBN: 978-1-61804-295-8

in so doing the value ξ_0 ($0 \le \xi_0 \le 1$) governs the energy distribution between two subsystems, X_1^1 and X_2^1, at the moment of impact.

Initial conditions. In order to construct the final solution of the problem under consideration, i.e. to solve the set of Eqs. 44-47 involving the functions $a_1(T_1)$, $a_2(T_1)$, or $\xi(T_1)$, as well as $\varphi_1(T_1)$, and $\varphi_2(T_1)$, or $\delta(T_1)$, it is necessary to use the initial conditions

$$w(x,y,0)=0, \tag{51}$$

$$\dot{w}(x_0,y_0,0)=\varepsilon V_0, \tag{52}$$

$$\frac{b_2}{k_2\omega_2}a_1^2(0)+\frac{b_1}{k_1\omega_1}a_2^2(0)=\frac{V_0}{2}. \tag{53}$$

The two-term relationship for the displacement w (8) within an accuracy of ε according to (17) has the form

$$w(x,y,t)=\varepsilon\left[X_{\alpha\beta}^1(T_0,T_1)\sin\left(\frac{\alpha\pi x}{a}\right)\sin\left(\frac{\beta\pi y}{b}\right)+X_{\gamma\delta}^1(T_0,T_1)\sin\left(\frac{\gamma\pi x}{a}\right)\sin\left(\frac{\delta\pi y}{b}\right)\right]+O(\varepsilon^2). \tag{54}$$

Substituting (21) in (54) with due account for (43) yields

$$\begin{aligned}w(x,y,t)&=2\varepsilon\left\{a_1(\varepsilon t)\cos\left[\omega_1 t+\varphi_1(\varepsilon t)\right]+a_2(\varepsilon t)\cos\left[\omega_2 t+\varphi_2(\varepsilon t)\right]\right\}\sin\left(\frac{\alpha\pi x}{a}\right)\sin\left(\frac{\beta\pi y}{b}\right)\\&+2\varepsilon\left\{\alpha_1 a_1(\varepsilon t)\cos\left[\omega_1 t+\varphi_1(\varepsilon t)\right]+\alpha_2 a_2(\varepsilon t)\cos\left[\omega_2 t+\varphi_2(\varepsilon t)\right]\right\}\sin\left(\frac{\gamma\pi x}{a}\right)\sin\left(\frac{\delta\pi y}{b}\right)+O(\varepsilon^2)\end{aligned} \tag{55}$$

Differentiating Eq. 55 with respect to time t and limiting ourselves by the terms of the order of ε, we could find the velocity of the shell at the point of impact as follows

$$\begin{aligned}\dot{w}(x_0,y_0,t)&=-2\varepsilon\left\{\omega_1 a_1(\varepsilon t)\sin\left[\omega_1 t+\varphi_1(\varepsilon t)\right]+\omega_2 a_2(\varepsilon t)\sin\left[\omega_2 t+\varphi_2(\varepsilon t)\right]\right\}s_1\\&-2\varepsilon\left\{\alpha_1\omega_1 a_1(\varepsilon t)\sin\left[\omega_1 t+\varphi_1(\varepsilon t)\right]+\alpha_2\omega_2 a_2(\varepsilon t)\sin\left[\omega_2 t+\varphi_2(\varepsilon t)\right]\right\}s_2+O(\varepsilon^2).\end{aligned} \tag{56}$$

Substituting (55) in the first initial condition (51) yields

$$\varphi_1(0)=\pm\frac{\pi}{2},\quad \varphi_2(0)=\pm\frac{\pi}{2}, \tag{57}$$

and

$$\cos\delta_0=\cos\left[2\varphi_2(0)-\varphi_1(0)\right]=0,\ \text{or}\ \ \delta_0=\pm\frac{\pi}{2}\pm 2\pi n. \tag{58}$$

The signs in (57) should be chosen considering the fact that the initial amplitudes are positive values, i.e. $a_1(0)>0$ and $a_2(0)>0$. Assume for definiteness that

$$\varphi_1(0)=-\frac{\pi}{2},\quad \varphi_2(0)=\frac{\pi}{2}. \tag{59}$$

Considering (59), from Eqs. 52 and 53 we could determine the initial amplitudes

$$a_2(0)=\frac{\omega_1(s_1+\alpha_1 s_2)}{\omega_2(s_1+\alpha_2 s_2)}a_1(0)-\frac{V_0}{2\omega_2(s_1+\alpha_2 s_2)}, \tag{60}$$

$$c_1 a_1^2(0)+c_2 a_1(0)+c_3=0, \tag{61}$$

where

$$c_1 = 1 + \frac{b_1 k_2 \omega_1 (s_1 + \alpha_1 s_2)^2}{b_2 k_1 \omega_2 (s_1 + \alpha_2 s_2)^2}, \quad c_2 = \frac{b_1 k_2 (s_1 + \alpha_1 s_2) V_0}{b_2 k_1 \omega_2 (s_1 + \alpha_2 s_2)^2}, \quad c_3 = \frac{b_1 k_2 V_0^2}{4 b_2 k_1 \omega_1 \omega_2 (s_1 + \alpha_2 s_2)^2} - \frac{k_2 \omega_2 V_0}{2 b_2}.$$

Finally from (49) we find the value of the constant $G_0 = 0$. Thus, we have determined all necessary constants from the initial conditions, therefore we could proceed to the construction of the solution for the contact force.

Contact force. Substituting relationship (56) differentiated one time with respect to time t in Eq. 3, we could obtain the contact force $P(t)$

$$\begin{aligned} P(t) &= 2\varepsilon M \left\{ \omega_1^2 a_1(\varepsilon t) \cos\left[\omega_1 t + \varphi_1(\varepsilon t)\right] + \omega_2^2 a_2(\varepsilon t) \cos\left[\omega_2 t + \varphi_2(\varepsilon t)\right] \right\} s_1 \\ &+ 2\varepsilon M \left\{ \alpha_1 \omega_1^2 a_1(\varepsilon t) \cos\left[\omega_1 t + \varphi_1(\varepsilon t)\right] + \alpha_2 \omega_2^2 a_2(\varepsilon t) \cos\left[\omega_2 t + \varphi_2(\varepsilon t)\right] \right\} s_2 + O(\varepsilon^2). \end{aligned} \tag{62}$$

From Eqs. 45 and 47 it follows that

$$\varphi_1(T_1) = \text{const} = \varphi_1(0), \qquad \varphi_2(T_1) = \text{const} = \varphi_2(0). \tag{63}$$

Considering (63) and (30), Eq. 62 is reduced to

$$P(t) = 2\varepsilon M \omega_2^2 \{8(s_1 + \alpha_1 s_2) a_1(\varepsilon t) \cos\omega_2 t - (s_1 + \alpha_2 s_2) a_2(\varepsilon t)\} \sin\omega_2 t. \tag{64}$$

Substituting (50) in Eq. 64, we finally obtained

$$P(t) = \varepsilon M \omega_2^2 \sqrt{2V_0} \{8(s_1 + \alpha_1 s_2) \sqrt{\frac{k_2 \omega_2}{b_2}} \sqrt{\xi(\varepsilon t)} \cos\omega_2 t - (s_1 + \alpha_2 s_2) \sqrt{\frac{k_1 \omega_1}{b_1}} \sqrt{1 - \xi(\varepsilon t)}\} \sin\omega_2 t. \tag{65}$$

Since the duration of contact is a small value, then $P(t)$ could be calculated via an approximate formula, which is obtained from Eq. 64 at $\varepsilon t \approx 0$

$$P(t) \approx 16\varepsilon M \omega_2^2 (\cos\omega_2 t - \frac{1}{8} æ)(s_1 + \alpha_1 s_2) a_1(0) \sin\omega_2 t, \tag{66}$$

where $æ = \frac{(s_1 + \alpha_2 s_2)}{(s_1 + \alpha_1 s_2)} \frac{a_2(0)}{a_1(0)}$.

The dimensionless time $\tau = \omega_2 t$ dependence of the dimensionless contact force P^*

$$P^*(\tau) = \left(\cos\tau - \frac{1}{8} æ \right) \sin\tau, \tag{67}$$

where $P^*(\tau) = \frac{P(t)}{16\varepsilon M \omega_2^2 (s_1 + \alpha_1 s_2) a_1(0)}$, is shown in Fig. 1 for the different magnitudes of the parameter æ: 0.008, 1, 2, and 4. Reference to Fig. 1 shows that the decrease in the parameter æ results in the increase of both the maximal contact force and the duration of contact.

Conclusion

The procedure proposed in the present paper allows one to investigate the dynamic response of a nonlinear doubly curved shallow shell with rectangular base under the low-velocity impact by an elastic sphere. It has been assumed that the shell is simply supported and partial differential equations have been obtained in terms of shell's transverse displacement and Airy's stress function, in so doing the local bearing of the shell and impactor's materials was neglected with respect to the shell deflection in the contact region. The equations of motion have been reduced to a set of infinite nonlinear ordinary differential equations of the second order in time and with cubic and quadratic nonlinearities in terms of the generalized displacements. Assuming that only two natural modes of vibrations dominate during the process of impact and applying the method of multiple time scales, the set of equations has been obtained, which allows one to investigate the case of the impact induced two-to-one internal resonance and to find the time dependence of the contact force.

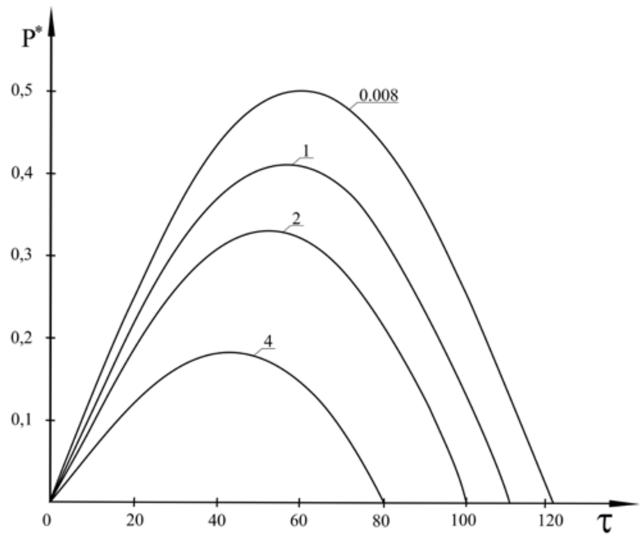

Figure 1. Dimensionless time dependence of the dimensionless contact force

Acknowledgment

This research was supported by the Grant No. 2014/19 as a Government task from the Ministry of Education and Science of the Russian Federation to Voronezh State University of Architecture and Civil Engineering.

Corresponding Author

Prof. M.V. Shitikova, MVS@vgasu.vrn.ru, +7-910-3450412

References

[1] A.W. Leissa and A.S. Kadi: J. Sound Vibr. Vol. 16 (1971), p. 173

[2] A.S. Volmir: *Nonlinear Dynamics of Plates and Shells* (in Russian). Nauka, Moscow (1972).

[3] M. Amabili: Int. J. Non-Linear Mech. Vol. 40 (2005)

[4] F. Alijani and M. Amabili: Int. J. Struct. Stability Dyn. Vol. 12 (2012) 1250047, 23 pages

[5] M. Amabili and M.P. Paidoussis: Appl. Mech. Rev. Vol. 56 (2003), p. 349), p.683

[6] C.Y. Chia: Ing-Archive Vol. 58 (1988), p. 252

[7] K. Chandrashekhara and T. Schoeder: J. Composite Mat. Vol. 29 (1995), p. 2160

[8] C. Cho, G. Zhao and C.B. Kim: KSME Int. J. Vol. 14 (2000), p. 666

[9] Y.M. Fu and Y.Q. Mao: Acta Materiae Compositae Sinica Vol. 25 (2008), p. 166

[10] S. Kumar: Struct. Eng. Mech. Vol. 35 (2010), p. 349

[11] Yu.A. Rossikhin, M.V. Shitikova and Salih Khalid J. M., in: *Recent Advances in Mathematical Methods in Applied Sciences*, edited byY.B. Senichenkov et al., volume 32 of Mathematics and Computers in Science and Engineering Series, Europment (2014), p.109

[12] A.H. Nayfeh: *Perturbation Methods*. Wiley, New York (1973).

[13] Yu.A. Rossikhin and M.V. Shitikova: Materials Science Forum vol. 440-441 (2003), p. 29

Preliminary Study on Fluidic Actuators. Design modifications.

D. del Campo; JM Bergada; V. del Campo.

***Abstract*—**As fluidic actuators have the advantage of lacking moving parts, their use in real applications brings high reliability. This is why, once having overcome their drawbacks, which means being able to provide the appropriate momentum and frequency, they could extensively be used in a wide range of applications. The present paper will present a CFD evaluation of the flow inside a fluidic oscillator. Initially a standard fluidic actuator will be simulated and the results compared with existing experimental data. In a second step, several geometric parameters will be modified; the actuator performance under these new conditions is reported. The paper aims to be an aid for future innovative oscillator designs.

***Keywords*—**Fluidic actuators design, CFD, flow control..

I. Introduction

FLOW control actuators have long been in the focus of research in the fluid mechanics field since they are able to reduce drag on bluff bodies, increase lift on airfoils or enhance mixing. However their performance in real applications, must assure reliability and long lifetime. Among the different existing actuators, ZNMF (zero net mass flow), plasma actuators, MEMS (Micro-Electro-Mechanical Systems), fluidic oscillators and combustion driven jet actuators [1,2], only the plasma, fluidic and pulsed combustion actuators do not have moving parts, which a priory give confidence regarding their reliability. At the moment, plasma actuators are not able to produce the needed momentum to modify the boundary layer in a real application, since it appears that the voltage differential used is not sufficiently ionizing the fluid to create the necessary fluid jet momentum. Pulsed combustion actuators provide a huge flow momentum, although, due to the combustion created temperatures, such actuators can just be used for very specific applications where high temperature fluid is tolerable. Fluidic oscillators, on the other hand, are able to produce a pulsating jet with the required momentum, although it appears their design needs to be adapted to each particular application. It must be taken into consideration that nowadays the use of MEMS is steadily increasing, especially in the microfluidics field [3,4], where small amount of flow is required. ZNMF actuators have been and are extensively studied and used, some relevant papers on development and applications are [5-9]. They provide enough momentum to modify the main flow boundary layer and thus to maintain high vorticity flux downstream. Despite the fact that they are widely used, their reliability might be compromised due to their moving parts.

Original fluidic actuators design goes back to the 60s and 70s, left nearly unchanged for over 40 years. The possible output frequency ranges from several Hz to KHz and the flow rate is usually of a few dm^3/min. Among their applications in flow control, it is worth to mention their use in combustion control [10-12], mixing enhancement and flow deflection [13], modifying flow separation in airfoils [14], boundary layer control on hump diffusers used in turbomachinery [15], flow separation control on stator vanes of compressors [16], drag reduction on trucks [17], and cavity noise reduction [18].

Following the present introduction it appears that fluidic actuators could be much widely used in the future, and it is according to the authors, worthy to better understand their behaviour in order to further improve their performance.

Regarding the fluidic oscillator design two main groups exist. The one based on Coanda effect [19], and the one based on a jet mixing chamber, also called vortex oscillators [20]. The former group had an early application as pressure, temperature and flow measuring devices [21-23], the latter group, has recently been applied as flow control devices [24].

Depending on the application to be used, fluidic actuators shall produce pulsating flow at a range of different frequencies and flow rates. To push forward such boundaries several fluidic oscillators designs have been recently created. Uzol and Camci [25] studied experimentally and by Computational Fluid Dynamics (CFD) a fluidic oscillator based on two elliptical cross-sections placed transversally and an afterbody located in front of them. Such configuration was in fact proposed by Bauer's patent [26,27]. The device operates at frequencies of around 30 Hz, and under laminar flow. The relation frequency versus Reynolds number was found to be perfectly linear.

Huang and Chang [28] performed a deep experimental study on a V-shaped fluidic oscillator, playing with the dimensions and the internal oscillator circular cavity, they defined the regimes under which oscillation was generated and they proved that

D.Del Campo. Lecturer at the Aerospace Department. Polytechnical University of Catalonia (UPC, ETSEIAT-Terrassa)
J.M.Bergada. Associate Professor at the Fluid Mechanics Department. Polytechnical University of Catalonia (UPC, ETSEIAT-Terrassa)
V.Del Campo. Lecturer at the Aerospace Department. Polytechnical University of Catalonia (UPC, ETSEIAT-Terrassa)

frequencies from few Hz to several KHz could be obtained by modifying oscillator parameters. Additionally, an analysis of the streamline patterns behind the oscillator was also presented. Khelfaoui et al [29], presented an experimental and numerical analysis of non-symmetrical mini and micro oscillators. The numerical analysis being based on a hybrid simulation, they simulated the central part of the oscillator by CFD, while the oscillator feedback was modelled analytically. They found a linear relationship between the actuator frequency and the feedback channel volume and noticed that above a certain input pressure choked flow appears. From this point on, the relation frequency versus pressure threshold difference decreased linearly. Gebhard et al [30] studied a micro-oscillator operated with water, finding a linear relationship between the output frequency and the input volumetric flow. Raman and Raghu [18] evaluated the decrease of a cavity tone by using fluidic oscillators. The main acoustic frequency was reduced by over 10 dB, concluding that fluidic excitation is a candidate in noise control applications. A numerical simulation of a two dimensional fluidic oscillator by using Navier-Stokes equations in laminar and incompressible flow, was performed by Nakayama et al [31]. They were able to visualize the periodical flow movement and measured the temporal axial and tangential fluid velocities, oscillation frequency being of 40Hz.

Gregory and Raghu [32], created quite recently a fluidic oscillator based on Coanda effect but driven by piezoelectric devices. One of the main interesting performances of such device is that the oscillating frequency can be decoupled from the input flow and pressure differential. Frequency just depends on input electrical signal, being the oscillator able to work at a range of velocities which goes up to sonic conditions.

At this point it seems clear that most of the research being done on fluidic actuators is focused in evaluating new configurations [20,25,28,29,32], performing numerical or CFD models, often under laminar conditions [25,29,30,31] and mostly in evaluating their performance experimentally whether by themself or in a given application [10-17,20-25,28-29,18,32].

The present paper will present a numerical evaluation of a fluidic oscillator. The CFD model used is based on unsteady Reynolds averaged Navier-Stokes equations (URANS) considering turbulent compressible flow. In fact, the fluidic actuator presented here was previously studied in [33, 34]. They performed and extensive CFD model including the analysis of several turbulent models in order to find out which one was the most appropriate. They also performed an experimental study obtaining a good agreement between experimental and CFD results. In the present paper, experimental results obtained in [33, 34] will be compared with the new CFD calculations. Finally, a discussion regarding how different fluidic oscillator parts and dimensions may affect its performance will be carried on. The idea is to give to the reader some hints to be able to modify a given oscillator to fulfil a particular application.

It needs to be clarified that the information presented here has to be seen as preliminary, then as it will be further explained, the simulation performed has some deficiencies therefore not allowing to fully trusting the results obtained. Nevertheless, the qualitative information presented shall be seen as fully relevant.

II. CFD MODEL OF THE FLUIDIC ACTUATOR.

As previously seen, many of the CFD simulations done until now were carried out in laminar flow. In fact, inside the fluidic actuators, especially when high speeds are required and or low density fluids are used, the flow is expected to be turbulent. In the present study flow will be considered as turbulent and incompressible.

The fluidic oscillator used for the present work is presented in figure 1. A very similar design has already been used in combustion control [10-12] giving notorious benefits regarding the stability behaviour of the combustor.

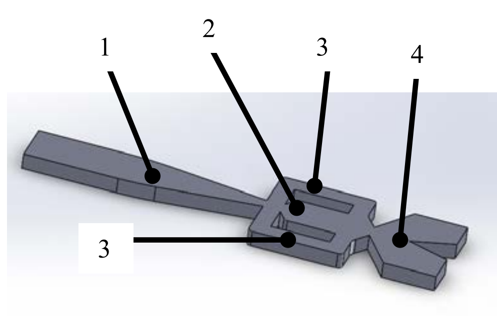

a)

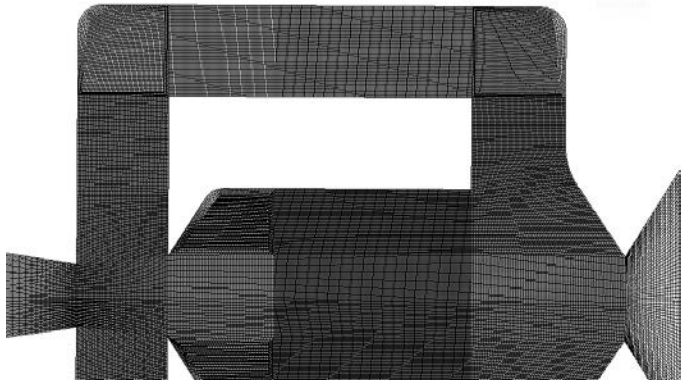

b)

Fig 1 a) main view of the fluidic oscillator. b) zoomed view of the grid used in the present study.

Notice that the oscillator consists of a conical input pipe (1), a mixing chamber (2), where two feedback channels (3) can be seen on both sides, and an external chamber (4), where a cone is placed in its centre; the two outlets are located at the end of the external chamber. A zoomed view of the grid used to perform the 2D simulations is presented in figure 1b, the grid it is of structured type and consists of 121551 nodes. The turbulence model used was the K-ω Shear Stress Transport (SST), then as found in [33], this model produces the closest results to experimental ones. Boundary conditions employed were, velocity at the entrance, $1.01*10^5$Pa absolute pressure at the output and Dirichlet boundary conditions were set to all walls. A range of different input velocities were studied, fluid employed was water. The software Ansys FLUENT (version 15.0) was used to perform all simulations. The finite volumes approach was employed.

III. MODIFICATIONS PERFORMED WITH RESPECT TO THE ORIGINAL MODEL DIMENSIONS.

The most interesting part of the preset study is based on analyzing the effect of several dimensions modifications. Four different modifications were evaluated, see figure 2.

Fluidic amplifier mixing chamber inlet diameter, point (1) in figure 2, was the first modification to be computed. 14 different diameters were analyzed, the maximum diameter was having an increment of 61.5% versus its original dimension, and the minimum was having a decrement of 61.5%.

The mixing chamber inlet angle, point (2) of figure 2, was progressively increased and decreased until reaching a 46.5% increase and decrease versus the original one. A total of 11 different angles were evaluated.

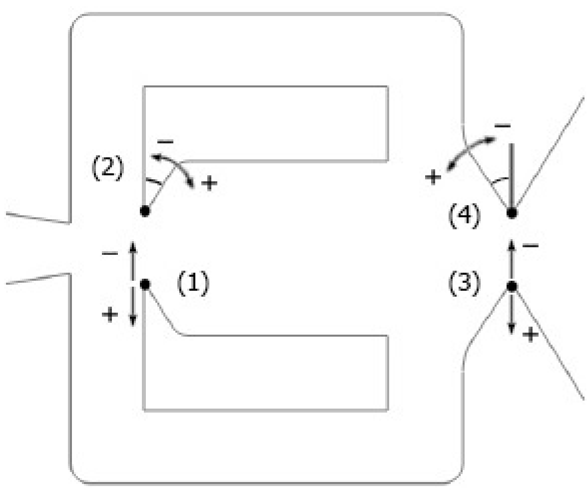

Fig 2 dimensional parameters modified in the present study.

Mixing chamber outlet diameter, point (3) of figure 2, was progressively increased until reaching a diameter 58.8% bigger than the original one. Outlet diameter maximum decrease was also of 58.8% versus its original dimension. A total of 12 different diameters were analyzed.

The mixing chamber outlet angle, point (4) of figure 2, was progressively increased and decreased versus its original value until reaching a percentage change in both directions of 58.8%. A total of 9 different angles were studied.

IV. Results

A. Original Fluidic Amplifier

One of the characteristics of fluidic actuators is its linear frequency behaviour versus the inlet mass flow, usually represented as a function of Reynolds number. In order to calibrate the simulation performed, CFD results for a set of different Reynolds numbers, were compared versus the ones obtained experimentally in [33], such comparison is presented in figure 3. The first thing to be noticed is that the agreement seems to be rather acceptable at low Reynolds numbers but the linear tendency is disappearing at high Reynolds numbers. These characteristics raise further issues regarding the validity of the CFD model. From the grid analysis, it was noticed that the grid used may not be dense enough nearby the walls. A second problem could be associated to the two dimensionality of the grid, clearly the experimental results were three dimensional, and therefore the use of a 3D CFD model appears to be the appropriate thing to do. At the moment authors are working on solving these two problems.

It is relevant to highlight that all results about to be presented are made non dimensional. The parameters used to obtain non dimensional variables were, the characteristic dimension of the original fluidic amplifier. At the inlet and outlet, the original diameters and angles were used as characteristic length and characteristic angles respectively. Original fluidic amplifier mass flow of 0.257kg/s and frequency of 46.84 Hz for a Reynolds number of Re= 51408, were used as characteristic parameters.

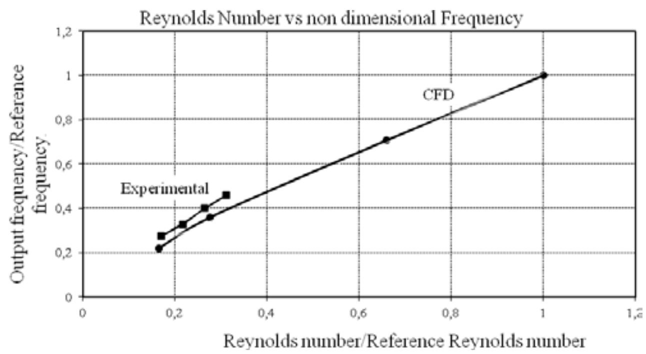

Fig 3 comparison experimental and CFD results. Non dimensional

B. Effect of dimensions modification on frequency

In the present section, it will be presented the different results obtained when the dimensional modifications introduced in section 3, were applied. The first modification to be considered is the variation of mixing chamber inlet diameter, figure 4 introduces this effect. The first thing to be noticed is that whenever the diameter falls below a minimum or is higher than a maximum, the actual fluidic amplifier is not producing any outgoing frequency, simply the flow crosses the amplifier as a jet. What it is also interesting to realize is that it exist a particular diameter at which the outgoing flow frequency falls to a minimum, a small increase or decrease from this diameter causes a slight increase of actuator frequency.

This phenomenon has to be related to the mixing chamber Coanda effect existence. When the diameter falls to a minimum or exceeds a certain level, two vortices of the same size appear on each side of the mixing chamber, the jet is not able to generate a stagnation pressure on the mixing chamber outlet inclined walls, high enough to create a pressure wave travelling upstream through the feedback channels and able to push the jet towards one side thus generating the Coanda effect. Whenever the inlet diameter reaches a certain value, the jet bending is minimum, low intensity vortices are being generated alternatively on both sides of the mixing chamber.

As diameter keeps increasing from this particular minimum value or decreasing from the maximum value, vortex intensity on both sides of the mixing chamber will also increase. This produces a huge reattachment of the jet alternatively on both sides of the mixing chamber, to bend the jet towards the other side. A high pressure wave must be send backwards and through the feedback channels, from the mixing chamber outlet to the inlet. Bending the jet to a maximum extend and building a pressure wave high enough to push the jet towards the other side, takes a while. This explains the small decrease of frequency as diameter changes from any border to the optimum one.

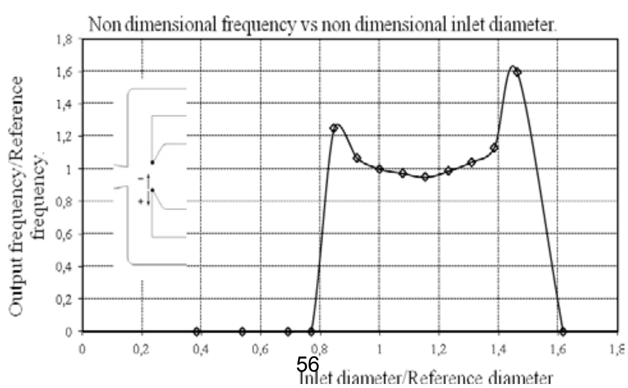

Fig 4 non dimensional frequency as a function of different mixing chamber inlet diameters. The rest of the dimensions were kept at its original value. Reynolds number Re= 51408.

The second modification to evaluate is the mixing chamber inlet angle. Figure 5 presents the outcome of the simulations performed. It was realized that for the angular values evaluated, a minor effect was observed. It appears as if a modification of the inlet mixing chamber angular value simply pushes the vortex being generated alternatively on both sides of the chamber back and forward. Its intensity, related with the minimum pressure at its central core, is not greatly affected by the angle used, thus frequency remains rather constant.

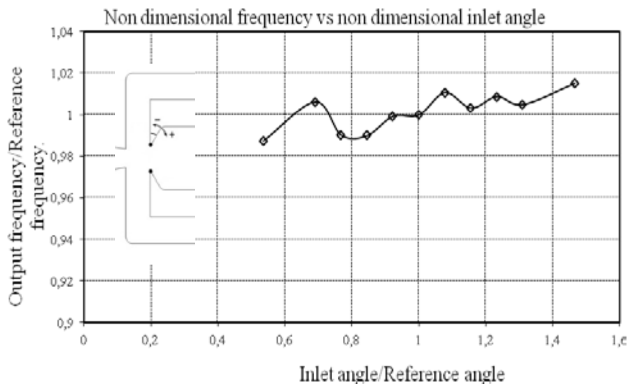

Fig 5 non dimensional frequency as a function of mixing chamber inlet angle. The rest of the dimensions were kept at its original value. Reynolds number Re= 51408.

A third dimensional evaluation undertaken was to see the effect of modifying the mixing chamber outlet diameter. Again for the values evaluated a negligible effect was obtained, except for a very small diameter which increases pulsating frequency, see figure 6. In fact outlet diameter is very likely a parameter which is not producing a key effect on the pulsating flow, yet, as can be seen in figure 6, whenever this diameter falls to a minimum, acts as a restrictor increasing the downstream stagnation pressure and the overall pressure of the amplifier, forcing the jet to flip over, in a smaller amount of time thus increasing frequency. Although not evaluated, and therefore not seen in figure 6, it is expected the frequency to increase if a further diameter decrease is to be produced.

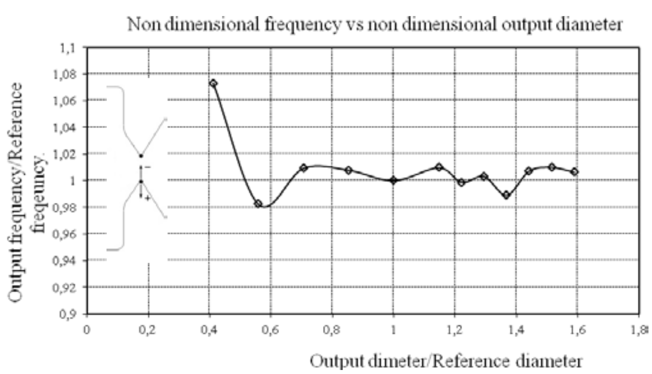

Fig 6 non dimensional frequency as a function of mixing chamber outlet diameter. The rest of the dimensions were kept at its original value. Reynolds number Re= 51408.

The final dimensions modification performed was the variation of mixing chamber outlet angle. Figure 7 shows the results obtained. Clearly this parameter is the most relevant among the studied ones. Frequency keeps decreasing as inclination angle increases. This effect is clearly understandable once it is realized that the mixing chamber outlet inclination wall, plays a key role regarding the feedback effect. Not only the stagnation pressure position will be modified by this angle but also its magnitude will be affected. High frequencies are linked to high stagnation pressure values and vice versa.

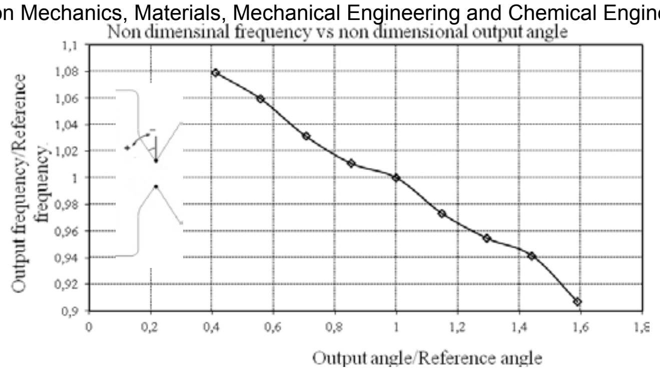

Fig 7 non dimensional frequency as a function of mixing chamber outlet angle. The rest of the dimensions were kept at its original value. Reynolds number Re= 51408.

C. Effect of dimensions modification on mass flow amplitude.

In the present section, the amplitude of the outlet mass flow oscillations will be presented and discussed. For all cases, the mean outlet mass flow flowing though both outlets, was 0.257 kg/s. The amplitude of the mass flow fluctuations for the reference case was 0.652 kg/s, 2.54 times the mean value. This means that reverse flow appears alternatively in both outlets during a fraction of the oscillation cycle.

In figure 8 it is shown the effect of modifying the inlet diameter. As presented in the previous section, for inlet diameters exceeding a limit in any direction, whether too big or too small, the flow stops oscillating and therefore the amplitude decays to zero. For the intermediate values it is seen that the amplitude is not much affected by the inlet diameter (except near the limits of the working range). It is also seen that the tendency is opposed to that of the frequency: and the highest amplitudes are found in the middle diameter values, where the frequencies are slightly smaller, see figure 4.

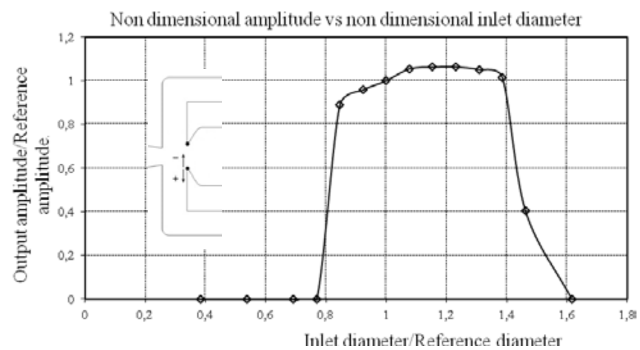

Fig 8 non dimensional mass flow amplitude as a function of mixing chamber inlet diameter. The rest of the dimensions were kept at its original value. Inlet Reynolds number Re = 51408.

In figure 9 it is shown the effect of modifying the inlet angle. It is seen that this parameter has a negligible effect regarding the mass flow amplitude. This is not surprising as the frequencies were also very little affected by this parameter.

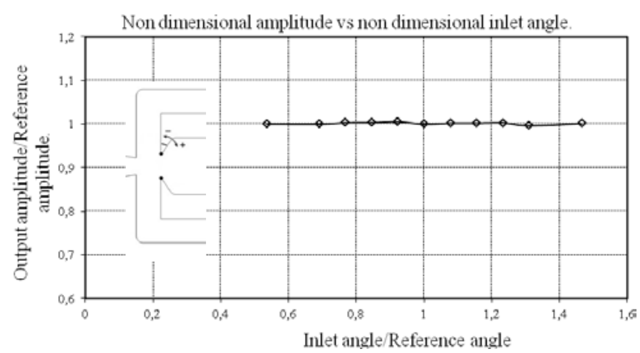

Fig 9 non dimensional mass flow amplitude as a function of mixing chamber inlet angle. The rest of the dimensions were kept at its original value. Inlet Reynolds number Re = 51408.

In figure 10 it is shown the effect of modifying the outlet diameter. It is seen that, outlet amplitude decays almost linearly while increasing the outlet diameter. A lower amplitude of the mass flow oscillations indicates a smaller deflection of the jet while

ISBN: 978-1-61804-295-8

passing through the output nozzle. It is reasonable to think that when the flow is forced to pass through a smaller throat area in a pulsating regime, the deflection should decrease. Therefore it can be stated that despite the outlet area is not having a very significant effect on the frequency, it can be effectively used to control the output oscillations amplitude.

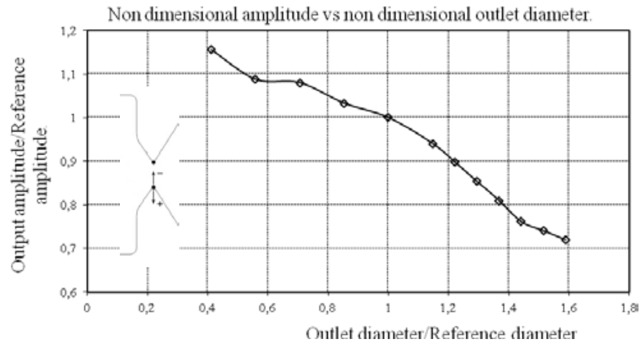

Fig 10 non dimensional mass flow amplitude as a function of mixing chamber outlet diameter. The rest of the dimensions were kept at its original value. Inlet Reynolds number Re = 51408.

Finally, in figure 11 it is presented the effect of modifying the outlet angle on the mass flow oscillations amplitude. Here can also be observed a nearly linear decay with increasing angles, similar to the one observed with increasing diameters. Nevertheless, the effect is much weaker. Therefore mixing chamber outlet angle, can also be used to control the outlet amplitude but not as effectively as using the outlet diameter.

Notice that the maximum mass flow amplitude variation, when modifying the outlet angle, is around 10%. Its effect can be explained taking into account that a higher angle tends to direct the jet towards the central axis, decreasing its deflection and therefore reducing the oscillations amplitude. It was seen in figure 7, that this parameter was particularly relevant when considering frequency variation, but its effect on mass flow amplitude it is much less relevant.

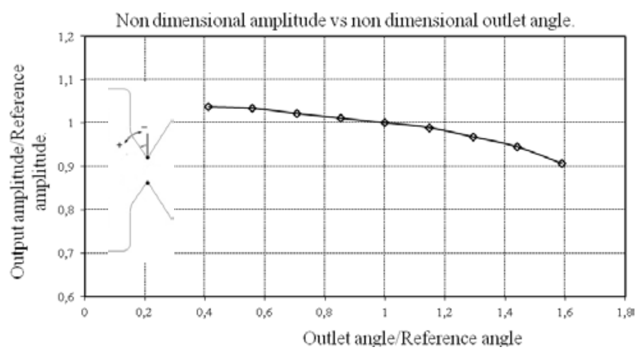

Fig 11 non dimensional mass flow amplitude as a function of mixing chamber outlet angle. The rest of the dimensions were kept at its original value. Inlet Reynolds number Re = 51408.

Furthermore, for the smallest outlet diameter simulated, it was observed a secondary oscillation on the outlet mass flow. This effect can be seen in figure 12, which represents the non dimensional flow through one of the outlets along one oscillation cycle, comparing the reference case and the one with the smallest outlet diameter. Notice that the secondary oscillation indicates that the outgoing jet, is not just oscillating from one fluidic amplifier outlet to the other, but presents a second an much smaller oscillation within a single amplifier outlet. This effect appears to be related to the small oscillating jet section at the fluidic amplifier outlet. As the jet section is much smaller than the outlet section, the jet has enough space to generate a second fluctuation whenever any small perturbation interacts with the flow.

ISBN: 978-1-61804-295-8

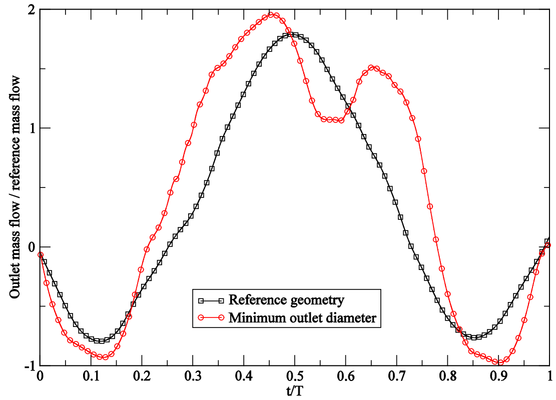

Fig 12 non dimensional mass flow amplitude as a function of mixing chamber outlet angle. The rest of the dimensions were kept at its original value. Inlet Reynolds number Re = 51408. Original mass flow amplitude 0.652 kg/s

V. Conclusion

A careful CFD evaluation of a fluidic oscillator under turbulent conditions has been performed. Numerical results obtained were compared with previous experimental work showing a reasonable agreement and giving hints of how to improve the CFD model performed.

Several dimensional parameters have been modified showing its relevance regarding the modification of fluidic actuator frequency. The most relevant parameter regarding frequency control is the mixing chamber outlet angle.

The parameter which allows modifying mass flow amplitude at the output, is the fluidic amplifier outlet diameter.

The authors expect that the information presented will be useful to other researchers to design fluidic actuators for future specific applications.

Acknowledgment

The authors would like to acknowledge the work performed by Mikel Ruiz Arozarena and Manuel Sarmiento Calderó, then the information presented in the present paper is based on their respective end of studies projects.

References

[1] Cattafesta L.N; Sheplak M. "*Actuators for Active Flow Control*". Annu. Rev. Fluid Mechanics. 43, pp 247-72. 2011.

[2] Corke T.C; Lon Enloe C; Wilkinson S.P. "*Dielectric Barrier Discharge Plasma Actuators for Flow Control*". Annu. Rev. Fluid Mechanics. 42, pp 505-29. 2010.

[3] Bell D.J; Lu T.J; Fleck N.A; Spearing S.M; "*MEMS actuators and sensors: observations on their performance and selection for purpose*". Journal of Micromechanics and Microengineering 15, pp 153-164. 2005.

[4] Huang A; Folk C; Silva C; Christensen B; Chen Y; Ho C.M; Jiang F; Grosjean C; Tai Y.C; Lee G.B; Chen M; Newbern S. "*Application of MEMS Devices to delta Wing Aircraft: From concept development to Transonic Flight Test*". 39th AIAA aerospace Sciences meeting & Exhibit. January 2001. Reno, NV

[5] Glezer A; Amitay M. "*Synthetic Jets*". Annu. Rev. Fluid Mechanics. 34, pp 503-29. 2002.

[6] Cater J.E; Soria J. "*The evolution of zero-net-mass-flux jets*". J. Fluid Mechanics. 472, pp 167-200. 2002.

[7] Raju R; Aram E; Mittal R; Cattafesta L. "*Simple models of Zero-Net Mass-Flux Jets for Flow Control Simulations*". International Journal of flow Control. 1, 3 pp 179-197. 2009.

[8] Kotapati R.B; Mittal R; Cattafesta L.N. "*Numerical study of a transitional synthetic jet in quiescent external flow*". J. Fluid mechanics. 581, (2007) 287-321. 2007.

[9] Nagib HM; Kiedaisch JW; Wygnanki IJ; Stalker AD; Wood T; McVeigh MA. "*First-in-Flight Full-Scale Application of Active Flow control*": The XV-15 Tiltrotor Download Reduction. RTO AVT specialists meeting on Enhancement of NATO military Flight Vehicle performance by Management of Interacting Boundary layer Transition and Separation. Prague 4-7 October 2004.

[10] Guyot D; Paschereit C.O; Raghu S. "*Active Combustion Control Using a Fluidic Oscillator for Asymmetric Fuel Flow Modulation*". International Journal of Flow Control. 1,2 (2009) 155-166

[11] Lacarelle A. "*Model, control and optimization of fuel/air mixing in a lean premixed swirl combustor using fuel staging to reduce pressure pulsations and NOx emission*". PhD. TU-Berlin. 2011.

[12] Abdelrazek A. "*Interactions of Flow Field and Combustion Characteristics in a Swirl Stabilized Burner*". PhD. TU-Berlin. 2011.

[13] Raman G; Packiarajan S; Papadopoulos G; Weissman C; Raghu S. "*Jet thrust vectoring using a miniature fluidic oscillator*". The Aeronautical Journal.pp 129-138. 2005.

[14] Seele R; Tewes P; Woszidlo R; McVeigh A; Lucas N.J; Wygnanski I.J. "*Discrete Sweeping Jets as Tools for Improving the performance of the V-22*". Journal of Aircraft. 46,6 pp 2098-2106. 2009.

[15] Cerretelli C; Kirtley K. "*Boundary Layer Separation Control With Fluidic Oscillators*". Journal of Turbomachinery. 131, 041001-1-9. 2009.

[16] Culley D.E; Bright M.M; Prahst P.S; Strazisar A.J. "*Active Flow Separation Control of a Stator Vane Using Surface Injection in a Multistage compressor Experiment*". NASA National Technical Information Service. NASA/TM (2003) 212356.

[17] Seifert A; Stalnov O; Sperber D; Arwatz G; Palei V; David S; Dayan S; Fono I. "*Large Trucks Drag Reduction Using Active Flow Control*". Tel Aviv University internal report.

[18] Raman G; Raghu S. "*Cavity Resonance Suppression Using Miniature Fluidic Oscillators*". AIAA Journal. 42,12 pp 2608-2611. 2004.

[19] Giles B.D. "*Fluidics, the Coanda Effect, and some Orographic winds*". Arch. Met. Geoph. Biokl. Ser.A, 25, pp 273-279. 1977.

[20] Campagnuolo C.J; Lee H.C. "*Fluidic Oscillators*". Instruments and Control Systems. pp 99-103. 1970.

[21] Andreiev N. "*Fluidic Oscillator Measures Flow*". Control Engineering pp 56-57. 1973.

[22] Maas M.A. "*Pressure and Temperature-Insensitive Fluidic Oscillator*". Design News. pp 50-51. 1969.

[23] Campagnuolo C.J; Gehman S.E. *"Fluidic Oscillator Design".* Instruments & control Systems pp 91-95. 1969.

[24] Gregory J.W; Sullivan J.P; Raman G; Raghu S; "*Characterization of a micro Fluidic Oscillator for flow control"*. 2nd AIAA Flow Control Conference. Portland OR. June 28-July 1, (2004).

[25] Uzol O; Camci C. "*Experimental and computational Visualization and Frequency measurements of the jet Oscillation inside a Fluidic oscillator*". Journal of Visualization 5,3 pp 263-272. 2002.

[26] Bauer P. "*Fluidic Oscillator and Spray Forming Output Chamber*". United States patent No. 4,184,636.1980

[27] Bauer P. "*Fluidic Oscillator Flowmeter*". United States patent No. 4,244,230. 1981.

[28] Huang R.F; Chang K.T. "*Fluidic Oscillation Influences on V-Shaped Bluffbody Fow*". AIAA Journal 43,11 pp 2319-2328. 2005.

[29] Khelfaoui R; Colin S; Orieux S; Caen R; Baldas L. "*Numerical and Experimental Analysis of Monostable Mini and Micro-Oscillators."* Heat Transfer Engineering, 30 (1-2) pp 121-129. 2009.

[30] Gebhard U; Hein H; Schmidt U. "*Numerical investigation of fluidic micro-oscillators"* J. Micromech, Microeng. 6, pp 115-117. 1996.

[31] Nakayama A; Kuwahara F; Kamiya Y. "*A two-dimensional numerical procedure for a three dimensional internal flow through a complex passage with a small depth. (its application to numerical analysis of fluidic oscillators)"*. International Journal of Numerical Methods for Head and Fluid Flow. 15, 8 pp 863-871. 2005.

[32] Gregory JW. Raghu S. "*Variable-Frequency Fluidic oscillator Driven by a Piezoelectric Bender*". AIAA Journal. 47,11 pp 2717-2725. 2009.

[33] Bobusch BC. *"Experimentelle und Numerische Bestimmumg der Innerdurschtrömung eines Fluidisched Oszillators*". Diplomarbeit. TU Berlin 2010.

[34] Bobusch BC; Woszidlo R; Bergada JM; Nayeri CN; Paschereit CO. *"Experimental study of the internal flow structures inside a fluidic oscillator*". Exp. Fluids 54:1559. 2013.

ISBN: 978-1-61804-295-8

Experimental investigation into suitability of smart polymers as an impact-absorbing material for an improved rugby headgear

Mladenko Kajtaz, Joseph Karren, and Aleksandar Subic

***Abstract*—**Concussion in Rugby is an important public health issue and there is a clear need for concussion-reducing headgear. It is not clear whether currently available soft headgear can mitigate the effects of a concussive impact and it is concerning that a notable proportion of the playing population have a misbelief in their protective effect. In order to enhance development of modern and effective headgear, this study investigated suitability of smart polymer materials via both standardised and novel biomechanical test methodologies. Superior performances of the smart polymers to that of the existing products were generally observed and resulted in the reductions of at least 40% in the probability of concussion. Diffuse Axonal Injury (DAI) severity rating suggested two-fold improvement over the existing headgear if the smart polymers were used as a replacement for the cushioning material in the current products.

***Keywords*—** biomechanical head impact testing, concussion, smart polymers, sport

I. Introduction

COMPETITIVE sports offer the ability to participate in a wide variety of school, collegiate, recreational and professional arenas. However, risk of injury is inherent in any sport, especially in contact sports such as Rugby (Rugby Union). Rugby is a ball carrying, collision team sport played at school, collegiate, club and professional levels in more than 100 countries across 5 continents [1]. Contesting for possession of the ball, players must cohesively and forcefully defend their goal line by tackling the ball carrier to interrupt the opposing play. Although tackles above the shoulders of a player are not permitted under the rules of the game, inadvertent head impacts are a common occurrence. As with other types of injury, the frequency and severity of head injury in sport is a function of the nature of the game, the rules, the regulations and the actions of participants. The retirement of several high-profile athletes as a result of concussion has increased the awareness of the sporting community to the pertinence of this issue. Much is unknown about the pathogenesis and long-term implications of sub-concussive and concussive blows, but what is known is that concussion is a complex phenomenon resulting from both linear and rotational injury mechanisms. Even though Rugby headgear are permitted under the rules of the game, their effectiveness in mitigating concussive impacts is not fully understood and their role is contentious. Many advocate that it only protects the wearer's head from abrasions, while others suggest that its role should be to act as a shock absorber. Pettersen [2] investigated the attitudes of Canadian Rugby players and found that most (62%) believe that headgear can protect against concussion. Finch et al. [3] also found that a large proportion of Australian school-age Rugby players believe that wearing soft headgear gives them more confidence in a tackle. A misbelief in the protective ability of headgear may be a catalyst for more severe head injury, so it is crucial for the role of soft headgear to be more adequately defined. As kinetic energy is applied to the cranium, the resulting inertial acceleration/deceleration and rotation of the brain causes internal strains that disrupt the cerebral anatomy and neurological framework [4]. For a protective headgear to function effectively, it must attenuate this impact energy to decrease the magnitude of the impact force to the head [5]. Kemp et al. [6] observed 13 English Rugby premiership teams and found no significant reduction in injury risk among headgear wearers. A randomised cluster controlled trial (RCT) by McIntosh and McCrory [5] involving Australian players yielded similar findings. Laboratory tests [7-9] have also found that many commercially available soft headgear perform poorly under simulated impact conditions.

To make headgear more effective, several studies have suggested the use of thicker, denser padding [8-10], but sanctions within the sport prevent such improvements from being made. The International Rugby Board (IRB) is the governing body for the global sport of Rugby Union, and imposes restrictions on the design and performance of approved headgear (in contrast, Rugby

M. Kajtaz is with RMIT University, School of Aerospace, Mechanical and Manufacturing Engineering, GPO Box 2476, Melbourne, VIC, 3001, Australia (e-mail: mladenko.kajtaz@rmit.edu.au).

J. Karren was with The University of Sydney, School of AMME. He is now with Human Impact Engineering, Sydney, NSW, Australia (e-mail: jkarren@humanimpacteng.com).

A. Subic is with RMIT University, School of Aerospace, Mechanical and Manufacturing Engineering, GPO Box 2476, Melbourne, VIC, 3001, Australia (e-mail: aleksandar.subic@rmit.edu.au).

League and Australian Rules football do not impose such regulations). The controversy over whether headgear prevent concussion has caused confusion as to their role in the game, and with rising participation and popularity in the sport, more focused research is necessary. Despite these sanctions and restrictions, a few studies have investigated changes to padding thickness and density in new headgear designs. In a laboratory study by Hrysomallis [8] it was suggested that padding of at least 15mm on the front and sides had the potential to offer adequate impact protection. In another investigation, a thickness increase of 5mm significantly reduced the mean linear headform acceleration maxima, concluding that it could be possible to use thicker foams to reduce concussion [9].

Unlike the existing investigations, this paper explores an application of smart polymers in new headgear designs. In addition to the standardized tests, this study in a unique way uses crash test dummies as surrogates to represent Rugby players in a tackle. This utilization of the crash test dummies is embodied in a novel and recently developed sport-specific testing methodology that allows for an introduction of other advanced and more relevant head injury criteria that were not typically a part of the existing and commonly used standardised tests.

II. Head Impact, Concussion and Injury Criterion

A head impact causes both contact and inertial loading at the impact location, whereby the direct focal contact forces at the impact site are linked to skull fracture and brain contusion resulting from skull deformation; while the inertial movement of the brain within the cranial cavity is linked to 'coup/contre-coup' type brain contusions (a coup type brain contusion occurs when the rapidly decelerating head forces the cerebrum towards the point of impact, whereas a contre-coup type contusion occurs when the movement of the brain causes negative suction pressures on the side of the brain diametrically opposite to the impact area). During this motion, the brain may also glide over the irregular, jagged contours of the skull causing cerebral lacerations [11]. Mild traumatic brain injury (mTBI), or commonly concussion, is a common head injury associated with many of these head impacts. New understanding of the pathophysiological underpinnings of this injury as well as its short and long-term effects has recently been a cause for concern in the realm of sports medicine [12]. It has been shown that repetitive concussive and subconcussive blows may increase the risk of developing neurocognitive impairment in later life [13]. A large body of the research has shown that concussive injury is primarily the result of the inertial and impulsive loading experienced throughout the brain during impact, rather than the result of acute coup/contre-coup type contusions and skull fractures.

Although, with the head and neck motions that occur in a typical oblique head impact, both linear and rotational forces inside the skull cause intracranial damage, early efforts to understand the biomechanical basis of concussion focused predominantly on linear force/acceleration and its effect on human injury. Lissner et al. [14] attributed intracranial damage to the skull deformation and pressure gradients caused by direct head impacts to cadaver heads and developed the Wayne State Tolerance Curve (WSTC) (see **Fig 1**), implying that linear acceleration has a strong association with brain injury pathogenesis and it could be adapted and used as a criterion for milder brain injury types [15, 16]. Today these indices are used to measure the likelihood of head injury in a range of vehicle, personal protective gear, and sports equipment standards for the prevention of both mild and severe forms of TBI. However, because they are based purely on linear acceleration, their validity in assessing concussion has been debated and many preeminent researchers have questioned their ability to diagnose injury risk because most impacts also involve rotational loading on the head. Importantly, brain tissue deforms readily in response to rotational forces since the bulk modulus of brain tissue is approximately 10^5 times its shear modulus, hence there is a general consensus in the literature that shear deformation caused by rotational motion is the predominant mechanism of brain injury [17, 18]. Studies showed [19] that it is difficult to produce traumatic unconsciousness in the absence of rotational motion but the likelihood of an unconscious episode is substantially increased once it is introduced. Early research by Ommaya and Hirsch [20] estimated that angular acceleration greater than 1,800 rad/sec^2 is likely to cause cerebral concussion in humans; while. Pincemaille et al. [21] established a concussion threshold of 13,000-16,000 rad/sec^2. Currently, rotational criteria are not incorporated into a vast majority of sports and recreational helmet standards due to the lack of extensive evaluation and review needed for them to be accepted by the scientific and sporting community.

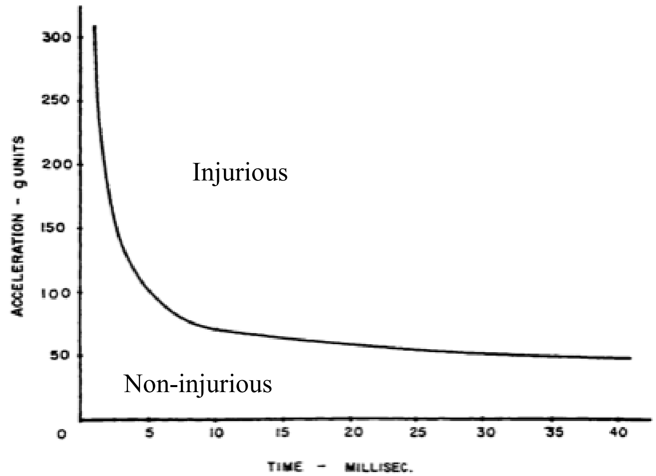

Fig 1. Wayne State Tolerance Curve, plotting acceleration as a function of impact duration to predict injury

However, recent investigations have made use of new technology to more accurately measure human tolerance to both linear and rotational acceleration in sport. In particular, many injury biomechanics researchers have investigated mild brain injury using accelerometers placed inside American football players' helmets. By observing the acceleration data of medically validated cases of concussion, these studies have proposed thresholds ranging from 70 to 165 g in padded impacts [22-25]; or a linear injury threshold of 78 g and a rotational threshold of 6322 rad/s^2 to represent a 50% risk of concussion, as proposed by Newman et al. [26]. Similarly, Rowson et al. [27] analysed concussions in a large number of NFL helmet impacts and proposed a linear acceleration injury threshold of 80g and a rotational threshold of 6383 rad/s^2 and 28.3 rad/s (peak resultant angular acceleration and maximum change in resultant angular velocity respectively). Other studies have observed similar thresholds for concussion [23, 24, 28, 29].

III. EXISTING RUGBY HEADGEAR

As head impact involves a transfer of energy and momentum due to changes in the relative velocities between the head and another object, a concept of placing a protective material between the head and the striking object to attenuate and distribute the impact force over a larger area is the basis for wearing head protection. Protection, as a safety concept, is defined as a reduction of impact severity to a level that the brain can tolerate whereby the tolerance is defined by an injury threshold/criterion. Since the majority of sports and recreational helmet standards specify the safety criteria in terms of linear acceleration only, current helmets are primarily designed to reduce the linear acceleration component of head impact [30].

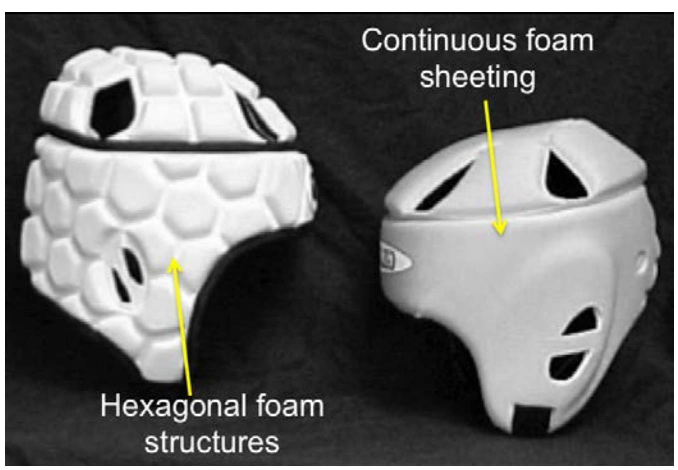

Fig 2. Typical headgear construction – honeycomb (left) and continuous (right).

There are several types of protective headgear available for use in Rugby Union, which typically have thickest padding at the forehead and sides, and thinnest at the top and back of the head. Honeycomb configurations (**Fig 2a**), featuring small, polygonal-shaped blocks of foam under a fabric skin, and continuous configurations (**Fig 2b**), constructed of larger foam sheets that extend over a greater area; are two most common designs of headgear construction. Impact testing by McIntosh et al. [9] found that the

ISBN: 978-1-61804-295-8

continuous arrangement performed better than the honeycomb arrangement due to improved load distribution and lateral stability, however it seems that the aesthetic and/or comfort value honeycomb-type headgear has resulted in their popularity in recent years and a decline in the availability of continuous types.

A. Use of protective headgear in Rugby

Pettersen [2] investigated headgear-wearing rates in Canadian Rugby players, and found that while 62% believed that headgear could offer them protection from head injury, only 26% admitted to wearing them. Primary reasons for not wearing headgear were that it caused players to become “too hot”, “uncomfortable” and impeded their ability to communicate on field. An Australian study by [3] found that over 70% of school-age Rugby players reported to regularly wear soft headgear and 67% believed that wearing headgear made them feel “safer” on field. Both these studies observed an assumption that headgear is protective. Garraway et al. [31] suggested that players use protective headgear with the expectation that it will reduce the severity of impact so they can tackle harder when wearing them. Such “risk-compensation” by players may result in a paradoxical increase in the risk of head injury. It is especially concerning that most players who wear headgear are young players who, as mentioned above, exhibit higher vulnerability to concussion compared to mature players. However, the idea that athletes wearing headgear will play more aggressively has yet to be substantiated, and despite the predominant belief that headgear are protective, it has been shown through the use of an instrumented tackle bag that players do not tackle harder when wearing headgear [32].

B. Performance and Safety Aspects of Existing Rugby Helmets

The presumption that headgear protects the wearer from concussion makes their role in Rugby very controversial. While some argue that they should be used for protection against impact, others believe that they should only be used to reduce lacerations and abrasions to the scalp. Prevention of lacerations and abrasions has been confirmed by a number of studies, including an investigation by [33] who concluded that headgear were associated with a significant reduction in bleeding head injuries in a cohort of English Rugby players. On the other hand, a number of investigations on the impact attenuation of headgear have revealed their poor performance and there is currently not enough evidence to suggest that they can protect the wearer from concussion [6, 34, 35]. Similarly, various laboratory studies have also found headgear do not attenuate sufficient impact energy to be able to protect players on the field [7, 36, 37].

IV. RUGBY HEADGEAR TESTING

In order to evaluate the protective capability of soft headgear without human subjects, head impact attenuation tests are devised to reconstruct concussive tackles. These sport-specific test methodologies need to simulate typical head impacts so that the results of these tests are delineated to the playing field. Therefore, helmet/headgear performance test methods tend to contain three essential items: a test system that is a good representation of reality; a durable headform that has a similar dynamic and kinematic response as the human head; and an injury criterion that is applicable to the test configuration. Van den Bosch [38] developed a load-injury head impact model (see **Fig 3**), which highlights the predicament faced when attempting to replicate head impacts in a laboratory setting. In particular, during a Rugby head impact, a mechanical load is applied to the head which will cause a unique biomechanical response that depends on: the impact attenuation characteristics of the headgear, the interaction between the head and the headgear and the head impact site (e.g. side, front, back). A tissue damage by means of linear and rotational forces is assumed if the biomechanical response exceeds a certain threshold for a specific impact type. Obviously, this head impact testing offers a means to crudely simulate the loading conditions and dynamic responses of a human collision. Even then, determining the injury risk depends on injury assessment tools that are largely unrefined, as mentioned previously.

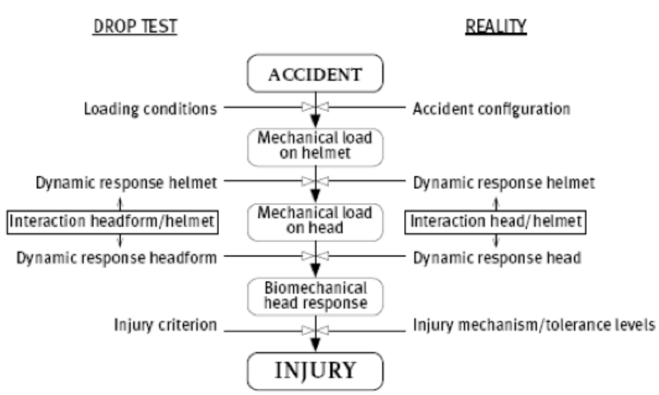

Fig 3. Load-injury head impact model comparing a laboratory test to reality [38]

ISBN: 978-1-61804-295-8

A. Helmet Testing Standards

A typical headgear performance testing involves similar methods to the AS/NZS 2512.1.1 head drop system (see **Fig 4**), which uses a magnesium alloy artificial headform guided in free-fall from a height onto a rigid, flat surface. Accelerometers in the headform measure its response and any effect of headgear in dissipating the impact energy. The majority of the abovementioned literature regarding headgear effectiveness (e.g. [5, 9], and the IRB standard [39], have utilised this form of drop test. Historically, this methodology has not been entirely satisfactory in evaluating headgear performance as it fails to represent the actual character of brain trauma [40]. Furthermore, this headgear evaluation test has a number of distinct limitations. Firstly, the use of a linear head drop system only assesses the linear acceleration of the impact and does not account for rotational injury mechanisms. Second, it also does not reflect the speed and severity of collisions experienced by Rugby players. The drop height of 300 mm specified in the IRB performance standard delivers impacts (2.4 m/s, 14.7 J) that are of significantly lower severity than the collisions experienced by Rugby players (5±1 m/s, 50-60 J). Third, in these tests there is no requirement for headform stiffness to correlate with that of the human skull, nor is there a requirement for the impacting surface to match any object likely to impact the player on field. Rigid metal headforms have demonstrated unrealistic impact responses compared to cadaver models and there is no way to delineate the human equivalent of a rigid headform impact, nor the protective capacity of any helmet using this technique (Mills 1990). Hrysomallis [8] argued that since bodily segments respond with motion and deformation during a head impact, deformable surfaces should be used to simulate real play. A possible explanation for incorporating hard surfaces may be in inability to produce repeatable results if the surfaces were allowed to deform [40].

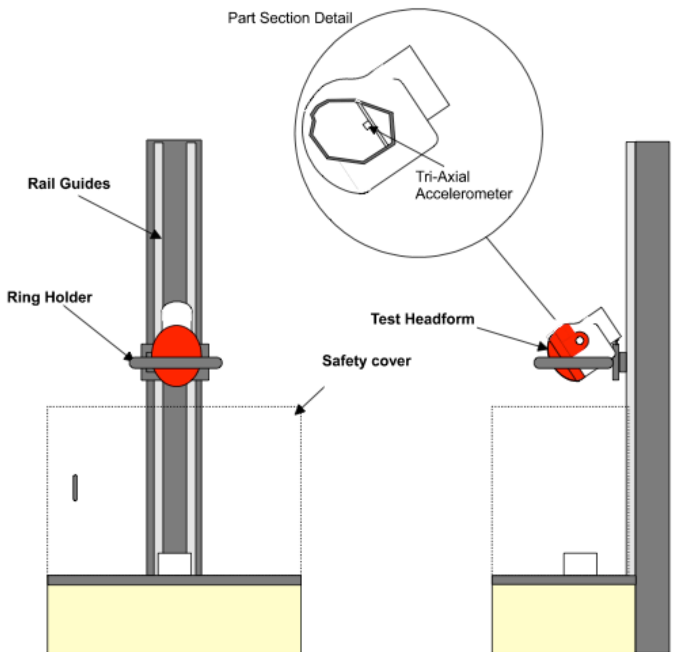

Fig 4. Standardised head drop system used by the IRB and others, similar to AS/NZS 2512. [39].

V. METHODOLOGY

The impact attenuation potential of alternative and non-traditional materials (i.e the smart polymers) was investigated using two laboratory tests. The first test methodology was the standardised head drop system used by the IRB and others, which was extensively discussed in the previous sections. Despite its numerous distinct limitations, this test is the only standardised and widely recognised methodology, which provides a basis for all further comparisons. The second test methodology was a novel, non-standard and sport-specific test methodology developed to reconstruct a typical concussive head impact scenario in Rugby

A. The Standardised Test Methodology

A guided drop test rig was used to impact a 5.5 kg hemispherical impactor (D=145mm) instrumented with a uniaxial accelerometer onto stationary flat sheets of the sample impact-absorbing materials (see **Fig 5**). The history of acceleration was recorded and the peak acceleration was presented as g-force as per the IRB Regulation 12 [39]. The samples were all tested at the same ambient temperature of 23C.

ISBN: 978-1-61804-295-8

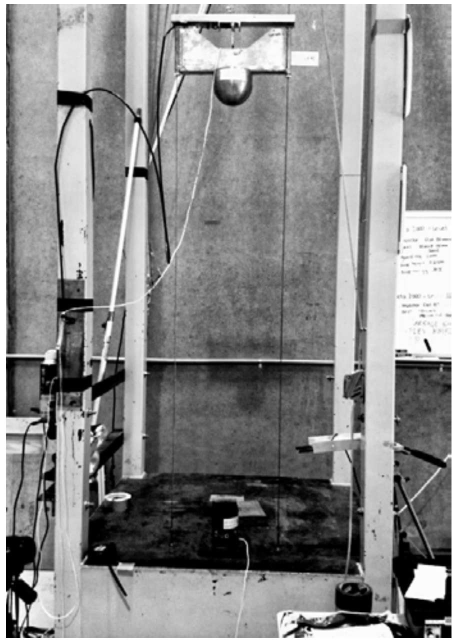

Fig 5. A setup of the standard impact drop test

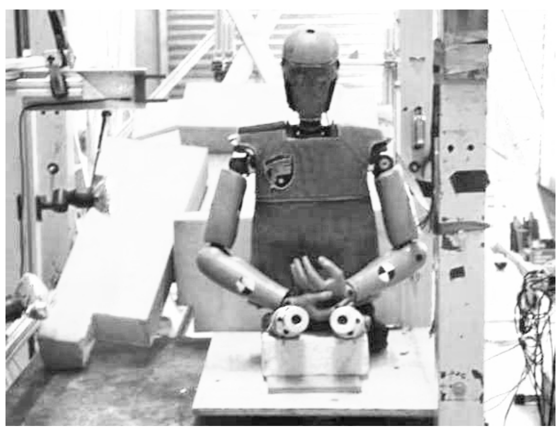

Fig 6. THOR - an advanced impact dummy

B. The New Sport-Specific Test Methodology

This test methodology was developed by one of the authors [41, 42] and consists of utilising a THOR (Test Device for Human Occupant Restraint) ATD to reconstruct a typical concussive head impact scenario in Rugby. Shown in **Fig 6**, THOR is an advanced impact dummy and is based on improved biomechanical knowledge compared to the commonly used Hybrid III, making it one of the most biofidelic devices available [43]. THOR also uniquely incorporates a specifically designed shoulder complex that simulates human shoulder seatbelt loading in frontal crashes [44, 45] that allowed this dummy to be used in a controlled impact-testing environment to reconstruct concussive shoulder-head tackles.

ISBN: 978-1-61804-295-8

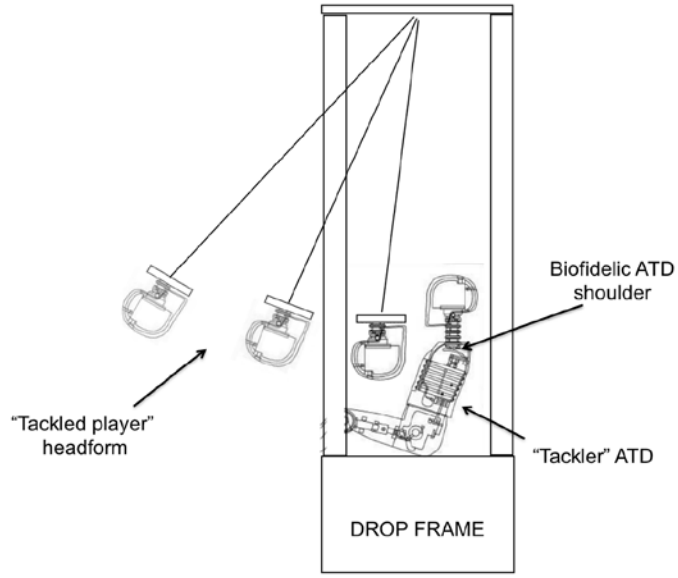

Fig 7. Schematics of the new biomechanical and rugby-specific testing setup

Fig 7 schematically shows the test setup by depicting a pendulum drop testing apparatus that guides a swinging THOR headform into impact with the acromioclavicular region (shoulder) of a THOR torso, similarly to the head of a tackled player coming into contact with the tackler's shoulder. Instrumentation within the headform measured the linear and rotational acceleration at the centre of gravity (cg) of the headform as it collided with the surrogate shoulder. An impact velocity of 4.65 m/s, which is in the range of impact velocities found to cause concussion in Rugby players (5±1 m/s) was used in this test and only temporoparietal impacts (side impacts) were considered in this study (see **Fig 8**).

Fig 8. Temporoparietal "patch" samples modelled off the side region of a standard headgear.

C. *Material Test Samples – Material Solutions*

Test samples of the impact-absorbing materials were prepared from flat material sheets provided by commercial suppliers, namely Rogers Corporation from the USA, D3O from the UK and Albion Sports from Australia.

Poron XRD is a lightweight, thin and breathable material that's engineered for repeated impact and shock absorption, provided by Rogers Corporation. Poron XRD is a urethane based and highly damped strain-rate sensitive material with a memory-foam-like properties that exploits the glass transition temperature (Tg) of the urethane molecules to enhance its impact attenuation properties. Three different densities of Poron XRD were investigated in this study (144, 192 and 240 kg/m3). The thickness for all was 9.6mm.

D3O is a British-based impact protection solutions company that markets a unique patented technology used to produce a shock absorbing material. Using a proprietary formula to engineer non-newtonian materials, D3O has the ability to engineer a number of dilatant materials and, using a patented technology, incorporate them into polymer. Two of their materials AERO (220 kg/m3) and DECELL (330 kg/m3), with two different thicknesses (6 and 10mm) were investigated in this study. The AERO material is a urethane based like Poron XRD, while the DECELL is based on an ethylene vinyl acetate (EVA).

Traditional foams were provided by Albion Sports, the Australian leading manufacturer in sports protection equipment and a

ISBN: 978-1-61804-295-8

former manufacturer of Rugby headgear. Samples of their EVA (40 kg/m3) and expanded polystyrene (EPS) (80 kg/m3) protective liners that are used in their hard shell helmets (cricket and cycling helmets) were included in this comparative study as examples of impact-absorbing materials used in other sports helmets. The test thickness for both materials was 10mm.

Headgear: Samples of two generic models of IRB-approved rugby soft helmets were obtained from a supplier of retail rugby headgear: an entry level; and a top end headgear. The entry level headgear was easily identifiable by a poorer quality of manufacturing upon an inspection.

VI. Results

A. Results of the Standard Tests

A total of 13 different solutions were investigated resulting in 39 individual tests. The results, shown in **Fig 9**, are averages of three repeated trials for each solution and since minimal variations between the trials were observed, the overall repeatability was deemed acceptable. Peak linear acceleration, as the injury assessment criterion in this test, was expressed in terms of "g-force". As expected, worst performing solutions were commercial headgear with their peak linear accelerations in excess of 350g because they were designed to adhere the IRB Standard, which enforces the minimum level of impact attenuation performance (i.e. cannot be lower/better than 200g) and the upper limit was historically kept to 550g. According to LOGIST plot relating the risk of concussion to peak linear accelerations that were developed by [46] (see **Fig 10**), such an inadequate performance of the commercial headgear undermines the philosophy of protective equipment in general, and demonstrate that the IRB does not support the use of headgear for impact protection.

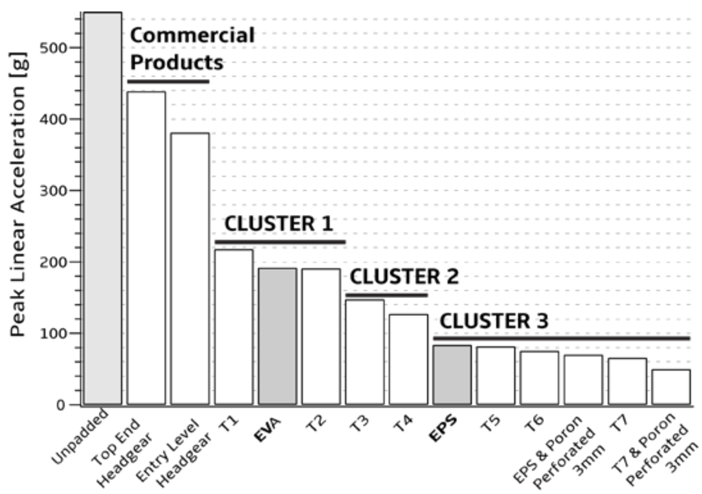

Fig 9. Result of the standard impact testing

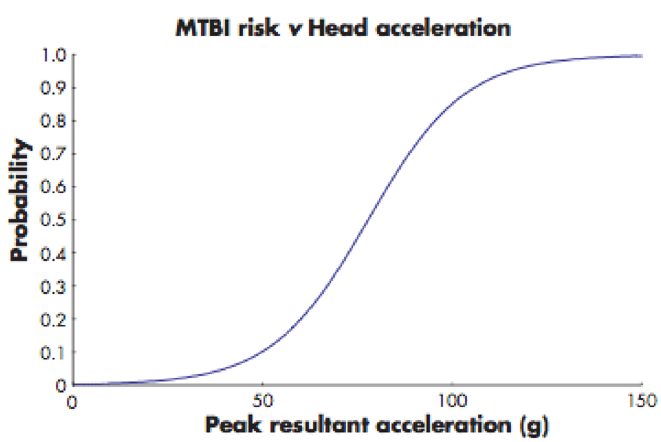

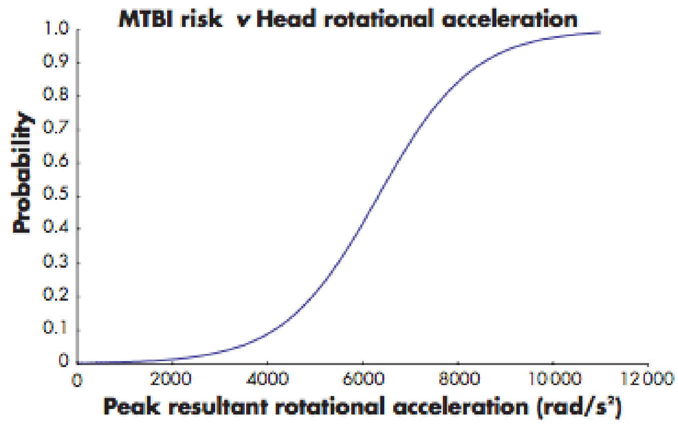

Fig 10. Probability risk curve for linear (top) and rotational accelerations (bottom) [46].

For confidentiality reasons, non-identifiable labelling of the smart polymer materials needed to be used, thus trends and general observations are discussed rather than the individual solutions. As it can be observed, the range of observed peak linear accelerations values is significantly large, which ultimately suggests a possibility of finding a balanced solution that encompasses an increased protection and an elimination of the concerns that such headgear may be a catalyst for more severe head injury. It can also be observed that the solutions could be grouped into three clusters based on their performance. The first cluster ("Cluster 1"), grouped around the EVA solution, includes soft and under-performing solutions and although these solutions may provide significant improvements to the existing rugby headgear, they still fail to reduce any risk of concussion (i.e. >150g). The second cluster ("Cluster 2") can be considered as the solutions with a transitional and relatively mediocre performance with some tendency to reduce the risk of concussion. The EPS solution separates the final cluster ("Cluster 3") and high performing solutions from the rest. These solutions are capable of at least halving the probability of concussion. When multi-layered solutions were considered, an addition of a 3mm thick layer of perforated Poron XRD to the EPS foam, improved its impact attenuation performance by 10%. The best performing solution was a multi-layered solution consisting of a high performance solution and the 3mm thick layer of perforated Poron XRD, which reduced the risk of concussion below 10%.

B. The New Sport-Specific Test Methodology Results

Unlike the standard test methodology which only had the peak linear acceleration as the injury assessment criterion, this newly developed test allowed the head injury risk to be quantified via several parameters: the peak linear acceleration, angular acceleration and angular velocity. Withnall et al. [46] also developed the LOGIST plot representing the injury risk for peak angular acceleration (see **Fig 10**). Furthermore, a biofidelic injury criterion called the Cumulative Strain Damage Measure (CSDM05) available via the simulated injury monitor (SIMon) finite element head model [47], was additional criterion used in this test methodology. The CSDM calculates the cumulative proportion of brain volume that has reached a threshold of ≥5% stretch over the duration of the load from the three-dimensional kinematic data of the headform [47-50]. Only the smart polymer materials and the commercial headgear were tested using this methodology, resulting in 18 individual tests. The results, shown in **Figs 11a-d**, are averages of two repeated trials for each solution and since minimal variations between the trials were observed, the overall repeatability was deemed acceptable. Since both the headform and the surrogate shoulder were deformable, the test reference involving the bare headform impact was also produced. As it can be observed from the figure, the best performing foam (T1) gave an approximate 37% reduction on the bare headform Peak g while the worst performing foam (T2) gave only around 15% of the reduction. The top three performing solutions reduced the concussion likelihood from 50% to 10% according to the LOGIST curves in **Fig 10**. Rotational acceleration was lower in the across all solutions compared to the bare headform condition, and the top three performing solutions offered reductions of approximately 40% in the probability of concussion. The angular accelerations were similar in order performance to the linear acceleration results for each solution, however angular velocity was relatively constant across all tests. According to SIMon, the lowest and the highest DAI severity ratings (CSDM05: 0.096, 81% reduction on the bare headform performance; and CSDM05: 0.311, 38% reduction, respectively) were assigned to two solutions with ***similar*** linear and rotational performance measures. Similarly, the repeated trials of the same solutions that had very similar linear and rotational components would show high variability in the CSDM05 value, which suggested repeatability issues. Bartsch et al. [51] reported a similar situation in their study and they attribute this inherent variability to high sensitivity of the FE model to rotational acceleration of the head about the coronal plane, which again may emphasizes the importance of considering the rotational acceleration as a vital part of any head injury criterion and targeting rotational acceleration reduction in future headgear may be critically important to their overall effectiveness

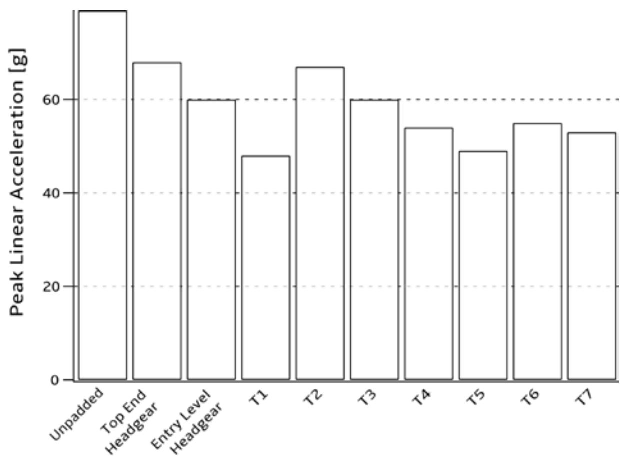

Fig 11a. Results of the side impact foam samples testing, showing linear acceleration

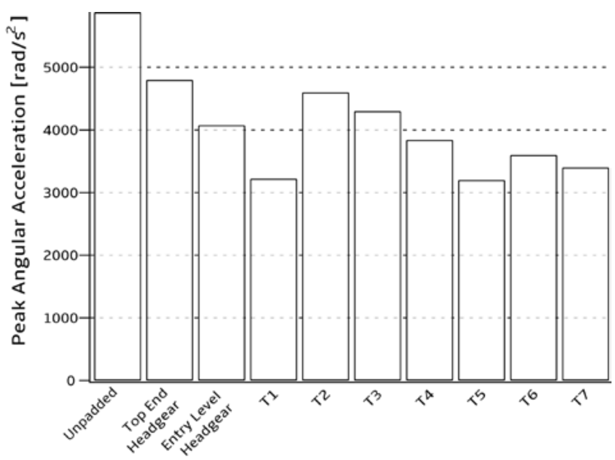

Fig 11b. Results of the side impact foam samples testing, showing angular acceleration

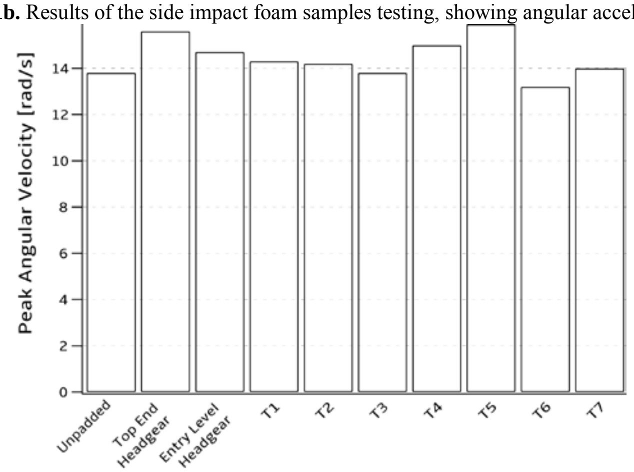

Fig 11c. Results of the side impact foam samples testing, angular velocity

ISBN: 978-1-61804-295-8

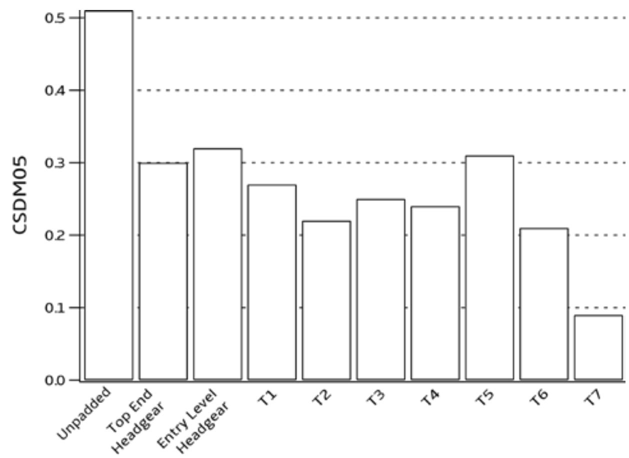

Fig 11d. Results of the side impact foam samples testing, showing CSDM05

C. Performance Comparison across the Two Tests

The peak linear acceleration, as the common parameter in both tests, contrasts the test methodologies and also provides additional insight into the performances of the tested materials (see **Fig 12**). An immediate distinction is the order of magnitudes between the outputted values. While the unpadded contact between an impactor and a base in the standard test was capped to 800g, the bare headform impact in the new biomechanical test was only 80g. This observation is in an agreement with other similar studies [7, 8, 37], which may demonstrate that the incorporation of yielding impact surfaces is an important improvement to the conventional linear head drop system. The trends and the performance of the tested materials generally tend to be corresponding and translate adequately but with one exception (T1) that was confirmed to be valid reading (consistent values during the repeatability testing). In order to suggest an explanation, the mechanical properties of the individual solution would need to be discussed, which carries a risk of identifying the material. However, it is another consequence of the introduction of yielding impact surfaces. Another noticeable distinction is that the erstwhile superior performance of the smart polymers is less augmented in the biomechanical test results, which may also demand a different approach to post-processing of results from a typical comparison of face values (eg. different scaling or performance indicators in order to decompress or increase a differentiation between points).

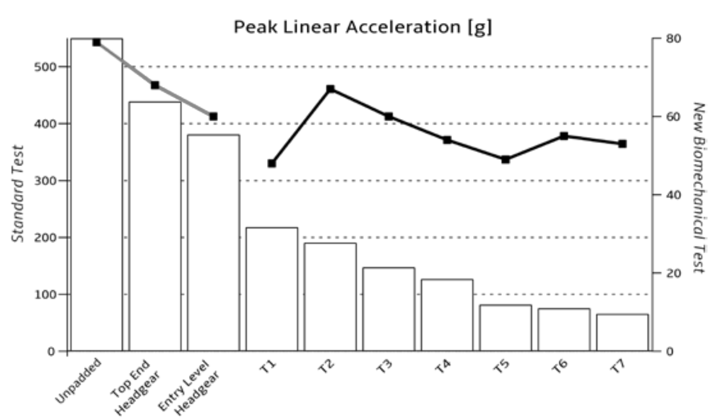

Fig 12. Performance comparison across the tests – peak linear acceleration

VII. Conclusions

The rate and severity of concussion in the sport of Rugby is concerning in light of recent findings relating repeated head impacts to neurological dysfunction and degeneration. Since much is still unknown about causes and effects of concussion, the minimization and the prevention of mild brain injury is of paramount importance to the short and long term health of all who play contact sports. Utilising a recently developed repeatable biomechanical test method to better recreate a common impact scenario resulting in concussion to Rugby players, this study explored application of smart polymers in new headgear designs by comparing their impact attenuation properties with those of the current products and more traditional foams. This study found:

- The current products do not provide sufficient protection.
- *Based on the peak linear acceleration injury criterion:* The majority of the solutions based on the tested smart polymer materials is capable of reducing the probability of concussion below 50%, according to the probability risk curve for

linear acceleration.

- The best performing solution was a multi-layered solution that reduced the risk of concussion below 10%
- *Based on the peak rotational acceleration injury criterion*: A smart polymer material is capable of offering reductions of approximately 40% in the probability of concussion according to the probability risk curve for rotational acceleration.
- *Based on a biofidelic injury criterion Diffuse Axonal Injury (DAI) severity rating*: A smart polymer material is capable of offering reductions of approximately 80% in contrast to the bare biomechanical headform performance, which is more than twice the reduction of the current products.

REFERENCES

[1] Patricios, J.S. and S. Kemp, "Chronic traumatic encephalopathy: rugby's call for clarity, data and leadership in the concussion debate," *British Journal of Sports Medicine*, vol. 48, no. 2, p. 76-79, 2014.
[2] Pettersen, J.A., "Does rugby headgear prevent concussion? Attitudes of Canadian players and coaches," *British Journal of Sports Medicine*, vol. 36, no. 1, p. 19-22, 2002.
[3] Finch, C.F., A.S. McIntosh, and P. McCrory, "What do under 15 year old schoolboy rugby union players think about protective headgear?," *British Journal of Sports Medicine*, vol. 35, no. 2, p. 89-94, 2001.
[4] Giza, C.C. and D.A. Hovda, "The Neurometabolic Cascade of Concussion," *Journal of Athletic Training*, vol. 36, no. 3, p. 228-235, 2001.
[5] McIntosh, A.S., P. McCrory, and J. Comerford, "The dynamics of concussive head impacts in rugby and Australian rules football," *Medicine & Science in Sports & Exercise*, vol. 32, no. 12, p. 1980-1984, 2000.
[6] Kemp, S.P., et al., "The epidemiology of head injuries in English professional rugby union," *Clinical Journal of Sport Medicine*, vol. 18, no. 3, p. 227-234, 2008.
[7] Knouse, C.L., et al., "Efficacy of Rugby Headgear in Attenuating Repetitive Linear Impact Forces," *Journal of Athletic Training*, vol. 38, no. 4, p. 330-335, 2003.
[8] Hrysomallis, C., "Impact energy attentuation of protective football headgear against a yielding surface," *Journal of science and medicine in sport*, vol. 7, no. 2, p. 156-164, 2004.
[9] McIntosh, A., P. McCrory, and C.F. Finch, "Performance enhanced headgear: a scientific approach to the development of protective headgear," *British Journal of Sports Medicine*, vol. 38, no. 1, p. 46-49, 2004.
[10] McIntosh, A.S., et al., "Rugby headgear study," *Journal of Science and Medicine in Sport*, vol. 6, no. 3, p. 355-358, 2003.
[11] Bailes, J.E. and V. Hudson, "Classification of Sport-Related Head Trauma: A Spectrum of Mild to Severe Injury," *Journal of Athletic Training*, vol. 36, no. 3, p. 236-243, 2001.
[12] Slobounov, S., et al., "Sports-related concussion: ongoing debate," *British Journal of Sports Medicine*, 2013.
[13] Gavett, B.E., R.A. Stern, and A.C. McKee, "Chronic traumatic encephalopathy: a potential late effect of sport-related concussive and subconcussive head trauma," *Clinical Sports Medicine*, vol. 30, no. 1, p. 179-188,xi, 2011.
[14] Lissner, H.R., M. Lebow, and F.G. Evans, "Experimental studies on the relation between acceleration and intracranial pressure changes in man," *Surgery, gynecology & obstetrics*, vol. 111, p. 329-338, 1960.
[15] Gadd, C., "Use of a weighted impulse criterion for estimating injury hazard," *10th Stapp Car Crash Conference Proceedings*, p. 164-174, 1966.
[16] Ono, K., et al., "Human head tolerance to sagittal impact. Reliable estimation deduced from experimental head injury using subhuman primates and human cadaver skulls," *SAE Technical Paper* 801303, 1980.
[17] Unterharnscheidt, F. and L.S. Higgins, "Traumatic lesions of brain and spinal cord due to nondeforming angular acceleration of the head," *Texas reports on biology and medicine*, vol. 27, no. 1, p. 127-166, 1968.
[18] Gennarelli, T.A., et al., "Diffuse axonal injury and traumatic coma in the primate," *Annals of neurology*, vol. 12, no. 6, p. 564-574, 1982.
[19] Ommaya, A.K. and T. Gennarelli, "Cerebral concussion and traumatic unconsciousness correlation of experimental and clinical observations on blunt head injuries," *Brain*, vol. 97, no. 4, p. 633-654, 1974.
[20] Ommaya, A.K. and A.E. Hirsch, "Tolerances for cerebral concussion from head impact and whiplash in primates," *Journal of Biomechanics*, vol. 4, no. 1, p. 13-21, 1971.
[21] Pincemaille, Y., et al., "Some new data related to human tolerance obtained from volunteer boxers," *Proceedings of the 33rd Stapp Car Crash Conference*, 1989.
[22] Funk, J.R., et al., "Biomechanical risk estimates for mild traumatic brain injury," *Annual proceedings/Association for the Advancement of Automotive Medicine*, vol. 51, no., p. 343-361, 2006.
[23] Pellman, E.J., D.C. Viano, and null, "Concussion in professional football: summary of the research conducted by the National Football League's Committee on Mild Traumatic Brain Injury," *Neurosurgical focus*, vol. 21, no. 4, p. E12, 2006.
[24] Pellman, E.J., et al., "Concussion in professional football: helmet testing to assess impact performance – Part 11," *Neurosurgery*, vol. 58, no. 1, p. 78-96, 2006.
[25] Rowson, S., et al., "Linear and angular head acceleration measurements in collegiate football," *Journal of Biomechanical Engineering*, vol. 131, no. 6, p. 61016, 2009.
[26] Newman, J., et al., "A new biomechanical assessment of mild traumatic brain injury. Part 2: results and conclusions," *Proceedings of the 2000 international IRCOBI Conference on the Biomechanics of Impact, Montpellier, France*, 2000.
[27] Rowson, S., et al., "Rotational head kinematics in football impacts: an injury risk function for concussion," *Annals of biomedical engineering*, vol. 40, no. 1, p. Jan-14, 2012.
[28] Zhang, L., K.H. Yang, and A.I. King, "A proposed injury threshold for mild traumatic brain injury," *Journal of Biomechanical Engineering*, vol. 126, no. 2, p. 226-236, 2004.
[29] Duma, S.M., et al., "Analysis of realtime head accelerations in collegiate football players," *Clinical Journal of Sport Medicine*, vol. 15, no. 1, p. 3-9, 2005.
[30] McIntosh, A.S., et al., "Sports helmets now and in the future," *British Journal of Sports Medicine*, vol. 45, no. 16, p. 1258-1265, 2011.
[31] Garraway, W.M., et al., "Impact of professionalism on injuries in rugby union," *British Journal of Sports Medicine*, vol. 34, no. 5, p. 348-351, 2000.
[32] McIntosh, A., C. Caponecchia, and J. Usman, "Tackling risk compensation – a psycho-physical approach to measuring behaviour change," *British Journal of Sports Medicine*, vol. 45, no. 4, p. 362, 2011.
[33] Jones, S.J., et al., "Effectiveness of rugby headgear in preventing soft tissue injuries to the head: a case-control and video cohort study," *British Journal of Sports Medicine*, vol. 38, no. 2, p. 159-162, 2004.

[34] McIntosh, A.S. and P. McCrory, "Effectiveness of headgear in a pilot study of under 15 rugby union football," *British Journal of Sports Medicine*, vol. 35, no. 3, p. 167-169, 2001.
[35] McIntosh, A.S., et al., "Does padded headgear prevent head injury in rugby union football?," *Medicine & Science in Sports & Exercise*, vol. 41, no. 2, p. 306-313, 2009.
[36] Kuncir, E.J., R.W. Wirta, and F.L. Golbranson, "Load-bearing characteristics of polyethylene foam: an examination of structural and compression properties," *Journal of rehabilitation research and development*, vol. 27, no. 3, 1990.
[37] McIntosh, A.S. and P. McCrory, "Impact energy attenuation performance of football headgear," *British Journal of Sports Medicine*, vol. 34, no. 5, p. 337-341, 2000.
[38] Bosch, H.L.A.v.d., "Crash helmet testing and design specifications," *PhD Thesis, Technische Universiteit Eindhoven,* Eindhoven, 2006.
[39] IRB, "Regulation 12: Provisions Relating to Players' Dress," *International Rugby Board*, Dublin, 1998.
[40] Viano, D.C., et al., "Injury biomechanics research: an essential element in the prevention of trauma," *Journal of Biomechanics*, vol. 22, no. 5, p. 403-417, 1989.
[41] Karren, J., et al., "Design of a Test Methodology to Measure Rugby Headgear Effectiveness," *9th Australasian Biomechanics Conference*, Wollongong, Australia, 2014.
[42] Karren, J., "Effectiveness of Rugby Headgear in the Prevention of Concussion," *Honours Thesis, School of Aeronautical, Mechanical and Mechatronic Engineering, University of Sydney*, Sydney, 2014.
[43] Whyte, T., et al., "Dead Injury and Effective Motorcycle Helmets," *Proceedings of Enhanced Safety of Vehicles Conference, Seoul*, Paper Number 13-0108, 2013.
[44] Shaw, G., J. Crandall, and J. Butcher, "Comparative evaluation of the THOR advanced frontal crash test dummy," *International Journal of Crashworthiness*, vol. 7, no. 3, p. 239-254, 2002.
[45] Vezin, P., et al., "Comparison of Hybrid III, Thor-alpha and PMHS Response in Frontal Sled Tests," *Stapp Car Crash Journal*, vol. 46, no., p. 1-28, 2002.
[46] Withnall, C., et al., "Biomechanical investigation of head impacts in football," *British Journal of Sports Medicine*, vol. 39, Suppl 1, p. i49-57, 2005.
[47] Takhounts, E.G., et al., "Investigation of Traumatic Brain Injuries Using the Next Generation of Simulated Injury Monitor (SIMon) Finite Element Head Model," *Stapp Car Crash Journal*, vol. 52, p. 1-33, 2008.
[48] Bandak, F., et al., "Simon: a simulated injury monitor; application to head injury assessment," *SAE Technical Paper*, vol. 2001-06-0222, 2001.
[49] Takhounts, E.G., et al., "On the development of the SIMon finite element head model," *Stapp car crash journal*, vol. 11, no. 47, p. 107-33, 2003.
[50] Marjoux, D., et al., ""Head injury prediction capability of the HIC, HIP, SIMon and ULP criteria"," *Accident Analysis & Prevention*, vol. 40, no. 3, p. 1135-1148, 2008.
[51] Bartsch, A., et al., "Impact test comparisons of 20th and 21st century American football helmets: Laboratory investigation," *Journal of neurosurgery*, vol. 116, no. 1, p. 222-233, 2012.

Investigation of Hydrothermal Processing of Strontium Peroxyapatite Synthesis

Agnese Osite[1, a] *, Karlis Agris Gross[2, b], Arturs Viksna[1, c], Juris Prikulis[3, d] and Aizhan Sainova[4,e]

[1]Department of Analytical Chemistry, University of Latvia, K. Valdemara Str. 48, Riga, LV-1013, Latvia

[2]Institute of Biomaterials & Biomechanics, Riga Technical University, Azenes Str. 14/24, Riga, LV-1048, Latvia

[3]Institute of Chemical Physics, University of Latvia, Kronvalda Blvd. 4, Riga, LV- 1010, Latvia

[4]Institute of Strength Physics and Materials Science SBRAS, 2/4, Academichesky ave., Tomsk, Russian Federation

[a]agnese.osite@lu.lv, [b]Karlis-Agris.Gross@rtu.lv, [c]arturs.viksna@lu.lv, [d]juris.prikulis@lu.lv, [e]aizhanochik@mail.ru

Keywords: strontium peroxyapatite, hydrogen peroxide, permanganatometric titration, hydrothermal processing

Abstract

The experimental research was devoted to the peroxide ions' incorporation in strontium hydroxyapatite (SrHAp) by exposure to 50 % wt. H_2O_2 during hydrothermal processing in the closed steel vessel system under relatively mild conditions at temperature range from 150 to 110 ^oC. Peroxide enriched strontium apatite (SrPerAp) was subjected to quantitative chemical analysis - content of peroxide was determined by classical permanganometric titration and stability of peroxide content was evaluated within three months. The structure of synthesised powders was characterized with X – Ray Difraction. This study continued from the previous ones. The objective was to obtain apatite, with a higher peroxide ion content incorporated in apatitic channels of strontium substitute lattice with synthesis at notably lower temperature and shorter time.

Introduction

Hydroxyapatite, (HAp), $[Ca_{10}(PO_4)_6(OH)_2]$ is one of the most promising biomaterials among all the calcium orthophosphates. Since chemically synthesized apatite indicates structure similarities to naturally formed mineral fraction of bone, HAp become one of the main bioceramics. In addition HAp exhibits several practical applications as a catalyst, LC column, lighting material or chemical sensor. But more essential is its emploing in clinical applications for bone and dental regeneration due to its excellent biocompability [1].

Cationic and anionic substitutions of initial calcium phospate can enrich the hosting material with additional well valued properties. Strontium which as trace element is present in the mineral phase of bone is one of wery comonly used for calcium substitution to improve bone strength and even reduce risks of osteoporosis [2, 3, 4]. Strontium hydroxyapatite as bioactive bone cement is used in spinal and bone fracture surgery, in bone replacement, bone fillings and bone adhesives [5].

Despite broad research in hydroxyapatite field still there are some improvements to be done to impart antibacterial capability. To exterminate or at least to minimize the undesirable infection threats, it is necessary to improve hydroxyapatite antibacterial properties. Hydrogen peroxide (H_2O_2) has an antibacterial effect and although it was widely thought that H_2O_2 is very toxic in vivo and must be rapidly eliminated employing several enzymes, also is found in the human body – it is generated by phagocytes to modulate the inflammatory processes [6].

Incorporation of both Sr and peroxide in apatite lattice structure would result by biomaterials having antiseptic and anti – inflammatory properties. There are several ways of synthesis of such materials, for example, treatment at 1000 ^oC temperature which lasted at least two days [7] or annealing treatment which was conducted at 800 ^oC for 2h [8]. Despite the increased research of

ISBN: 978-1-61804-295-8

hydroxyapatites during last decades, there is still informational lack in basics of peroxyapatite and the most appropriate synthesis routes have still not been developed.

Experimental

Strontium hydroxyapatite (SrHAp) powder was obtained by wet chemical method using two solutions. Solution A consisted from 0.02 mol of $Ca(NO_3)_2$, 0.06 mol of $Sr(NO_3)_2$, and 0.4 mol of NH_3 water solution, but 0.03 mol of $(NH_4)_2HPO_4$ and additive of $(NH_4)_2CO_3$ was used for preparing of solution B. Analytical grade chemicals were dissolved in deionized water and the two solutions mixed, the obtained suspension was stirred for 10 minutes, filtered, washed, and dried at 100 ^oC for 30 minutes.

SrHAp was used as the host powder for peroxide ions to create strontium peroxyapatite. Synthesis of SrPerAp was performed in a closed system - hydrothermal steel pressure vessel (total volume $2.5 \cdot 10^{-5}$ m^3) at temperature diapason from 150 till 110 ^oC, contrary to the higher temperatures used in the previous research works and contrary to notably higher temperatures used by other authors [7, 8, 9]. After loading 0.05 g of SrHAp powder and 4 mL of concentrated H_2O_2 solution in the hydrothermal steel pressure vessel, the hydrothermal pressure system was heated for 1, 3 and 6 hours and afterwards cooled under cool air flow with cooling rate $1{,}5^o$ per min.

The classical permanganometric redox titration was applied to determine the content of H_2O_2 in peroxyapatite. After dissolving SrPerAp in concentrated perchloric acid and diluting with deionized water, the titration was applied using potassium permanganate solution (0.001 M) until the stoichiometric point was reached. To clarify extent of peroxide decomposition during hydrothermal processing, the same redox titration method was used to determine concentration of residual peroxide solution.

The physico-chemical characteristics were followed by other complementary technique. The obtained powder of SrPerAp was investigated by X-ray diffraction on a D8 Advance diffractometer (Bruker), recorded from 5^o till 60 ^{o} using Cu Kα radiation (λ = 1.54180Å generated at 40 mA and 40 kV).

Results and Discussion

X-Ray Difraction analysis. As it was predicted by lowering the hydrothermal treatment temperature until 110 ^oC, the results of XRD analysis of synthesized powders displayed two types of patterns depending on the heating temperature, Fig. 1. Diffraction peaks of peroxyapatite samples obtained at temperatures 150 and 130 ^oC (samples treated for 3 and 6 hours) are sharp and characteristic of a well-crystallized peroxyapatite, the hydrothermal process treatment has apparently improved the crystallinity of strontium peroxyapatite samples. This shows that the previously developed method of peroxyapatite synthesis is reproducible also at lower temperature range [10]. XRD results indicated that the hydrothermal treatment of the apatite samples at 110 ^oC was insufficient to obtain well-crystallized peroxyapatite although at treatment duration - 6 hours small diffractions peaks started to form but the corresponding pattern of sample treated for 1h is witnessing the similar structure of amorphous SrHAp, Fig.1. The powder color serves as a visual characterizing parameter of successful hydrothermal process. Those samples showing amorphous structure in XRD patterns remained in white color, but SrPerAp samples with crystalline structure changed their coloration to light yellow, what is in a good agreement with other studies [7].

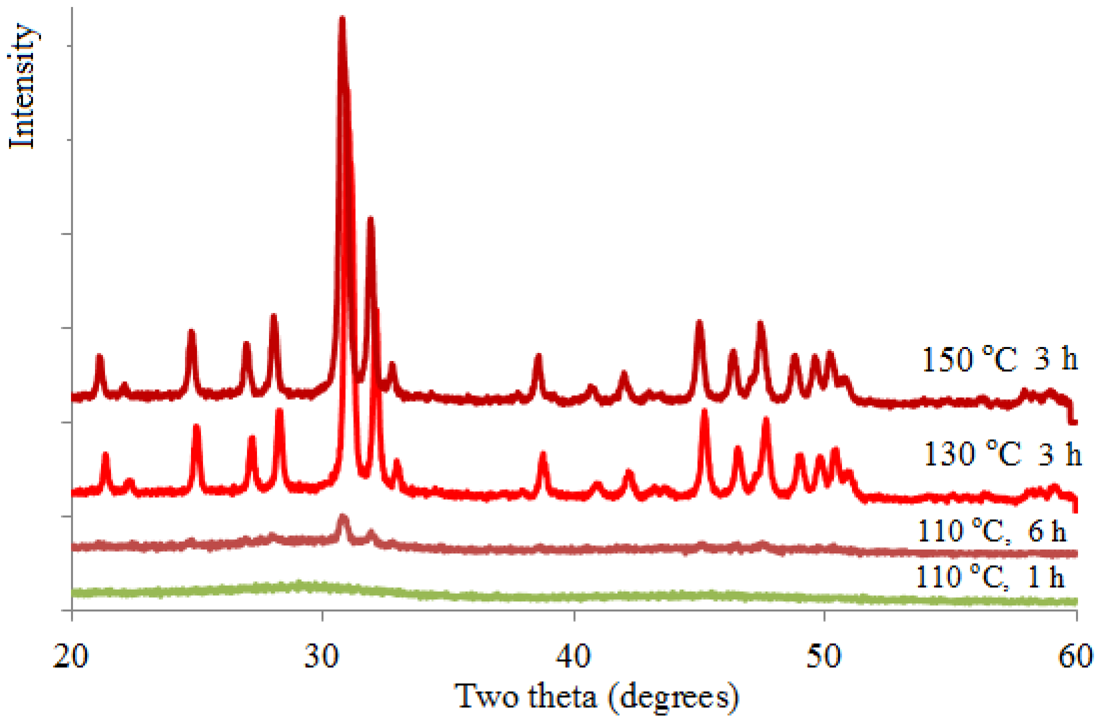

Fig. 1 XRD results of strontium substituted apatite samples after hydrothermal treatment in H_2O_2 medium

Peroxide quantification. A classical redox titration served for the peroxide quantification in obtained strontium peroxyapatite samples, leading to a peroxide content in ranges of 1.0 to 2.9 %. As it can be observed from Fig. 2a, peroxide content varies depending on the hydrothermal processing duration and temperature. Higher values of peroxide content in strontium peroxyapatite were obtained during SrHAp hydrothermal processing at 110 and 130 ^{o}C if duration of process was only 1 hour. But we must admit that theoretical value of peroxide ion weight percent 2.4 % are exceeded in particular samples. It testifies thus not only peroxide incorporation in an apatitic lattice channels occurs but possibly H_2O_2 molecules could be associated to an apatite like water molecules or some other oxygenated species (for example O_2^-) may be present after hydrothermal processing as it was described previously [10]. These results confirmed the presence of peroxide ions in the composition of strontium apatite samples treated in H_2O_2 medium even at 110 ^{o}C.

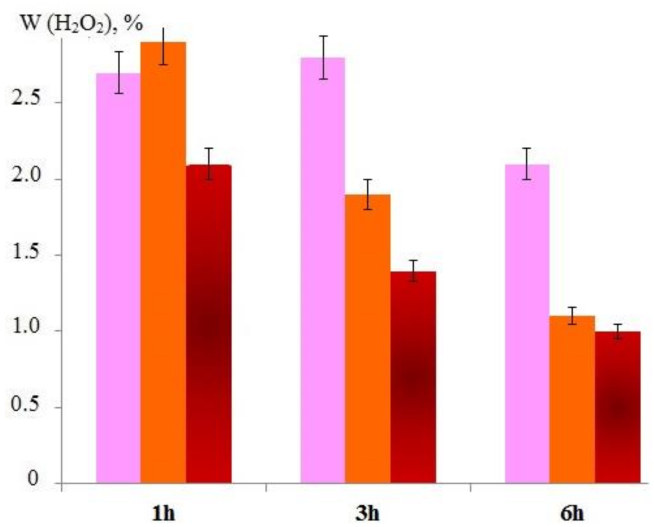

Fig.2a Weight percentage of H_2O_2 after SrHAp treatment at 110, 130 and 150 ^{o}C for 1, 3 and 6 hours.

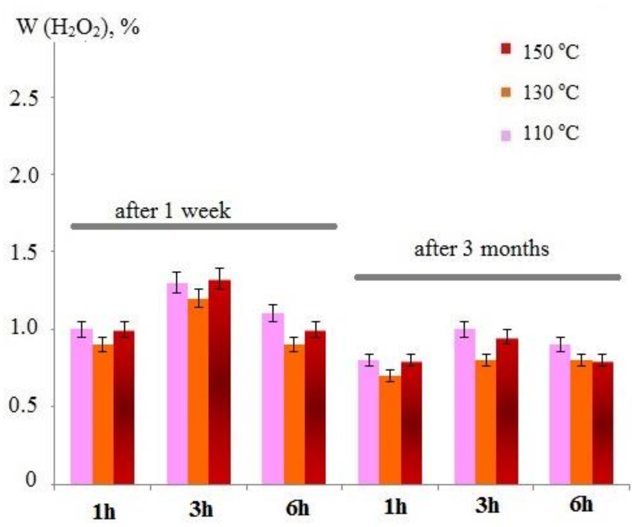

Fig. 2b Weight percentage of H_2O_2 after one week and three months.

Stability of SrPerAp. Investigation of peroxide content in SrPerAp powders has showed noteworthy changes over time. The highest peroxide concentrations are detected by redox titration just after the synthesis process. Repeated titration already one day after hydrothermal powder treatment indicated reduction in approximately 5-7 % of previously determined peroxide content, the most remarkable decrease (50-60 %, Fig. 2b) occurs after one week of powder storage at 4 ^oC. In Fig. 2b we can also observe that minor changes of peroxide content have affected samples treated at higher temperature ranges and with longer processing duration. Peroxide content in SrPerAp powders remain rather stable (0.8 – 0.9 % wt) after three months storage and the total average loss of initially determined peroxide content approach 70 %. Such stable peroxiapatites could be favorable material for implants, which are safe for a living body.

Impact of hydrothermal process. Originally the critical pressure and temperature of the hydrothermal pressure processing was calculated and these results adverted that heating temperature should not reach 180 ^oC for safety reasons. Analysis of apatite powder obtained after hydrothermal synthesis process at severe temperatures indicated that the detected peroxide amount increased by lowering the temperature from 170 ^oC (previous work [11]) until 110 ^oC, but unfortunately the remarkable loss of initially determined peroxide attested week peroxide incorporation in the apatitic lattice. This brought us to the efficiency verification of hydrothermal process therefore after hydrothermal treatment concentrations of residual peroxide solution were determined also by permanganometric titration (molar concentration of $KMnO_4$ was 0.02M). Results testified that used 50 % wt H_2O_2 solution is very well stabilised and increased temperature and pressure during hydrothermal processing leads to poor peroxide decomposition – around 15 % of initial concentrated peroxide that gives approximately 5 mmols O_2. Obtained load of O_2 did not show significant variations depending on hydrothermal processing duration and temperature, exception was 6 hours' process at 150 ^oC which gave higher O_2 amount. Regarding above mentioned, the usage of the catalyst containing Mn^{2+} ions was supported. The peroxide decomposition experiments showed that previously achieved 15 % of initial peroxide solution decomposition has been approached during the first minutes of experiment. The usage of catalyst during apatite hydrothermal processing will be developed in future studies.

As it was found out that peroxide decomposition and formation of O_2 is not the only process accountable to peroxyapatite formation, and since the 50 % H_2O_2 solution boiling point is 114 ^oC, peroxide gaseous phase may give some contribution.

Conclusion

Modifying strontium hydroxyapatite by hydrothermal processing at 130 – 150 ^oC in peroxide medium it is possible to obtain well crystalized strontium peroxyapatite with average peroxide weight percentage 1.7 % (substitution 0.74), at lower temperature – 110 ^oC, determined average peroxide content is higher – 2.8 %, but X-Ray Difraction patterns indicate still amorphous structure. Although treated powders with higher detected peroxide content are not stable and within several weeks peroxide content is decreased by 70 %. To achieve complete hydrogen peroxide decomposition during hydrothermal process and more effective peroxide incorporation in apatitic lattice, a catalyst will be used in further work.

Acknowledgement

Support from the ESF project 2013/0028/1DP/1.1.1.2.0/13/APIA/VIAA/054 is gratefully acknowledged.

References

[1] N. Rangavittal, A.R. Landa-ca´ novas, J.M. Gonza´ lez-Calbet, M.Vallet-Regı´. J. Biomed.Mater. Res. 51, 2000, 660–668.

[2] A. Bigi, E. Boanini, C. Capucini, M. Gazzano, Inorganica Chimica Acta. 360, 2007, 1009-1016.

[3] L. Yingguang, Y. Zhuoru, C. Jiang, W. Lianshi, J. of Wuhan University of Technology-Mater. 2008, 475-479.

[4] S.P. Nielsen, Bone, 35, 2004, 583-588.

[5] M.D. Grynpas, E. Hamilton, R. Cheung, Y. Tsouderos, P. Deloffre, M. Hott, P.J. Marie, Bone 18, 1996, 253.

[6] B. Halliwella et. al. FEBS Letters, 486, 2000, 10-13.

[7] J.C. Trombe, G. Montel, J. inorg. nucl. Chem. 40, 1978, 23-26.

[8] H. Zhao, X. Li, J. Wang, S. Qu, J. Weng, X. Zhang, J. Biomed Mater. Res. 52, 2000, 157-163.

[9] P.E. Kazin, M.A. Zykin, R.E. Dinnebier, O.V. MagDysyuk, Y.D. Tretyakov, M. Jansen, Z. Allg. Chem. 638 (2012) 909-919.

[10] A. Osite, K. A. Gross, A.Viksna and R. Poplausks. Mat. Sc. Eng., submitted.

[11] K.A. Gross, A. Jersova, A. Viksna, Key Eng. Mater., 631, 2014, 88.

Nonlinear Dynamic Response of a Fractionally Damped Thin Plate with 1:1:1 Internal Resonance

Yury Rossikhin[1,a], Marina Shitikova[1,b*] and Jean Claude Ngenzi[1,2,c]

[1]Research Center of Wave Dynamics, Voronezh State University of Architecture and Civil Engineering, Voronezh 394006, Russia

[2]Ecole Normale Supérieure, ENS Burundi

[a]yar@vgasu.vrn.ru , [b]mvs@vgasu.vrn.ru , [c]jngenzi@vgasu.vrn.ru

* the corresponding author

Keywords: Dynamics of nonlinear thin plate, fractional derivative, method of multiple time scales, fractional viscoelastic medium, one-to-one-to-one internal resonance

Abstract. Nonlinear vibrations of a thin plate, the motion of which is described by a set of three nonlinear differential equations, are studied for the case when the plate is embedded in a fractional derivative viscoelastic medium and the natural frequencies of different modes of in-plane and out-of-plane vibrations are approximately equal to each other, i.e., the 1:1:1 internal resonance takes place. Using the approach recently proposed, it is possible first to uncouple the coupled linear parts of equations of motion of the plate, and then to solve nonlinear governing equations by the method of multiple time scales.

Introduction

In the present paper, nonlinear free vibrations of a thin plate described by three coupled nonlinear differential equations [1] are considered when the plate is being under the conditions of the 1:1:1 internal resonance resulting in the interaction of three different types of modes corresponding to the three mutually orthogonal displacements. The displacement functions are determined in terms of eigenfunctions of linear vibrations. The procedure resulting in decoupling linear parts of equations proposed in [2] with the further utilization of the method of multiple time scales [3] for solving nonlinear governing equations of motion has been generalized for the case of the 1:1:1 internal resonance, in so doing the amplitude functions are expanded into power series in terms of the small parameter and depend on different time scales. It is shown that the phenomenon of internal resonance can be very critical, since in a thin plate internal resonance of different types are always present.

Problem Formulation and the Method of Solution

Let us consider the dynamic behavior of a free supported nonlinear thin rectangular plate, vibrations of which in a viscoelastic medium are described in the Cartesian system of coordinates by the following three differential equations written in the dimensionless form [1]:

$$u_{xx} + \frac{1-\nu}{2}\beta_1^2 u_{yy} + \frac{1+\nu}{2}\beta_1 v_{xy} + w_x\left(w_{xx} + \frac{1-\nu}{2}\beta_1^2 w_{yy}\right) + \frac{1+\nu}{2}\beta_1^2 w_y w_{xy} = \ddot{u} + æ_1 D^\gamma u, \tag{1}$$

$$\beta_1^2 v_{yy} + \frac{1-\nu}{2} v_{xx} + \frac{1+\nu}{2}\beta_1 u_{xy} + \beta_1 w_y\left(\beta_1^2 w_{yy} + \frac{1-\nu}{2} w_{xx}\right) + \frac{1+\nu}{2}\beta_1 w_x w_{xy} = \ddot{v} + æ_2 D^\gamma v, \tag{2}$$

$$\frac{\beta_2^2}{12}(w_{xxxx}+2\beta_1^2 w_{xxyy}+\beta_1^4 w_{yyyy})-w_{xx}(u_x+\nu\beta_1 v_y)-w_x(u_{xx}+\nu\beta_1 v_{xy})$$
$$-\quad \frac{1-\nu}{2}\beta_1[w_{xy}(\beta_1 u_y+v_x)+w_y(\beta_1 u_{xy}+v_{xx})]-\quad \beta_1^2[w_{yy}(\nu u_x+\beta_1 v_y)+w_y(\nu u_{xy}+\beta_1 v_{yy})] \tag{3}$$
$$-\quad \frac{1-\nu}{2}\beta_1[w_{xy}(\beta_1 u_y+v_x)+w_x(\beta_1 u_{yy}+v_{xy})]=-\ddot{w}-æ_3 D^\gamma w,$$

subjected to the initial

$$u|_{t=0}=0,\quad v|_{t=0}=0,\quad w|_{t=0}=0, \tag{4}$$
$$\dot{u}|_{t=0}\ =\ \varepsilon U^0(x,y),\quad \dot{v}|_{t=0}=\varepsilon V^0(x,y),\quad \dot{w}|_{t=0}=\varepsilon W^0(x,y), \tag{5}$$

as well as the boundary conditions

$$w|_{x=0}=w|_{x=1}=0,\quad v|_{x=0}=v|_{x=1}=0,\quad u_x|_{x=0}=u_x|_{x=1}=0,\quad w_{xx}|_{x=0}=w_{xx}|_{x=1}=0, \tag{6}$$
$$w|_{y=0}=w|_{y=1}=0,\quad u|_{y=0}=u|_{y=1}=0,\quad v_y|_{y=0}=v_y|_{y=1}=0,\quad w_{yy}|_{y=0}=w_{yy}|_{y=1}=0, \tag{7}$$

where $u=u(x,y,t)$, $v=v(x,y,t)$, and $w=w(x,y,t)$ are the displacements of points located in the plate's middle surface in the $x-$, $y-$, and $z-$directions, respectively, ν is Poisson's ratio, $\beta_1=a/b$ and $\beta_2=h/a$ are the parameters defining the dimensions of the plate, a and b are the plate's dimensions along the $x-$ and $y-$axes, respectively, h is the thickness, t is the time, an overdot denotes the time-derivative, lower indices label the derivatives with respect to the corresponding coordinates, $æ_i$ ($i=1,2,3$) are damping coefficients, $U^0(x,y)$, $V^0(x,y)$, and $W^0(x,y)$ are the functions describing the distribution of the initial velocities of the points locating within the middle surface of the plate, ε is a small value, and D^γ is the Riemann-Liouville fractional derivative of the γ-order [4]

$$D^\gamma F=\frac{d}{dt}\int_0^t \frac{F(t-t')}{\Gamma(1-\gamma)t'^\gamma}\,dt'. \tag{8}$$

In Eqs. 1-7 , the dimensionless values are introduced similarly as it has been done in [5].
We seek the solution of Eqs. 1- 3 in the form

$$u(x,y,t)=\sum_{m=1}^{\infty}\sum_{n=1}^{\infty}x_{1mn}(t)\eta_{1mn}(x,y),\quad v(x,y,t)=\sum_{m=1}^{\infty}\sum_{n=1}^{\infty}x_{2mn}(t)\eta_{2mn}(x,y),\quad w(x,y,t)=\sum_{m=1}^{\infty}\sum_{n=1}^{\infty}x_{3mn}(t)\eta_{3mn}(x,y), \tag{9}$$

where $x_{1mn}(t)$, $x_{2mn}(t)$, and $x_{3mn}(t)$ are the generalized displacements corresponding to the displacements in the plane of the plate and to its deflection, respectively, but the natural functions satisfying the boundary conditions Eq. 6 and Eq. 7 have the form

$$\eta_{1mn}(x,y)=\cos\pi mx\sin\pi ny,\quad \eta_{2mn}(x,y)=\sin\pi mx\cos\pi ny,\quad \eta_{3mn}(x,y)=\sin\pi mx\sin\pi ny, \tag{10}$$

and m and n are integers.

Substituting Eq. 9 into Eqs. 1-3, multiplying Eqs. 1, 2, and 3 by η_{1lk}, η_{2lk}, and η_{3lk}, respectively, integrating over x and y, and using the orthogonality conditions for linear modes within the domains of $0\le x,y\le 1$, we are led to a coupled set of nonlinear ordinary differential equations of the second order in $x_{i\,mn}$ $(i=1,2,3)$:

$$\ddot{x}_{\alpha\,mn}+æ_\alpha D^\gamma x_{\alpha\,mn}+S_{\alpha\beta}^{mn}x_{\beta\,mn}=-F_{\alpha\,mn}\quad (\alpha,\beta=1,2), \tag{11}$$

$$\ddot{x}_{3\,mn} + æ_3 D^{\gamma} x_{3\,mn} + \omega_{3mn}^2 x_{3\,mn} = -F_{3\,mn}, \tag{12}$$

where the summation is carried out over two repeated indices, the nonlinear parts $F_{i\,mn}$ are presented in [2], and the elements of the matrix S_{ij}^{mn} are defined as

$$S_{11}^{mn} = \pi^2 \left(m^2 + \frac{1-\nu}{2} \beta_1^2 n^2 \right), \quad S_{12}^{mn} = S_{21}^{mn} = \frac{1+\nu}{2} \beta_1 \pi^2 mn, \quad S_{22}^{mn} = \pi^2 \left(\frac{1-\nu}{2} m^2 + \beta_1^2 n^2 \right). \tag{13}$$

Since the second-rank tensor $S_{\alpha\beta}^{mn}$ is symmetric, then it has two real eigenvalues $\omega_{\alpha\,mn}$

$$\omega_{1\,mn}^2 = \pi^2 (m^2 + \beta_1^2 n^2), \qquad \omega_{2\,mn}^2 = \frac{1-\nu}{2} \omega_{1mn}^2, \tag{14}$$

which are in correspondence with two mutually orthogonal eigenvectors

$$\vec{L}_{mn}^{\mathrm{I}} \left\{ L_{1\,mn}^{\mathrm{I}} = \frac{\pi m}{\omega_{1\,mn}}, \ L_{2\,mn}^{\mathrm{I}} = \frac{\pi \beta_1 n}{\omega_{1\,mn}} \right\}, \qquad \vec{L}_{mn}^{II} \left\{ L_{1\,mn}^{II} = \frac{\pi \beta_1 n}{\omega_{1\,mn}}, \ L_{2\,mn}^{II} = -\frac{\pi m}{\omega_{1\,mn}} \right\}, \tag{15}$$

i.e., $L_{\alpha\,mn}^{\mathrm{I}} L_{\alpha\,mn}^{\mathrm{I}} = L_{\alpha\,mn}^{II} L_{\alpha\,mn}^{II} = 1, \quad L_{\alpha\,mn}^{\mathrm{I}} L_{\alpha\,mn}^{II} = 0.$

Thus, the matrix $S_{\alpha\beta}^{mn}$ and the generalized displacements $x_{\alpha\,mn}$ entering in Eqs. 11 and 12 could be expanded in terms of the vectors defined in Eq. 15 [2] as

$$S_{\alpha\beta}^{mn} = \omega_{1\,mn}^2 L_{\alpha\,mn}^{\mathrm{I}} L_{\beta\,mn}^{\mathrm{I}} + \omega_{2\,mn}^2 L_{\alpha\,mn}^{II} L_{\beta\,mn}^{II}, \quad x_{\alpha\,mn} = X_{1\,mn} L_{\alpha\,mn}^{\mathrm{I}} + X_{2\,mn} L_{\alpha\,mn}^{II}. \tag{16}$$

Substituting Eq. 16 in Eqs. 11 and 12 and then multiplying Eq. 11 successively by $L_{i\,mn}^{\mathrm{I}}$ and $L_{i\,mn}^{II}$, we obtain the following three equations:

$$\ddot{X}_{1mn} + æ_1 D^{\gamma} X_{1mn} + \omega_{1mn}^2 X_{1mn} = -\sum_{\alpha=1}^{2} F_{\alpha\,mn} L_{\alpha\,mn}^{\mathrm{I}}, \tag{17}$$

$$\ddot{X}_{2mn} + æ_2 D^{\gamma} X_{2mn} + \omega_{2mn}^2 X_{2mn} = -\sum_{\alpha=1}^{2} F_{\alpha\,mn} L_{\alpha\,mn}^{II}, \tag{18}$$

$$\ddot{X}_{3mn} + æ_3 D^{\gamma} X_{3mn} + \omega_{3mn}^2 X_{3mn} = -F_{3\,mn}, \tag{19}$$

where $X_{3mn} = x_{3mn}$, and $\omega_{3\,mn}^2 = \dfrac{\pi^4 \beta_2^2}{12} (m^2 + \beta_1^2 n^2)^2$.

It should be emphasized that left-hand side parts of Eqs. 17-19 are linear and independent of each other, while Eqs. 17-19 are coupled only by nonlinear terms in their right-hand sides.

In order to show the influence of the initial conditions presented in Eqs. 4 and 5 on the solution to be constructed, let us expand the desired functions X_{imn} $(i = 1,2,3)$ in a series in terms of the small parameter ε

$$X_{imn} = \varepsilon X_{imn}^0 + \varepsilon^2 X_{imn}^1 + \ldots \quad (i = 1,2,3). \tag{20}$$

Substituting Eq. 20 in the set of Eqs. 17-19 and restricting ourselves by the terms of the order of ε, we are led to a linear homogeneous set of differential equations

$$\ddot{X}_{imn}^0 + \omega_{imn}^2 X_{imn}^0 = 0 \quad (i = 1,2,3). \tag{21}$$

The solution of Eqs. 21 has the form

$$X_{imn}^0 = A_{imn}(\varepsilon t) \exp(i\omega_{imn} t) + \bar{A}_{imn}(\varepsilon t) \exp(-i\omega_{imn} t) \quad (i = 1,2,3), \tag{22}$$

where $A_{imn}(\varepsilon t)$ and $\bar{A}_{imn}(\varepsilon t)$ are complex conjugate functions to be found.

Representing functions $A_{imn}(\varepsilon t)$ in the polar form

$$A_{imn}(\varepsilon t) = a_{imn}(\varepsilon t)e^{i\psi_{imn}(\varepsilon t)} \quad (i = 1,2,3), \tag{23}$$

the solution (20) is reduced to

$$X_{imn} = \varepsilon X_{imn}^{0} = 2\varepsilon a_{imn}(\varepsilon t)\cos\left[\omega_{imn}t + \psi_{imn}(\varepsilon t)\right] \quad (i = 1,2,3), \tag{24}$$

where $a_{imn}(\varepsilon t)$ and $\psi_{imn}(\varepsilon t)$ are the amplitudes and phases of non-linear vibrations, respectively.

Differentiating Eq. 24 with respect to time t and ignoring the terms of the order of ε^2, we obtain

$$\dot{X}_{imn} = -2\varepsilon a_{imn}(\varepsilon t)\omega_{imn}\sin\left[\omega_{imn}t + \psi_{imn}(\varepsilon t)\right] \quad (i = 1,2,3). \tag{25}$$

Now substituting Eq. 16 in Eq. 9 with due account for (24), we have

$$\begin{aligned}
u(x,y,t) &= 2\varepsilon\sum_{m=1}^{\infty}\sum_{n=1}^{\infty}\left\{a_{1mn}(\varepsilon t)\cos\left[\omega_{1mn}t + \psi_{1mn}(\varepsilon t)\right]L_{1mn}^{\mathrm{I}}\right. \\
&+ \left. a_{2mn}(\varepsilon t)\cos\left[\omega_{2mn}t + \psi_{2mn}(\varepsilon t)\right]L_{1mn}^{\mathrm{II}}\right\}\eta_{1mn}(x,y), \\
v(x,y,t) &= 2\varepsilon\sum_{m=1}^{\infty}\sum_{n=1}^{\infty}\left\{a_{1mn}(\varepsilon t)\cos\left[\omega_{1mn}t + \psi_{1mn}(\varepsilon t)\right]L_{2mn}^{\mathrm{I}}\right. \\
&+ \left. a_{2mn}(\varepsilon t)\cos\left[\omega_{2mn}t + \psi_{2mn}(\varepsilon t)\right]L_{2mn}^{\mathrm{II}}\right\}\eta_{2mn}(x,y), \\
w(x,y,t) &= 2\varepsilon\sum_{m=1}^{\infty}\sum_{n=1}^{\infty}a_{3mn}(\varepsilon t)\cos\left[\omega_{3mn}t + \psi_{3mn}(\varepsilon t)\right]\eta_{3mn}(x,y).
\end{aligned} \tag{26}$$

Using the initial conditions (4) and (5) with due account for relationships (25), from Eqs. 26 at $t = 0$ we obtain an infinite set of algebraic equations for determining $a_{imn}(0)$ and $\psi_{imn}(0)$ ($i = 1,2,3$)

$$\begin{aligned}
&a_{1mn}(0)L_{1mn}^{\mathrm{I}}\cos\psi_{1mn}(0) + a_{2mn}(0)L_{1mn}^{\mathrm{II}}\cos\psi_{2mn}(0) = 0, \\
&a_{1mn}(0)L_{2mn}^{\mathrm{I}}\cos\psi_{1mn}(0) + a_{2mn}(0)L_{2mn}^{\mathrm{II}}\cos\psi_{2mn}(0) = 0, \\
-\ &a_{1mn}(0)\omega_{1mn}L_{1mn}^{\mathrm{I}}\sin\psi_{1mn}(0) - a_{2mn}(0)\omega_{2mn}L_{1mn}^{\mathrm{II}}\sin\psi_{2mn}(0) = æ_{1mn}, \\
-\ &a_{1mn}(0)\omega_{1mn}L_{2mn}^{\mathrm{I}}\sin\psi_{1mn}(0) - a_{2mn}(0)\omega_{2mn}L_{2mn}^{\mathrm{II}}\sin\psi_{2mn}(0) = æ_{2mn}, \\
&a_{3mn}(0)\cos\psi_{3mn}(0) = 0, \\
-\ &a_{3mn}(0)\omega_{3mn}\sin\psi_{3mn}(0) = æ_{3mn},
\end{aligned} \tag{27}$$

where

$$æ_{1mn} = \frac{\int_0^1\int_0^1 U^0(x,y)\eta_{1mn}(x,y)dxdy}{\int_0^1\int_0^1 \eta_{1mn}^2(x,y)dxdy}, \quad æ_{2mn} = \frac{\int_0^1\int_0^1 V^0(x,y)\eta_{2mn}(x,y)dxdy}{\int_0^1\int_0^1 \eta_{2mn}^2(x,y)dxdy},$$

$$æ_{3mn} = \frac{\int_0^1\int_0^1 W^0(x,y)\eta_{3mn}(x,y)dxdy}{\int_0^1\int_0^1 \eta_{3mn}^2(x,y)dxdy}.$$

All subsequent approximations are determined from an inhomogeneous set of differential equations with known right parts. Since the general solution of such a system is the sum of two solutions, a particular solution of the inhomogeneous system and a general solution of the

ISBN: 978-1-61804-295-8

corresponding homogeneous system, then arbitrary constants could be chosen in such a way that the initial conditions of all subsequent approximations would be zero ones.

It is known [6] that during nonstationary excitation of thin bodies not all possible modes of vibration would be excited. Moreover, the modes which are strongly coupled by any of the so-called internal resonance conditions are initiated and dominate in the process of vibration, resulting in the energy transfer from one subsystem to another between the coupled modes, in so doing the types of modes to be excited are dependent of the character of the external excitation. As a result of damping, the modes that are not excited directly by an external excitation or through an internal resonance will die out, and only three modes will dominate the motion of the plate in three directions.

Following [2], assume hereafter that the vibration process occurs in such a way that only three natural modes corresponding to the generalized displacements $X_{1s_1s_2}$, $X_{2l_1l_2}$, and $X_{3k_1k_2}$ are excited and dominate over other natural modes. In this case, the right parts of Eqs. 17-19 are significantly simplified, and omitting hereafter the subindices s_1s_2, k_1k_2, and l_1l_2 for ease of presentation equations of free vibrations take the form

$$\begin{gathered}\ddot{X}_1 + æ_1 D^\gamma X_1 + \omega_1^2 X_1 + \zeta_1 X_3^2 = 0, \qquad \ddot{X}_2 + æ_2 D^\gamma X_2 + \omega_2^2 X_2 + \zeta_2 X_3^2 = 0, \\ \ddot{X}_3 + æ_3 D^\gamma X_3 + \omega_3^2 X_3 + X_3\left(\zeta_{13}X_1 + \zeta_{23}X_2\right) = 0,\end{gathered} \tag{28}$$

where ζ_1, ζ_2, ζ_{13}, and ζ_{23} are known coefficients.

Method of Solution

An approximate solution of Eqs. 28 for small but finite amplitudes weakly varying with time can be represented by a second-order uniform expansion in terms of different time scales in the following form [3]:

$$X_i = \varepsilon X_{i1}(T_0, T_1, T_2 \ldots) + \varepsilon^2 X_{i2}(T_0, T_1, T_2 \ldots) + \ldots, \tag{29}$$

where $i = 1,2,3$, ε is a small dimensionless parameter of the same order of magnitude as the amplitudes, $T_n = \varepsilon^n t$ are new independent variables, among them: $T_0 = t$ is a fast scale characterizing motions with the natural frequencies, and $T_1 = \varepsilon t$ and $T_2 = \varepsilon^2 t$ are slow scales characterizing the modulation of the amplitudes and phases of the modes with nonlinearity.

Recall that the first and the second time-derivatives are defined, respectively, as follows

$$\frac{d}{dt} = D_0 + \varepsilon D_1 + \varepsilon^2 D_2 + \ldots, \quad \frac{d^2}{dt^2} = D_0^2 + 2\varepsilon D_0 D_1 + \varepsilon^2\left(D_1^2 + 2D_0 D_2\right) + \ldots, \tag{30}$$

while the fractional-order time-derivative could be represented as [5]

$$\left(\frac{d}{dt}\right)^\gamma = \left(D_0 + \varepsilon D_1 + \varepsilon^2 D_2 + \ldots\right)^\gamma = D_0^\gamma + \varepsilon\gamma D_0^{\gamma-1} D_1 + \frac{1}{2}\varepsilon^2\gamma\left[(\gamma-1)D_0^{\gamma-2}D_1^2 + 2D_0^{\gamma-1}D_2\right] + \ldots, \tag{31}$$

where $D_n = \partial/\partial T_n$, and D_0^γ, $D_0^{\gamma-1}$, $D_0^{\gamma-2}$,... are the Riemann-Liouville fractional derivatives in time t defined in Eq. 8. Considering that the viscosity is small, i.e., $æ_i = \varepsilon^2 \mu_i \tau_i^\gamma$, where τ_i is the relaxation time of the i-th generalized displacement and μ_i is a finite value, substituting Eqs. 29-31 in Eqs. 28, after equating the coefficients at like powers of ε to zero, we are led to a set of recurrence equations to various orders:

to order ε

$$D_0^2 X_{11} + \omega_1^2 X_{11} = 0, \qquad D_0^2 X_{21} + \omega_2^2 X_{21} = 0, \qquad D_0^2 X_{31} + \omega_3^2 X_{31} = 0; \tag{32}$$

ISBN: 978-1-61804-295-8

to order ε^2

$$D_0^2X_{12}+\omega_1^2X_{12}=-2D_0D_1X_{11}-\zeta_1X_{31}^2,\qquad D_0^2X_{22}+\omega_2^2X_{22}=-2D_0D_1X_{21}-\zeta_2X_{31}^2,$$
$$D_0^2X_{32}+\omega_3^2X_{32}=-2D_0D_1X_{31}-\zeta_{13}X_{11}X_{31}-\zeta_{23}X_{21}X_{31},\tag{33}$$

to order ε^3

$$D_0^2X_{13}+\omega_1^2X_{13}=-2D_0D_1X_{12}-\left(D_1^2+2D_0D_2\right)X_{11}-2\zeta_1X_{31}X_{32}-\mu_1\tau_1^\gamma D_0^\gamma X_{11},$$
$$D_0^2X_{23}+\omega_2^2X_{23}=-2D_0D_1X_{22}-\left(D_1^2+2D_0D_2\right)X_{21}-2\zeta_2X_{31}X_{32}-\mu_2\tau_2^\gamma D_0^\gamma X_{21},$$
$$D_0^2X_{33}+\omega_3^2X_{33}=-2D_0D_1X_{32}-\left(D_1^2+2D_0D_2\right)X_{31}$$
$$-\zeta_{13}\left(X_{11}X_{32}+X_{12}X_{31}\right)-\zeta_{23}\left(X_{21}X_{32}+X_{22}X_{31}\right)-\mu_3\tau_3^\gamma D_0^\gamma X_{31}.\tag{34}$$

We shall seek the solution of Eqs. 32 in the form

$$X_{j1}=A_j(T_1,T_2)\exp(i\omega_jT_0)+\bar{A}_j(T_1,T_2)\exp(-i\omega_jT_0)\quad(j=1,2,3),\tag{35}$$

where $A_j(T_1,T_2)$ $(j=1,2,3)$ are unknown complex functions, and $\bar{A}_j(T_1,T_2)$ are the complex conjugates of $A_j(T_1,T_2)$.

Substituting Eqs. 35 in the right-hand side of Eqs. 33 with due account for Eqs. 30 yields

$$D_0^2X_{12}+\omega_1^2X_{12}=-2i\omega_1D_1A_1(T_1)\exp(i\omega_1T_0)-\zeta_1\left[A_3^2\exp(2i\omega_3T_0)+A_3\bar{A}_3\right]+\text{cc},$$
$$D_0^2X_{22}+\omega_2^2X_{22}=-2i\omega_2D_1A_2(T_1)\exp(i\omega_2T_0)-\zeta_2\left[A_3^2\exp(2i\omega_3T_0)+A_3\bar{A}_3\right]+\text{cc},$$
$$D_0^2X_{32}+\omega_3^2X_{32}=-2i\omega_3D_1A_3(T_1)\exp(i\omega_3T_0)-\zeta_{13}\left\{A_1A_3\exp\left[i(\omega_1+\omega_3)T_0\right]+A_1\bar{A}_3\exp\left[i(\omega_1-\omega_3)T_0\right]\right\}$$
$$-\zeta_{23}\left\{A_2A_3\exp\left[i(\omega_2+\omega_3)T_0\right]+A_2\bar{A}_3\exp\left[i(\omega_2-\omega_3)T_0\right]\right\}+\text{cc},\tag{36}$$

where cc is the complex conjugate part to the preceding terms.

To eliminate circular terms in Eqs. 36, it is necessary to vanish to zero the coefficients standing at $\exp\left(\pm i\omega_jT_0\right)$, i.e., $D_1A_j(T_1,T_2)=0$, whence it follows that A_j ($j=1,2,3$) are T_1-independent.

Then solution of Eqs. 36 has the form

$$\begin{aligned}X_{12}&=F_1(T_2)\exp(i\omega_1T_0)+k_1A_3^2\exp(2i\omega_3T_0)+k_2A_3\bar{A}_3+\text{cc},\\X_{22}&=F_2(T_2)\exp(i\omega_2T_0)+k_3A_3^2\exp(2i\omega_3T_0)+k_4A_3\bar{A}_3+\text{cc},\\X_{32}&=F_3(T_2)\exp(i\omega_3T_0)+k_5A_1A_3\exp\left[i(\omega_1+\omega_3)T_0\right]\\&+k_6A_2A_3\exp\left[i(\omega_2+\omega_3)T_0\right]+k_7A_3\bar{A}_1\exp\left[i(\omega_3-\omega_1)T_0\right]+k_8A_3\bar{A}_2\exp\left[i(\omega_3-\omega_2)T_0\right]+\text{cc},\end{aligned}\tag{37}$$

where $F_j(T_2)$ ($j=1,2,3$) are new functions to be determined, and coefficients k_i $(i=1,2,...,8)$ have the form

$$k_1=\frac{\zeta_1}{4\omega_3^2-1},\quad k_2=-\frac{\zeta_1}{\omega_1^2},\quad k_3=\frac{\zeta_2}{4\omega_3^2-1},\quad k_4=-\frac{\zeta_2}{\omega_2^2},\quad k_5=\frac{\zeta_{13}}{\omega_1(\omega_1+2\omega_3)},$$

$$k_6=\frac{\zeta_{23}}{\omega_2(\omega_2+2\omega_3)},\; k_7=\frac{\zeta_{13}}{\omega_1(\omega_1-2\omega_3)},\; k_8=\frac{\zeta_{23}}{\omega_2(\omega_2-2\omega_3)}.$$

Considering that $D_0^\gamma e^{i\omega_jt}\approx(i\omega_j)^\gamma e^{i\omega_jt}$ [4] and Eqs. 37, Eqs. 34 take the form

$$\begin{aligned}
D_0^2 X_{13} + \omega_1^2 X_{13} = &-\left[2i\omega_1 D_2 A_1 + \mu_1 \tau_1^\gamma (i\omega_1)^\gamma A_1 + 2\zeta_1 k_5 A_1 A_3 \overline{A}_3\right]\exp(i\omega_1 T_0) - 2\zeta_1 \{F_3 A_3 \exp(2i\omega_3 T_0) \\
&+ \overline{F}_3 A_3 + k_5 A_1 A_3^2 \exp\left[i(\omega_1 + 2\omega_3)T_0\right] + k_6 A_2 A_3^2 \exp\left[i(\omega_2 + 2\omega_3)T_0\right] \\
&+ k_6 A_2 A_3 \overline{A}_3 \exp(i\omega_2 T_0) + k_7 \overline{A}_1 A_3^2 \exp\left[i(2\omega_3 - \omega_1)T_0\right] + k_8 A_3^2 \overline{A}_2 \exp\left[i(2\omega_3 - \omega_2)T_0\right]\Big\} + \mathrm{cc},
\end{aligned} \tag{38}$$

$$\begin{aligned}
D_0^2 X_{23} + \omega_2^2 X_{23} = &-\left[2i\omega_2 D_2 A_2 + \mu_2 \tau_2^\gamma (i\omega_2)^\gamma A_2 + 2\zeta_2 k_6 A_2 A_3 \overline{A}_3\right]\exp(i\omega_2 T_0) - 2\zeta_1 \{F_3 A_3 \exp(2i\omega_3 T_0) \\
&+ \overline{F}_3 A_3 + k_5 A_1 A_3^2 \exp\left[i(\omega_1 + 2\omega_3)T_0\right] + k_6 A_2 A_3^2 \exp\left[i(\omega_2 + 2\omega_3)T_0\right] \\
&+ k_6 A_2 A_3 \overline{A}_3 \exp(i\omega_2 T_0) + k_7 \overline{A}_1 A_3^2 \exp\left[i(2\omega_3 - \omega_1)T_0\right] + k_8 A_3^2 \overline{A}_2 \exp\left[i(2\omega_3 - \omega_2)T_0\right]\Big\} + \mathrm{cc},
\end{aligned} \tag{39}$$

$$\begin{aligned}
D_0^2 X_{33} + \omega_3^2 X_{33} = &-\Big[2i\omega_3 D_2 A_3 + \mu_3 \tau_3^\gamma (i\omega_3)^\gamma A_3 + (\zeta_{13} k_2 + \zeta_{23} k_4) A_3^2 \overline{A}_3 \\
&+ \zeta_{13} k_7 A_1 \overline{A}_1 A_3 + \zeta_{23} k_8 A_2 \overline{A}_2 A_3\Big]\exp(i\omega_3 T_0) - (\zeta_{13} k_1 + \zeta_{23} k_3) A_3^3 \exp(3i\omega_3 T_0) \\
&- \zeta_{13}\left\{(F_3 A_1 + F_1 A_3)\exp\left[i(\omega_3 + \omega_1)T_0\right] + (A_3 \overline{F}_1 + \overline{A}_1 F_3)\exp\left[i(\omega_3 - \omega_1)T_0\right]\right\} \\
&- \zeta_{23}\left\{(F_3 A_2 + F_2 A_3)\exp\left[i(\omega_3 + \omega_2)T_0\right] + (A_3 \overline{F}_2 + \overline{A}_2 F_3)\exp\left[i(\omega_3 - \omega_2)T_0\right]\right\} \\
&- \zeta_{13}\left\{k_5 A_1^2 A_3 \exp\left[i(2\omega_1 + \omega_3)T_0\right] + k_7 A_1^2 \overline{A}_3 \exp\left[i(2\omega_1 - \omega_3)T_0\right]\right\} \\
&- \zeta_{23}\left\{k_6 A_2^2 A_3 \exp\left[i(2\omega_2 + \omega_3)T_0\right] + k_8 A_2^2 \overline{A}_3 \exp\left[i(2\omega_2 - \omega_3)T_0\right]\right\} \\
&- (\zeta_{13} k_6 + \zeta_{23} k_5) A_1 A_2 A_3 \exp\left[i(\omega_1 + \omega_2 + \omega_3)T_0\right] - (\zeta_{13} k_6 + \zeta_{23} k_7) \overline{A}_1 A_2 A_3 \exp\left[i(\omega_2 + \omega_3 - \omega_1)T_0\right] \\
&- (\zeta_{13} k_8 + \zeta_{23} k_5) A_1 \overline{A}_2 A_3 \exp\left[i(\omega_1 - \omega_2 + \omega_3)T_0\right] - (\zeta_{13} k_8 + \zeta_{23} k_7) \overline{A}_1 \overline{A}_2 A_3 \exp\left[i(\omega_3 - \omega_1 - \omega_2)T_0\right],
\end{aligned} \tag{40}$$

where k_i ($i = 1,2,...,8$) are known coefficients.

Reference to Eqs. 38-40 shows that along with the internal resonance 1:1 and combinational internal resonances of the additive-difference type considered in [7], there could occur one more type of the internal resonance which couples three different modes of vibration:

$$\omega_1 \approx \omega_2 \approx \omega_3 \tag{41}$$

Governing Nonlinear Differential Equations Describing Amplitude-Phase Modulation for the 1:1:1 Internal Resonance

Considering condition (41) and eliminating secular terms in Eqs. 38-40, we obtain the following solvability equations:

$$\begin{aligned}
&2i\omega_1 D_2 A_1 + \mu_1 (i\omega_1 \tau_1)^\gamma A_1 + 2\zeta_1 k_5 A_1 A_3 \overline{A}_3 + 2\zeta_1 k_6 A_2 A_3 \overline{A}_3 + 2\zeta_1 k_7 \overline{A}_1 A_3^2 + 2\zeta_1 k_8 \overline{A}_2 A_3^2 = 0, \\
&2i\omega_2 D_2 A_2 + \mu_2 (i\omega_2 \tau_2)^\gamma A_2 + 2\zeta_2 k_6 A_2 A_3 \overline{A}_3 + 2\zeta_2 k_5 A_1 A_3 \overline{A}_3 + 2\zeta_2 k_7 \overline{A}_1 A_3^2 + 2\zeta_2 k_8 \overline{A}_2 A_3^2 = 0, \\
&2i\omega_3 D_2 A_3 + \mu_3 (i\omega_3 \tau_3)^\gamma A_3 + (\zeta_{13} k_2 + \zeta_{23} k_4) A_3^2 \overline{A}_3 + \zeta_{13} k_7 A_1 \overline{A}_1 A_3 + \zeta_{23} k_8 A_2 \overline{A}_2 A_3 \\
&\quad + \zeta_{13} k_7 A_1^2 \overline{A}_3 + \zeta_{23} k_8 A_2^2 \overline{A}_3 + (\zeta_{13} k_6 + \zeta_{23} k_7) \overline{A}_1 A_2 A_3 + (\zeta_{13} k_8 + \zeta_{23} k_5) A_1 \overline{A}_2 A_3 = 0.
\end{aligned} \tag{42}$$

Let us multiply the first, second and third equations of Eqs. 42, respectively, by $\overline{A}_1$, $\overline{A}_2$, and $\overline{A}_3$ and find their complex conjugates. Adding every pair of the mutually adjoint equations with each other and subtracting one from another, and considering that $A_i = a_i e^{i\varphi_i}$ $(i = 1,2,3)$, as a result we have

$$
\begin{aligned}
&\left(a_1^2\right)^{\cdot} + s_1 a_1^2 = -2\omega^{-1}\zeta_1\left[k_7 a_1^2 \sin 2(\varphi_3-\varphi_1) + k_6 a_1 a_2 \sin(\varphi_2-\varphi_1) + k_8 a_1 a_2 \sin(2\varphi_3-\varphi_2-\varphi_1)\right]a_3^2,\\
&\left(a_2^2\right)^{\cdot} + s_2 a_2^2 = -2\omega^{-1}\zeta_2\left[k_8 a_2^2 \sin 2(\varphi_3-\varphi_2) - k_5 a_1 a_2 \sin(\varphi_2-\varphi_1) + k_7 a_1 a_2 \sin(2\varphi_3-\varphi_2-\varphi_1)\right]a_3^2,\\
&\left(a_3^2\right)^{\cdot} + s_3 a_3^2 = \omega^{-1}\left[\zeta_{13}k_7 a_1^2 \sin 2(\varphi_3-\varphi_1) + \zeta_{23}k_8 a_2^2 \sin 2(\varphi_3-\varphi_2)\right]a_3^2,\\
&\dot{\varphi}_1 = \frac{1}{2}\sigma_1 + \omega^{-1}\zeta_1\left[k_5 + k_7\cos 2(\varphi_3-\varphi_1) + k_6 a_1^{-1}a_2\cos(\varphi_2-\varphi_1) + k_8 a_1^{-1}a_2\cos(2\varphi_3-\varphi_2-\varphi_1)\right]a_3^2,\\
&\dot{\varphi}_2 = \frac{1}{2}\sigma_2 + \omega_2^{-1}\zeta_2\left[k_6 + k_8\cos 2(\varphi_3-\varphi_2) + k_5 a_1 a_2^{-1}\cos(\varphi_2-\varphi_1) + k_7 a_1 a_2^{-1}\cos(2\varphi_3-\varphi_2-\varphi_1)\right]a_3^2,\\
&\dot{\varphi}_3 = \frac{1}{2}\sigma_3 + \frac{1}{2}\omega^{-1}\left[\zeta_{13}k_7 a_1^2 + \zeta_{23}k_8 a_2^2 + \left(\zeta_{13}k_2 + \zeta_{23}k_4\right)a_3^2\right] + \frac{1}{2}\omega^{-1}\left[\zeta_{13}k_7 a_1^2\cos 2(\varphi_3-\varphi_1)\right.\\
&\qquad\left. + \zeta_{23}k_8 a_2^2\cos 2(\varphi_3-\varphi_2)\right] - \frac{2}{3}\omega^{-3}\zeta_{13}\zeta_{23}a_1 a_2\cos(\varphi_2-\varphi_1).
\end{aligned}
\tag{43}
$$

where a dot denotes differentiation with respect to T_2, $s_i = \mu_i \tau_i^\gamma \omega_i^{\gamma-1}\sin\psi$, $\sigma_i = \mu_i \tau_i^\gamma \omega_i^{\gamma-1}\cos\psi$, $\psi = \pi\gamma/2$ $(i=1,2,3)$, and $\delta = 2\varphi_3 + \varphi_1 - \varphi_2$.

The nonlinear set of Eqs. 43 with the initial conditions (4) and (5) completely describe the vibrational process of the mechanical system being investigated under the condition of the internal resonance 1:1:1 and could be solved numerically.

Summary

Nonlinear free vibrations of a thin plate described by three coupled nonlinear differential equations are considered when the plate is being under the conditions of the 1:1:1 internal resonance resulting in the interaction of three modes corresponding to three different mutually orthogonal displacements. The procedure resulting in decoupling linear parts of equations is proposed with the further utilization of the method of multiple time scales for solving nonlinear governing equations of motion, in so doing the amplitude functions are expanded into power series in terms of the small parameter and depend on different time scales. It is shown that the phenomenon of internal resonance can be very critical, since in a thin plate internal resonance of different types are always present.

Acknowledgment

This research was made possible by the Grant No. 7.22.2014/K as a Government task from the Ministry of Education and Science of the Russian Federation.

References

[1] Yu.A. Rossikhin and M.V. Shitikova: Int. J. Non-Linear Mech. Vol. 41 (2006), p. 313

[2] Yu.A. Rossikhin and M.V. Shitikova: Appl. Mech. Materials Vol. 518 (2014), p. 60

[3] A. Nayfeh: *Perturbation Methods,* Wiley, New York (1973).

[4] Yu.A. Rossikhin and M.V. Shitikova: Appl. Mech. Reviews Vol. 63 (2010), p. 010801-1

[5] Yu.A. Rossikhin and M.V. Shitikova: Mater. Sci. Forum Vol. 440-441 (2003), p. 29

[6] A.H. Nayfeh: *Nonlinear Interaction: Analytical, Computational, and Experimental Methods*, Wiley, New York (2000).

[7] Yu.A. Rossikhin and M.V. Shitikova: Appl. Mech. Materials Vol. 595 (2014), p. 105

Need for mechanical protection of Gabcikovo ship lock

Dipl.Eng. Danka Rakusova, PhD[a], [1]*

[1]Faculty of Special Technology, Trencin University of Alexander Dubcek, Trencin, Slovakia

[a]danka.rakusova@tnuni.sk*

Keywords: Ship locks, vessel, hydro-electric plant, chamber, fender

Abstract. The ship lock in Gabčíkovo has been for more than 20 years in operation, providing services for ships from many countries and nowadays is in an emergency state, when both chambers need to be closed because of damages on a gate and on structural parts of the lock chamber. Mechanical protection is the way how to increase its service life.

1. Introduction

Danube is the E80 trunk waterway connecting countries up to Black Sea. Gabčíkovo ship lock (Fig.1) with a hydroelectric dam feeder is located in a short distance from Slovak-Hungarian border and it has been operating from fall 1992. Lock chambers of the water structure Gabčíkovo are 275 meters long and 34 meters wide.

The feeder canal provides the water delivery to the turbines and a shipway into the Gabčíkovo ship lock chambers. The Shipping companies are organized by the Danube Commission and transportation of cargoes on the Danube is defined by Bratislava Accord, that evaluates one day of delay of the vessel of 1 300 deadweight tons for 430 Euros. A tugboat set may consist of several such vessels. An average number of tugs is about 20 per a lock/day. The costs for repair works only on a left lock, lasting four days, amounted 300 000 Euros. The ship lock has been providing services for ships from many countries and nowadays it

Fig.1 The Gabcikovo ship locks

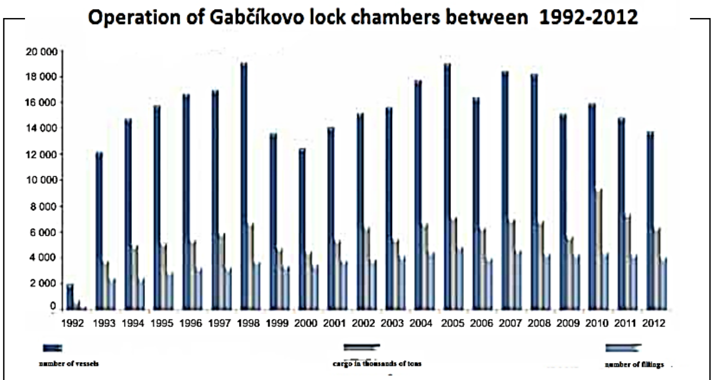

Fig. 2 Operation of the Gabčíkovo lock

is in an emergency state, when both chambers needed to be closed for a short period because of damages on a gate and structural parts of the lock chamber. The importance and construction costs for Gabčikovo ship lock are enormous. In 2012, there were made 4063 fillings of the lock chambers and total of 13,767 vessels passed through. Since commencement of operation of the Gabčíkovo water structure a total of 318,176 vessels have passed through, which represents 122 901 099 tons of freight and 5 731 255 passengers.[1] When such amount of vessel float between the dams and ship lock walls many contacts happen between vessels and ship lock chamber walls and a dam blacktop revetment**.**

2. History

Hydro-electric plant with ship locks had been built from 1977 as an original hydro-electric plant Gabčíkovo-Nagymaros based on an international agreement aiming to prevent from regular (in 1954, 1965) floods in this area. In 1989, Hungary suspended the works on the Gabčíkovo – Nagymaros water structure system and despite a series of unsuccessful inter-governmental negotiations between 1990 and 1991, the Czechoslovak Government decided, mainly due to increasing economic and environmental losses, to start the operation of the Gabčíkovo water structure using a temporary solution known as the "C alternative". The decision was speeded up also by an oil crisis in 1973. The hydro-electric plant was commissioned into operation in 1992. Recession from contract by Hungary had been for long years a subject of an international legal process between Slovakia (as an successor of liabilities after Czechoslovakia splitting-up) and Hungary. International Court of Justice decided in October 1997, that the international agreement from 1977 has been still valid.

The water structure system Gabčíkovo –Nagymaros consists of the following components:

- Hrušov – Dunakiliti weir at the Danube River kilometers 1,860 – 1,842(hereinafter referred to as "rkm") with a maximum upper reach of 131.10 m above sea level on Slovak and Hungarian territory;
- Dunakiliti weir with an auxiliary ship-lock at rkm 1,842 on Hungarian territory;
- Derivation canal (intake and discharge canal) at rkm 1,842 – 1,811 on Slovak territory;
- Segment on the derivation canal on Slovak territory, consisting of a hydropower plant with an installed output of 720 MW, two lock chambers and facilities;
- Regulated old riverbed of the Danube at rkm 1,842–1,811 on the common Slovak-Hungarian section;
- Dredged and regulated old riverbed of the Danube at rkm 1 811 – 1 791 on the common Slovak-Hungarian section.[2]

3. Ship lock operation

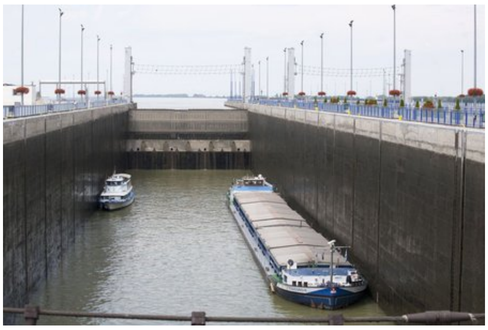

Fig.3 Vessels waiting in a chamber

Lock mooring is a commonly used method of navigating into a lock by a barge travelling upstream.(Fig. 3) The barge would be directed to the slack water to one side of the lock gates and as the volume of water decreased as the lock emptied the barge or boat is effectively sucked out of the slack water into the path of the lock gates. The effort required to navigate the barge or boat into the mouth of the lock is therefore substantially reduced. Ship lock chamber is a place, where the ships sailing on the Danube river pass through a weir. There are two chambers in Gabčikovo; their depth is approximately 32 meters. A vessel floating down-the-river enters into a chamber), then a part of water is drained from a weir and a vessel continues in shipping. It takes about 15 minutes. The water flows into, or on contrary, flows out through orifices in the bottom. An exploitable length of each ship lock chamber is 275 meters and width of 34 meters that is more than in the Panama Canal.

ISBN: 978-1-61804-295-8

4. Damages on a feeder canal and shiplock chambers.

Only the most experienced captains are allowed to operate a vessel within the ship lock chamber. Nevertheless, recently a number of accidents in the chambers has increased. Despite the fact of its great importance, the ship lock has not been protected against any irresponsible and inexperienced captains causing damages on the ship locks structure by hitting with vessels to the walls and gates of the ship lock. The hits on walls of the chamber or on the gate supports are not sporadic and

Fig.5 A damaged wall of a feeder canal

Fig. 6 Damaged supports of an upper left gate

a subsequent investigation of an offending personnel or organization does not bring satisfactory results. Even water police is unable to prevent hitting the wall of a chamber. From a classification of damages on a feeder canal and its asphalt-concrete isolator there are horizontal and vertical cracks over the water level and asphalt leaked out mainly in a transition curve between a water-side slope and a dam crest. Under the minimum operational water level the dents were found caused by impacts of vessels floating in a feeder canal (Fig. 5) The only way that is able to reduce inevitable damages resulting from hits is mechanical protection of the chamber as well as of the vessels entering into a ship lock chamber. An increased number of non-convenient and non-competent shipping and vessel leadership has resulted in repeated damage of the upper support of the lock gate. The company carried out regular repairs and maintenance of specific water structures as well as repairs of damaged technical equipment. In 2012, the VV Inc. Company, repaired right lock chamber on the water structure Gabčíkovo (Fig. 6.) Total debt rate of the Gabčíkovo ship lock operator is almost 39%, so the new investments are not feasible. The Gabčíkovo ship locks are similar to Panama locks with respect to technical features, however Panama locks have been operating for more than 80 years and they are still in excellent conditions.

5. Calculation of fenders capacity

The principal function of the fender system is to prevent the vessel or the dock from being damaged during the mooring process or during the berthing periods. Forces during the vessel berthing may be in the form of impact, abrasive action from vessels, or direct pressure. These forces may cause an extensive damage to the ship and structure if suitable means are not employed to counteract them. The amount of energy absorbed and the maximum impact force imparted are the primary criteria applied in accepted fender design practices.

ISBN: 978-1-61804-295-8

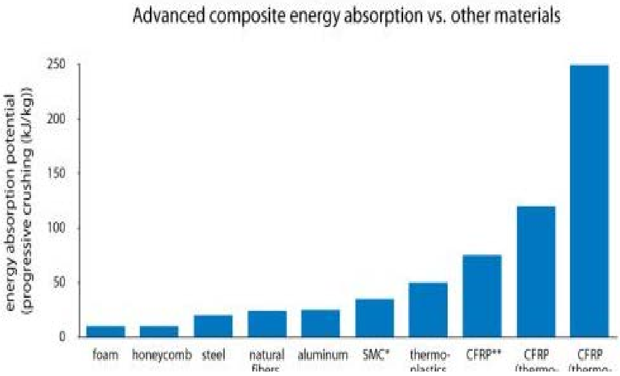

Figure 7 . Energy absorption by different materials

A variety of factors affect the proper selection of a fender system. These include, but not limited to, local shipping environment, class and configuration of ships, speed and direction of approach of ships when berthing, available docking assistance, type of berthing structure, and even the skills of pilots or ship captains. It is considered impractical to standardize fender designs since berthing conditions are rarely identical.

In boating, a fender is a bumper used to absorb the kinetic energy of a boat or vessel berthing against a jetty, ship lock wall or other vessel. To prevent the vessels from damage, fenders usually have high energy absorption and low reaction force. Fenders are typically manufactured out of rubber, foam or plastic. Their absorption features are compared in the Figure 7. Rubber fenders are either extruded or made in a mould. Designing a fender system basically is determining what the berthing energy of a vessel or range of vessels will be, and then determine what capacity the fender needs to have to absorb that kinetic energy and finally how to find a way to avoid the reaction force creating too much hull pressure. Composites have dramatically higher specific energy absorption than steel or aluminum. Composite-based crush cones and similar structures built into berthing wall can absorb 120 kJ/kg, even up to 240, vs. about 20 for steel. Crush properties and costs can also be optimized by mixing costlier carbon fiber with lower-cost materials like fiberglass.

6. Calculation of berthing energy

The method to define kinetic energy can be used in the determination of berthing energy of the ship. Work is closely related to energy

$$W = F.\ s \qquad (1)$$

if a force of 10 Newtons (F = 10 N) acts along a point that travels 1 metres (s = 1 m), then it does the work W = (10 N)(1 m) = 10 N m = 10 J. Transferred into tons and km the above mentioned is equal to

10×10^{-3} ton $\times 1\mathrm{x}10^{-3}$ km = 10 J

The kinetic energy method has been the widely accepted method for piers, wharves and ship lock facilities. When the tonnage of the ship is known, the energy equation can be written as:

$$E\mathrm{ship} = F\ .\ s = \frac{1}{2}mv^2 \qquad (2)$$

where Eship = Berthing energy of ship (MJ)
m = weight of the ship in tons
v = Berthing velocity normal to the berth (km/hour = 0,278 x 10^{-3} km/s), speed of the center of mass of the vessel body.
Since the kinetic energy increases with the square of the speed, an object doubling its speed has four times as much kinetic energy.
The kinetic energy of a vessel is related to its momentum by the equation

$$E_k = \frac{p^2}{2m} \qquad (3)$$

ISBN: 978-1-61804-295-8

p- is momentum
m – is mass of the vessel

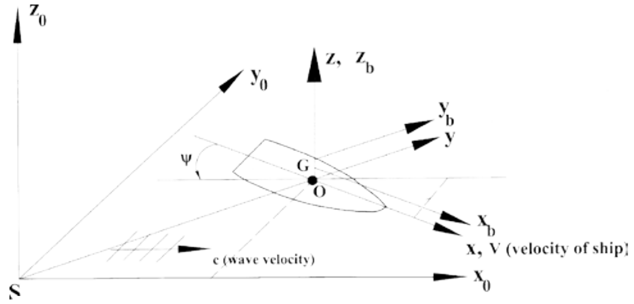

The kinetic energy of such systems depends on the choice of reference frame: the reference frame that gives the minimum value of that energy is the center of momentum frame, i.e. the reference frame in which the total momentum of the system is zero. This minimum kinetic energy contributes to the invariant mass of the system as a whole.

Fig. 8 Coordinate system of the vessel´s center of gravity

In principle, a berthing energy calculation is a simple kinetic energy calculation, adjusted for specific behavior of a berthing vessel or the specific characteristics of the berthing location or structure.The time-dependent motions of the ship shall be studied using the coordinate system seen in Figure 8, where xb, yb, zb are the coordinates relative to the center of gravity of the ship G; xo, yo, zo are the global coordinates relative to a point S in the space, where S is on the free surface of otherwise calm water; and x, y, z are the ship-fixed coordinate system relative to the center of gravity of the ship G, moving together with the ship. The angular motions of the ship shall be relative to those three axes: roll, pitch, or yaw.

The work done accelerating a particle during the infinitesimal time interval dt is given by the dot product of force and displacement:

$$\mathrm{F.dx} = \mathrm{F.vdt} = \frac{\mathrm{dp}}{\mathrm{dt}}\mathrm{.vdt} = \mathrm{v.dp} = \mathrm{v.d(mv)} \ (4)$$

where we have assumed the relationship p = m v.
Applying the product rule we see that:

$$d(\mathbf{v}.\mathbf{v}) = (d\mathbf{v}).\mathbf{v} + \mathbf{v}.(d\mathbf{v}) = \mathbf{2}\ (\mathbf{v}.\ d\mathbf{v})\ \mathbf{(5)}$$

Therefore (assuming constant mass so that dm=0), the following can be seen:

$$\mathbf{v}.d(m\mathbf{v}) = \frac{m}{2}d(\mathbf{v}.\mathbf{v}) = \frac{m}{2}\ dv^2 = d\left(\frac{mv^2}{2}\right) (6)$$

Since this is a total differential (that is, it only depends on the final state, not how the particle got there), we can integrate it and call the result kinetic energy. Assuming the object was at rest at time 0, we integrate from time 0 to time t because the work done by the force to bring the object from rest to velocity v is equal to the work necessary to do the reverse:

$$E_k = \int_0^t \mathbf{F}.d\mathbf{x} = \int_0^t \mathbf{v}.d(m\mathbf{v}) = \int_0^v d\left(\frac{mv^2}{2}\right) = \frac{mv^2}{2} (7)$$

The abovementioned relations were applied during calculations of kinetic energy produced by the types of vessels commonly operated on the Danube river: DNL2000, KVC1000, UC1500 (Fig.9), DE1600, VC850, Ro-ro at angles 5,10,15,20,25,30,35,40 and 45 degrees and velocity of berthing operation from 0,1 up to 5,0 km/h and their combinations.(Fig.10)

ISBN: 978-1-61804-295-8

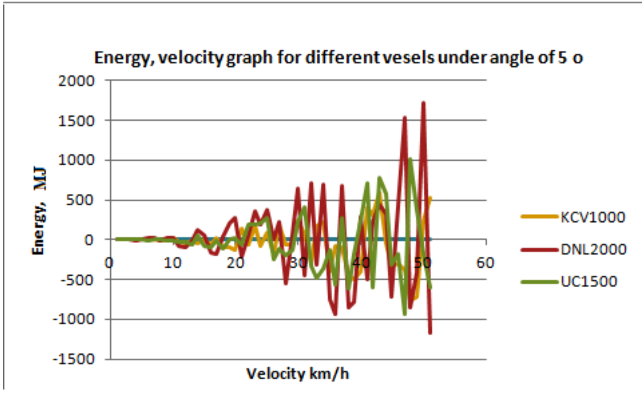

Fig.9 Energy and velocity graph for different vessels

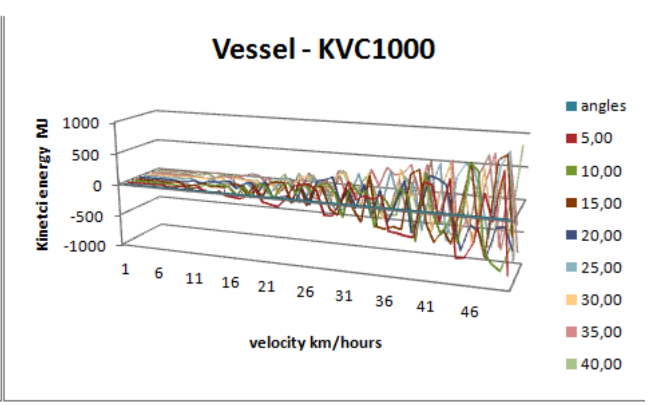

Fig.10 Energy , velocity, angles graph for KVC1000 vessel

However there are several factors that modify the actual energy to be absorbed by the fender system. The energy absorbed by the ship depends on the relative stiffness of the ship and the obstruction. The deformation coefficient varies from 0.9 for a non-resilient fender to nearly 1.0 for a flexible fender. For larger ships on energy-absorbing fender systems, little or no deformation of the ship takes place; therefore, a coefficient of 1.0 is recommended. Configuration Coefficient (Cc) is implied when the water between the berthing ship and the structure is squeezed, which introduces a cushion effect that represents an extra force on the ship away from the berth and reduces the energy to be absorbed by the fender system. Experience has indicated that for a solid quay wall about one quarter of the energy of the berthing ship is absorbed by the water cushion. For berths with different

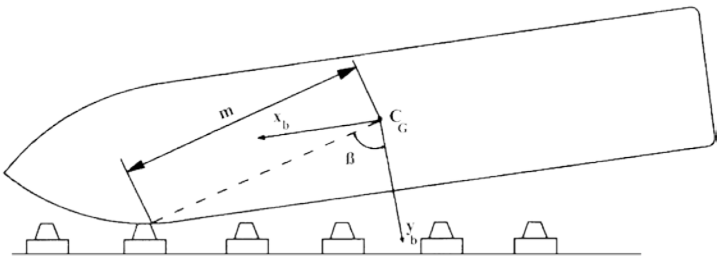

Fig. 11 Geometry of berthing

conditions, Cc might be chosen somewhere between these values 0,8-1,0.

When a ship approaches a ldock, the berthing impact is induced not only by the mass of the moving ship, but also by the water mass moving along with the ship. The latter is generally called the "hydrodynamic" or "added" mass. In determining the kinetic energy of a berthing ship, the effective or virtual mass (a sum of ship mass and hydrodynamic mass) should be used. The hydrodynamic mass does not necessarily vary with the mass of the ship, but is closely related to the projected area of the ship at right angles to the direction of motion. Other factors, such as the form of ship, water depth, berthing velocity, and acceleration and deceleration of the ship, will have some effect on the hydrodynamic mass.

7. Measures to reduce the damages on a ship lock

Various kinds of measures (Table 1) can reduce the unfavourable effects of the environment and forces having impact on the vessel in the chamber. There are many factors having an influence on the situation in the chamber, namely experience of the captain, size of a vessel, speed of filling in, speed of emptying the chamber, water regime, speed of water current, speed of a vessel, composition of vessels formation, day or night time, visibility conditions, availability of a port tug with a navigating personnel, training of personnel, competence, staffing of vessel crews, level of responsibility and liability for damages, and the last but not the least discipline of captains, their nationality, different national shipping regulations and legal regulations. These measures differ in fund and time demandingness.

Table 1. Investments in mechanical protective measures aiming to reduce damages

Protected object	Investments		
	Long-term investments	Medium-term measures	Immediate measures
vessel	-higher quality of material used during vessel construction -tug fenders	-equipment improving towing and tugging maneuverability of the vessel, -quick release hooks	-wooden fender -tires hanging on ropes or chain -ropes tying up the vessels
Ship lock chamber	- Higher quality of material used during ship lock construction, - length of an intake and discharge canal, -mooring equipment for vessels -permanent fenders on lock walls -mooring equipment for vessels waiting for a ship lock chamber	-renovation of ship lock wall fenders -roller fenders -wooden timbering on walls -application of quick release hooks on mooring -pneumatic fenders	-wooden fenders -tires hanging on ropes or chain

7.1. Wooden fender

As far back in the history common people knew that wooden pieces effectively damp an impact force. In general the wood fenders were fitted to gates in places where they might be hit by vessels. In the case of miter gates they are recommended to be fitted with wood fender

Fig.12 Wooden fender on a ship and a lock wall

on the outside surface of the opened gates to protect the construction from damage caused by inbound and outbound vessels.

ISBN: 978-1-61804-295-8

However all loosen objects, which fall down into water and get in between the gates, may destroy the gate, therefore permanently installed or fixed and movable fenders on a chain are preferred.

7.2 Truck tire fender

The simplest and the less expensive way how to protect both chamber wall and a vessel is a truck tire.

Fig.13 Tires protecting a wall from a vessel impact

Fig. 14 Roller fender

Roller fenders are usually installed to guide ships in restricted spaces like walls of locks and docks. They can also be used on corners and lock entrances where lower energies are needed. Features of a roller fender include good energy absorption, gentle contact face, low rolling resistance, use singly or in multiple stacks, composite and stainless steel bearings, low maintenance frame design. Roller fenders use stainless steel and composite bearings which give a very low rolling resistance and require virtually zero maintenance. Wheel fenders are widely used on environments with exposed corners to help ships maneuver into berths and narrow channels such as locks and dry-dock entrances. The main axle slides on bearings and the wheel reacts against back rollers to provide high energy and minimal rolling resistance, whilst the stainless steel and composite bearings are almost zero maintenance.

7.3. Foam fenders

Fig.15 Foam fender

In order to enable safe ship-to-ship and ship-to-quay berthing operations and meet the most stringent quality and performance demands the manufactures produce foam fenders as an alternative to the standard pneumatic fenders and shock absorbers. Foam fenders, all share the same manufacturing technology centered on an outer reinforced skin. Foam fenders absorbs the impacts whilst the skin resists wear and tear in use in any tough conditions, thus providing tough, heavy-duty fendering systems for harbors, offshore and ship-to-ship applications. The key attributes of the foam fenders include high energy absorption and low reaction force, a foam fender conforms to hull protrusions, it has an ultra-tough, unsinkable design, it remains fully functional even if skin is punctured and requires low maintenance and an easy installation.[.5]

7.4. Prevention from damage on a vessel hull

Fig. 16 Tug fender

Design of all fender systems is to prevent permanent deformation of the ship's hull. It is much more expensive to repair a ship's hull than rehabilitate a damaged fender system. The composition of a typical river ship hull is steel plating welded to longitudinal (horizontal) stiffeners at 0.6 to 1.2 m on center. The stiffeners span from 1.5 to 7.6 m depending on the vessel. Generally, the stiffeners are of sufficient strength to preclude failure from fender loading. However, the hull plating may yield when subjected to a uniformly distributed overload on the panel. Fender systems with rigid face elements or in combination with rigid camels tend to concentrate the reaction forces on the ships frames versus the hull plating due to the relative stiffness of the frames.

Tug fenders must work harder, for longer and under more extreme conditions than any other fender type. Tugs may be fitted with up to four types of fender – each type serving a particular application. As many tugs become more powerful, some exceeding 100t bollard pull, choosing the right type, size and arrangement of fenders becomes critical. Cylindrical tug fenders are fitted to the bow/stern of tugs and usually used to push against flared hulls and in open river conditions. Large cylindrical fenders are often used as the primary pushing fenders on the bow or stern of modern tugs. Their round shape is ideal for working with large bow flares (like container ships), but are equally good for pushing flat-sided vessels. Tug cylindrical come in diameters to 1000 mm and in very long continuous or spigot-joined lengths. A longitudinal chain runs down the centre of the fender, supplemented by circumferential straps or chains which are recessed into grooves. Tapered ends are also available.

7.5. Pneumatic fenders

Floating pneumatic fenders with chain and truck tire net or tire netting**.** The pneumatic fender of the net with chain and tire protects the fender body from damaged by sharp objects, the net also via the absorption of sheer loads during berthing. The better the pneumatic fender net, the more protection it will offer.

Fig. 17 Floating pneumatic fenders

8. Preservative Treatment.

All timber members, with the exception of some fender piling, exposed to the water and air environment and immersed in water should be pressure treated with oilborne (creosote, pentachlorophenol) or waterborne

ISBN: 978-1-61804-295-8

chemical preservatives to protect against deleterious effects of decay, insects, and borers. If possible, pressure treatment after all holes and cuts are made. When holes and cuts are made in the field, timber members with preservative should be treated to prevent decay from starting in the holes or cuts.

Therefore, whenever possible, design and detailing should avoid the necessity for making cuts or holes on underwater timber members. For example, avoid bracing or connections below mean high water are to be avoided.

9. Conclusion

The practice has shown that no protection of estates is the worst behavior of the owner, should it be anyone, a natural person, joint-stock company or a state organization. The Gabčíkovo water structure was built in hard economic and political conditions when Slovakia has taken over all responsibility for its completion and operation. Even the previous generations knew how to protect such huge water structures. An excuse for non-protecting the water structure due to lack of funds does not work at all, as many protective measures need no funds. Old truck tires protect the ship lock chamber in the same way as a hull of a vessel. Very rough calculation of economical consequences resulted from negligence to irresponsibility and incompetency of some vessel captains is breath-taking. The Gabčíkovo water structure brings only benefits and nowadays great incomes, so it should be protected by all available means, including the mechanical ones.

References

[1]“Výročné správy“ available:

http: //www.vvb.sk/cms/index.php?page=vyrocne-spravy/ . [Online]. [Accessed Nov. 25, 2014].

[2]“Európske vodné cesty“ available:
file:///C:/Users/DANA%20PC/Downloads/Priloha_1a_ku_KRVD%20(2).pdf[Online]. Accessed Nov. 7, 2014].
[3] „Náklady na opravu horných vrát sú vyčíslené“ available on
http://www.vvb.sk/cms/index.php?mact=News,cntnt01,detail,0&cntnt01articleid=49&cntnt01origid=56&cntnt01returnid=39. /[Online]..[Accessed Nov. 7, 2014].
[4]“Podmienky pre plavbu cez Gabčíkovo sa výrazne sprísnia“ available:
http://www.vvb.sk/cms/index.php?mact=News,cntnt01,detail,0&cntnt01articleid=50&cntnt01origid=70&cntnt01returnid=39, [Online].Accessed Nov. 25, 2014].
[5]“Trelleborg docking and mooring systems.“ [Online].available:
http://www.vvb.sk/cms/index.php?mact=News,cntnt01,detail,0&cntnt01articleid=50&cntnt01origid=70&cntnt01returnid=39, Accessed Nov. 25, 2014].
[6] Gökdeniz N.“Dynamics of ships and fenders during berthing in
a time domain“ / Ocean Engineering 33 (2006) 1919–1934.

Acknowledgement

This publication was created in the frame of the project "Alexander Dubček University of Trenčín wants to offer high-quality and modern education“, ITMS code 26110230099, based on the Operational Programme Education and funded from the European Social Fund.

On Prediction of Surface Roughness of Al7075alloy during Slot Milling using NN Modeling

J. KECHAGIAS[1, a*], P. KYRATSIS[2, b] and N. MASTORAKIS[3, c]

[1]Department of Mechanical Engineering, Technological Educational Institute of Thessaly, Larissa, Greece.

[2]Department of Mechanical Engineering and Industrial Design, Technological Education Institution of Western Macedonia, Kila Kozani, Greece.

[3]Departmentof Industrial Engineering, Technical University of Sofia, Sofia, Bulgaria.

[a]jkechag@teilar.gr, [b]pkyratsis@teiwm.gr, [c]mastor@tu-sofia.bg

Keywords: Neural Networks, Modelling, Face Milling, Surface Texture Parameters.

Abstract: Surface roughness as an indicator of surface quality is one of the mostly specified customer requirements in a machining process. Mastering of surface quality issues helps avoiding failure, enhances component integrity and reduces overall costs. Al7075 alloy surface quality, achieved in slot milling, constitutes the subject of the current research study. Twenty seven slots were cut using different cutting conditions by a KC633M drill-slot end mill cutter. The independent variables considered were the depth of cut (a_p, mm), cutting speed (V_c, m/min), and feed rate (f, mm/rev). Process performance is estimated using the statistical surface texture parameters R_a, RS_m, and R_t; all measured in microns. To predict the surface roughness within the limits of the parameters involved, an artificial feed forward back propagation neural network model was designed for the data obtained.

Introduction

Aluminum alloys are extensively used as a main engineering material in various industries such as automotive and aerospace industries, the mould and die components manufacture and every case in which weight is the most important factor [1]. Surface roughness has an important role in the performance of finished components. It refers to the third up to the sixth order deviation from the nominal surface and all different order deviations are superimposed and form the surface roughness profile [2]. Surface properties dominate the quality of the finished component, since they influence features like dimensional accuracy; tribological characteristics such as the friction coefficient and wear; post processing requirements; appearance and cost. Besides the obvious problems related to correct dimensions, one of the more significant problems is achieving the appropriate finish or surface smoothness on the workpiece. Surface quality is important for a number of reasons i.e. aesthetic (a smooth and free from scratches surface is more likely to give a favorable impression to the customer), surfaces affect safety and they interact with the environment due to their influence on mechanical properties [3]. Surface roughness or texture constitutes a measure for achieving finer surface irregularities in the finished product, while three components i.e., roughness, waviness, and form are required for its determination [4].

A number of methodologies investigating the relations of the cutting parameters with the produced surface quality are reported in literature. Response surface methodology (RSM) is one of the mostly used in order to build mathematical models based on the Taguchi theory [5]. Other researchers are combining the application of fuzzy logic with the Taguchi method and optimise the surface roughness achieved [6, 7].

The present paper deals with the effects of different process parameters: depth of cut (a_p), cutting speed (V_c), and feed rate (f)on the surface quality, when slot milling Al7075 alloy workpieces. A set of experiments using Taguchi design and Neural Networks modelling were used and the surface texture parameters measured during this study were the following: R_a (the arithmetic mean surface roughness), RS_m (average groove width) and R_t (total height of the roughness profile), all measured in μm. Experimental results are used in order to train a feed forward back propagation neural network (FFBP-NN) and predict the surface texture parameters in finish slot milling of Al7075 alloy parts. The use of the FFBP-NN together with the orthogonal matrix experiment results in a successful way to model the process and predict the surface texture parameters when different cutting parameters apply.

Experimental setup

The material used for cutting is specified as Al 7075 (90% Al, 5.6% Zn, 2.5% Mg, 1.6% Cu, and 0.23% Cr).A two flute end mill cutter (KC633M) made by Kennametal was used to cut 27 slots upon three plates. The cutter diameter was 12mm, the length 83mm and the helix angle 30o (Fig. 1).

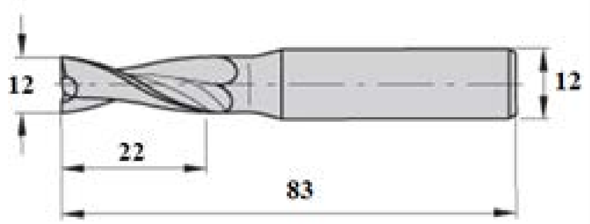

Fig. 1: Cutting tool main dimensions

Three Al7075 plates with a thickness of 12mm (150mm in length and 50mm in width) were used to cut the slots (Fig. 2). A four axis HAAS VF1 CNC machining center with continuous speed and feed control within their boundaries was used for twenty seven slotting operations (Fig. 3). During cutting operations an appropriate coolant fluid was used.

Fig. 2: Machined specimens of Al7075 alloy

Surface roughness is a widely used index characterising a product's quality, and is measured off-line, when the component is already machined. The three surface texture parameters measured during this study were the following(Fig.4):

- R_a(μm): the arithmetic mean surface roughness (arithmetical mean of the sums of all profile values),
- RS_m(μm): average groove width (mean value of the width of the profile elements Xsi), and
- R_t(μm): total height of the roughness profile (sum from the height Zp of the highest profile peak and the depth Zv of the lowest profile valley within the measured length).

Measurements were conducted using the Mitutoyo portable Surftest SJ-210 tester (Fig. 5). Its Zaxis measuring range is between -200μm & +160μm and depending on the measurement is able to achieve up to 0.002μm resolution. The tester is able to measure a great deal of different surface parameters based on different standards and can apply online a series of filters if required.

ISBN: 978-1-61804-295-8

The experimental procedure was designed using the Taguchi method [8], which uses an orthogonal array to study the entire parametric space with a limited number of experiments. For the purposes of the current research, a full factorial experiment plan was used and the basics of Taguchi's DOE were taken into account [8, 9].

Fig. 3: HAAS VF1CNC machine centre (7500 rpm, 15 KW)

The main cutting parameters (depth of cut - a_p, mm; cutting speed - V_c, m/min; and feed rate - f, mm/rev) were assigned on a standard L_{27} (3^{13}) orthogonal array to explore the entire parametric space with a limited number of experiments. Three levels were specified for each of the three cutting parameters (Table 1).

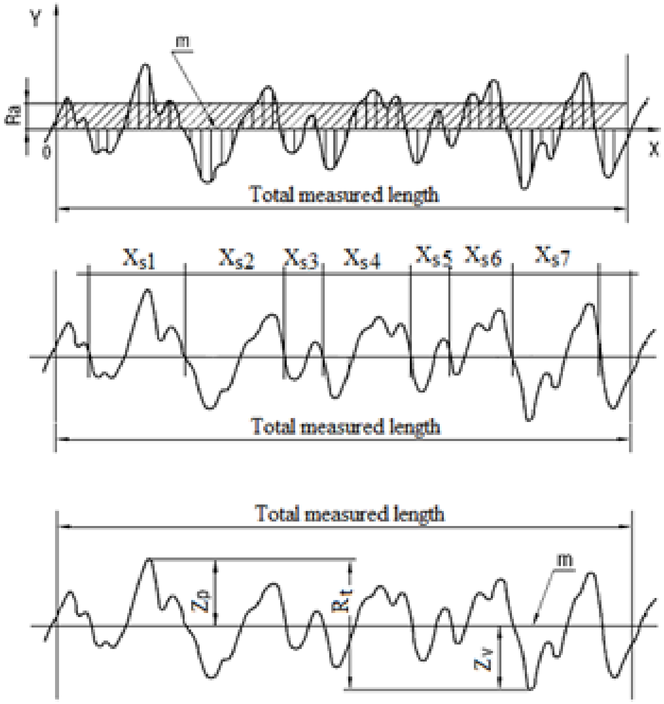

Fig. 4: Surface texture parameters

Fig. 5: Machined specimen and surface tester

Table 1: Parameter design.

		Levels		
No	Process Parameters	1	2	3
1	Depth of cut (a_p, mm)	0.5	1	1.5
2	Cutting Speed (V_c, m/min)	50	100	150
3	Feed Rate (f, mm/rev)	0.05	0.08	0.11

Based on the three-level orthogonal array factor assignment for high resolution number, the main cutting parameters occupied the columns 1, 2, and 5 of L_{27} orthogonal array whereas the rest left vacant (Table 2).

Specifically, depth of cut (mm) was assigned to column 1, cutting speed (m/min) was assigned to column 2, and feed rate (mm/rev) was assigned to column 5. It is mentioned that the selection of L27 was done by taking into account preliminary experimentation in which strong interactions among cutting parameters were noticed.

Table 2. L_{27} (3^{13}) orthogonal array [8].

	Columns												
Exp.	1	2	3	4	5	6	7	8	9	10	11	12	13
1	1	1	1	1	1	1	1	1	1	1	1	1	1
2	1	1	1	1	2	2	2	2	2	2	2	2	2
3	1	1	1	1	3	3	3	3	3	3	3	3	3
4	1	2	2	2	1	1	1	2	2	2	3	3	3
5	1	2	2	2	2	2	2	3	3	3	1	1	1
6	1	2	2	2	3	3	3	1	1	1	2	2	2
7	1	3	3	3	1	1	1	3	3	3	2	2	2
8	1	3	3	3	2	2	2	1	1	1	3	3	3
9	1	3	3	3	3	3	3	2	2	2	1	1	1
10	2	1	2	3	1	2	3	1	2	3	1	2	3
11	2	1	2	3	2	3	1	2	3	1	2	3	1
12	2	1	2	3	3	1	2	3	1	2	3	1	2
13	2	2	3	1	1	2	3	2	3	1	3	1	2
14	2	2	3	1	2	3	1	3	1	2	1	2	3
15	2	2	3	1	3	1	2	1	2	3	2	3	1
16	2	3	1	2	1	2	3	3	1	2	2	3	1
17	2	3	1	2	2	3	1	1	2	3	3	1	2
18	2	3	1	2	3	1	2	2	3	1	1	2	3
19	3	1	3	2	1	3	2	1	3	2	1	3	2
20	3	1	3	2	2	1	3	2	1	3	2	1	3
21	3	1	3	2	3	2	1	3	2	1	3	2	1
22	3	2	1	3	1	3	2	2	1	3	3	2	1
23	3	2	1	3	2	1	3	3	2	1	1	3	2
24	3	2	1	3	3	2	1	1	3	2	2	1	3
25	3	3	2	1	1	3	2	3	2	1	2	1	3
26	3	3	2	1	2	1	3	1	3	2	3	2	1
27	3	3	2	1	3	2	1	2	1	3	1	3	2

Experimental Results

The Taguchi design method is a simple and robust technique for optimizing the process parameters. In this method, main parameters, which are assumed to have an influence on process results, are located at different rows in a designed orthogonal array. With such an arrangement randomized experiments can be conducted. In general, signal to noise (S/N) ratio (n, dB) represents

ISBN: 978-1-61804-295-8

quality characteristics for the observed data in the Taguchi design of experiments. In the case of surface roughness amplitude [8-13], lower values are desirable. These S/N ratios in the Taguchi method are called as the smaller-the-better characteristics and are defined as follows:

$$\eta = -10\log_{10}\left[\frac{1}{n}\sum_{i=1}^{n} y_i^2\right] \qquad (1)$$

where yi is the observed data at the ith trial and n is the number of trials. From the S/N ratio, the effective parameters having an influence on process results can be obtained and the optimal sets of process parameters can be determined. Based on robust design, the standard orthogonal array L27 (313) has been selected in order to perform the matrix experiment (Table 3). Three levels for each factor were selected (Table 1). Following the (L27) orthogonal array twenty seven experiments were performed with each experiment producing a test part which was tested for Ra, RSm, and Rt, all measured in μm.

Neural Network Architecture

Aiming in the prediction of the produced surface roughness parameters (Ra, RSm, and Rt) during slot milling of an AL7075 alloy, a NN model has been developed. The three (3) factors studied were used as input parameters of the NN model plus the constant number one (1). Previous studies [14] indicate that by using Taguchi's DoE methods, a structured method of NN parameter-setting can be implemented, which identify NN and training parameter settings resulting in enhanced NN performance. Training samples are presented to the NN during training, and the network is adjusted according to its error. The twenty seven (27) experimental data samples (Table 3), were separated into three groups, namely the training, the validation and the testing samples (70%, 15%, and 15% respectively). Training samples were presented to the network during training and the network was adjusted according to its error. Validation samples were used to measure network generalization and to halt training when generalization stopped improving. Testing samples have no effect on training and so they provide an independent measure of network performance during and after training (confirmation runs).

In general, a standard procedure for calculating the proper number of hidden layers and neurons does not exist. For complicated systems the theorem of Kolmogorov or the Widrow rule can be used for calculating the number of hidden neurons [15]. In this work, the feed-forward with back-propagation learning (FFBP) architecture has been selected to analyze the surface texture parameters. These types of networks have an input layer of X inputs, one or more hidden layers with several neurons and an output layer of Y outputs. In the selected ANN, the transfer function of the hidden layer is hyperbolic tangent sigmoid, while for the output layer a linear transfer function was used. The input vector consists of the three process parameters of Table 3 and the constant number one (1). The output layer consists of the performance measures, namely the Ra, RSm, and Rt surface texture parameters. According to ANN theory FFBP-NNs one hidden layer is appropriate to model each mapping between process parameters and performance measures in engineering problems [16].

In the present work, five trials using FFBP-NNs with one hidden layer were tested having 7, 8, 9, 10, and 11 neurons each; see Figure 6. The one with 9 neurons on the hidden layer gave the best performance, as indicated from the results tabulated in Table 4.

The one-hidden-layer 9-neurons FFBB-NN was trained using the Levenberg-Marquardt algorithm (TRAINLM) and the mean square error (MSE) was used as the objective function. The data used were randomly divided into three subsets, namely the training, the validation and the testing samples.

Back-propagation ANNs are prone to the overtraining problem that could limit their generalization capability [15]. Overtraining usually occurs in ANNs with a lot of degrees of freedom [16, 17] and after a number of learning loops, in which the performance of the training data set increases, while the performance of the validation data set decreases. Mean squared error (MSE) is the average squared difference between network output values and target values. Lower values are better. Zero means no error. The best validation performance is equal to 0.7477 at epoch 4 (Fig. 7).

Table 3: Matrix of experiments

Ex.	ap	Vc	f	Ra	RSm	Rt
1	0.5	50	0.05	0.474	54	4.072
2	0.5	50	0.08	0.685	61.2	3.862
3	0.5	50	0.11	0.971	113.6	4.517
4	0.5	100	0.05	0.378	48.3	2.279
5	0.5	100	0.08	0.5	76.8	4.173
6	0.5	100	0.11	0.873	114.4	4.478
7	0.5	150	0.05	0.393	44.6	3.667
8	0.5	150	0.08	0.888	89.8	7.446
9	0.5	150	0.11	0.731	93	4.666
10	1	50	0.05	0.597	73.1	4.005
11	1	50	0.08	0.788	87.2	5.359
12	1	50	0.11	0.905	106.6	5.964
13	1	100	0.05	0.57	106.7	4.298
14	1	100	0.08	0.767	81.6	4.045
15	1	100	0.11	0.95	111.8	4.613
16	1	150	0.05	0.411	64.4	3.202
17	1	150	0.08	0.735	85.3	3.891
18	1	150	0.11	0.766	85.5	4.265
19	1.5	50	0.05	0.464	52.1	2.428
20	1.5	50	0.08	0.559	80.1	3.728
21	1.5	50	0.11	0.968	115.1	5.022
22	1.5	100	0.05	0.49	58.4	5.094
23	1.5	100	0.08	0.734	85.1	3.579
24	1.5	100	0.11	0.972	115.9	4.457
25	1.5	150	0.05	0.523	67.4	3.503
26	1.5	150	0.08	0.741	88	4.115
27	1.5	150	0.11	0.825	104.3	7.665

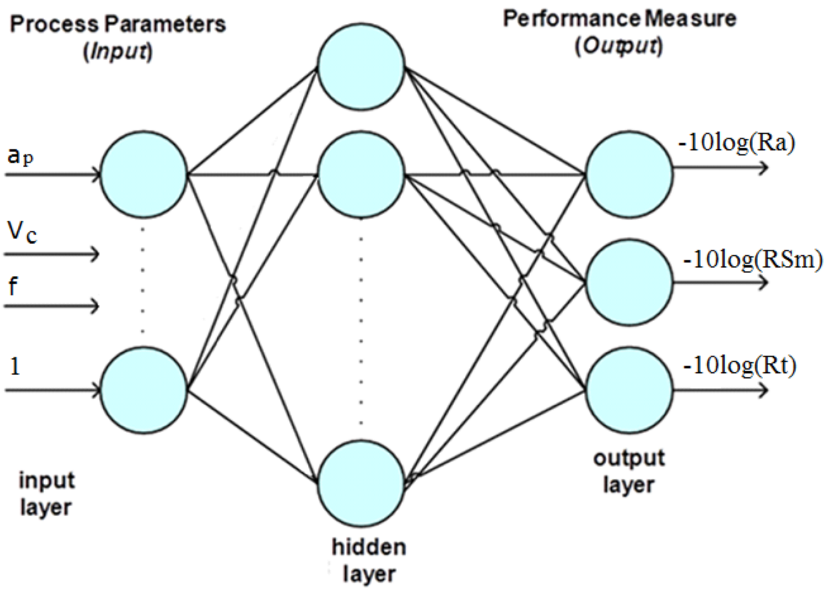

Fig. 6: The selected ANN architecture (feed-forward with back-propagation learning).

ISBN: 978-1-61804-295-8

Table 4. Best performance of ANN architecture.

	ANN Architecture				
	4x7x3	4x8x3	**4x9x3**	4x10x3	4x11x3
Training	0.9997	0.9996	0.9996	0.9993	1
Validation	0.9597	0.9779	0.9827	0.9778	0.9584
Test	0.9932	0.9944	0.9887	0.9814	0.9922
All	0.9902	0.9945	**0.9944**	0.9902	0.9907
Best val. perf.	3.1316	2.374	**0.7477**	3.139	3.111
epoch	4	2	**4**	2	2

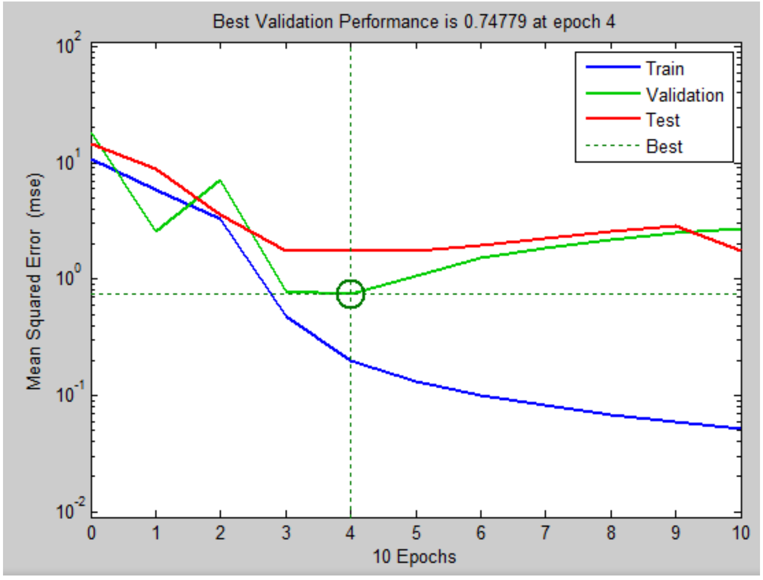

Fig. 7: The selected ANN architecture (feed-forward with back-propagation learning).

Another performance measure for the network efficiency is the regression (R) (Figs 8-11). Regression values measure the correlation between output values and targets. The acquired results show a good correlation between output values and targets during training (R=0.9996), validation (R=0.9827), and testing procedure (R=0.9887).

The trained ANN model can be used for the optimization of the cutting parameters during slot milling of Al7075 alloy.

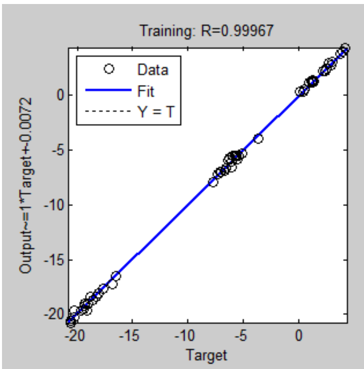

Fig. 8: Regression plots-Training

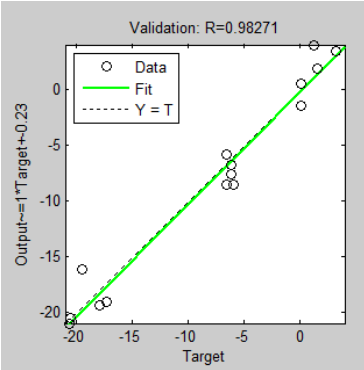

Fig. 9: Regression plots-Validation

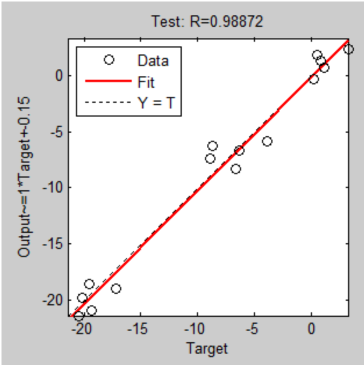

Fig. 10: Regression plots-Test

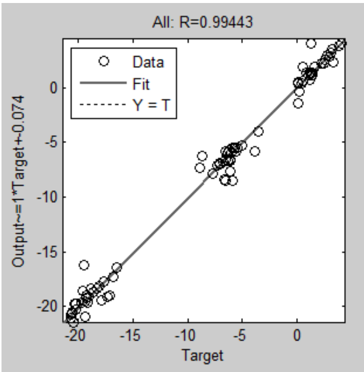

Fig. 11: Regression plots-Validation

This can be done by testing the behavior of the response variable (Ra, RSm, and Rt) under different variations in the values of depth of cut (ap), cutting speed (Vc), and feed rate (f) (Fig. 12-14).

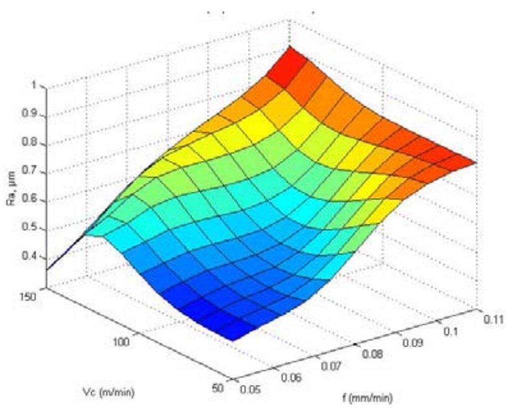

Fig. 12: Ra vs. feed rate and cutting speed (ap=1.5mm)

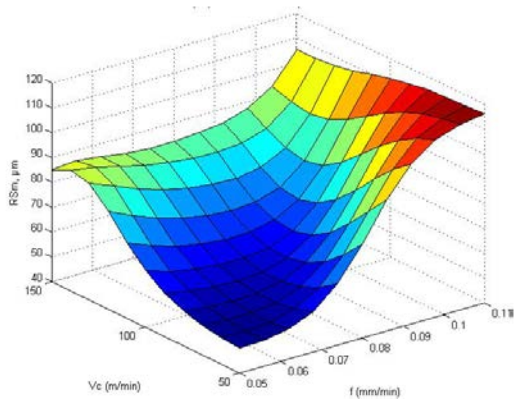

Fig. 13: Rsm vs. feed rate and cutting speed (ap=1.5mm)

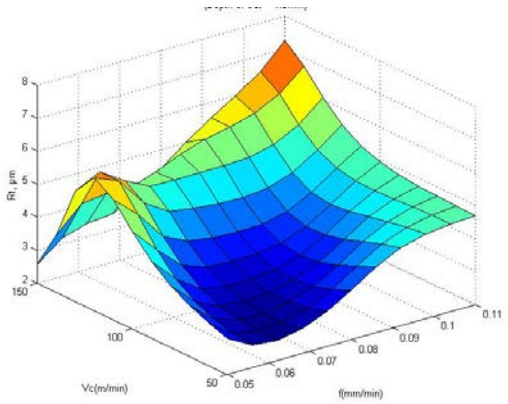

Fig. 14: Rt vs. feed rate and cutting speed (ap=1.5mm)

Conclusions

The surface texture parameters (Ra, RSm, and Rt) of Al7075 parts during slot milling were measured according to a matrix of experiments. The results were used to train a feed forward back propagation neural network with a topology of 4X9X3 neurons. The proposed NN can be used to predict the surface texture parameters as well as to optimize the process according to each one of the surface texture parameters. As a future work, authors plan to improve the performance of FFBP-NN incorporating more experiments as well as investigate the performance of alternatives training algorithms. In addition, a comparison among other approaches such as regression and additive modeling will be performed. Using the extracted NN, the surface response of Ra, RSm, and Rt can be drawn and the effects of process parameters can be estimated inside the experimental region in which the designed experiments were conducted. This methodology could be easily applied to different materials and initial conditions for optimization of other material removal processes.

Acknowledgements

The authors express special thanks to Mr Konstantinos Sirgkanis and the undergraduate student Aris Tsiolikas for their support on the developed laboratory activities.

References

[1] S. Rawangwong, J. Chatthong, R. Burapa, W. Boonchouytan, An investigation of optimum cutting conditions in face milling semi-solid AA7075 using carbide tool, International Journal of Innovation, Management and Technology, 3(6)(2012) 692-696.

[2] D. Vakondios, P. Kyratsis, S. Yaldiz, A. Antoniadis, Influence of milling strategy on the surface roughness in ball end milling of the aluminum alloy Al7075-T6, Measurement, 45(6)(2012) 1480-1488.

[3] P. Munoz-Escalona, P. Maropoulos, A geometrical model for surface roughness prediction when face milling Al 7075-T7351 with square insert tools, Journal of Manufacturing Systems, (2014)doi:10.1016/j.jmsy.2014.06.011.

[4] S. Karagiannis, P. Stavropoulos, C. Ziogas, J. Kechagias, Prediction of surface roughness magnitude in computer numerical controlled end milling processes using neural networks, by considering a set of influence parameters: An aluminium alloy 5083 case study, Proc IMechE Part B: J Engineering Manufacture, 228(2)(2014) 233–244.

[5] M.Y.Wang, H.Y. Chang, Experimental study of surface roughness in slot end milling AL2014-T6, International Journal of machine Tools & Manufacture, 44(2004) 51-57.

[6] T.P. Mahesh, R. Rajesh, Optimal selection of process parameters in CNC end milling of Al7075-T6 aluminum alloy using a Taguchi-Fuzzy approach, Procedia Materials Science, 5(2014) 2493-2502.

[7] S. Karagiannis, V. Iakovakis, J. Kechagias, N. Fountas, N. Vaxevanidis, Prediction of Surface Texture Characteristics in Turning of FRPs using ANN, Communications in Computer and Information Science 383(2013) 144-153.

[8] M.S. Phadke, Quality Engineering using Robust Design, Prentice-Hall, Englewood Cliffs, NJ, 1989.

[9] N. Vaxevanidis, J. Kechagias, N. Fountas, D.E. Manolakos, Three component cutting force system modeling and optimization in Turning of AISI D6 tool steel using design of experiments and Neural Networks, In Proceedings of the World Congress on Engineering 2013London, U.K, Vol. I, July 2-6, (2013).

[10] J. Kechagias, V. Iakovakis, A neural network solution for LOM process performance, The International Journal of Advanced Manufacturing Technology, 43(11)(2009) 1214-22.

[11] M. Pappas, J. Kechagias, V. Iakovakis, S. Maropoulos, Surface roughness modelling and optimization in CNC end milling using Taguchi design and Neural Networks, ICAART 2011 – In Proceedings of the 3rd International Conference on Agents and Artificial Intelligence 1(2011) 595-598.

[12] D. Montgomery, Design and Analysis of Experiments, 7th Edition, John Wiley & Sons (2008).

[13] C.C. Tsao, Grey–Taguchi method to optimize the milling parameters of aluminum alloy, The International Journal of Advanced Manufacturing Technology, Vol. 40(2009) 41–48.

[14] W. Sukthomaya, J. Tannock, The optimisation of neural network parameters using Taguchi's design of experiments approach: an application in manufacturing process modelling, Neural Computing and Applications, 14(4)(2005) 337-344.

[15] S.G. Tzafestas, P.J. Dalianis, G. Anthopoulos, On the overtraining phenomenon of backpropagation NNs., Mathematics and Computers in Simulation, 40(1996) 507-521.

[16] C.T. Lin, G.C.S. Lee, , Neural fuzzy systems- A neuro-fuzzy synergism to intelligent systems. Prentice Hall (1996).

[17] L. Prechelt, Automatic early stopping using cross validation: quantifying the criteria, Neural Networks, 11(4)(1998) 761–767.

Pattern Analysis of Pediatric Foot Disorders using Decision Tree

Jungkyu Choi[1,a], Hwa-In Kim[2,b], Yonggwan Won[3,c] and Jung-ja Kim[4,5,d *]

[1]Department of Healthcare Engineering, Chonbuk National University, 567 Baekje-daero, Deokjin-gu, Jeonju-si, Jeollabukdo, 561-756, Republic of Korea

[2]The Foot Clinic of Jeonju Pediatrics, 485-42, Junghwasan-dong 2, Wansan-gu, Jeonju, Jeolabuk-do, Republic of Korea

[3]School of Electronics and Computer Engineering, Chonnam National University, 77 Yongbong-ro, Buk-gu, Gwangju, 500-757, Republic of Korea

[4]Division of Biomedical Engineering, Chonbuk National University, 567 Baekje-daero, Deokjin-gu, Jeonju-si, Jeollabukdo, 561-756, Republic of Korea

[5]Research Center of Healthcare & Welfare Instrument for the Aged, Chonbuk National University, 567 Baekje-daero, Deokjin-gu, Jeonju-si, Jeollabukdo, 561-756, Republic of Korea

[a]chaosjoozak@nate.com, [b]mssy1016@yahoo.com, [c]ykwon@jnu.ac.kr, [d]jungjakim@jbnu.ac.kr

Keywords: Pediatric Foot, Lower limb, Disorder, Pattern classification, Decision tree.

Abstract. In modern medical field, the explosive increase of clinical data has happened by development of computer information technology and tools. For a large amount of clinical data, data mining, the extraction method of hidden predictive information, has been recognized by many studies. The purpose of the study was to find out significant knowledge between the foot disorder groups and biomechanical parameters related to symptom on the basis of the pediatric clinical data by developing a prediction model of the decision tree. The first examination clinical data of 174 pediatric patients diagnosed with complex disorder including pes planus basically was used for analysis, in total 279 records. For analysis, the dependent variable was consisted of five complex disorder groups, and 14 of 34 independent variables related to disorder groups were selected by importance. The analysis data was partitioned into training data and test data to generate an ideal prediction model. After developing the prediction model by C5.0 algorithm, the prediction rate was verified. In conclusion, 13 diagnosis patterns were figured out, and major symptom information was confirmed. To improve accuracy of classification, the detailed preprocessing of variables and meticulous analysis will be performed from now on.

Introduction

The bipedalism, including walking, running and jumping, is the most fundamental human activity, and natural behavior that anyone is able to perform easily in everyday life, if normal [1]. For this movement, the lower limbs, including foot, are very important organ of the body. However, the close collaboration of different skeletal muscles, join and nervous system is necessary to get a high amount of balancing and stability on gait. That is why the foot has a highly complex structure composed of 28 bones, 55 small joint and 23 muscles, despite just 5% surface of the body. When a human walks for 1 km, there is about 15 t weight-bearing increase on the foot. In addition, the weight-bearing with push-off exercise of gait causes stress or soft tissue strain on the lower limbs. This problem deforms

ISBN: 978-1-61804-295-8

the leg and foot shape, and the abnormal lower limbs have a bad influence on the balance of the spine and pelvis [2. In case of children, the level of deformation is different from adult because pediatric foot have characteristic differences in structure and function [3]. For this reason, Muller, Carlsohn, Muller, Baur, Mayer performed the study to acquire static and dynamic foot characteristics in childhood, and to establish data for age groups of a population of 1–13 year old infants and children based on a cohort of 7788 subjects [4]. Although there is difference by a variety of causes, the foot commonly grow up by age 5 and 7 quickly. Since then, it maintains growth by age 10 and 14 at constant rate [5]. During that time, the foot shape is changing from pes planus to normality, and the leg shape also alters in the same order as follows: genu varum, genu valgum and normality [6]. If the shape of the lower limb does not become normality until about 12 years old, it is more likely to be cause of the adult foot disorder. In addition, treatment of non-invasive method is only efficient in childhood. Jay, Schoenhaus, Seymour, Gamble confirmed that there was significant improvement in the resting calcaneal stance position (RCSP) of children, aged 20 months to 14 years with pes planus, who were prescribed with a custom-made orthosis [7]. Lincoln, Suen noted that out-toe gait was observed in children with pes planus, and its patterns may result from abnormal conditions of the hip, tibia and femoral region [8]. There are close connections between abnormal shape and cause of various disorders in the lower limbs. However, the disorders appear multiply and symptoms are not clear, on the average. Accordingly, more intelligent analysis is necessary to figure out pattern of symptoms.

In modern medical field, the explosive increase of clinical data has happened by development of computer information technology and tools [9,10]. For a large amount of clinical data, data mining, the extraction method of hidden predictive information, has been recognized by many study [11]. It is method to handle large data and to find out desired important and meaningful knowledge with utilizing pattern recognition technology, statistics technique or mathematic algorithm [12]. Decision-tree, which is a key issue of representative technique in the data mining, is an algorithm to classify or predict a couple of subgroup from interested object group by modeling rule and observing relation [13]. This method is a model of decisions and a special form of tree structure. Therefore, it has advantage to understand analysis process and results easily [14]. According to previous studies, data mining was adopted for analysis of medical data. Breault, Goodall and Fos applied Classification and Regression Trees (CART) of data mining for analysis of diabetic data warehouse. They figured out that the most important variable associated with bad glycemic control was younger age, not the comorbidity index or whether patients had related disorders [15]. Kim presented that age, associated disorder, pathology scale, course of hospitalization, respiratory failure and congestive heart failure were came out to be danger factors on death of pneumonia by using data mining for analysis of death factor on pneumonia patient [16]. Stoean, Stoean, Lupsor, Stefanescu, and Badea reported that the evolutionary-driven support vector machine of data mining was utilized to anticipate stage of hepatic fibrosis that determine hardness degree of liver or operation in chronic hepatitis C [17]. Lim, Ryu, Park and Ryu the logistic regression and neural network were applied to extract attribute and perform learning based on widespread clinical data of acute myocardial infarction for forecast short-term relapse mortality of ST-segment elevation myocardial infarction (SEMI) patients. Through this study, the model to foresee short-term mortality of SEMI patients was suggested [18]. In addition, the four decision tree algorithms were used to analyze postoperative status of ovarian endometriosis patient under different conditions. This study reported new meaningful information about recurrent ovarian endometriosis [10]. However, most previous study about the lower limbs just noted simple comparison analysis based on quantitative values. In addition, a study in respect of the pediatric foot disorder is insufficient, despite the symptoms are commonly complicated. More integration analysis with data mining technique is necessary, and interpretation of interconnection between several clinical parameters and the foot disorder is important.

Accordingly, the purpose of this study was to find out significant knowledge between the foot disorder groups and biomechanical parameters related to symptom on the basis of the pediatric clinical data in the Foot clinic by developing a prediction model of the decision tree.

Study Procedure

Subject. The first examination clinical data of total 279 pediatric patients diagnosed with complex disorder, including pes planus basically, was used from the Foot Clinic of Jeonju Pediatrics. To diagnose disorder, total 34 attributes, Resting Calcaneal Stance Position (RCSP), the Tibia TransMalleolar Angle (Tibia TMA), the Knee Internal Malleolus Distance (Knee IMD), etc., were measured and patient charts was made up by a podiatrist, as shown in Fig. 1. 64 patients records with missing values were excluded, and complex disorder groups above 5% of data were selected for analysis. Analysis data was composed of 174 patient records with five groups for the complex disorder.

Fig 1. Measurement of RCSP and patient charts

Variables. A dependent variable in the study was consisted of five complex disorder group such as A: Pes planus and Achilles tendinitis, B: Pes planus, C: Pes planus and Intoe gait, D: Pes planus, Intoe gait and Genu valgum and E: Pes planus and Genu valgum, as shown in Table 1.
Independent variable was preprocessed through statistical validity and importance analysis. Therefore, 14 of 34 independent variables related to disorder closely were selected and optimized, as shown in Table 2.

Table 1. Dependent variable

Class	Disorder
A	Pes planus, Achilles tendinitis
B	Pes planus
C	Pes planus, Intoe gait
D	Pes planus, Intoe gait, Genu valgum
E	Pes planus, Genu valgum

Study Process. In the study, combination of independent variables meant each of the foot disorder group. Therefore, 14 independent variables were inserted into C5.0 algorithm of decision tree at the same time. Data analysis was performed by IBM SPSS statistics 18 (SPSS Inc., Chicago, IL, USA)

ISBN: 978-1-61804-295-8

Table 2. Independent variable

Variable	Type	Description
Sex	Nominal	Male, Female
(L) TibiaTMA	Numeric	Angle of the left tibia transmalleolar
(R) TibiaTMA	Numeric	Angle of the right tibia transmalleolar
KneeIMD	Numeric	The knee internal malleolus distance
(L) Talocalcaneal	Numeric	Left angle between the talus and the calcaneus
(R) Talocalcaneal	Numeric	Right angle between the talus and the calcaneus
(L) CuboidAbduction	Numeric	Left angle of the cuboid abduction
(R) CuboidAbduction	Numeric	Right angle of the cuboid abduction
(L) Intermetatarsal	Numeric	Left angle of the metatarsus primus adductus
(R) Intermetatarsal	Numeric	Right angle of the metatarsus primus adductus
(L) TalarDeclination	Numeric	Angle of the left talus declination
(R) TalarDeclination	Numeric	Angle of the right talus declination
(L) RCSP	Numeric	Left Resting calcaneal stance position angle
(R) RCSP	Numeric	Right Resting calcaneal stance position angle

and IBM SPSS Modeler 14.2 (SPSS Inc., Chicago, IL, USA). For generating an ideal model, it was effective to develop a couple of the prediction model and perform comparison analysis [19]. Consequently the entire data was partitioned into training data (70%) and test data (30%) at random, and the prediction models of data were developed by C5.0 algorithm, as shown fig. 1. The prediction rate was verified through the analysis node after development of model. The prediction model of tree-structured decision tree is comprised of organization as ‘If A, then B. Else B2’ [20].

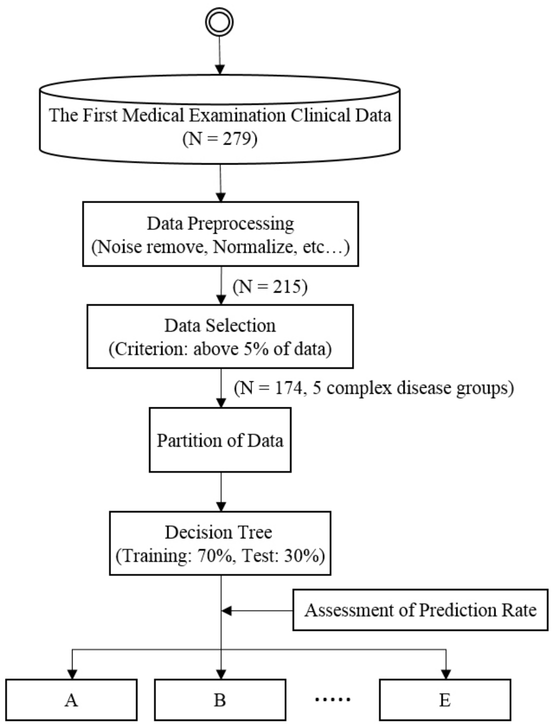

Fig 2. Mining procedure

Results

The first clinical data of 174 pediatric patients with complex disorder, including pes planus basically, was utilized for the study. The prediction model was created to analyze pattern of the foot disorder group by applying the C5.0 algorithm. The measured prediction rate was Correct: 92.44 % and

ISBN: 978-1-61804-295-8

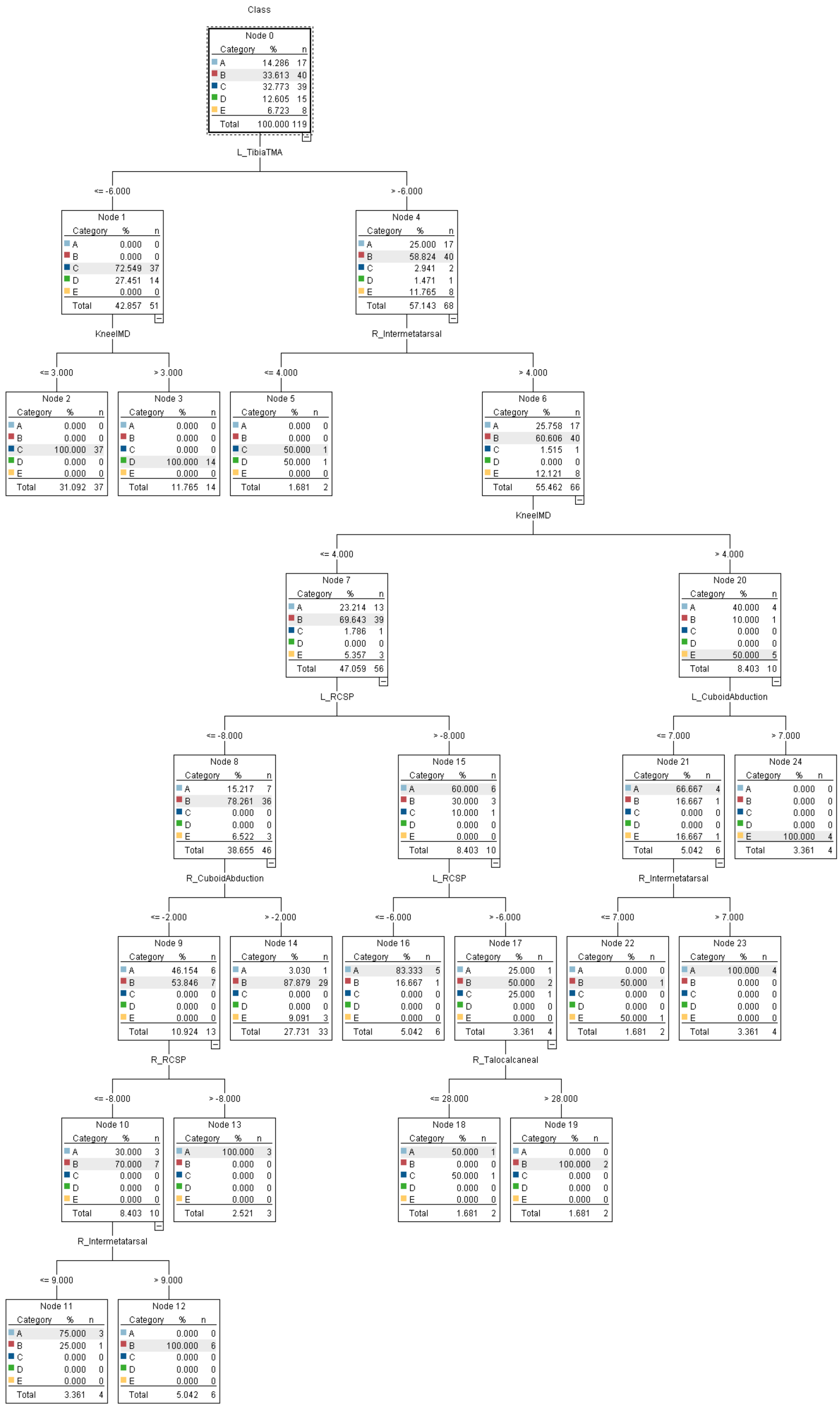

Fig 3. The result of decision tree

Wrong: 7.56 % in the training data, and Correct: 74.07 % and Wrong: 25.93 % in the test data.

As a result of analysis on five complex disorder groups by using decision tree, 13 rules were discovered : (1) If '(L) Tibia TMA' was above -6°, '(R) Intermetatarsal' was above 4°, 'KneeIMD' was below 4 cm, '(L) RCSP' was below -8°, '(R) Cuboidabduction' was below -2°, '(R) RCSP' was below -8 and '(R) Intermetatarsal' was below 9°, then 'A', (2) If '(L) Tibia TMA' was above -6°, '(R) Intermetatarsal' was above 4°, 'KneeIMD' was below 4 cm, '(L) RCSP was below -8°, '(R) Cuboidabduction' was below -2° and '(R) RCSP' was above -8°, then 'A', (3) If '(L) Tibia TMA' was above -6°, '(R) Intermetatarsal' was above 4°, 'KneeIMD' was below 4 cm, '(L) RCSP' was below -6 ° ~ above -8°, then 'A', (4) If '(L) Tibia TMA' was above -6°, '(R) Intermetatarsal' was above 4°, 'KneeIMD' was below 4 cm, '(L) RCSP' was above -6° and '(R) Talocalcaneal' was below 28°, then 'A', (5) If '(L) Tibia TMA' was above -6°, '(R) Intermetatarsal' was above 4°, 'KneeIMD' was above 4 cm, '(L) Cuboidabduction was below 7° and '(R) Intermetatarsal' was above 7°, then 'A', (6) If '(L) Tibia TMA' was above -6°, '(R) Intermetatarsal' was above 4°, 'KneeIMD' was below 4 cm, '(L) RCSP' was below -8°, '(R) Cuboidabduction' was below -2°, '(R) RCSP' was below -8 and '(R) Intermetatarsal' was above 9°, then 'B', (7) If '(L) Tibia TMA' was above -6°, '(R) Intermetatarsal' was above 4°, 'KneeIMD' was below 4 cm, '(L) RCSP' was below -8° and '(R) Cuboidabduction' was above -2°, then 'B', (8) If '(L) Tibia TMA' was above -6°, '(R) Intermetatarsal' was above 4°, 'KneeIMD' was below 4 cm, '(L) RCSP' was above -6° and '(R) Talocalcaneal' was above 28°, then 'B', (9) If '(L) Tibia TMA' was above -6°, '(R) Intermetatarsal' was above 4°, 'KneeIMD' was above 4 cm, '(L) Cuboidabduction was below 7° and '(R) Intermetatarsal' was below 7°, then 'B', (10) '(L) Tibia TMA' was below -6° and 'KneeIMD' was below 3 cm, then 'C', (11) '(L) Tibia TMA' was above -6° and '(R) Intermetatarsal' was below 4°, then 'C', (12) '(L) Tibia TMA' was below -6° and 'KneeIMD' was above 3 cm, then 'D', (13) If '(L) Tibia TMA' was above -6°, '(R) Intermetatarsal' was above 4°, 'KneeIMD' was above 4 cm and '(L) Cuboidabduction was above 7°, then 'E', as shown in Fig. 3 and Fig. 4.

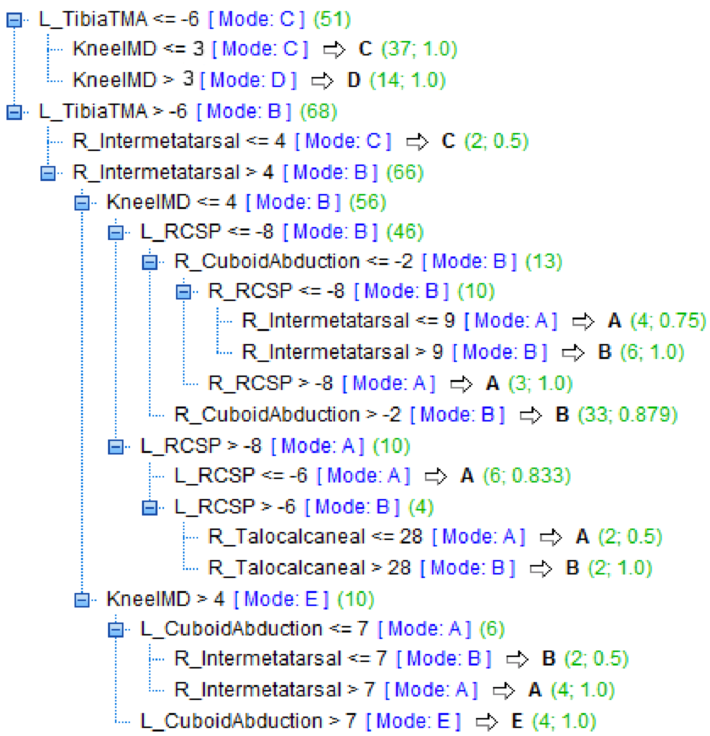

Fig 4. The result of C5.0 decision tree

Conclusion

In the study, the object was to find out significant knowledge between the foot disorder groups and biomechanical parameters related to symptom on the basis of the pediatric clinical data by developing

a prediction model of the decision tree. The first examination clinical data of 174 pediatric patients diagnosed with complex disorder including pes planus basically was used for analysis. The dependent variable was consisted of five groups, and the 14 independent variables were selected by importance. The analysis data was partitioned into training data and test data to generate an ideal prediction model. After developing the prediction model by C5.0 algorithm, the prediction rate was verified.
In conclusion, we were able to confirm that the variable of each node was a key diagnosis factor to discriminate the foot disorder. As follow rules of result, major symptom pattern information of disorder was confirmed as follows. The class A had two patterns; (a) the left tibia transmalleolar angle above -6°, the right intermetatarsal angle above 4°, the knee internal malleolus distance below 4 cm, left resting calcaneal stance position angle below -8°, the right cuboid abduction angle below -2° and right resting calcaneal stance position angle above -8°, (b) the left tibia transmalleolar angle above -6°, the knee internal malleolus distance above 4 cm, the left cuboid abduction angle below 7° and the right intermetatarsal angle above 7°. The class B also had two patterns; (a) the left tibia transmalleolar angle above -6°, the right intermetatarsal angle above 4°, the knee internal malleolus distance below 4 cm, both resting calcaneal stance position angle below -8°, the right cuboid abduction angle below -2° and the right intermetatarsal angle above 9°, (b) the left tibia transmalleolar angle above -6°, the right Intermetatarsal angle above 4°, the knee internal malleolus distance below 4 cm, left resting calcaneal stance position angle above -6° and the right talocalcaneal angle above 28°. The class C had one pattern; (a) the left tibia transmalleolar angle bellow -6° and the knee internal malleolus distance bellow 3 cm. In case of the class D, it had one pattern; (a) the left tibia transmalleolar angle bellow -6° and the knee internal malleolus distance above 3 cm. The class E also had one pattern; (a) the left tibia transmalleolar angle above -6°, the right intermetatarsal angle above 4°, the knee internal malleolus distance above 4 cm and the left cuboid abduction angle above 7°.

The symptom of the foot disorder was commonly complicated, not obvious. In case of children, especially, classification of disorder was more difficult than adult due to the soft bones or growth. For these reasons, the error rate of the prediction rate was relatively high in test data. Therefore, detailed preprocessing of variables and meticulous analysis will be performed to improve accuracy of classification. Also, other decision tree algorithms will be applied to develop additional model and carried out comparison analysis for an ideal model from now on.

Acknowledgements

This work was supported by National Research Foundation of Korea (NRF) grant funded by the Korea government (MSIP) (NRF-2013R1A2A2A04016782) and by Basic Science Research Program through the National Research Foundation of Korea (NRF) funded by the Ministry of Education, Science and Technology (NRF-2012R1A1B3003952).

References

[1] R.A. Donatelli, The Biomechanics of the foot and ankle, The F. A. Davis Company, Philadelphia, 1995.

[2] D.J. Lott, M.K. Hastings, P.K. Commean, K.E. Smith, M.J. Muller, Effect of footwear and orthotic devices on stress reduction and soft tissue strain of the neuropathic foot, Clinical Biomechanics. 22 (2007) 352–359.

[3] J.H. Chang, S.H. Wang, C.L. Kuo, H.C. Shen, Y.W. Hong, L.C. Lin, Prevalence of flexible flatfoot in Taiwanese school-aged children in relation to obesity, gender, and age, European journal of pediatrics. 169(4) (2010) 447-452.

[4] S. Muller, A. Carlsohn, J. Muller, H. Baur, F. Mayer, Static and dynamic foot characteristics in children aged 1–13 years: A cross-sectional study, Gait & posture, 35(3) (2012) 389-394.

[5] M. Anderson, M.M. Blais, W.T. Green, Lengths of the growing foot, J Bone Joint Surg Am. 38 (1956) 998-1000.

[6] M. Pfeiffer, R. Kotz, T. Ledl, G. Hauser, M. Sluga, Prevalence of flat foot in preschool-aged children, Pediatrics. 118(2) (2006) 634-639.

[7] R.M. Jay, H.D. Schoenhaus, C. Seymour, S. Gamble, The Dynamic Stabilizing Innersole System (DSIS): the management of hyperpronation in children, The Journal of foot and ankle surgery. 34(2) (1995) 124-131.

[8] Y.J. Ko, H.W. Kim, Diagnosis and Conservative Treatment of Common Foot Disorders, Journal of the Korean Medical Association. 47(3) (2004) 247-257.

[9] J. Han, and M. Kamber, Data mining: concepts and techniques, Morgan Kaufmann, San Francisco, 2001.

[10] N. Duru, An application of apriori algorithm on a diabetic database, Knowledge-Based Intelligent Information and Engineering Systems, Springer Berlin Heidelberg, (2005) 398-404.

[11] A.R. Islam, T.S. Chung, An Improved Frequent Pattern Tree Based Association Rule Mining Technique, Information Science and Applications (ICISA), 2011 International Conference on. IEEE. (2011), 1-8.

[12] T.L. Lincoln, P.W. Suen, Common rotational variations in children. Journal of the American Academy of Orthopedic Surgeons 11(5) (2003) 312–320.

[13] M.Y. Chang, C.C. Shih, D.A. Chiang, C.C. Chen, Mining a Small Medical Data Set by Integrating the Decision Tree and t-test, Journal of Software. 6(12) (2011) 2515-2520.

[14] J.Y. Song, H.K. Kim, A Study of Decision Tree in Detecting Intrusions, Journal of the Korean Data Analysis Society. 12 (2010) 983-996.

[15] J.L. Breault, C.R. Goodall, P.J. Fos, Data mining a diabetic data warehouse, Artificial Intelligence in Medicine. 26(1) (2002) 37-54.

[16] Y.M. Kim, A study on analysis of factors on in-hospital mortality for community-acquired pneumonia, Journal of the Korean Data & Information Science Society. 22(3) (2011) 389-400.

[17] R. Stoean, C. Stoean, M. Lupsor, H. Stefanescu, R. Badea, Evolutionary-driven support vector machines for determining the degree of liver fibrosis in chronic hepatitis C, Artificial intelligence in medicine. 51(1) (2011) 53-65.

[18] K.H. Lim, K.S. Ryu, S.H. Park, H.S. Shon, K.H. Ryu, Short-term Mortality Prediction of Recurrence Patients with ST-segment Elevation Myocardial Infarction, Journal of The Korea Society of Computer and Information. 17(10) (2012) 145-154.

[19] M. Park, S. Choi, A.M. Shin, H. Chul, Analysis of the Characteristics of the Older Adults with Depression Using Data Mining Decision Tree Analysis, J Korean Acad Nurs. 43 (2013) 1-10.

[20] M.H. Huh, Y.G. Lee, Data mining modeling and case, second ed., Hannarae, Seoul, 2008.

Materials used in a construction of a camshaft mechanism

SŇAHNIČAN František[1,a] BARBORÁK Oto [2,b*] and RAKÚSOVÁ Danka [3,c]

František Sňahničan, University of Defence, Brno, Czech Republic

Oto Barborák, Trencin University of Alexander Dubcek in Trencin, Trencin, Slovak Republic

Danka Rakúsová, Trencin University of Alexander Dubcek in Trencin, Trencin, Slovak Republic

[a]Frantisek.snahnican@unob.cz, [b]oto.barborak@tnuni.sk[*], [c]danka.rakusova@tnuni.sk

Key words: Mechanism, camshaft, production engineering and special equipment, material composition, technical parameters of camshafts

Abstract: The paper deals with an importance of camshafts as important parts of mechanisms being used in production engineering as well as in special equipment. Material composition of camshafts together with a complexity of its profile construction and character of motion has impact on kinetic and dynamic parameters of a mechanism as well as a whole machine.

1. Introduction

Several mechanisms enabling transformation of motion, thus a change of its kind are used in mechanical engineering practice. In practice the mechanisms the most often used for a transition of a rotational movement into a straight-line one are worm-geared, screwed, camshaft and cranked ones. There are basic kinds of transformation mechanisms illustrated in the Fig. 1 – a screwed mechanism, a gear wheel and a gear rack, a worm and a worm rack, cam mechanisms, cranked mechanism centrical and eccentric, a cranked mechanism with a bar link, a cranked mechanism with a rotating block.

2. Camshaft mechanism

Camshaft and eccentric mechanisms transform a rotational motion into an advance reversible motion with a small travel. A cam is mounted on a shaft. The motion and a force are transferred from a driving shaft through a lever-type mechanism on a working unit. Requested speed and trajectory course will be reached through a cam shaping.

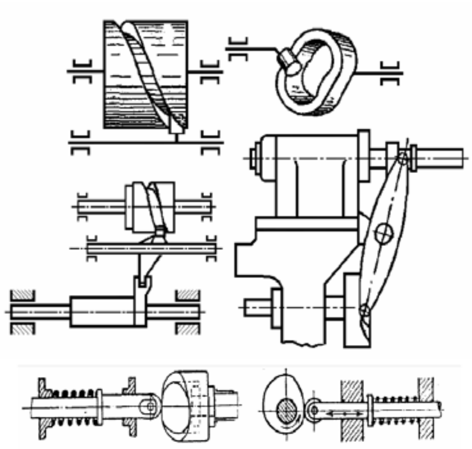

Fig.1 Examples of application of cam mechanisms for a transition of a rotation movement into a straight-line one

The cam mechanisms are plane or triaxle curvilinear mechanisms. The cam mechanisms are used to transform a rotational motion into a periodical straight-line motion, or a periodical rocking or a rotational motion (Fig.2).

From a construction view the cam mechanisms fit the best to perform short travels. The trajectories of such motions can be increased through engagement of a gearing mechanism (a gear lever or a gear lever system) with a needed gear ration between a cam and an effective body. An advantage is a simple performance of a requested motion of a driven element and a simple replacement of a kinetic relation, travel size and a motion time through a replacement of a cam.

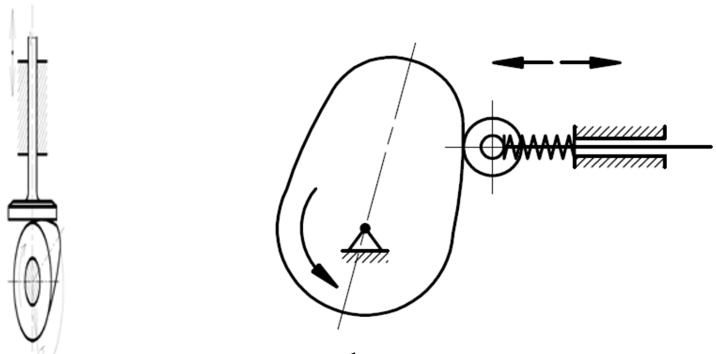

a b

Fig. 2 Cams used in
a- automotive industry, b- in production engineering

Advantages:

Possibility to reach ideal dynamic ratios for a straight-line motion, applicability mainly for mass production automatic machines

Disadvantages:

A small travel, demanding production, higher demands on material hardness (resistance to impression and wear)

<u>A cam mechanism consists of:</u>

1. A frame that is a fixed part of a machine,
2. A driving element – a cam that can begin through its construction a loose (Fig.3/a) or a forced motion of an effective element of a mechanism (Fig.3/b)
3. A driven element that used to be an effective element of a mechanism (a pulley, a tappet).

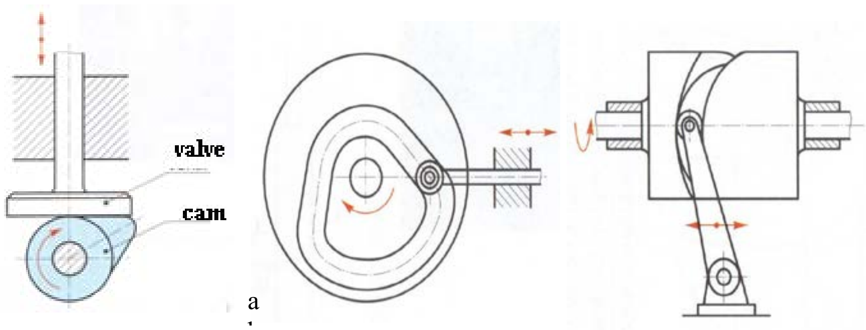

Fig. 3 Main joints of a cam with an effective
body od a mechanism
a- loose joint, b- forced joint

A main element of a camshaft mechanism is a cam, an associated element is a pulley or a tappet that does not roll away as a pulley, but it slides. Contact of a pulley, a tappet is a force one and it used to be secured with a spring.

<u>Classification of camshaft mechanisms:</u>

- A tappet with a tip, an axis passes through a cam rotation axis (Fig.4/a),
- A tappet with a pulley, an axis passes through a cam rotation axis (Fig.4/b),
- A tappet with a pulley, the axes are skew (Fig.4/c),
- A rocker arm with a pulley (Fig.4/d),
- A flat tappet (Fig.4/e),
- A flat rocker arm (Fig.4/f).

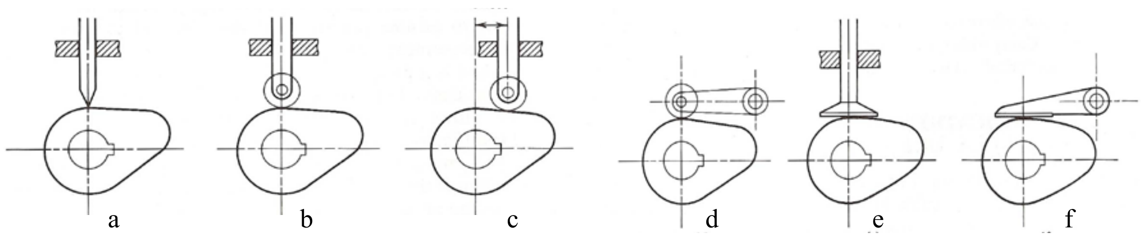

Fig.4 Kinds of cams with a different tappet construction

3. Cam production and used material

A cam – is a disk, whose each point on its circumference is a part of a circle with a slot or a nib. In fact a cam profile represents a trajectory of a motion of a driven element; an instantaneous velocity and acceleration depend of its position and subsequently its dynamic parameters as well. These parameters cause inter alia large, often impact stress on a cam, and become evident in its wear and in a change of its kinematic parameters in relation with a driven element. It finally results in non-standard parameters of bending up to mechanism destruction.

<u>AS profile of each cam is composed of:</u>

- A basic circle,
- Two effective parts (sides)and a cylindrical part,
- A leading and a finishing parts (a transition part).

Just a selection of a suitable material for production of a cam and mainly quality of its surface at loose as well as at forced motion is a significant factor for an application of a camshaft mechanism of a given construction in production engineering and often in special equipment as well.

A cam is a component or a component part (as an example of a camshaft) characterized by its general shape – particular points of a cam surface are at a different distance from a rotation axis. A function of a cam is to transform a rotational motion into a straight-line reversible one so that its shape in rotation causes a motion of another component leaning against a cam – e.g. in control of valves of a combustion engine (Fig.5).

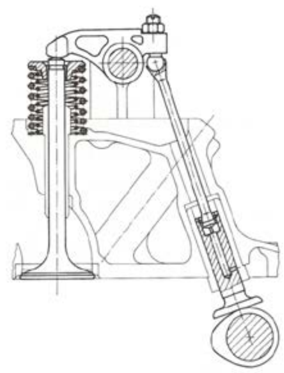

Fig.5 Camshaft mechanism for valve control

The paper deals with material composition of cams that are largely applied in mechanisms in production engineering as well as in special equipment. They exercise a significant influence on kinematic and dynamic parameters of a whole mechanism as well as a machine through their variable technical parameters and their location in a construction of mechanisms. Especially a material composition of cams predetermines their particular practical application from a view of an operational stress.

As a rule nowadays the cams are produced by milling operations on CNC machines. After then they are ground aiming to increase an accuracy and surface quality. An option is an application of a copier, where another cam serves as a counter gear. If an absolute accuracy of production is not required, the consideration about pressing operations or exact shearing comes on force. In case when the cams are heavy stressed and therefore they need to be produced from strong hardly Machin able materials, an electro erosive machining is used.

3.1 A tappet

The main task of a tappet is to absorb a tangential force from a cam and a subsequent transfer onto a distribution pushrod (Fig.4). Tappets used to be hollow bucket-type with a cylindrical profile or with a disk profile. An advantage of bucket-type tappets is a possibility to replace it without dismantling of a camshaft, on contrary, an advantage of disk tappets is a simpler production due to a cylindrical line of a smaller diameter. The mentioned valve distribution disposes of disk tappets.

A contact area with a cam (from a view of a material and a surface treatment highly significant area) used to be hardened from 50 HRC up to 60 HRC hardness, then processed through finishing technologies, in particular ground and lapped ones. A pushrod sits on a base of a tappet or on a top end. Lubrication is performed through a pressure of oil assigned for lubrication of bearings on a rocker arm.

Theoretical contact area between a cam and a tappet is a line (eventually a point). In order to prevent from a significant wear of a contact area, the tappet used to be shifted from an axis by 2mm up to 3 mm, resulting in tappet swiveling.

3.2 Cam material

A cam has homogenous mechanical features in its whole volume. Choice of a suitable material depends on a maximum value of a contact pressure in a working cycle of a cam mechanism that has been obtained by calculation from a dynamic solution of a particular cam.

Table 1. Materials used for production of a cam with no tempered surface layer

steel STN	Way of material treatment	Cam width l[mm]	Minimum tensile strength R [MPa]	Tensile yield point R_p 0,2 [MPa]	Hardness HB	Admissible pressure „p „ for 10^8 life cycles [MPa]
11 500	Thermally non-treated	130	490	265	141	313
11 600	Thermally non-treated	130	588	314	169	375
11 700	Thermally non-treated	130	686	363	197	437
12 050	Normalizing	100	530	305	152	337
12 050	Heat treatment	40	640	390	192	426
12 061	Normalizing	100	660	382	189	419

ISBN: 978-1-61804-295-8

12 061	Heat treatment	40	720	420	210	466
13 240	Heat treatment	40	780	540	239	530
13 240	Heat treatment	25	880	635	269	596
14 140	Heat treatment	40	883	637	270	599
14 140	Heat treatment	100	785	539	240	532
15 241	Heat treatment	40	1177	981	359	796
15 241	Heat treatment	40	1716	1372	51 HRC	1099
16 640	Heat treatment	140	1569	1275	49 HRC	1045
14 209	Quenching	40	2100	1700	61 HRC	1392

For some cams it is more suitable to reach different features of a surface and a kernel. Mechanical features differ in a cam section. On a functional surface area the hardened layer is created through chemical-and-heat treatment, it means quenching, cementing, nitriding or a combination of technologies, nitro carburizing or carbonitriding.

Table 2 Materials for a cam with a hardened surface layer

	Kernel			Surface layer		
steel STN	Cam width l[mm]	Minimum tensile strength R [MPa]	Tensile yield point R_p 0,2 [Mpa]	Way of treatment	hardness HRC	Admissible pressure p for 10^8 life cycles [Mpa]
12 020.4	30	490	295	cementing, quenching	58 up to 61	1300 up to 1390
14 220.4	30	785	588			

ISBN: 978-1-61804-295-8

14 223.4	15	883	687			
14 230.4	40	981	794			
16 220.4	30	883	637			
16 420.4	30	932	735			
15 230.6	250	780	635	nitriding	60	1360
15 330.6	250	834	637			
14 140.4	40	1716	1373	Nitro carburizing, quenching,	56 up to 60	1240 up to 1360
11 600.1	60	580	314	Surface hardening	55 up to 59	1210 up to 1330
11 700.1	60	686	363			
12 051.6	30	640	390			
14 140.7	25	932	785			
15 241.7	40	1177	981			

3.3 Camshaft

Straining of a camshaft is the same as for a crankshaft – mostly fatigue and wear. Its task is to open and to close valves on cylinders by rotation of special shaped cams. This directly implies that number of revolutions of a camshaft per minute will be equal to a half of revs of a crank shaft. The most common material for a production of a cam shaft is nowadays a shortly chilled grey cast iron Fe-3.2C-2Si- 0.8Mn-0.8Cr-0.2Mo, or Fe-32.C-2Si- 0.8Mn-1.2Cr-0.6Mo. An effect of a short chilling causes, that a kernel does not have enough time to cool down at a needed speed and it still remains as a grey cast metal, meanwhile the surface has changed into a white cast metal. In some engines there is applied a lighter camshaft made of a forged steel Fe-0.2C-0.3Si-0.8Mn-1Cr- 0.2Mo, which is carburized after forging. Reduction in weight while keeping requested mechanical features is achieved also with a sintered alloy Fe- 0.9C-0.2Si-0.4Mn-4.5Cr-5Mo-3Cu-2V- 6W. Heavy stressed camshaft is coated as a rule with a TiN layer through PVD method.

4. Straining of cams through impacts effects

An impact is a dynamic interaction of two bodies, whereby mechanical energy is transferred. Impact energy is transformed into tensile, deformation and heat energy. Generally, the impacts in mechanisms are unfavorable phenomena.

What do the impacts cause:

- Wear of functional areas,
- Functional areas impression,
- increase of clearances,
- degradation of working accuracy,
- they are sources of unwanted vibration and noise.

Sources of impact rise:

- inappropriate kinematic links (improper construction of a mechanism),
- unbalanced rotating masses.
- insufficient lubrication (self-excited vibrations),
- hard impacts,
- inadmissible overloading of a machine.

Measures to decrease a size of impacts:

- higher accuracy of produced components,
- balancing of rotors and accurate mounting of components,
- frame of a machine and a base stiff enough,
- use of machine in accordance with regulations, proper maintenance,
- application of damping and tensile elements in kinematic chains,
- better machine design concept (relieved construction of movable parts,).

5. Conclusion

A cam forms a significant part of three-element mechanisms. Its profile, dimensions of driving and driven elements define a lifting relation taking into consideration individual deformation ratios and a rigidity of an element for requested operation. During its movement the cam is exposed to effects of significant forces at a contact performing a direct influence on its surface that may result in damaging of contact areas. Such damage becomes evident in form of pitting that develops from small cracks on a surface of a working surface. Therefore a correct choice of material of particular elements in a design of a cam mechanism, especially a cam, is the first presumption for a reliable operation of the mechanism.

Reference

[1] Barborak O., Bartosova L., Barborakova S., *Základy technickej mechaniky*. - 1.vyd. - Trenčín : GC TECH, 2013. - 151 s., CD ROM. - ISBN 978-80-971446-0-9.

[2] Hires O., Liptak P., *Metallurgy and features of NiCrMo steel*. - 1. vyd. - Rzeszów : RSdruk, 2013. - 124 s. - ISBN 978-83-63666-97-2.

[3] Koloc Z., Václavík M.: *Vačkové mechanizmy*. SNTL/LAFA, Praha, 1988, 04-226-88, 384 s.

This publication was created in the frame of the project "Alexander Dubček University of Trenčín wants to offer high-quality and modern education", ITMS code 26110230099, based on the Operational Programme Education and funded from the European Social Fund. The authors have agreed on portion 0,7/0,2/0,1.

Active Driving Content in RFLP Structured Product Model

László Horváth[a*] and Imre J. Rudas[b]

Óbuda University, H-1034, Budapest, Bécsi u. 96/b, Hungary

[a]horvath.laszlo@nik.uni-obuda.hu, [b]rudas@uni-obuda.hu

Keywords: product lifecycle management, multidisciplinary product model, RFLP structure, IBCA structure, knowledge driven product definition

Abstract. Engineering application of advanced computer methods has been developed into product lifecycle management (PLM) which relies upon single but very complex and comprehensive model of product. Recently, generic product models are in the possession of self adaptive capability for the generation their instances considering well defined situations and events. The Laboratory of Intelligent Engineering Systems (LIES) at the Óbuda University, Budapest, Hungary joined to efforts in research for new product modeling methods in this area. One of recent LIES researches targets new methods for requirements engineering (RE) based and relevant company intelligent property (IP) driven generation of elements in requirements, functional, logical, and physical (RFLP) structure based product models. This seems suitable contribution to solutions for unified conceptual modeling of multidisciplinary products. In this paper, discussion of essential problem with modeling increasingly multidisciplinary industrial products in engineering is followed by discussion of recent issues of RFLP structured product model in PLM system. In this context, contributions in this paper are new concept of multilevel abstraction for mechanical and materials engineering centered PLM model, control of RFLP structure element generation by the new multilevel initiative, behavior, context, and action (IBCA) structure, and the integration of IBCA structure in PLM model.

Introduction

Development of engineering systems in computer systems greatly contributed to well-engineered products during the past two decades. This was greatly stimulated by new demands which enforced better and better engineered products, accurate prototyping, and constantly decreasing innovation cycles. It would be impossible to fulfill these demands without powerful engineering modeling systems. The history of model based engineering, simulation, and manufacturing started with the application of mathematical shape definitions, numerical methods in shape related load analysis, and computer controlled production equipment. One of the essential objectives was integration of theory and practice in a model environment which increasingly relies upon high level information and computer technology. The result was the product lifecycle management (PLM) paradigm which conceptualizes information technology support of all engineering activities using single, highly integrated and complex model of product. This generic model serves lifecycle engineering of product families at industrial companies. As a previous milestone, concept and methodology of product modeling were grounded in a giant project for Integrated Product Information Model (IPIM) during the eighties and nineties. This was the basis of the ISO 10303 standard by the International Standards Organization.

While PLM models were developed on the classical way of knowledge based feature driven methodology during the last decade of past century and first decade of this century, mechanical product structures were integrated with, electric, control electronic, hardware, and software units. The separated or only slightly integrated mechanical engineering modeling increasingly demanded multidisciplinary integration. However, unified multidisciplinary model can be realized only on the level of product concept. As a solution, systems engineering (SE) methodology was introduced in leading PLM modeling systems in the form of requirements, functional, logical, and physical (RFLP) structure. At the same time, knowledge in company environment and active knowledge in product model has become much more organized in the form of intelligent property (IP) of company.

The main contribution in this paper is about one of the latest results in multidisciplinary product modeling at the Laboratory of Intelligent Engineering Systems (LIES). The LIES is active in the organization of the Óbuda University, Budapest, Hungary. On the basis of former results in product model integration [1], feature driven product definition [2], and including content behind model information in product model [3], research at LIES turned to the new problem which was caused by the complexity of RFLP structure elements definition in engineer dialogues. In order to integrate requirement originated active driving knowledge content in product model, the new initiative, behavior, context, and action (IBCA) structure was conceptualized and developed. In this paper, PLM methodology related contribution concentrates on new concept of multilevel abstraction in PLM model, driving RFLP structure element generation by the multilevel IBCA structure, and integration of the IBCA structure in PLM model. The main objective is bridging the current gap between human intent and PLM model entity generation in PLM model definition process. This modeling needs new theoretical and methodological content which is suitable for industrial engineering practice.

Essential Problem at Multidisciplinary Product Engineering Modeling

Development, production, marketing, and application of multidisciplinary products need coordination vast amounts of model information and representations for lifecycle. Although contextual connections between model representations of two different discipline related parts or units is possible on the physical level of modeling, integrated definition must be raised to conceptual level of product design. The classical feature driven PLM model (Fig. 1) is restricted for the physical level where physical product objects are represented and connected. Main groups of product features and their information connections are shown in Fig. 1. Feature modifies earlier defined contextually connected features. The well proven feature principle was originally implemented as the Form Feature Information Model (FFIM) in the ISO 10303 standard. By now, leading PLM modeling systems extended the feature principle to all modeled product objects. Features are placed in object model where suitable object classes and taxonomy are defined.

In the classical product model, product features represent parts and their functionally originated elements. Analysis features represent analysis information for product features. Knowledge features are active at product feature definition for lifecycle. Despite of their key role in contextual chains, less attention is paid for material features in classical product modeling. In Fig 1, connections of material features with product, analysis, and knowledge features are emphasized.

Knowledge features actively modify contextually defined product features when well defined situations and events change [4]. Manufacturing features constitute model of manufacturing activities and process in contextual connection with analysis and knowledge features. This concept by the authors of this paper refuses direct connection between product and manufacturing features and enforces their knowledge based connection. This is considered as important theoretical issue in the future development of classical product modeling and will be topic of future research at the LIES. Using decision results at this level, equipment control features receive information from knowledge and product features. Manufacturing system features are controlled by manufacturing and equipment control features. They are also in connection with resource model features. However, resource model is not issue in this paper and is omitted from Fig. 1.

Conceptual level of product engineering needs abstraction on three levels. These levels are requirements against product, functions of products which are appropriate for the requirements, and system of overall logical connections within the whole multidisciplinary product model. For this purpose, recent leading PMM modeling systems introduced a new four leveled structure of product model using the RFLP structure. This is big change because RFLP structure offers possibility of handling product and its model as systems. RFLP methodology is applied from systems engineering (SE).

Research at the LIES revealed that definition of elements on levels of RFLP structure is a new challenge for engineers who use dedicated dialogue surfaces for this purpose in PLM modeling systems. The initiative, behavior, context, and action (IBCA) structure [5] was intended to fill the above gap between the engineer who defines requests and associated knowledge for product definition and the procedures which generate RFLP elements. This work at LIES is very difficult because comprehensive PLM modeling environment is required which is purposed and configured for research on global level of product definition. As it is shown in Fig. 1, global level modeling in IBCA structure is product requirements initiated. The IBCA structure represents active knowledge content and has driving actions on RFLP structure elements. Its utmost purpose is providing engineers with communication surface for the communication of naturally available information with the IBCA structure in order to generate theory and practice conform RFLP structure elements. Dashed lines in Fig. 1 represent contextual connections which are not essential but possible and available. Because IBCA structure is devoted as fully integrated unit in PLM model, it must have connections both to classical feature driven and RFLP structure based model entities. Driving active knowledge relies upon company expertise and experience in a contextual generic product model.

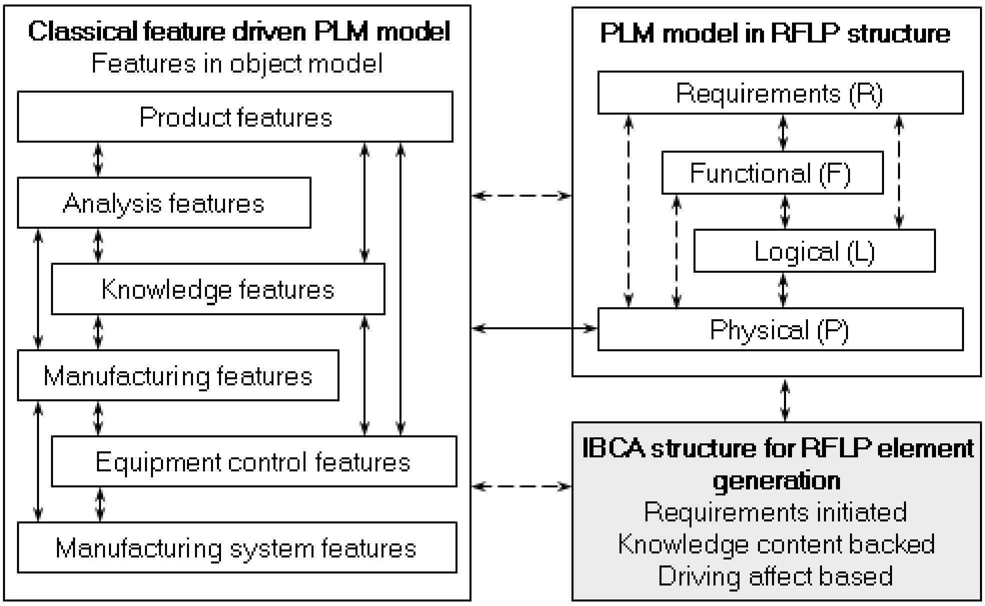

Fig. 1 Place and role of the IBCA structure in PLM model

Including Systems Engineering in the Form of RFLP Structure

As it was emphasized above, conceptual product definition requires high level abstraction and handling product and its model as systems. For this purpose, RFLP structure was introduced in leading PLM technology during recent years [6]. Researchers at the LIES recognized importance of abstraction on higher level than representation of physical product objects in the course of their earlier works. Results were published in [3]. After RFLP structure based product definition was made available in PLM systems, reconsidered and redeveloped version of the abstraction in [3] was analyzed in order to establish content basis for the generation of elements on R, F, and L levels.

Known RFLP implementations [6] had structure which was considered suitable for the IBCA structure. It is important that each level of RFLP structure is also structure in itself. Moreover, additional substructures can be defined as necessary. In order to achieve application related product model user defined elements can be related on levels of the RFLP structure. Ports are opened on element for the purpose of content supply, control, and establishing connections with other elements. Fig. 2 shows ports for content (P_{co}), communication (P_{cm}), and element control (P_{cn}) in case of elements on requirements (R_e), functional (F_e), logical (L_e), and physical (P_e) levels.

The above mentioned redeveloped abstraction levels and their content related connections with elements on levels of the RFLP structure is summarized in Fig. 2. Content for abstraction is placed on five levels. This content is intended to drive RFLP structure element generation. On the first level of abstraction, intent of authorized humans is recorded as required product functions and objects, contextual connections, and demanded or proposed methods for the generation of relevant product objects. This level provides content for R and F level elements. On the second level of abstraction, concepts are included for the interpretation of meaning of new human intent. This is a means of introduction new theoretical contributions for the RFLP structure. On the third level of abstraction, engineering objectives are represented as demanded or proposed behaviors. Behaviors are important because F and L levels in [6] can accommodate various behavior definitions in order to make product model virtually executable. Because recent product models are fully contextual, importance of contextual connections on the fourth level of abstraction for the first three levels of abstraction is inevitable. Context content is communicated with elements on the L level of the RFLP structure. Finally, fifth level of abstraction includes decisions on physical level objects in change affect zones (CAZ) of product model. Concept and methodology of CAZ was published in [7].

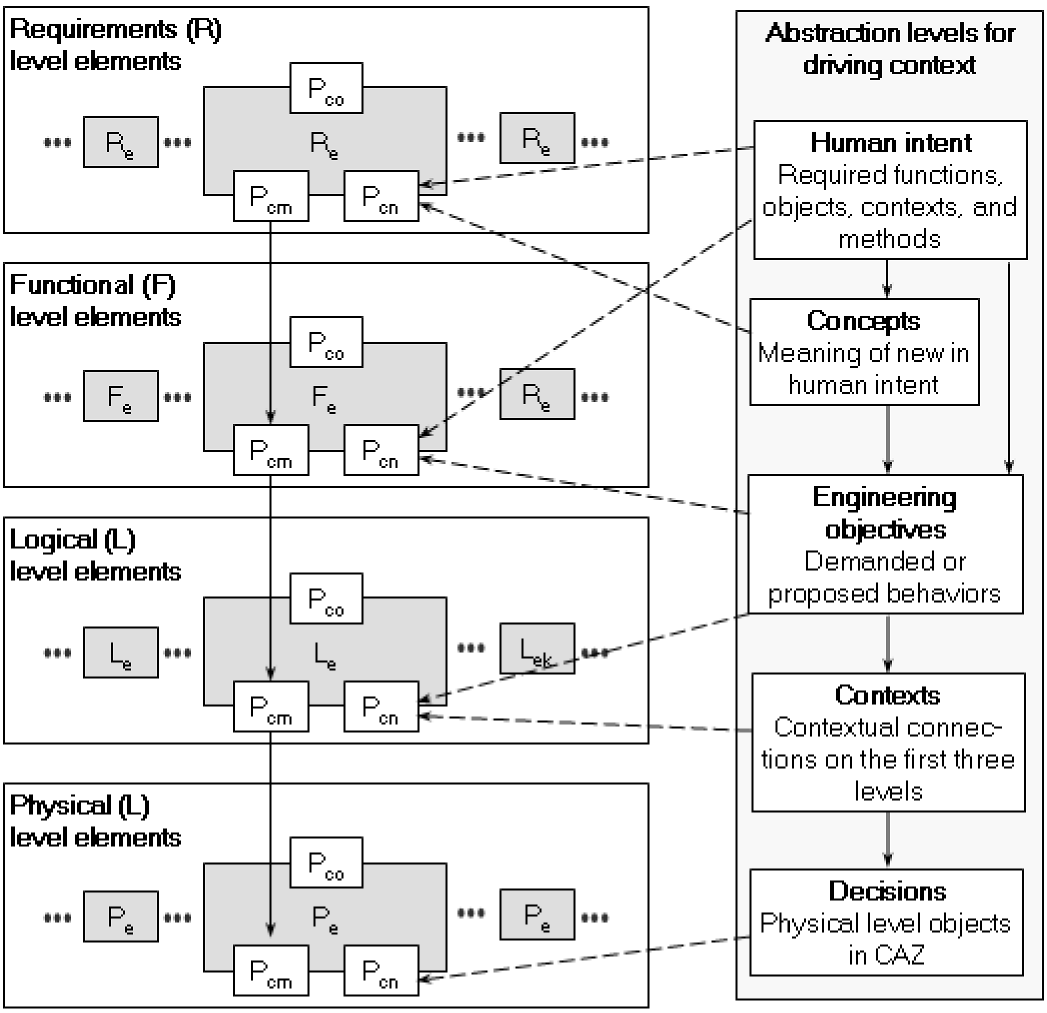

Fig. 2 RFLP structure connections of the proposed abstraction

New Concept for Multilevel Abstraction Based Content in PLM Model

The next question is how the above introduced multilevel model of abstraction content controls generation of RFLP structure elements. First of all, it must be decided how can be modeled this content. As in case of latest classical product models, this control must be adaptive through

ISBN: 978-1-61804-295-8

contextual chains of object parameters and must be maintained for the entire lifecycle of product. The content for driving abstractions is proposed to represent in contextual substructures on the levels of IBCA structure. While definition and connection of IBCA elements are free for authorized engineers, the substructures and their connections are proposed as there are shown in Fig. 3. On the Initiatives (I) level, engineers define elements for initiative definition (DI), specification (SI), product function (FI), product definition method (MI), product configuration (CI), and process of product definition (PI). After initial definition, this level follows changes of accepted and rejected personal originated definitions. In this way, relevant model content is collected in these substructures during the entire lifecycle of product. In this context, product lifecycle starts from the first concept and ends with successful recycling.

On the behaviors (B) level of IBCA structure, definite demands for product are represented in behavior definitions (DB), situations (SB) are configured to define behaviors by a set of object parameter values, and relevant simulations (MB) are defined for behavior analysis. On the contexts (C) level of IBCA structure three categories of contextual definitions are structured for the product model. They are for product definition activity (AC), adaptive drive of model entity generation (DC), and product feature connection (FC). Finally, actions (A) level of IBCA structure serves physical level object definition. Actions are included for product definition activity (AA), adaptive drive of features (DA), and direct product feature actions (FA).

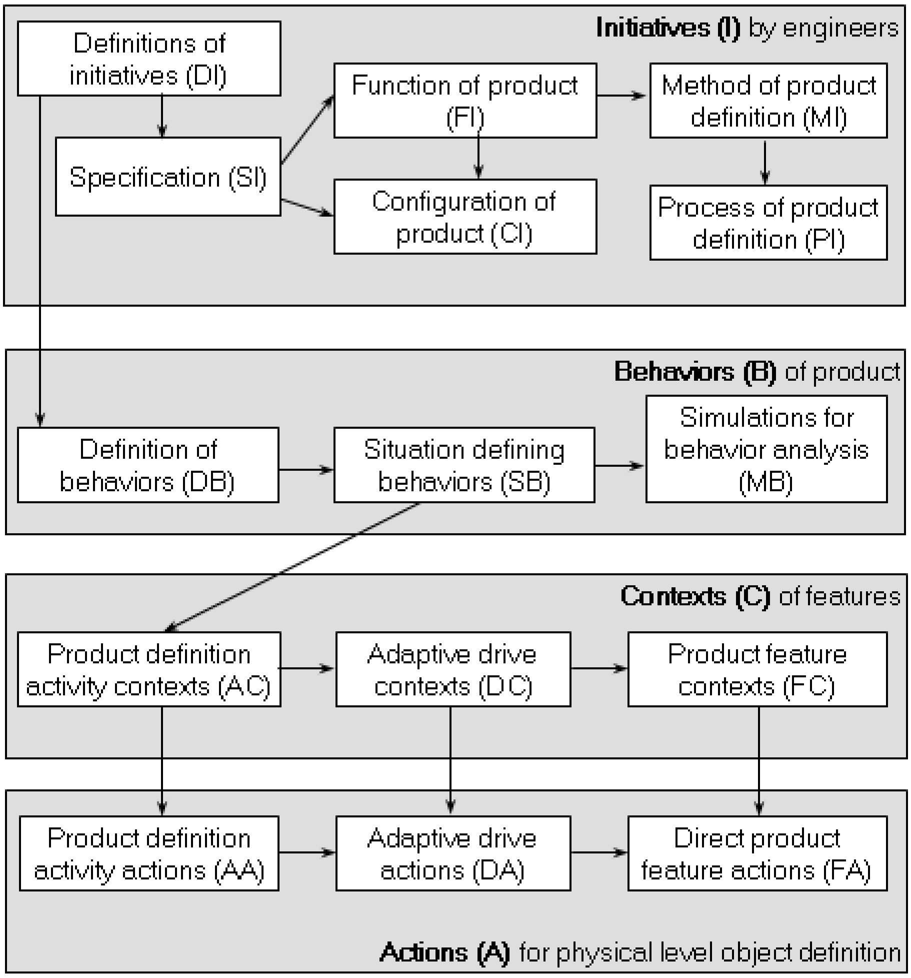

Fig. 3 Contextual substructures of content for driving abstractions on IBCA structure levels

Control of RFLP structure element generation by IBCA structure

As it was stated above, IBCA structure controls element generation for RFLP structured PLM model. Initial basics of IBCA concept were published in [8]. Some advanced structures complete RFLP structure by simulation structures and product definition processes. The latter one serves

ISBN: 978-1-61804-295-8

advanced automation of product entity generation by built in content. At the same time, IBCA structure support is also demanded for classical feature structures where RFLP structure is not available or is not applied at a given PLM modeling. Fig 4 shows driving connections from substructures on IBCA structure levels. Some substructures have not direct driving affect on RFLP structure elements; they act indirectly through elements in other substructures.

On the initiative (I) level of IBCA structure, driving content of DI, FI, CI, and PI substructure elements drive R, F, L, and product definition process elements, respectively (Fig. 4). At the same time, CI substructure elements also can drive features in classical structures. SB behavior (B) substructure provides behavior content for F and L level elements. MB substructure can provide content for simulation structures available in leading industrial PLM technology [6]. Content in context (C) substructures drives L level elements in RFLP structure. Action (A) level substructures drive P level elements. At the same time, FA substructure is capable of providing direct actions on product features as it was discussed above.

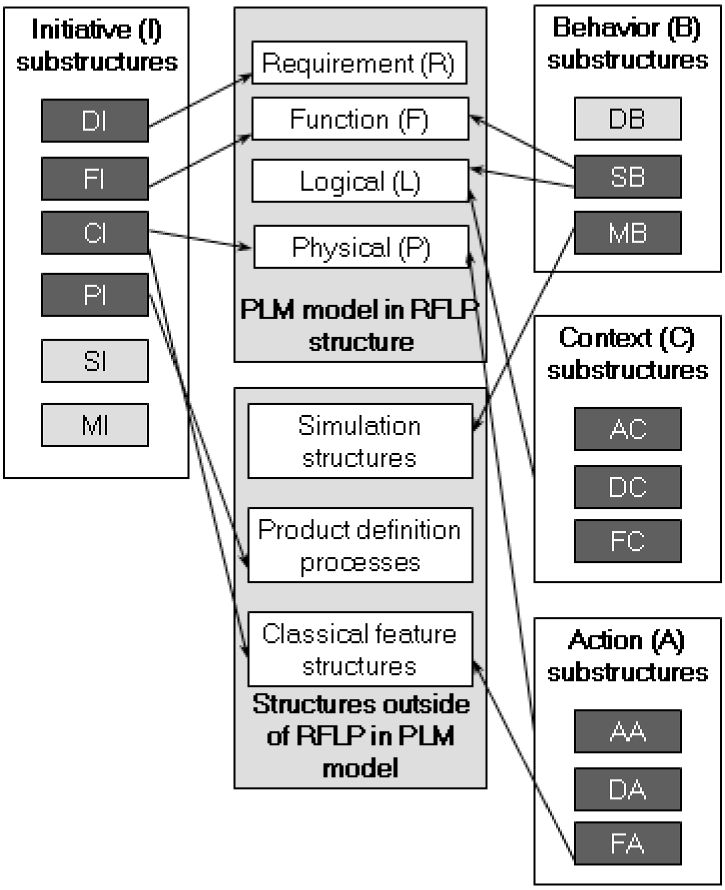

Fig. 4 IBCA structure controlled RFLP structured PLM model

IBCA structure in PLM Model

RFLP based PLM model have a structure which is organized accordingly. The question is how IBCA structure can be integrated in this structure. PLM modeling systems are open for definition of new object classes, parameters, and relationships in contextual connection with existing PLM model entities. In this way, modeling capabilities of PLM system can be extended to IBCA structure. Driving contexts between a pair of elements from the F and I structures in Fig. 5 illustrate active connection between RFLP and IBCA structures. Any change in an IBCA element is propagated in the product model to contextual IBCA and RFLP elements along contextual chains of elements.

During the work for concept and integration of IBCA structure relevant results in related research issues were considered mainly from the area of feature driven modeling, knowledge engineering, soft computing, requirements engineering (RE), and systems engineering (SE). Several of them are

ISBN: 978-1-61804-295-8

cited below. In the future, analysis of application product modeling in system of systems (SoS) engineering environment also must be considered [15].

Paper [9] discusses importance of specific knowledge management tools and proper decisional model for knowledge based definition of product model in order to ensure high design performance. Process of human-computer interaction (HCI) is evaluated in the context of requirements engineering in [10]. HCI functional allocation heuristics is considered in order to control system requirements for decision making. Knowledge based support of design is analyzed in Chapter [14] to achieve organizing design activities, capturing relevant knowledge and embedding this knowledge in engineering model. Authors refer to Dassault Systems V6 system.

One of the actual problems in PLM modeling is application of the highly theoretical intelligent computing in the industrial practice of PLM modeling. Paper [11] discusses how fuzzy logic, genetic algorithms, and neural networks can support engineering activities. On the physical level of PLM model, definition of features and their connections has key importance especially in case of knowledge feature based form and other features.

Paper [12] discusses modification of complex product model through its contextual connections. Large models including units with different types may cause inconsistency. Manual handling of this problem often fails in these systems. Paper [13] shows the way towards automatic inconsistency handling which can generate repair plans using configurable search space and combinatorial type of problem solving.

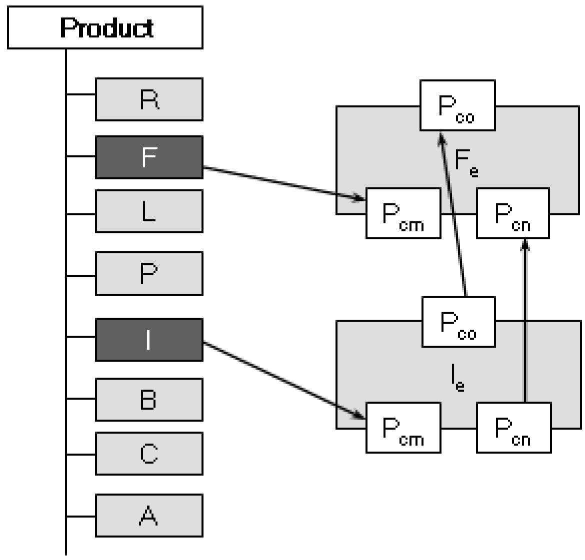

Fig. 5 Connections RFLP and IBCA levels

Because RFLP structure represents new leading virtual engineering technology, it is not available in numerous conventional PLM modeling environments. Moreover, it is subject of project specific decision that RFLP or classical feature structure is developed. Sometime classical solution is enough for an actual engineering task. For this purpose, direct drive of classical product feature structures using direct product feature actions (FA) substructure elements is explained by the example on Fig. 6. In this example FA elements act through four contextual connections for driving PF1, PF2, and PF3 product features in a subset, formula F1, rule R1, and reaction Re1. Parameter P1 is defined in the context of form feature PF1 while PF2 is defined in its context. Rule R1 is also defined in the context of F1 and PF3 is defined in its context. Reaction Re1 is also defined in the context of FF3. In the industrial classical PLM modeling, rule connects a set of feature parameters and activities while reaction recognizes communicated or sensed event.

Although the simple knowledge entities on Fig. 6 are understandable for mechanical and materials engineers, this method makes definition of complex knowledge based adaptive structure along much more complex contextual chains possible. In case of RFLP structure based model, authorized engineer defines these knowledge features and their contextual connections on physical level or raise them to higher abstraction levels. This is a task dependent important decision.

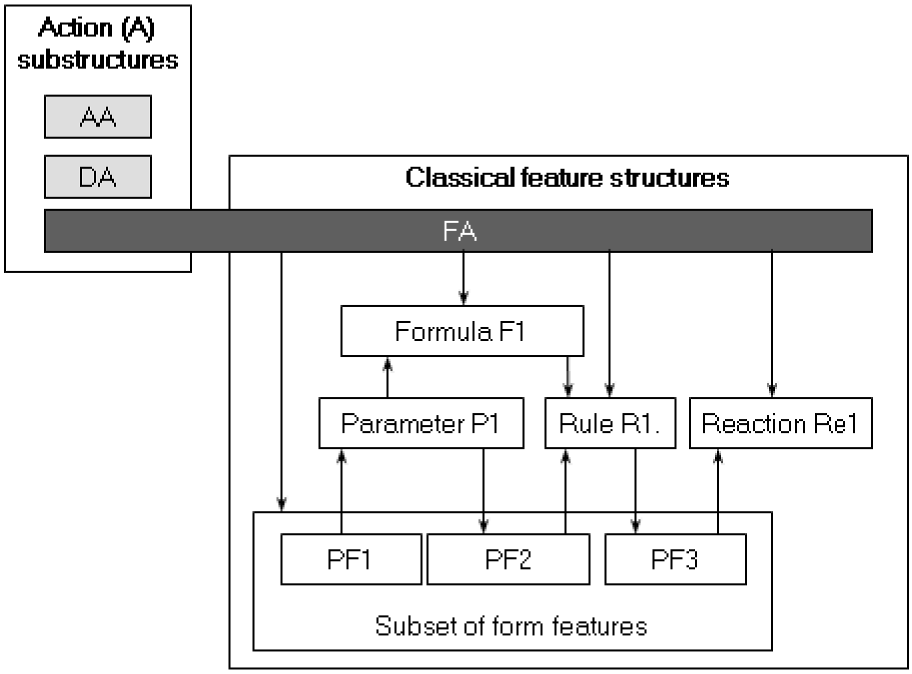

Fig. 6 Direct control of classical feature structures

Implementation and future research

Important preliminary of the research in this paper provided systemic analysis of classical PLM modeling methodology [9]. LIES and former laboratories installed the Dassault Systemes V6 PLM system and its former V4 and V5 versions as leading representative PLM modeling environment. Currently, installation of research configuration of this system is under preparation for IBCA experiments at LIES. Integration of IBCA structure is planned in close connection with RFLP structure. The main objective is application of advanced element and feature definition, and PLM model structure configuration capabilities of PLM system for IBCA model development at application environment. The remained modeling will be considered as development through application programming interface (API).

Future research will start with experimental driving chains between representative IBCA and RFLP structures. A good example for this research is RFLP structured model of robot system using content in IBCA structure. Content communication needs analysis of requirement representation capabilities of IBCA structure and comparison of user surface characteristic in IBCA and RFLP structures.

Summary

Conventional mechanical and materials engineering concepts, methods and processes should be revised in order to prepare the change for PLM modeling of multidisciplinary products. Fortunately, advanced PLM systems rely upon modeling methodology in which modeling and simulation of mechanical structures together with associated materials engineering related modeling are in the centre. Higher level abstraction in RFLP structured product model offers solution for multidisciplinary modeling on the level of conceptual product design. However, conventional dialogue based definition of RFLP structure elements is made almost impossible when complex content including complex knowledge must be handled. The IBCA structure concept of representation active driving content for RFLP structure elements may be one of the possible solutions. Its structure conforms to both RFLP structured and conventional feature driven PLM modeling. Moreover, it can serve as a new connection between these model structures.

References

[1] L. Horváth, I. J. Rudas, Virtual technology based associative integration of modeling of mechanical parts. Journal of Advanced Computational Intelligence and Intelligent Informatics, 5(5) (2001) pp. 269-278.

[2] L. Horváth, I. J. Rudas, S. G. Tzafestas, Relating Shape and Robot Process Model Features. International Journal of Mechanics and Control, 4(2) (2003) 27-31.

[3] L. Horváth: A New Method for Enhanced Information Content in Product Model. WSEAS Transactions on Information Science and Applications, 5(3) (2008) 277-285.

[4] A. Brière-Côté, L. Rivest, A. Desrochers, Adaptive generic product structure modelling for design reuse in engineer-to-order products, Computers in Industry, 61(1) (2010) 53–65.

[5] L. Horváth, I. J. Rudas, Active Knowledge for the Situation-driven Control of Product Definition, Acta Polytechnica Hungarica, 10(2) (2013) 217-234.

[6] S. Kleiner, C. Kramer, Model Based Design with Systems Engineering Based on RFLP Using V6., in: M. Abramovici, R. Stark (eds.) Smart Product Engineering, Springer, Berlin, Heidelberg, 2013, pp 93-102.

[7] L. Horváth, I. J. Rudas, J. Bitó, G. Hancke, Intelligent Computing for the Management of Changes in Industrial Engineering Modeling Processes, Computing and Informatics, 24 (2005) 549-562.

[8] L Horváth, I. J. Rudas, New Method for Generation of RFLP Structure Elements in PLM Model, in: New Trends in Software Methodologies, Tools and Techniques, IOS Press, Delft, Netherlands, 2014. pp. 310-324.

[9] Y. Bodeinab, B. Rosec, E. Caillaudd, "Decisional Model for KBE Implementation in a Commercial CAD Software, Computer-Aided Design and Applications, 9(2) (2012) 121-131.

[10] A. Sutcliffe, S. Thew, P. Jarvis, Experience with user-centered requirements engineering, Requirements Engineering, 16(4) (2011) 267-280.

[11] K. M. Saridakis, A. J. Dentsoras, Soft computing in engineering design. A review, Advanced Engineering Informatics, 22(2) (2008) 202–221.

[12] J. Lee and D. Muthig, Feature-Oriented Analysis and Specification of Dynamic Product Reconfiguration, in: M. Hong (Ed.), High Confidence Software Reuse in Large Systems, Springer Berlin, Heidelberg, 2008, pp. 154-165.

[13] M. A. Almeida da Silva, A. Mougenot, X. Blanc, R. Bendraou, Towards Automated Inconsistency Handling in Design Models, in: C. Salinesi, M. C. Norrie, O. Pastor (Eds.) Advanced Information Systems Engineering, Lecture Notes in Computer Science, Springer Berlin, Heidelberg, Vol. 6051, pp 348-362 (2010).

[14] M. Hirz, W. Dietrich, A. Gfrerrer, J. Lang, Knowledge-Based Design, in: Integrated Computer-Aided Design in Automotive Development, Springer, Berlin, Heidelberg, 2013, pp 309-330.

[15] L. Horváth, I. J. Rudas, Towards interacting systems in product lifecycle management, In: proc of the 8th International Conference on System of Systems Engineering (SoSE), Maui, Hawaii, USA, 2013, pp. 267-272.

Mathematical modeling of forest canopy ignition due to ruptured pipeline

Valeriy A. Perminov

Abstract— Accidents occurring at the sites of pipelines, accompanied by environmental damage, economic loss, and sometimes loss of life. Thermal radiation can result in serious additional damage by igniting combustible materials, e.g., finely, divided or thin fuels such as dried leaves and wood. Thus, fires may be started in buildings and forests and may spread rapidly to considerable distances. These catastrophes, as a rule, are known to accompany by the initiation of forest fires. Mathematical model of forest fire was based on an analysis of experimental data and using concept and methods from reactive media mechanics. The paper suggested in the context of the general mathematical model of forest fires give a new mathematical setting and method of numerical solution of a problem of a forest fires initiation. The boundary-value problem is solved numerically using the method of splitting according to physical processes In this paper attention is given to questions of description of the initial stage in the development of a mass forest fires initiated by high radiative energy sources such as fireballs.

Keywords— forest fire, mathematical model, discrete analogue, ignition, radiation, pipeline accident, fireball.

I. Introduction

As a rule, a large man-made catastrophes in the trunk pipelines accompanied by the appearance of fireballs, which under the influence of possible ignition nearby vegetation. In this connection it is interesting to predict the occurrence and development of fires that occurred in the vicinity of the place of an emergency. Since the full-scale studies in solving these problems is not possible, are actual methods of mathematical modeling. In the mathematical model used, the integral parameters (the maximum size of the fireball lifetime and lifting height of the burning clouds, the radiation power per unit area) as a function of the mass of fuel involved, derived from empirical relationships by treating the experimental results and the rapid analysis of accidents [1]. Mathematical models obtained from studies can be used to predict the effects and preventive measures.

II. Physical and Mathematical model

Let consider that the source of radiant energy is upward to the height H of the Earth's surface (see Fig. 1). Since its dimensions are small compared to the radius of the Earth, we assume that a point source of radiation, D - the distance from the source to the center point of the surface of the forest, h - the height of forest, r_* is the radius of the ignition zone. On the upper boundary z = h forest acts intense radiant flux $q_R(r, t)$, which is attenuated with increasing distance from the epicenter 0. Maximum intensity of the source is reached at t = to, further, it decays to zero according to $q_R(r, t)$, which can be approximated as follows: [2]

$$q_R(r,t) = \frac{t_p P_m \sin L}{4\pi D^2} \begin{cases} t/t_m, & ,t < t_m \\ \exp(-k_0(t/t_m - 1)), & t \geq t_m \end{cases}, \quad (1)$$

$$t_0 = 0.032 w_0^{0.5}, P_m = 4 w_0^{0.5} kT/c.$$

Here t_m- at maximum heat radiation source, s;

D - distance from the radiation source to the forest canopy, m;

t_p - the transmittance of the atmosphere;

P_m- maximum value of a light pulse at time t_m, kT/s;

L - the angle between the vector of the radiation flux density and an upper limit of vegetation;

w_0 - power source, kT;

k_0 - approximation coefficient (k_0 = 0.75).

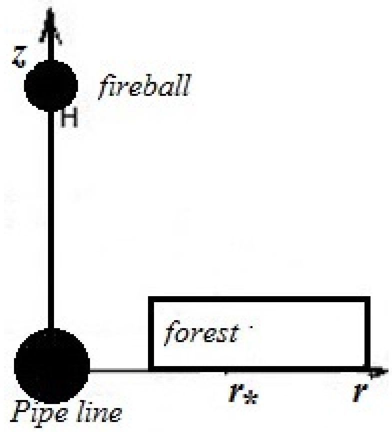

Fig. 1.
The scheme of burning domain.

Receipt of radiant energy in the vegetation cover ($z_o \leq z \leq h$) causes heating of forest fuel, evaporation and subsequent thermal decomposition of the solid material with the release of the volatile pyrolysis products, which then ignite. Due to the presence of gravity, the heated air volumes begin to emerge up, so processes surround the ignition of forest vegetation are, in general, related to the hydrodynamics of the flow. Due to the fact that at the periphery of the epicenter intensity of the radiant flux in the forest canopy is small, there is no ignition. Thus, during the action of the radiation source is formed by this initial ignition forest radius r_*. Ideally, it has a circular shape in plan. Its subsequent development is determined by the interaction of ascending currents of the wind field as they make the surface layer of the atmosphere and carried a spread in the surrounding area of burning solid elements, as well as meteorological and geographical conditions in a given area. [3]. For the purposes of this study, it is assumed that the wind velocity in the atmosphere is relatively low and the energy is mainly transferred by radiation. This allows us to consider the problem in the axisymmetric formulation. Since the combination of different physical factors accompanies the ignition process of the forest, it is advisable to carry out the description at different levels of complexity. The hierarchy of physical models, including more complex to evaluate the role of individual factors that are omitted to simplify the description of the phenomenon [3].

The paper will be given basic physical assumptions and representations of the object of research needed to understand the mathematical model. It is believed that: for symmetric about the vertical axis z, having started in the center of the area under consideration (Figure 1) and directed vertically upward, the flow is developed turbulent and molecular transport is neglected in comparison with the turbulent, gas phase density does not depend on pressure because the flow velocity is small in comparison with the speed of sound, the forest canopy is considered to be non-deformable medium. We assume that the forest canopy can be modeled by a uniform two-temperature multiphase porous reactive medium. Provided the temperature of condensed (solid) T_s and T gas phase. The first is the dry organic matter, moisture, condensed pyrolysis products and mineral part of forest fuels. In the gas phase will be distinguished only necessary to describe the combustion reaction components, i.e. the mass concentrations c_α (α = 1 - oxygen, 2 - combustible pyrolysis products are wood fuels, 3 - other inert ingredients, including water vapor). The solid phase, which combustible material (thin needles and twigs of up to 6 mm), water in liquid state and drip-condensed pyrolysis products has its own velocity and the volume fraction, when compared with the gas phase can be neglected in the appropriate equations as per unit volume of wood is <0.5 kg. From the standpoint of hydrodynamics, this porous medium, nevertheless, offers resistance to any force $\vec{F} = \rho s c_d |\vec{v}| \vec{v}$ displacement of air masses. It is believed that the medium is locally thermodynamic equilibrium. Turbulent convective transport due to the action of gravity, is described with the Reynolds equation [3]. We will also take into account the physical and chemical processes occurring in the forest canopy, the rate of chemical reactions which R_i (i = 1, 2, 3, 5) as a function of temperature and other parameters assumed to be known. Determining the mechanism of energy transfer in this case is the radiation. In the forest canopy absorbs, reflects and emits mainly solid phase. To describe transport in such a specific Continuum will use the diffusion approximation. This is justified, since the mean free path of the radiation in the canopy $l_R << l_o$, $l_0 \sim$ 10-15 м, $l_R \sim$ 1 m (*lo* - the characteristic scale height) [3]. The z-axis is directed vertically upwards and r - axis along the earth's surface (see Fig. 1). To describe the heat and mass transfer in the amount of forest vegetation with the general conservation laws are used for the multiphase medium. Since any movement of air currents in the atmosphere is turbulent, then to describe them using the Reynolds equation. The problem formulated in a cylindrical coordinate system is reduced to solving the following equations [3]:

$$\frac{\partial \rho}{\partial t} + \frac{1}{r}\frac{\partial}{\partial r}(r \ \rho v) + \frac{\partial}{\partial z}(\rho w) = \dot{m}; \qquad (2)$$

$$\frac{\partial}{\partial t}(\rho v)+\frac{1}{r}\frac{\partial}{\partial r}(r\rho v^2)+\frac{\partial}{\partial z}(\rho v w)=-\frac{\partial p}{\partial r}+\frac{1}{r}\frac{\partial}{\partial r}(-r\rho\overline{v'^2})+ \quad (3)$$
$$+\frac{\partial}{\partial z}(-\rho\overline{v'w'})-\rho s c_d v\sqrt{v^2+w^2};$$

$$\frac{\partial}{\partial t}(\rho w)+\frac{1}{r}\frac{\partial}{\partial r}(r\ \rho v w)+\frac{\partial}{\partial z}(\rho w^2)=-\frac{\partial p}{\partial z}+ \quad (4)$$
$$+\frac{1}{r}\frac{\partial}{\partial r}(-r\ \rho\overline{v'w'})+\frac{\partial}{\partial z}(-\rho\overline{w'^2})-\rho s c_d w\sqrt{v^2+w^2}-\rho g;$$

$$\frac{\partial}{\partial t}(\rho c_p T)+\frac{1}{r}\frac{\partial}{\partial r}(r\ \rho v c_p T)+\frac{\partial}{\partial z}(\rho w c_p T)=$$
$$=\frac{1}{r}\frac{\partial}{\partial r}(-r\rho c_p\overline{v'T'})+\frac{\partial}{\partial z}(-\rho c_p\overline{w'T'})+k_g(cU_R-4\sigma T^4)+ \quad (5)$$
$$+q_5R_5+\alpha_v(T_s-T);$$

$$\frac{\partial}{\partial t}(\rho c_\alpha)+\frac{1}{r}\frac{\partial}{\partial r}(r\ \rho v c_\alpha)+\frac{\partial}{\partial z}(\rho w c_\alpha)= \quad (6)$$
$$=\frac{1}{r}\frac{\partial}{\partial r}(-r\rho\overline{v'c'_\alpha})+\frac{\partial}{\partial z}(-\rho\overline{w'c'_\alpha})-R_{5\alpha},\alpha=1,2;$$

$$\frac{\partial}{\partial z}\left(\frac{c}{3k}\frac{\partial U_R}{\partial z}\right)-kcU_R+4k_g\sigma T^4+4k_S\sigma T_s^4=0; \quad (7)$$

$$\sum_{i=1}^{4}\rho_i c_{pi}\varphi_i\frac{\partial T_s}{\partial t}=q_3R_3-q_2R_2+k_S(cU_R-4\sigma T_s^4)+ \quad (8)$$
$$+\alpha_V(T-T_s);$$

$$\rho_1\frac{\partial\varphi_1}{\partial t}=-R_1,\rho_2\frac{\partial\varphi_2}{\partial t}=-R_2,\rho_3\frac{\partial\varphi_3}{\partial t}=\alpha_c R_1-\frac{M_c}{M_1}R_3, \quad (9)$$
$$\rho_4\frac{\partial\varphi_4}{\partial t}=0;$$

$$\sum_{\alpha=1}^{3}c_\alpha=1,\ p_e=\rho RT\sum_{\alpha=1}^{3}\frac{c_\alpha}{M_\alpha},$$

$$\dot{m}=(1-\alpha_c)R_1+R_2+\frac{M_c}{M_1}R_3,R_{51}=-R_3-\frac{M_1}{2M_2}R_5, \quad (10)$$
$$R_{52}=\nu(1-\alpha_c)R_1-R_5;$$

$$R_1=k_1\rho_1\varphi_1\exp\left(-\frac{E_1}{RT_S}\right),\ R_2=k_2\rho_2\varphi_2T_S^{-0.5}\exp\left(-\frac{E_2}{RT_S}\right),$$
$$R_3=k_3\rho\varphi_3 s_\sigma c_1\exp\left(-\frac{E_3}{RT_S}\right),$$
$$R_5=M_2k_5\left(\frac{c_1M}{M_1}\right)^{0.25}\left(\frac{c_2M}{M_2}\right)T^{-2.25}\exp\left(-\frac{E_5}{RT}\right).$$

The system of equations (1)–(10) must be solved taking into account the initial and boundary conditions:

$$t=0: v=0, w=0, T=T_e, c_\alpha=c_{\alpha e}, T_s=T_e, \varphi_i=\varphi_{ie}; \quad (11)$$

$$r=0: v=0, \frac{\partial w}{\partial r}=0, \frac{\partial T}{\partial r}=0, \frac{\partial c_\alpha}{\partial r}=0, \frac{\partial U_R}{\partial r}=0; \quad (12)$$

$$r=r_e: \frac{\partial v}{\partial r}=0, \frac{\partial w}{\partial r}=0, \frac{\partial c_\alpha}{\partial r}=0, \frac{\partial T}{\partial r}=0, \frac{c}{3k}\frac{\partial U_R}{\partial r}+\frac{c}{2}U_R=0; \quad (13)$$

$$z=z_0: \frac{\partial v}{\partial z}=0, \frac{\partial w}{\partial z}=0, \frac{\partial T}{\partial z}=0, \frac{\partial c_\alpha}{\partial z}=0, -\frac{c}{3k}\frac{\partial U_R}{\partial z}+\frac{c}{2}U_R=0; \quad (14)$$

$$z = h: \frac{\partial v}{\partial z} = 0, \frac{\partial w}{\partial z} = 0, \frac{\partial T}{\partial z} = 0, \frac{\partial c_\alpha}{\partial z} = 0,$$
$$\frac{c}{3k}\frac{\partial U_R}{\partial z} + \frac{c}{2}U_R = 2q_R(r,z). \quad (15)$$

here and above v, w – velocity projection on the r axes and z ; α_V is the coefficient of phase exchange; ρ - density of gas – dispersed phase, t is time; v_i - the velocity components; T, T_S, - temperatures of gas and solid phases, U_R - density of radiation energy, k - coefficient of radiation attenuation, P - pressure; c_p – constant pressure specific heat of the gas phase, c_{pi}, ρ_i, φ_i – specific heat, density and volume of fraction of condensed phase (1 – dry organic substance, 2 – moisture, 3 – condensed pyrolysis products, 4 – mineral part of forest fuel), R_i – the mass rates of chemical reactions, q_i – thermal effects of chemical reactions; k_g , k_S - radiation absorption coefficients for gas and condensed phases; T_e - the ambient temperature; c_α - mass concentrations of α - component of gas - dispersed medium, index α=1,2,3, where 1 corresponds to the density of oxygen, 2 – gas products of pyrolysis(carbon monoxide CO and etc.), 3 - to carbon dioxide and inert components of air; R – universal gas constant; M_α , M_C, and M molecular mass of α -components of the gas phase, carbon and air mixture; g is the gravity acceleration; c_d is an empirical coefficient of the resistance of the vegetation, s is the specific surface of the forest fuel in the given forest stratum. To define source terms which characterize inflow (outflow of mass) in a volume unit of the gas-dispersed phase, the following formulae were used for the rate of formulation of the gas-dispersed mixture $\dot{m}$, outflow of oxygen R_{51}, changing carbon monoxide R_{52}. Reaction rates of these various contributions (pyrolysis, evaporation, combustion of coke and volatile combustible products of pyrolysis) are approximated by Arrhenius laws whose parameters (pre-exponential constant k_i and activation energy E_i) are evaluated using data for mathematical model [3]. The initial values for volume of fractions of condensed phases are determined using the expressions:

$$\varphi_{1e} = \frac{d(1-\nu_z)}{\rho_1}, \varphi_{2e} = \frac{Wd}{\rho_2}, \varphi_{3e} = \frac{\alpha_c \varphi_{1e}\rho_1}{\rho_3}$$

where d -bulk density for surface layer, ν_z – coefficient of ashes of forest fuel, W – forest fuel moisture content. It is supposed that the optical properties of a medium are independent of radiation wavelength (the assumption that the medium is “grey”), and the so-called diffusion approximation for radiation flux density were used for a mathematical description of radiation transport during forest fires. To close the system (1)–(10), the components of the tensor of turbulent stresses, and the turbulent heat and mass fluxes are determined using the local-equilibrium model of turbulence (Grishin, [3]). The system of equations (1)–(10) contains terms associated with turbulent diffusion, thermal conduction, and convection, and needs to be closed. The components of the tensor of turbulent stresses $\rho\overline{v'w'}$, as well as the turbulent fluxes of heat and mass are written in terms of the gradients of the average flow properties. It should be noted that this system of equations describes processes of transfer within the entire region of the forest massif, which includes the space between the underlying surface and the base of the forest canopy, the forest canopy and the space above it, while the appropriate components of the data base are used to calculate the specific properties of the various forest strata and the near-ground layer of atmosphere. This approach substantially simplifies the technology of solving problems of predicting the state of the medium in the fire zone numerically. The thermodynamic, thermophysical and structural characteristics correspond to the forest fuels in the canopy of a different (for example pine [3,4]) type of forest. The system of equations (1)–(10) must be solved taking into account the initial and boundary conditions.

III. Calculation Methods and Results

The boundary-value problem Eq. (1)–(10) was solved numerically using the method of splitting according to physical processes. In the first stage, the hydrodynamic pattern of flow and distribution of scalar functions was calculated. The system of ordinary differential equations of chemical kinetics obtained as a result of splitting was then integrated. A discrete analog was obtained by means of the control volume method using the SIMPLE like algorithm [5]. Difference equations that arise in the course of sampling were resolved by the method of SIP [6]. The accuracy of the program was checked by the method of inserted analytical solutions. The time step was selected automatically. On the basis of a mathematical model described numerical calculations were carried out to determine the pattern of occurrence of ignition process of forest cover due to the formation of the fireball and the effects of thermal radiation on the underlying surface. The result obtained by numerical integration of the field of mass concentrations of the components of the gas phase, the temperature, the volume fractions of the components of the solid phase. Figures 2 - 3 illustrate the time dependence of dimensionless temperatures of gas and condensed phases (Fig.2) and concentrations of oxygen and gas products of pyrolysis (Fig.3) at the upper boundary of the forest (z=h) for different horizontal distances from epicenter of fireball (solid curves — temperature of solid phase; dash curves — temperature of gas phase). Fig. 3 (solid curves — concentration of oxygen; broken curves — concentration of combustible products of pyrolysis(CO)) illustrate the distribution of concentrations of components of the gas phase. At the moment of ignition the gas products of pyrolysis burns away, and the concentration of oxygen is rapidly reduced. The temperatures of both phases reach a maximum value at the point of ignition.

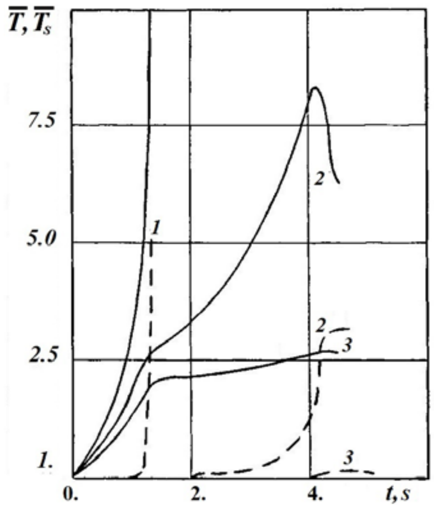

Fig.2.

1 – *r=0, 2 – r=36 m, 3 – r=50 m.*

$$\overline{T} = T / T_e,\ \overline{T_s} = T_s / T_e, T_e = 300K.$$

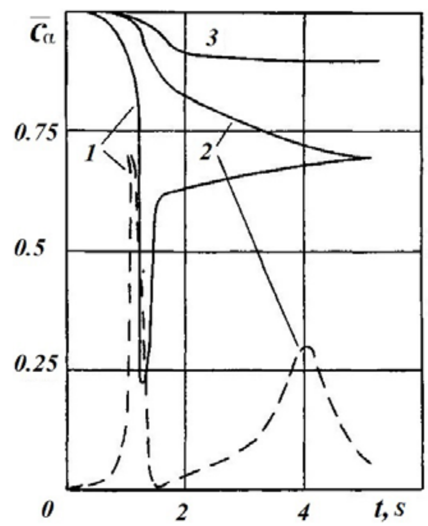

Fig.3.

$$\overline{c}_\alpha = c_\alpha / c_{1e}, c_{1e} = 0.23.$$

On the basis of these data determined the values of the radii of the ignition of forests under the influence of the thermal radiation of the fireball, which depend on the moisture content of the underlying surface and the mass of the spilled fuel. According to the results, a table depending on the size of the radii of the zones of the mass of spilled ignition of combustible material and the moisture content of forest fuels.

Table 1

The values of radii of ignition for different quantity of spilled fuel and moisture of forest combustible materials

Mass of spilled fuel, kg	The radius of the ignition of forest cover, m			
	moisture of forest combustible materials, *W*			
	0,2	0,4	0,6	0,8
10^4	15,8	11,3	0	0
$20 \cdot 10^3$	24,9	21,4	18,3	14,8
$30 \cdot 10^3$	30,9	27,4	23,9	21,9

$40 \cdot 10^3$	36,9	33,4	28,4	24,4
$60 \cdot 10^3$	44,9	41,9	36,9	35,4

The radius of the ignition of vegetation maximum at a moisture content W = 0.2 and mass spilled flammable liquid $m = 60 \cdot 10^3$ kg. With increasing moisture content of forest combustible materials the sizes of ignition (radius) are decreased. The results of mathematical modeling of such phenomena can be used to develop preventive measures, as well as the liquidation of their consequences.

IV. Conclusion

1. On the basis of the theory of general mathematical model of forest fires [1] have developed a new mathematical model of ignition of forest as a result of emergency situations. It is taken into account turbulent flow, two-temperature environment and the main physical and chemical processes (drying and pyrolysis of forest fuels, chemical reaction of combustion of gaseous and condensed pyrolysis products afterburner).
2. Based on the finite volume method it is developed a method of numerical solution of unsteady two-dimensional equations of the theory of forest fires.
3. Analysis of the results of the numerical solution of the problem of forest massif ignition revealed that the following stages of the process: the heating of the ground cover and canopy, the formation of gaseous pyrolysis products of the soil cover, their inflammation, the formation of gaseous products of pyrolysis of forest canopy and the ignition .
4. It was found that the radius of forest massif ignition decreases when moisture content of vegetation increases.
5. As a result of numerical calculations show that the ignition of forest fuel is a gas-phase nature.

References

[1] I.A.Bolodyan.,Ya.N. Shebeko, Karpov V.L. and etc. Guidance on fire risk assessment for industrial enterprises. FGU VNIIPO of EMERCOM of Russia, M. 2006.
[2] S.Glastone (Ed.). The Effects of Nuclear Weapons, U.S. Gov't. Printing Office, Washington, 1962.
[3] A.M.Grishin, Mathematical Modeling Forest Fire and New Methods Fighting Them, Publishing House of Tomsk University, Tomsk (Russia), 1997.
[4] A.M. Grishin., V.A.Perminov, An ignition of forest massifs under the influence of high altitude radiant energy, Combustion, Explosion and Shock Waves»,32(5), 1996. pp. 108-115
[5] S.V. Patankar, Numerical Heat Transfer and Fluid Flow, Hemisphere Publishing Corporation, New York, 1981.
[6] H.L.Stone, Iterative solution of implicit approximations of multidimensional partial differential equations, SIAM Journal of Numerical Analysis, 5, 1968, pp. 530-558.

Invited-by-Zoe-Michel-perminov@tpu.ru

VALERIY A. PERMINOV obtained his PhD at Tomsk University for a thesis on the mathematical modeling of forest fires. In 2011 he became a Doctor of Physical and Mathematical Sciences. Since 2011 he is a Professor of Tomsk Polytechnic University, Department of Ecology and Basic Safety (Russia). His scientific interest is connected with mathematical and computational models for physical processes and their applications to ecology and forest fires initiation and development and environmental pollution. Dr. Perminov is a member in Council on combustion and explosion of Siberian Department of Russian Academy of Science and a member of American Chemical Society.

Evaluation for Postural Balance Pattern of Patients with Adolescent Idiopathic Scoliosis using Pressure Sensor Systems

Ji-Yong Jung[1,a], Soo-Kyung Bok[2,b], Bong-Ok Kim[2,c], Yonggwan Won[3,d] and Jung-Ja Kim[4,5,e*]

[1]Department of Healthcare Engineering, Chonbuk National University, Jeonju, South Korea

[2]Department of Rehabilitation Medicine, Chungnam National University Hospital, Daejeon, South Korea

[3]Department Electronics and Computer Engineering, Chonnam National University, Gwangju, South Korea

[4]Division of Biomedical Engineering, Chonbuk National Univeristy, Jeonju, South Korea

[5]Research Center of Healthcare & Welfare Instrument for the Aged, Chonbuk National University, Jeonju, South Korea

[a]cholbun@hanmail.net, [b]skbok@cnuh.ac.kr, [c]bokim@cnu.ac.kr, [d]ykwon@jnu.ac.kr, [e]jungjakim@jbnu.ac.kr

Keywords: Adolescent idiopathic scoliosis, Postural balance, Pressure sensor systems, Plantar pressure, Body pressure.

Abstract. Abnormal lateral curvature of the spine may affect postural balance pattern in static and dynamic condition. Previous studies demonstrated asymmetrical balance patterns of adolescent patients with idiopathic scoliosis during sitting and walking. However, pressure distribution data have been rarely used to analyze asymmetrical postural pattern of scoliotic patients. In this study, pressure data analysis for evaluation of postural balance in patients with idiopathic scoliosis was conducted by utilizing two types of pressure sensor systems. Subjects were classified into a control group, scoliosis with left convex side of the curve group, and scoliosis with right convex side of the curve group. All subjects were instructed to walk and sit on pressure sensor systems which is consist of a lot of capacitive sensors. Pressure distribution data were subdivided into two regions of masks and analyzed for maximum force, peak pressure, and contact area. There were significant differences in pressure distribution patterns between scoliosis patient groups according to the direction of the curve during walking and sitting. From these results, it was concluded that idiopathic scoliosis cause postural asymmetry and unequal weight distribution during walking and sitting. Furthermore, pressure sensor systems can be used to detect asymmetrical balance and postural change of patients with idiopathic scoliosis and provide accurate diagnosis and rehabilitation method for individuals.

Introduction

Postural balance is the ability to keep the line of gravity of a body within the base of support. The ability to keep balance is one of the most essential factors in activities of daily living. Human body tries to maintain its correct posture under static and dynamic conditions against gravity. Good posture provides normal biomechanical functions of the musculoskeletal system. However, improper postural alignment and trunk stability including asymmetrical pelvic tilt in the three different planes (frontal, sagittal, and transverse) and excessive curvature of the spine such as lordosis, kyphosis, and scoliosis can cause spinal deformities as well as influence on our balance system negatively. Previous studies discovered that abnormalities in balance function caused by progressive curve were found to be associated with pelvic deformities in the sagittal and frontal plane [1].

Scoliosis is a three-dimensional deformity defined as an abnormal lateral curvature of the spine. It is divided into two categories: congenital and idiopathic. Congenital is caused by vertebral anomalies

ISBN: 978-1-61804-295-8

present at birth and idiopathic means the identifying cause of the disease is unknown. Idiopathic scoliosis is defined by the age of onset such as infantile, juvenile, and adolescent. Generally, curve types of scoliosis are classified as C-shaped and S-shaped based on the direction and location of the curve in spinal deformity. C-shaped and S-shaped curves refer to a single and double curve, respectively, in the thoracic, lumbar, or thoracolumbar region. These curve types are connected to asymmetrical rotation, elevation, and tilting of the pelvis which can cause various pain-related symptoms.

Adolescent idiopathic scoliosis (AIS) is the most common type that is present in 2 to 4 % of children between the ages of 11-17 years [2]. More severe curve that requires treatment is present more frequently in females than males. Initial asymmetry of the body during growth phases may affect progression of AIS. Progressive curve is related to posture asymmetry, and it can affect physical activity in adolescent. Scoliosis in adolescent has been closely associated with excessive spinal curvature, asymmetrical load on the spine, and progressive loss of both trunk and lower limb balance [3]. In biomechanics, the trunk and pelvis plays a fundamental role in the maintenance of body balance. Therefore, convexity and concavity of the spinal curve with pelvic inequality would alter the postural balance pattern in standing, sitting, and during walking. The scoliosis patients group displayed increasing displacement of the center of pressure (COP) and the center of mass (COM) excursion [4]. Aggravated scoliosis with pelvic imbalance leads to increasing several trunk muscle contraction, postural instability, and asymmetrical tilting angle while standing and sitting [5,6]. Shamberger [7] described the connection between asymmetrical alignment of the lower extremities and compensatory curvatures of the spine. Additionally, patients with idiopathic scoliosis showed asymmetrical gait in kinematic and ground reaction force (GRF) due to changes in postural control strategies [8].

To date, many studies related to postural balance of idiopathic scoliosis in adolescent have been conducted by utilizing various balance assessment systems. Muscle imbalance in the lumbar or thoracolumbar area on the convex side of patients with idiopathic scoliosis was observed by measuring electromyography (EMG) signals in thoracic, lumbar, and abdominal trunk muscles [9]. More reduced step length, pelvis, hip, and shoulder frontal motion, hip transversal motion, knee sagittal motion of scoliosis patients than normal subjects was observed by using three-dimensional motion analysis equipment [10]. However, pressure distribution data have been rarely used to analyze asymmetrical postural pattern of scoliotic patients in the literature. It is crucial to assess the pressure distribution pattern for patients with idiopathic scoliosis because pressure distribution data is useful to get the quantitative information about normal or abnormal balance pattern for individuals in static and dynamic conditions. In addition, in recent years, adolescent students spend most of time sitting with the increase in sedentary activities such as studying, watching television, and playing computer game. Bennett [11] reported that patients with AIS have muscular imbalance between concave and convex side of the spine as they spend most of time sitting. Accordingly, there is need to investigate the weight distribution pattern of AIS patients during sitting and effect of sitting balance control on body balance system during gait.

Pressure sensors are commonly used in various medical fields to provide the information about postural balance of patients by converting electric signal into physical output. There are many pressure measurement methods including resistive, inductive, capacitive, and piezoelectric for measuring pressure between two contacting surfaces. Especially, capacitive sensors are more suitable than other sensors for assessing interface pressure due to its advantage of high sensitivity and linear characteristics. Platform system with capacitive sensors has been utilized to collect pressure distribution of the foot during walking [12]. In addition, capacitance mapping system was used to analyze the effect of the body asymmetry, trunk mobility, postural change caused by prolonged sitting in working conditions on spinal deformity [13].

The purpose of this study was to assess the postural balance pattern of AIS patients and to analyze the correlation between compensatory strategies of subjects during sitting and walking by utilizing two types of pressure sensor systems based on capacitive sensors.

Methods

Subjects

Eighteen adolescents were recruited from the Department of Rehabilitation Medicine of Chungnam National University Hospital in Daejeon, South Korea. Subjects were consisted of three groups as shown in Fig. 1. The control group (CG) consisted of 6 adolescents without spinal deformation, previous history of injury, and abnormal gait pattern. The scoliosis patient group was divided into two subgroups according to the direction of the curve in scoliosis: scoliosis group 1 (SG 1) and scoliosis group (SG 2). The inclusion criteria for scoliosis patients were anteroposterior (AP) full spine standing X-ray evidence of idiopathic scoliosis with a C-shaped lumbar or thoracolumbar curve and no previous conservative or surgical treatment for the scoliosis. The SG 1 consisted of 6 adolescents with the left convex side of the curve and SG 2 consisted of 6 adolescents with the right convex side of the curve.

(a) (b) (c)

Fig. 1. (a) Control group; (b) Scoliosis group 1; (c) Scoliosis group 2

All adolescents and their parents provided written informed consent prior to their voluntary participation. Characteristics of subjects about demographic data including mean age, height, body weight, body mass index (BMI), and Cobb angle are shown in Table 1.

Table 1 Characteristics of subjects

	Control group (mean±SD) (n = 6)	Scoliosis patients (mean±SD)	
		Group 1 (n = 6)	Group 2 (n = 6)
Age (years)	15.17±2.04	14.50±2.17	15.17±2.14
Height (cm)	166.17±7.78	159.67±10.37	164.67±6.15
Body weight (kg)	62.51±5.40	52.17±5.42	53.33±14.75
BMI (kg/m^2)	22.87±2.09	20.66±1.53	18.92±4.73
Cobb angle (°)	-	14.63±3.48	16.47±7.38

Pressure Sensor System

ISBN: 978-1-61804-295-8

Two types of pressure sensor systems were utilized to detect postural balance of AIS patients during walking and sitting, as shown in Fig. 2. The emed-at platform (Novel Gmbh, Munich, Germany) is a plantar pressure measurement system. This system contains 1,760 capacitive sensors with an individual sensor area of 0.25 cm^2 in an array to determine the local loading on the foot during walking. The dimension of the platform were 610 mm × 323 mm × 18 mm with a sensor dimension of 389 mm × 226 mm, at a sampling rate of 50 Hz. Sitting balance was assessed by using Pliance seat sensor system (Novel Gmbh, Munich, Germany). It is consists of a flexible 256 capacitive sensors with an individual sensor area of 1.5 cm^2 in a matrix configuration for measuring weight distribution of the body during sitting. The dimension of the sensor mat were 150 mm × 100 mm × 40 mm with a sampling frequency of 100 Hz in a matrix configuration for measuring weight distribution of the body during sitting.

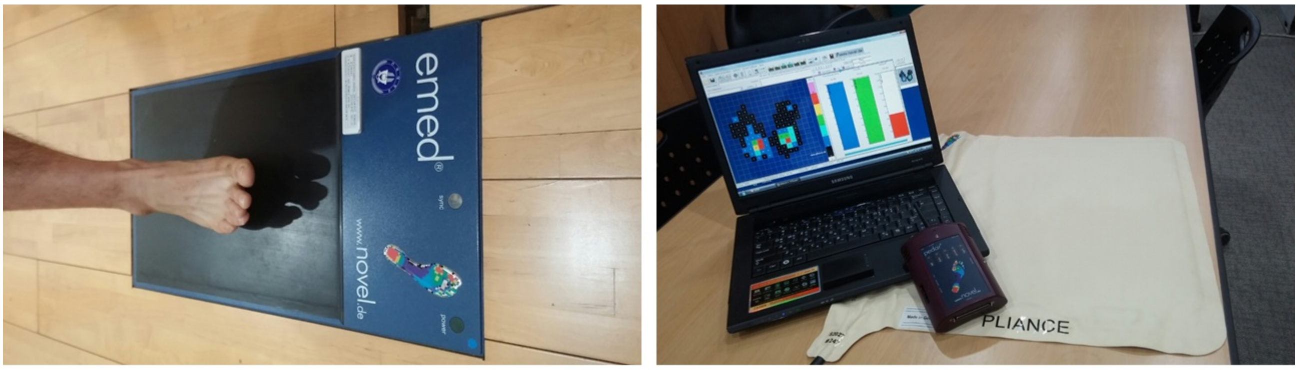

(a) (b)

Fig. 2. (a) Emed-at platform system; (b) Pliance seat sensor system

Procedure

Subjects were instructed to walk over the plantar pressure measurement system which is embedded in the floor by using the two-step protocol [14] and to sit in the usual manner on the capacitive seat sensor system with arms crossed on contra-lateral shoulder for 30 seconds. Plantar pressure measurement system starts recording automatically when the subject's foot touches the platform. Seat sensor system was located on the unstable board (length: 335 mm, width: 305 mm, height: 36 mm). The curvature radius of the board was 320 mm. Symmetrical or asymmetrical postural pattern of patient can be detected by its unstable structure. This unstable structure has been used to assess the ability of postural control of the spine in the frontal and sagittal plane while sitting [15]. Additionally, a foot support was employed to adjust the knee and ankle at 90° to prevent leg movements.

Data analysis

Pressure distribution data were subdivided into two regions of masks (left and right side) and analyzed for maximum force, peak pressure, and contact area by using Novel software (Novel Gmbh, Munich, Germany). Plantar pressure distribution and body weight distribution data was displayed in 2D and 3D, and the pressure values are shown according to the corresponding color scale.

Statistical analysis was conducted using SPSS PASW statics 18 software (SPSS Inc, Chicago, USA). A t-test was used to examine the differences in pressure distribution between left and right side, at the $p < .05$ level. Comparisons were also made for measured variables in experimental results between the groups by using one-way ANOVA with Post Hoc Scheffé test, at the $p < .05$ level.

Results

Comparisons of plantar pressure distribution between the groups are presented in Table 2. Maximum force, peak pressure, and contact area of the SG 1 increased on the left side, while plantar pressure distribution of the SG 2 decreased on the right side during gait. There were no significant differences in the maximum force and peak pressure between both sides or between the groups. However, contact area between the left and right side of SG 1 was only different significantly ($p < 0.05$).

Table 2 Differences in plantar pressure distribution between the groups

			Left	Right	p-value
	Maximum	CG	760.01±114.09	763.18±98.73	0.929
	Force	SG 1	638.93±87.41	627.85±69.15	0.772
	(N)	SG 2	660.96±153.42	666.06±147.05	0.920
Plantar	Peak	CG	558.06±140.94	559.44±108.22	0.974
Pressure	Pressure	SG 1	463.61±108.01	442.22±104.86	0.551
Distribution	(kPa)	SG 2	384.44±38.38	416.94±82.05	0.615
	Contact	CG	130.22±9.26	129.69±6.69	0.846
	Area	SG 1	126.42±8.65	120.42±6.02	0.022*
	(cm^2)	SG 2	117.83±13.63	125.5±16.54	0.567

M±SD, *p-value < .05

Comparisons of body pressure distribution between the groups are presented in Table 3. Maximum force, peak pressure, and contact area of the SG 1 increased on the left side, while plantar pressure distribution of the SG 2 decreased on the right side during sitting. There were no significant differences in the maximum force and contact area between both sides or between the groups. However, peak pressure between the left and right side of SG 2 was only different significantly ($p < 0.05$).

Table 3 Differences in body pressure distribution between the groups

			Left	Right	p-value
	Maximum	CG	205.45±38.74	206.90±36.51	0.908
	Force	SG 1	163.99±31.89	145.48±33.13	0.097
	(N)	SG 2	155.62±40.64	177.31±51.76	0.171
Body	Peak	CG	46.71±15.73	45.31±15.42	0.789
Pressure	Pressure	SG 1	39.31±15.94	35.85±19.27	0.561
Distribution	(kPa)	SG 2	41.15±11.84	55.10±12.33	0.001*
	Contact	CG	294.57±38.97	294.46±39.57	0.993
	Area	SG 1	259.11±66.69	248.10±65.11	0.620
	(cm^2)	SG 2	226.09±60.38	233.43±73.22	0.745

M±SD, *p-value < .05

Figure 3 illustrates the differences in plantar pressure distribution between the groups by using 2D and 3D display mode. As compared with plantar pressure among CG, SG 1, and SG 2, pressure distribution pattern of SG 1 and SG 2 were tilted in accordance with their direction of scoliosis curve, respectively.

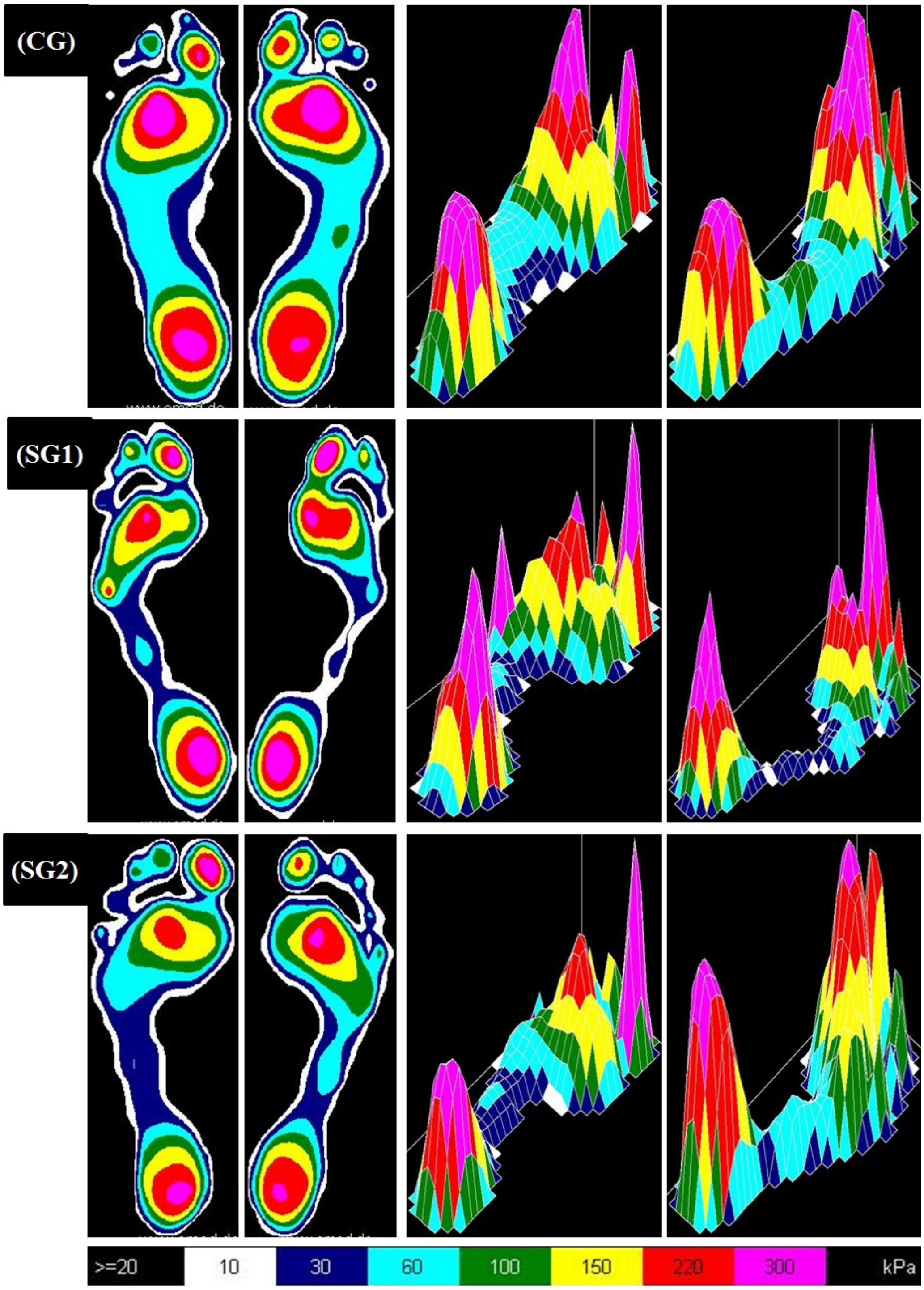

Fig. 3. Differences in 2D and 3D plantar pressure distribution between the groups

Figure 4 illustrates the differences in body pressure distribution between the groups by using 2D and 3D display mode. As compared with body pressure among CG, SG 1, and SG 2, pressure distribution pattern of SG 1 and SG 2 were tilted in accordance with their direction of scoliosis curve, respectively.

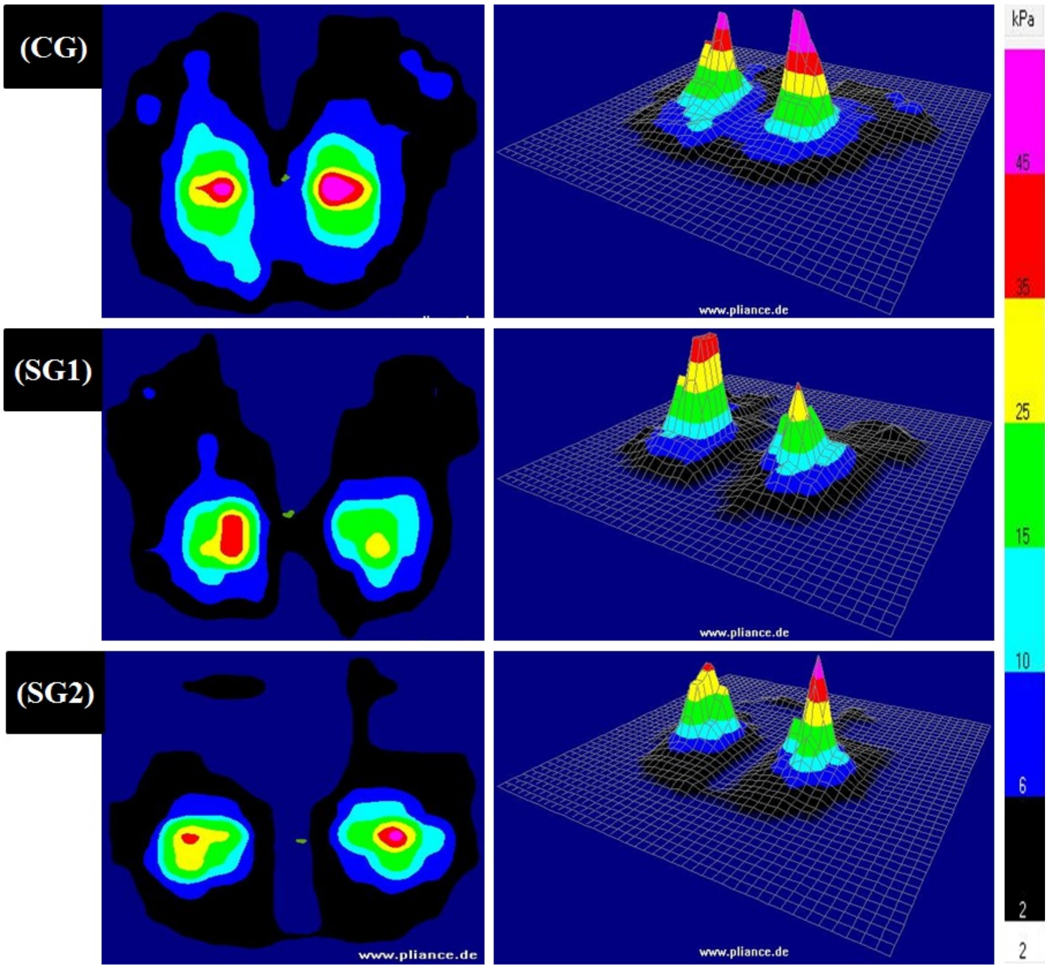

Fig. 4. Differences in 2D and 3D body pressure distribution between the groups

Conclusion

In this study, postural balance pattern of patients with idiopathic scoliosis in adolescent was evaluated by using pressure measurement system based on capacitive sensors.

Progressive idiopathic scoliosis would alter the postural balance pattern during sitting. We hypothesized that altered sitting postural balance caused by abnormal lateral curvature of the spine may affect the plantar pressure distribution during gait. Generally, scoliosis patients with C-shaped curve tend to have more severe thoracolumbar spinal imbalance than patients with S-shaped curve [16]. Accordingly, we focused on patients with C-shaped lumbar or thoracolumbar curve and classified into two groups according to direction of scoliosis curve. Scoliosis patients group with left convex side of the curve showed more tilted plantar and body pressure distribution to the left side than the right side. In contrast, plantar and body pressure of scoliosis patients group with right convex side of the curve increased on the right side. It means that direction of scoliosis curve may affect directly the asymmetrical pressure pattern during walking and sitting. These asymmetrical patterns are connected to significant difference in the contact area and peak pressure of scoliosis patients in accordance with their characteristic of spinal curve. From the results of this study we confirmed that AIS have influence on postural imbalance and control problem in walking and sitting conditions.

It has been reported that unbalanced pressure distribution can cause pressure ulcers and advance deformation of the spine. Therefore, studies about postural balance in patients with AIS have been emphasized by other investigators. Measurement of balance abnormalities in adolescents with idiopathic scoliosis is very important to prevent progression of the curve and to treat pain caused by spinal deformities.

Postural balance pattern of scoliosis patients with lumbar or thoracolumbar curve were analyzed by using plantar and body pressure measurement system. Asymmetrical pressure distribution pattern was caused by direction of scoliosis curve during walking and sitting. These asymmetrical patterns are connected to significant difference in pressure distribution between scoliosis patient groups in accordance with their characteristic of spinal curve. Consequently, it was concluded that idiopathic scoliosis in adolescent can have a significant effect on postural balance and pressure distribution. Furthermore, this paper suggested that pressure sensor systems which is consist of a lot of capacitive sensors with high sensitivity and linear characteristics can provide accurate information about postural balance of patients with idiopathic scoliosis and can be utilized to prevent progression of postural asymmetry caused by abnormal lateral curvature of the spine by measuring plantar and body pressure of patients during walking and sitting.

Acknowledgements

This work was supported by National Research Foundation of Korea (NRF) grant funded by the Korea government (MSIP) (NRF-2013R1A2A2A04016782).

References

[1] P. Mahaudens, J. L. Thonnard, C. Detrembleur, Influence of structural pelvic disorders during standing and walking in adolescents with idiopathic scoliosis, Spine. Vol. 5 (2005) 427-433.

[2] M. J. Slomito, M. C. Lee, D. R. Peterson, Using motion analysis technology to reduce radiographs in patients with scoliosis, Proceeding of the 37th IEEE Annual Northeast Conference on Bioengineering (2011) 1-2.

[3] M. K. Ireneusz, P. F. Halina, S. Piotr, Z. S. Katarzyna, D. Aneta, K. Marek, R. Juozas, Analysis of the sagittal plane in standing and sitting position in girls with left lumbar idiopathic scoliosis, Pol. Ann. Med. 21 (2013) 30-34.

[4] M. L. Nault, P. Allard, S. Hinse, R. Le Blanc, O. Caron, H. Labelle, H. Sadeghi, Relationship between standing stability and body posture parameters in adolescent idiopathic scoliosis, Spine. 27 (2002) 1911-1917.

[5] A. V. Bruyneel, P. Chavet, G. Bollini, S. Mesure, Gait initiation reflects the adaptive biomechanical strategies of adolescents with idiopathic scoliosis, Ann. Phys. Rehabil. Med. 53 (2010) 372-386.

[6] S. Sahli, H. Rebai, S. Ghroubi, A. Yahia, M. Guermazi, M. H. Elleuch, The effects of backpack load and carrying method on the balance of adolescent idiopathic scoliosis subjects, Spine. J. 13 (2013) 1835-1842.

[7] W. Shamberger, The Malalignment Syndrome., Churchill Livingstone, London, 2002.

[8] A. H. Abdul Razak, A. Zayegh, R. K. Begg, Y. Wahab, Foot plantar pressure measurement system: A review, Sensors. 12 (2012) 9884-9912.

[9] D. Odermatt, P. A. Mathieu, M. Bequsejour, H. Labelle, C. E. Aubin, Electromyography of scoliotic patients treated with a brace, J. Orthop. Res. 21 (2003) 931-936.

[10] P. Mahaudens, X. Banse, M. Mousny, C. Detrembleur, Gait in adolescent idiopathic scoliosis: kinematics and electromyographic analysis, Eur. Spine. J. 18 (2009) 512-521.

[11] M. J. Hessert, M. Vyas, J. Leach, K. Hu, L. A. Lipsitz, V. Novak, Foot pressure distribution during walking in young and old adults, BMC. Geriatr. 5 (2005) 8.

[12] T. W. Kernozek, P. A. Wilder, A. Amundson, J. Hummer, The effects of body mass index on peak seat-interface pressure of institutionalized elderly, Arch. Phys. Med. Rehabil. 83 (2002) 868-871.

[13] B. C. Bennett, M. F. Abel, K. P. Granata, Seated postural control in adolescents with idiopathic scoliosis, Spine. 29 (2004) E449-E454.

[14] K. J. Mickle, B. J. Munro, S. R. Lord, H. B. Menz, J. R. Steele, Gait, balance and plantar pressures in older people with toe deformities, Gait and Posture. 34 (2011) 347-351.

[15] S. P. Silfies, J. Cholewicki, A. Radebold, The effects of visual input on postural control of the lumbar spine in unstable sitting, Human Movement Science. 22 (2003) 237-252.

[16] E-L. Larsson, S. Aaro, H. Normelli, B. Öberg, Weight distribution in the sitting position in patients with paralytic scoliosis: pre-and postoperative evaluation, Eur. Spine. J. 11 (2002) 94-99.

Diurnal Variations of BTEX in ambient air of a site located in the center zone of Orizaba Veracruz, Mexico during autumn 2014

Rodriguez-Guzmán, A[2a]., Cerón-Bretón, J.G. [1b*], Cerón-Bretón, R.M[1c]., Ramírez-Lara, E[4d]., Rustrián-Portilla, E[2e]., Houbron, E.P [2f]., Aguilar-Ucán, C.A[1g]., Montalvo-Romero, C[1h]., Córdova-Quiroz, A.V[1i]., Alderete-Chavez, A [3j].

[1]Chemistry Faculty. Autonomous University of Carmen. Ciudad del Carmen, Campeche, Mexico
[2]Chemistry Faculty. Universidad Veracruzana. Orizaba, Veracruz, Mexico.
[3]Research Center on Environmental Sciences. Autonomous University of Carmen. Ciudad del Carmen, Campeche, Mexico
[4]Chemistry Faculty. Autonomous University of Nuevo Leon. San Nicolás de los Garza, Nuevo León, Mexico
[a]abril708@hotmail.com, [b]jceron@pampano.unacar.mx, [c]rceron@pampano.unacar.mx, [d]evangelina.ramirezlr@uanl.edu.mx, [e]erustrian@uv.mx, [f]ehoubron@uv.mx, [g]caguilar@pampano.unacar.mx, [h]cmontalvo@pampano.unacar.mx, [i]acordova@delfin.unacar.mx, [j]aalderete@pampano.unacar.mx

Abstract— Atmospheric levels of BTEX (benzene, toluene, ethyl benzene and p-xylene) were measured in an urban site located in Orizaba, Veracruz, Mexico during autumn 2014. 1.5 h-samples were collected at 07:00 h, 14:00 h and 17:30 h, and then analyzed using gas chromatography with flame ionization detector (GC-FID). The relative abundance of BTEX followed the order: benzene> toluene >p-xylene>ethyl benzene with mean concentrations of 74.50 µg m^{-3}, 5.32 µg m^{-3}, 3.34 µg m^{-3} and 2.25 µg m^{-3}, respectively. Benzene and ethyl benzene did not show a specifically behavior and the highest mean levels for toluene were obtained during the afternoon sampling period. p-xylene showed the highest levels during midday. During the whole sampling period the influence of the vehicular sources was evident due to the highway Veracruz-Mexico which is located in these directions (SE, S, SSE). We can infer that the high benzene concentrations found in this study were influenced by vehicular traffic.

Keywords—BTEX, Orizaba, VOCs, air pollution, Mexico, autumn.

Rodríguez-Guzmán, A. is with Chemistry Faculty of the Universidad Veracruzana in Orizaba, Veracruz, Mexico. e-mail: abril708@hotmail.com.
Cerón-Bretón, J.G. is with Chemistry Faculty of the Autonomous University of Carmen in Ciudad del Carmen, Campeche, Mexico. (corresponding author). Phone: (52) 938 38 1 10 18, ext 2106; e-mail: jceron@pampano.unacar.mx.
Cerón-Bretón, R.M. is with Chemistry Faculty of the Autonomous University of Carmen in Ciudad del Carmen, Campeche, Mexico. e-mail: rceron@pampano.unacar.mx.
Ramírez-Lara, E. is with the Chemistry Faculty. Autonomous University of Nuevo Leon in San Nicolás de los Garza, Nuevo León, Mexico. e-mail: evangelina.ramirezlr@uanl.edu.mx.
Rustrián-Portilla, E. is with Chemistry Faculty of the Universidad Veracruzana in Orizaba, Veracruz, Mexico. e-mail: erustrian@uv.mx.
Houbron, E. is with Chemistry Faculty of the Universidad Veracruzana in Orizaba, Veracruz, Mexico. e-mail: ehoubron@uv.mx.
Aguilar-Ucán, C.A.. is with Chemistry Faculty of the Autonomous University of Carmen in Ciudad del Carmen, Campeche, Mexico. (e-mail: caguilar@pampano.unacar.mx).
Montalvo-Romero, C. is with Chemistry Faculty of the Autonomous University of Carmen in Ciudad del Carmen, Campeche, Mexico. (e-mail: cmontalvo@pampano.unacar.mx).
Córdova-Quiroz, A.V. is with Chemistry Faculty of the Autonomous University of Carmen in Ciudad del Carmen, Campeche, Mexico. (e-mail: acordova@delfin.unacar.mx).
Alderete-Chávez, A. is with Ecological Restoration Master Degree Program, Research Center on Environmental Sciences, Autonomous University of Carmen in Ciudad del Carmen, Campeche, Mexico. (e-mail: aalderete@pampano.unacar.mx).

I. Introduction

VOLATILE Organic Compounds (VOCs) in the atmosphere have received special attention during the last decades due to the fact that they are important tropospheric ozone precursors, contribute to photochemical smog formation and due to their possibilities of causing adverse health effects [1-3]. VOCs have been defined as organic compounds whose vapor pressure is 0.01 kPa or higher at 20ºC [31]. VOC group include compounds like alkanes, alkenes, alkynes, aldehydes, alcohols, ketones, chlorofluorocarbons, chlorinated organic compounds and aromatics. This last group includes a sub-group named as “BTEX” which includes to benzene, toluene, ethyl-benzene, 1,2,4-trimethyl-benzene, o-xylene, m-xylene and p-xylene, all of them considered as air toxic pollutants and some of them as carcinogenic species [4].These compounds can be emitted from several and different sources: biogenic [5]; gasoline powered [6] and diesel powered [7] moto vehicles; fuel storage and fuel combustion [8], biomass burning [9]; natural gas [10]; LPG [11], industrial processes and solvents [8]. Due to their ubiquitous character, multiple emission sources, to that they can be transported over large distances, and to that exposure to some BTEX can cause acute non lym-phocytic leukemia and a variety of other blood-related disorders in humans, it is very important to know their diurnal and seasonal levels and to identify their probable sources in urban areas in order to gain a better understanding of their role in the photochemistry of regional troposphere. In spite of the well-known toxic effects of these compounds, available data in Mexico are very limited. Few studies have reported BTEX levels in Mexico mega-cities [17-19] and there are not studies on other important cities in Mexico. Veracruz State has about one-fourth of Mexico’s petroleum reserves and ranks third in petroleum production [12-13]. Orizaba is one of the most important cities in Veracruz, which is located in the mountainous central region and at 266 km from Mexico City. The municipality population is of more than 120,000 and it has an area of 27.97 km2 [13], and its economy and industrial activity has grown significantly in the last years. For all these reason, the number of vehicles, industries and services has increased in Orizaba and air quality in this region has suffered a gradual decline in recent years. The present study is an attempt to envisage about the BTEX levels and their probable sources in terms of their inter-species and meteorological parameters correlations using a principal component analysis (PCA) and meteorological analysis (wind roses and backward trajectory analysis using HYSPLIT from NOAA) in an urban site located in the west area of Orizaba, Veracruz, Mexico during autumn 2014.

II. Methodology

A. Study Area

Orizaba is located at latitude of 18º51’N and the longitude of 97º06’W with an altitude of 1236 m above sea level. Its climate is pleasant, though often cloudy and rainy and the soil of the valley is extraordinary fertile. Overlooking the valley from the north is the Pico de Orizaba, a volcano that at 5636 m, is the highest mountain in Mexico and the third highest in North America. The mean annual rainfall is 1800 mm. January is the coldest month (7-10 ºC). The average annual high and low temperatures are of 27 ºC and 13 ºC, respectively. Mean annual temperature is of 21 ºC. The air in Orizaba is wet for most of the year with very high relative humidity from November to February (almost 100%) and temperature inversions are common in winter. The specific sampling site location can be observed in Fig. 1.

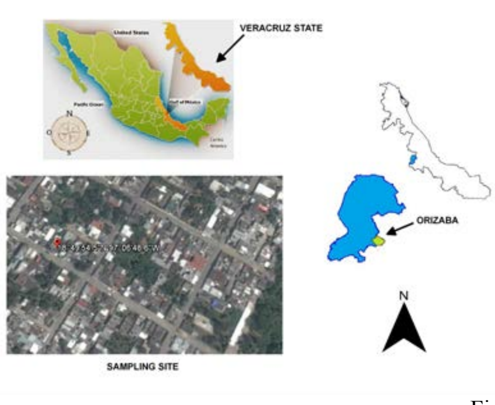

Fig. 1 Location of the sampling site

B. Sampling Method

A total of 33 samples were collected from November 7 to November 27, 2014, during the autumn season. Benzene (B), ethyl benzene (Ebz), toluene (T) and p-xylene (X) were determined in all ambient air samples. Samples were collected using glass tubes containing 226-01 Anasorb CSC (SKC) with following features: length 70 mm; inner diameter 4.0 mm; outer diameter 6 mm packed in two sections with 100 mg and 500 mg of active carbon, separated by a glass wool section (Method INSHT MTA/MA-030/A92) [14-15] b). The downstream end of the glass tube was connected to a calibrated flow meter. Ambient air was passed through the glass tubes at a flow rate of 200 ml min-1 at 1.5-hour intervals (morning, midday and afternoon). Samples with a sampling volume lower than 5 liters were discarded. Sampling was carried out using a Universal XR pump model PCXR4 (SKC), at three sampling periods (local time): B1 (from 07:00 to 08:30 h), B2 (from 14:00 to 15:30 h) and B3 (from 17:30 to 19:00 h). Sampling tubes were protected from adverse weather conditions by aluminum shelters. After the exposure time, the adsorption tubes were labeled and capped tightly with PTFE caps and transferred to the laboratory in cold boxes. Samples were analyzed within three weeks after sample collection at the Environmental Sciences Laboratory of the Autonomous University of Carmen City (UNACAR).

C. Analytical Method

Samples were extracted with 1 ml of CS_2 for each section of the sample tubes, and shaken for 30 s to assure maximum desorption. Extracted samples were analyzed using a TRACE GC Ultra gas chromatograph (Thermoscientific) and one flame ionization detector (FID; Thermoscientific Technologies, Inc) (Method INSHT MTA/MA-030/A92) [15]. The analytical column used was a capillary column (57 m, 0.32 mm i.d., 0.25 µm film thickness). Operation of the instrument was controlled using a Trace Chemstation data system. The oven temperature program was initially set to 40 °C for 4 min, then increased at a rate of 5 °C/min up to 100 °C, and finally maintained for 10 min at 100 °C. The FID temperature was set to 250 °C using a hydrogen/air flame with constant flows of 35 ml min-1 and 350 ml min-1 for ultra-pure hydrogen and extra-dried air, respectively. The ultra-pure nitrogen carrier (99.999%) gas flow rate was 1 ml min-1 [15]. Four BTEX were investigated: benzene, p-xylene, ethyl benzene, and toluene.

D. Monitoring of Meteorological parameters

Wind conditions (speed and direction), relative humidity, temperature and barometric pressure were monitored during and autumn, 2014 (from November 7 to November 27) using a Davis Vantage Pro II model portable meteorological station. Wind frequency statistics were determined using WRPLOT software [24]. This station was located specifically in the sampling site.

E. Correlation and Principal Component Analysis (PCA)

Pearson correlation analysis was applied to all data collected at the sampling site. To assess the relationships between BTEX concentrations, meteorological parameters and criteria air pollutants; a factor analysis (Principal Component Analysis) was applied using XLSTAT software (Statistics Package for Microsoft Excel) [16].

III. Results and Discussion

A. Diurnal Variation

Diurnal variation and descriptive statistics for autumn sampling period can be observed in Fig 2. During this period, Benzene (B), Toluene (T), Ethyl benzene (Ebz), and p-xylene (X) showed different diurnal patterns. B and Ebz did not show significant differences among the different sampling periods (B1: morning sampling, B2: midday sampling, and B3: afternoon sampling). T presented higher levels during the mornings (B1), decreasing during the midday (B2) and presenting the lowest values during the afternoons (B3). X had the highest concentrations during midday (B2) and the lowest levels during the afternoon sampling period (B3). The relative abundance of BTEX exhibited the following order during both sampling periods: B > T> X > Ebz. Mean concentration levels were 74.51 $\mu g\ m^{-3}$ for B, 5.33 $\mu g\ m^{-3}$ for T, 2.26 $\mu g\ m^{-3}$ for Ebz and 3.35 $\mu g\ m^{-3}$ for X.

BTEX levels in different cities are influenced by several factors including sampling season, sampling duration, sampling location, meteorological conditions, site topography and sampling methods. Bearing these factors in mind, BTEX levels in the study site could be compared in a cautious way with those levels reported in other cities around the world (Table 1). It can be observed that, during autumn sampling period, benzene levels found in this study were similar to those reported for Greater Cairo and Algeriers, whereas, Toluene levels were lower than those found in Seoul, Korea ut higher than those reported by Pankow [20] in New Jersey. Ethylbenzene levels in the study site were similar to those found in Seoul and p-xylene levels were higher than those reported for New Jersey.

Table 1 Comparison of atmospheric concentrations of BTEX found in this study with data of other studies around the world.

Loca-tion	B		T		EBz		X	
	1	2	1	2	1	2	1	2
Rowan College, NJ (James F. Pankow, 2003)		**0.36**		**0.56**		**0.09**		**0.29**
Haram, Greater Cairo (Khoder, 2007)	**33.33-58.56**		**78.41-138.69**		**16.61-32.48**		**51.51-99.64**	
Seoul, Korea (Kwangsam, Na, 2001)		**1.00**		**6.4**		**0.7**		**2.3**
Algeriers, Africa (Kerbachi, 2012)	**1.1-26.8**		**3.5-63.3**		**2-12**		**4.9 - 46.8**	
Present Study	**74.50**	**24.25**	**5.32**	**2.08**	**2.25**	**0.52**	**3.34**	**0.77**

[1]: µg/m^3; [2]: ppbv; B: Benzene; T: Toluene; Ebz: Ethylbenzene; X: p-Xylene

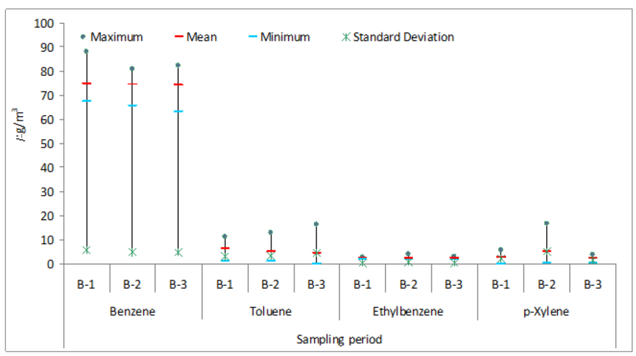

Fig. 2 Diurnal variation and descriptive statistics for measured BTEX during the autumn sampling period, 2014. B1 (07:00-08:30 h), B2 (14:00-15:30 h) and B3 (17:30-19:00 h).

B. Meteorological Influence

Winds during the autumn sampling period were quite un-stables but always showing a south component coming from the highways 180 and 190 located in this direction. Fig. 3a, Fig. 3b and Fig. 3 c show the daily meteorological influences for each BTEX for B1, B2 and B3 sampling periods, respectively. During the mornings (B1), BTEX showed the highest values when winds blew from SSE and S. During the midday sampling period (B2) the highest values of concentration were found for B when winds blew from SW, for T when air masses came from SE, for Ebz when winds came from SSW and for X when winds blew from SSE. During the afternoon sampling period (B3), winds had a more stable behavior: B presented the highest levels when winds came from SSE, whereas, T, Ebz and X showed the highest concentrations when winds blew from SE. 24 h backward air masses trajectories were calculated in order to infer the origin of air masses at three different levels (50, 100 and 500 MAGL) using the hybrid Lagrangian model HYSPLIT from NOAA (Fig. 4 a, Fig. 4b and Fig. 4 c). The wind conditions are used to identify the probable sources of the measured BTEX compounds. During the whole sampling period the influence of the vehicular sources was evident due to the highway Veracruz-Mexico which is located in these directions (SE, S, SSE). We can infer that the high benzene concentrations found in this study were influenced by vehicular traffic.

ISBN: 978-1-61804-295-8

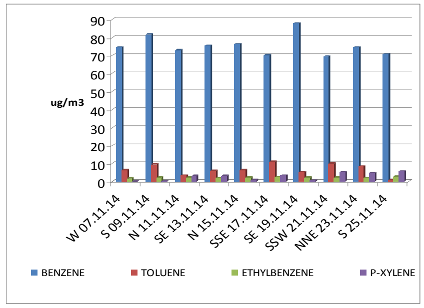

B1)

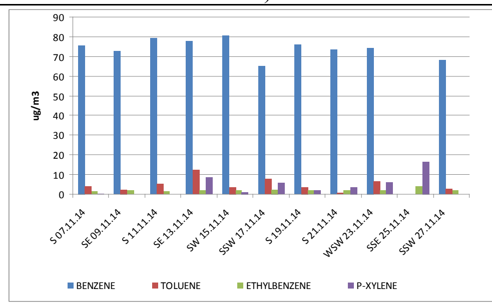

B2)

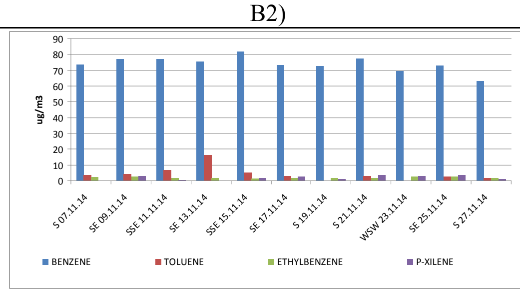

B3)

Figure 3. Meteorological influence on BTEX levels: a (B1: 07:00- 080:30 h); b (B2: 14:00-15:30 h); and c (B3: 17:30-19:00 h)

a)

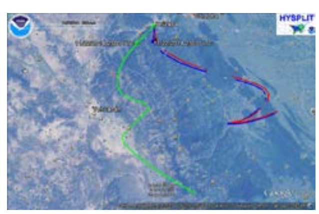

b)

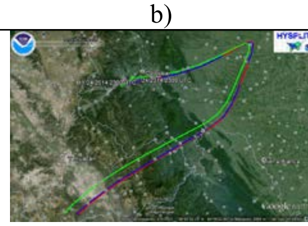

c)

Figure 4. Representative 24-h backward air masses trajectories for autumn period: a) November 21, 2014, for b) November 23, 2014 and for c) November 25, 2014.

C. Toluene to Benzene Ratio (T/B ratio)

The T/Bz ratio has been commonly used as an indicator of traffic emissions. Bz and T are constituents of gasoline and are emitted into the atmosphere by motor vehicle exhaust. The toluene content of gasoline and motor vehicle exhaust is 3-4 times higher than Bz content [26]. T/Bz values lower than 2-3 are characteristic of vehicular emissions in many urban areas worldwide [19, 25], whereas values higher than 3 may indicate that BTEX levels could be associated with industrial facilities and area sources (evaporative emissions, painting, cooking processes, among others). During the whole sampling period this ratio was of 0.0864 for B1, of 0.0689 for B2 and 0.0583 for B3, being higher during the morning sampling period. These values are in agreement with typical values of vehicular emissions reported for other urban areas, suggesting that this site was under the influence of mobile sources.

D. P-Xylene/Ethylbenzene Ratio (X/Ebz ratio)

The p-Xylene to Ethyl benzene (X/Ebz) ratio is commonly used as an indicator of the photochemical age of the air masses. A ratio of 3.6: 1 of (X/Ebz) has been established as a typical emission relation for these species. This ratio is related to the atmospheric residence time of these pollutants: high values of indicate aged air masses (old emissions), and low values indicate fresh air masses (recent emissions). Kuntasal et al. [26] used a value of 3.8 for this ratio. Fresh gasoline emissions provide values between 3.8 and 4.4 for this ratio. In this study, the whole period registered low values for this ratio, indicating that most of the air masses correspond to “fresh emissions”. A mean value of 1.2798 for this ratio was obtained (B1: 1.1104; B2: 1.8025; B3: 0.9263). Taken together, the T/Bz and X/Ebz ratio results suggest that these fresh emissions correspond to vehicular emission from mobile sources

E. Pearson Correlation and Principal Component Analysis (PCA)

Meteorological analysis and Toluene to Benzene ratios and Xylene to Ethyl benzene ratios suggest that autumn BTEX levels at the site under study were influenced in a dominant way by vehicular traffic emissions (see sections 4.2, 4.3 and 4.4). However, PCA analysis can reveal more detailed information about the behavior of the studied pollutants. While BTEX ratios are used as markers of fresh, local traffic emissions, different gasoline formulations can result in different T/B ratios. These ratios must therefore be used with caution. In addition, low values for the T/B ratio may indicate the presence of other benzene sources in this area in addition to motor vehicle emissions. Therefore, it is necessary to investigate the relationship among BTEX and meteorological parameters in order to elucidate the possible source for the BTEX. Pearson correlation matrixes were constructed for each sampling period (B1, B2 and B3) (Tables 2-4). A good mutual correlation among the species indicates that they might primarily originated from the same source and a good mutual correlation between Ebz and X indicates that they might possibly originated from gasoline vehicles and gasoline stations [27-31]. A low correlation factor indicates towards the spiking of BTEX from some additional sources apart from vehicular inputs. For B1 sampling period low correlations between benzene and the rest of BTEX were found, indicating that excepting benzene, the other studied BTEX could have their origin in sources different from vehicular emissions. It was found a good correlation between relative humidity and wind speed (0.830) and a good negative correlation between temperature and relative humidity (-0.750). Toluene-p-Xylene and Ethyl benzene-p-Xylene showed good correlations during the midday sampling period (B2) (Table 3), 0.645 and 0.865, respectively. Benzene and Ethyl benzene showed a significant negative correlation (-0.661) indicating that Ethyl benzene was probably precursor of benzene. Wind direction showed a significant negative correlation with relative humidity. In Table 4 it can be observed that benzene had good correlation with relative humidity (0.627), whereas toluene showed good correlation with barometric pressure (0.606). Ethyl benzene and p-xylene once again showed good correlation (0.639) indicating that these pollutants probably had common sources. Good correlations between wind speed-wind direction, barometric pressure and benzene were found. In addition, a Principal component analysis (PCA) was used to study the variability patterns present in this multivariate data set. A PCA model was developed for air pollutants levels (benzene, toluene, ethyl benzene and p-xylene) and the meteorological parameters (temperature: T, barometric pressure: P, relative humidity: RH, wind direction: WD, and wind speed: WS). The PCA biplot obtained for the morning (B1), midday (B2) and afternoon (B3) sampling periods during autumn season is shown in Fig. 5, Fig. 6 and Fig. 7. PCA for the morning sampling period (B1) gave two principal components (F1 and F2) expressing about 55.60% of the total variance. In figure 5 it can be observed that B was influenced by wind direction, it means that this pollutant was probably transported from the highway Veracruz-Mexico. Ebz and X did not show correlation between each other indicating that they probably had their origin in different sources. In Fig. 6 it can be observed that ethyl benzene and p-xylene had a good relation indicating that they probably had common sources. Toluene had a negative correlation with wind speed, indicating that this pollutant was probably dispersed by wind effects. Temperature and relative humidity, once again showed a negative correlation. In Fig. 7 it can be observed that ethyl benzene and p-xylene showed a good relation each other and that benzene and toluene had good correlation with barometric pressure, whereas, Benzene and relative humidity showed a good relation too.

Table 2 Pearson correlation matrix for B1 sampling period during autumn 2014

Variables	Benzene	Toluene	Ethylbenzene	p-Xylene	Wind speed	Wind direction	Relative Humidity	Temperature	Barometric Pressure
Benzene	**1**	0.069	-0.137	-0.528	0.048	-0.095	0.244	-0.151	0.406
Toluene	0.069	**1**	-0.339	-0.015	0.168	-0.257	0.026	0.170	0.060
Ethylbenzene	-0.137	-0.339	**1**	0.125	0.173	0.073	0.252	-0.211	-0.350
p-Xylene	-0.528	-0.015	0.125	**1**	-0.159	-0.231	-0.170	0.493	-0.445
Wind speed	0.048	0.168	0.173	-0.159	**1**	-0.225	**0.830**	**-0.802**	-0.080
Wind direction	-0.095	-0.257	0.073	-0.231	-0.225	**1**	0.112	-0.001	0.572
Relative Humidity	0.244	0.026	0.252	-0.170	**0.830**	0.112	**1**	**-0.750**	0.169
Temperature	-0.151	0.170	-0.211	0.493	**-0.802**	-0.001	**-0.750**	**1**	0.095
Barometric Pressure	0.406	0.060	-0.350	-0.445	-0.080	0.572	0.169	0.095	**1**

Table 3 Pearson correlation matrix for B2 sampling period during autumn 2014

Variables	Benzene	Toluene	Ethylbenzene	p-Xylene	Wind speed	Wind direction	Relative Humidity	Temperature	Barometric Pressure
Benzene	**1**	-0.079	**-0.661**	-0.464	0.535	0.046	0.015	0.441	0.562
Toluene	-0.079	**1**	0.345	**0.645**	-0.450	-0.282	0.185	-0.014	0.183
Ethylbenzene	**-0.661**	0.345	**1**	**0.865**	-0.318	-0.106	0.157	-0.135	-0.458
p-Xylene	-0.464	**0.645**	**0.865**	**1**	-0.308	-0.258	0.288	-0.087	-0.356
Wind speed	0.535	-0.450	-0.318	-0.308	**1**	0.506	-0.108	0.293	-0.078
Wind direction	0.046	-0.282	-0.106	-0.258	0.506	**1**	**-0.613**	0.551	-0.321
Relative Humidity	0.015	0.185	0.157	0.288	-0.108	**-0.613**	**1**	-0.461	0.355
Temperature	0.441	-0.014	-0.135	-0.087	0.293	0.551	-0.461	**1**	0.037
Barometric Pressure	0.562	0.183	-0.458	-0.356	-0.078	-0.321	0.355	0.037	**1**

Table 4 Pearson correlation matrix for B3 sampling period during autumn 2014

Variables	Benzene	Toluene	Ethylbenzene	p-Xylene	Wind speed	Wind direction	Relative Humidity	Temperature	Barometric Pressure
Benzene	**1**	0.374	-0.130	0.031	-0.484	-0.416	**0.627**	0.393	**0.606**
Toluene	0.374	**1**	-0.209	-0.545	-0.226	-0.533	0.395	-0.103	**0.641**
Ethylbenzene	-0.130	-0.209	**1**	**0.639**	-0.128	0.077	-0.060	0.010	-0.096
p-Xylene	0.031	-0.545	**0.639**	**1**	-0.150	0.203	0.023	0.108	-0.456
Wind speed	-0.484	-0.226	-0.128	-0.150	**1**	**0.616**	-0.493	-0.055	-0.169
Wind direction	-0.416	-0.533	0.077	0.203	**0.616**	**1**	**-0.746**	0.513	-0.483
Relative Humidity	**0.627**	0.395	-0.060	0.023	-0.493	**-0.746**	**1**	-0.341	0.319
Temperature	0.393	-0.103	0.010	0.108	-0.055	0.513	-0.341	**1**	0.174
Barometric Pressure	**0.606**	**0.641**	-0.096	-0.456	-0.169	-0.483	0.319	0.174	**1**

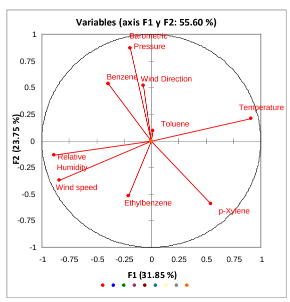

Fig. 6 Multivariate set Biplot from the PCA for B1 sampling period.

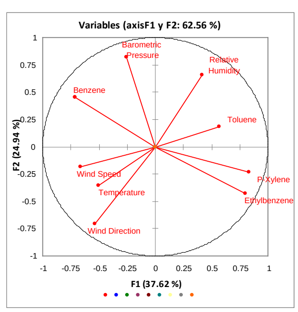

Fig. 7 Multivariate set Biplot from the PCA for B2 sampling period.

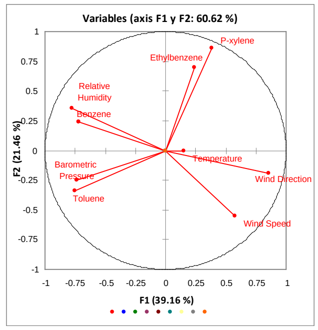

Fig. 8 Multivariate set Biplot from the PCA for B3 sampling period.

IV. Conclusion

Benzene was the dominant BTEX in the study site and its levels were strongly influenced by winds blowing from the S and SSE where an important highway is located (highway Mexico-Veracruz), indicating that benzene was originated from vehicular sources. Benzene concentrations were similar to those reported in other large cities like Great Cairo and Algeriers, whereas, the levels of Ethyl benzene were similar to those reported for Seoul, Korea. P-Xylene and Toluene showed a clear diurnal pattern but benzene and ethyl benzene did not show significant differences between the different sampling periods. T/B and X/Ebz ratios showed that BTEX were influenced by fresh vehicular emissions. PCA analysis showed that benzene was probably transported from the highways 180 and 190 and that additional sources beyond traffic related emissions could influence the levels of ethyl benzene and p-xylene.

References

[1] H.B. Singh, L.J. Salas, A.J. Smith, H. Shigeishi. " Measurements of some potentially hazardous organic chemicals in urban environments", *Atmospheric Environment* Vol. 15, pp. 601-612, 1981.

[2] S.A. Edgerton, M.W. Holdren, D.L. Smith, J.J. Shah. "Interurban comparison of ambient volatile organic compound concentrations in U.S. Cities", *Journal of Air and Waste Management Association* Vol. 44, pp. 881-899, 1989.

[3] S. Sillman. "The relation between zono, NOx and hydrocarbons in urban and polluted rural environments", *Atmospheric Environment* Vol. 33 no. 12, pp. 1821-1845, 1999.

[4] Air Resources Board of California, USA. http:/www.arb.ca.gov/toxics/id/taclist.htm

[5] A. Guenther, T. Karl, P. Harley, C. Wiedinmyer, P.J. Palmer, C. Geron. "Estimates of Global terrestrial isoprene emissions using MEGAN (Model of emission of gases and aerosols from nature)", *Atmos. Chem. Phys*. Vol. 6, pp. 3181-3210, 2006.

[6] H. Hellen, H. Hakola, T. Laurib. "Determination of source contributions of NMHCs in Helsinki (60ºN 25ºE) using chemical mas balance and the Unmix multivariate receptor models", *Atmos. Environ.* Vol. 37, pp. 1413-1424, 2003.

[7] S. Demir, A. Saral, F. Erturk S.L. Kuzu, B.I. Goncaloglu, G. Demir. "Effect of diurnal changes in VOC source strenghts on performances of receptor models", *Environ, Sci. Pollut. Res.* http://dx.doi.org/10.1007/s11356-011-0636-8. 2011.

[8] V.A. Lanz, B. Buchmann, C. Hueglin, R. Locher, S. Reimann, J. Staehelin. " Factor analytical modeling of C2-C7 hydrocarbon sources at an urban background site in Zurich (Switzerland). Changes between 1993-1994 and 2005-2006", *Atmos. Chem. Phys. Discuss*. Vol. 8, pp. 907-955, 2008.

[9] R.J.Yokelson, T.J. Christian, T.G. Karl, A. Guenther. "The tropical forest and fire emissions experiment: laboratory fire measurements and synthesis of campaign data". *Atmos. Chem. Phys*. Vol. 8, pp. 3509-3527, 2008.

[10] A. Latella, G. Stani, L. Cobelli, M. Duane, H. Junninen, C.Astorga, B.R. Larsen. " Semicontinuous GC analysis and receptor modeling for source apportionment of ozone precursor hydrocarbons in Bresso, Milan, 2003", *J. Chromatogr*. A. Vol. 1071, pp. 29-39, 2005.

[11] C.H.Lai, K.S. Chen, Y.T. Ho, Y.P. Peng, Y.M. Chou. "Receptor modelling of source contributions to atmospheric hydrocarbons in urban Kaohsiung, Taiwan", *Atmos. Environ*. Vol. 39, pp. 4543-4559, 2005.

[12] INFDM. Instituto Nacional para el Federalismo y Desarrollo Municipal. 2005. Enciclopedia de los municipios de Mexico: Veracruz de Ignacio de la Llave. Retrieved August 3, 2010.

[13] INEGI. Instituto Nacional de Estadística, Geografía e Informática. 2005. Mexico en cifras. Retrieved, April 9, 2011.

[14] J.G. Cerón- Bretón, R.M. Cerón-Bretón, M. Rangel-Marrón, G.X. Villarreal-Sánchez, A.Y. Uresti-Gómez. " Determination of BTX levels in ambient air of one urban site located at the southwest of Mexico City during spring 2013" In: *Proc. 4th International Conference on Development, Energy, Environment and Economics (DEEE'13), Recent Advances in Energy, Environment, Economics and Technological Innovation,* Paris, France, October 29-31, 2013.

[15] INSHT Method MTA/MA-030/A92 (1992) Aromatic hydrocarbons determination in air (benzene, toluene, ethylbenzene, p-xylene, 1, 2, 4-trimethyl-benzene): Adsorption in activated carbon/gas chromatography method, Social and Occupacional Affairs Office, Spain.

[16] D. Facundo, E. Ramírez Lara, J.G. Cerón Bretón, R.M. Cerón Bretón. "Measurements of carbonyls and its relation with criteria pollutants (O3, NO, NO2, NOx, CO and SO2) in an urban site within the Metropolitan Area of Monterrey, in Nuevo Leon, Mexico", In: . *Proceedings of the 1st International Conference on Sustainable Development, Sustainable Chemical Industry, Pollution, Hazards and Environment (SDSCIPHE '12)*, pp. 122-127, Iasi, Romania, June 13-15, 2012.

[17] V. Mugica, E. Vega, H. Ruiz, G. Sánchez, E. Reyes, A. Cervantes. "Photochemical reactivity and sources of individual VOCs in Mexico City", In: *Brebbia C A and Martin-Duque J F (Eds) Air Pollution X,* WIT PRESS, London, U.K pp. , 209-217. 2002.

[18] V. Mugica, M.E. Ruiz, J. Watson, J. Chow. "Volatile Aromatic Compounds in Mexico City atmosphere:Levels and Source apportionment", *Atmosfera* Vol. 16, pp. 5-27, 2003.

[19] F. James, W.L. Pankow. "Concentrations and co-occurrence correlations of 88 volatile organic compounds (VOCs) in the ambient air of 13 semi-rural to urban locations in the United States", *Atmospheric Environment* Vol. 5, pp. 2023-2046, 2003.

[20] Y.K. Kerbachi. "Measurement of BTEX (benzene, toluene, ethybenzene, and xylene) levels at urban and semirural areas of Algiers City using passive air samplers", *Journal of the Air & Waste Management Association* Vol. 1, pp. 1370-1379, 2012.
[21] M. Khoder. " Levels of volatile organic compounds in the atmosphere of Greater Cairo", *Atmospheric Environment* Vol. 41, pp. 554-566, 2007.
[22] Kwangsam Na, Y. C. King, K.C. Moon, I. Moon, K. Fung. "Concentrations of volatile organic compounds in an industrial area of Korea", *Atmospheric Environment* Vol. 35, pp. 2747-2756, 2001.
[23] Lakes Environmental, WRPLOT View version 7.0: Wind Rose Plots for Meteorological Data, http://www.weblakes.com/products/wrplot/index.html.
[24] T. Elbir, B. Cetin, E. Cetin, A. Bayram, M. Odabasi. "Characterization of volatile organic compounds (VOCs) and their sources in the air of Izmir, Turkey*", Environ. Monit. Assess* Vol. 133, pp. 149-160, 2007.
[25] B. Pekey, H. Yilma. "The use of passive sampling monitor spatial trends of volatile organic compounds (VOCs) at one industrial city of Turkey", *Microchemical Journal* Vol. 9 no. 2, pp. 213-219, 2011.
[26] O.O. Kuntasal, D. Karman, D. Wang, S. Tuncel, G. Tuncel. "Determination of volatile organic compounds in microenvironments by multibed adsorption and short-path thermal desorption followed by gas chromatographic-mass spectrometric analysis", *Journal of Chromatography* A Vol. 1099, pp. 43-54, 2005.
[27] R.R. Hoque, P.S. Khillare, T. Agarwal, V.Shridhar, S. Balachandran. "Spatial and temporal variation of BTEX in the urban atmosphere of Delhi, India", *Science of the Total Environment* Vol. 392, pp. 30-40, 2008.
[28] J.M. Baldasano, R. Delgado, J. Calbó "Applying receptor models to analyze urban/suburban VOC sair quality in Martorell (Spain)", *Environ. Sci. Technol.* Vol. 32, pp. 404-412, 1998.
[29] X.M. Wang, G.Y. Sheng, J.M. Fum, C.Y. Chan, S.C. Lee, L.Y. Chan, Z.S. Wang. " Urban roadside aromatic hydrocarbons in three cities of the Pearl River Delta, People`s Republic of China", *Atmos. Environ*. Vol. 36, pp. 5141-5148, 1993.
[30] Union, C.D. (1999). Reducing the emissions of volatile organic compounds (VOCs) 1999/13/EC.
[31] J.G. Cerón-Bretón, R.M. Cerón-Bretón, J.D.W. Kahl, E. Ramírez-Lara, C. Guarnaccia, C. Aguilar-Ucán, C.Montalvo-Romero, F.Anguebes-Franseschi, U. López-Chuken. "Diurnal and seasonal variation of BTEX in the air of Monterrey, Mexico: preliminary study of sources and photochemical ozone pollution", *Air Quality, Atmosphere and Health*, DOI 10.1007/S11869-014-0296-1, pp. 1-14, 2014.

Retrospective Examination of Relative Permeability Data on Steady-State Two-Phase Flow in Porous Media

Marios Valavanides[1,a], Eraldo Totaj[1,b] and Minas Tsokopoulos[1,c]

[1]Department of Civil Engineering, TEI Athens, Ag. Spyridonos, GR-12210 Greece

[a]marval@teiath.gr, [b]mssy1016@yahoo.com, [c]ykwon@jnu.ac.kr, [d]jungjakim@jbnu.ac.kr

Keywords: Two-phase flow, porous media, steady-state, operational efficiency

Abstract. Experimental evidence on the phenomenology of steady-state two-phase flow in porous media processes is recorded in the well-known relative permeability diagrams published in the literature. In the present work, the preliminary results of an extensive retrospective examination comprising a total of 88 published relative permeability diagrams, pertaining to a variety of steady-state two-phase flow conditions and types of porous media, are presented. Relative permeability data sets cropped from these diagrams were transformed into process operational efficiency data sets. Operational efficiency is considered as the ratio of oil transport over mechanical power supplied to the process ("oil produced per kW dissipated in pumps"). The re-examination revealed a universal, latent process characteristic: the existence of optimum operating conditions, i.e. conditions whereby process efficiency attains a maximum value. Its appearance and its correlation with the process conditions merit further investigation.

Introduction

Two-phase flow in porous media is a physical process whereby a wetting phase ("water") displaces a non-wetting phase ("oil") within a porous medium. It occupies a central position in physically important processes with practical applications of industrial and environmental interest, such as enhanced oil recovery, groundwater and soil contamination and subsurface restoration, the operation of multiphase trickle-bed reactors, the operation of proton exchange membrane fuel cells (PEMFC), etc. The majority of those applications are based on inherently transient processes. Nevertheless, to understand the physics of such processes in a deeper context, we need first to understand the stationary case, steady-state flow in macroscopically homogeneous p.m. or pore networks, whereby the two immiscible phases, "oil" & "water", are forced to flow at pre-selected, constant flowrates.

The concept of relative permeability is basic when the two immiscible phases flow simultaneously within a porous medium. It has been contrived to extend Darcy's law in accounting the phenomenology of the process. The, so-called, fractional Darcy's law takes the form

$$\widetilde{U}_i = k_{ri} \frac{\widetilde{k}}{\widetilde{\mu}_i}\left(-\frac{\Delta\widetilde{p}}{\Delta\widetilde{z}}\right)_i \qquad i = o, w \tag{1}$$

where $\widetilde{U}_o$ and $\widetilde{U}_w$ are the superficial velocities of "oil" (the non-wetting phase = "o") and "water" (the wetting phase – "w"), e.g. oil/water, gas/oil, etc; $\widetilde{\mu}_o, \widetilde{\mu}_w$ are the dynamic viscosities of the two phases and $\left(-\Delta\tilde{p}/\Delta\tilde{z}\right)_i$ represents the macroscopic pressure gradient in each phase, $i = o, w$. The relative permeabilities of oil and water (dimensionless variables) are denoted by k_{ro} and k_{rw} respectively. *Note*: In this paper, a tilde (~) denotes a dimensional variable.

In general, relative permeabilities are measured either by *steady-state* or *unsteady-state* methods (for a brief review of the methods commonly used to determine relative permeability, see Honarpour *et al.* [1]). In steady-state methods, the two-phases are simultaneously injected at a fixed ratio into a porous medium. When the system reaches steady-state conditions, the differential pressure and the saturation (by convention) of the wetting phase, S_w, are measured and the relative permeabilities can be calculated by using Darcy's law, eqn. (1). Steady-state methods are in general relatively accurate, easy to understand and implement straightforward and acceptable data processing procedures, namely regular/special core analysis. However, since the process needs to reach steady-state conditions it is, in general, time-consuming. Relative permeability curves are produced for a given porous medium and for a given pair of fluids by laboratory measurements when different flow conditions are imposed.

Diagrams of relative permeability for oil and water provide valuable and necessary data input in reservoir studies when estimating the producible reserves and the ultimate recovery. Nevertheless, we must point out that, at present, pragmatic sustainability issues on energy production/management (hydrocarbons, fuel cells, catalytic or trickle-bed reactors) shifted "recovery optimization" trends into "process efficiency optimization" scopes and targets. As a consequence, new challenges emerge within a wide spectrum of technological problems, extending from laboratory to industrial scale, e.g. unconventional/ enhanced oil recovery /carbon capture & sequestration processes, soil and aquifer pollution & remediation, operation of trickle-bed reactors [2]. To address these issues we need first to examine if any efficiency characteristics are inherent in the sought process, starting from its simpler form, immiscible steady-state.

The scope of the present work is to collect data from laboratory studies of steady-state two-phase flow in porous media, in order to examine if operational characteristics of such processes show a universal trend and, if that trend can be exploited in a systematic way.

Operational Efficiency Aspects of Two-Phase Flow in Porous Media

Consider the simultaneous flow of oil and water through a pore network. In order to induce and sustain specific flowrates of oil, $\tilde{q}_o$, and water, $\tilde{q}_w$, corresponding pressure differences, $\Delta\tilde{p}_o$ and $\Delta\tilde{p}_w$, must be effected upon the two phases. Consequently, an amount of mechanical power, $\tilde{W}$,

$$\tilde{W} = \tilde{q}_o\Delta\tilde{p}_o + \tilde{q}_w\Delta\tilde{p}_w \tag{2}$$

must be externally supplied to the system to balance the rate of mechanical energy dissipation within the process. The later is caused interstitially (a) by bulk viscous stresses in combination with the local rates of deformation, and, (b) by the velocities of moving menisci moving against local capillary pressure differences induced by contact angle hysteresis. The relative magnitude of the two contributions depends -among other factors- on the degree of disconnection of oil.

The reduced rate of mechanical energy dissipation, W, is defined as [3]

$$W = \frac{\tilde{W}}{\tilde{W}^{1\Phi}} = \tilde{W}\frac{\tilde{k}\tilde{\mu}_w}{\left(\tilde{\gamma}_{ow}Ca\right)^2} \tag{3}$$

where $\widetilde{W}^{1\Phi}$ equals the rate of mechanical energy dissipation of the equivalent one phase flow of water at a rate $\widetilde{q}^{1\Phi} = \widetilde{q}^{o} + \widetilde{q}^{w}$. $Ca = \widetilde{\mu}_w \widetilde{U}_w / \widetilde{\gamma}_{ow}$ is the capillary number, $\widetilde{\gamma}_{ow}$ the interfacial tension between the two phases and $r = \widetilde{q}_o / \widetilde{q}_w = \widetilde{U}_o / \widetilde{U}_w$ is the oil-water flowrate ratio. The value of Ca provides a measure of the viscous forces over the capillary forces. Ca and r, comprise the essential independent variables of the process (also called *operational parameters*) [3].

The efficiency of the process, with respect to the oil transport over the mechanical power supplied to it or "oil produced per kW of mechanical power dissipated in pumps", may be assessed by the values of the energy utilization coefficient, f_{EU}, a macroscopic quantity originally defined by Valavanides & Payatakes in the context of the development of the *DeProF* mechanistic model [3], as

$$f_{EU} = \frac{r}{W(Ca, r)} \tag{4}$$

The mechanistic model *DeProF* for immiscible steady-state two-phase flow in pore networks [3], predicts the relative permeability of each phase using the concept of decomposition in prototype flows. It combines effective medium theory with appropriate expressions for pore-to-macro scale consistency for oil and water mass transport and takes into account the pore-scale mechanisms and the network-wide cooperative effects as well as the sources of non-linearity, caused by the motion of interfaces and other complex effects. Using the *DeProF* model, one can obtain the solution to the problem of steady-state two-phase flow in porous media in terms of the capillary number, Ca, the oil/water flowrate ratio, r, the oil/water viscosity ratio, $\kappa = \widetilde{\mu}_o / \widetilde{\mu}_w$, the advancing and receding contact angles, and a parameter vector, comprising not only the absolute permeability but also dimensionless parameters describing geometrical and topological characteristics of the porous medium affecting the flow (the latter are regarded as the *system parameters*).

Extensive simulations using the *DeProF* model algorithm revealed that a continuous line, r*(Ca), exists in the (Ca, r) domain for which the energy utilization index takes locally maximum values. This line appears when the ridge of the f_{EU}(Ca,r) surface is projected on the (Ca, r) plane, see Fig. 1, whereby the effect of Ca and r on the energy utilization index, f_{EU}, is depicted by "mountain-range" or "half-croissant" shaped surfaces).

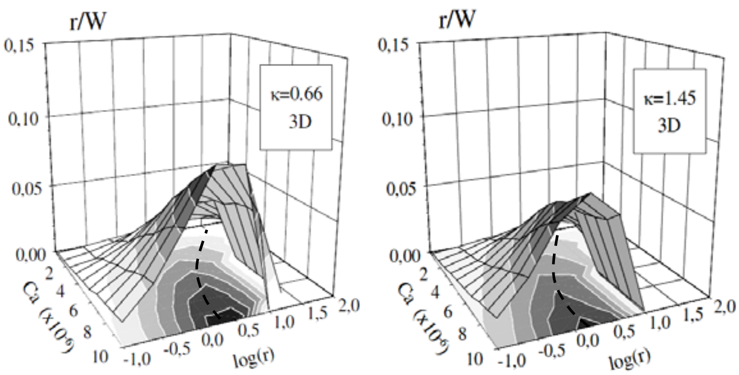

Fig 1. Energy utilization factor, f_{EU}=r/W, as a function of Ca and r. The diagrams pertain to 3D pore network *DeProF* simulations for two o/w systems with viscosity ratios $\kappa = 0{,}66$ and 1,45 [3]. Dashed lines represent the projection of the ridge of the f_{EU}(Ca,r) surface on the (Ca,r) planeeasurement of RCSP and patient charts

The existence of 'optimum conditions' for oil transport in two-phase flow in pore networks is a consequence of the remarkable internal adaptability of the flow to externally imposed flow constraints (Ca, r) and its inherent characteristic in self adjusting the connected versus disconnected moving-oil

ISBN: 978-1-61804-295-8

balance. Detecting and setting such conditions is of ample importance in real processes of industrial scale. It is therefore imperative to challenge the *DeProF* theory claims regarding the existence of optimum operating conditions (OOC) in such processes and in the course of the present work we will provide the necessary experimental evidence. To this end, relative permeability diagrams for steady-state two-phase flow in porous media published in the literature are examined.

Transformation of Relative Permeability Data into Operational Efficiency Data

The transformation originally introduced by Valavanides [3] for steady-state two-phase flows in porous media,

$$r = \frac{\tilde{q}_o}{\tilde{q}_w} = \frac{\tilde{U}_o}{\tilde{U}_w} = \frac{k_{ro}/\tilde{\mu}_o}{k_{rw}/\tilde{\mu}_w} = \frac{1}{\kappa}\frac{k_{ro}}{k_{rw}} \qquad \& \qquad f_{EU} = \frac{k_{ro}}{\kappa(r+1)} = \frac{r k_{rw}}{r+1} = k_{ro}\left(\frac{k_{ro}}{k_{rw}} + \kappa\right)^{-1} \quad (5)$$

where $\kappa = \tilde{\mu}_o/\tilde{\mu}_w$ is the oil/water viscosity ratio, is valid for steady-state flow conditions. It was implemented in reconstructing measured relative permeability vs saturation data sets, $\{k_{ro}, k_{rw}, S_w\}$, into corresponding energy utilization vs flowrate ratio data sets, $\{f_{EU}, r\}$. The proof of eqns (5) is based on the observation that in steady-state conditions, the pressure gradient is the same in both phases, or, equivalently, the mobility ratio equals the flowrate ratio ([3], [6]).

Table 1. Classification of the re-examined laboratory studies [4-27] pertaining to a variety of steady-state flows in sand packs, plug cores, glass micromodels and virtual p.m. and fluid systems.

Core plug type	**Lab runs**
Berea sandstone	36
Carbonate core	3
Glass (incl. Pyrex^{TM}) pore network models	15
Loudon core	3
Teflon (consolidated, porous)	3
Propant pack	2
Bentheimer	2
Clashach sandstone	1
Virtual cores (L-B or CFD simulations)	19
Outcrop chalk	2
Pyrex (crushed)	2
In total	**88**

Viscosity ratio $\kappa = \tilde{\mu}_o/\tilde{\mu}_w$	**Lab runs**
Favorable, $\kappa < 1$	31
$\kappa = 1$	8
Unfavorable, $1 < \kappa$	48
Undisclosed	1
In total	**88**

Constant Ca runs	**53**

By using eqs. (5), reconstructions of $\{k_{ro}, k_{rw}, S_w\}$, into $\{f_{EU}, r\}$ data sets were produced for a total of 88 steady-state relative permeability diagrams from 24 published laboratory studies [4-27]. The re-examined systems and flow conditions examined have been coarsely classified in Table 1, whereas representative diagrams are presented in Figs. 2, 3 and 4.

The typical reconstruction of $\{k_{ro}, k_{rw}, S_w\}$, into $\{f_{EU}, r\}$ data sets is presented in Fig. 2, whereby steady-state relative permeability diagrams published in [4] & [10], are transformed into energy utilization diagrams.

ISBN: 978-1-61804-295-8

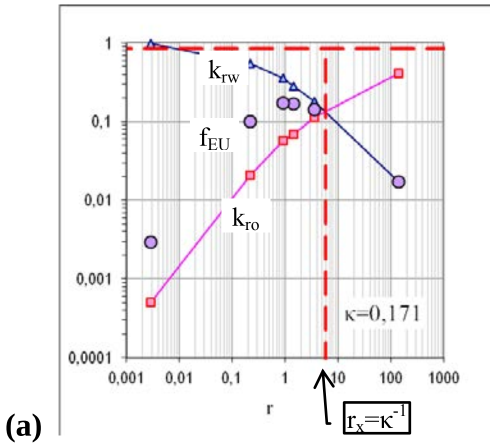

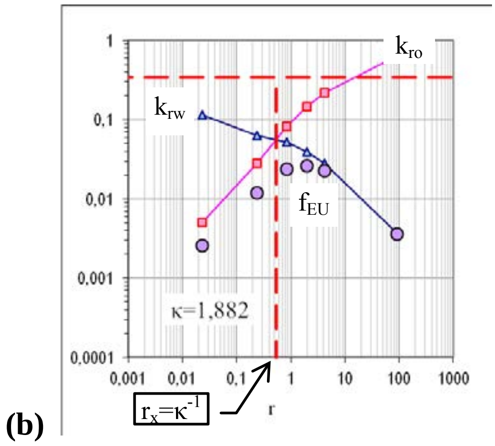

Fig. 2: Typical data sets of relative permeabilities for oil, k_{ro} (▫), & water, k_{rw} (▵) and energy utilization index, f_{EU}, (○) against flowrate ratio, r. The values of r & f_{EU} -computed through eqs (5) from source data- pertain to two typical systems: **(a)** favorable viscosity ratio in Berea sandstone [10] and **(b)** unfavorable viscosity ratio, in Clashach sandstone [4].

Results

The source relative permeability diagrams that were re-examined, together with the corresponding extracted data values and the diagrams produced from these data -when transformed by eqs. (5)- have been systematically recorded in a technical report (*ImproDeProF* project report, [28]). Here, the most representative diagrams are presented in Figs. 2, 3 and 4.

Referring to Figs. 2 - 4, the relative permeability data, k_{ri}, i=o,w and the corresponding logr and f_{EU} values, have been plotted together in appropriate (log-log) diagrams. Every set of {f_{EU}, logr} values, corresponding - through transformation eqs. (5)- to a {k_{ro}, k_{rw}} data set, presents a local maximum.

The majority of the examined relative permeability diagrams may be transformed into diagrams appearing as slide-cuts or curved-slice-cuts of surface diagrams similar to the f_{EU}(Ca, logr) diagrams predicted by the *DeProF* model (Fig. 1). In our review we found a few exceptional cases where there is either a lack of sufficient data, or, the original study was performed over a narrow span of flow conditions and optimum operating conditions have not been reached.

In all of the re-examined diagrams (Figs. 2 - 4 and [28]) the following trends are observed:

(a) Depending on the imposed flow conditions, the operational efficiency may vary by even two orders of magnitude. Optimum operating conditions, r*, are smooth functions of r in all diagrams and optimum operational efficiency can be reached in a smooth and continuous manner – there are no peaks or abrupt changes in f_{EU} with changes in r. Both attributes are of paramount importance when process efficiency is considered for industrial scale applications.

(b) Optimum operation conditions, r*, seem to depend primarily on the viscosity ratio, κ. The effect of other physicochemical parameters, e.g. wettability, porous medium structure is less obvious; to this end a systematic laboratory study should be designed.

(c) The dashed vertical line (in red) indicates the critical flowrate, r_x, for which the two relative permeabilities are equal. In all diagrams, the value of r_x is equal to the inverse of the viscosity ratio, $r_x = \kappa^{-1}$. The dashed horizontal line (in red) indicates the upper limit of the operational efficiency of the process, corresponding to pure viscous flow conditions ($Ca \to \infty$) [28].

(d) The flowrate ratio corresponding to the maximum value of f_{EU}, r*, is in general different than r_x. In systems with favorable viscosity ratios ($\kappa < 1$), $r^* < r_x$, whereas in systems with unfavorable viscosity ratios ($1 < \kappa$), $r_x < r^*$. The "distance" between these two figures, $|r^* - r_x|$, seem to correlate to the values of the system parameters and the imposed flow conditions.

ISBN: 978-1-61804-295-8

Favorable viscosity ratio, $\kappa = \tilde{\mu}_o / \tilde{\mu}_w < 1$

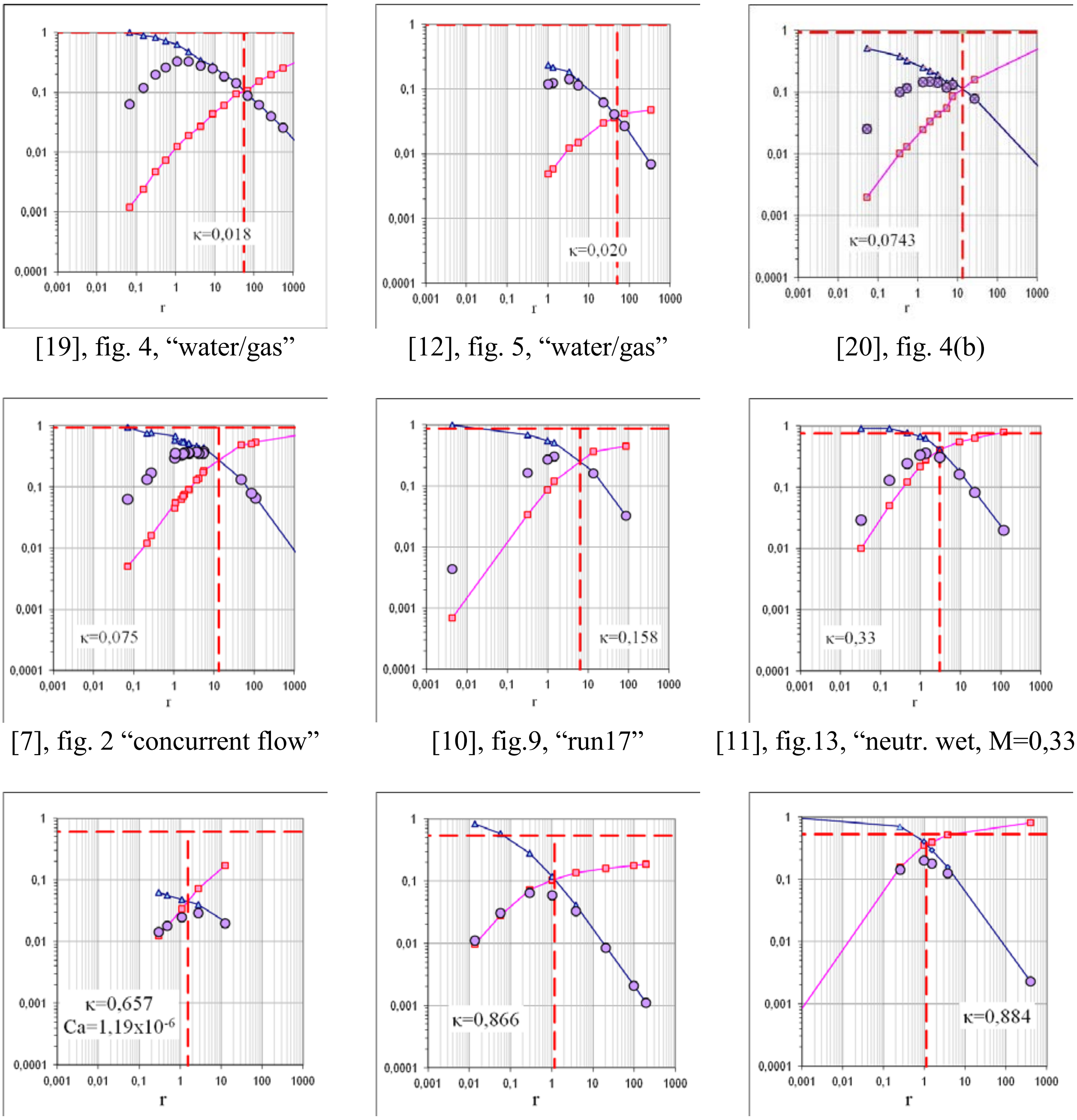

[19], fig. 4, "water/gas" — [12], fig. 5, "water/gas" — [20], fig. 4(b)

[7], fig. 2 "concurrent flow" — [10], fig.9, "run17" — [11], fig.13, "neutr. wet, M=0,33"

[5] "fig. 9(a)" — [25], fig. 2, "0,2cc/min" — [10], fig. 5, "run11"

Fig. 3 Relative permeabilities for "oil" (□) & "water" (△) and energy utilization index, f_{EU}, (○) against flowrate ratio, r, for "oil/water" systems with favorable viscosity ratios $\kappa = \tilde{\mu}_o / \tilde{\mu}_w < 1$ and for various flow conditions. Sub-legends refer source data.

ISBN: 978-1-61804-295-8

Unfavorable viscosity ratio, $1 < \kappa = \tilde{\mu}_o / \tilde{\mu}_w$

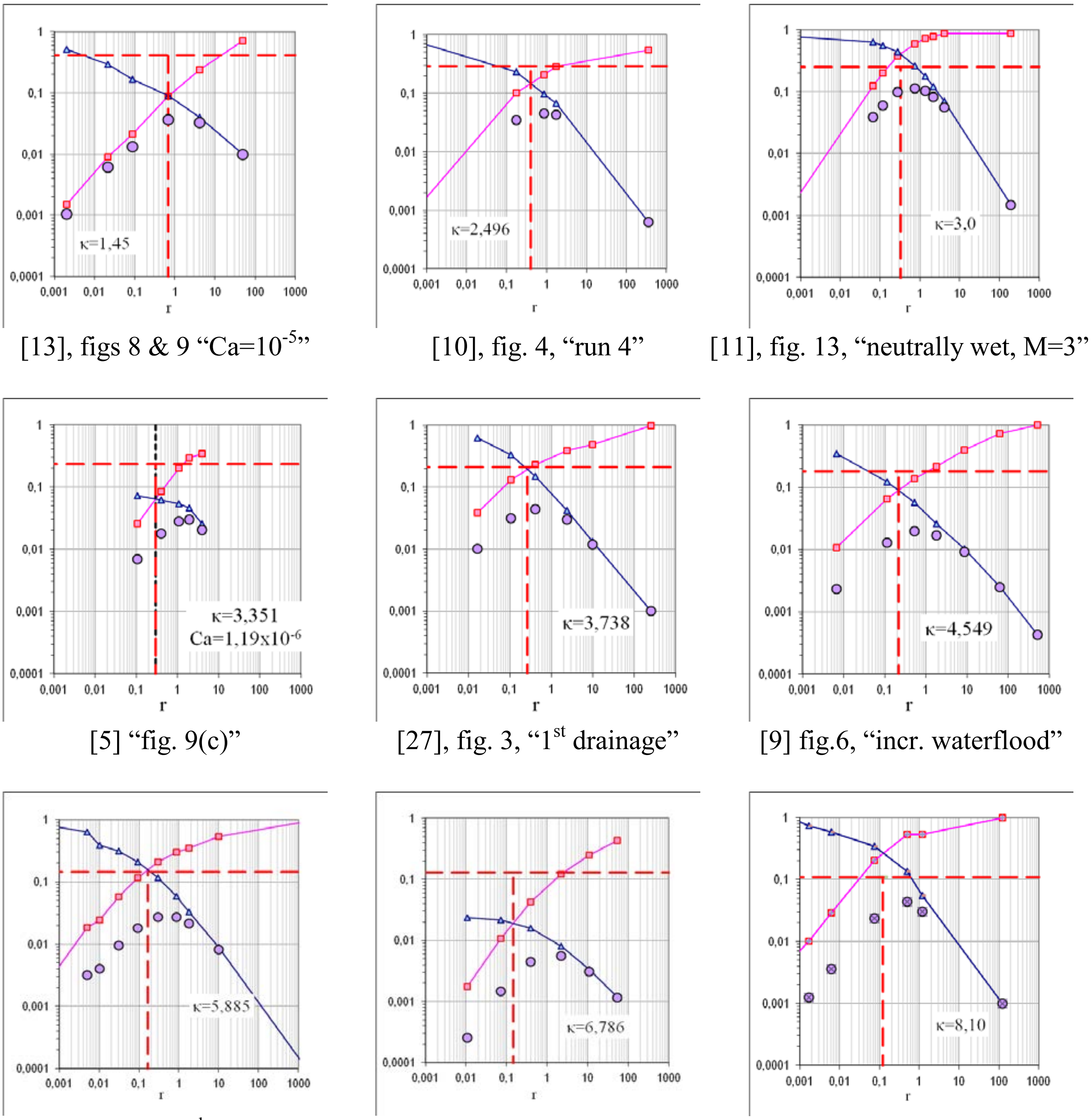

[13], figs 8 & 9 "Ca=10^{-5}" | [10], fig. 4, "run 4" | [11], fig. 13, "neutrally wet, M=3"

[5] "fig. 9(c)" | [27], fig. 3, "1st drainage" | [9] fig.6, "incr. waterflood"

[17], fig. 14, "2nd drainage" | [8] | [24], fig. 3, "drainage"

Fig. 4 Relative permeabilities for "oil" (□) & "water" (△) and energy utilization index, f_{EU}, (○) against flowrate ratio, r, for "oil/water" systems with unfavorable viscosity ratios $1 < \kappa = \tilde{\mu}_o / \tilde{\mu}_w$ and for various flow conditions. Sub-legends refer source data.

Conclusions

An extensive –but not at all exhaustive- retrospective examination was performed comprising a total of 88 published relative permeability diagrams, pertaining to a variety of steady-state two-phase flow conditions and types of porous media. Each set of relative permeability data was transformed into a corresponding operational efficiency diagram. In all cases, a local maximum of the process operational efficiency for that particular system and for the set of flow conditions examined was obvious.

The trend of the measured values of (r, f_{EU}) corresponding to (k_{rw}, k_{ro}) is remarkably similar –not to say identical at this stage- to the trend of the f_{EU}(Ca,r) values predicted by the *DeProF* model/algorithm. Moreover, in general, the derived diagrams can be seen as lateral curved "slice" cut-outs of the f_{EU}(Ca,r) diagrams in Fig. 1; this is so because most of the relative permeability curves published in the literature are furnishing permeability measurements at steady-state conditions but at different values of the capillary number. This experimental evidence supports the universality of the *DeProF* theory findings with respect to the existence of optimum operating conditions in steady-state two-phase flow in porous media and reveals an opportunity of further deciphering the physics of the sought process.

Two-phase flow in p.m. is "burdened": (a) with oil disconnection and capillarity effects that restrain or inhibit -to a certain extent- the superficial transport of oil & water, (b) the bulk phase viscosities of oil & water. Process engineers can take advantage of these natural intrinsic characteristics and judge where to set the balance between capillarity or viscosity.

The results also indicate there is a potential for normative flow characterization, as to its capillary or viscous character, based on a few appropriately selected, non-dimensional physical variables. To do so, the conditions whereby process efficiency attains a maximum value and its correlation with the process characteristics (oil-water-porous medium system properties and flow conditions) merit a systematic investigation.

Acknowledgements

This research work has been co-funded by the European Union (European Social Fund) and Greek national resources in the frameworks of the "Archimedes III: Funding of Research Groups in TEI of Athens" (MIS 379389) research project of the "Education & Lifelong Learning" Operational Program.

References

[1] M. Honarpour, L. Koederitz, A.H. Harvey, *Relative Permeability of Petroleum Reservoirs*, Boca Raton, Florida, USA, CRC Press, 1986, ISBN 0-8493-5739-X

[2] M.S. Valavanides, C.D. Tsakiroglou, M.A. Ioannidis, O. Vizika, "Unconventional modelling of multi-phase flows in porous media", *Minisymposium 1.03, 7th International Conference on Porous Media*, Padova, Italy, May 18-21, 2015. Available: http://www.interpore.org/padova.

[3] M.S. Valavanides, "Steady-State Two-Phase Flow in Porous Media: Review of Progress in the Development of the *DeProF* Theory Bridging Pore- to Statistical Thermodynamics- Scales", *Oil & Gas Science and Technology*, vol. 67, pp. 787-804, 2012. Available: http://dx.doi.org/10.2516/ogst/2012056 .

[4] F.R. Allen, D.A. Pucket, "Theoretical and experimental studies of rate-dependent two-phase immiscible flow", SPE10972, AEE Winfrith, Dorset, U.K. (1986) pp. 62-74

[5] D.G. Avraam, A.C. Payatakes, "Flow Regimes and Relative Permeabilities during Steady-State Two-Phase Flow in Porous Media", *J. Fluid Mech*, vol. 293, pp. 207-236, 1995.

[6] D.G. Avraam, A.C. Payatakes, “Flow Mechanisms, Relative Permeabilities and Coupling Effects in Steady-State Two-Phase Flow in Porous Media. Case of Strong Wettability”, *Industrial & Engineering Chemistry Research*, vol. 38, pp. 778-786, 1999.
[7] R.G. Bentsen, “Interfacial Coupling in Vertical, Two-Phase Flow Through Porous Media”, *Journal of Petroleum Science & Technology*, vol. 23 pp. 1341-1380, 2005.
[8] E.M. Braun, R.J. Blackwell, “A steady-state technique for measuring oil-water relative permeability curves at reservoir conditions”, SPE 10155 pp. 1-10, 1981.
[9] O.O. Eleri, A. Graue, A. Skauge, “Steady-state and unsteady-state two-phase relative permeability hysteresis and measurements of three-phase relative permeabilities using imaging techniques”, SPE 30764, University of Bergen, Norway 1995, pp. 643-653.
[10] R.A. Fulcher, T. Ertekin, C.D. Stahl, “Effect of capillary number and its constituents on two-phase relative permeability curves”, *Journal of Petroleum Technology*, vol. 37, pp 249-260, 1985.
[11] A. Ghassemi, A. Pak, “Numerical study of factors influencing relative permeabilities of two immiscible fluids flowing through porous media using lattice Botzmann method”, *Journal of Petroleum Science and Engineering*, vol. 77, pp. 135–145, 2011
[12] B. Lai, J. Miskimins, “A new technique for accurately measuring two-phase relative permeability under non-Darcy flow conditions” SPE 134501, *ATCE2010*, Florence, Italy, 2010, pp. 1-14.
[13] H. Li, C. Pan, C.T. Miller, “Pore-scale investigation of viscous coupling effects for two-phase flow in porous media”, *Phys. Rev. E,* vol. 72, no 26705, pp. 1-14, 2005.
[14] H.Y. Lo, N. Mungan, “Effect of temperature on water-oil relative permeabilities in oil-wet and water-wet systems”, SPE 4505 Dallas, Texas (1973) pp. 1-12.
[15] D.G. Longeron, L. Cuiec, F.A. Yahya, “Water-oil relative permeabilities in the case of a mixed-wet carbonate reservoir: influence of experimental conditions”, SCA 9324 *Annual Symposium of the Society of Core Analysts*, 1993, pp. 1-16.
[16] D. Maloney, K. Doggett, A. Brinkmeyer, “Special core analyses and relative permeability measurements on almond formation reservoir rocks” *NIPER*, vol. 648, pp. 1-30, 1993.
[17] S.K. Masalmeh, “The effect of wettability heterogeneity on capillary pressure and relative permeability”, *Journal of Petroleum Science and Engineering*, vol. 39, pp. 399-408, 2003.
[18] J.E. Nordtvedt, H. Urkedal, A.T. Watson, E. Ebeloft, K. Kolltveit, K. Langaas, I.E.I. Oxnevad, “Estimation of relative permeability and capilary pressure functions using transient and equilibrium data from steady-state experiments”, SCA 9418 *Annual Symposium of the Society of Core Analysts*, pp. 197-206, 1994.
[19] M.J. Oak, L.E. Baker, D.C. Thomas, “Three-phase relative permeability of berea sandstone”, *Journal of Petroleum Technology*, vol. 42, pp. 1054-1061, 1990.
[20] J-C Perrin, M. Krause, C-W Kuo, L. Miljkovic, E. Charob, S.M. Benson, “Core-scale experimental study of relative permeability properties of CO2 and brine in reservoir rocks”, *Energy Procedia*, vol. 1, pp. 3515-3522, 2009.
[21] T. Ramstad, N. Idowu, C. Nardi, P.E. Oren, “Relative permeability calculations from two-phase flow simulations directly on digital images of porous rocks”, *Transport in Porous Media*, vol. 94, pp. 487-504, 2012.
[22] J.L. Shafer, E.M. Braun, A.C. Wood, J.M. Wooten, “Obtaining relative permeability data using a combination of steady-state and unsteady-state core floods”, SCA 9009 *Annual Symposium of the Society of Core Analysts* Houston, Texas, 1990, pp. 1-16.
[23] Q. Sheng, K.E. Thompson, J.T Fredrich, P.A. Salino, “Numerical Prediction of Relative Permeability from MicroCT Images: Comparison of Steady-State versus Displacement Methods”, SPE 147431 pp. 1-16, 2011.
[24] A.W. Talash, “Experimental and Calculated Relative Permeability Data for Systems Containing Tension Additives”, AIME SPE5810, pp. 177-188, 1976.

[25] G.A. Virnovsky, Y. Guo, S.M. Skjaeveland, P. Ingsoy, “Steady-state relative permeability measurements and interpretation with account for capillary effects”, SCA 9502 *Annual Symposium of the Society of Core Analysts*, pp. 1-10, 1995.
[26] V.A. Virnovsky, K.O. Vatne, S.M. Skjaeveland, A. Lohne, “Implementation of multirate technique to measure relative permeabilities accounting for capillary effects”, SPE 49321, New Orleans, Louisiana, pp. 901-911, 1998.
[27] F.H.L. Wang, “Effect of wettability alteration on water/oil relative permeability dispersion and flowable saturation in porous media”, *SPERE* 15019, pp. 617-628, 1988.
[28] M.S. Valavanides, E. Totaj, M. Tsokopoulos, “Retrospective Examination of Relative Permeability Data on Steady-State 2-Ph Flow in Porous Media Transformation of Rel-Perm Data (k_{ro}, k_{rw}) into Operational Efficiency Data (f_{EU})”, ImproDeProF /Archimedes III, project internal report, 2014. Available: http://users.teiath.gr/marval/ArchIII/retrorelperm.pdf

CFD Simulation of Fractal Impeller and Baffle for Stirred Tank Reactor with a Single Stage 4 Blade Rushton Turbine

MANSHOOR Bukhari[1, a], MOHD JAMALUDIN Saddam[2,b], KHALID Amir[3,c] and ZAMAN Izzuddin[4,d]

[1,2,3,4]Centre for Energy and Industrial Environment Studies (CEIES),

Faculty of Mechanical and Manufacturing Engineering

Universiti Tun Hussein Onn Malaysia

86400 Pt. Raja, Batu Pahat, Johor

Malaysia

[a]bukhari@uthm.edu.my, [b]saddamjamaludin@gmail.com, [c]amirk@uthm.edu.my,

[d]izzuddin@uthm.edu.my

Keywords: CFD, Fractal, Mixing, Stirred tank

Abstract. Implementing the fractal design for baffles and impellers in stirred tank believe will influence the flow characteristic inside the stirred tank. Since the fractal pattern was proven as a good turbulent generator, a new concept of baffles and impellers which used a fractal design was proposed in a stirred tank to predict the fluid flow pattern and study an effectiveness of the new design in term of mixing performance. In order to investigate the kinds of flow properties, a commercial CFD software package was used to simulate the behaviour of flow pattern inside the stirred tank equipped with fractal baffles and also fractal impellers. Four configurations were simulated which are normal baffles and normal impellers, normal baffles and fractal impellers, fractal baffles and normal impellers, and the last configuration is fractal baffles and fractal impellers. The normal baffles and normal impellers were used as a reference for determination of mixing performance and the simulation was carried out by using the standard k-ε turbulence model. The results show that the stagnant regions were reducing significantly when the fractal baffles applied in the stirred tank. Besides that, high concentration of the velocity occurred when normal baffles used while the concentration just above the normal impellers was reduced by the usage of fractal impellers. It showed that the implementation of the fractal design was gave a certain level of mixing efficiency in stirred tank. The simulation by using the CFD software package also gives a good agreement with the experimental results and gave a high confidence for the results in order to determine the flow pattern in stirred tank with a new concept of baffles and impellers.

Introduction

Stirred tank reactor was commonly used in many industries such as chemical biotechnologies, chemical, food processing and many more [1]. Many design and specification were come out for stirred tanks and they were different according to its use [2]. Most of the study is to make the optimum stirred tank design configuration with good efficiencies of mixing process. Factors that influence the performance of mixing process are, mixing time, the type of blade, blade numbers, sizing and speed of the rotating blade and the use of baffle [3].

The performance of the stirred tank here was referred on how fast the mixing completed their process while at the same time can maintain or even reduce the operation cost. According to the interest in designing the most effective stirred tank, many researches, was focused on the optimization of the design of the stirred tanks and impellers geometry. For the effect of the number

ISBN: 978-1-61804-295-8

of impellers implemented in stirred tank, Franco et al. [4] was found that the effect of the vortex at the impeller blades shows turbulent fluid flow and mixing time shorter than one impeller. In order to carry out an analysis for the stirred tank, there are various technique was used. For example, Zalc et al. [5] was simulated a laminar flow in an impeller stirred tank using CFD tools. They were studied an effect of mixing time performance as a function of the impeller speed. Since the CFD can simulate various configuration of the stirred tank included the impellers and baffles, a lot of analysis can be done numerically.

On the basis of the previous research, there are a lot of study had been conducted on the mechanical stirred tank, particularly those equipped by various numbers of blades. However, there is lack of some particular system which is discuss regarding the design the blade itself and at the same time the rule of baffles to enhance the mixing process. In this paper, a simulation work has been carried out by using ANSYS Fluent software package to determine the fundamental mechanisms of mixing with a new pattern multi stage stirred tanks with fractal pattern baffled. At the same time, an effect of baffles in the stirred tank on the mixing performance also been discussed. For the simulation work, the authors have focused on the low Reynolds number mixing regime because this situation are the most common problem occurs in practical applications.

Fractal concept. Fractal is basically a repeated shape and self-similarity to an infinitely small scale [6]. According to Karl Weiertrass, the mathematician who was introduced Weierstrass function in 1923, the fractal is continuous everywhere but differential nowhere. Helge Von Koch in 1904 then refined the definition of the Weierstrass function and adds on a more geometric definition that called Koch snowflake. As a high turbulent level occurred when a fluid flow through the fractal pattern [7], we expect that the fractal shape can give a significant effect on mixing effectiveness due to their self similar shape. Another advantages of the fractal pattern that motivated us to apply as a pattern for baffles and impellers in stirred tanks because of low pressure drop across them [8]. Research on the space filling fractal were carried out by Hurst & Vassilicos [9] who found that the static pressure drop for the space filling fractals is independent of the thickness factor; moreover, away from the grids the homogeneity is improved as a function of the thickness factor. In this research, square grid fractal was chosen as a pattern that will apply to the baffles and impeller for the purpose of research. The square grid fractal is as in Fig. 1 below.

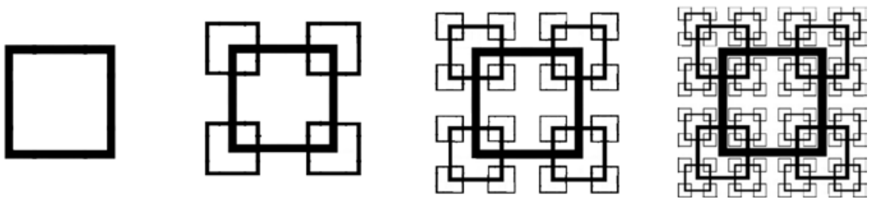

Initiator 2nd iterations 3rd iterations 4th iterations

Fig. 1: Square grid space filling fractal from initiator to higher order iterations up to the 4th level of fractal [7]

Simulation Model

For the simulation work, the model of stirred tank was build to investigate flow behaviour in the stirred tank equipped with a fractal impellers and baffles. The model of stirred tank used here is a clear cylindrical tank with a diameter, T = 300mm. The rest of stirred tank components dimension are referred to the diameter of the tank. This tank was equipped with 4-blade multi-stage impellers with the impeller shaft located at the axis of the tank, a flat bottomed and fitted with four symmetrical baffles at 90◦ interval against the tank wall. The model of stirred tank that was set up for the simulation work is shown in Fig. 2 and the dimensions of the tanks are given in Table 1.

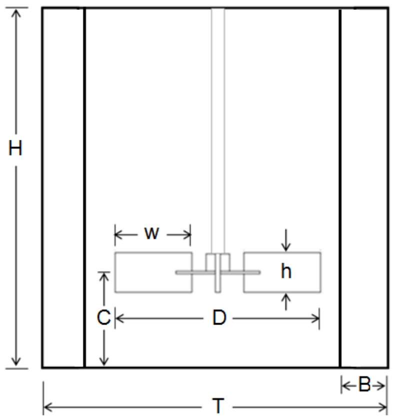

Fig. 2: Schematic diagram of a baffled tank with a multi-stage turbine impeller.

Table 1 Dimensions of the stirred tank designed

General parameters	Dimension (mm)
Tank diameter, (*T*)	*300*
Depth of liquid, (*H*)	*1T*
Impeller diameter, (*D*)	*T/3*
Impeller blade width, (*w*)	*D/4*
Impeller blade height, (*h*)	*D/5*
Baffles width, (*B*)	*T/10*
Impeller clearance, (*C*)	*T/3*

In this simulation, four configurations of the simulation models were set up and the configurations were chose in order to determine the effect of each configuration for the flow pattern in the stirred tank. The configurations are Standard Baffles and Standard Impellers (*SBSI*), Fractal Baffles and Standard Impellers (*FBSI*), Standard Baffles and Fractal Impellers (*SBFI*) and Fractal Baffles and Fractal Impellers (*FBFI*). Summary of the configurations are shown in Table 2 below. The simulation model and the meshing were shown in Fig. 3 below. In order to investigate the effect of the baffles and impellers configuration, the working fluid used in this simulation was air.

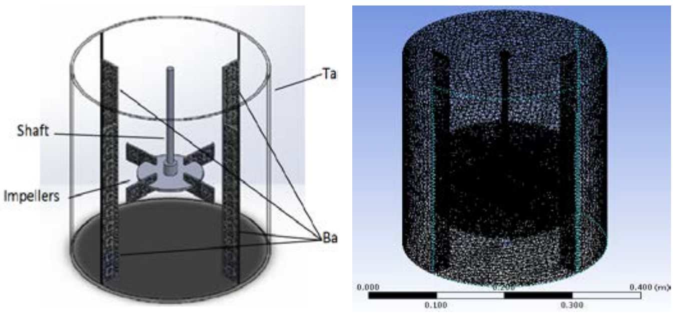

Fig. 3. Simulation model for the stirred tank with fractal baffles and impellers and the meshing of the model

Table 2. Configurations used for simulation work

Configuration	**Baffles**	**Impeller**
1^{st} (*SBSI*)	Standard	Standard
2^{nd} (*FBSI*)	Fractal	Standard
3^{rd} (*SBFI*)	Standard	Fractal
4^{th} (*FBFI*)	Fractal	Fractal

Simulation Model

The simulation results for the fractal impeller and baffle for stirred tank reactor with a single stage 4-blade rushton turbine were presented by a velocity contour at the vertical cross section of the tank and also at the blade cross section as in Fig. 4. A significant effect of the fractal pattern in the stirred tank in clearly showed in the figure in term of velocity distribution. The first image was a figure for SBSI which is a common flow occurred in current stirred tank available nowadays. The combination of standard baffles and impellers shows the flow distribution are mostly scattered in all regions around the tank and a little bit small vortex occur between the impellers.

Second configuration which is FBSI, it showed that the flow have a nearly similar pattern as in the first configuration. However the flow moved smoothly around the baffles and this give advantages due to low pressure drop when the fractal baffles implemented to the stirred tank. Again for the implementation of fractal baffles for the third configuration, SBFI, the flow pattern are clearly similar when it cross the fractal impellers and the flow around the impellers had a good movement without any concentrated particles around that.

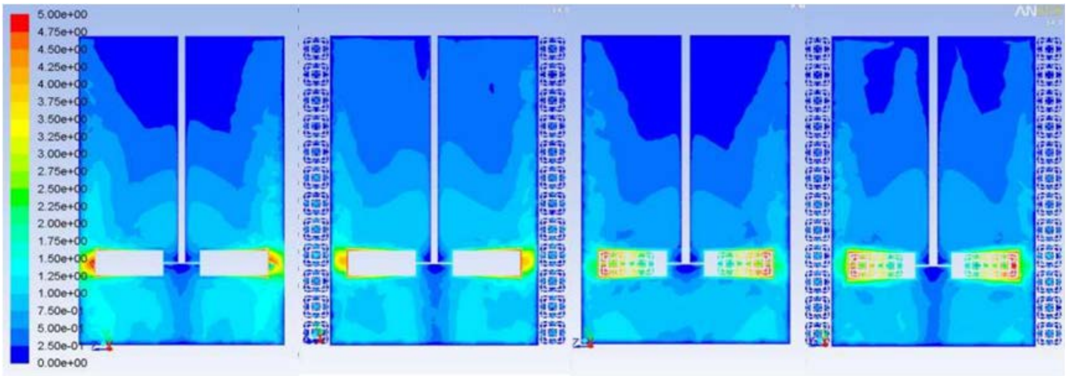

SBSI *FBSI* *SBFI* *FBFI*

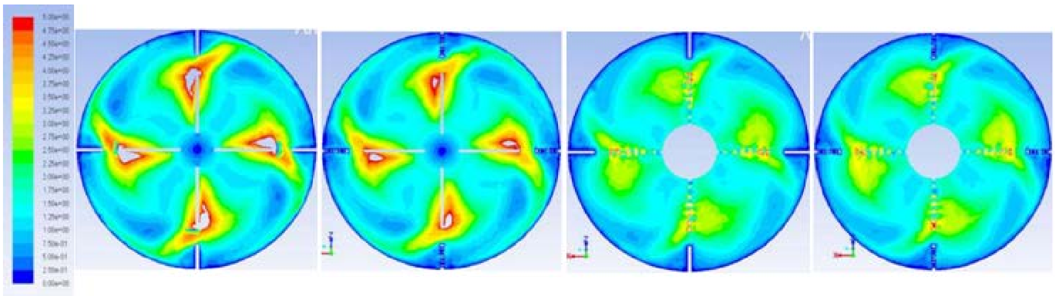

SBSI *FBSI* *SBFI* *FBFI*

Fig. 4: Velocity contour and velocity vector for four configurations of simulation models

The last configuration which is the implementation of fractal pattern for both baffles and impellers give the best configuration in this study. The results showed in the last image in Fig. 4 above gave a clear view on how the fractal pattern influenced the flow in the stirred tank. The velocity contour seems to be fairly distributed in the tank and there is no fluid concentration on the fractal baffle as compared to normal baffle on other configurations. The results gave a good agreement with a previous research which is the fractal pattern can generate high turbulent level; hence enhance the mixing in the stirred tank.

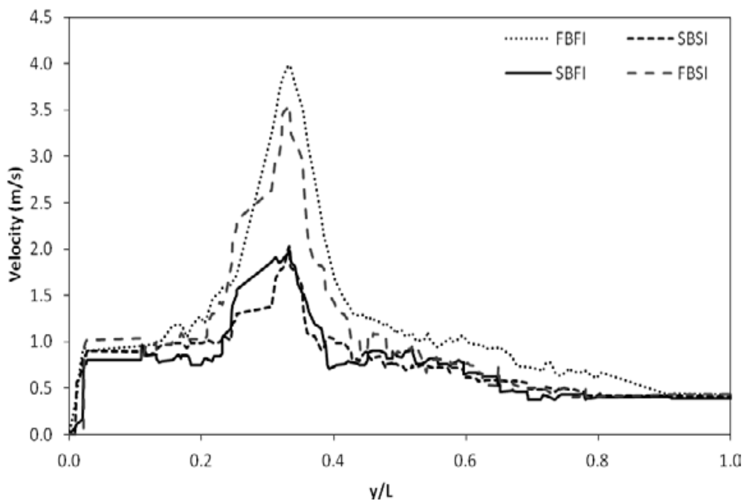

Fig. 5. Velocity distribution along the vertical line at distance T/4 from centre of stirred tank

Besides the flow pattern that clearly gave a good result in term of the implementation of fractal baffles and impellers for a stirred tank, the velocity plot along a selected vertical location in the stirred tank also were come out as a result in this paper. Fig. 5 showed a velocity distribution along the vertical line at distance T/4 from the centre of stirred tank. As we can see from the figure, high velocity occurred at the area near the impeller tips. More interesting here is the highest velocity occurred at the fractal impeller where it is important for a fluid mixing to have a high velocity to ensure a homogeneous mixing in the tank.

Conclusion

As a conclusion, this research study of the new approaches of fractal baffles and impellers have successfully done by fulfilling the requirement of main objectives for this study. The concept of the square grid was developed based on fractal pattern and had been applied to generate a new approach of baffles and impellers in stirred tank. The simulation results were showed that the velocity contour and velocity magnitude have a different flow pattern in stirred tank by using fractal design on four blade single-stage impellers and baffles. Besides that, the highest velocity occurred at the fractal impellers tips and it gave advantages of the fractal designed impeller where the highest velocity can give an influence in mixing criteria in stirred tank. Although this idea is a basic concept, it can be improved in order to provide better results in term of fluid mixing and also the flow pattern in stirred tank.

Acknowledgements

Partial support was provided by MOHE (Ministry of Higher Education, MALAYSIA) and Universiti Tun Hussein Onn Malaysia (UTHM) under the Fundamental Research Grants Scheme (FRGS), vote 1466.

References

[1] Zadghaffari R, Moghaddas J.S. and Revstedt J., *A Study on Liquid-Liquid Mixing in a Stirred Tank with a 6-Blade Rushton Turbine*, Iranian Journal of Chemical Engineering. (2008) **5**(4): 12-22.

[2] Aubin J., Kresta S.M., Bertrand J., and Fletcher D.F., *Alternate Operating Methods for Improving the Performance of a Continuous Stirred Tank Reactor*, Trans IChemE, (2006) 84:569-582.

[3] M.P. Isabela and S.O. Leandro, *CDF Modelling and Simulation of Transesterification Reactions of Vegetable Oils with an Alcohol in Baffled Stirred Tank Reactor,* Applied Mechanics and Materials. Vol.390 (2013) pp 86-90

[4] Franco M., Giuseppina M., Davide P., and Alessandra P, *Mixing time in high aspect ratio vessel with multiple impeller*, Chemical Engineering Science, (2013) 101:712-720

[5] Zalc J.M., Szalai E.S., Alvarez M.M. and Muzzio F.J., *Using CFD to understand chaotic mixing in laminar stirred tanks*, AIChE Journal, (2002), 48;2124-2134.

[6] Manshoor B, Zaman I, Othman M.F and Amir Khalid, *Experimental Study of Circle Grid Fractal Pattern on Turbulent Intensity in Pipe Flow*, IOP Conference Series: Material Science and Engineering. 50 (2013) 012014

[7] Manshoor B and Amir Khalid, *Numerical Investigation of the Circle Grids Fractal Flow Conditioner for Orifice Plate Flowmeter*. Applied Mechanics and Materials, (2012) 229-231: 700-704

[8] Manshoor B, Zaman I. and Amir Khalid. *Experimental study of pressure drop after the circle grids fractal orific*e. Applied Mechanics and Materials. (2013) 390:111-115

[9] Hurst D. and Vassilicos J.C., *Scalings and decay of fractal-generated turbulence*. Physics of Fluids. (2007) **19**(3).

Cell Model for Electromagnetic Axial Flow over a Cylinder: Part II. Transverse Radial Magnetic Field

Sunil Datta[1,a], Manju Agarwal[1,b], Anatoly Filippov[2,c]* and Sergey Vasin[2,d]

[1]Department of Mathematics and Astronomy, Lucknow University, Lucknow, 226007, India

[2]Department of Higher Mathematics, Gubkin Russian State University of Oil and Gas,

Leninsky pr., 65-1, Moscow, 119991, Russia, e-mail:

[a] sv.datta@gmail.com, [b] manjuak@yahoo.com, [c] filippov.a@gubkin.ru, [d] s.vasin@rambler.ru

Keywords: cell model, magnetic field, cylinders covered by a porous shell, hydrodynamic permeability

Abstract. In this paper we consider the filtration problem across a membrane composed of an aggregate of parallel circular cylinders wherein each cylinder is covered by a concentric porous shell and subject to transverse radial magnetic field. The cell model is applied so that system is taken as equivalent to a single cylinder encased in the porous shell and enclosed by a concentric cylindrical enveloping surface under axial flow of a conducting fluid subject to approximately radial magnetic field. Our aim is to evaluate the effect of magnetic field on the permeability parameter. The results are then graphically presented and discussed. The analysis reveals that hydrodynamic permeability decreases with Hartmann number M for all given values of porosity and that increasing the porosity increases the permeability for all values of M.

Introduction

Cell model was advanced by Happel in 1959 [1] and Kuwabara also in 1959 [2] to obtain in a simple manner the analytical results for the complex problem of flow past a concentrated assemblage of particles. The method is dealt with in the above papers and also in the book *Low Reynolds Number Hydrodynamics* by Happel and Brenner [3]. The cell method is concerned with the study of slow flow past a swarm of concentrated particles. The essence of the method consists of replacing the swarm by a single particle enclosed in an envelope and the interaction effect of the multitude of particles being accounted by suitable boundary conditions at the enveloping surface. The use of this method in our context follows from observing that filtration membrane is composed of an aggregate of tiny particles through which a fluid percolates slowly.

Vasin and Filippov (2004) [4] used cell model to evaluate the hydrodynamic permeability for a system of solid spherical particles covered with a porous shell and in a subsequent paper [5] extended the results for the more general problem of a complex porous media. In another paper (2009) [6] they investigated the flows in a concentrated media composed of rigid impenetrable cylinders covered with a porous layer; both transverse and longitudinal flows of filtering fluid were taken up. Amongst similar works, we may mention the contributions of Kirsh [7, 8].

Here we aim to study the controlling factor of electromagnetic Lorentz force when the fluid is electrically conducting and flows through a membrane composed of array of parallel circular non-conducting cylinders with each cylinder covered by a porous layer and subject to transverse radial magnetic field. We take into consideration two scales of porosity, namely, *microporosity* – porosity of the layer which covers impermeable cylindrical fibers, and *macroporosity* – a fraction of free space between cylindrical fibers with a porous layer. The flow in the clear fluid is governed by Stokes' equation and in the porous medium by Brinkman equation [9].

In previous papers [10, 11] of this study of cell model for hydromagnetic axial flow over a cylinder, we have studied the case of uniform transverse magnetic field. But here we introduce an additional parameter in the form of porosity of the porous shell covering each of the constituent impermeable cylinders.

ISBN: 978-1-61804-295-8

1. Basic Equations

The basic hydromagnetic field quantities are velocity $\mathbf{u}'$, pressure p', magnetic field $\mathbf{B}'$, electric field $\mathbf{E}'$ and current density vector $\mathbf{J}'$. Let us consider in the polar coordinate system axial flow $\mathbf{u}'(r)$ along a cylindrical body (composed of a solid core covered by a concentric porous shell) of radius a and subject to “almost radial” magnetic field $\left(B_0 / r'\right)\mathbf{e}_r$ [See Figs.1, 2].

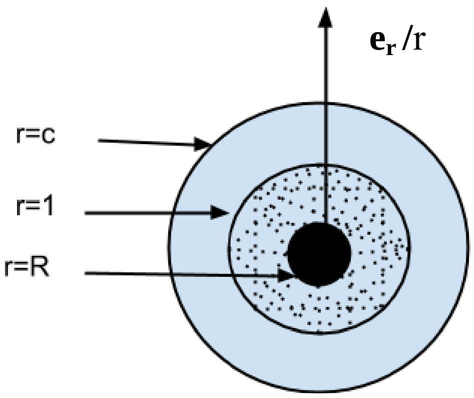

Fig.1. Normal section of the cell.

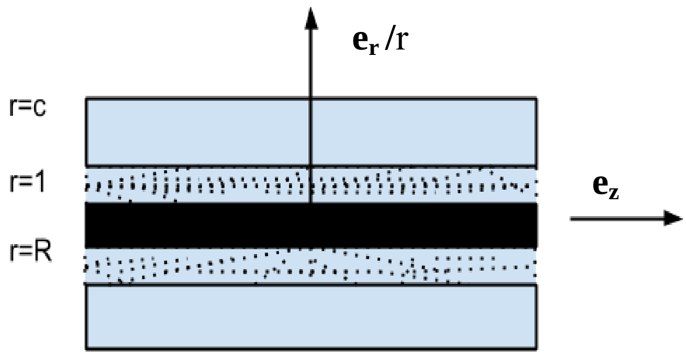

Fig.2. Transverse section of the cell.

It will be convenient to non-dimensionalize the quantities as follows

$$
\begin{aligned}
&r' = ar,\ z' = az,\ \mathbf{u}' = U_0\mathbf{u},\ p' = \frac{\mu U_0}{a} p, \\
&\mathbf{B}' = B_0\mathbf{B},\ \mathbf{E}' = U_0 B_0 \mathbf{E},\ \mathbf{J}' = \sigma\mu_m U_0 B_0 \mathbf{J},
\end{aligned} \tag{1}
$$

where U_0 is characteristic value of velocity, μ is viscosity of pure liquid, μ_m – magnetic permeability and σ – electric conductivity. Governing equations in non-dimensional form are as follows:

Stokes Equation:

$$\nabla p = \nabla^2 \mathbf{u} + M^2 \mathbf{J} \times \mathbf{B}, \tag{2}$$

$$\nabla . \mathbf{u} = 0. \tag{3}$$

Brinkman Equation:

$$\nabla p = m\nabla^2 \mathbf{u} - s^2 \mathbf{u} + M^2 \mathbf{J} \times \mathbf{B}, \tag{4}$$

$$\nabla . \mathbf{u} = 0. \tag{5}$$

Here $M^2 = \sigma a^2 B^2{}_0 / \mu$ is square of Hartmann number, $m = \mu_e / \mu$ is the ratio of effective viscosity in porous medium μ_e to viscosity of pure liquid μ, and $s^2 = \dfrac{a^2}{k}$ is dimensionless parameter (k being specific permeability of microporous medium).

Maxwell equations:

$$\nabla \times \mathbf{E} = 0,\ \nabla . \mathbf{E} = \rho_e, \tag{6}$$

$$\nabla \times \mathbf{B} = R_m \mathbf{J},\ \nabla . \mathbf{B} = 0, \tag{7}$$

ISBN: 978-1-61804-295-8

here $\rho_e = \rho_e' a / \left(\kappa U_0 B_0\right)$ is dimensionless total charge density (ρ_e' is dimensional total charge density, κ is dielectric constant), $R_m = \mu_m \sigma U_0 a$ is magnetic Reynolds number.

Ohm's law:

$$\mathbf{J} = \mathbf{E} + \mathbf{u} \times \mathbf{B}. \tag{8}$$

Continuity equation for current density vector:

$$\nabla.\mathbf{J} = 0. \tag{9}$$

Resler and Sears [12] pointed out that the term $\mathbf{u} \times \mathbf{B}$ in Ohm's can be taken to represent a tiny generator or source of e.m.f at any point in the moving fluid. The vector $\mathbf{E}$ represents the total electric field arising out of internal causes such as separation of charges or polarization and external causes such as charged boundaries of the flow. Thus the electric field *cannot be dissociated from the fluid motion*; its value within the fluid element is directly affected by the motion of the element and is taken to be of the order $\mathbf{u} \times \mathbf{B}$. Hence, keeping in view equation (9), we conclude that for $\mathbf{E}$ to vanish, we must have

$$\nabla.(\mathbf{u} \times \mathbf{B}) = 0. \tag{10}$$

2. Framing of the Problem

As noted earlier, the purpose of the work is to describe the process of filtration through a membrane consisting of impermeable cylindrical fibers coated with a microporous layer. The cell method simplifies the problem to consideration of uniform steady flow in the axial direction, taken along the z axis of a cylinder enveloped in a cell and subject to transverse radial magnetic field [See Figs.1, 2]. Thus, in the non-dimensional variables the particle is of unit radius, composed of an impermeable inner cylinder of radius $R = 1 - \delta$ and a microporous shell encasing it (δ - the thickness of microporous layer); the enveloping cylinder is of radius $c = 1/\gamma$ ($\varepsilon = 1 - \gamma^2$ is macroporosity). Flow velocity $\mathbf{u}$ is directed along the axis of the cylinder and applied magnetic field $\mathbf{e}_r / r$ in the transverse radial direction. It may be seen that except for pressure all quantities are independent of z and functions of r alone. Further, we assume that magnetic Reynolds number R_m is small and find that only z - component of magnetic field is induced. Also, we take $m = 1$ but the analysis may be extended to other positive values of m. Thus, the problem reduces to the determination of the differential equations and boundary conditions for the velocity $\tilde{u}(r)\mathbf{e}_z$ and induced magnetic field $b(r)\mathbf{e}_z$.

Thus, we take

$$\mathbf{u} = \tilde{u}(r)\mathbf{e}_z, \tag{11}$$

$$\mathbf{B} = \frac{\mathbf{e_r}}{r} + b(r)\mathbf{e}_z. \tag{12}$$

We find that

$$\mathbf{u} \times \mathbf{B} = \frac{\tilde{u}\mathbf{e}_\theta}{r}, \tag{13}$$

so that

ISBN: 978-1-61804-295-8

$$\nabla.\mathbf{u}\times\mathbf{B}=0. \tag{14}$$

Hence, we can take $\mathbf{E}=0$. We may check that all the hydromagnetic equations are satisfied with $\mathbf{u}$ and $\mathbf{B}$ given by (11) and (12). Now onwards, we shall designate velocity $\tilde{u}(r)$ in the Stokes region II $(1<r<c)$ by $u(r)$ and in the Brinkman region I $(R<r<1)$ by $v(r)$.

2.1 MHD equations for the problem

For the problem in hand, we find that the component Stokes, Brinkman and Maxwell equations (2)–(7) are expressible as below.

Stokes and Maxwell Equations in region II:

$$0=-\frac{\partial p}{\partial r}+\frac{M^2ub}{r}, \tag{15}$$

$$0=-\frac{\partial p}{\partial z}+\frac{1}{r}\frac{d}{dr}\left(r\frac{du}{dr}\right)-\frac{M^2u}{r^2}, \tag{16}$$

$$-\frac{\partial b}{\partial r}=\frac{R_m u}{r}. \tag{17}$$

The equation (16) shows that $\partial p/\partial z$ is constant and this leads to the determination of velocity u. Equation (17) provides the induced magnetic field b and then the first one the pressure as a function of r and z.

Brinkman and Maxwell Equations in region I:

$$0=-\frac{\partial p}{\partial r}+\frac{M^2vb}{r}, \tag{18}$$

$$0=-\frac{\partial p}{\partial z}+\frac{1}{r}\frac{d}{dr}\left(r\frac{dv}{dr}\right)-s^2v-\frac{M^2v}{r^2}, \tag{19}$$

$$-\frac{\partial b}{\partial r}=\frac{R_m v}{r}. \tag{20}$$

It may be noted that in the region I, we continue to write the same symbols for pressure p and induced magnetic field b, this is because pressure gradient $\partial p/\partial z=-P$ is constant and we are not here evaluating p as we are interested in finding the velocity field and for that equations (16) and (19) together with the boundary conditions are sufficient. The differential equations (16) and (19) with $P=1$ are

$$r^2\frac{d^2u(r)}{dr^2}+r\frac{du(r)}{dr}-M^2u(r)=-r^2, \text{ (Stokes' Region)} \tag{21}$$

$$r^2\frac{d^2v(r)}{dr^2}+r\frac{dv(r)}{dr}-\left(M^2+s^2r^2\right)v(r)=-r^2, \text{ (Brinkman's Region).} \tag{22}$$

2.2 Boundary Conditions

At the solid surface $r=R$ no slip:

ISBN: 978-1-61804-295-8

$$v(R) = 0\,. \tag{23}$$

At the interface $r = 1$ continuity of the velocity:

$$u(1) = v(1) \tag{24}$$

and continuity of the stress:

$$\frac{dv}{dr} = \frac{du}{dr}\,. \tag{25}$$

At the cell envelope $r = c$ Happel, Kuwabara, Kvashnin, Morse-Mehta/Cunningham conditions [6], all reduce to

$$\frac{du}{dr} = 0\,. \tag{26}$$

3. Solution of the problem

It may be observed that the two differential equations (21) and (22) of the second order posses three kinds of solution respectively for $M \neq 0;\, 2$, $M = 0$ and $M = 2$.

3.1. Solution for $M \neq 0;\, 2$

Thus we express below the solution of Stokes' equation (21)

$$u(r) = c_1 r^{-M} + c_2 r^{M} + \frac{r^2}{M^2 - 4} \tag{27}$$

and solution of Brinkman's equation (22)

$$v(r) = c_3 I_M(sr) + c_4 K_M(sr) - I_M(sr)\int_R^r x K_M(sx)dx + K_M(sr)\int_R^r x I_M(sx)dx\,, \tag{28}$$

here $I_M(sr)$ and $K_M(sr)$ are modified Bessel functions of first and second kind. Integrals in (28) are expressed in terms of Lommel's functions and have different types, depending on parameter *M*. Constants c_1, c_2, c_3, c_4 may be obtained by applying the boundary conditions (23)–(26), but their expressions are too unwieldy to be reproduced here.

3.2. Solution in the case of $M = 0$

In this case, we get

$$u(r) = \frac{I_0(Rs)[\gamma^2 K_2(s) - K_0(s)] - K_0(Rs)[\gamma^2 I_2(s) - I_0(s)] - 2(\gamma/s)^2}{2s\gamma^2[I_1(s)K_0(Rs) + I_0(Rs)K_1(s)]} + \frac{\ln r}{2\gamma^2} + \frac{1 - r^2}{4} \tag{29}$$

and

$$v(r) = \frac{s(\gamma^2 - 1)[K_0(rs)I_0(Rs) + K_0(Rs)I_0(rs)] - 2\gamma^2[K_0(rs)I_1(s) + K_1(s)I_0(rs)]}{2\gamma^2 s^2[I_1(s)K_0(Rs) + I_0(Rs)K_1(s)]} + \frac{1}{s^2}\,. \tag{30}$$

3.3. Solution for $M = 2$

In this case, we get

$$u(r) = c_1 r^2 + \frac{c_2}{r^2} - \frac{r^2 \ln r}{4} \tag{31}$$

and

$$v(r) = c_3 K_2(rs) + c_4 I_2(rs) + \frac{r^2}{4} I_2(rs) G_{1,3}^{3,0}\left(\frac{rs}{2}, \frac{1}{2}\middle| \begin{matrix} 0 \\ -1, -1, 1 \end{matrix}\right) + \frac{K_2(rs)[2 + rsI_1(rs) - 2I_0(rs)]}{s^2}, \tag{32}$$

where $G_{1,3}^{3,0}\left(\frac{rs}{2}, \frac{1}{2}\middle| \begin{matrix} 0 \\ -1, -1, 1 \end{matrix}\right)$ is the Meijer G function. The constants c_1, c_2, c_3, c_4 may be obtained by applying the boundary conditions (23)–(26), but the expressions are too unwieldy to be reproduced here.

4. Solution when Porous Shell is Absent

When the porous shell is absent $R = 1$ and there is no Brinkman's region. In the Stokes region $(1 < r < 1/\gamma)$ the governing equation is

$$r^2 \frac{d^2 u}{dr^2} + r \frac{du}{dr} - M^2 u = -r^2 . \tag{33}$$

The relevant boundary conditions are

$$u(1) = 0 \text{ and } \left.\frac{du}{dr}\right|_{r=1/\gamma} = 0 . \tag{34}$$

Thus, we get for
$M \neq 0; 2$:

$$u(r) = \frac{2\gamma^{-M}(1 - r^{2M}) + \gamma^2 M[(1 + \gamma^{-2M}) r^{2+M} - \gamma^{-2M} - r^{2M}]}{r^M \gamma^2 \left(1 + \gamma^{-2M}\right) M \left(M^2 - 4\right)}, \tag{35}$$

$M = 0$:

$$u(r) = \frac{1}{4}\left(1 - r^2 + \frac{2\ln r}{\gamma^2}\right), \tag{36}$$

$M = 2$:

$$u(r) = \frac{\left(r^4 - 1\right)\left(1 - 2\ln\gamma\right)}{8r^2\left(\gamma^4 + 1\right)} - \frac{r^2 \ln r}{4} . \tag{37}$$

5. Evaluation of Permeability

We shall now evaluate the permeability parameter L [3, 5] connecting Darcy law with the volume flux Q

ISBN: 978-1-61804-295-8

$$L = \frac{Q}{\pi c^2} = \frac{\gamma^2 Q}{\pi}, \tag{38}$$

where

$$Q = 2\pi[\int_R^1 rv(r)dr + \int_1^{1/\gamma} ru(r)dr]. \tag{39}$$

We can now obtain the values of the involved integrals by inserting the values of $u(r)$ and $v(r)$ obtained earlier and integrating.

The hydrodynamic permeability $L(M, R, \gamma, s)$ is a function of four arguments.

Parameter *M* is Hartmann's number, which characterizing intensity of the applied magnetic field; parameters *R* and *γ* determine the fraction of the porous phase in the particle per se and in the cell, respectively; parameter *s* characterizes drag force acting from the porous layer.

It may be noted here that the first integral vanishes on taking $R = 1$ and we have the non-porous case.

In general, the expression for the permeability has a complicated form and is not presented here. If the microporous layer is absent (*R*=1), the expressions for the permeability are as follows.

$M \neq 0; 2$:

$$L = \frac{16\left(\gamma^{-2M} - 1\right) + M\{32\gamma^{2-M} - 12 - \gamma^4 \left(M-2\right)^2 + M^2 + \gamma^{-2M}[M^2 - 12 - \gamma^4\left(M+2\right)^2]\}}{2M\gamma^2\left(1+\gamma^{-2M}\right)\left(M^2-4\right)^2}; \tag{40}$$

$M = 0$:

$$L = \frac{4\gamma^2 - \gamma^4 - 3 - 4\ln\gamma}{8\gamma^2}, \tag{41}$$

the last expression was obtained earlier [3, 6];

$M = 2$:

$$L = \frac{3 - 2\gamma^4 - \gamma^8 + 16\gamma^4 \ln\gamma\left(1 - \ln\gamma\right)}{32\gamma^2\left(1+\gamma^4\right)}. \tag{42}$$

6. Plots and Discussion

We present below some graphs to show the effects of various parameters on the velocity field *u*(*r*) in the Stokes region and *v*(*r*) in the Brinkman's region as well as permeability *L*.

Fig. 3 shows the dependence of longitudinal velocity *u*(*r*) in the Stokes region ($1 < r < 2$) and *v*(*r*) in the microporous region ($0.5 < r < 1$) for different values of the Hartmann number *M*. Due to effects of sticking and filtration through microporous layer the flow velocity decreases from the surface of the cell (*r* = 2) to the surface of the solid fiber (*r* = 0.5) (Fig. 3). When intensity of the applied magnetic field increases (enlargement of the parameter *M*) then induced Lorentz force increases too that gives an additional resistance to flow and leads to a decrease in flow rate (see Fig. 3).

Fig. 4 illustrates the dependence of the permeability *L* on parameter *M* for different values of the solid fiber radius *R*. When the Hartmann number *M* increases the flow velocity decreases (Fig. 3) and, consequently, the permeability decreases (Fig. 4). Growth of radius *R* of the cylindrical impermeable fiber with reducing thickness δ of the microporous layer leads to an increase in solid

ISBN: 978-1-61804-295-8

fraction of a membrane and to a reduction of the permeability (Fig. 4). At R = 1 the microporous layer is absent and hydrodynamic permeability is calculated using (40)–(42).

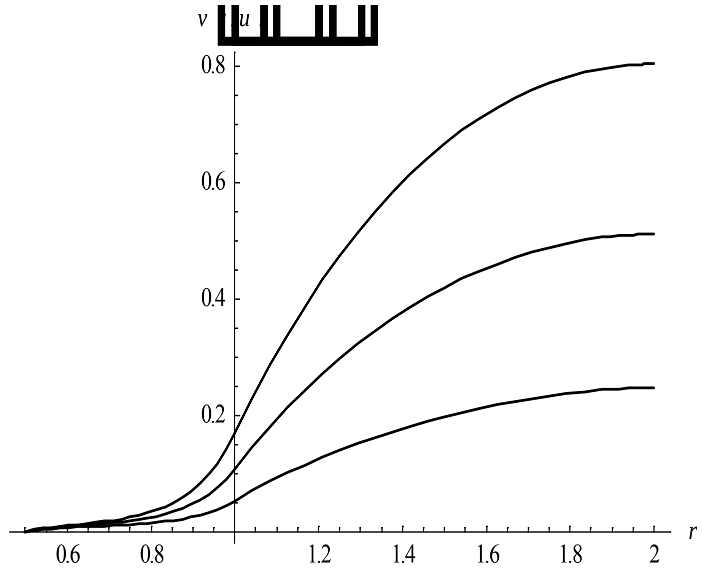

Fig. 3. Variation of velocity *v*(*r*), *u*(*r*) with *r* at $R = 0.5,\ \gamma = 0.5,\ s = 10,\ M = 0, 1.5, 3.$ **Parameter *M* increases from top to bottom curve.**

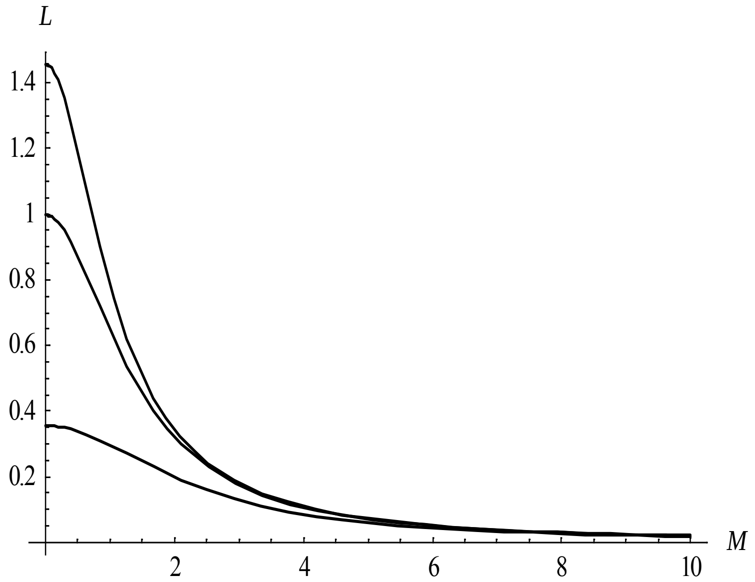

Fig. 4. Variation of permeability *L* with *M* at $\gamma = 0.5,\ s = 2,\ R = 0.1, 0.55, 1.$ **Parameter *R* increases from top to bottom curve.**

Dependence of hydrodynamic permeability L on parameter γ for different values of M is shown in Fig. 5. With increasing parameter γ the value of macroporosity decreases that leads to a decrease in the permeability (Fig. 5). At $\gamma \to 0$ the value of macroporosity tends to unity and hydrodynamic permeability tends to infinity (Fig. 5). At $\gamma = 1$ the value of macroporosity is equal to zero and filtration is going on only through a microporous medium so the permeability tends to the limiting value depending on the Brinkman parameter s. As previously observed the permeability decreases with increasing the Hartmann number M (Fig. 5).

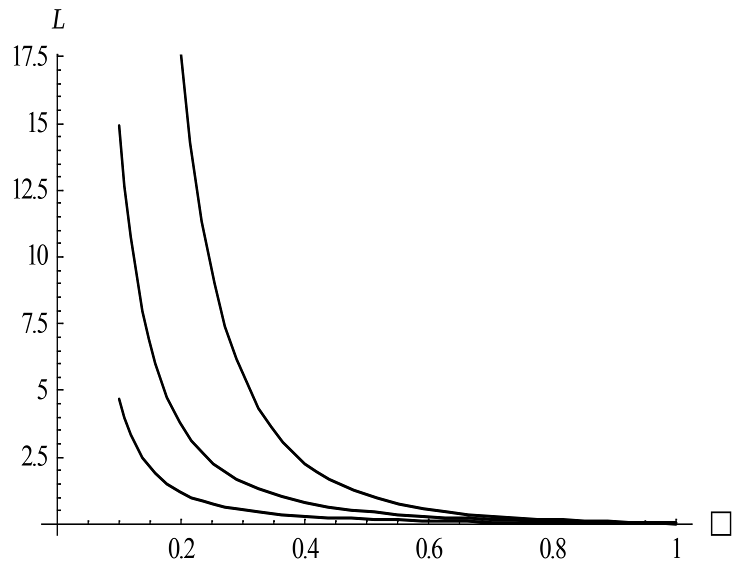

Fig. 5. Variation of permeability *L* with γ at $R = 0.6$, $s = 0.5$, $M = 0, 1.5, 3$. Parameter *M* increases from top to bottom curve.

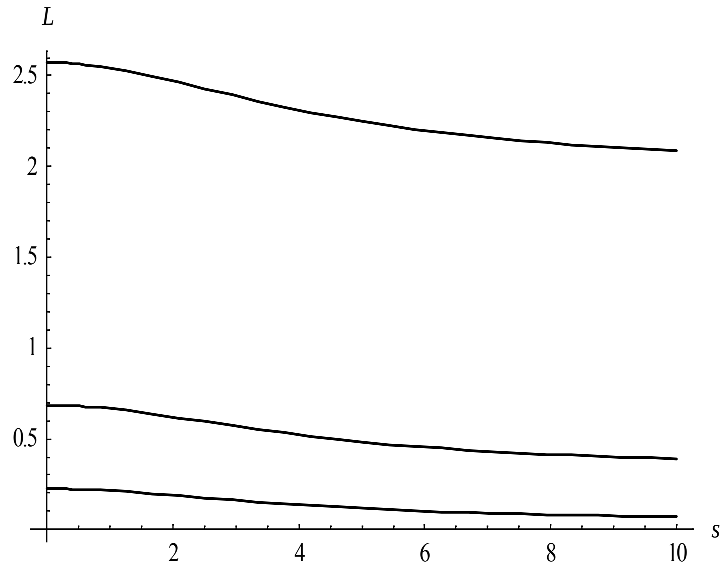

Fig. 6. Variation of permeability *L* with *s* at $R = 0.6$, $M = 1$, $\gamma = 0.3, 0.5, 0.7$. Parameter γ increases from top to bottom curve.

Fig. 6 shows the dependence of hydrodynamic permeability L on Brinkman's parameter s for different values of γ. Enlargement of parameter s increases resistance of the microporous layer, which covers impermeable cylindrical fibers, that leads to decreasing the permeability (Fig. 6). At $s \to \infty$ microporous layer becomes impermeable and filtration occurs through macropores that is characterized with flat parts on the graphs (Fig. 6). Under growth of parameter γ macroporosity decreases that leads to a drop of hydrodynamic permeability (Fig. 6).

The dependence of permeability L on radius R of the impermeable cylindrical fibers for different values of s is shown in Fig. 7. As noted earlier, growth of R leads to a decrease of the fraction of microporous medium in the membrane and as a consequence to a decrease of hydrodynamic permeability (Fig. 7). At $R = 1$ microporous layer is absent and hydrodynamic permeability of the membrane is calculated using (40)–(42) and apparently does not depend on Brinkman's parameter s as it is shown in Fig. 7.

ISBN: 978-1-61804-295-8

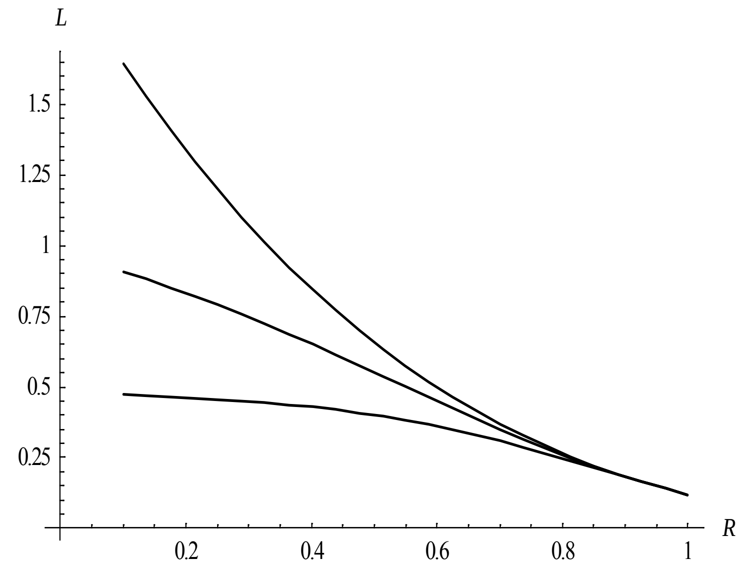

Fig. 7. Variation of permeability *L* with *R* at $\gamma = 0.6,\ M = 0.5,\ s = 0, 1, 3.$ **Parameter *s* increases from top to bottom curve.**

Remarks

- Expression for the velocity satisfying both Stokes and Brinkman equations and all the four boundary conditions have been obtained; but it is too unwieldy to work with and determine the permeability.
- While deriving the expressions for velocity and permeability, boundary conditions on magnetic field are not needed.
- The material presented here extends the hydromagnetic annulus flow studied by Globe [13] to the cell model.

Acknowledgements

Sunil Datta's and Manju Agarwal's research was supported by DST, New Delhi, Indo-Russian Project grant INT/RFBR[P-76]. Anatoly Filippov's research was partially supported by the Russian Science Foundation, project no. 14-19-01045 and CRDF-Global, project No. FSAX-14-60158-0.

References

1. J. Happel, AIChE J. 5 (1959) 174-177.
2. S. Kuwabara, Phys. Soc. Japan. 14 (1959) 527-532.
3. J. Happel and H. Brenner, Low Reynolds Number Hydrodynamics, Kluwer, Dordrecht, 1991.
4. S.I. Vasin and A.N. Filippov, Colloid J. 66 (2004) 266-270.
5. S.I. Vasin and A.N. Filippov, Colloid J. 71 (2009) 31-45.
6. S.I. Vasin and A.N. Filippov, Colloid J. 71 (2009) 141-155.
7. V.A. Kirsh, Colloid J. 58 (1996) 786-790.
8. V.A. Kirsh, Colloid J. 68 (2006) 198-206.
9. H.C. Brinkman, Appl. Sc. Res. 1 (1947) 27-34.
10. A. Tiwari, S. Deo and A. Filippov, Colloid J. 74 (2012) 515-522.
11. S. Datta, M. Agarwal, A. Filippov and S. Vasin, Colloid J. 75 (2013) 642-648.
12. E. Resler and W.R. Sears, Aeronautical Sci. 25 (1958) 235-245.
13. S. Globe, Physics of Fluids, 2 (1959) 404-407.

Variations in Dry Sliding Friction Coefficients with Velocity

James Moran[1,*] and Thawan Sucharitakul[2]

[1,2]Department of Mechanical Engineering, Faculty of Engineering, Chiang Mai University, Chiang Mai, 50200 Thailand

* Corresponding author: james@dome.eng.cmu.ac.th

Keywords: Dry sliding surfaces, Kinetic Friction Variations, Journal Bearings, Hertzian Stresses

Abstract. This paper examines the variation in the coefficient of friction with sliding velocity between different materials. Measurements are made of the average coefficient of friction as a function of sliding velocity but also the variation or standard deviation of the friction coefficient with velocity. The results found that the average coulomb friction coefficient was relatively constant with velocity as expected. However, the standard deviation of the friction coefficient changed dramatically with sliding velocity speed. This variation was not explained by electrical or angular resonances. Five different materials were used as the sliding surfaces in the experiments, Aluminum, Bronze, Mild Steel, Stainless Steel and Nylon.

Introduction

The motivation behind this research was to try and improve the durability and life of journal bearings. A full introduction to journal and every other kind of bearing can be found in Slocum [1]. The original purpose of this paper was to test new designs for low friction non-lubricated bearings and to compare their performance with regular journal bearings. The design and concept behind these bearings is described in [2]. They were to overcome some of the problems associated with regular bearings which can fail by seizure [3]. During the course of this journal testing an interesting phenomena was observed which is the subject of this paper. The sliding speed between the bearing and shaft was found to effect the fluctuation of the kinetic friction coefficient. The average friction stayed broadly constant with sliding speed as expected.

There are many different methods and standards used to measure friction. ASTM, The Society of Automotive Engineers, The Society of Motion picture Engineers, The Packaging Institute and The American National Standards Institute have all developed specialized friction test standards for their products. Friction can be measured between two flat surfaces using a simple inclinded plane device as per ASTM D-3248 but these will not show how the friction changes with time or with sliding speed. For curved surfaces there is the block on ring test ASTM G77 or the pin on disk test ASTM G99. The standards address the sample preparation method, cleaning, tolerances and measurement technique. The sample to be tested must be a certain shape and size. This is ideal for obtaining friction coefficents for materials but if you wanted to test the material in its end use condition then these general tests are unsuitable. A compilation of international friction and wear test standards was published in VAMAS on “Wear Test Methods” [4]. There are also a variety of specialized friction tests for measuring microfriction, friction between shoes and pavement and for detecting the degree of lubrication on processed photographic film (ANSI PH 1.47). The huge variety of standards testifies to the fact that no one friction test provides satisfactory information for all applications.Khun et al. [5] designed a specific rig for testing the rolling resistance of physical vapor deposition coatings and Wang [6] did the same for testing hip joints. Since the original goal of this project was to find the coefficient of friction, as a function of time, for novel unlubricated bearings it was decided to design a test specifically for this purpose.

An experimental setup was designed to measure the coefficient of friction between the two surfaces moving at different velocities. It rapidly measured the change in friction coefficient by

ISBN: 978-1-61804-295-8

recording the coefficient of friction every four milliseconds for a total of 2500 data points per sample. This allows for an average and variation in friction over a short 10 second time period to be calculated.

Friction Background

There has been many books and articles published over the past 300 years on friction, tribology, wear and lubrication, such as P. Blau [7].It is not the intention of this paper to go into this subject's history but only to give an overview that is relevant to this topic. There are three accepted sources of friction, adhesion which is chemical bonding between two surfaces, asperity interaction which is resistance to motion due to surface roughness and plowing which comes from embedded particles [8].

The relative magnitude of these three components can vary from system to system but Suh [9] in a series of publications made the argument that plowing was the most significant component. Suh and Sin [10] experimentally demonstrated that asperity interaction is primarily responsible for the static coefficient of friction, which can vary between 0 – 0.5. The adhesion component of friction between metals does not play much role in many engineering surfaces although it could vary between 0 – 0.4. Suh also performed experiments with undulated surfaces and concluded that when the plowing by wear particles is eliminated the friction between sliding surfaces can be as low as boundary lubricated surfaces. He demonstrated that friction with boundary lubricants can be caused by micro-plowing as did Kim et al. [11]. Even at low loads and hard surfaces plowing occurs [12]. Reduced friction has been found between undulated surfaces which allow for particles to escape [13]. Another way is to reduce the apparent area of contact to an extremely small size to allow the wear particles to escape. Low friction electrical power connectors have been constructed using a compliant surface which reduced friction from plowing[14], and structured surfaces are becoming more widely studied [15]. There is even the suggestion that the undulated surfaces on the body of a desert scorpion leads to reduced wear[16].

Journal bearings were designed for this project with compliant surfaces[17], the intention was that they would have a lower friction coefficient and longer life than regular journal bearings. The reason for assembling the experimental rig as described in this paper was to test these bearings. However, during initial trials of the system with regular bearings some surprising results kept repeating themselves and these are the subject of this paper.

Friction versus Velocity. The coefficient of kinetic friction,μ_k, is independent of sliding velocity. This is sometimes referred to as the third law of friction, Amonton's third lawor Coulomb's law of friction after it was proposed by Coulomb in 1781. This law does not apply at low velocities where adhesion can dominate. This is true for small areas where debris generated can escape. However for a bearing without a debris escape passage, Moslehet al.[18] demonstrated that the kinetic friction increases with time due to wear and plowing.

Stiction. Stiction or Stick-Slip can be a cause of vibration in sliding systems. It is sometimes called stick-slip, frictional vibration or frictional oscillation. It arises because the static friction coefficient is larger than the kinetic friction coefficient. At low velocities a shaft has to overcome this static friction force which can cause the shaft to twist. Then as the shaft begins to turn the friction reduces and the shaft rotates overshooting its equilibrium position. The process then repeats resulting in vibrations or oscillations. However as the sliding velocity increased the magnitude of the oscillations are expected to reduce [19] tending to zero for high velocities. This paper will present results showing the opposite happening, increased velocities resulting in higher frictional vibrations.

Experimental Setup

The experimental test bed was designed to measure the sliding friction. It is shown in Fig. 1. The premise is that two surfaces move against each other. One surface is a shaft and the other is a plain unlubricated bearing. The shaft is placed inside the bearing, a known load applied and the shaft is rotated. By measuring the torque applied to the bearing the friction coefficient can be obtained. The shafts used were all 12mm in diameter and the bearings used were all 32mm in length. The ends of the shafts were supports by ball bearings and great care was taken to align the shaft precisely.

Twoequal fixed loads, 1kg each,were applied both above and below the bearing. Symmetric loading in this way allowed for the load to be balanced at small angular offsets. A McLennan 50W brushless 24V DC motor was used to drive the shaft. There is a 2:1 gearing ratio connecting the motor to the shaft so the maximum angular speed of the shaft is 1800 rpm at a torque of 0.34 Nm assuming no gearing losses. The force between the shaft and bearing was measured with aHoneywell force sensor, FSG series with a sensitivity of 0.24 mV/gram and a maximum force of 1500 grams. This was situated 40 mm from the center of the shaft rotation. The force at this location was used to calculate the torque between the bearing and the shaft. A relay switch was used as a safety device to protect the motor from an over current.

The following is the list of main components of the set up.

1) 12mm stainless steel shaft
2) Motor for driving the shaft (BLDC 58 – 50L McLennan)
3) Bearing under load
4) Symmetric weights for loading

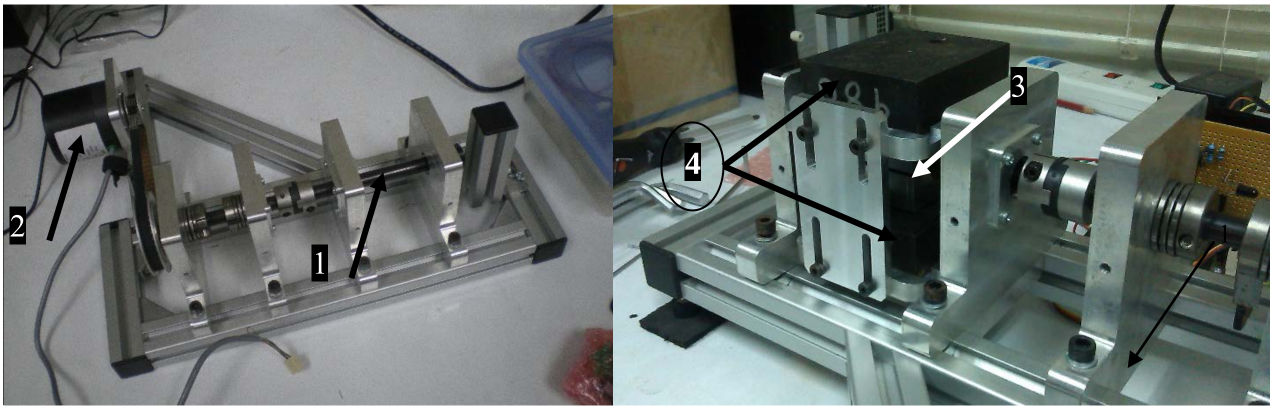

Figure 1: Completed Test Bed

An Arduino microcontroller was used to record data from the force sensor, the motor RPM output and the safety relay. An oscilloscope was connected to the force sensor. This was used for collecting 2500 data points from the force sensor in a 10 second period. The mean and standard deviation of the friction coefficient can thus be calculated for that specific time interval.

To calculate the friction coefficient (μ), it is helpful to look at the setup as shown in Fig. 2. The whole assembly in Fig. 2 is capable of rotation. The force sensor prevents that from happening so the only item rotating is the shaft. The reason for two weights is to prevent a bias reading as during tests the appartus can tilt at a slight angle.

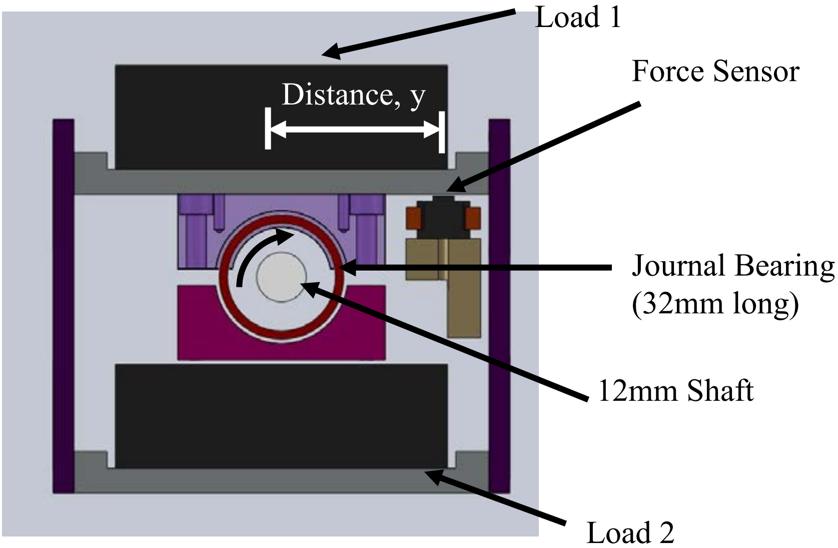

Figure 2: Sketch of Apparatus

a) F_{sensor} = Force experienced by the Force sensor
b) N = Total weight applied to the bearings (Including weight of support and screws)
c) F_{shaft} = Force applied by the rotating shaft on to the bearing
d) y = distance from the middle of the shaft to the middle of the force sensor

The coefficient of friction μ, between the bearing and the shaft is given by:

$$\mu = \frac{F_{shaft}}{N} \tag{1}$$

The torque applied to the bearing must be counteracted by the torque from the force sensor.

$$F_{sensor} * y = F_{shaft} * r_{shaft} \tag{2}$$

Therefore the coefficient of friction can be obtained from:

$$\mu = \frac{F_{sensor} * y}{r_{shaft} * N} \tag{3}$$

The coefficient of friction can be calculated from Eq.(3). The variable F_{sensor} is continuously measured during each test and a data point taken every 4 milli-seconds. The force sensor was calibrated before each test so that its output in milli-volts could be converted to force.
All shafts and bearings were made up in five different materials, four metals and one plastic, which are listed in Table 1.

Table 1: Materials used for Shaft and Bearing

Material for both Shaft and Bearing	Ultimate Tensile Strength [Mpa]	Young's Modulus [Gpa]	Hardness Brinell	Poisson's ratio
Superlene Nylon	75	2.4	10	0.39
Aluminum 6061	300	69	95	0.33
Bronze SAE 660	240	100	65	0.35
Mild Steel S45	570	200	180	0.26
Stainless Steel SS440	720	200	570	0.30

Each test was run with new materials for both the shaft and bearing since running a test can damage the surface of both materials. They were not reused again. Both surfaces were thoroughly cleaned with alcohol beforehand to remove any traces of dirt or grime. A load was applied and the shaft was spun. The shaft angular velocity and output from the force sensor were recorded. The angular velocity was then increased and the data collection repeated up to the maximum angular velocity of the motor. Care was taken to complete the test quickly, in under five minutes as the friction coefficient does increase with time due to plowing [4].

Results

Friction Variations. To check that the data gathered was not corrupted by noise or other variations a simple test was performed. A bronze bearing was used with a mild steel shaft at a fixed angular speed of 370 rpm. The friction coefficient was measured. The test was repeated again, except a small quantity of lubricating oil was placed on the shaft. Fig.3 shows the friction results of this test. The dry surfaces had an average friction value of 0.34, which is within expectations,and a standard deviation of 0.24. The lubricated surfaces had a reduced mean friction coefficient (0.01) and also a much lower standard deviation (0.03). This gave confidence that the observed large fluctuations in the dry case was real and not some unknown external cause.

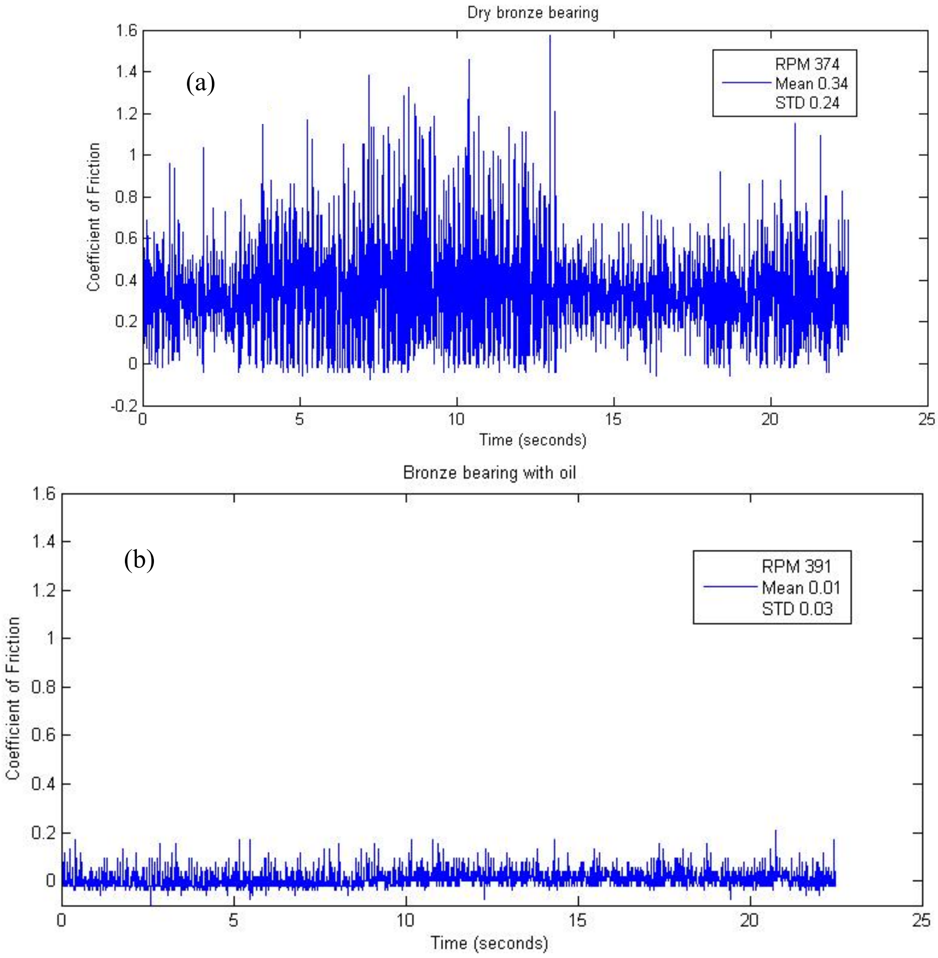

Figure 3: Oscilloscope reading of (a) dry and (b) lubricated bearing at 370 RPM

The variation in the friction coefficient at different rotational speeds was measured for all five different materials. Fig. 4 shows results of the friction coefficient for a mild steel shaft and an aluminum bearing at two different rotational speeds.

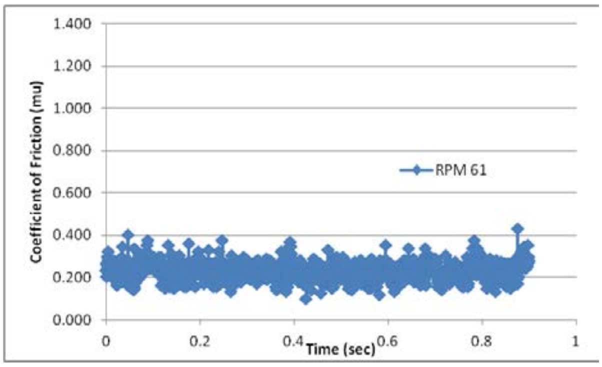

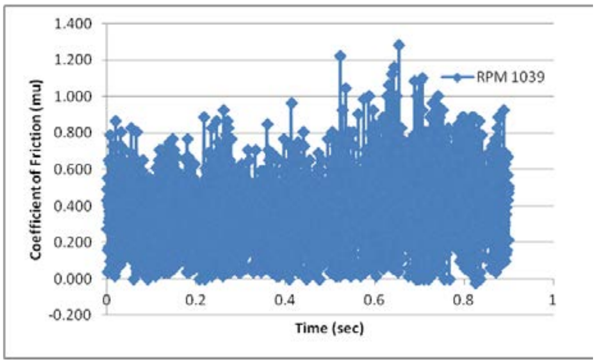

Mild Steel Shaft and Aluminum Bearing; Friction coefficient at 60RPM and 1039RPM respectively

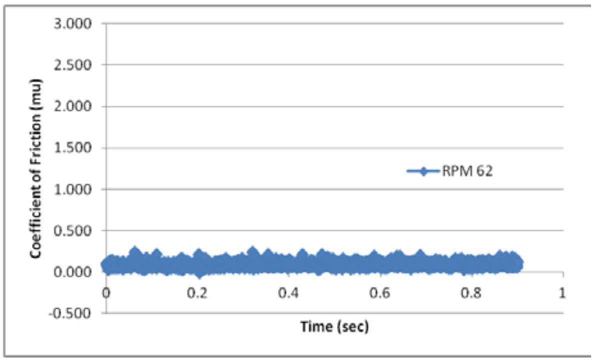

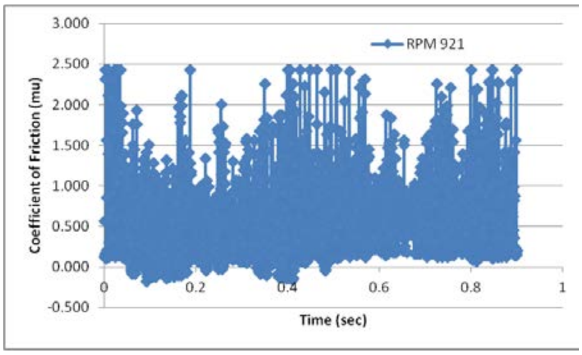

Mild Steel shaft and Stainless Steel Bearing; Friction coefficient at 62 RPM and 921 RPM respectively

Figure 4: Friction coefficient versus time for different shaft speeds and materials

As can be seen in Fig. 4 the standard deviation in the friction coefficient changes dramatically with the rotational speed. This could be explained by the rotational nature of the test. A large asperity will be contacted more frequently at higher speeds and therefore result in larger fluctuations or mislaignment may cause this. In Fig. 5 a power spectrum from the FFT is plotted for an Aluminium shaft on Aluminium bearing rotating at 17 Hz, selected because it is the highest value. The average friction coefficent was 0.93 and its standard deviation was 0.75. The power spectrum does show peaks at 17Hz and multiples of 17Hz. Using a notch filter these frequencies were removed and the data plotted again in Fig. 5(c). The average friction was constant at 0.93 and the standard deviation was lowered to 0.65. Therefore the rotational nature of the test does have some effect on the standard deviation. It was decided to run 25 tests in total, testing all the different shafts against all the bearings for a variety of rotational speeds. Fig. 6 shows the mean friction coefficient as a function of speed for all five different shafts.

ISBN: 978-1-61804-295-8

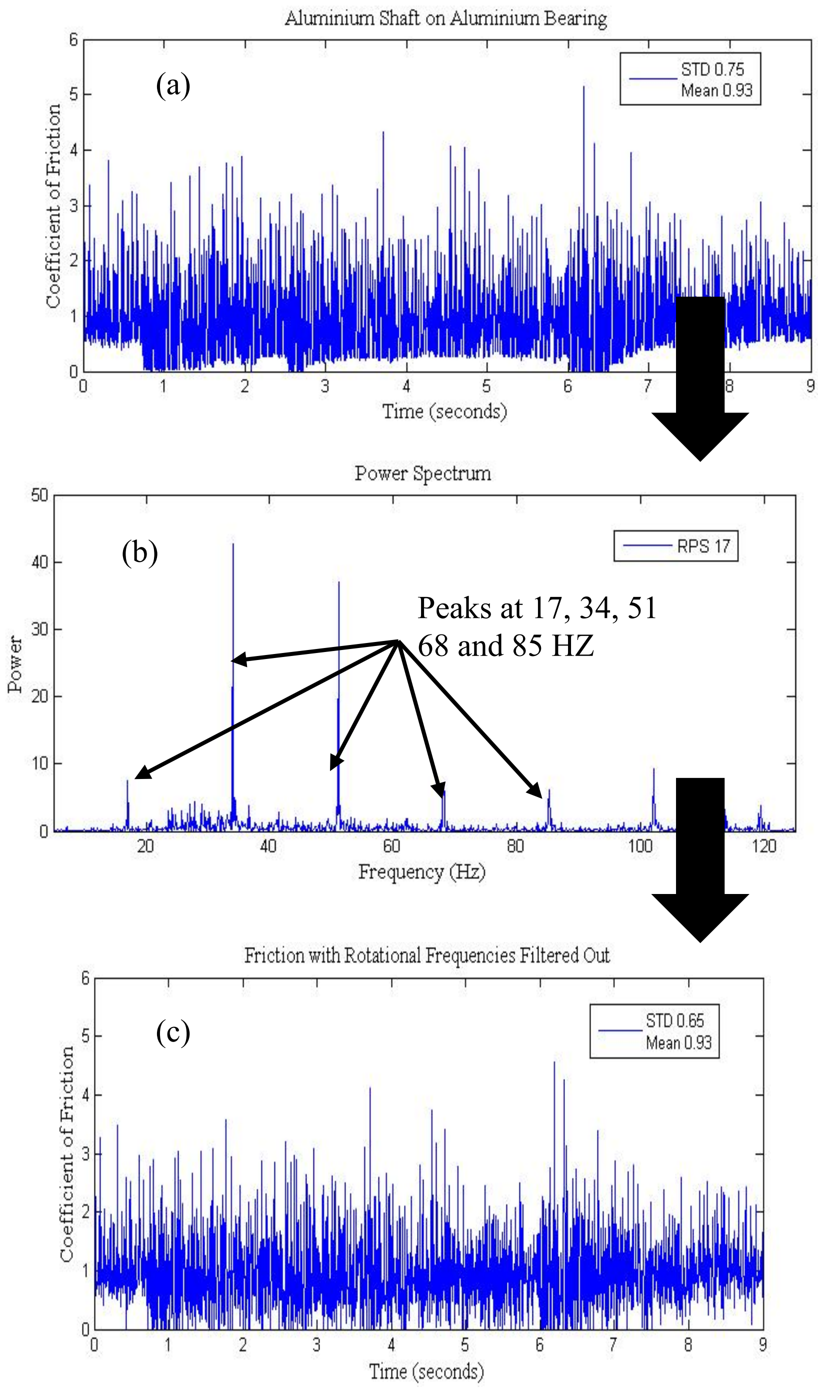

Figure 5(a): Friction Data for a Speed of 17 RPS (b) Power Spectrum (c) Friction with Filtered Rotational Frequencies

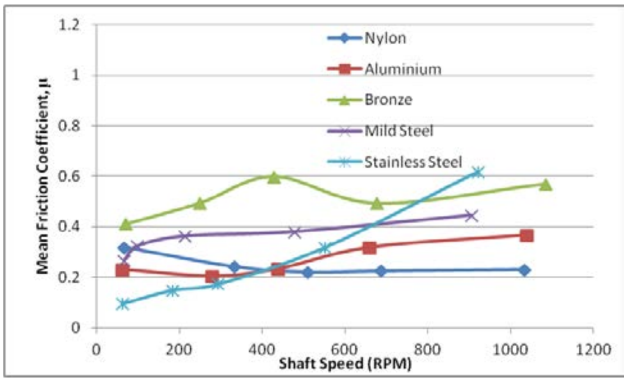

Mild Steel Shaft

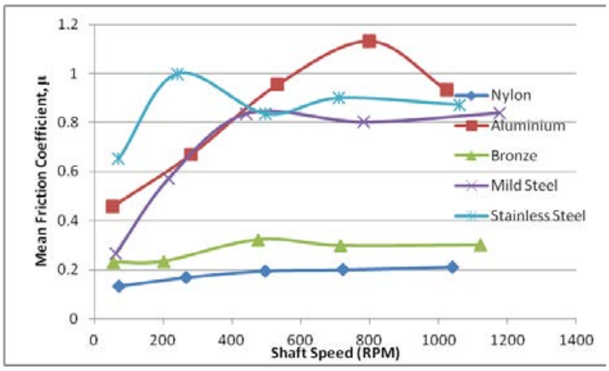

Aluminum Shaft

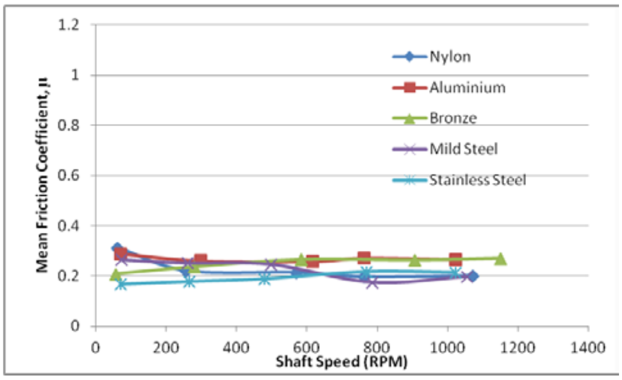

Bronze Shaft

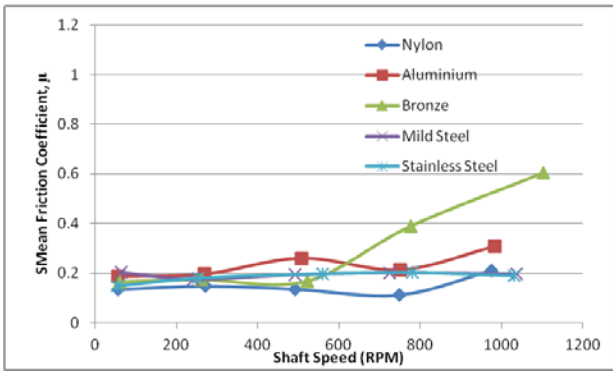

Nylon Shaft

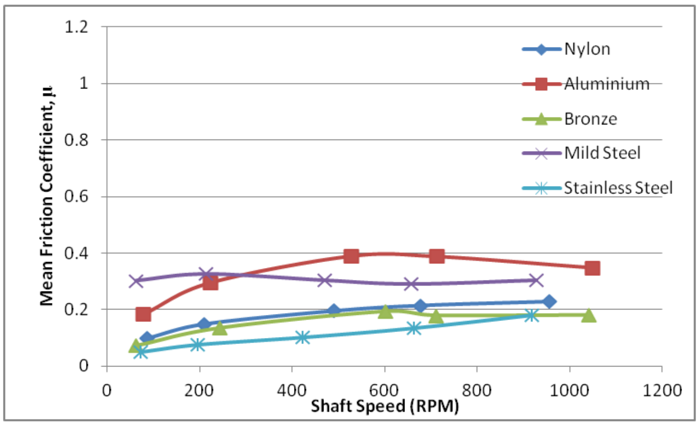

Stainless Steel Shaft

Figure 6: Mean friction coefficients as a function of rotational speed

As can be seen the average friction coefficient changes slightly, with rotational speed. It was not the purpose of this experiment to analyze the effects of time on friction. Each experiment was only run for a short time, less than 5 minutes, to reduce the effect of plowing. Each data point was acquired in 10 seconds. A comparisonbetween the measured kinetic friction coefficient and published kinetic friction coefficientsobtained from the Handbook of Lubrication[19] is shown in Table 2.

ISBN: 978-1-61804-295-8

Table 2: Coefficient of Kinetic Friction from[19] and Experiments

Material	Material	Friction Coefficient, μ_k (Dry Surface)	Measured μ_k
Aluminum	Aluminum	1.4	0.83
Aluminum	Mild Steel	0.47	0.46
Nylon	Nylon	0.2	0.15
Mild Steel	Bronze	0.44	0.37
Mild Steel	Mild Steel	0.57	0.35
Hard Steel	Hard Steel	0.12	0.10

Given the dependence on the friction coefficient on the condition of the surface, surface roughness, environment, time of contact, cleaning methods, area of contact and precise grade of material the results from the experiments match well with the standards. There were some material combinations, nylon on metal, for which a friction coefficient could not be looked up. However nylon on nylon has a coefficient of 0.2 which matches well with the data, giving credibility to our nylon on metal results. In situations where there are two dissimilar metals the average friction was used when both materials were the shaft. Interestingly the friction coefficient changed depending on which material was moving, i.e which material was the shaft.

The interesting results from these tests are not the average friction coefficient, which after all are already known but arise from the variation in the friction coefficient.Plotting the standard deviation of this sample set as shown in Fig.7.

ISBN: 978-1-61804-295-8

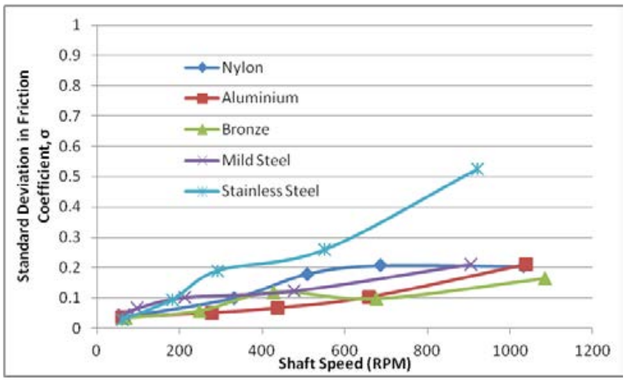

Mild Steel Shaft

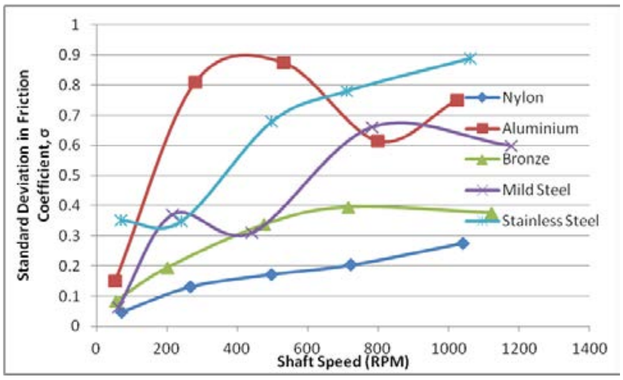

Aluminum Shaft

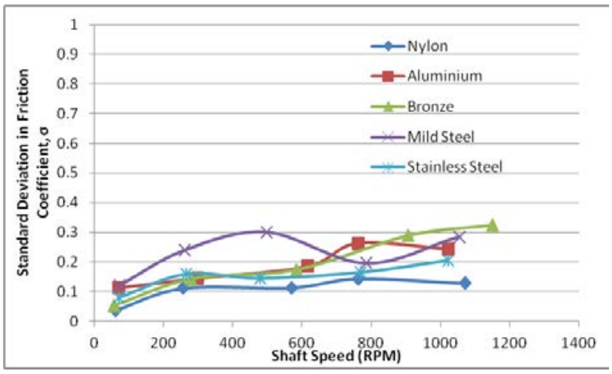

Bronze Shaft

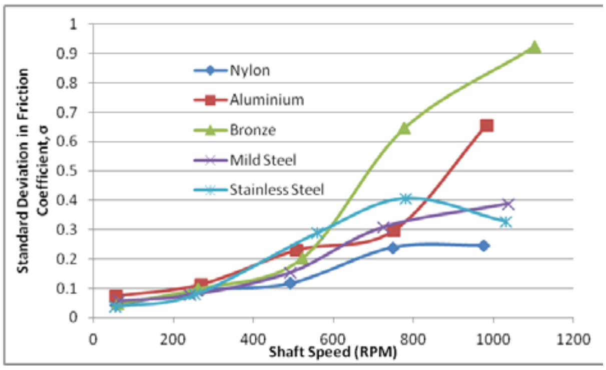

Nylon Shaft

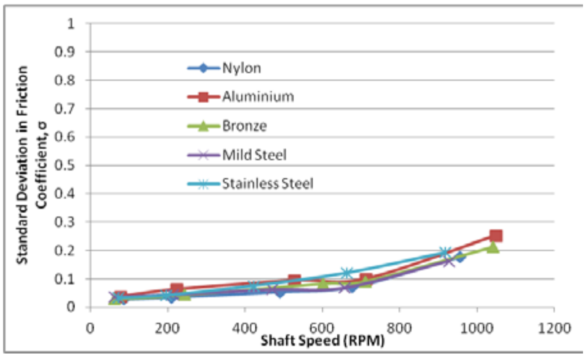

Stainless Steel Shaft

Figure 7: Standard deviation in friction coefficient at different rotational speeds

There is an increase in the standard deviation with rotational speed. It applies to all materials, and holds true even if the bearing is worn in beforehand.

Discussion

The Hertzian contact stresses between the various materials can be calcualted from Hertz's equations [7]. These are for static, elastic contacts only. The contact stress for a cylinder on a flat surface can be calculated from:

$$S_c = 0.798\sqrt{p/DE^*} \tag{4}$$

Where: p is the force per unit length, D is the diameter of the cylinder and E^* is given from:

$$E^* = \left[\left\{\frac{1-\nu_1^2}{E_1}\right\} + \left\{\frac{1-\nu_2^2}{E_2}\right\}\right] \tag{5}$$

Table 3: Contact Stresses in [Mpa]

	Superlene Nylon	Aluminum 6061	Bronze SAE 660	Mild Steel S45	Stainless Steel SS440
Superlene Nylon	7.6	10.6	10.7	10.7	10.7
Aluminum 6061	10.6	40.0	43.7	48.5	48.7
Bronze SAE 660	10.7	43.7	48.6	55.5	55.8
Mild Steel S45	10.7	48.5	55.5	66.7	67.1
Stainless Steel SS440	10.7	48.7	55.8	67.1	67.5

The higher stresses are on the materials with the higher Young's modulus. The weaker shafts made from Nylon and Aluminium gave the highest fluctuations.

It matters which material is the shaft and which is the bearing. The shaft is rotating while the bearing is stationary. Using identical materials but changing their relative shaft/bearing positions produces different results. The Stainless Steel shaft produces the least amount of oscillations for all bearing materials however the Stainless bearing on an Aluminium shaft produces the most. This suggests that the oscillations depends on which of the materials is in relative motion.

A new shaft and bearing was used for each test. The oscillations may be a result of the bearing getting worn in and over time the oscillations may all converge. To test this explanation a bearing was worn in for an hour. The coefficient of friction did rise up to a steady state value. The tests were repeated and the same pattern observed, increased oscillations at higher speeds.

The standard deviation to mean ratio σ/μ versus the linear speed was plotted for all five materials. The graph is shown in Fig. 8. Both shaft and bearing are the same material. The softer materials, Nylon and Al, display wide fluctuations. The stiffer metals display a linear correlation with the speed.

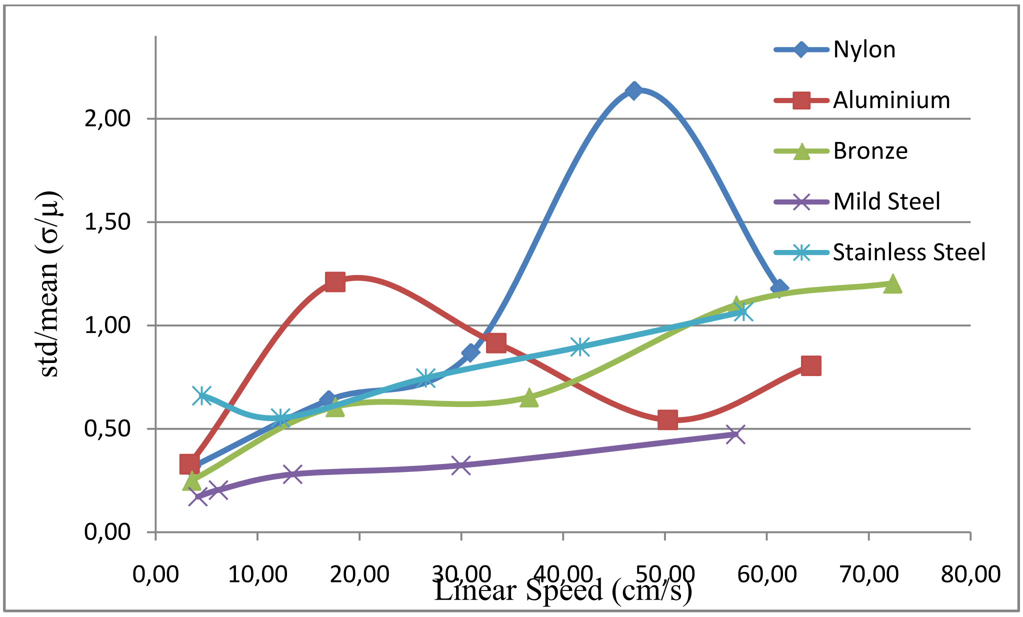

Figure 8: Standard deviation/mean ratio versus linear speed

Conclusions

Plain journal bearings and shafts were made from five different materials. Each material was made into a 12mm diameter shaft and a plain journal bearing that was 32mm long. The friction coefficient was measured between all shafts and sleeves for different sliding speeds. The aggregated results are shown in Figs 6 and 7.

For all material sets the average kinetic friction coefficient stayed fairly constant over a wide range of speeds. This is consistent with Coulombs Law. There was a slight increase observed with speed which can be explained by debris agglomeration and plowing. Care was taken to minimize the time the shaft was spinning in the sleeve but a finite time was needed to run the test. The average kinetic friction results obtained are consistent with published values.

However the standard deviation of the kinetic friction coefficent increased with increasing velocity. Across all material combinations this trend was observed. It was still observed after harmonic frequencies from angular rotation was filtered out. A notch filter was used to remove these harmonic frequencies which resulted in a 13% lower standard deviation, significant but not enough to alter the general conclusions. The effect from these harmonic frequencies needs to be quantified more precisely. Increasing fluctuations with velocity is counter to the frictional oscillation theory which implies that increasing velocity results in less oscillations. This frictional oscillation could have an effect on material wear, particle agglomeration, plowing and the time change of friction. For bearings this could mean a reduced life or seizure. Future work is focussing on designing compliant surface bearings that limit the effect of surface plowing and determining if the friction oscillations decrease. If so, these could result in bearings that have reduced wear, increased durability and increased life.

Acknowledgements

The authors would like to express their thanks to Chiang Mai University for funding this research

References

[1] A. Slocum, Precision Machine Design, NY: Prentice-Hall, 1992.

[2] J. Moran, P. Tangsukkasemsan and S. Asadatorn, "New Design Concepts for Low Friction Plain Journal Bearings," in *TSME International Conference on Mechanical Engineering*, Ubon Ratachani, 2010.

[3] Q. Wang, "Seizure failure of journal-bearing conformal contacts," *Wear,* no. 210, pp. 8-16, 1997.

[4] P. Blau, "A Compilation of International Standards for Friction and Wear Testing of Materials"," VAMAS, Report No. 14, Gaithersburg, 1993.

[5] M. Khun, P. Gold and J. Loos, "Wear and friction characteristics of PVD-coated roller bearings," *Surface and Coatings Technology,* vol. 177, no. 1, pp. 469 - 476, 2004.

[6] A. Wang, "A unified theory of wear for ultra-high molecular weight polyethylene in multi-directional sliding," *Wear,* vol. 248, pp. 38-47, 2001.

[7] P. J. Blau, Friction Science and Technology, New York: Marcel Dekker, 1996.

[8] E. Avalonne, T. Baumeister and A. Sadegh, Mark's Standard Handbook for Mechanical Engineers, NY: McGraw-Hill, 2006.

[9] N. Suh, Tribophysics, Prentice-Hall, 1986.

[10] N. Suh and H. Sin, "The genesis of friction," *Wear,* vol. 69, pp. 91-114, 1981.

[11] D. Kim, K. Cha and L. Sung, "Design of surface micro-structures for friction control in micro-systems applications," *CIRP Annals - Manufacturing Technology,* vol. 51, no. 1, pp. 495-498, 2002.

[12] M. Mosleh and N. Suh, "Investigation of dry friction of submicrometer thick polyurethane films on a hard, smooth substrate," *Surface and Coating Technology,* no. 85, pp. 138 - 145, 1996.

[13] N. P. Suh and N. Saka, "Surface Engineering," *Annals of CIRP,* vol. 36, pp. 403-408, 1987.

[14] J. Moran, M. Sweetland and N. P. Suh, "Low friction and wear on non-lubricated connector contact surfaces," in *Proceedings of the 50th IEEE Holm Conference*, Seattle, 2004.

[15] C. Evans and J. Bryan, "Structured, textured or engineered surfaces," *Ann. CIRP,* vol. 48, pp. 541-556, 1999.

[16] H. Zhiwu, Z. Junqiu, G. Chao, W. Li and L. Ren, "Erosion resistance of bionic functional surfaces inspired from desert scorpions," *Langmuir,* vol. 28, pp. 2914-2921, 2012.

[17] J. Moran and P. Tangsukkasemsan, "Time to seizure comparisons between different plain journal bearings," in *The 3rd TSME International Conference on Mechanical Engineering*, Chiang Rai, 2012.

[18] M. Mosleh, N. Saka and N. Suh, "A mechanism of high friction in dry sliding bearings," *Wear,* no. 252, pp. 1-8, 2002.

[19] R. E. Booser, Handbook of Lubrication, New York: CRC Press, 1983.

Throughfall deposition patterns for Nitrogen and Sulphur on ecosystems adjacent to one sour gas recompression plant in Campeche, Mexico

Cerón-Bretón, R.M. [1, a *], Cerón-Bretón, J.G.[1,a], García-Montero, A. [2,c], Ramírez-Lara, E.[3,d], Aguilar-Ucán, C.A.[1,e], Montalvo-Romero, C. [1,f], Córdova-Quiroz, A.V. [1,g], Alderete-Chavez, A. [2,h], Jetta,S[1i]; Cruz-Camacho, G[1j]

[1]Chemistry Faculty. Autonomous University of Carmen. Ciudad del Carmen, Campeche, Mexico
[2]Research Center on Environmental Sciences. Autonomous University of Carmen. Ciudad del Carmen, Campeche, Mexico
[3]Chemistry Faculty. Autonomous University of Nuevo Leon. San Nicolás de los Garza, Nuevo León, Mexico
[a]rceron@pampano.unacar.mx, [b]jceronbreton@gmail.com, [c]antoniogarciamontero@hotmail.com, [d]evangelina.ramirezlr@uanl.edu.mx, [e]caguilar@pampano.unacar.mx, [f]cmontalvo@pampano.unacar.mx, [g]acordova@delfin.unacar.mx, [h]aalderete@pampano.unacar.mx, [i]jettasatyanarayana@gmail.com, [j]gcruz@pampano.unacar.mx

***Abstract*—** In this study, throughfall deposition of N and S was measured from June 6, 2014 to January 6, 2015 at Xicalango-Atasta region, this zone is exposed to both, emissions from a local sour gas recompression plant and meteorological conditions that transport emission from offshore platforms in the Gulf of Campeche during autumn and winter seasons. Passive throughfall collectors based on a mixed bed ion exchange resin column (IER) were used to collect samples in thirteen sampling points distributed along this zone in a multiple transects design. Ions retained (NO_3^-, NH_4^+, and SO_4^{2-}) by the resin column were extracted within the same sampling column with 2N KCl, and analyzed by colorimetry and turbidimetry. Mean throughfall deposition fluxes for N (NO_3^- + NH_4^+) and S (SO_4^{2-}) were 0.8 and 9.22 Kg ha^{-1} yr^{-1}, respectively. N deposition flux did not exceed the critical load proposed for sensitive ecosystems; however, throughfall deposition flux for S was 3 times higher than those proposed for sensitive areas, and 2 times higher than value reported for natural forests, suggesting that S deposition could be a threat for the mangrove ecosystems and fisheries in the region. Regional contribution was significant mainly during autumn and winter seasons, when long-range transported air pollutants from platforms enhanced the background levels. However, it was clear that the local sour gas recompression plant had a great influence on these background levels in the region Xicalango-Atasta.

***Keywords*—** Throughfall deposition, Nitrogen, Sulphur, Campeche, Mexico.

Cerón-Bretón, R.M. is with Chemistry Faculty of the Autonomous University of Carmen in Ciudad del Carmen, Campeche, Mexico. (corresponding author). Phone: (52) 938 38 1 10 18, ext 2106; e-mail: rceron@pampano.unacar.mx.

Cerón-Bretón, J.G. is with Chemistry Faculty of the Autonomous University of Carmen in Ciudad del Carmen, Campeche, Mexico. (e-mail: jceron@pampano.unacar.mx).

García-Montero, A. is with Ecological Restoration Master Degree Program, Research Center on Environmental Sciences, Autonomous University of Carmen in Ciudad del Carmen, Campeche, Mexico. (e-mail: antoniogarciamontero@hotmail.com).

Ramírez-Lara, E. is with the Chemistry Faculty. Autonomous University of Nuevo Leon in San Nicolás de los Garza, Nuevo León, Mexico. (e-mail: [d]evangelina.ramirezlr@uanl.edu.mx).

Aguilar-Ucán, C.A.. is with Chemistry Faculty of the Autonomous University of Carmen in Ciudad del Carmen, Campeche, Mexico. (e-mail: caguilar@pampano.unacar.mx).

Montalvo-Romero, C. is with Chemistry Faculty of the Autonomous University of Carmen in Ciudad del Carmen, Campeche, Mexico. (e-mail: cmontalvo@pampano.unacar.mx).

Córdova-Quiroz, A.V. is with Chemistry Faculty of the Autonomous University of Carmen in Ciudad del Carmen, Campeche, Mexico. (e-mail: acordova@delfin.unacar.mx).

Alderete-Chávez, A. is with Ecological Restoration Master Degree Program, Research Center on Environmental Sciences, Autonomous University of Carmen in Ciudad del Carmen, Campeche, Mexico. (e-mail: aalderete@pampano.unacar.mx).

Jetta, S. is with Chemistry Faculty of the Autonomous University of Carmen in Ciudad del Carmen, Campeche, Mexico. (e-mail: jettasatyanarayana@gmail.com).

Cruz-Camacho, G. is with Chemistry Faculty of the Autonomous University of Carmen in Ciudad del Carmen, Campeche, Mexico. (e-mail: gcruz@pampano.unacar.mx).

I. Introduction

ACIDIFICATION damages aquatic and terrestrial ecosystems, not only in the vicinity of industrial sources but also in sensitive background regions. Because of the widespread and largely detrimental aspects of atmospheric deposition in elevated amounts, the quantification of N and S inputs to the ecosystems is needed. It is clear that the changes on elemental biogeochemical cycles as a result of human activities have serious repercussions not only at ecosystem level, but also at regional and global level (with their corresponding adverse effects on sensible species). Biodiversity at the Southeast of Mexico is strongly affected by the deposition of nitrogen and sulphur. Since a great proportion of the economical incomes in Mexico come from ecotourism industry, exist an increasing concern about the potential ecological effects of acid deposition on the ecosystems and historical heritage. Particularly, the main terrestrial and offshore facilities for the oil and gas exploration and production are located in Campeche State, therefore, in this region, archaeological monuments, natural protected areas and petroleum industry co-exist, resulting in a complex environmental frame.

The composition of throughfall and stemflow had been studied in a number of locations around the world, especially in Europe and North America. In Mexico, there are only a few descriptions of this kind; some of the most extensive forest (particularly mangrove ecosystems) remains unstudied. Critical loads estimation method allows to quantify the grade of damage derived from atmospheric pollutants deposition on ecosystems. In spite of in North America and European countries, the standardized and systematic monitoring of atmospheric deposition at a long-term has been carried out since several years (resulting in the establishment of critical loads and reference values for different sensible ecosystems); in Mexico, critical load values and ecological effects related to acid deposition are unknown.

A variety of approaches, such as the inferential method, simulation modeling, the assessment of wet and dry deposition fluxes of trace elements and throughfall deposition estimations [1] have been used to determine N and S deposition. However, the quality of precipitation falling on forests is altered during the interaction with the surface of trees, resulting in additional deposition of mineral matter by throughfall and stemflow to the forest soils [2]. Throughfall and stemflow constitute the main pathways in the nutrient cycling; therefore, the estimation of deposition fluxes from these pathways plays an important role in the nutrient budgets studies in forest ecosystems. The study of atmospheric deposition chemistry has increased the last years, and nutrient budgets for disturbed and undisturbed forest ecosystems provide the framework for the assessment of the response of the ecosystems to the atmospheric deposition in diverse geographical regions.

Throughfall data and information on stand structure, seasonal trends and spatial distribution are needed to quantify elements deposition to forests exposed to chronic air pollution. Because of the difficulty in measuring dry deposition inputs, throughfall measurements are often used as an estimate of atmospheric deposition inputs to forests [3,4,5]. However, stand-level estimates of atmospheric inputs of N and S to forests in Mexico have been limited to studies carried out in pine forests at the surroundings of Mexico Valley [6,7,8].

In Mexico, atmospheric deposition studies focused to the establishment of critical loads are not available. The estimation of the exceedances to these critical loads let to identify vulnerable ecosystems and to develop policies to reduce and control emissions in these sites. This work constitutes the first step to diagnose the sensitivity of the region to the acidity and to carry out the mapping of N and S throughfall deposition. The most of annual precipitation at the Southeast of Mexico occurs during the period summer-autumn-winter, when Yucatan Peninsula is exposed to trade winds and cold fronts ("Nortes"), respectively; transporting regional pollutants that enhance the atmospheric background levels and the total deposition fluxes of N and S in Campeche State. Therefore, in this paper, throughfall deposition fluxes for N and S were measured during the summer, autumn and winter seasons at the surroundings of one sour gas recompression plant in Campeche State.
Procedure for Paper Submission

II. Methodology

A. *Sampler design and analysis*

Throughfall deposition consists of collected solutes in deposition under the forest canopies. This method is widely used to estimate atmospheric deposition inputs to the forest ecosystems, since; it includes both, wet and dry deposition. Because of the high cost associated to automatic collectors, and considering the complex process of the estimation of dry deposition, throughfall collectors constitute a good choice to measure in a reliable way the atmospheric deposition in forest stands. In addition, passive sampling devices (as throughfall collectors) let to increase the density of the sampling grid at a low cost, and to sample in a simultaneous way at different locations in a given region.

A resin column design was chosen, considering that it is a highly efficient technique for ion capture from throughfall samples as the flow is directed through the ionic exchange resin (IER) column, enhancing contact of the solutions with the resin [9,10]. Other advantages of the IER column design are that the resins are not in contact with the soil or forest floor and that the resins can be extracted easily in the laboratory from the same columns used during the field sampling.

Samples were collected with a funnel; the solution was channeled to the mixed resin bed (Amberlite TM IRN150) through the column where ions were retained. The funnel was connected to the IER column (a 1.27 cm x 35.6 cm polyvinyl chloride [PVC] tube) with PVC fittings and tubing. A double-walled white plastic tube (7.1 cm i.d.) was placed around the IER column to protect it from direct solar radiation. The resin used for the IER collectors is a mixed bed polystyrene anion and cation exchange resin (Amberlite™ IRN150). During all period (summer-autumn-winter seasons), a fine mesh screen was placed in the funnel opening to keep out debris. 30 g of resin were added to PVC columns and rinsed with distilled water. This volume of resin was sufficient to collect N and S. Glass fiber was inserted at the bottom (as a support platform) and top (as a filter) of the resin columns. The bottom end of the IER column was closed using a standard PVC cap with an “X” cut into it to allow for drainage.

At the end of each sampling period (two months), retained ions were extracted by using 2N KCl as extractant solution. Extraction efficiency was approximately 98.6%. Recovery percentage of N and S for the third extraction was not significant; therefore, only two sequential extractions were carried out in this study. Nitrate and ammonium were determined by colorimetry [11,12] and sulfate was analyzed by turbidimetry [13]. The surface area of the funnel opening and the sampling period were used to estimate the deposition fluxes of N (as $NO_3^- + NH_4^+$) and S (as SO_4^{2-}) in Kg per land area per year (Kg ha^{-1} yr^{-1}).

B. Study Area and Field Sampling

Research was conducted in the region of Xicalango-Atasta, in the state of Campeche at the Southeast of Mexico (Fig. 1). In this region, a sour gas recompression station is located at 2 km from the sampling sites. This station re-compresses sour gas obtained from offshore platforms sending it to petrochemical complexes. This region constitutes a hotspot in Mexico due to the following reasons: 1) its proximity to the sour gas recompression station and offshore platforms area in the Gulf of Campeche, and 2) its proximity to the Natural Protected Area “Laguna de Términos”.

Climate in this region is sub-humid warm with rains occurring along the summer. The annual mean precipitation is 1300 mm and the annual mean temperature is 27 °C. The prevailing winds come from NE from October to March when the region is under the influence of cold fronts or “Nortes”, and from SE from April to September, when this site is under the influence of tropical maritime air as a result of trade winds. Since this region is surrounded by water bodies (Terminos and Pom-Atasta Lagoons), this study site is influenced by land and sea breezes as a result of the heating difference between water and the terrestrial surface.

A multiple transect sampling schema was designed (13 sampling points were considered along a narrow continental extension known as region Xicalango-Atasta) in order to assess the spatial and temporal distribution of N and S deposition. Specific sampling points are presented in Figure 1. Throughfall deposition was collected in this study site from July 6, 2014 to January 6, 2015. Passive sampling devices were exposed during two months for three periods (a total of six months) during 2014-2015, including summer, autumn and winter seasons in each of the thirteen sampling points. Samples were collected and extracted at the end of each period (two months).

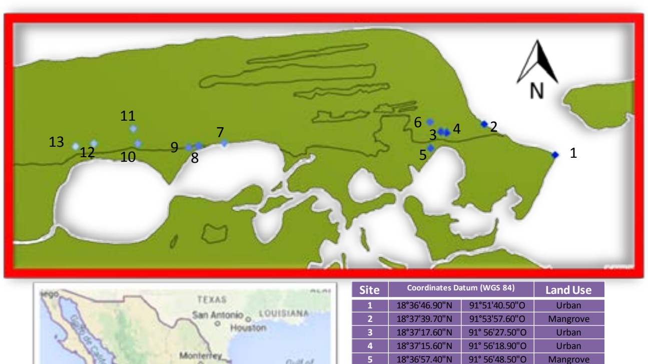

Site	Coordinates Datum (WGS 84)		Land Use
1	18°36'46.90"N	91°51'40.50"O	Urban
2	18°37'39.70"N	91°53'57.60"O	Mangrove
3	18°37'17.60"N	91° 56'27.50"O	Urban
4	18°37'15.60"N	91° 56'18.90"O	Urban
5	18°36'57.40"N	91° 56'48.50"O	Mangrove
6	18°37'54.70"N	91° 56'44.90"O	Farming
7	18°37'12.90"N	92° 6'55.20"O	Mangrove
8	18°37'12.90"N	92° 7'14.30"O	Mangrove
9	18°37'16"N	92° 05'48.5"O	Farming
10	18°37'7.80"N	92° 9'32.40"O	Industrial
11	18°37'47.7"N	92°09'48.6"O	Industrial
12	18°36'58.70"N	92°11'8.50"O	Industrial
13	18°37'1.70"N	92°12'18.40"O	Urban

Fig. 1 Sampling sites location

III. RESULTS AND DISCUSSION

In Mexico, critical loads for atmospheric deposition are not available, and only few studies have been carried out in pine forests at the surroundings of Mexico Valley. It has been reported an input of 15 Kg N ha^{-1} yr^{-1} for pine stands in Desierto de los Leones [6]; whereas in Zoquiapan [8], the reported inputs were 5.5 and 8.8 Kg ha^{-1} yr^{-1} for N and S, respectively. On the other hand, a critical load value of 5 Kg N ha^{-1} yr^{-1} has been proposed for alpine ecosystems [14,15], whereas for New Mexico and California, values of 3-8 and 4-7 Kg N ha^{-1} yr^{-1} respectively have been found [16,17]. On the other hand, a value of 3 Kg S ha^{-1} yr^{-1} has been proposed as a reference value for very sensitive areas, and a range of 2-5 Kg ha^{-1} yr^{-1} as critical load for natural forests in European countries [18].

In this study mean fluxes of throughfall deposition for N (NO_3^- + NH_4^+) and S (SO_4^{2-}) at Xicalango-Atasta region were 0.8 and 9.22 Kg ha^{-1} yr^{-1}, respectively. Throughfall deposition fluxes for N did not exceed critical loads proposed for sensitive ecosystems. However, throughfall deposition fluxes for S were 3 times higher than those proposed for sensitive areas, and 2 times higher than value reported for natural forests, suggesting that S deposition could be a threat for the mangrove ecosystems in the region. Throughfall deposition fluxes found in this study for S were comparable with those reported for forests located in the surrounding of the Mexico Valley [8], forests that can be considered as perturbed. Escoffie et al [19] measured throughfall deposition fluxes for N and S in Carmen Island, a city located at East from the studied region in this research, due to the high density of vehicular traffic in Carmen Island, N deposition fluxes were almost 3 times higher than the values reported here. However, in the case of S deposition fluxes, values (4.7 Kg ha^{-1} yr^{-1}) reported by Escoffie et al [19] were almost half of values found in this study (9.22 Kg ha^{-1} yr^{-1}). Therefore, this high sulfate contribution to deposition in the region of Xicalango-Atasta could be attributed to air pollutants emitted by sour gas re-compression station located in this zone. The safety system of this recompression plant has four flare burners that use sour gas as fuel, releasing air pollutants to the atmosphere, mainly SO_2 that is deposited as SO_4^{2-} in the surroundings of this station.

To infer the local or regional influence of N and S, the sulfate:nitrate ratio in throughfall deposition was estimated. A ratio of 13 was obtained, almost three times higher that obtained by Escoffie et al [19] for Carmen Island; suggesting that this region is subjected to the influence of long-range transport. It is agree with the local and regional character of nitrate and sulfate, respectively.

Nitrate and Ammonium showed an opposite seasonal pattern, suggesting that they were originated from different sources. From Fig. 2, it can be observed that NO_3^- deposition fluxes were higher during the summer, whereas NH_4^+ fluxes were higher during winter season. On the other hand, SO_4^{2-} deposition fluxes were higher during winter and autumn seasons, just in the plenitude of the rainy season, and at the beginning of the cold fronts named “Nortes”. These meteorological phenomena promote the long-range transport of air pollutants from offshore platforms in the Gulf of Campeche, where, flares (that are used as safety systems in platforms to avoid over-pressure in compression equipments) are burning sour gas periodically, as a result of a lack of capacity in the gas management system.

Sampling points in which throughfall deposition was collected, were grouped in four zones according the land use in each of the sites. Identified zones were the following: mangrove zone, industrial zone, urban zone and farming zone. From Fig. 3 and Fig. 4, it can be observed that mean throughfall deposition fluxes for nitrate were higher in the sampling points labeled as 8, 10, 11 and 12, corresponding to a land use of farming and industrial type. However, it is necessary to consider that these points are located just at federal highway 180, therefore, nitrate origin can be attributed to both, industrial and vehicular sources. In addition, sampling points 10-12 are located in the surrounding of gas recompression plant.

In the case of ammonium, mean throughfall deposition fluxes were higher in the sampling points 3 and 12. NH_3 emissions from gasoline and diesel vehicles have been reported by Bishop et al [20], this NH_3 is finally deposited as NH_4^+ on soils and receptors. Point labeled as “3” is located at federal highway 180, specifically next to a parking lot for heavy vehicles that travel to Yucatan Peninsula by this way, therefore, the high ammonium levels found in this sampling site could be attributed to these sources.

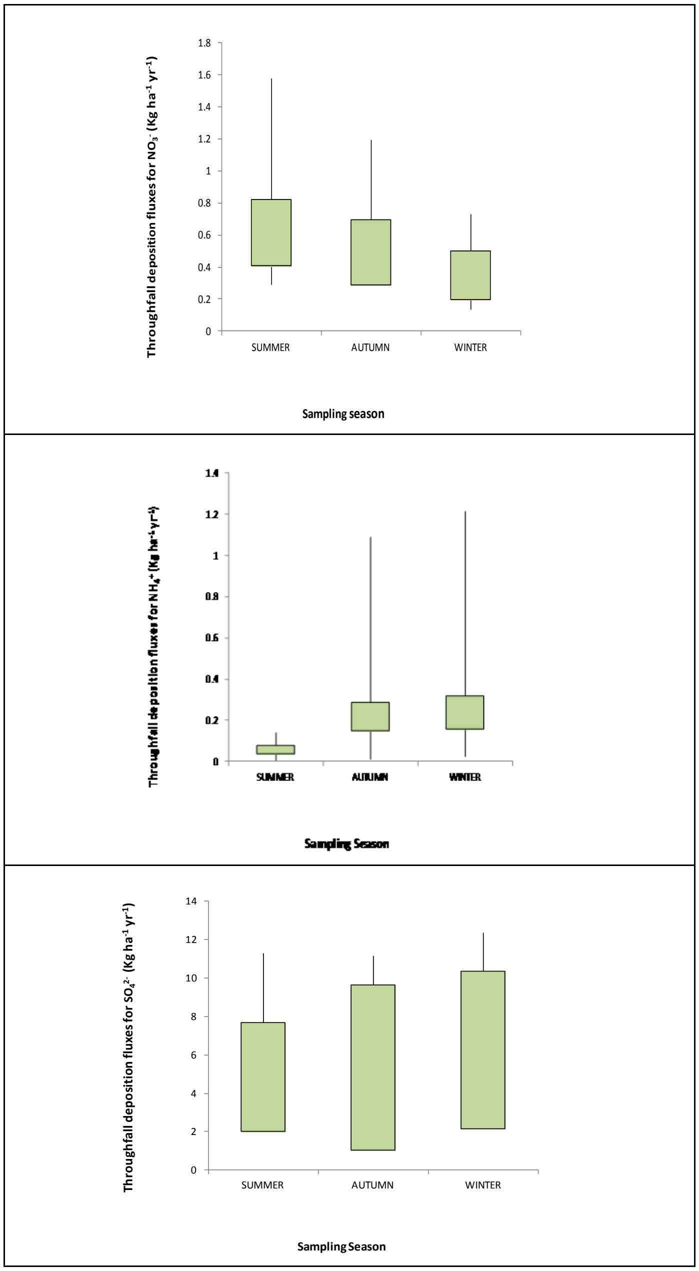

Fig. 2 Atmospheric deposition fluxes for NO_3^-, NH_4^+, and SO_4^{2-} at Xicalango-Atasta region for each sampling period.

Finally, SO_4^{2-} deposition fluxes were higher in sampling points 10, 11 and 12, that correspond to a land use of industrial type; therefore these high sulfate levels can be attributed to local sources as flares in the recompression plant that are burning periodically sour gas. However, it is necessary to consider the significant contribution of regional sources (offshore platforms) during autumn and winter seasons as a result of the cold fronts that transport pollutants from these sources.

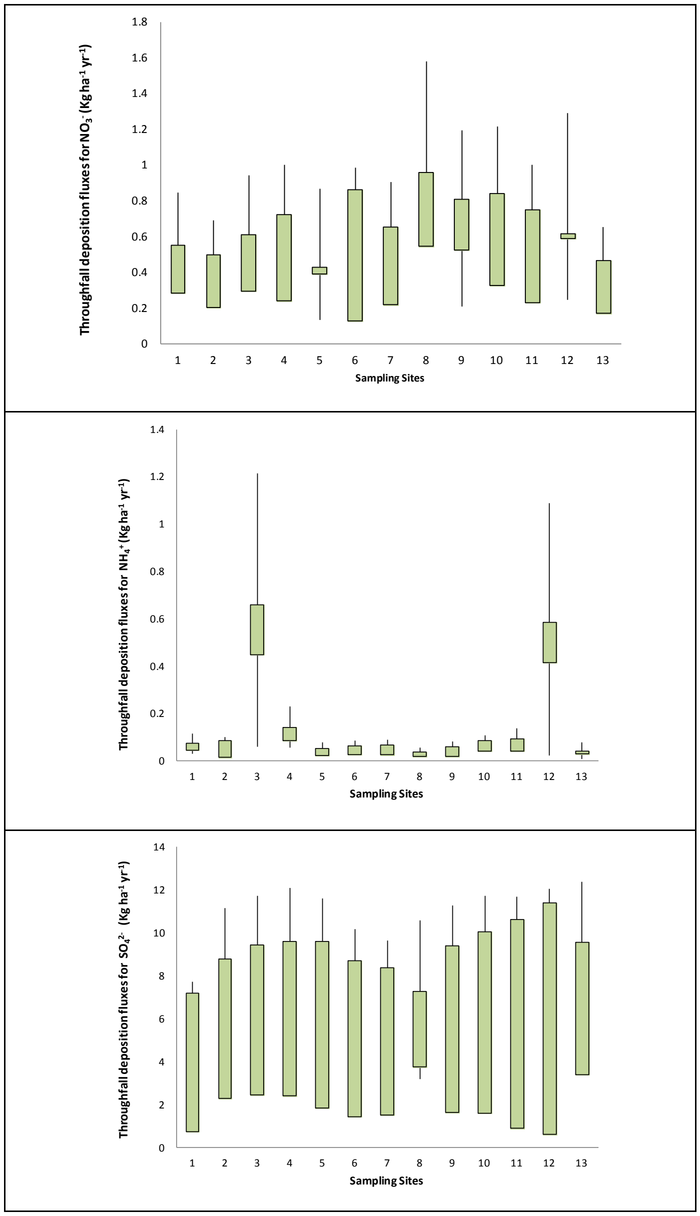

Fig. 3 Atmospheric deposition fluxes for NO_3^-, NH_4^+, and SO_4^{2-} at Xicalango-Atasta region for each sampling site.

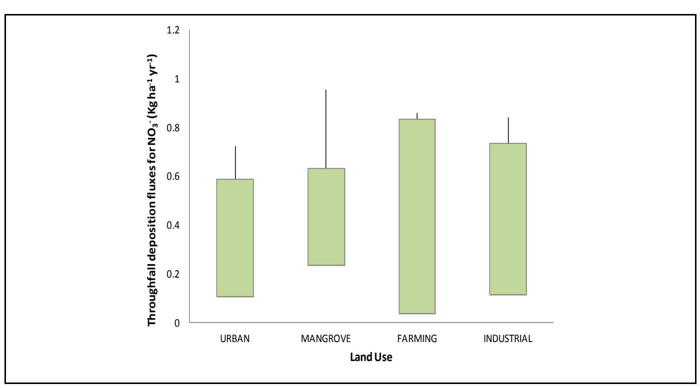

ISBN: 978-1-61804-295-8

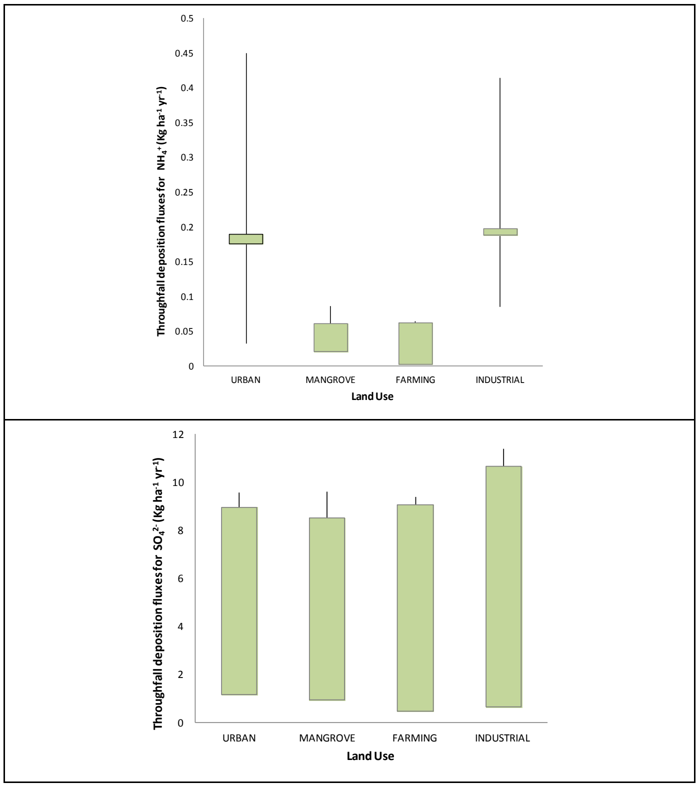

Fig. 4 Atmospheric deposition fluxes for NO_3^-, NH_4^+, and SO_4^{2-} at Xicalango-Atasta for different land use.

IV. Conclusion

Results found in this research work suggest that NO_3^- and NH_4^+ levels had a local origin, whereas, sulfate levels can be attributed to both, local and regional sources. Regional contribution is significant mainly during autumn and winter seasons, when long-range transported air pollutants from platforms enhanced the background levels in this region. However, it was clear that the sour gas recompression plant had a great influence on these background levels in the region Xicalango-Atasta. S atmospheric deposition can be considered as a serious threat to the mangrove ecosystem and the fisheries in this region. Data obtained in this study are preliminary, once the database is completed, interpolation kriging will be applied to obtain distribution maps of throughfall deposition fluxes in geographic information system (GIS). From these maps it will be possible to identify vulnerable zones to develop regional policies focused to regulate and control emission sources to protect the biodiversity in this region

References

[1] G.M. Lovett. " Atmospheric deposition of nutrients and pollutants in North America: an ecological perspective", *Ecol. Applic.* Vol. 4, pp. 629-650, 1994.

[2] L. Ling-Hao, L. Peng, L. "Throughfall and stemflow nutrient depositions to soil in a subtropical evergreen broad-leaved forest in the Wuyi Mountains", *Journal of Environmental Sciences*, Vol. 10, pp. 426-432, 1998.

[3] J.D. Joslin, M.H. Wolfe. "Tests of the use of net throughfall sulfate to estimate dry and occult sulfur deposition", *Atmospheric Environment*, Vol. 26, pp. 63-72, 1992.

[4] S.E. Lindberg, G.M. Lovett. "Deposition and forest canopy interactions of airborne sulfur-Results from the Integrated Forest Study", *Atmospheric Environment*, Vol. 26, pp. 1477-1492, 1992.

[5] T.J. Butler, G.E. Likens. "A direct comparison of throughfall plus stemflow to estimates of dry and total deposition for sulfur and nitrogen", *Atmospheric Environment*, Vol. 29, pp. 1253- 1265, 1998. doi: 10.1016/1352- 2310(94)00339- M.

[6] M.E. Fenn, M.A. Poth. "Temporal and spatial trends in streamwater nitrate concentrations in the San Bernardino Mountains in Southern California", *J. Environ. Qual.*, Vol. 28, pp. 822- 836, 1999. doi: 10.2134/jeq1999.00472425002800030013x.

[7] M.E. Fenn, L.I. De Bauer, T. Hernandez- Tejed. "Summary of air pollution impacts on forest in the Mexico City Air Basin". In: Fenn ME, Bauer LI, Hernandez- Tejeda T. eds., *Urban Air Pollution and Forests: Resources at Risk in the Mexico City Air Basin*. Ecological Studies Series, Volume 156, 2002. Springer- Verlag, New York, NY.

[8] M. Pérez-Suárez, M.E. Fenn, V.M. Cetina-Alcalá, A. Alderete. "The effects of canopy cover on throughfall and soil chemistry in two forest sites in the Mexico City Air Basin", *Atmósfera*, Vol. 21, pp. 83- 100, 2008.

[9] M.E. Fenn, L.I. De Bauer, K. Zeller, A. Quevedo, C. Rodríguez, T. Hernández-Tejeda. "Nitrogen and sulfur deposition in the Mexico City Air basin: Impacts on forest nutrient status and nitrate levels in drainage waters". In: M.E. Fenn et al eds. ***Urban Air Pollution and Forests.*** Springer- Verlag, New York. 2001, pp. 319.

[10] M.E. Fenn, M.A. Poth. " Monitoring nitrogen deposition in throughfall using ion exchange resin columns: A field test in the San Bernardino Mountians", ***J. Environ. Qual***. Vol. 30., pp. 2007- 2014, 2004.

[11] NMX- AA- 079- SCFI- 2001, 2001. Análisis de aguas. Determinación de nitratos en aguas naturales, potables, residuales y residuales tratadas.

[12] W. Fresenius, K.E. Quentin, W. Schneider (Eds.), *Water Analysis*. 1988. Springer Verlag, Berlín: 804 p.

[13] NMX- AA- 074- SCFI- 1981, 1981. Análisis de aguas. Determinación del ión sulfato en aguas naturales, residuales y residuales tratadas.

[14] H. Dieter, T. Gouger. " Critical load, dynamic modeling and impact assessement in Europe". C.E.E. Status. Report. 2000.

[15] E. Hiltbrunner, M. Schwikowski, C. Korner. "Inorganic nitrogen storage in alpine snow pack in the Central Alps (Switzerland)", *Atmospheric Environment,* Vol. 39, pp. 2249-2259, 2005. doi: 10.1016/j.atmosenv.2004.12.037.

[16] M.E. Fenn, R. Haueber, G.S. Tonnesen, J.S. Baron, S. Grossman-Clarke, D. Hope, D.A. Jaffe, S. Copeland, L. Geiser, H.M. Rueth, J.O. Sickman. " Nitrogen emission, deposition and monitoring in the Western United States", ***Bioscience,*** Vol. 53, pp. 391-403, 2003.

[17] L. Pardo, M.E. Fenn, C.L. Goodale, L.H. Geiser, C.T. Driscoll, E.B. Allen, J.S. Baron, R. Bobbink, W.D.Bowman, C.M. Clark, B. Emmet, F.S. Gillian, T.L.Greaver, S.J. Hall, E.A. Lileskov, L. Liu, J.A. Lynch, K.J. Nadelhoffer, S.S. Perakis, M.J. Robin-Abbot, J.L. Stoddard, K.C. Weather, R.L. Dennis. "Effects of nitrogen deposition and empirical nitrogen critical loads for ecoregions of the United States", ***Ecol. Applic,*** Vol. 21, pp. 3049-3082, 2011.

[18] P. Grennfelt, J. Nilsson. "Critical loads for sulphur and nitrogen". Report from a workshop held at Skokloster, Sweden. March 19- 24, 1988. The Nordic Council of Ministers Report 1988: 15, Copenhagen, Denmark. ISBN: 87- 7303- 248- 4.

[19] R. Escoffie, R. Cerón, R., J. Cerón, E. Guevara, C. Carballo, J. Benítez, J. Zavala, F. Anguebes, M. Ramírez. " Throughfall deposition of N and S to mangrove ecosystems in the Southeast of Mexico". In: *Latest trends in Energy, Environment and Development*. WSEAS 7th International Conference on Environmental and Geological Science and Engineering. June 3-5. 2014. Salerno, Italy.

[20] G.A. Bishop, A.M. Peddle, D.H. Stedman. "On- road emission measurements of reactive nitrogen compounds from three California cities", ***Environ, Sci. Technol.*** Vol. 44, pp. 3616- 3620, 2010. doi: 10.1021/es903722p.l

Modeling by Finite Elements Method of Nonlinear Conductivity in Corrosive Mediums

D. BOUKHLEF[1, a*], D. BOUGHRARA[2, b] and H. MOHELLEBI[3, c]

[1]Unité de Recherche en Energies Renouvelables en Milieu Saharien, URERMS, Centre de Développement des Energies Renouvelables, CDER, (01000), Adrar, Algeria

[2] Physics and Chemistry of Materials Laboratory, UMMTO, Tizi- Ouzou,

[3] Numerical Modeling of Electromagnetic Phenomenon and Components Laboratory, UMMTO, Tizi- Ouzou, (15000), BP 17, Algeria.

[a]boukhlefdjidji@gmail.com, [b]d_boughrara@yahoo.fr, [c] mohellebi@yahoo.fr

Keywords: Finite Elements, Electric Potential, Current Density, Nonlinear Electric Conductivity, Corrosion.

Abstract: The objective of this work is to apply a numerical model of electrical conductivity in order to predict the distribution of electric potential and total current density, and put together comparisons between both linear and nonlinear models by considering the electric conductivity as a function of electric potential for nonlinear study. Solving the Laplace equation allows us to present the distribution of potential and total current density. The found results allow us to illustrate that potential and current density distribution is important in the linear case than in nonlinear.

Introduction

Galvanic corrosion, resulting from a metal contacting an -other conducting material in a corrosive medium, is one of the most common types of corrosion [1]. Galvanic corrosion can occur when two dissimilar metallic alloys are in electrical contact with each other for electron transport and are exposed to a conductive environment such as salt water that provides a medium for ionic flow. A material with a lower free corrosion potential in a galvanic couple becomes more active and corrodes preferentially. Corrosion severity of a galvanic couple depends upon various factors such as potential difference between the dissimilar metal alloys, polarization behavior of individual alloys, anode to cathode area ratio, electrolyte conductivity, distance between the dissimilar metal alloys, etc [2,3]. The alloy Al-Mg is widely used in automotive, aerospace and maritime industry for its light weight. The high relative weight strength makes it a good engineering material. The disadvantage is that this alloy is sensitive to different types of surface damage, for reasons of corrosion or degradation of the physical contact with other metals. The objective of this study is to found a nonlinear model of electric conductivity to compare the two cases linear and nonlinear.

Finite Elements Modeling

Numerical model. The relationship between the electric field intensity (E) and the electric potential (ϕ) is,

$$\vec{E} = -\nabla\vec{\phi}. \tag{1}$$

and Ohm’s Law gives the electrolyte current density J, by the following formula :

$$\overrightarrow{J} = \sigma.\vec{E}. \tag{2}$$

ISBN: 978-1-61804-295-8

where σ is the conductivity of the electrolyte.

From the above, the continuity equation becomes,

$$-\nabla(\sigma\nabla\phi) = 0. \tag{3}$$

The calculations were performed by exploiting the software COMSOL Multiphysics for the resolution of the equation of the electric conduction. The distribution of the electric potential, (in volts), on the surface of the anode, the cathode and in the electrolyte surrounding the two metal surfaces is governed by the Laplace (Eq. 3).

When the electrical conductivity σ is considered constant, Eq. 3, is expressed in cylindrical co-ordinates and when using Galerkin method, the finite elements formulation becomes as follow [5]:

$$\iint_\Omega \left(\frac{\partial}{\partial r}\left(\frac{\sigma}{r}\frac{\partial\phi}{\partial r}\right) + \frac{\partial}{\partial z}\left(\frac{\sigma}{r}\frac{\partial\phi}{\partial z}\right)\right)\alpha_j.\,dr.\,dz =$$

$$\iint_\Omega \sigma\left(\frac{\partial\phi}{\partial r}\frac{\partial\alpha_j}{\partial r} + \frac{\partial\phi}{\partial z}\frac{\partial\alpha_j}{\partial z}\right)\frac{dr.dz}{r} + \int_\Gamma \sigma\left(\frac{\partial\phi}{\partial r}n_r + \frac{\partial\phi}{\partial z}n_z\right)\alpha_j.\frac{d\Gamma}{r}. \tag{4}$$

$$\phi(x,y) = \sum_{i=1}^{N}\alpha_i\,(x,y)\phi_i. \tag{5}$$

α_i : finite elements function called form function and $\phi_i$the nodal unknown at node i of the electric potential.
N: total number of nodes at the solving domain.
α_j : projection function which is considered the same one as finite elements function α_i.

The conduction problem is associated to geometry deformation problem. The "Arbitrary Lagrangian Eulerian (ALE)" method which is time dependent, is used in order to track the frontier displacement and the current density distribution in exploiting the ‘’moving mesh’’ technique [3]. The deformation velocity normal to the anodic surface becomes as followed:

$$v.n = -K.\,J_n. \tag{6}$$

where, K is a proportionality coefficient (equal to 3,49 10^{-11} $C^{-1}.m^3$).

At the cathode, the velocity is zero when the surface of cathode is not changed.

When the electrical conductivity (σ) is variable, we need to find a non-linear relationship, which connect the electrical conductivity and electrical potential (ϕ).
On one point i, we can write:

$$\sigma_i = -\frac{J_{si}}{E_i}. \tag{7}$$

We can also write the average electric field on item i:

$$E_{moy} = \frac{\nabla\phi_{moy}}{d_{moy}}. \tag{8}$$

We can write (7) as follows:

$$\sigma = -J_s\frac{d_{moy}}{\nabla\phi_{moy}}. \tag{9}$$

ISBN: 978-1-61804-295-8

The formula of the equation used during our work is:

$$\sigma = -J_s \frac{d}{\phi}. \tag{10}$$

where,
d: the distance between the electrodes,
J_s : the source current density.

Geometry. The Laplace equation is solved in the electrolyte with the area of boundary conditions as presented in Fig. 1.

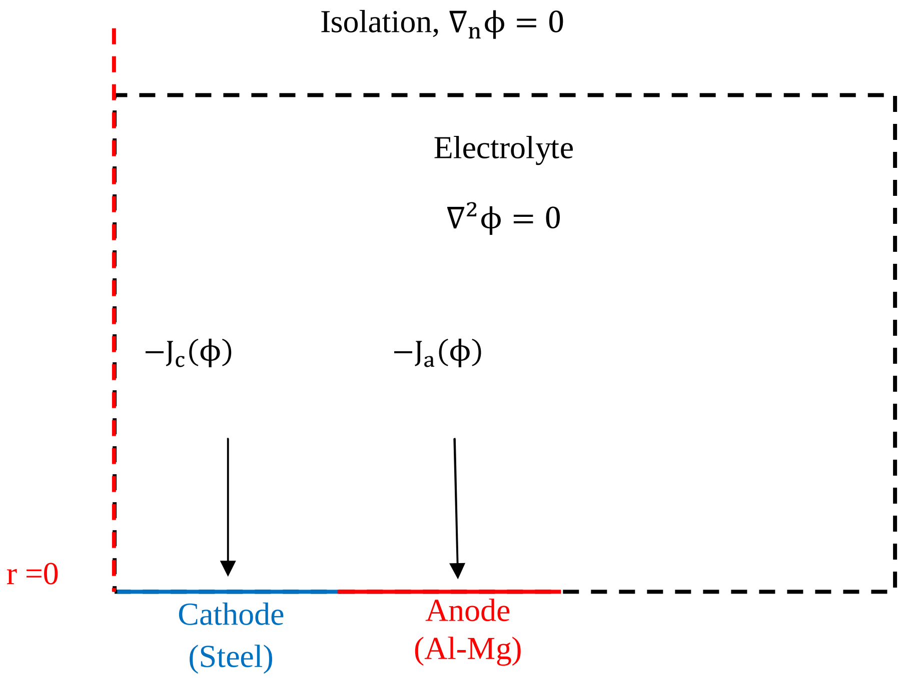

Fig.1. Geometry of the system and boundary conditions.

Application and results

Study of linear problem. The geometry of the model consists of two coplanar electrodes of the same size (2.5 mm) and at their interface an electrolyte square of 1 cm area of the side. The surface plot of electric potential at electric conductivity equal 0.06 S/m is presented in Fig. 2.

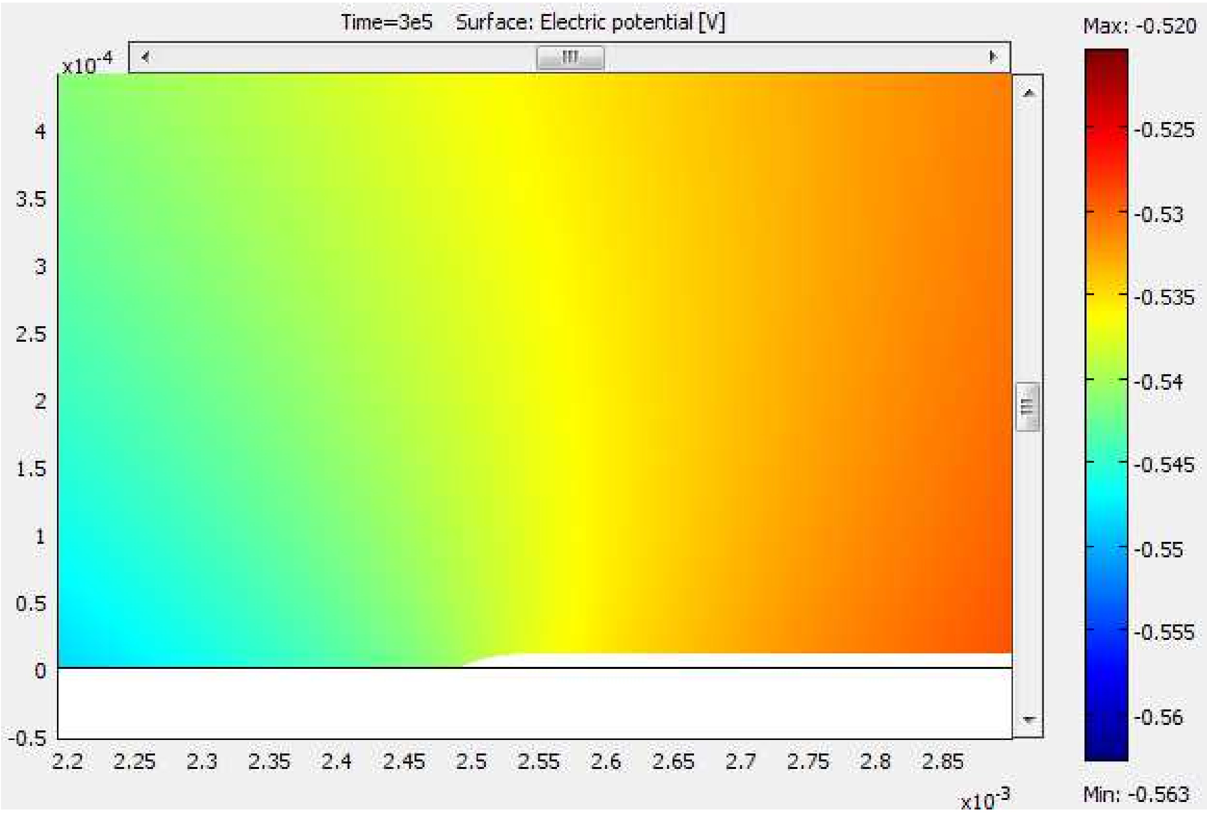

Fig.2. Surface plot of electric potential for steel/Al-Mg after time = 3. 10^5s.

The resolution of the equation of Laplace enables us to present distribution of potential and total current density, on surface of electrodes steel/Al-Mg [6]. The distributions for various values of conductivities are presented on the Fig. 3 and Fig. 4, respectively.

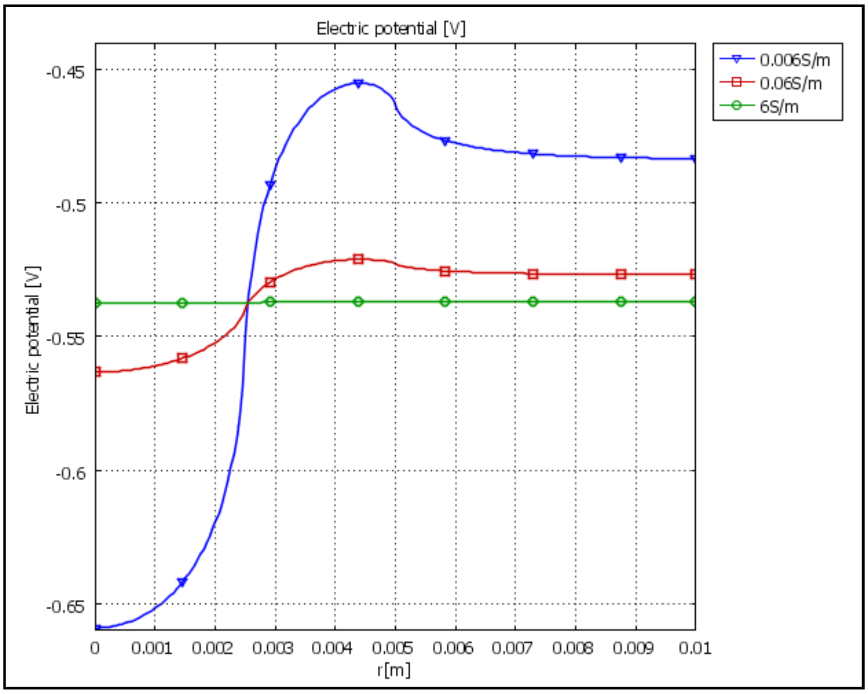

Fig.3. Distribution of electric potential for various values of electric conductivity.

On level of cathode (Fig. 3), the potential is proportional with electric conductivity, in contrast, on level of anode, the variations of potential are more significant for lower values of conductivity, and then it decreases to reach constant values on level of isolation. To note also that throughout surface the potential is constant for a conductivity of 6 S/m.

Fig. 4 shows the distribution of current density for three values of conductivity. The total current is highly distributed on steel (cathode) and on Al - Mg alloy (anode), the values of current densities increase with conductivity. They are in higher range at the junction interface of steel and Al-Mg, and annul at the insulator.

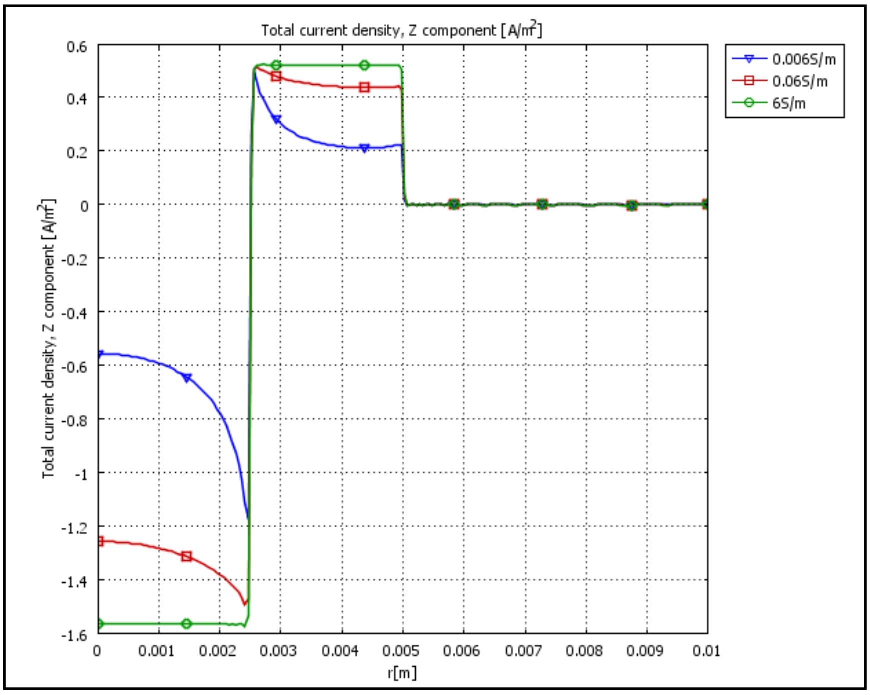

Fig.4. Distribution of total current density for various values of electric conductivity.

Study of nonlinear problem. The electrolyte at the surface of anode and cathode is controlled by the following equation, with a nonlinear variable conductivity:

$$-\vec{\nabla}.\left(\sigma(\phi)\vec{\nabla}\phi\right) = 0. \tag{11}$$

Where,

$$\sigma(\phi) = -J_s\frac{d}{\phi}. \tag{12}$$

To apply the non-linear simulation, the selected values of currents density J_s, and that of the distance d are 1.5 A/dm² and 6 mm, respectively [7].

The finite elements formulation in case of nonlinear study is as follow:

$$\iint_\Omega \left(\frac{\partial}{\partial r}\left(\frac{\sigma(\phi)}{r}\frac{\partial\phi}{\partial r}\right) + \frac{\partial}{\partial z}\left(\frac{\sigma(\phi)}{r}\frac{\partial\phi}{\partial z}\right)\right)\alpha_j.\,dr.\,dz =$$

$$\iint_\Omega \sigma(\phi)\left(\frac{\partial\phi}{\partial r}\frac{\partial\alpha_j}{\partial r} + \frac{\partial\phi}{\partial z}\frac{\partial\alpha_j}{\partial z}\right)\frac{dr.dz}{r} + \int_\Gamma \sigma(\phi)\left(\frac{\partial\phi}{\partial r}n_r + \frac{\partial\phi}{\partial z}n_z\right)\alpha_j.\frac{d\Gamma}{r}. \tag{13}$$

ISBN: 978-1-61804-295-8

The Fig. 5 shows the result of surface plot of electric potential.

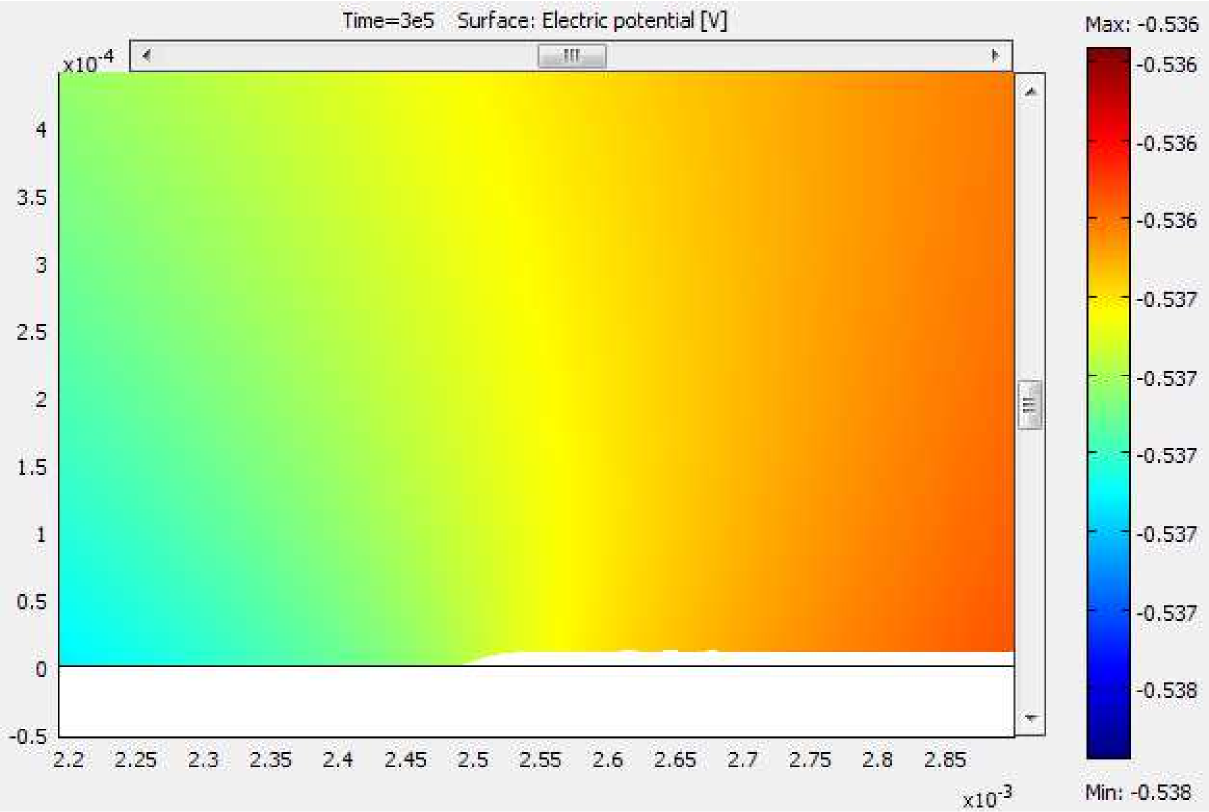

Fig.5. Surface plot of electric potential for steel/Al-Mg with a nonlinear conductivity.

To compare the distribution of potential in the linear and nonlinear case, it is necessary to trace this evolution for the two cases (Fig. 6).

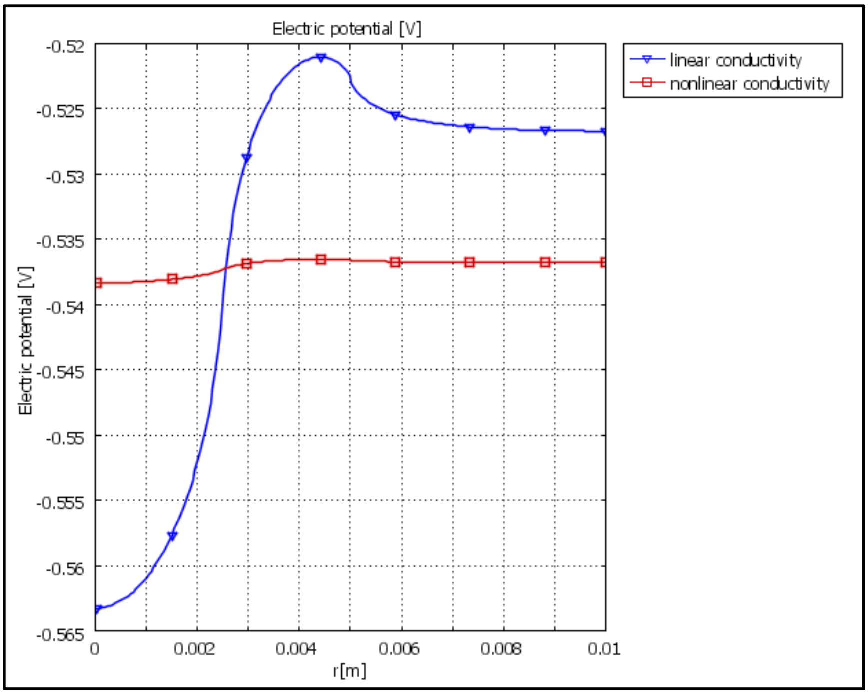

Fig.6. Distribution of electric potential in the linear and nonlinear case.

ISBN: 978-1-61804-295-8

The Fig. 7 shows the distribution of current density for the two cases. The current density is greater in the nonlinear case, its value is then more important at cathode, it decreases to anode, to reach a less value then annuls on the insulator.

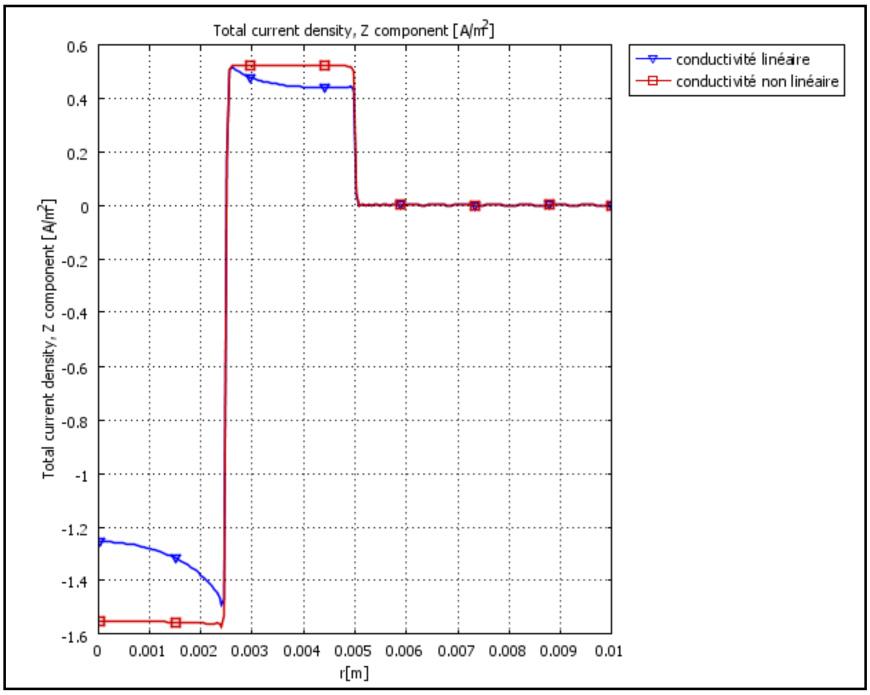

Fig.7. Distribution of current density in the linear and nonlinear case.

The Fig. 8 shows the distribution of electric potential for different values of source current density. At anode, the potential is greater for a low value of current density, and then decreases to constant values at the insulator.

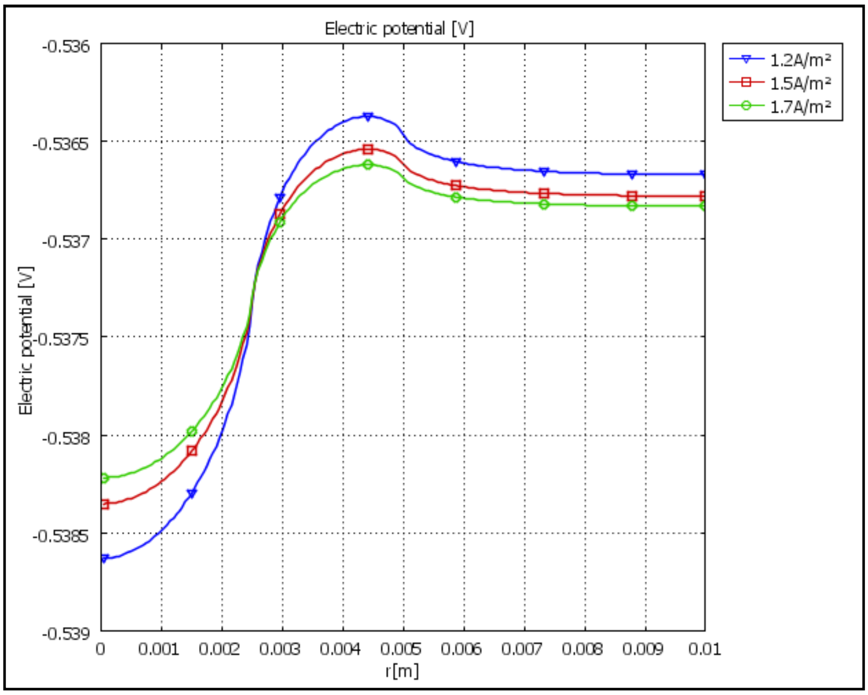

Fig.8. Distribution of electric potential for different values of source current density.

The Fig. 9 shows the variation of the electric conductivity according to electric potential for a source current density of 1.5 A/dm².

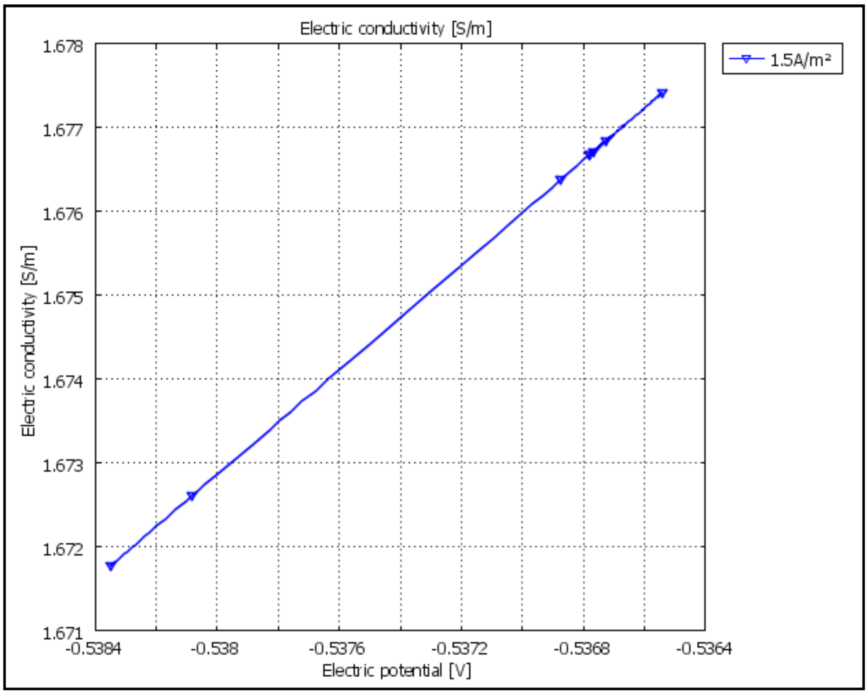

Fig.9. Variation of electric conductivity according to electric potential.

Conclusion

The study of linear electric potential partial differential equation was performed by considering a constant electric conductivity. The finite elements solution was coupled to an analytic solution representing the boundaries conditions of the interface electrolyte/anode-cathode-insulator. The model has been achieved and a follow-up of the distortion of the border is simulated. The nonlinear case yields to a distribution of potential and current density values less important than the linear solution.

References

[1] X. G. Zhang, Galvanic corrosion, Teck Metals Ltd, Mississauga, Ontario, Canada.

[2] ASTM Standard G82-98, Development and Use of a Galvanic Series for Predicting Galvanic Corrosion Performance, Annual Book of ASTM Standards, ASTM International, Philadelphia, 2003.

[3] Kiran B. Deshpande, Corros. Sci. 52 (2010) 3514-3522.

[4] M. E. Turner, Finite Element Modeling of Galvanic Corrosion of Metals, Rensselaer Polytechnic Institute Hartford, CT, December 2012.

[5] H. Mohellebi, M. Féliachi, K. Srairi, Coupled 2D-Analytical and Finite Elements Analysis for the Eddy Current Computation, the Third International Workshop on Electric and Magnetic Field-Liège, Belgium, 6-9 Mai (1996) 339-341.

[6] L. Lacroix, Mécanismes de corrosion localisée de l'alliage d'aluminium 2024, Apport de la Microscopie à Force Atomique (AFM) couplée au Mode Kelvin (KFM) et des alliages modèles, thèse de Doctorat, Université de Toulouse 2008.

[7] D. Landolt, Corrosion et chimie de surfaces des métaux. Ed Press. Polytechniques et universitaires, 1997.

Size-dependent pull-in analysis of electrically actuated micro-plates based on the modified couple stress theory

Arman Mohsenzadeh[1,a], Masoud Tahani[2,b*], Amir Reza Askari[3,c]

[1,2,3]Department of Mechanical Engineering, Faculty of Engineering, Ferdowsi University of Mashhad, Mashhad, Iran

[a]Armanmohsenzadeh@yahoo.com, [b]mtahani@um.ac.ir, [c]amaskari@gmail.com

Keywords: MEMS, Modified couple stress theory, Pull-in analysis, Extended Kantorovich method.

Abstract. In view of the difficulties arisen in determining the solutions of linear eigenvalue problems of fully-clamped rectangular micro-plates, the size-dependent pull-in analysis of such systems has not been carried out yet. Therefore, size-dependent pull-in analysis of such systems is the main goal of the present work. To this end, the size-dependent equation of equilibrium for an electrically actuated fully-clamped rectangular micro-plate based on the combination of the modified couple stress theory and the Kirchhoff plate model is utilized and solved through the computationally efficient single mode Galerkin reduced order method. The linear and un-damped mode-shapes of the system, which are obtained by the extended Kantorovich method (EKM), are employed as the weight functions in the Galerkin procedure. The findings of the present work are compared and validated against the available results in the literature and excellent agreements between them are observed. The results show that considering the effect of couple stress components increases the instability threshold of the system.

Introduction

Thanks to recent advances in the technology of micro-electro-mechanical systems (MEMS), micro sensors and actuators are widely used in different applications and industries. Nowadays, MEMS are key components of many devices because of their small size, low power consumption, high reliability and the ability of batch fabrication [1].

MEMS devices are produced in different types such as micro-beams, micro-plates and micro-mirrors. Parallel rectangular micro-plates are the building blocks of plate-type MEMS. These structures consist of two parallel electrodes which act by applying an external voltage. One of these electrodes is stationary and considered as a rigid substrate and the other one is a flexible micro-plate. Electrostatic force made by applying the external voltage, forces the flexible electrode to deflect toward the rigid substrate. In this manner the mechanical elastic restoring force is the only source which resists against the electrostatic attraction. It is noteworthy that the applied voltage has an upper limit in which the elastic restoring force cannot overcome the electrostatic attraction and the structure suddenly collapses toward the rigid substrate. This phenomenon is called pull-in instability and the minimum associated voltage with that is called pull-in voltage. Pull-in instability was observed by Nathanson et al. [2] for the first time.

Recent experiments show that the mechanical behaviors of materials in micron scales are size-dependent [3]. Size-dependency is an inherent property of the certain materials which emerges when the characteristic size of the structure (e.g. the diameter or the thickness) is comparable to the material length scale parameter. Material length scale parameter is one of the mechanical properties and can be determined by some typical experiments such as micro-torsion test [3] and micro-bend test [4].

The common classical theory (CT) of continuum mechanics cannot predict the size-dependent behavior of materials in micron and sub-micron scales. Therefore, the size-dependent theories have been developed. These theories contain some additional material constants besides two classical Lame's constants for isotropic materials: The classical couple stress theory (CCST), the classical strain gradient theory (CSGT), the modified couple stress theory (MCST) and the strain gradient (SGT) theory of elasticity include two, five, one and three additional material constants,

ISBN: 978-1-61804-295-8

respectively [3, 5-7]. Many researches have been done to investigate the size-dependent behavior of the materials and a lot of them are concentrated on micro-beams while there are a few researches done on micro-plates especially in the case of using MCST. Tsiatas [8] presented a size-dependent model for thin plates based on the Kirchhoff's assumptions. He solved the boundary value problem using the method of fundamental solutions (MFS) which is a boundary-type meshless method. He showed that the deflection of the micro-plates decreases nonlinearly with the increase of material length scale parameter and the MCST to CT ratio of the deflection is influenced only by the Poisson's ratio of the micro-plate. Jomehzadeh et al. [9] investigated the natural frequencies of thin micro-plates with both circular and rectangular shapes. However, their research was limited to rectangular micro-plates with two opposite edges simply supported. They found that considering the size effect increases the natural frequencies of the system. Roque et al. [10] used the MCST together with the first-order shear deformation plate model to study the size-dependent bending of simply supported isotropic micro-plates. They solved the equilibrium equations numerically through a meshless method. Ke et al. [11] investigated the size-dependent bending, buckling and free vibrations of annular Mindlin micro-plates made of functionally graded materials (FGMs) based on the MCST. They solved their equations using differential quadrature method. They found that when the thickness is much greater than the length scale parameter in micro-plates, the size effect is negligible. Ke et al. [12] also developed a similar model for the free vibration analysis of rectangular Mindlin's micro-plates and found that the size effect is significant when the thickness of micro-plate is close to its material length scale parameter. They utilized the p-version of the Ritz method to solve the governing equations of motion. Thai and Choi [13] presented size-dependent models for bending, buckling, and free vibrations of non-linear functionally graded Kirchhoff's and Mindlin's simply supported micro-plates based on the MCST. Although, they could not solve their governing equations for non-linear FG plates and they presented some analytical solutions for other cases of simply supported micro-plates. Zhang et al. [14] presented a novel size-dependent plate element including 4 nodes and 15 degrees of freedom for each node based on a framework of the MCST and the Mindlin's plate model for analyzing the static bending, free vibration and buckling behaviors of thick rectangular micro-plates.

Size-dependent pull-in analysis of plate-type MEMS has not been carried out yet in the open literature. The main aim of this study is to present a size-dependent pull-in analysis for a fully-clamped rectangular micro-plate using the MCST. To this end, the governing partial differential equation (PDE) of equilibrium is investigated and reduced to an algebraic equation through the Galerkin weighted residual method. The linear and un-damped mode-shapes of the micro-plate, which are obtained by the EKM, are utilized as the admissible basis functions. It is found that using only the first mode not only can provide high accurate results in comparison with available empirical observations in the literature, but also it can remove the small gap between the findings of CT and experiments [15]. A detailed parametric study is also conducted to illustrate the significant effects of couple stress components on the pull-in instability threshold of rectangular micro-plates. It is found that the ratio of MCST to CT pull-in voltages is independent of the plate aspect ratio and only depends on Poisson's ratio for systems without the effect of axial residual stresses.

Size-dependent mathematical modeling

Consider two parallel rectangular electrodes of plate-type MEMS. One of them is an isotropic fully-clamped rectangular micro-plate and the other one is a stationary rigid substrate. The length, width, thickness, density, Young's modulus of elasticity, and Poisson's ratio of the flexible electrode are a, b, h, ρ, E, and ν respectively. The initial gap between two electrodes is d. Also X, Y, and Z are the respective coordinates along the length, width, and thickness, and W is the deflection. It is to be noted that, for convenience, the coordinate system is attached at the center of the mid-plane of the micro-plate. According to the MCST presented by Yang et al. [7], the strain energy density consists of both the strain and curvature components which are conjugated with the classical stress and couple stress components, respectively. Also the MCST includes only one additional constant parameter known as the material length scale parameter. Considering the MCST and

Kirchhoff plate model, the governing equation of equilibrium for an electrically actuated rectangular micro-plate can be written as [8, 16]:

$$\left(\frac{Eh^3}{12\left(1-v^2\right)}+\frac{Ehl^2}{2\left(1+v\right)}\right)\left(\frac{\partial^4 W}{\partial X^4}+2\frac{\partial^4 W}{\partial X^2\partial Y^2}+\frac{\partial^4 W}{\partial Y^4}\right)-\left(\hat{N}_x\frac{\partial^2 W}{\partial X^2}+\hat{N}_y\frac{\partial^2 W}{\partial Y^2}\right)=\frac{\varepsilon V^2}{2\left(d-W\right)^2} \tag{1}$$

where l is the material length scale parameter, V is the polarized DC voltage and $\hat{N}_x$ and $\hat{N}_y$ are the axial residual forces in the X and Y directions, respectively. To non-dimensionalize the governing PDE, dimensionless parameters $x = X/a$, $y = Y/b$, and $w = W/d$ are introduced. By substituting these parameters into Eq. 1, the non-dimensionalized form of the governing equation takes the form:

$$\left(1+6\alpha_2\right)\left(\frac{\partial^4 w}{\partial x^4}+2\alpha_1^{\,2}\frac{\partial^4 w}{\partial x^2\partial y^2}+\alpha_1^{\,4}\frac{\partial^4 w}{\partial y^4}\right)-\left(N_x\frac{\partial^2 w}{\partial x^2}+\alpha_1^{\,4}N_y\frac{\partial^2 w}{\partial y^2}\right)=\frac{\beta}{(1-w)^2} \tag{2}$$

where

$$\alpha_1=\frac{a}{b},\ \alpha_2=\frac{1-v}{\left(h/l\right)^2},\ \beta=\frac{\varepsilon a^4V^2}{2Dd^3},\ D=\frac{Eh^3}{12(1-v^2)},\ N_x=\frac{a^2\hat{N}_x}{D},\ N_y=\frac{b^2\hat{N}_y}{D} \tag{3}$$

Solution procedure

According to the Galerkin weighted residual method, the static deflection of the micro-plate can be expressed as [1, 17]:

$$w\left(x,y\right)=\sum_{i=1}^{n}\varphi_i\left(x,y\right)u_i \tag{4}$$

where n is the number of degrees of freedom, φ_i is the ith linear and un-damped mode-shape of the micro-plate, and u_i is the ith un-known generalized coordinate which should be determined. It is proved that, for micro-plates' problems, utilizing only the first linear and un-damped mode-shape for the transverse deflection can provide sufficient accuracy [18, 19]. Hence, the solution is expressed as:

$$w\left(x,y\right)=\varphi_{11}\left(x,y\right)u \tag{5}$$

Substituting Eq. 5 into Eq. 2 and applying the Galerkin weighted residual method [17], one can obtain:

$$\begin{aligned}&\left[\left(1+6\alpha_2\right)\int_{-1/2}^{1/2}\int_{-1/2}^{1/2}\left(\frac{\partial^4\varphi_{11}}{\partial x^4}+2\alpha_1^{\,2}\frac{\partial^4\varphi_{11}}{\partial x^2\partial y^2}+\alpha_1^{\,4}\frac{\partial^4\varphi_{11}}{\partial y^4}\right)\varphi_{11}dxdy\right.\\&\left.-\int_{-1/2}^{1/2}\int_{-1/2}^{1/2}\left(N_x\frac{\partial^2\varphi_{11}}{\partial x^2}+\alpha_1^{\,4}N_y\frac{\partial^2\varphi_{11}}{\partial y^2}\right)\varphi_{11}dxdy\right]u=\beta\int_{-1/2}^{1/2}\int_{-1/2}^{1/2}\frac{\varphi_{11}}{\left(1-u\varphi_{11}\right)^2}dxdy\end{aligned} \tag{6}$$

In Eq. 6, the first linear and un-damped mode-shape of the plate (i.e. φ_{11}) is obtained through the EKM. To do so, the mode-shape of the rectangular micro-plate is considered as a multiplication of two separable functions as [19, 20]:

$$\varphi_{11}\left(x,y\right)=f\left(x\right)g\left(y\right) \tag{7}$$

According to the iterative procedure of the EKM [19, 20], the variational form of the linear and un-damped eigenvalue problem associated with the present micro-plate problem is considered. At the first iteration step, one of the aforementioned separable functions (for example $g(y)$) is considered as a known guess function such that it satisfies all corresponding separated boundary conditions [19]. By choosing $g(y)=(4y^2-1)^2$ and substituting this function into the variational form of the present eigenvalue PDE and employing the fundamental lemma of variational calculus [17], the other separable function (i.e. $f(x)$) will be determined through solving a resultant linear ordinary differential equation (ODE) with its corresponding separated boundary conditions [19]. At the next step of iteration, the determined $f(x)$ is employed as the known function and import into the variational form of the eigenvalue PDE again. Utilizing the mentioned procedure $g(y)$ can be obtained by solving another ODE with its corresponding separated boundary conditions. This procedure should be continued till the convergence is achieved. It is proved that only one iteration yields the mode-shape of a fully clamped rectangular micro-plate accurately [19]. Following the EKM procedure, the eigenvalue PDE will be separated to two following ODEs as [19, 20]:

$$\frac{d^4f}{dx^4}-I_1\frac{d^2f}{dx^2}+\left(I_2-\bar{\alpha}_2\omega_{mn}^2\right)f=0 \tag{8a}$$

$$\frac{d^4g}{dy^4}-I_1'\frac{d^2g}{dy^2}+\left(I_2'-\bar{\alpha}_2'\omega_{mn}^2\right)g=0 \tag{8b}$$

where

$$I_1=\frac{2\alpha_1^2(1+6\alpha_2)\int_{-1/2}^{1/2}\left(\frac{dg}{dy}\right)^2dy+N_x\int_{-1/2}^{1/2}g^2\,dy}{(1+6\alpha_2)\int_{-1/2}^{1/2}g^2\,dy},\ I_2=\frac{\alpha_1^4\left[(1+6\alpha_2)\int_{-1/2}^{1/2}\left(\frac{d^2g}{dy^2}\right)^2dy+N_y\int_{-1/2}^{1/2}\left(\frac{dg}{dy}\right)^2dy\right]}{(1+6\alpha_2)\int_{-1/2}^{1/2}g^2\,dy}$$

$$I_1'=\frac{2(1+6\alpha_2)\int_{-1/2}^{1/2}\left(\frac{df}{dx}\right)^2dx+\alpha_1^2N_y\int_{-1/2}^{1/2}f^2\,dx}{\alpha_1^2(1+6\alpha_2)\int_{-1/2}^{1/2}f^2\,dx},\ I_2'=\frac{(1+6\alpha_2)\int_{-1/2}^{1/2}\left(\frac{d^2f}{dx^2}\right)^2dx+N_x\int_{-1/2}^{1/2}\left(\frac{df}{dx}\right)^2dx}{\alpha_1^4(1+6\alpha_2)\int_{-1/2}^{1/2}f^2\,dx} \tag{9}$$

$$\bar{\alpha}_2=\frac{1}{1+6\alpha_2},\ \bar{\alpha}_2'=\frac{1}{\alpha_1^4(1+6\alpha_2)}$$

The mode-shapes of a fully-clamped rectangular micro-plate will be obtained by applying the separated boundary conditions on the solutions of Eqs. 8. By substituting the first determined linear and un-damped mode-shape of the plate, the only unknown of the non-linear algebraic Eq. 6 can be obtained iteratively. To do so, the non-linear Eq. 6 is linearized using the zeroth order Tailor's expansion of its non-linear terms about the unknown generalized coordinate u and the following iterative solution is obtained:

$$u_{N+1}=\frac{\beta\int_{-1/2}^{1/2}\int_{-1/2}^{1/2}\frac{\varphi_{11}}{(1-(u_N\varphi_{11}))^2}dxdy}{\int_{-1/2}^{1/2}\int_{-1/2}^{1/2}\left((1+6\alpha_2)\left(\frac{\partial^4\varphi_{11}}{\partial x^4}+2\alpha_1^2\frac{\partial^4\varphi_{11}}{\partial x^2\partial y^2}+\alpha_1^4\frac{\partial^4\varphi_{11}}{\partial y^4}\right)-\left(N_x\frac{\partial^2\varphi_{11}}{\partial x^2}+\alpha_1^4N_y\frac{\partial^2\varphi_{11}}{\partial y^2}\right)\right)\varphi_{11}dxdy} \tag{10}$$

At the first step, the value of the unknown parameter u (i.e. u_0) is assumed to be zero. This iterative procedure will be continued till the convergence is occurred or pull-in is happened. The convergence criteria and pull-in condition are set to $(u_{N+1}-u_N)/u_N\le 10^{-6}$ and $w_{\text{mid-point}}=\varphi_{11}(0,0)u_{N+1}\ge 1$, respectively [19, 21].

Results and discussions

In order to verify the present study, the results are validated by the experimental observations of Francais and Dufour [15]. In this case the axial residual stresses are neglected and the specifications of the system are given in Table 1.

Table 1. Material and geometrical parameters of the system

p	E	v	h	d	l [22]
$2320\,\mathrm{kg/m^3}$	$169\,\mathrm{GPa}$	0.3	$20\,\mu\mathrm{m}$	$5\,\mu\mathrm{m}$	$0.592\,\mu\mathrm{m}$

According to Fig. 1 the results are in excellent agreement with those obtained by Francais and Dufour [15]. To find the results of the CT using the present procedure the value of the material length scale parameter is set to zero (i.e. $l=0$). Fig. 1 also shows the comparison between the MCST and CT results. It is seen that use of the MCST increases the pull-in voltage and makes the results more accurate and compatible with the empirical observations.

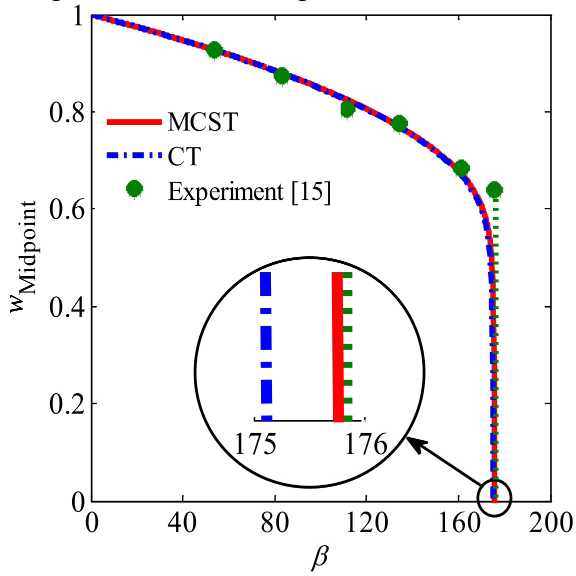

Fig. 1. Non-dimensional midpoint deflection versus non-dimensional applied voltage

According to Eq. 3 the coefficient of the MCST (i.e. α_2) is a function of h/l. On the other hand, to investigate the effect of using the MCST in compare to the CT the ratio of the pull-in voltage in the both theories is considered (i. e. $\beta_{\mathrm{PI}}{}^{\mathrm{MCST}}/\beta_{\mathrm{PI}}{}^{\mathrm{CT}}$). Fig. 2 represents $\beta_{\mathrm{PI}}{}^{\mathrm{MCST}}/\beta_{\mathrm{PI}}{}^{\mathrm{CT}}$ versus h/l for different values of aspect ratio when there exists no axial load.

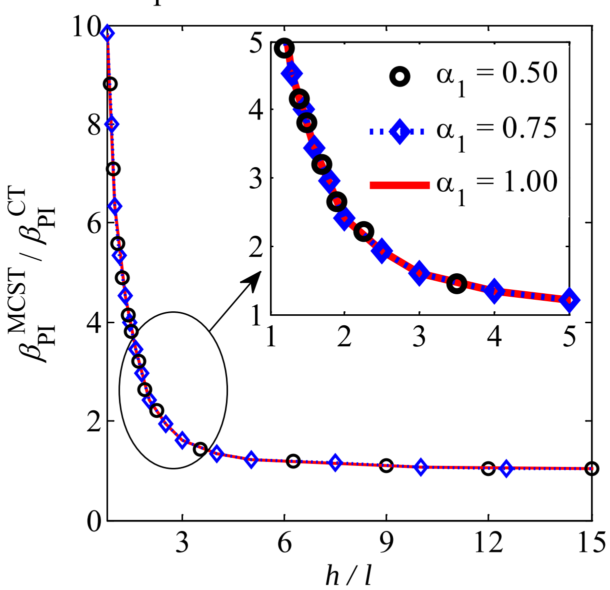

Fig. 2. Effect of plate's aspect ratio on $\beta_{\mathrm{PI}}{}^{\mathrm{MCST}}/\beta_{\mathrm{PI}}{}^{\mathrm{CT}}$ ($N_x = N_y = 0$)

As it is seen in Fig. 2, when there exists no axial load, the ratio of the pull-in voltage found by both of the theories is independent of the plate's aspect ratio. Fig. 3 shows the ratio of $V_{\mathrm{PI}}^{\mathrm{MCST}}/V_{\mathrm{PI}}^{\mathrm{CT}}$ considering the axial loads. It is to be noted that the ratio of $V_{\mathrm{PI}}^{\mathrm{MCST}}/V_{\mathrm{PI}}^{\mathrm{CT}}$ can be calculated as $\sqrt{\beta_{\mathrm{PI}}{}^{\mathrm{MCST}}/\beta_{\mathrm{PI}}{}^{\mathrm{CT}}}$. As It is observed form Fig.3, the ratio of $V_{\mathrm{PI}}^{\mathrm{MCST}}/V_{\mathrm{PI}}^{\mathrm{CT}}$ increases by applying compressive axial load and decreases when tensile axial loads are applied. Also the effect of compressive axial load is more than that of tensile one. In this case the ratio of $V_{\mathrm{PI}}^{\mathrm{MCST}}/V_{\mathrm{PI}}^{\mathrm{CT}}$ decreases by reducing the plate's aspect ratio.

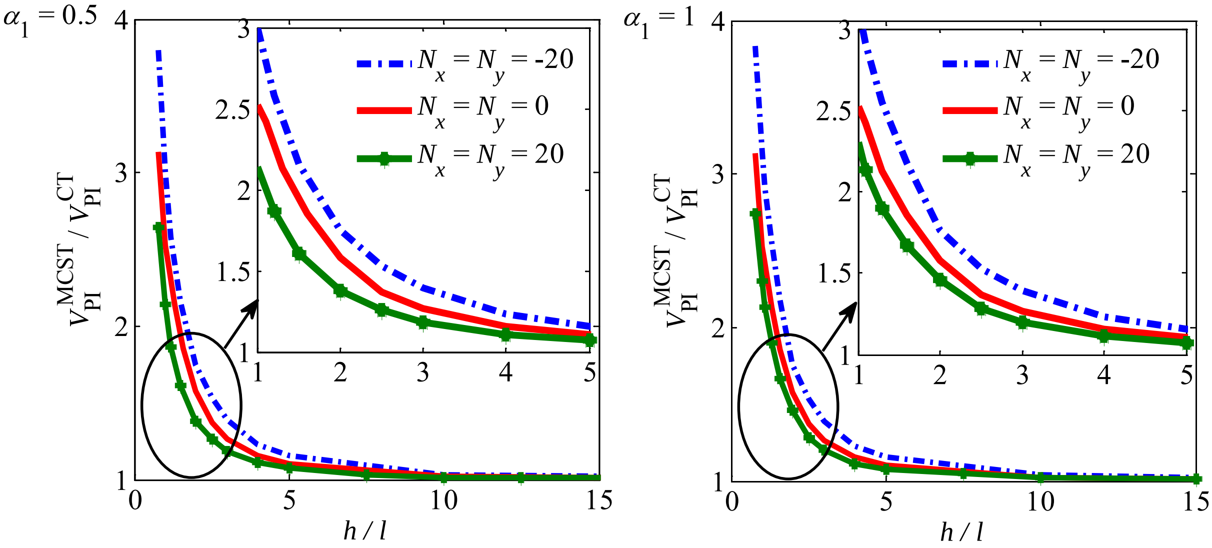

Fig. 3. Effects of plate's aspect ratio and applied axial loads on the ratio of $V_{\mathrm{PI}}^{\mathrm{MCST}}/V_{\mathrm{PI}}^{\mathrm{CT}}$

Summary

In this study, a combination of the Galerkin projection method and the EKM has been successfully utilized to investigate the size-dependent pull-in instability of fully clamped rectangular micro-plates based on the MCST. The main conclusions of the present work can be summarized to:

- The decrease of the size effect parameter (i.e. h/l) increases the difference between the results of the MCST and CT.
- The differences between the MCST and CT results for pull-in voltage, are usually negligible when $h/l \geq 10$. However, this range will be extended more for axially compressed micro-plates.
- The ratio of $V_{\mathrm{PI}}^{\mathrm{MCST}}/V_{\mathrm{PI}}^{\mathrm{CT}}$ is independent of the plate's aspect ratio for axially unstressed micro-plates.
- The ratio of $V_{\mathrm{PI}}^{\mathrm{MCST}}/V_{\mathrm{PI}}^{\mathrm{CT}}$ decreases non-linearly by a decrease of plate's aspect ratio for axially stressed micro-plates.

References

[1] M.I. Younis: *MEMS Linear and Nonlinear Statics and Dynamics*, (Springer, New York 2011).

[2] H.C. Nathanson, W.E. Newell, R.A. Wickstrom and J.R. Davis: The resonant gate transistor, IEEE T. Electron. Dev. 14 (3) (1967), pp. 117-133

[3] N.A. Fleck, G.M. Muller, M.F. Ashby and J.W. Hutchinson: Strain gradient plasticity: theory and experiment, Acta Metall. Mater. 42 (1994), pp. 475–487

[4] J.S. Stolken and A.G. Evans: Microbend test method for measuring the plasticity length scale, Acta Mater. 46 (1998), pp. 5109-5115

[5] R.D. Mindlin and H.F. Tiersten: Effects of couple-stresses in linear elasticity, Arch. Ration. Mech. An. 11 (1) (1962), pp. 415-448

[6] D.C.C. Lam, F. Yang, A.C.M. Chong, J. Wang and P. Tong: Experiments and theory in strain gradient elasticity, J. Mech. Phys. Solids. 51 (2003), pp. 1477-1508

[7] F. Yang, A.C.M. Chong, D.C.C. Lam and P. Tong: Couple stress based strain gradient theory for elasticity, Int. J. Solids Struct. 39 (2002), pp. 2731-2743

[8] G.C. Tsiatas: A new Kirchhoff plate model based on a modified couple stress theory, Int. J. Solids Struct. 46 (2009), pp. 2757–2764

[9] E. Jomehzadeh, H.R. Noori and A.R. Saidi: The size-dependent vibration analysis of micro-plates based on a modified couple stress theory, Physica E. 43 (2011), pp. 877–883

[10] C.M.C. Roque, A.J.M. Ferreira and J.N. Reddy: Analysis of Mindlin micro plates with a modified couple stress theory and a meshless method, Appl. Math. Model. 37 (2013), pp. 4626–4633

[11] L.L. Ke, J. Yang, S. Kitipornchai and M.A. Bradford: Bending, buckling and vibration of size-dependent functionally graded annular microplates, Compos. Struct. 94 (2012), pp. 3250–3257

[12] L.L. Ke, Y.S. Wang, J. Yang and S. Kitipornchai: Free vibration of size-dependent Mindlin microplates based on the modified couple stress theory, J. Sound Vib. 331 (2012), pp. 94–106

[13] H.T. Thai and D.H. Choi: Size-dependent functionally graded Kirchhoff and Mindlin plate models based on a modified couple stress theory, Compos. Struct. 95 (2013), pp. 142–153

[14] B. Zhang, Y. He, D. Liu, Z. Gan and L. Shen: A non-classical Mindlin plate finite element based on a modified couple stress theory, Eur. J. Mech. A-Solid. 42 (2013), pp. 63-80

[15] O. Francais and I. Dufour: Normalized abacus for the global behavior of the diaphragms: pneumatic, electrostatic, piezoelectric or electromagnetic actuation, J. Modeling Simulation Microsys. 12 (2) (1999), pp. 149-160

[16] R.C. Batra, M. Porfiri and D. Spinello: Review of modeling electrostatically actuated microelectromechanical systems, Smart Mater. Struct. 16 (2007), pp. R23-31

[17] J.N. Reddy: *Energy Principles and Variational Methods in Applied Mechanics*, (John Wiley & Sons, New York 2002).

[18] R.C. Batra, M. Porfiri and D. Spinello: Reduced-order models for microelectromechanical rectangular and circular plates incorporating the Casimir force, Int. J. Solids Struct. 45 (2008), pp. 3558-3583

[19] A. Mohsenzadeh, M. Tahani and A.R. Askari: A novel method for investigating the Casimir effect on pull-in instability of electrostatically actuated fully clamped rectangular nano/micro-plates, J. Nanoscience. Accepted for publication

[20] A.R. Askari and M. Tahani: Analytical determination of size-dependent natural frequencies of fully clamped rectangular micro-plates based on the modified couple stress theory, J. Mech. Sci. Technol. Accepted for publication

[21] M. Tahani and A.R. Askari: Accurate electrostatic and van der Waals pull-in prediction for fully clamped nano/micro-beams using linear universal graphs of pull-in instability, Physica E. 63 (2014), pp. 151-159

[22] M. Rahaeifard, M.H. Kahrobaiyan, M. Asghari and M.T. Ahmadian: Static pull-in analysis of microcantilevers based on the modified couple stress theory, Sensor Actuat. A-Phys. . 171 (2011), pp. 370-374

Levels and origin of aromatic hydrocarbons in air of an urban site located at the center of the Veracruz State 2014

Cruz-Cruz, A.I[2a]. , Cerón-Bretón, J.G[1b]*., Cerón-Bretón, R.M[1c]. , Ramírez-Lara, E[3d]. , Rustrián-Portilla, E[2e]. , Houbron, E. [2f], Aguilar-Ucán, C.A[1g]. , Montalvo-Romero, C[1h]. , Anguebes-Franseschi,F[1i]., Gonzalez, G.I[2j]., Cima-Mukul, C[1k].

[1]Chemistry Faculty. Autonomous University of Carmen. Ciudad del Carmen, Campeche, Mexico
[2]Chemistry Faculty. Universidad Veracruzana. Orizaba, Veracruz, Mexico.
[3]Chemistry Faculty. Autonomous University of Nuevo Leon. San Nicolás de los Garza, Nuevo León, Mexico
[a]anitha_rock@hotmail.com, [b*]jceron@pampano.unacar.mx, [c]rceron@pampano.unacar.mx, [d]evangelina.ramirezlr@uanl.edu.mx, [e]erustrian@uv.mx, [f]ehoubron@uv.mx, [g]caguilar@pampano.unacar.mx, [h]cmontalvo@pampano.unacar.mx, [i]fanguebes@pampano.unacar.mx, [j]giglzlz2@hotmail.com, [k]ccima@pampano.unacar.mx

Abstract — BTEX (Benzene, toluene, ethylbenzene, and p-xylene) were sampled in ambient air of Orizaba, Veracruz, Mexico. Mean concentrations found in this study were 80.06 μgm^{-3}, 14,60 μgm^{-3}, 2.74 μgm^{-3}, and 2.25 μgm^{-3} for benzene, toluene, ethylbenzene and p-xylene, respectively. Benzene did not show a clear diurnal pattern. From the meteorological analysis, Toluene/Benzene and p-xylene/ethylbenzene ratios, spearman correlation coefficients and principal component analysis (PCA) it was possible to elucidate the probable sources for BTEX. Benzene was associated to vehicular exhaust emissions from mobile sources, whereas the rest of BTEX could have their origin from other sources different from vehicular emissions.

***Keywords*—**BTEX, air pollution, VOCs, atmospheric pollution, Orizaba, Veracruz.

Cruz-Cruz, A.I.. is with Chemistry Faculty of the UniversidadVeracruzana in Orizaba, Veracruz, Mexico. e-mail: anitha_rock@hotmail.com.

Cerón-Bretón, J.G. is with Chemistry Faculty of the Autonomous University of Carmen in Ciudad del Carmen, Campeche, Mexico. (corresponding author). Phone: (52) 938 38 1 10 18, ext 2106; e-mail: jceron@pampano.unacar.mx.

Cerón-Bretón, R.M. is with Chemistry Faculty of the Autonomous University of Carmen in Ciudad del Carmen, Campeche, Mexico. e-mail: rceron@pampano.unacar.mx.

Ramírez-Lara, E. is with the Chemistry Faculty. Autonomous University of Nuevo Leon in San Nicolás de los Garza, Nuevo León, Mexico. e-mail: evangelina.ramirezlr@uanl.edu.mx.

Rustrián-Portilla, E. is with Chemistry Faculty of the UniversidadVeracruzana in Orizaba, Veracruz, Mexico. e-mail: erustrian@uv.mx.

Houbron, E. is with Chemistry Faculty of the Universidad Veracruzana in Orizaba, Veracruz, Mexico. e-mail: ehoubron@uv.mx.

Aguilar-Ucán, C.A.. is with Chemistry Faculty of the Autonomous University of Carmen in Ciudad del Carmen, Campeche, Mexico. e-mail: caguilar@pampano.unacar.mx.

Montalvo-Romero, C. is with Chemistry Faculty of the Autonomous University of Carmen in Ciudad del Carmen, Campeche, Mexico. e-mail: cmontalvo@pampano.unacar.mx.

Anguebes-Franseschi, F. is with Chemistry Faculty of the Autonomous University of Carmen in Ciudad del Carmen, Campeche, Mexico. e-mail: fanguebes@pampano.unacar.mx.

González, G.I. is with Chemistry Faculty of the Universidad Veracruzana in Orizaba, Veracruz, Mexico. e-mail: giglzlz2@hotmail.com.

Cima-Mukul, C. is with the Autonomous University of Carmen in Ciudad del Carmen, Campeche, Mexico. e-mail: ccima@pampano.unacar.mx.

I. Introduction

TROPOSPHERIC ozone levels, photochemical smog fomation, degradation of air quality and concerns about effects in public health have been associated to the presence of volatile organic compounds (VOCs) in urban areas [1]. For all these reason it is crucial to characterize the sources and distribution of these polutants in urban areas. Within this group of compounds there is a subgroup named as "BTEX" which includes to benzene and its derivatives (toluene, ethyl-benzene, 1,2,4-trimethyl-benzene, p-xylene, o-xylene, m-xylene, among others). Recent studies have focused on BTEX due to their carcinogenic potential and abundance in urban ambient air [2]. These compounds are ubiquitous in the atmosphere, due to both natural and anthropogenic emissions [3]. Anthropogenic sources include vehicle exhaust emissions, solvent and gas emissions from manufacturing and chemical facilities as the major contributors [4].BTEX variation and sources have been broadly characterized in the last two decades in megacities around the world [5-7]. However, in Mexico there is enough information about the diurnal, seasonal distribution of these pollutants. Most of the information have been focused on Mexico city and its surroundings [8-11] and megacities like Monterrey [12, 14]. Veracruz State is located in the middle of the Gulf of Mexico Coast and it includes important cities like Coatzacoalcos, Poza Rica, Xalapa and Orizaba. Many industries, educational and bussiness centers are located in Orizaba. Orizaba is located at 18° 53' N and 97° 10' W This municipality represents the 0.04% of Veracruz's state Surface and it have had an increased economic development in the last years. As a consequence this city has experimented a population grown (more than 120 000 inhabitants) and an increase in its economic activity and its vehicular fleet. Therefore, the objectives of this study are to investigate the correlation inter-species of BTEX and their relation with meteorological parameters using a principal component analysis (PCA) and meteorological analysis (wind roses and 24 h backward air masses trajectories). This work constitute the first study on air quality in this region and it will let us to infer the probable origin of BTEX and to know the influence of meteorological parameters on BTEX levels in the study site during autumn 2014.

II. Methodology

A. Study Area

Orizaba City is located at 18° 53'and 18° 50' N; and 97° 04' and 97° 10' W. This municipality has borders at the north with Ixhuatlancillo, Mariano Escobedo, Atzacan e Ixtaczoquitlán; at the east with Ixtaczoquitlán; at the south with Ixtaczoquitlán, Rafael Delgado, Huiloapan and Rio Blanco; and at the west with Rio Blanco and Ixhuatlancillo. This city is on the Neovolcanic axis and "Sierra Madre del Sur". Orizaba has two types of weather one is wet semiwarm with a lot of rain in summer and the other is wet temperate with abundant rainfall in summer. In Fig. 1 it can be observed the specific sampling site which was located in the urban center of the city where many commercial and bussines activities are performed along one avenue with high vehicular traffic at 18º51'02.2"N and 97 º06'13.6"W and at 1172 masl.

B. Sampling Method

A total of 36 samples were collected from November 6 to November 28, 2014, during the autumn season. Benzene (B), ethyl benzene (Ebz), toluene (T) and p-xylene (X) were determined in all ambient air samples. Samples were collected using glass tubes containing 226-01 Anasorb CSC (SKC) with following features: length 70 mm; inner diameter 4.0 mm; outer diameter 6 mm packed in two sections with 100 mg and 500 mg of active carbon, separated by a glass wool section (Method INSHT MTA/MA-030/A92) [13]. The downstream end of the glass tube was connected to a calibrated flow meter. Ambient air was passed through the glass tubes at a flow rate of 200 ml min-1 at 1.5-hour intervals (morning, midday and afternoon). Sampling was carried out using a Universal XR pump model PCXR4 (SKC), at three sampling periods (local time): B1 (from 07:00 to 08:30 h), B2 (from 14:00 to 15:30 h) and B3 (from 17:30 to 19:00 h). Sampling tubes were protected from adverse weather conditions by aluminum shelters. After the exposure time, the adsorption tubes were labeled and capped tightly with PTFE caps and transferred to the laboratory in cold boxes. Samples were analyzed within three weeks after sample collection at the Environmental Sciences Laboratory of the Autonomous University of Carmen City (UNACAR).

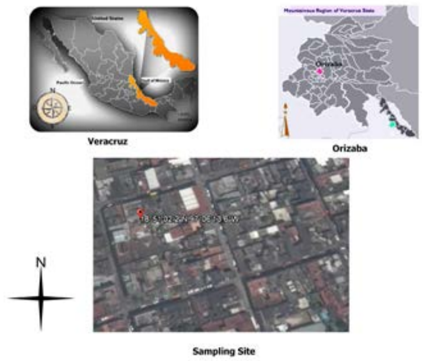

Fig. 1 Location of the sampling site

C. Analytical Method

Samples were extracted with 1 ml of CS_2 for each section of the sample tubes, and shaken for 30 s to assure maximum desorption. Extracted samples were analyzed using a TRACE GC Ultra gas chromatograph (Thermoscientific) and one flame ionization detector (FID; Thermoscientific Technologies, Inc) (Method INSHT MTA/MA-030/A92) [13]. The analytical column used was a capillary column (57 m, 0.32 mm i.d., 0.25 µm film thickness). Operation of the instrument was controlled using a Trace Chemstation data system. The oven temperature program was initially set to 40 °C for 4 min, then increased at a rate of 5 °C/min up to 100 °C, and finally maintained for 10 min at 100 °C. The FID temperature was set to 250 °C using a hydrogen/air flame with constant flows of 35 ml min-1 and 350 ml min-1 for ultra-pure hydrogen and extra-dried air, respectively. The ultra-pure nitrogen carrier (99.999%) gas flow rate was 1 ml min-1 [13]. Four BTEX were investigated: benzene, p-xylene, ethylbenzene, and toluene. Method detection limits (MDL) for each compound were calculated by multiplying the standard deviation obtained from seven replicate measurements of the first level of calibration by 3.14 (Student's t-value). The analytical results showed that the MDLs for the four VOC compounds of benzene, ethyl benzene, p-xylene, and toluene, were 0.0517, 0.0566, 0.0600, and 0.025 µg m^{-3}, respectively.

D. Monitoring of Meteorological parameters

Wind conditions (speed and direction), relative humidity, temperature and barometric pressure were monitored during autumn, 2014 (from November 6 to November 28) using a Davis Vantage Pro II model portable meteorological station. Wind frequency statistics were determined using WRPLOT software (Lakes Environmental). This station was located specifically in the sampling site.

E. Correlation and Principal Component Analysis (PCA)

Pearson correlation analysis was applied to all data collected at the sampling site. To assess the relationships between BTEX concentrations, and meteorological parameters; a factor analysis (Principal Component Analysis) was applied using XLSTAT software [12].

III. RESULTS AND DISCUSSION

A. BTEX distribution and Diurnal Variation

BTEX levels and their diurnal variation and descriptive statistics for the autumn sampling period can be observed in Fig 2 a and in Fig. 2 b it can be observed each aromatic hydrocarbon contribution to Total BTEX. All BTEX showed different diurnal pattern. Benzene (B) levels remain almost unaltered without significant differences among the three different sampling periods (B1, B2 and B3). Toluene (T) had the highest levels during the afternoon sampling period (B3) followed by the morning sampling period (B1) and having the lowest concentrations during the midday sampling period (B2). Ethylbenzene (Ebz) presented the maximum concentrations during the midday followed by the afternoon sampling period and having the minimum levels during the mornings. Finalley, p-Xylene had the highest values of concentration during the afternoon, decreasing during the midday and presenting the lowest values during the afternoons. The relative abundance of BTEX exhibited the following order during both sampling periods: B > T> EBz > X. Mean concentration levels were 80.06 µg m^{-3} for B, 14.60 µg m^{-3} for T, 2.74 µg m^{-3} for EBz and 2.25 µg m^{-3} for X.

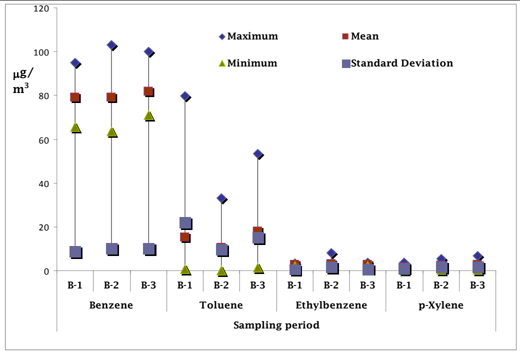

a)

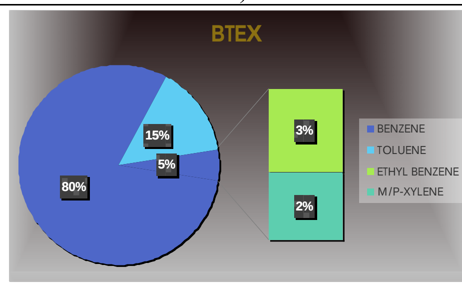

b)

Fig. 2 a) Diurnal variation and descriptive statistics for measured BTEX during the autumn sampling period, 2014. b) Aromatic hydrocarbon contribution to th Total BTEX. B1 (07:00-08:30 h), B2 (14:00-15:30 h) and B3 (17:30-19:00 h).

Table 1 Comparison of atmospheric concentrations of BTEX found in this study with data of other studies around the world

LOCATION	BENZENE	TOLUENE	ETHYLBENZENE	P-XYLENE
	µg/m³	µg/m³	µg/m³	µg/m³
Ramsis, Greater Cairo Khoder, 2007)	72.35-107.37	159.65-363.44	30.36-59.53	102.55-171.61
Tijuca,Rio de Janeiro (Eduardo Monteiro Martins, 2007)	0.3-3.3	1.4-16.9	1.6-6.6	4.7-21.3
Roadsite, Tokyo Metropolitan (Jun-ya Hoshi, 2008)	2.3	19	3.9	4.6
Ankara, Turkey (Sema Yurdakul, 2013)	2.18±2.25	7.89±9.64	0.85±0.91	2.21±2.50
This Study	80.06	14.60	2.74	2.24

Comparing the BTEX levels obtained in the study site with those reported in other cities around the world, it can be observed in Table 1 that levels ob benzene obtained in this study are comparable to those reported in Greater Cairo by Khoder and collaborators [17] but higher than those found in Tokyo [16] and Ankara [1]. Toluene levels in his study were lower than those reported for El Cairo but higher than those found in Río de Janeiro. Tokyo and Ankara. Ethylbenzene and p-Xylene levels foun in this research were similar to those reported for Tokyo [16].

B. Meteorological Analysis

Winds during the autumn sampling period were quite unstable. T, Ebz and X levels were higher when winds blew with a West component (W, SW, SSW). B showed a different pattern presenting the highest concentrations when winds came from North and from the SE. It was expected since that the sampling site is located along an avenue with high vehicular traffic and due to the vehicular flux goes from the north to the south along this avenue. At SE of the sampling site is located the main avenue of the city with and intensive vehicular flux and an important industrial area located in the Ixtaczoquitlán municipality. At W, SW, and SSW, are located many induatrial facilities, gas service stations and fuel storage facilities. All these sources could influence the

BTEX levels in the study site. Fig. 3a, Fig. 3b and Fig. 3 c show the daily meteorological influences for each BTEX for B1, B2 and B3 sampling periods, respectively.

During the mornings (B1), B showed the highest values when winds blew from N, T showed the maximum when wids came from W and Ebz and X showed the highest levels when wind direction was from SW. During the midday sampling period (B2), B and T had their maximum concentration values when winds blew from SE, Ebz had the highest levels when wind direction was from S and X had their maximum levels when winds came from WSW. During the afternoon samplin period (B3), winds had a more stable behaviour blowing almost all the time from SW. B presented the highest levels when winds came from SE, whereas, T, Ebz and X showed the highest concentrations when winds blew from SW. 24 h backward air masses trajectories were calculated in order to infer the origin of air masses at three different levels (50, 100 and 500 magl) using the hybrid lagrangian model HYSPLIT from NOAA (Fig. 4 a, Fig. 4b and Fig.4 c). The wind conditions are used to identify the probable sources of the measured BTEX compounds. According to the meterological analysis we can infer that BTEX had mixed and different sources but being evident that benzene had its origin in vehicular emission from mobile sources.

C. Toluene to Benzene Ratio (T/B ratio)and p-xylene to Ethylbenzene Ratio (X/Ebz ratio)

BTEX ratios can be indicative of sources or photochemical age. Studies have looked at toluene to benzene (T/B) ratios as an indicator of emission sources in North America [2] and internationally [6, 17-19]. These studies reported T/B values from 1.5 to 4.0 in urban areas impacted by mobile sources. Similarly, the ratio of p-xylene to ethylbenzene has been identified as an indicator of photochemical age [20]. These species are typically emitted in a ratio of approximately 3.6 in urban areas regardless of geographic location [21] and are removed from the air by dispersion, deposition, and chemical reaction. However, the removal of p-xylene via chemical reaction is approximately 3 times faster than that of ethylbenzene. Therefore, this ratio typically decreases with photochemical aging [22]. T/Bz values lower than 2-3 are characteristic of vehicular emissions in many urban areas worldwide [10, 23], whereas values higher than 3 may indicate that BTEX levels could be associated with industrial facilities and area sources (evaporative emissions, painting, cooking processes, among others). During the whole sampling period this ratio was of 0.1113 for B1, of 0.1047 for B2 and 0.1728 for B3, being higher during the afternoon sampling period. These values are in agreement with typical values of vehicular emissions reported for other urban areas, suggesting that this site was under the influence of mobile sources. The p-Xylene to Ethylbenzene (X/Ebz) ratio is commonly used as an indicator of the photochemical age of the air masses. This ratio is related to the atmospheric residence time of these pollutants: high values of indicate aged air masses (old emissions), and low values indicate fresh air masses (recent emissions). Kuntasal et al. [24] used a value of 3.8 for this ratio. Fresh gasoline emissions provide values between 3.8 and 4.4 for this ratio. In this study, the whole period registered low values for this ratio, indicating that most of the air masses correspond to “fresh emissions”. A mean value of 0.8664 for this ratio was obtained (B1: 0.6467; B2: 0.8853; B3: 1.0678). Taken together, the T/Bz and X/Ebz ratio results suggest that these fresh emissions correspond to vehicular emission from mobile sources.

D. Pearson Correlation and Principal Component Analysis (PCA)

Meteorological analysis, T/B and X/Ebz ratios suggest that autumn BTEX levels at the site under study were influenced by mixed and different sources (see sections 4.2, 4.3 and 4.4). A PCA analysis was carried out in order to get more detailed information about the behavior of the studied pollutants. Therefore, it was necessary to investigate the relationship among BTEX and meteorological parameters in order to elucidate the possible source for VOCs. The spearman rank correlation coefficients indicate consistency in spatial patterns for each compound. A strong positive correlation with one another indicates that both pollutants could have their origin in common sources. A strong negative correlation can be indicative that one compound could be a precursor of the other one. Pearson correlation matrixes were constructed for each sampling period (B1, B2 and B3)(Tables 2-4). A good mutual correlation between Ebz and X indicates that they might possibly originated from gasoline vehicles and gasoline stations [24]. A low correlation factor indicates towards the spiking of BTEX from some additional sources apart from vehicular inputs. In Table 2 it can be observed that Benzene and Toluene had a good significant mutual correlation, indicating that during the mornings these compounds could have their origin in common sources probably vehicular emissions. A low correlation with ethylbenzene and p-xylene is an indicative that these pollutants had their origin in sources different from vehicular exhaust, probably evaporative emissions and industrial sources. Temperature and wind direction had good correlation and a negative strong correlation (-0.834) between relative humidity (RH) and temperature was found indicating that high values of RH could contribute to decrease temperature in the study site (chilling effect). In Table 3 it can be observed that BTEX did not had mutual correlation each other, indicating that during this sampling period, BTEX probably had mixed and different sources. In Table 4 it can be observed that Toluene and Ethylbenzene had a good mutual correlation (0.600) indicating that they probably were originated from the same sources. Once again temperature and relative humidity (RH) showed a strong negative correlation, it shows the influence of RH on temperature in the study site. A Principal component analysis (PCA) was used to study the variability patterns present in this multivariate data set.

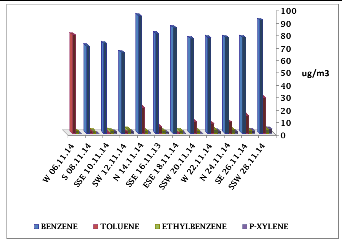

a) B1

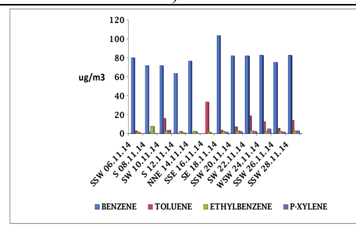

b) B2

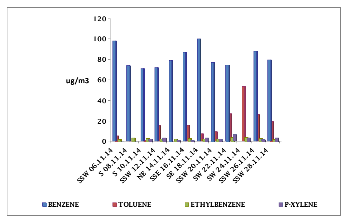

c) B3

Fig. 3 Meteorological influence on BTEX levels: a (B1: 07:00- 080:30 h); b (B2: 14:00-15:30 h); and c (B3: 17:30-19:00 h).

a) B1

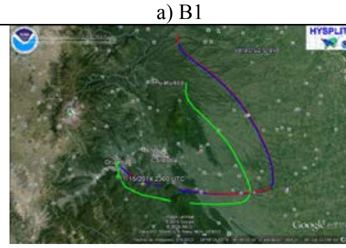

b) B2

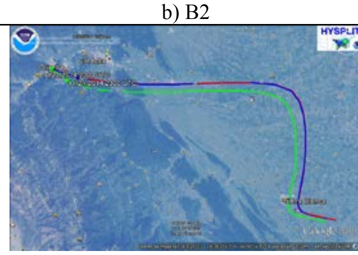

c) B3

Fig. 4 Representative 24-h backward air masses trajectories for autumn period: a) November 28, 2014, for b) November 16, 2014 and for c) November 22, 2014.

A PCA model was developed for air pollutants levels (benzene, toluene, ethylbenzene and p-xylene) and the meteorological parameters (temperature: T, barometric pressure: P, relative humidity: RH, wind direction: WD, and wind speed: WS). The PCA biplot obtained for the morning (B1), midday (B2) and afternoon (B3) sampling periods during autumn season is shown in Fig. 5, Fig. 6 and Fig. 7. PCA for the morning sampling period (B1) gave two principal components (F1 and F2) expressing about 58.14% of the total variance. In Fig. 5 it can be observed that B showed a close relation with toluene, whereas ethylbenzene, p-xylene showed a moderate relation. Two principal components (F1 and F2) were enough to express about 53.19% of the total variance (Fig. 6) for the midday sampling period (B2).

Table 2 Pearson correlation matrix for B1 sampling period during autumn 2014

Variables	Benzene	Toluene	Ethylbenzene	p-Xylene	Wind speed	Wind direction	Relative Humidity	Temperature	Barometric Pressure
Benzene	**1**	**0.698**	-0.252	-0.263	-0.178	0.306	0.021	-0.263	-0.023
Toluene	**0.698**	**1**	-0.189	-0.171	-0.197	0.323	-0.161	0.043	0.107
Ethylbenzene	-0.252	-0.189	**1**	0.302	0.091	0.406	-0.547	0.503	-0.293
p-Xylene	-0.263	-0.171	0.302	**1**	-0.066	-0.160	-0.180	-0.139	-0.542
Wind speed	-0.178	-0.197	0.091	-0.066	**1**	0.098	-0.475	0.337	-0.338
Wind direction	0.306	0.323	0.406	-0.160	0.098	**1**	**-0.606**	**0.656**	-0.012
Relative Humidity	0.021	-0.161	-0.547	-0.180	-0.475	**-0.606**	**1**	**-0.834**	0.275
Temperature	-0.263	0.043	0.503	-0.139	0.337	**0.656**	**-0.834**	**1**	0.069
Barometric Pressure	-0.023	0.107	-0.293	-0.542	-0.338	-0.012	0.275	0.069	**1**

Table 3 Pearson correlation matrix for B2 sampling period during autumn 2014

Variables	Benzene	Toluene	Ethylbenzene	p-Xylene	Wind speed	Wind direction	Relative Humidity	Temperature	Barometric Pressure
Benzene	**1**	0.173	-0.276	-0.083	0.537	-0.092	0.096	-0.272	-0.401
Toluene	0.173	**1**	-0.229	-0.096	0.454	0.295	-0.414	0.376	-0.130
Ethylbenzene	-0.276	-0.229	**1**	0.349	0.100	0.043	0.244	-0.051	0.158
p-Xylene	-0.083	-0.096	0.349	**1**	-0.079	0.553	-0.563	0.453	-0.129
Wind speed	0.537	0.454	0.100	-0.079	**1**	-0.058	0.098	0.129	0.257
Wind direction	-0.092	0.295	0.043	0.553	-0.058	**1**	**-0.681**	0.413	-0.439
Relative Humidity	0.096	-0.414	0.244	-0.563	0.098	**-0.681**	**1**	-0.505	0.294
Temperature	-0.272	0.376	-0.051	0.453	0.129	0.413	-0.505	**1**	0.178
Barometric Pressure	-0.401	-0.130	0.158	-0.129	0.257	-0.439	0.294	0.178	**1**

Table 4 Pearson correlation matrix for B3 sampling period during autumn 2014

Variables	Benzene	Toluene	Ethylbenzene	p-Xylene	Wind speed	Wind direction	Relative Humidity	Temperature	Barometric Pressure
Benzene	**1**	-0.183	-0.407	-0.103	-0.218	-0.175	0.163	-0.384	0.109
Toluene	-0.183	**1**	**0.600**	0.412	0.018	0.413	-0.142	0.205	-0.470
Ethylbenzene	-0.407	**0.600**	**1**	0.273	0.092	0.202	-0.157	0.453	-0.126
p-Xylene	-0.103	0.412	0.273	**1**	0.517	0.426	-0.206	0.173	-0.566
Wind speed	-0.218	0.018	0.092	0.517	**1**	0.412	0.127	-0.147	-0.234
Wind direction	-0.175	0.413	0.202	0.426	0.412	**1**	-0.552	0.263	-0.433
Relative Humidity	0.163	-0.142	-0.157	-0.206	0.127	-0.552	**1**	**-0.744**	-0.226
Temperature	-0.384	0.205	0.453	0.173	-0.147	0.263	**-0.744**	**1**	0.343
Barometric Pressure	0.109	-0.470	-0.126	-0.566	-0.234	-0.433	-0.226	0.343	**1**

It can be observed that benzene and toluene had a good relation indicating that they probably had common sources and p-xylene and temperature showed a close relation indicating that this compound could be originated from evaporative emissions during the midday sampling period. Temperature and relative humidity, once again showed a negative correlation. Two principal components (F1 and F2) were enough to express about 57.92% of the total variance (Fig. 7) for the afternoon sampling period (B3). It can be observed that benzene had a different source than the rest of BTEX, probably it was originated from vehicular exhaust from mobile sources. The rest of BTEX showed s good relation with wind direction indicating that theses pollutants could be transported from other surroundings areas. The effect of RH on temperature was evident once again.

IV. CONCLUSION

The probable origin of BTEX and their diurnal distribution were investigated for an urban site in in center of Veracruz in Mexico. From the meteorological analysis, BTEX ratios and a principal component analysis (PCA) it was possible to infer the origen of the measured compounds. This study showed that benzene had their origin from vehicular exhaust of mobile sources, whereas, the rest of BTEX were originated from different and mixed sources.

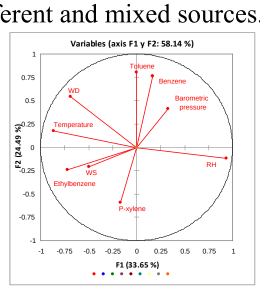

Fig. 5 Multivariate set Biplot from the PCA for B1 sampling period.

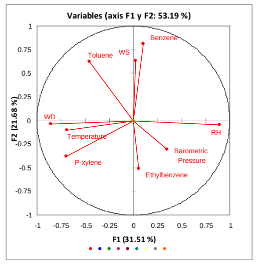

Fig. 6 Multivariate set Biplot from the PCA for B2 sampling period

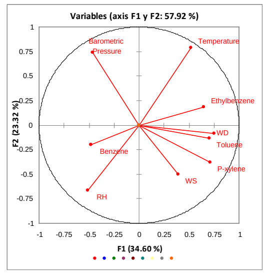

Fig. 7 Multivariate set Biplot from the PCA for B3 sampling period

Benzene concentrations were higher than other cities around the world and it could constitute a potential risk to the Orizaba citizen's health. This is the first study on air quality in this area and these preliminary results will be useful in order to stablish an intensive monitoring campaign in a short future in the study area.

References

[1] S. Yurdakul, M. Civan, G. Tuncel. "Volatile organic compounds in suburban Ankara atmosphere, Turkey: sources and variability", *Atmospheric Research* Vol. 120-121, pp. 298-311, 2013.

[2] L. Miller, X. Xu, A. Grgicak-Mannion, J. Brook, A. Wheeler. "Multi-season, muti.year concentrations and corelations amongst the BTEX group of VOCs in an urbanized industrial city", *Atmospheric environment* Vol. 61, pp. 305-315, 2012.

[3] J. Zheng, J.P. Gazón, M. Huertas, R. Zhang, M. Levy, Y. Ma, J.I. Huertas, R.T. Jardon, L.G. Ruiz, H. Tan, H; L.T. Molina. "Volatile organic compunds in Tijuana during the Cal-Mex 2010 campaign: measurements and source apportionment", *Atmospheric Environment* Vol. 70, pp. 521-531, 2013.

[4] A. Srivastava, R. Sengupta, S.A. Dutta. "Source apportionment of ambient VOCs in Delhi city", *Science of The Total Environment* Vol. 343, pp. 207-220, 2005.

[5] F. James, W.L. Pankow. "Concentrations and co-occurrence correlations of 88 volatile organic compounds (VOCs) in the ambient air of 13 semi-rural to urban locations in the United States", *Atmospheric Environment* Vol. 5, pp. 2023-2046, 2003.

[6] R.R. Hoque, P.S. Khillare, T. Agarwal, V. Shridhar, S. Balachandran. "Spatial and temporal variation of BTEX in the urban atmosphere of Delhi, India", *The Science of the Total Environment* Vol. 392, pp. 30-40, 2008.

[7] H. Guo, K.L. So, I.J. Simpson, B. Barletta, S. Meinardi, D.R. Blake. " C1-C8 Volatile organic compounds in the atmosphere of Hong Kong: overview of atmsopheric processing and source apportionment", *Atmospheric environment* Vol. 41, pp. 1456-1472, 2007.

[8] A.H. Bravo, E.R. Sosa, A.P. Sánchez, E. Bueno, R.L. González. "Concentrations of benzene and toluene in the atmosphere of the southwestern area at the Mexico City Metropolitan Zone". *Atmospheric Environment* Vol. 36, pp. 3843-3849, 2002.

[9] V. Mugica, E. Vega, H. Ruiz, G. Sánchez, E. Reyes, A. "Cervantes, Photochemical reactivity and sources of individual VOCs in Mexico City", In: *Brebbia C A and Martin-Duque J F (Eds) Air Pollution X, WIT PRESS, London, U.K,* pp. 209-217, 2002.

[10] V. Mugica, M.E. Ruiz, J. Watson, J. Chow. "Volatile Aromatic Compounds in Mexico City atmosphere: Levels and Source apportionment", *Atmosfera* Vol. 16, pp. 5-27, 2003.

[11] J.G. Cerón-Bretón, R.M. Cerón-Bretón, M. Rangel-Marrón, G.X.Villarreal-Sánchez, A.Y. Uresti-Gómez. "Determination of BTX levels in ambient air of one urban site located at the southwest of Mexico City during spring 2013". In: *Proc. 4th International Conference on Development, Energy, Environment and Economics (DEEE'13), Recent Advances in Energy, Environment, Economics and Technological Innovation*, Paris, France, October 29-31, 2013.

[12] D. Facundo, E. Ramírez Lara, J.G. Cerón Bretón, R.M. Cerón Bretón, et al., "Measurements of carbonyls and its relation with criteria pollutants (O3, NO, NO2, NOx, CO and SO2) in an urban site within the Metropolitan Area of Monterrey, in Nuevo Leon, Mexico", *International Journal of Energy and Environment* Vol. 6, no. 5, pp. 524-531, 2012.

[13] INSHT Method MTA/MA-030/A92 (1992) Aromatic hydrocarbons determination in air (benzene, toluene, ethylbenzene, p-xylene, 1, 2, 4-trimethyl-benzene): Adsorption in activated carbon/gas chromatography method, Social and Occupacional Affairs Office, Spain.

[14] J.G. Cerón-Bretón, R.M. Cerón-Bretón, J.W.D. Kahl, E. Ramírez-Lara, C. Guarnaccia, C.A. Aguilar-Ucán, C. Montalvo-Romero, F. Anguebes-Franseschi, U. López-Chuken. " Diurnal and seasonal variation of BTEX in the air of Monterrey, Mexico: preliminary study of sources and photochemical ozone pollution", *Air Quality, Atmosphere and Health*, DOI 10.1007/S11869-014-0296-1, pp. 1-14, 2014.

[15] E. Monteiro, G.A. Martins. "Atmospheric levels of aldehydes and BTEX and their relationship with vehicular fleet changes in Rio de Janeiro urban area", *Chemosphere* Vol. 67, pp. 2096-2103, 2007.

[16] S.A. Jun-ya Hoshi. " Investigation and estimation of emission sources of 54 volatile organic compounds in ambient air in Tokyo", *Atmospheric Environment* Vol. 24, no. 1, pp. 2383-2393, 2008.

[17] M. Khoder. "Levels of volatile organic compounds in the atmosphere of Greater Cairo". *Atmospheric Environment* Vol. 41, pp. 554-566, 2007.

[18] A.B. Hansen, F. Palmgren. "VOC air pollutants in Copenhagen", *The Science of the Total Environment* Vol. 189, pp. 451-457, 1996.

[19] A.J. Buczynska, A. Krata, M. Stranger, A. Flavia Locateli Godoi, V. Kontozova-Deutsch, L. Bencs, I. Naveau, E. Roekens, R. Van Grieken. "Atmospheric BTEX concentrations in an area with intensive street traffic", *Atmospheric Environment* Vol. 43, pp. 311-318, 1993.

[20] J. Zhang, T. Wang, W.L.Chameides, C. Cardelino, D.R. Blake, D.G. “Streets, Source characteristics of volatile organic compounds during high ozone episodes in Hong Kong, southern China”, *Atmospheric Chemistry and Physics* Vol. 8, pp. 4983-4996, 2008.

[21] A. Monod, B.C. Sive, P. Avino, T. Chen, D.R Blake, F.S. Rowland. “Monoaromatic compounds in ambient air of various cities: a focus on correlations between the xylenes and ethylbenzene”, *Atmospheric Environment* Vol. 35, pp. 135-149, 2001.

[22] P.F. Nelson, S.M. Quigle. “The m,p-xylenes:ethylbenzene ratio. A technique for estimating hydrocarbon age in ambient atmospheres”, *Atmospheric Environmen*t Vol. 17, pp. 659-662, 1983.

[23] T. Elbir, B. Cetin, E. Cetin, A. Bayram, M. Odabasi. “Characterization of volatile organic compounds (VOCs) and their sources in the air of Izmir, Turkey”, *Environ. Monit. Assess* Vol. 133, pp. 149-160, 2007.

[24] O.O. Kuntasal, D. Karman, D. Wang, S. Tuncel, G. Tuncel. “Determination of volatile organic compounds in microenvironments by multibed adsorption and short-path thermal desorption followed by gas chromatographic-mass spectrometric analysis”, Journal of Chromatography A Vol. 1099, pp. 43-54, 2005.

ISBN: 978-1-61804-295-8

Visual Examination of the Effects of the Different Operating Conditions on the Residence Time Distribution in a Single-Screw Extruder with Transparent Barrel

M. Fatih Ergin*, Ismail Aydin, A. Tugrul Albayrak
Rheology Laboratory, Chemical Engineering Department, Engineering Faculty, Istanbul University, Avcilar Campus, 34320 Avcilar, Istanbul
*e-mail: mfergin@istanbul.edu.tr

Keywords: Polymers; extrusion; EVA; plastics industry; melting

Abstract: In this study, the residence times of the polymeric materials were calculated via styropor grains as tracers under different operating conditions using a single-screw extruder with a transparent barrel as the first novel design in the literature and the performance values of the single-screw extruder system with a glass barrel were confirmed by the distribution results of the tracers. EVA was used as the polymeric material. In the studies, the motions of the tracers in different regions of the single-screw extruder were observed with naked eye and the movement from the regions towards the extruder exit was recorded by means of a camera. It was observed that the tracers proceeded in bulk for the solid conveying, the melt and the melt pumping zones in the extruder as the screw speed increased. Due to an increase in temperature, the low viscosity led to a wider dispersion of the tracers.

Introduction

The residence time distribution, RTD, is considered as one of the key parameter for characterizing the performance of an extruder. Since the shape of RTD functions depends on the combined effect of the flow patterns developed, the existing mixing mechanisms and also of heat transfer and reaction processes, RTD is often used to monitor and control important process attributes, such as consistency, extent of polymer degradation and degree of mixing [1]. The shear and temperature history of extruded product, conversion in reactive extrusion etc. are directly dependent on the RTD [2]. Hence, knowing and controlling RTD in industrial extruders are important to the quality of the output. For example, in the case of PVC, polymer chains exposed to high extrusion temperatures for prolonged periods of time are more likely to degrade to toxic products. In these cases, it is desirable to minimize the RTD in the extruder [3] as it is directly linked to contact time of reactants [4]. Also, the rheological properties of the polymer have a significant impact on fluid flow in an extruder [5, 6]. In addition, screws of good performance should not only have good plastication behavior, stable extrusion characteristics, and high output rate but also a good mixing capability [7].

There are many publications dealing with the RTD in an extruder in the literature. Ainsworth et al. [8] studied the effects of feed rate and screw speed on RTD of tarhana in a twin-screw extruder and found that increasing feed rate or screw speed, while keeping the other operating conditions constant, reduced the mean residence time (MRT) with the feed rate having a more pronounced effect than the screw speed and the flow in the extruder approached plug flow as the feed rate increased, whereas an increase in the screw speed resulted in the flow approaching mixed flow. De Ruyck [9] showed that the greatest influences on the MRT and RTD of wheat flour in a twin screw extruder were obtained by changing screw profile, screw speed and feed supply. Yeh et al. [10] modelled RTDs for single screw extrusion process and reported that increasing the feed rate caused the reduction in RT. Also high screw speed resulted in short RT, but large dispersion number. They showed that [11] the flow pattern in a single screw extruder can be obtained by regression without knowing the characteristics of the screw profile or the extruder for an extrusion cooking. To measure the RTD in real time, Hu et al. [12] constructed a fluorescence monitoring device in which the source of fluorescence emission was an anthracene-bearing substance that was injected to the flow stream as a pulse (tracer) in very small amounts and demonstrated that this device was accurate and reliable for on-line monitoring of the RTD in screw extruders. Iwe et al. [13] studied the influence of feed composition, screw rotation speed and die diameter on RTD of soy-sweet potato samples using congo red as a tracer in a single-screw extruder and found that the mean residence time depended significantly on the level of soy flour in the mixture as well as on the screw speed of the extruder and the flow of the mixtures was mainly plug flow. Apruzzese et al. [14] carried out in-line measurement of RTD in a co-rotating twin-screw extruder and showed that the rapid, simple in-line method accurately predicted the effects of temperature, feed and water rate as the three extrusion parameters on RT and mixing inside the extruder.

Seker [15] investigated RTD of starch extruded with sodium hydroxide and sodium trimetaphosphate in a single-screw extruder at 40% moisture content and showed that the increase in screw speed from 90 to 140 rpm reduced the MRT of the starch sample with a mixing element, but replacing the screw having one mixing element with a screw having two mixing elements increased MRT. The researcher recommended increasing the number of mixing elements at high screw speed for homogeneous treatment and reaction of the feed material in the extruder. A non-labor intensive, non-destructive method based on digital image processing was developed to measure RTD in a laboratory extrusion process by Kumar et al. [16] and it is shown that the increase in screw speed and temperature resulted in decrease in the MRT and an increase in degree of mixing. Waje et al. [17] studied RTD in a pilot-scale screw conveyor dryer (SCD) and revealed that the increase of screw speed resulted in a decrease in MRT and an increase in degree of mixing. Also they demonstrated that the flow in a SCD approaches plug flow as the feed rate was increased, whereas an increase in the screw speed resulted in a mixed flow.

Bi et al. [18] developed a convenient, inexpensive and simple digital image processing (DIP) method for measuring the RTD in a plasticating extruder and it was found that the repeatability and the linear relationship between the red color intensity and the concentration of the tracer proved the feasibility of the DIP method, so did the comparative experiment and in addition, the MRT was proportional to reciprocal values of the feed rate and the screw speed. Nikitine et al. [19] studied the RTD of Eudragit E100 polymer/supercritical CO_2 ($scCO_2$) through a single screw extruder which allowed injection of $scCO_2$ used as physical foaming agent and it was reported that high screw speed or high temperature gave short RT, but these parameters did not have the same effect on polymer flow.

Besides in the flow rate range studied, it was observed that $scCO_2$ had no significant influence on the RTD curves. Nwabueze et al. [20] extruded African breadfruit mixtures to assess RTD of them in a single screw extruder and it was found that extrudate temperature was linearly and quadratically influenced by feed composition, feed moisture and screw speed depending on the process conditions and also an increase in screw speed (100-180 rpm) and decrease in feed moisture (27-15%) increased thermal and shear energies, and hence, extrudate temperature.

Experimental Methods

Equipment and experimental set-up: Single-screw extruder system containing a transparent barrel used in this study is shown in Fig. 1. The transparent glass readily enables observation of the flow characteristic of the flowing material inside the barrel and facilitates the temperature measurement via an infrared thermometer. The steel screw in the transparent glass barrel is directly connected to the gear box of the motor. The control of the motor is governed by means of a driver. Transparent glass barrel is separated into four distinct temperature zones. Each zone is isolated by teflon o-ring. Consequently, the temperature of each zone is individually controlled. The hot oil system is used to set the barrel temperature to the desired temperature.

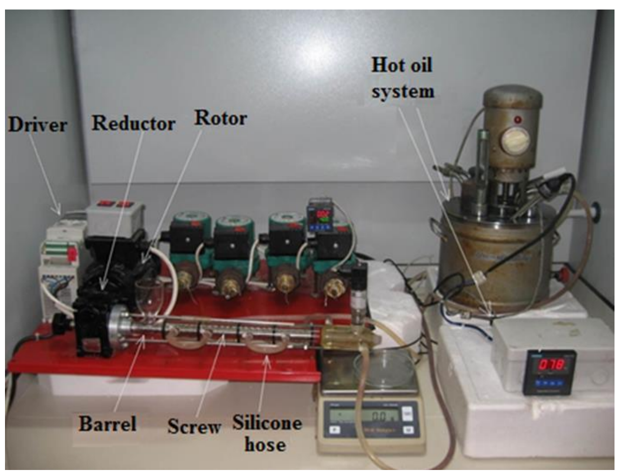

Fig. 1 Extruder system with transparent barrel.

Barrel: The extruder barrel in this study is composed of two nested-glass tubes. One is inner glass barrel enclosing the screw and the other is the outer glass jacket which retains the hot-oil as shown in Fig. 2. The area between the inner and the outer barrel comprises four zones that are not only separated from each other by teflon separator but also with the inlet and outlet sections for recirculation of the heat transfer oil used for heating.

ISBN: 978-1-61804-295-8

Fig. 2 Heating zones on the barrel.

Screw: Each one of the three different screws used in this study has different feeding and metering zone lengths and a unique design. The screws have such a length that they embody the feeding, the compressive and the melt conveying zones. The melting zone lengths of all the screws in Fig. 3 are the same. The feeding and the metering zone length for the first, the second and the third screw all of which are manufactured by Mikrosan Corporation are 15D and 7D, 13D and 9D, 11D and 11D, respectively. In our study, L/D ratio is 29 and compression ratio, i.e. the flight depth in the feeding zone/the flight depth in the melt conveying, is 2.5/1.5.

Fig. 3 The screws used in this study (the colored zones indicate the melting zone).

Materials: In the experiments, Elvax 40W (ethylene-vinyl acetate) copolymer provided by Dupont-Belgium was used. Some physical and chemical properties of Elvax 40W are given in Table 1.

Table 1 Some physico-chemical properties of Elvax 40W.

Property	**Elvax 40W (DuPont)**
VA content (weight percent)	39 – 42

ISBN: 978-1-61804-295-8

Melt index (g/10 minutes)	48 – 66
Melting temperature (◦C)	~ = 50
Crystallinity (%)	<10
Tensile strength at break (MPa)	4.8 – 6.2
Elongation at break (%)	1000 – 1300
Hardness (Shore A)	40
Density (g/cm^3)	0.965

EPS (expanded polystyrene) provided by EastChem Corporation (Izmir, Turkey) was used as tracer in the experiments and its some physical properties are given in Table 2.

Table 2 Some physical properties of EPS used as tracer.

Properties	**Sytrafor (EastChem)**
	Eurocell® 200F
Size range of grains (mm)	0.9 – 1.25
Sieve analysis (mm)	0.9 – 1.4 (min. 96 %)
Bulk density (kg/m^3)	≈ 615 kg/m^3

Residence Time Distribution (RTD): In this study, residence time distributions in the single-screw extruder with glass barrel were found by using pulse method. The bulk material (EVA 40W) is fed into the extruder from the feed hopper until the extruder system is reached steady state which implies that the flow rate, pressure and temperature are not changing. 0.250 g of the tracer was instantly fed into the system following the steady state. The mixture of the melted bulk material and the tracers was collected every 10 seconds. The collected samples were transformed into the film form (Fig. 4). This treatment was carried out for the temperature values of 55, 65, 75 °C and at the screw speeds of 30, 50 and 70 rpm. The three different screws and each experiment were repeated at least three times. Residence time distribution E(t) in Eq. 1 and the mean residence time τ in Eq. 2 were calculated using the obtained data. The mathematical relationships for each one of these terms are as follows:

Residence time distribution (E(t)):

$$E(t) = \frac{c(t)}{\int_0^{\infty} c(t)dt} \tag{1}$$

Mean residence time (τ):

$$\tau = \int_0^{\infty} tE(t)dt \tag{2}$$

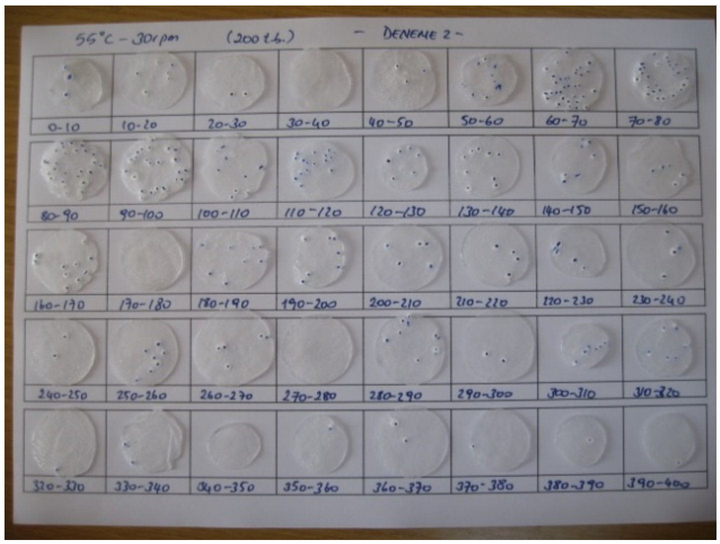

Fig. 4 The films obtained by hot-pressing bulk material-tracer mixture to determine the RTD.

Results and Discussion: In the following sections, the effects of screw speed and temperature on the extruder system are demonstrated.

The effect of screw speed on RTD: The residence time distributions based on the different screw speeds at 55, 65 and 75 °C are shown in Figs. 5, 6 and 7, respectively. From Fig. 5, it is reported that the RTDs decreased as the screw speeds for all the screw geometries increased at 55 °C. Also, the MRT decreases since the screw speed increases at the same temperature as in Fig. 8(a). The RTDs of screws 1 and 2 are similar to each other at 30 rpm and 55 °C, but there is little difference between the three screws at high screw speeds, especially at 50 and 70 rpm.

ISBN: 978-1-61804-295-8

As seen from Fig. 6, a narrower RTD is obtained compared to that in 55 °C as the screw speed increases at 65 °C, leading to a decrease in MRT. It is observed from Fig. 8(b) that as the screw speed increases at 65 °C, the effect of all the screw geometries on RTD diminishes, particularly at 70 rpm.

As the screw speed increases from 30 to 70 rpm for all the screw geometries, the RTDs, shown in Fig. 7, becomes narrower, consequently causing the MRTs to decrease as seen in Fig. 8(c). It is observed from Fig. 8(c) that, the screw geometries have a slight effect on RTDs obtained at 30 and 70 rpm for 75 °C. However, the RTDs at this temperature are significantly different for 50 rpm. The widest RTD were obtained using screw 1. It can be inferred from Fig. 8 that the narrowest RTD was obtained using screw 3 at 50 rpm for all the temperatures. The reason for that is the solid conveying length of screw 3 is smaller than the other screw geometries.

The temporal dispersion of the tracer inside the solid conveying, the melting and the metering zone of the glass-barrel extruder is videotaped as shown in Fig. 9. The effect of the lengths of the three different regions in the extruder on mixing was examined. An increase in the solid conveying zone length leads to bulk flow of the tracer such that the axial mixing decreases. The lengths of the melting zones of all the screws are the same. However starting from the entrance to the melting zone, the dispersion of the tracer increases rapidly for each screw geometry. The complete melting of the bulk material in the metering zone occurs. Therefore the viscosity of the bulk material decreases depending on the temperature and the friction and the molten pool takes place such that the tracers can move independently from each other. As a result of this movement, the distance between each tracer increases and accordingly, the axial mixing increases.

Increasing screw speed leads to a better axial mixing; on the other hand, the time required for mixing decreases. This also negatively affects obtaining a good mixing. The MRTs obtained at 70 rpm for all the temperatures in this study is lower compared with those at 30 and 50 rpm. Although the degree of the dispersion is high at high screw speeds, a screw speed of 70 rpm may not be the best operation condition.

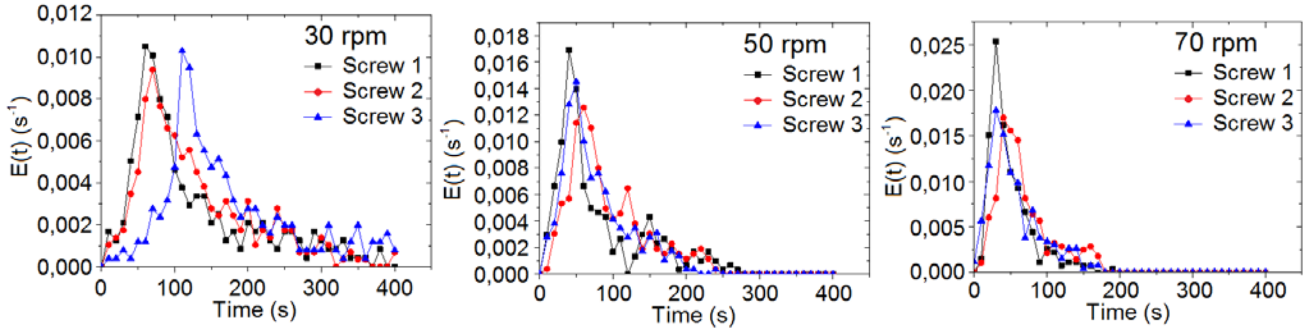

Fig. 5 The effect of the different screw geometries on RTD at 30, 50 and 70 rpm for 55 °C.

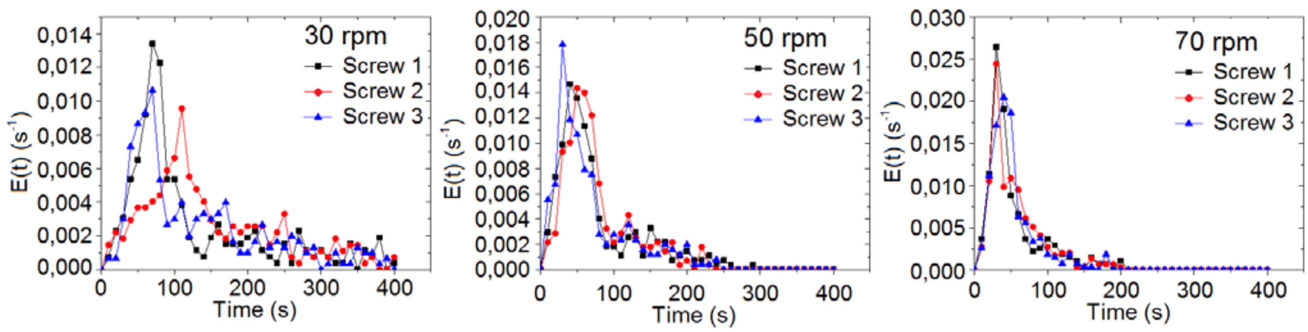

Fig. 6 The effect of the different screw geometries on RTD at 30, 50 and 70 rpm for 65 °C.

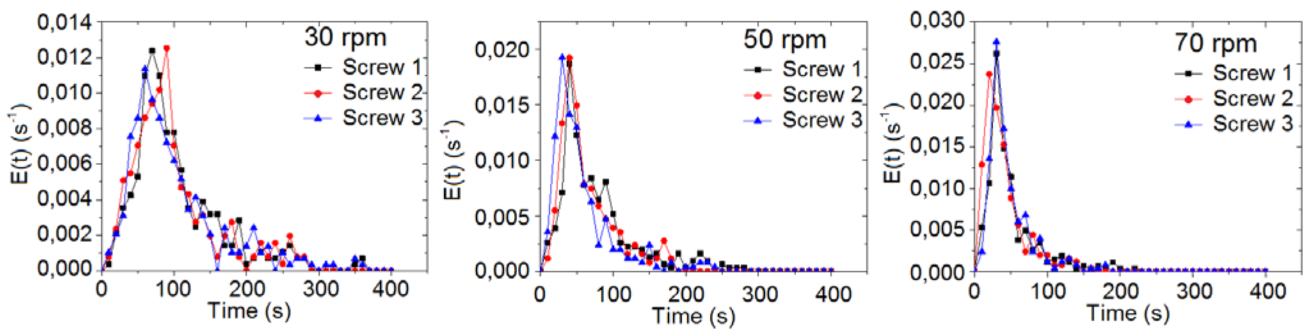

Fig. 7 The effect of the different screw geometries on RTD at 30, 50 and 70 rpm for 75 °C.

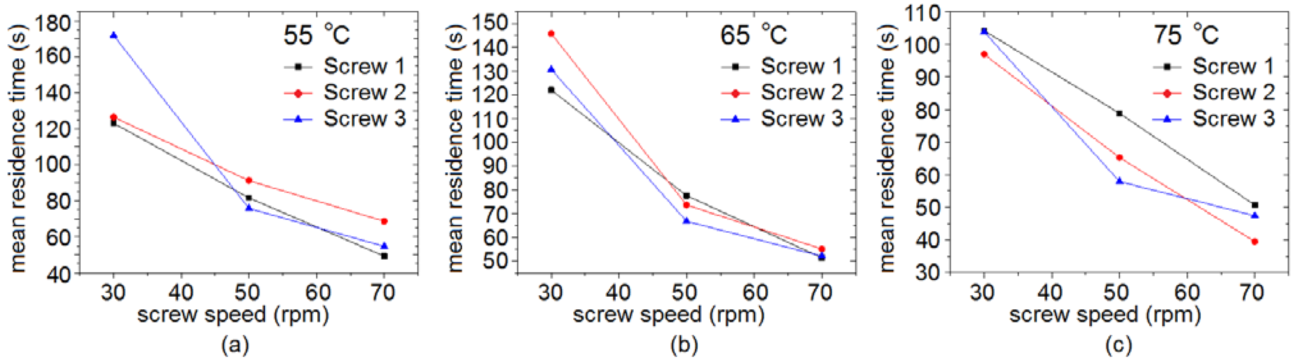

Fig. 8 The effect of the different screw designs and the different screw speeds on MRT at (a) 55, (b) 65 and (c) 75 °C.

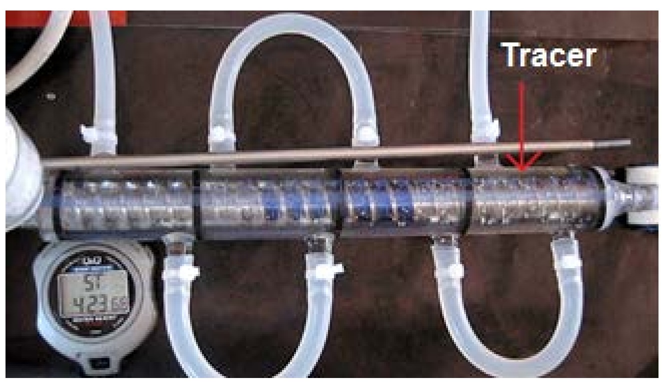

Fig. 9 The temporal dispersion of the tracer in the different zones of the single-screw extruder with the glass barrel

ISBN: 978-1-61804-295-8

Conclusions: Single-screw extrusion process in this study was investigated. A glass-barrel extruder produced and designed specifically was used to clearly observe the material flow in the solid conveying, the melting and the metering zones. To date, this extruder is not available in the literature and it is established that a net flow of the material inside the extruder was seen apparently and it behaves as a melt in a major part of the barrel. It is determined that the material floats on the molten shortly after some degrees of the melting are taken place by compression, i.e., the first melting seen in the solid conveying zone. Thus solid profile X/W, the flow rate in the solid bed V_{sz}, the positions of the upper melt, the melt pool and the occurrence of the solid bed breaking was monitored sensitively. The numerous dynamic properties of extrusion such as non-plug solid conveying, the breaking of the solid bed and the melting of the breaking solid granules were tracked in-situ constantly behind the glass-barrel extruder.

The output increases in direct proportion to the screw speed. Increasing the screw speed causes a decrease in MRT. The reduction in MRT is more pronounced using screw 2 and 3 because of an increase in screw speed. Among the three screw types, the shortest mean residence time is reached using screw 3 at 50 rpm for all the temperatures. The RT in the solid conveying zone of the extruder decreases with increasing screw speed.

The RTD becomes narrower as the temperature increases from 55 to 75 °C, but at the same time the axial mixing increases with the increasing of temperature. There is a considerable temperature effect on the RTDs obtained using screws 2 and 3 because the length of the metering section, where the polymer is completely in the molten state, of screws 2 and 3 is bigger than that of screw 1. Increasing temperature from 55 to 75 °C improves the axial mixing at 70 rpm for screws 1 and 2. The blend homogeneity increases as temperature increases for all the relevant screws.

With this study, the dispersion of the tracers in the completely transparent glass barrel can be observed and the flow regime can be determined. Also, it will give insight into the understandings of flow characteristics of polymeric materials.

References

[1] Carneiro, O.S., Covas, J. A., Ferreira, J. A., Cerqueira, M. F., On-line monitoring of the residence time distribution along a kneading block of a twin-screw extruder, Polymer Testing, 23 (2004) 925-937.

[2] Mudalamane, R., Bigio, D. I., Tomayko, D. C., Meissel, M., Behavior of fully filled regions in a non-intermeshing twin-screw extruder, Polymer Engineering and Science, 43 (8) (2003) 1466-1476.

[3] Gendron, R., Daigneault, L. E., Tatibouet, J., Dumoulin, M. M., Residence time distribution in extruders determined by in-line ultrasonic measurements, Advances in Polymer Technology, 15 (2) (1996) 111-125.

[4] Baron, R., Vauchel, P., Kaas, R., Arhaliass, A., Legrand, J., Dynamical modelling of a reactive extrusion process: Focus on residence time distribution in a fully intermeshing co-rotating twin-screw extruder and application to an alginate extraction process, Chem. Eng. Sci., 65 (2010) 3313-3321.

[5] Elkouss, P., Bigio, D. I., Wetzel, M. D., Raghavan, S. R., Influence of polymer viscoelasticity on the residence time distributions of extruders, AIChE Journal, 52 (4) (2006) 1451-1459,.

[6] Raza, A., Aydin, I., Lai-Fook, R., Briscoe, B., Lawrence C., Rheological Models for Finite Element Analysis, The 1998 IChemE Event, London, Vol. 1, (1998) 305-311.

[7] Wong, A. C-Y., Lam, J. C. M., Liu, T., Zhu, F., Visualization studies on the comparison of mixing characteristics of single-screws having different mixing elements, Advances in Polymer Technology, 19 (1) (2000) 1-13.

[8] Ainsworth, P., Ibanoglu, S., Hayes, G. D., Influence of process variables on residence time distribution and flow patterns of tarhana in a twin-screw extruder, Journal of Food Engineering, 32 (1997) 101-108.

[9] De Ruyck, H., Modelling of the residence time distribution in a twin screw extruder, Journal of Food Engineering, 32 (1997) 375-390.

[10] Yeh, A., Jaw, Y., Modelling residence time distributions for single screw extrusion process, Journal of Food Engineering, 35 (1998) 211-232.

[11] Yeh, A., Jaw, Y., Predicting residence time distributions in a single screw extruder from operating conditions, Journal of Food Engineering, 39 (1999) 81-89.

[12] Hu, G., Kadri, I., On-line measurement of the residence time distribution in screw extruders, Polymer Science and Engineering, 39 (5) (1999) 930-939.

[13] Iwe, M. O., Van Zuilichem, D. J., Ngoddy, P. O., Ariahu, C. C., Residence time distribution in a single-screw extruder processing soy-sweet potato mixtures, LWT- Food Science and Technology, 34 (2001) 478-483,.

[14] Apruzzese, F., Pato, J., Balke, S. T., Diosady, L. L., In-line measurement of residence time distribution in a co-rotating twin screw extruder, Food Research International, 36 (2003) 461-467.

[15] Seker, M., Distribution of the residence time in a single-screw extruder with differing numbers of mixing elements, International Journal of Food Science and Technology, 39 (2004) 1053-1060.

[16] Kumar, A., Ganjyal, G. M., Jones, D. D., Hanna, M. A., Digital image processing for measurement of residence time distribution in a laboratory extruder, Journal of Food Engineering, 75 (2006) 237-244.

[17] Waje, S. S., Patel, A. K., Thorat, B. N., Mujumdar, A. S., Study of residence time distribution in a pilot-scale screw conveyor dryer, Drying Technology, 25 (2007) 249-259.

[18] Bi, C., Jiang, B., Li, A., Digital image processing method for measuring the residence time distribution in a plasticating extruder. Polymer Eng.&Sci., 47 (7) (2007) 1108-1113.

[19] Nikitine, C., Rodier, E., Sauceau, M., Jacques, F., Residence time distribution of a pharmaceutical grade polymer melt in a single screw extrusion process. Chem. Eng. Res. Des., 87 (2007) 809-816.

[20] Nwabueze, T. U., Iwe, M. O., Residence time distribution (RTD) in a single screw extrusion of African breadfruit mixtures, Food Bioprocess Technol., 3 (2010) 135-145.

Numerical Study on condensation Process of Steam Flow in Nozzles

A. S. Hegazy, W. A. El-Askary, A. A. El-Terhy and M. S. Farag

Mechanical Power Engineering Department - Faculty of Engineering
Menoufiya University - Shebin El-kom-Egypt

Abstract

Steam ejector is an important component in engineering applications, which require high vacuum, such as steam plant condenser. Prediction of steam ejector performance is very significant tool for the design of the ejector. The steam ejector consists of three parts; nozzle, mixing chamber and diffuser. The nozzle has the task of creating the vacuum required. In the current paper numerical treatment of wet steam flow through the nozzle of an ejector is presented. The first task of this work is to test and evaluate several turbulence models on a generic case, constructed for turbulent steam flow in a convergent-divergent nozzle. The effect of pressure ratios, that is responsible for controlling the location or absence of the generated shock wave as well as the impact of the shock wave on the condensation of steam inside the nozzle are numerically concerned. These features are clearly observed from the pressure distribution, Mach number, liquid mass fraction, droplet nucleation rate, droplet critical radius and static temperature. It is concluded from the current work that the standard k-ω model is the most appropriate turbulence model for simulating this complex flow compared to the other considered models for nozzle steam flow sumulation.

Keywords: **CFD; Nozzle; Wet steam model; Turbulence Models; Shock Wave and Two Phase Flow (Steam condensing).**

1 - INTRODUCTION

Nozzles are the main parts in many industrial applications, such as jet pump and ejector. Supersonic flow in a convergent–divergent nozzle is a fundamental fluid phenomenon that affects a large variety of applications. When a supersonic nozzle is operated at suitable pressure ratios well below its design point, a shock wave forms inside the nozzle and flow downstream of the shock separates from the nozzle walls. Even though flow separation is typically viewed as an undesirable occurrence, it may have some interesting applications in the area of fluid mixing. During the rapid expansion of steam, a condensation process will take place shortly after the state path crosses the vapor-saturation line. The expansion process causes the super-heated dry steam to first subcool and then nucleates to form a two-phase mixture of saturated vapor and fine liquid droplets known as wet steam. Modeling wet steam is very important in the analysis and design of steam nozzles. An increase in wetness fraction at nozzle exit is gained by decreasing exit pressure. This leads to a reduction in aerodynamic efficiency of the nozzle operating in the wet steam region.

Avetissian et al. [1] noticed that the standard k–ε turbulence model can be invalid for predicting two-phase flows in transonic nozzles. The influence of inlet moisture on spontaneously condensing flow resembles the effect of turbulence. Pressure based Eulerian–Eulerian multi-phase models for non-equilibrium condensation in transonic steam flow were studied by **Gerber and Kermani [2]**. The equations were applied to predict the moisture distribution in low and high pressure steam flow in a Laval nozzle. Numerical analyses of spontaneously condensing phenomena in nozzle of steam-jet vacuum pump were introduced by **Wang et al. [3]**. The condensation heat produced during wet steam condensation in the nozzle increases the pressure and decreases the velocity at the outlet of the nozzle which would depress pumping performance of steam-jet pump and the supersonic steam condensation in the nozzle may be avoided or weakened by enhancing steam superheat degree. Numerical modelling of steam condensing flow in low and high-pressure nozzles were considered by **Dykas and Wróblewski [4]**. The implemented condensation model predicted the condensation onset correctly both for low and high pressures. The applied droplet growth model was found to be strongly dependent on the value of Knudsen numbers, which differs significantly for the low and high pressure values used. **Yang and Shen [5]** distinguished the numerical simulation on non-equilibrium spontaneous condensation in supersonic steam flow. Different from the isentropic expansion, in supersonic steam flow non-equilibrium spontaneous condensation will occur in the form of "condensation shock" downstream of the nozzle throat at a certain value.

Single- and two-fluid models for steam condensing flow modeling were introduced by **Dykas and Wróblewski [6]**. **Cinar et al. [7]** studied the nucleation of steam during expansion through a nozzle. The initial centers of nucleation, which have sufficient time to grow at relatively small values of expansion rate, affect the subsequent history of the flow; the effect of pressure ratio is important in the case of low expansion rate. Viscous and unsteady flow calculations of condensing steam in nozzles were studied by **Simpson and White [8]**. Viscous calculations for steady flow indicate that growth of the boundary layer has a significant impact on the predicted pressure distributions and droplet sizes, at least for cases where two-dimensional effects are prominent.

In the present study, different turbulence models are considered to simulate the steam flow in convergent–divergent nozzle. These turbulence models are standard $k-\varepsilon$ model, Realizable $k-\varepsilon$ model, RNG $k-\varepsilon$ model, standard $k-\omega$ model and SST $k-\omega$ model. The main aim of the study is to prediction of flow characteristic of wet steam and to validate the results obtained from simulation against experimental data available in literature. Also, selection of the most appropriate turbulence model that can handle steam flow through nozzle is discussed, and extended for further simulation handling different effects on nozzle performance.

2 - MATHEMATICAL MODEL

The mathematical model of homogeneous condensation in wet steam flow is based on the physical model, which was executed by the general CFD Code FLUENT 6.3 **[9]**. This is namely thermodynamic non-equilibrium process, which can take place during the expansion of steam flow. This state is characterized by subcooling of steam, when the steam

ISBN: 978-1-61804-295-8

temperature is lower than the equilibrium temperature of saturated steam for the given pressure. The wet steam is a mixture of two phases, the primary phase is the gaseous - phase consisting of water vapor while the secondary phase is the liquid-phase composed of condensed water droplets. To simplify the present analyses, the following assumptions have been made : No slip velocity between the droplets and vapor surrounding them, the interactions between droplets are neglected, the wetness mass fraction is small, (less than 20%) ; 2-D; turbulent steady flow; adiabatic nozzle walls and viscous compressible flow.

This section presents the governing equations, which describe the ideal flow behavior through the nozzle. Based on the above mentioned assumptions, the governing equations of steam flow and energy exchange through supersonic nozzle have been developed. **Figure 1** shows cross section through the nozzle to be studied.

Equation of state

The steam equation of state used in the solver, which relates the pressure to the vapor density and temperature, is given by **[10]**:

$$P = \rho_v RT(1 + B\rho_v + C\rho_v^{\,2}) \qquad \textbf{(1)}$$

Where B (m^3 /kg) and C (m^6 /kg^2) are coefficients. The mixture density (ρ) can be related to the vapor density (ρ_v) by the following equation:

$$\rho = \frac{\rho_v}{(1-\beta)} \qquad \textbf{(2)}$$

Where β is Wetness mass fraction and is defined as: $\beta = \dfrac{m_l}{m_{tot}}$

Equation of Continuity

$$\frac{D\rho}{Dt} + \rho\nabla.\vec{V} = 0 \qquad \textbf{(3)}$$

Equation of Motion

r - Component

$$\rho\left[\frac{Dv_r}{Dt}\right] = -\frac{\partial p}{\partial r} + \frac{\partial}{\partial r}\left\{\mu\left(2\frac{\partial v_r}{\partial r} - \frac{2}{3}\nabla.\vec{V}\right)\right\} + \frac{\partial}{\partial z}\left\{\mu\left(\frac{\partial v_r}{\partial z} + \frac{\partial v_z}{\partial r}\right)\right\} + \frac{2\mu}{r}\left(\frac{\partial v_r}{\partial r} - \frac{v_r}{r}\right) \qquad \textbf{(4)}$$

z - Component

$$\rho\frac{Dv_z}{Dt} = -\frac{\partial p}{\partial z} + \frac{\partial}{\partial z}\left\{\mu\left(2\frac{\partial v_z}{\partial z} - \frac{2}{3}\nabla.\vec{V}\right)\right\} + \frac{1}{r}\frac{\partial}{\partial r}\left\{\mu r\left(\frac{\partial v_r}{\partial z} + \frac{\partial v_z}{\partial r}\right)\right\} \qquad \textbf{(5)}$$

Equation of energy

$$\rho\frac{D}{Dt}(C_P T) = \frac{Dp}{Dt} + \frac{\partial Q}{\partial t} + \frac{1}{r}\left(kr\frac{\partial T}{\partial r}\right) + \frac{\partial}{\partial z}\left(k\frac{\partial T}{\partial z}\right) + \phi \qquad \textbf{(6)}$$

Where

$$\frac{D}{Dt} \equiv v_r\frac{\partial}{\partial r} + v_z\frac{\partial}{\partial z} \qquad \textbf{(7)}$$

$$\nabla.\vec{V} = \frac{1}{r}\frac{\partial r v_r}{\partial r} + \frac{\partial v_z}{\partial z} \qquad \textbf{(8)}$$

$$\phi = \mu\left[2\left\{\left(\frac{\partial v_r}{\partial r}\right)^2 + \left(\frac{\partial v_r}{r}\right)^2 + \left(\frac{\partial v_z}{\partial z}\right)^2\right\} + \left(\frac{\partial v_r}{\partial z} + \frac{\partial v_z}{\partial r}\right)^2 - \frac{2}{3}(\nabla.\vec{V})^2\right] \quad \textbf{(9)}$$

Where μ represents the effective viscosity in which $\mu = \mu_l + \mu_t$, the laminar viscosity (μ_l) depends on the fluid pressure and temperature and μ_t is the turbulent viscosity that can be computed using the turbulence model.

For wet steam model, two additional transport equations are needed **[11].** The first transport equation governs the mass fraction of the condensed liquid phase (β):

$$\frac{\partial(\beta\rho)}{\partial t} + \nabla.(\rho\,\beta\,\vec{V}) = \Gamma \quad \textbf{(10)}$$

Where Γ is the mass generation rate due to condensation and evaporation (kg per unit volume per second). The second transport equation models the evolution of the number density of the droplets per unit volume (η):

$$\frac{\partial(\rho\eta)}{\partial t} + \nabla.(\rho\vec{V}\,\eta) = \rho\, I \quad \textbf{(11)}$$

The mass generation rate due to condensation and evaporation (Γ), which is correlated with nucleation rate I (number of new droplets per unit volume per second) and growth/demise of these droplets **[11]**. Therefore, Γ is written as:

$$\Gamma = \frac{4}{3}\pi\,\rho_l\, I\, r_*^3 + 4\pi\,\rho_l\,\eta\,\bar{r}^2\frac{\partial\bar{r}}{\partial t} \quad \textbf{(12)}$$

Where r_* is the Kelvin-Helmholtz critical droplet radius, above which the droplet will grow and evaporate. An expression for r_* is given by **[12].**

$$r_* = \frac{2\sigma}{\rho_l\, RT\, \ln S} \quad \textbf{(13)}$$

The condensation process involves two mechanisms, the transfer of mass from the vapor to the droplets and the transfer of heat from the droplets to the vapor in the form of latent heat. This energy transfer rate relation was presented in **[13]** and can be written as:

$$h_{lv}\,\rho_l\frac{\partial\bar{r}}{\partial t} = \frac{\partial Q}{\partial t} = \frac{p}{\sqrt{2\pi RT}}\frac{\gamma+1}{2\gamma}C_P\,(T_s - T) \quad \textbf{(14)}$$

Rearranging the terms in equation **(14)** we get

$$\frac{\partial\bar{r}}{\partial t} = \frac{p}{h_{lv}\,\rho_l\sqrt{2\pi RT}}\frac{\gamma+1}{2\gamma}C_P\,(T_s - T) \quad \textbf{(15)}$$

Where T_s is the saturation temperature.

In the model, the classical homogeneous nucleation theory describes the formation of a liquid-phase in the form of droplets from a saturated phase in the absence of impurities or foreign particles, and the nucleation rate is given by:

ISBN: 978-1-61804-295-8

$$I = \frac{q_c}{(1+\theta)}\left(\frac{\rho_v^{\,2}}{\rho_l}\right)\sqrt{\frac{2\sigma}{M_m^{\,3}\pi}}\; e^{-\left(\frac{4\pi r_*^2\sigma}{3K_bT}\right)} \quad \textbf{(16)}$$

Where q_c is the evaporation coefficient, K_b is the Boltzmann constant, M_m is mass of one molecule. The nonisothermal correction factor, θ, is given by **[12]**:

$$\theta = \frac{2(\gamma-1)}{(\gamma+1)}\left(\frac{h_{lv}}{RT}\right)\left(\frac{h_{lv}}{RT}-0.5\right) \quad \textbf{(17)}$$

Where $h_{lv} = (h_v - h_l)$ is the specific enthalpy of evaporation at pressure p and γ is the ratio of specific heat capacities.

The mixture properties are calculated using the following mixing relation:

$$\phi_m = \beta\,\phi_l + (1-\beta)\,\phi_v \quad \textbf{(18)}$$

where: ϕ represents any of the following thermodynamic properties: $h,\ s,\ C_P, C_V, \mu$ *and* K_t.

3 - COMPUTATIONAL METHOD

The finite volume solver, FLUENT 6.3, is used to perform the numerical solution of the two-dimensional compressible Reynolds Averaged Navier–Stokes (RANS) equations in connection with different turbulence models including standard $k-\varepsilon$, RNG $k-\varepsilon$, Realizable $k-\varepsilon$, standard $k-\omega$ and SST $k-\omega$ turbulence models.

3-1 Computational Domain and Mesh Definition

The details of the full 2D computational domain and geometry are presented in **Fig. 1**. The chosen grid represents a compromise between the accuracy and computer time **[14]** of steam nozzle simulation. The computational mesh generated is $(i \times j) = (170 \times 10)$, where i the number of points in the streamwise direction and j is the number of points in the direction normal to the axis.

3-2 Boundary Conditions

The 2-D computational domain with the assigned boundary conditions is shown in **Fig. 2**. The saturation properties (temperature and pressure), are considered at the flow inlet. The outlet pressure boundary condition must be identified.

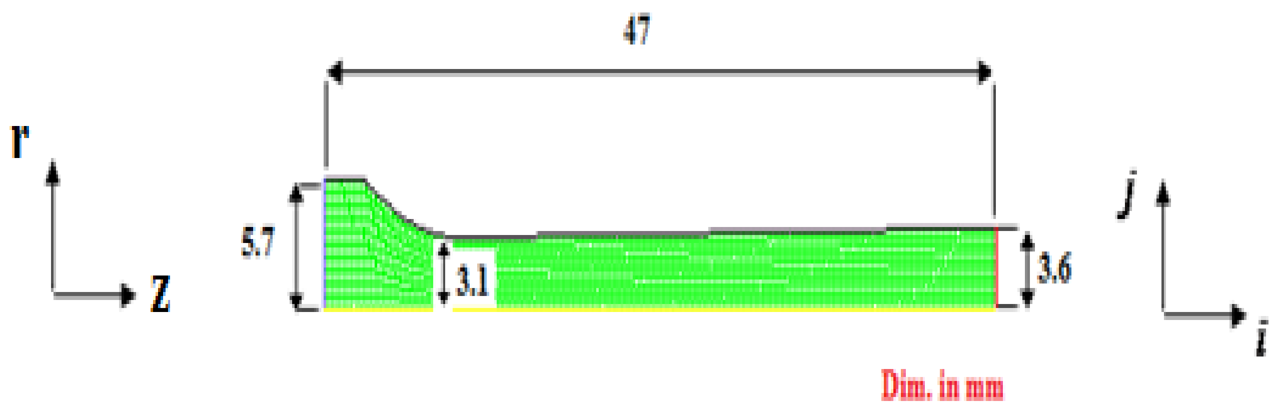

Fig. 1 Computational domain and geometry of steam nozzle

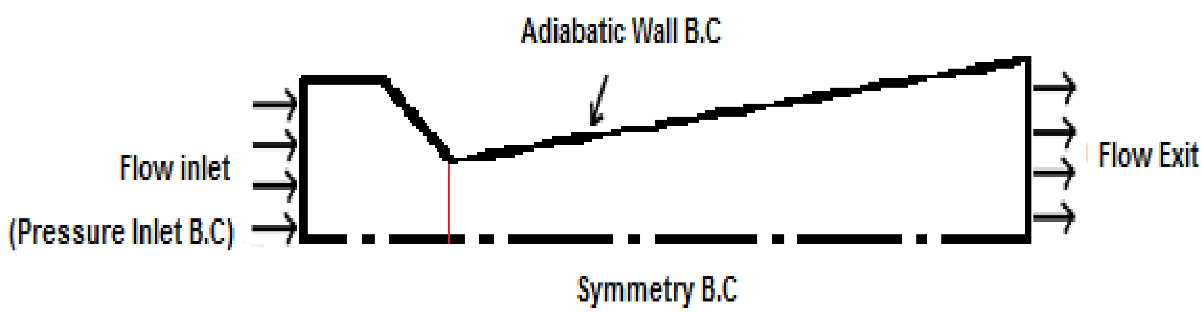

Fig. 2 Boundary conditions for computational domain of steam flow

4 – RESULTS AND DISCUSSIONS

4 – 1 Validation of Flow through Nozzle

It is first very important to determine the most appropriate turbulence model that can be used in the theoretical calculations from the comparison of the stated turbulence models. This choice is based on comparing the numerical results of the chosen turbulence models with the previously experimental published results.

The validations of the turbulence models in the present investigation are based on the comparison of the wall static pressure and Mach number with the experimental measurements of **[15]** at pressure ratio (PR) = 2. The PR is defined as the ratio between the stagnation pressure at the nozzle inlet (p_o) and the back pressure at the nozzle exit (p_b).This validation is presented in **Fig. 3**, in which it can be observed that the pressure decreases along the convergent part and it approaches to 0.27 p_o at the nozzle throat, see **Fig. 3 (a)**. After that, the flow is in continuous expansion along the nozzle divergent section. The reason of this behavior of pressure distribution is the low values of the back pressure (by which no internal shock is expected to occur). The results show that standard k-ω model gives an acceptable prediction of pressure distribution, especially through the divergent section (accuracy range).

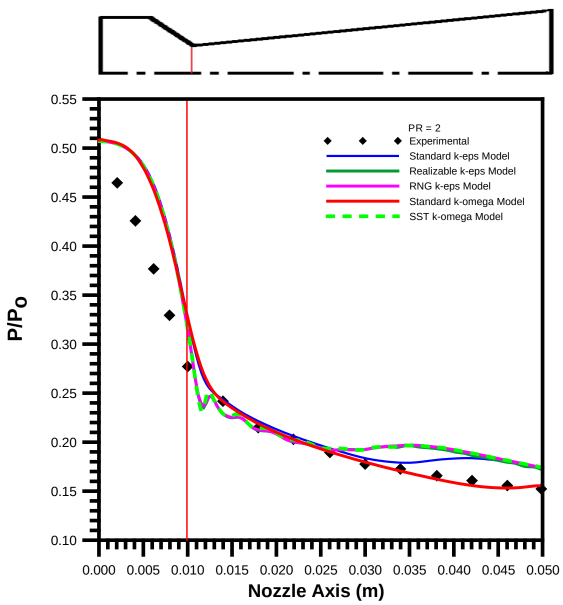

(a) Pressure Distribution

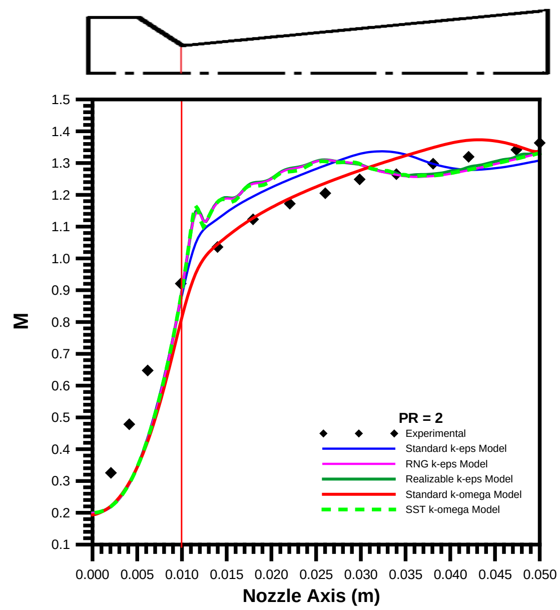

(b) Mach Number Distribution

Fig.3. Comparison of the predicted results using different turbulence models with the measurements of **[15]** along nozzle axis

The distribution of the Mach number along the nozzle axis is also shown in **Fig. 3 (b)**. From the figure it can be observed that flow doesn't reach to sonic case at the nozzle throat (M≈0.92). The flow reaches the exact sonic (M=1) after the throat section. The reason of this may return to the viscous effect. After that the Mach number increases along the divergent section and the flow becomes supersonic flow. Also, the figure leads to inferring that the standard k-ω model is the preferable turbulence model, which can predict the Mach number distribution along the steam nozzle, with the best accuracy.

4 – 2 Wet Steam Flow Characteristics in Nozzle

Some results of the flow characteristics will be discussed in the following subsections. These characteristics are distribution of pressure, Mach number, liquid mass fraction and droplet nucleation rate as well as droplet critical radius and temperature. It is worth mentioning that the computations are based on the standard $k-\omega$ as a turbulence model.

4 – 2 – 1 Pressure distributions along the nozzle axis

The effect of the pressure ratio on the pressure distribution is presented by **Fig. 4**. The pressure ratio has a direct effect on the flow behavior inside steam nozzle. At the low pressure ratio, the shock wave starts to appear near the nozzle exit as shown in the figure (i.e PR $\leq$ 1.8). The pressure ratio values strongly affect the position of shock wave. Increasing the pressure ratio moves the shock wave into direction of the nozzle exit. On the other hand, a condensation shock near the nozzle throat is clearly noticed. The reason for this may be due to the condensation of water vapour after the nozzle throat. The increase of the liquid mass fraction in this region is responsible for increasing the density and hence the pressure increases, causing weak shock (known as condensation shock) after the throat, see **Fig. 4**. Increasing the pressure ratio causes gradual disappearing of this weak shock.

4 – 2 – 2 Mach number distributions along the nozzle axis

The effect of the pressure ratio on the Mach number distribution along the nozzle axis is shown in **Fig. 5.** The increases in throat Mach number when PR is less than1.8 is due to the delaying of liquid formation in the nozzle. After the shock the flow returns to subsonic flow at all values of the pressure ratio less than 1.8.

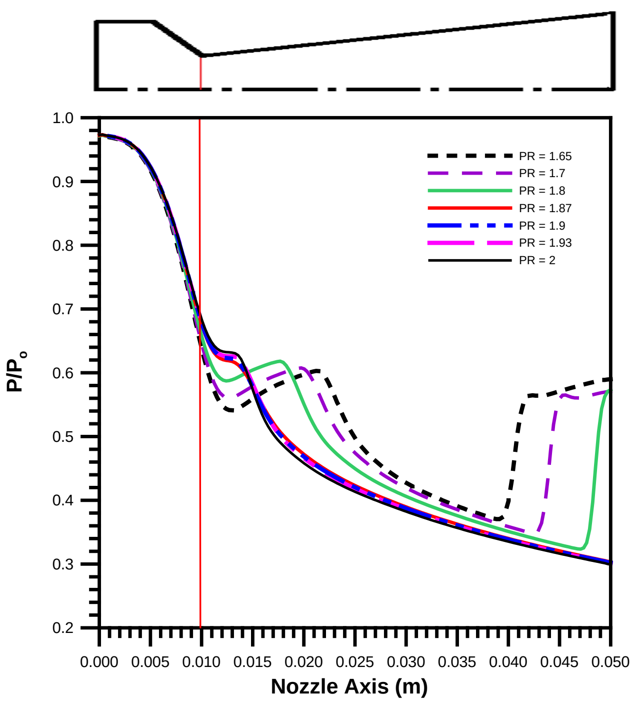

Fig. (4) Effect of pressure ratio on the pressure distribution along nozzle axis.

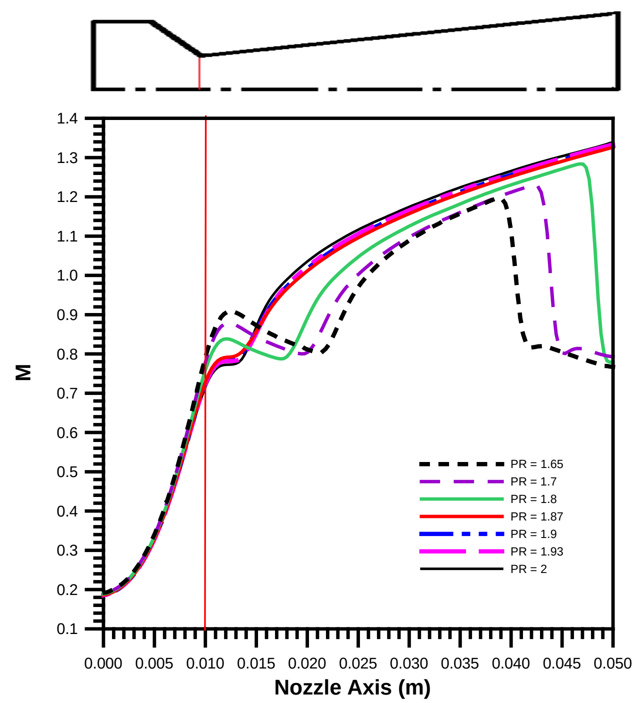

Fig. (5) Effect of pressure ratio on the Mach number distribution along nozzle axis.

4 – 2 – 3 Liquid mass fraction profile along nozzle

ISBN: 978-1-61804-295-8

Steam temperature is proportional to steam pressure. During flow through the nozzle the steam temperature decreases and reaches saturation temperature. If the temperature reaches the saturation temperature, condensation of steam (i.e. water droplet) is triggered. **Figure 6** shows the values of liquid mass fraction (mass of condensate steam to mixture of saturated water and saturated steam). From the figure it can be noticed that the liquid mass fraction is reduced after the shock wave near nozzle exit because of the increased temperature.

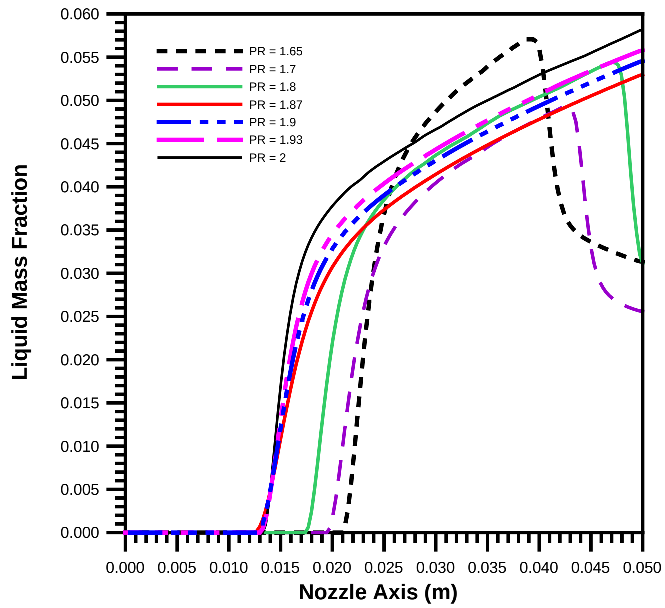

Fig. (6) Effect of pressure ratio on the liquid mass fraction along nozzle axis.

4 – 2 – 4 Droplet nucleation rate and temperature

Figures 7 and 8 show the changes of droplet nucleation rate and the droplet critical radius along nozzle axis at different pressure ratios, respectively. As clearly seen in **Fig.7**, the nucleation rate reaches its maximum value just upstream of the nozzle throat which is located at (x=0.01 m). As a result of that maximum nucleation rate, the droplets are formed downstream of the nozzle throat as shown in **Fig. 8**. For pressure ratios, PR= 1.65, 1.7 and 1.8 shock wave are clearly seen in **Figs. 4 and 5**. The droplet critical radius is decreased after shock wave, which may be (as discussed previously) due to the increase of temperature of the flow that causes evaporation of the droplet. The temperature distributions for different pressure ratios are observed in **Fig. 9**, in which the increase of temperature after the shock near the nozzle exit is observed. The ramp from after the nozzle throat is due to the condensation of vapor after the nozzle throat, see **Fig. 6.**

ISBN: 978-1-61804-295-8

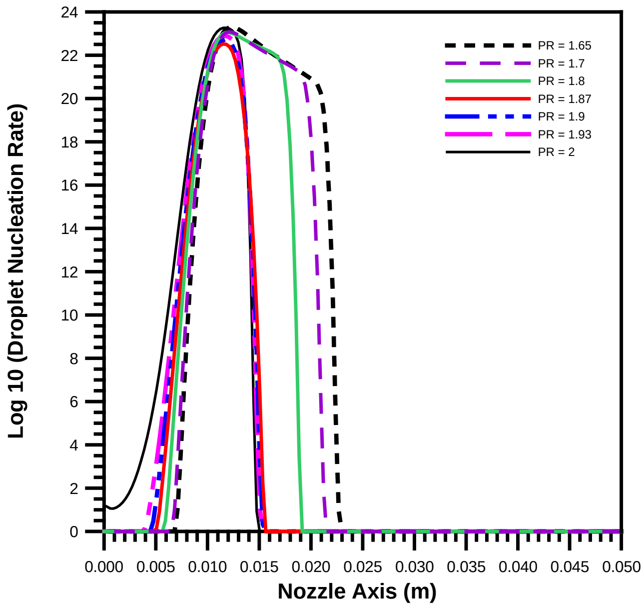

Fig. (7) Effect of pressure ratio on the droplet nucleation rate along nozzle axis.

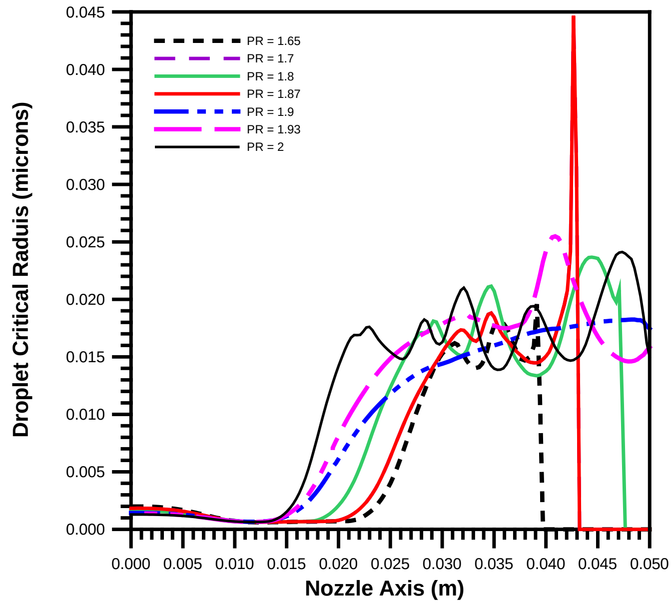

Fig. (8) Effect of pressure ratio on the droplet critical radius along nozzle axis.

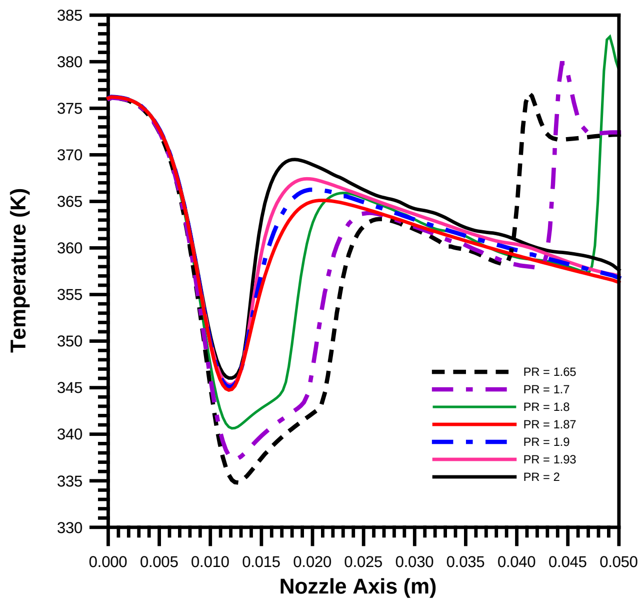

Fig. (9) Effect of pressure ratio on the temperature along nozzle axis.

5 – CONCLUSIONS

ISBN: 978-1-61804-295-8

The concern of the present work is to simulate steam flow passing through a convergent–divergent nozzle with a fixed geometry and different nozzle pressure ratios. The wall of the studied nozzle is assumed to be impermeable and adiabatic. The computational results are obtained by solving the RANS equations for steam flow in its conservative form coupled with both the energy equation and the wet steam equation of state using wet steam model. Different turbulence models are applied, namely the standard k-ε model, Realizable k-ε model, RNG k-ε model, standard k-ω Model and SST k-ω model. The standard k-ω model performs as the best one in views of the comparison with published experimental data. The pressure ratio values affect the position of shock wave. Increasing the pressure ratio moves the shock wave into the nozzle exit. The liquid mass fraction is decreased after the shock wave because of the enhanced temperature. The maximum nucleation rate of the droplets are formed starting downstream of the nozzle throat. The droplet critical radius is decreased after shock wave due to the increase in temperature of the flow that causes evaporation of the droplet. The present study will be extended to study the performance of steam ejectors.

REFERENCES

[1] A.R. Avetissian , G.A. Philippov and L.I. Zaichik, "Effects of turbulence and inlet moisture on two-phase spontaneously condensing flows in transonic", International Journal of Heat and Mass Transfer 51 (2008) 4195–4203.

[2] A.G. Gerber and M.J. Kermani "A pressure based Eulerian–Eulerian multi-phase model for non-equilibrium condensation in transonic steam flow", International Journal of Heat and Mass Transfer 47 (2004) 2217–2231.

[3] Xiao-Dong Wang , Jing-Liang Dong , Tian Wang and Ji-Yuan Tu "Numerical analysis of spontaneously condensing phenomena in nozzle of steam-jet vacuum pump", Vacuum 86 (2012) 861-866.

[4] Sławomir Dykas and Włodzimierz Wróblewski, "Numerical 11odeling of steam condensing flow in low and high-pressure nozzles", International Journal of Heat and Mass Transfer 55 (2012) 6191–6199.

[5] Yong Yang and Shengqiang Shen, "Numerical simulation on non-equilibrium spontaneous condensation in supersonic steam flow", International Communications in Heat and Mass Transfer 36 (2009) 902–907.

[6] Sławomir Dykas and Włodzimierz Wróblewski, "Single- and two-fluid models for steam condensing flow modeling", International Journal of Multiphase Flow 37 (2011) 1245–1253.

[7] G. Cinar, B. S. Yilbas and M. Sunar, "Study into nucleation of steam during expansion through a nozzle", Int. J. Multiphase Flow Vol. 23, No. 6 (1997) 1171-1188.

[8] D.A. Simpson and A.J. White, "Viscous and unsteady flow calculations of condensing steam in nozzles", International Journal of Heat and Fluid Flow 26 (2005) 71–79.

[9] Fluent, User's Guide Fluent 6.3.26, 2006.

[10] J. B. Young, "An Equation of State for Steam for Turbomachinery and Other Flow Calculations", Journal of Engineering for Gas Turbines and Power, Vol. 110, January (1988), 1-7.

[11] Yong Yang and Shengqiang Shen, “Numerical simulation on non-equilibrium spontaneous condensation in supersonic steam flow”, International Communications in Heat and Mass Transfer 36 (2009) 902–907.
[12] J. B. Young, “Two-Dimensional, Nonequilibrium, Wet-Steam Calculations for Nozzles and Turbine Cascades”, Journal of Turbomachinery, Vol. 11, July (1992) 569-579.
[13] Xiao-Dong Wang, Jing-Liang Dong , Tian Wang and Ji-Yuan Tu, “Numerical analysis of spontaneously condensing phenomena in nozzle of steam-jet vacuum pump”, Vacuum 86 (2012) 861-866.
[14] M. S. Farag, A. A. Hussien, W. A. El-Askary and A. S. Hegazy, “Numerical Simulation of Supersonic Steam Flow”, ICFDP 2013, Egypt.
[15] Assim H Yousif, Kassim K Abbas and Aqeel M Jary, “Simulation of spontaneous condensation of viscous steam flow in low-pressure convergent-divergent nozzles”, Eng. & Tech. Journal (2009), Vol. 27, No.13.

Nomenclature

C_p and C_V	Specific heat (J/kg. K)
h_{lv}	The specific enthalpy of evaporation at pressure P [Latent heat] (J/kg)
I	The nucleation rate (number of new droplets per unit volume per second)
k	Turbulent kinetic energy (m^2/s^2)
K_b	The Boltzmann constant
K_t	Thermal conductivity (w/m. K)
M_m	Mass of one molecule
m_l	Liquid mass flow rate (kg/s)
m_v	Vapor mass flow rate (kg/s)
m_{tot}	Total mass flow rate (kg/s) , $m_{tot} = m_l + m_v$
P	Pressure (Pa)
PR	Pressure ratio for nozzle
q_c	Evaporation coefficient
S	The super saturation ratio defined as the ratio of vapor pressure to the equilibrium saturation pressure [$S = \dfrac{p}{p_{Sat}(T)}$]
T_s	the saturation temperature (K)

Greek Symbols

β	Wetness mass fraction
ρ_l	The liquid density (kg/m^3)
ρ_v	The vapor density (kg/m^3)
Γ	The mass generation rate due to condensation and evaporation (kg per unit volume per

ISBN: 978-1-61804-295-8

	second)
η	The number of liquid droplets per unit volume
r_*	The Kelvin-Helmholtz critical droplet radius (m)
$\bar{r}$	The average radius of the droplet (m)
γ	The ratio of specificc heat capacities
μ	The dynamic viscosity (N.s/ m^2)
σ	the liquid surface tension
$\omega = \varepsilon / k$	Specific turbulent dissipation rate (1/s)
ε	Turbulent dissipation rate (m^2/s^3)

Abbreviations

RNG	The renormalization group
SFM	Single fluid model
SST	The shear stress transport
TFM	Two fluid model

Authors Index

ISBN: 978-1-61804-295-8